

DOCTORAL SCHOOL IN MATHEMATICS

Numerical methods for computationally efficient and accurate blood flow simulations in complex vascular networks: Application to cerebral blood flow

---

PHD CANDIDATE:
Beatrice GHITTI

SUPERVISORS:
Prof. Lucas O. MÜLLER
Prof. Eleuterio F. TORO

April 26, 2023

Doctoral thesis in **Mathematics**, XXV cycle
Department of Mathematics, **University of Trento**
Academic year: 2021/2022
Supervisors: **Prof. Lucas Omar Müller, Prof. Eleuterio Francisco Toro**, *University of Trento, Italy*

External examiner: **Leif Rune Hellevik**, Full Professor, *Biomechanics Group, Department of Structural Engineering, Norwegian University of Science and Technology (NTNU), Norway*
External examiner: **María Elena Vázquez Cendón**, Associate Professor, *Departamento de Matemática Aplicada, Universidade de Santiago de Compostela (USC), Spain*

University of Trento
Trento, Italy
April, 2022

Abstract

It is currently a well-established fact that the dynamics of interacting fluid compartments of the central nervous system (CNS) may play a role in the CNS fluid physiology and pathology of a number of neurological disorders, including neurodegenerative diseases associated with accumulation of waste products in the brain. However, the mechanisms and routes of waste clearance from the brain are still unclear. One of the main components of this interacting cerebral fluids dynamics is blood flow. In the last decades, mathematical modeling and fluid dynamics simulations have become a valuable complementary tool to experimental approaches, contributing to a deeper understanding of the circulatory physiology and pathology. However, modeling blood flow in the brain remains a challenging and demanding task, due to the high complexity of cerebral vascular networks and the difficulties that consequently arise to describe and reproduce the blood flow dynamics in these vascular districts.

The first part of this work is devoted to the development of efficient numerical strategies for blood flow simulations in complex vascular networks. In cardiovascular modeling, one-dimensional (1D) and lumped-parameter (0D) models of blood flow are nowadays well-established tools to predict flow patterns, pressure wave propagation and average velocities in vascular networks, with a good balance between accuracy and computational cost. Still, the purely 1D modeling of blood flow in complex and large networks can result in computationally expensive simulations, posing the need for extremely efficient numerical methods and solvers. To address these issues, we develop a novel modeling and computational framework to construct hybrid networks of coupled 1D and 0D vessels and to perform computationally efficient and accurate blood flow simulations in such networks. Starting from a 1D model and a family of nonlinear 0D models for blood flow, with either elastic or viscoelastic tube laws, this methodology is based on (i) suitable coupling equations ensuring conservation principles; (ii) efficient numerical methods and numerical coupling strategies to solve 1D, 0D and hybrid junctions of vessels; (iii) model selection criteria to construct hybrid networks, which provide a good trade-off between accuracy in the predicted results and computational cost of the simulations. By applying the proposed hybrid network solver to very complex and large vascular networks, we show how this methodology becomes crucial to gain computational efficiency when solving networks and models where the heterogeneity of spatial and/or temporal scales is relevant, still ensuring a good level of accuracy in the predicted results. Hence, the proposed hybrid network methodology represents a first step towards a high-performance modeling and computational framework to solve highly complex networks of 1D-0D vessels, where the complexity does not only depend on the anatomical detail by which a network is described, but also on the level at which physiological mechanisms and mechanical characteristics of the cardiovascular system are modeled.

Then, in the second part of the thesis, we focus on the modeling and simulation of cerebral blood flow, with emphasis on the venous side. We develop a methodology that, departing from the high-resolution MRI data obtained from a novel *in-vivo* microvascular imaging technique of the human brain, allows to reconstruct detailed subject-specific cerebral networks of specific vascular districts which are suitable to perform blood flow simulations. First, we extract segmentations of cerebral districts of interest in a way that the arterio-venous separation is addressed and the continuity and connectivity of the vascular structures is ensured. Equipped with these segmentations, we propose an algorithm to extract a network of vessels suitable and good enough, *i.e.* with the necessary properties, to perform blood flow simulations. Here, we focus on the reconstruction of detailed venous vascular networks, given that the anatomy and patho-physiology of the venous circulation is of great interest from both clinical and modeling points of view. Then, after calibration and parametrization of the MRI-reconstructed venous networks, blood flow simulations are performed to validate the proposed methodology and assess the ability of such networks to predict physiologically reasonable results in the corresponding vascular territories. From the results obtained we conclude that this work represents a proof-of-concept study that demonstrates that it is possible to extract subject-specific cerebral networks from the novel high-resolution MRI data employed, setting the basis towards the definition of an effective processing pipeline for detailed blood flow simulations from subject-specific data, to explore and quantify cerebral blood flow dynamics, with focus on venous blood drainage.

Acknowledgements

First and foremost I am extremely grateful to my supervisors, Prof. Lucas O. Müller and Prof. Eleuterio F. Toro for their invaluable advice, guidance and continuous support at every stage of my PhD program. Their knowledge and wealth of experience have inspired me throughout my doctoral studies and academic research.

I sincerely thank Dr. Pablo J. Blanco (National Laboratory for Scientific Computing LNCC, Petrópolis, Brazil) for his contribution to a relevant part of my PhD project, presented in Chapter 3 of this thesis, for the very useful discussions and his insightful comments.

I would like to express my gratitude to Prof. E. Mark Haacke (Wayne State University, Detroit, MI, USA) for the opportunity he gave me to visit his lab (SpinTech MRI, Bingham Farms, MI, USA) and spend a research period with his group. I sincerely thank Prof. Haacke and Dr. Sagar Buch (Wayne State University, Detroit, MI, USA) for providing the MRI data used in this thesis and for their invaluable collaboration in the development of the research project presented in Chapter 4.

I also thank the University of Trento, in particular the Department of Mathematics, for providing the financial and academic support to carry out this PhD research project, in terms of PhD scholarship, resources for participating in relevant conferences and advanced courses and funding for completing the research period in the USA.

Contents

Abstract v

Acknowledgements vii

Scientific publications xix

Scientific communications xxi

1 Introduction 1
- 1.1 Motivation and goals . . . 1
- 1.2 State of the art . . . 2
  - 1.2.1 Reduced-order models for blood flow in the vascular system . . . 2
  - 1.2.2 Computational efficiency of blood flow simulations . . . 5
  - 1.2.3 Techniques for vascular networks generation and reconstruction . . . 7
- 1.3 Contributions of this thesis . . . 8

2 Derivation of nonlinear lumped-parameter models for blood flow 11
- 2.1 Introduction . . . 11
- 2.2 1D blood flow model . . . 12
  - 2.2.1 1D blood flow model with elastic tube law . . . 13
  - 2.2.2 Dimensional analysis . . . 14
- 2.3 Derivation of lumped-parameter models for blood flow . . . 15
  - 2.3.1 Governing ODE system . . . 16
  - 2.3.2 Nonlinearity of the pressure-area relation . . . 17
  - 2.3.3 0D vessel configurations . . . 19
    - 2.3.3.1 (P_{in}, Q_{out})-type 0D vessel . . . 19
    - 2.3.3.2 (Q_{in}, P_{out})-type 0D vessel . . . 21
    - 2.3.3.3 (P_{in}, P_{out})-type 0D vessel . . . 22
    - 2.3.3.4 (Q_{in}, Q_{out})-type 0D vessel . . . 22
- 2.4 Stability analysis . . . 23
- 2.5 Junctions of vessels and coupling equations . . . 28
  - 2.5.1 1D coupling equations . . . 29
  - 2.5.2 Boundary conditions for 1D vessels . . . 30
  - 2.5.3 0D junctions and coupling equations . . . 31
    - 2.5.3.1 Two-vessel junction (J2) . . . 31
    - 2.5.3.2 Three-vessel junction (J3) . . . 32
    - 2.5.3.3 Generic 0D junction . . . 33
    - 2.5.3.4 Terminal vessels . . . 33
- 2.6 Numerical methods . . . 34
  - 2.6.1 Numerical scheme for 1D blood flow model . . . 34

2.6.2 1D numerical coupling strategy . . . 36
2.6.3 Numerical scheme for 0D blood flow models . . . 36
2.7 Numerical experiments . . . 37
2.7.1 Error calculations . . . 38
2.7.2 Analysis of relative contribution of convective terms . . . 39
2.7.3 Aortic bifurcation model . . . 41
2.7.4 37-artery network . . . 41
2.7.5 Reduced ADAN56 model . . . 44
2.7.6 CPU times . . . 47
2.7.7 Analysis of relative contributions of single nonlinear terms . . . 50

3 A hybrid 1D-0D solver for efficient blood flow simulations in complex vascular networks 59
3.1 Introduction . . . 59
3.2 Mathematical models . . . 60
3.2.1 1D blood flow model for viscoelastic vessels . . . 61
3.2.1.1 Variable material properties and augmented equations . . . 62
3.2.1.2 Mathematical reformulation: hyperbolic approximation . . . 63
3.2.2 0D blood flow models with viscoelastic pressure-area relation . . . 65
3.2.3 Coupling equations . . . 67
3.2.3.1 1D coupling equations . . . 67
3.2.3.2 0D coupling equations . . . 68
3.2.3.3 Hybrid coupling equations . . . 71
3.3 Hybrid networks and *a-priori* model selection criteria . . . 73
3.3.1 Numerical methods . . . 74
3.3.1.1 Numerical schemes for 1D and 0D blood flow models . . . 74
3.3.2 High-order numerical couplings . . . 75
3.3.2.1 0D coupling . . . 76
3.3.2.2 Hybrid coupling . . . 76
3.3.3 Adaptivity and *a-priori* model selection criteria . . . 78
3.3.4 Numerical experiments . . . 80
3.3.4.1 Convergence rate studies . . . 81
3.3.4.2 Application of the adaptive model selection strategy . . . 87
3.3.4.3 On the validity of 1D junction/bifurcation models . . . 96
3.4 An efficient hybrid network solver and its application to complex vascular models . . . 109
3.4.1 Numerical methods . . . 110
3.4.1.1 Path-conservative numerical scheme for PDE system . . . 110
3.4.1.2 1D temporal discretization strategies: GTS and LTS solvers . . . 113
3.4.1.3 An efficient strategy for solving large and stiff ODE systems . . . 117
3.4.1.4 0D temporal discretization strategy . . . 123
3.4.2 High-order numerical hybrid coupling strategy . . . 124
3.4.3 Numerical experiments . . . 126
3.4.3.1 Region-based hybrid networks . . . 127
3.4.3.2 ADAN model . . . 130
3.4.3.3 ADAN model coupled to CCO cerebral networks . . . 141
3.4.3.4 Concluding remarks . . . 150

4 Reconstruction of MRI-derived cerebral networks for blood flow simulations **155**
4.1 Introduction . . . 155
4.1.1 The MICRO method . . . 156
4.2 Reconstruction of arterio-venous segmentations of specific vascular territories . . . 157
4.2.1 Arterio-venous separation and Vessel Tracking (VT) algorithm . . . 160
4.2.2 Major-veins mask . . . 162
4.2.3 Major-arteries mask . . . 163
4.2.4 Micro-veins masks . . . 164
4.2.5 Thinning algorithm . . . 166
4.2.6 Small-arteries masks . . . 167
4.2.6.1 Extraction of superficial/cortical arteries . . . 170
4.2.7 A high-resolution map of the human brain's vasculature . . . 171
4.3 Extraction of a network of vessels . . . 174
4.4 Networks calibration and parametrization . . . 183
4.5 Blood flow simulations and results . . . 188
4.5.1 Steady state simulations . . . 188
4.5.2 Transient simulations . . . 189
4.5.3 Concluding remarks . . . 193

5 Conclusions **199**
5.1 Achievements . . . 199
5.1.1 Nonlinear lumped-parameter models for blood flow . . . 199
5.1.2 A hybrid network solver for efficient blood flow simulations in complex networks . . . 200
5.1.3 Reconstruction of MRI-derived human cerebral networks for blood flow simulations 201
5.2 Future works . . . 201

A Stability analysis **203**
A.1 First-order ordinary differential equations with periodic forcing function . . . 203
A.2 First-order system of ordinary differential equations with null eigenvalue . . . 204
A.2.1 Scalar case . . . 204
A.2.2 ODE system case . . . 205

B RK4 numerical method and coupling algorithm **209**

C Quantitative error analysis for ADAN model and CCO arteriolar networks **211**

Bibliography **217**

List of Figures

2.1 Examples of 0D representations for a two-vessel junction and a three-vessel junction 32
2.2 Example of a generic 0D junction 33
2.3 Schematic representation of a *RCR* Windkessel model 34
2.4 Aortic bifurcation: comparison of pressure and flow waveforms from 1D, nonlinear 0D and linear 0D models 43
2.5 Schematic representation of the 37-artery network 44
2.6 37-artery network: comparison of pressure and flow waveforms from 1D, nonlinear 0D and linear 0D models in aortic segments 46
2.7 37-artery network: comparison of pressure and flow waveforms from 1D, nonlinear 0D and linear 0D models in first-generation vessels 47
2.8 37-artery network: comparison of pressure and flow waveforms from 1D, nonlinear 0D and linear 0D models in second-generation vessels 48
2.9 37-artery network: comparison of pressure and flow waveforms from 1D, nonlinear 0D and linear 0D models in third-generation vessels 49
2.10 Schematic representation of ADAN56 model 50
2.11 ADAN56 model: comparison of pressure and flow waveforms from 1D, nonlinear 0D and linear 0D models in aortic segments 52
2.12 ADAN56 model: comparison of pressure and flow waveforms from 1D, nonlinear 0D and linear 0D models in first-generation vessels 53
2.13 ADAN56 model: comparison of pressure and flow waveforms from 1D, nonlinear 0D and linear 0D models in second-generation vessels 54
2.14 ADAN56 model: comparison of pressure and flow waveforms from 1D, nonlinear 0D and linear 0D models in third-/fourth-generation vessels 55
2.15 37-artery network: analysis of relative contributions of single nonlinear terms 57
2.16 ADAN56 model: analysis of relative contributions of single nonlinear terms 58

3.1 37-artery network: efficiency plots I 91
3.2 37-artery network: efficiency plots II 94
3.3 37-artery network: comparison of flow and pressure waveforms from the 1D, the 0D and a hybrid configuration with 1D-0D threshold of $V_0 = 6$ cm^3 in selected vessels 95
3.4 37-artery network: comparison of flow and pressure waveforms from the 1D, the 0D and a hybrid configuration with 1D-0D threshold of $C_0 = 1.5 \cdot 10^{-5}$ cm^5/dyne in selected vessels . 96
3.5 ADAN56 model: efficiency plots I 97
3.6 ADAN56 model: efficiency plots II 98
3.7 ADAN56: comparison of flow and pressure waveforms from the 1D, the 0D and a hybrid configuration with 1D-0D threshold of $V_0 = 3.5$ cm^3 in selected vessels I 99
3.8 ADAN56: comparison of flow and pressure waveforms from the 1D, the 0D and a hybrid configuration with 1D-0D threshold of $V_0 = 3.5$ cm^3 in selected vessels II 100

3.9 ADAN56: comparison of flow and pressure waveforms from the 1D, the 0D and a hybrid configuration with 1D-0D threshold of $C_0 = 7 \cdot 10^{-6}$ cm^5/dyne in selected vessels I 101
3.10 ADAN56: comparison of flow and pressure waveforms from the 1D, the 0D and a hybrid configuration with 1D-0D threshold of $C_0 = 7 \cdot 10^{-6}$ cm^5/dyne in selected vessels II 102
3.11 Aortic bifurcation: comparison of total pressure profiles from 3D and 1D junction models . . 103
3.12 Schematic representation of a hybrid network of 1D-0D vessels 119
3.13 Structure of the sparse Jacobian matrix corresponding to a fully 0D configuration of the ADAN model 122
3.14 Anatomically Detailed Arterial Network (ADAN) model with detail of the vasculature in the head 128
3.15 Detail of the CCO-generated cerebral peripheral beds 128
3.16 Radius and length distributions for the ADAN model and the CCO-generated cerebral arteriolar networks 129
3.17 Schematic representation of the region-based hybrid network configurations of the ADAN model 132
3.18 Elastic ADAN model: distribution of relative RMS errors for 0D and Test 3-hybrid results w.r.t. 1D results 136
3.19 Elastic ADAN model: distribution of relative systolic errors for 0D and Test 3-hybrid results w.r.t. 1D results 137
3.20 Elastic ADAN model: qualitative comparison between computational results from the 1D, 0D and Test3-hybrid configurations 138
3.21 Viscoelastic ADAN model: distribution of relative RMS errors for 0D and Test 1-hybrid results w.r.t. 1D results 141
3.22 Viscoelastic ADAN model: distribution of relative systolic errors for 0D and Test 1-hybrid results w.r.t. 1D results 142
3.23 Viscoelastic ADAN model: qualitative comparison between computational results from the 1D, 0D and Test1-hybrid configurations 143
3.24 Viscoelastic ADAN model: distribution of relative RMS errors for 0D and Test 2-hybrid results w.r.t. 1D results 144
3.25 Viscoelastic ADAN model: distribution of relative systolic errors for 0D and Test 2-hybrid results w.r.t. 1D results 145
3.26 Viscoelastic ADAN model: qualitative comparison between computational results from the 1D, 0D and Test2-hybrid configurations 146
3.27 Viscoelastic ADAN model: distribution of relative RMS errors for 0D and Test 3-hybrid results w.r.t. 1D results 147
3.28 Viscoelastic ADAN model: distribution of relative systolic errors for 0D and Test 3-hybrid results w.r.t. 1D results 148
3.29 Viscoelastic ADAN model: qualitative comparison between computational results from the 1D, 0D and Test3-hybrid configurations 149
3.30 Viscoelastic ADAN model: qualitative comparison between computational results from the 1D, 0D and Test3-hybrid configurations 150
3.31 Viscoelastic ADAN model + CCO network of lenticulostriate artery: distribution of relative RMS errors for 0D and hybrid results w.r.t. 1D results 151
3.32 Viscoelastic ADAN model + CCO network of lenticulostriate artery: distribution of relative systolic errors for 0D and hybrid results w.r.t. 1D results 152

3.33 Viscoelastic ADAN model + CCO network of lenticulostriate artery: qualitative comparison between computational results from the 1D, 0D and hybrid configurations I 153
3.34 Viscoelastic ADAN model + CCO network of lenticulostriate artery: qualitative comparison between computational results from the 1D, 0D and hybrid configurations II 154

4.1 Comparison between pre-contrast MRA, pre-contrast SWI and post-contrast SWI data 160
4.2 Selected slices from the MIP of the final *all-vessels mask* MVM 161
4.3 MIP of the major veins segmentation 163
4.4 3D volume rendering of the obtained main cerebral veins mask 164
4.5 MIP of the major arteries segmentation 165
4.6 3D volume rendering of the obtained main cerebral arteries mask 165
4.7 MIPs of the extracted micro-veins masks for the different cerebral districts of interest 168
4.8 MIPs of the extracted small-arteries masks for the different cerebral districts of interest 171
4.9 3D volume rendering of the extracted small-veins and small-arteries masks 172
4.10 3D volume rendering of the human brain's arterio-venous vasculature map reconstructed from the MICRO data 173
4.11 Schematic representation of how the minimum radius of the vessel section surrounding each centerlines point is calculated 177
4.12 Main cerebral arteries network 179
4.13 Main cerebral veins and venous sinuses network 179
4.14 Small-veins cerebral networks 180
4.15 Tube rendering of the main cerebral arteries network, scaled by the calculated radius 181
4.16 Tube rendering of the main cerebral veins network, scaled by the calculated radius 181
4.17 Tube rendering of the small-veins cerebral networks, scaled by the calculated radius 182
4.18 Schematic representation of the coupling between inlet node of a vessel and *RCR* model . . . 186
4.19 Time-varying pressure curves for boundary conditions to the cerebral venous networks . . . 187
4.20 Venous pressure throughout each cerebral network obtained at steady state 190
4.21 Wall shear stress and radius distributions in the RLEV venous network 191
4.22 Wall shear stress and radius distributions in the LLEV venous network 191
4.23 Wall shear stress and radius distributions in the RSV venous network 191
4.24 Wall shear stress and radius distributions in the LSV venous network 192
4.25 Mean venous pressure throughout RLEV and LLEV cerebral networks over a cardiac cycle . 193
4.26 Venous pressure distribution throughout the RLEV cerebral network at selected time points . 194
4.27 Venous pressure distribution throughout the LLEV cerebral network at selected time points . 195
4.28 Flow and pressure waveforms in selected vessels of the RLEV venous network 196
4.29 Flow and pressure waveforms in selected vessels of the LLEV venous network 197

List of Tables

2.1 Schematic representations and governing ODE systems of the four different 0D vessel configurations . . . 23
2.2 (Q_{in}, Q_{out})-type 0D vessel: quantitative assessment of factors f_1 and f_2 defining the discriminant Δ . . . 27
2.3 Computational parameters adopted in the 1D/0D numerical simulations . . . 38
2.4 Quantitative assessment of the relative importance of convective, pressure and friction terms within the momentum balance equation . . . 40
2.5 Geometrical and mechanical properties of the aortic bifurcation model . . . 42
2.6 Aortic bifurcation: quantitative pressure and flow error analysis between 1D and 0D results . 42
2.7 General model parameters of the 37-artery network . . . 44
2.8 37-artery network: quantitative pressure and flow error analysis between 1D and 0D results 45
2.9 General parameters of the reduced ADAN56 model . . . 47
2.10 ADAN56 model: quantitative pressure and flow error analysis between 1D and 0D results . 51
2.11 Comparison between CPU times per cardiac cycle for 1D, nonlinear 0D and linear 0D simulations . . . 51

3.1 Errors and empirical convergence rates for the single 1D vessel test problem . . . 82
3.2 Geometrical and mechanical properties of the upper thoracic aorta model . . . 84
3.3 Errors and empirical convergence rates for the test problem with a single 1D vessel coupled to an *RCR* Windkessel element . . . 84
3.4 Errors and empirical convergence rates for the 1D two-vessel closed-loop network test problem 85
3.5 Errors and empirical convergence rates for the 1D aortic bifurcation model (Test 1) . . . 86
3.6 Errors and empirical convergence rates for a hybrid configuration of the aortic bifurcation model I (Test 2) . . . 86
3.7 Errors and empirical convergence rates for a hybrid configuration of the aortic bifurcation model II (Test 3) . . . 86
3.8 Errors and empirical convergence rates for a hybrid configuration of the aortic bifurcation model III (Test 4) . . . 87
3.9 37-artery network: results from the adaptive model selection strategy I . . . 92
3.10 37-artery network: results from the adaptive model selection strategy II . . . 93
3.11 ADAN56 model: results from the adaptive model selection strategy I . . . 105
3.12 ADAN56 model: results from the adaptive model selection strategy II . . . 106
3.13 Geometrical and mechanical properties of the aortic bifurcation model . . . 106
3.14 Aortic bifurcation: relative errors in 1D solution with respect to 3D solution . . . 107
3.15 Aortic bifurcation: comparison between 1D and 3D total pressure variation across the junction 107
3.16 Aortic bifurcation: analysis of relative contributions of pressure and kinetic terms in the total pressure for 1D and 3D models . . . 107
3.17 Aortic bifurcation: analysis of energy dissipation for 1D and 3D aortic bifurcation models . . 108

3.18 General parameters of the ADAN model and of the CCO-generated cerebral arteriolar networks . . . 127
3.19 Computational parameters adopted in the simulations for the ADAN model and the CCO-generated cerebral arteriolar networks . . . 130
3.20 Anatomical regions of ADAN model . . . 131
3.21 Region-based hybrid configurations of ADAN model . . . 132
3.22 Code profiling output for the fully 0D simulation of the elastic ADAN model . . . 133
3.23 CPU times for elastic ADAN model . . . 134
3.24 CPU times for viscoelastic ADAN model . . . 134
3.25 CPU times for viscoelastic ADAN model + CCO network of lenticulostriate artery . . . 145
3.26 CPU times for viscoelastic ADAN model + CCO network of MCA's posterior parietal branch 146

4.1 Morphological properties and geometric features of the reconstructed cerebral networks . . . 178
4.2 Main features of the topology of the MRI-reconstructed small-veins cerebral networks . . . 186
4.3 Calibration results for the MRI-reconstructed small-veins cerebral networks . . . 186
4.4 Computational parameters adopted in the 1D numerical simulations . . . 188

C.1 Elastic ADAN model: quantitative pressure and flow error analysis for 0D and Test 3-hybrid results w.r.t. 1D results . . . 211
C.2 Viscoelastic ADAN model: quantitative pressure and flow error analysis for 0D and Test 1-hybrid results w.r.t. 1D results . . . 212
C.3 Viscoelastic ADAN model: quantitative pressure and flow error analysis for 0D and Test 2-hybrid results w.r.t. 1D results . . . 213
C.4 Viscoelastic ADAN model: quantitative pressure and flow error analysis for 0D and Test 3-hybrid results w.r.t. 1D results . . . 214
C.5 Viscoelastic ADAN model + CCO network of lenticulostriate artery: quantitative pressure and flow error analysis for 0D and hybrid results w.r.t. 1D results . . . 215

Scientific publications

Papers published during the PhD candidature or in preparation:

- Beatrice Ghitti, Lucas O. Müller, E. Mark Haacke, Eleuterio F. Toro and Sagar Buch. Extraction of MRI-derived *in-vivo* human cerebral networks and validation through subject-specific blood flow simulations. In preparation.
- Beatrice Ghitti, Pablo J. Blanco, Eleuterio F. Toro and Lucas O. Müller. A hybrid 1D-0D solver for efficient blood flow simulations in complex vascular networks: Application to the ADAN model. In preparation.
- Beatrice Ghitti, Pablo J. Blanco, Eleuterio F. Toro and Lucas O. Müller. Construction of hybrid 1D-0D networks for efficient and accurate blood flow simulations. *International Journal for Numerical Methods in Fluids.* 2023; 95(2):262-312. https://doi.org/10.1002/fld.5149
- Beatrice Ghitti, Eleuterio F. Toro and Lucas O. Müller. Nonlinear lumped-parameter models for blood flow simulations in networks of vessels. *ESAIM: Mathematical Modelling and Numerical Analysis*, 56(5):1579-1627, 2022. https://doi.org/10.1051/m2an/2022052

Scientific communications

Conference and seminar presentations during the PhD candidature:

- B. Ghitti, P.J. Blanco, E.F. Toro and L.O. Müller, *"Towards computationally efficient and accurate blood flow simulations in complex vascular networks"*, **Second Conference of Young Applied Mathematicians (YAMC 2022),** Arenzano (GE), Italy.
- B. Ghitti, E.F. Toro, F. Costanzo, B.M. Laudenzi, S. Buch, E.M. Haacke and L.O. Müller, *"A 1D coaxial model for coupled blood-CSF flow simulations in cerebral vascular-perivascular networks"*, **VPH 2022 Conference, Virtual Physiological Human,** Porto, Portugal.
- B. Ghitti, P.J. Blanco, E.F. Toro and L.O. Müller, *"Towards computationally efficient and accurate blood flow simulations in complex vascular networks"*, **7^{th} International Conference on Computational and Mathematical Biomedical Engineering (CMBE) 2022,** Milan, Italy.
- B. Ghitti, *"Towards computationally efficient and accurate blood flow simulations in the entire cardiovascular system"*, seminar for the **Neural Engineering Seminar Series 2022,** Center for Neural Engineering, The Pennsylvania State University, PA, USA.
- B. Ghitti, P.J. Blanco, E.F. Toro and L.O. Müller, *"Blood flow simulations in hybrid 1D-0D networks of vessels based on a-priori model selection criteria"*, **7^{th} International Conference on Numerical Methods for Hyperbolic problems (NumHyp) 2021,** Trento, Italy.
- B. Ghitti, C. Berthon, M.H. Le and E.F. Toro, *"Derivation of fully well-balanced schemes for the 1D blood flow equations"*, **SIAM Conference on Mathematical & Computational Issues in the Geosciences (GS21), 2021,** online conference.
- B. Ghitti, E.F. Toro and L.O. Müller, *"Towards an adaptive model selection strategy: 1D models vs 0D models"*, **VPH 2020 Conference, Virtual Physiological Human,** online conference.

Chapter 1

Introduction

1.1 Motivation and goals

It is currently a well-established fact that the dynamics of interacting fluid compartments of the central nervous system (CNS) may play a role in the CNS fluid physiology and pathology of a number of neurological disorders, including neurodegenerative diseases associated with misaccumulation of waste products in the brain. For example, in Alzheimer's Disease, the pathological hallmark is the accumulation of toxic protein aggregates that fail to be eliminated from the CNS by fluid transport [109]. However, the brain parenchyma lacks a conventional lymphatic system for the elimination of metabolic products, and the mechanisms and routes of waste clearance from the brain are still unclear and source of controversy [1, 69, 70]. Cerebrospinal fluid (CSF) flow in perivascular spaces (PVS) surrounding cerebral arteries and, possibly, veins is acknowledged as a potential key mechanism for brain solute transport and clearance, but the nature and driving forces of CSF flow and solute transport remain unclear and controversial [72, 73, 109, 29, 9, 90, 1, 115]. On the other hand, recent research in physiology and medicine brought attention to the blood flow circulation, especially the venous one, prompting the urgent question whether vascular anatomical abnormalities could alter the dynamics of interacting fluid compartments of the CNS, to the extent of becoming a triggering mechanism in the onset of neurological diseases [137]. In [155], Zamboni and collaborators established a strong association between extracranial venous anomalies, such as stenoses, and a range of diseases with no cure and unknown cause, affecting the CNS, such as Multiple Sclerosis. In this complex scenario, the available evidence is, however, partial, scattered and controversial, pointing to a knowledge gap in CNS fluids. Then, mathematical modeling and fluid dynamics simulations may contribute to the definition of a quantitative and comprehensive approach for the description of flow and transport in the brain parenchyma, and the interaction of intracranial fluids, including arterial and venous blood, CSF and interstitial fluid.

This thesis focuses on the modeling of one of the main components of this interacting cerebral fluids dynamics, blood flow, with emphasis on the modeling and simulation of cerebral blood flow dynamics and, in particular, the venous haemodynamics, given also its potential connection to some neurodegenerative diseases. Computational modeling and simulation of blood flow represent indeed a valuable complementary tool to experimental approaches, contributing to a deeper understanding of the circulatory physiology and pathology. However, modeling blood flow in the brain remains a challenging and demanding task, due to the high complexity of cerebral vascular networks and the difficulties that consequently arise to describe and reproduce the blood flow dynamics in these vascular districts.

For this reason, in this thesis we aim at developing a novel modeling and computational framework which allows to perform computationally efficient and accurate blood flow simulations in complex vascular networks, including cerebral networks, where the complexity does not only depend on the anatomical detail by which a network is described, but also on the level at which physiological mechanisms and mechanical characteristics of the cardiovascular system are modeled. We propose an efficient hybrid network

solver, which is based on both a one-dimensional and a lumped-parameter description of blood flow in vascular segments, to construct hybrid networks of 1D and 0D vessels coupled together and to perform simulations on such networks providing a good balance between computational efficiency and accuracy in the predicted results.

Furthermore, modeling and simulating blood flow in detailed, real arterio-venous cerebral networks may contribute to investigate, quantify and better characterize cerebral blood flow, potentially providing some insights into its complex dynamics and mechanisms. Motivated by this, in this thesis we propose a methodology that, departing from *in-vivo* high-resolution MRI data in human brain, allows to extract subject-specific arterial and venous networks of cerebral districts of interest, which are suitable to perform blood flow simulations. We note that the MRI data employed here were never used before to extract networks of vessels and to perform blood flow simulations. Hence, this work represents a first step towards the definition of an effective processing pipeline for the extraction and parametrization of real cerebral networks and blood flow simulations from subject-specific data.

The ultimate goal behind this thesis is indeed to apply this framework to a more complete mathematical model of the human circulation [99, 100, 144], which allows to account for the interaction of blood, CSF and brain tissue, and where the reconstructed cerebral vascular networks can be integrated to provide a detailed description of cerebral blood flow dynamics and its interaction with other intracranial fluids. Furthermore, we will consider the one-dimensional co-axial model proposed in [80], extending the original model of Toro *et al.* [143], which describes the coupled blood and CSF flow dynamics in cerebral vessels and surrounding CSF-filled PVS. Based on more detailed approaches modeling CSF flow in a single perivascular space [77, 78], our aim is to apply the proposed 1D co-axial model to networks of cerebral vessels and surrounding PVS. Hence, cerebral arterial and venous networks reconstructed with the methodology proposed in this thesis will be the departing point for describing the CSF flow dynamics through PVS surrounding cerebral vessels and its interaction with blood flow, adopting the modeling strategy presented in [80]. This framework will allow us to investigate the coupled blood-CSF flow dynamics and to explore current hypotheses about the nature, mechanisms and driving forces of CSF flow and solute transport through PVS and their role in brain waste clearance. Finally, 1D vascular(-perivascular) models could also be coupled with the 3D elastic tissue of the brain, by following the multiscale coupling approach proposed by Heltai *et al.* [68] for the simulation of vascularized tissues.

1.2 State of the art

1.2.1 Reduced-order models for blood flow in the vascular system

In the last decades, mathematical modeling and simulation of blood flow have become of primary importance in different contexts, such as biomedical engineering, and with a vast range of applications, from basic research to clinic, strongly contributing to the deep understanding of the circulatory physiology and pathology. Cardiovascular modeling has been pursued employing different levels of model complexity and sophistication, from lumped-parameter (0D) to distributed (1D and 3D) models. The selection of the appropriate dimensionality in a model representation, from 0D to 3D, depends on problem-specific characteristics, like flow conditions and spatial/temporal scales, the aim of the application in mind and thus, the required level of accuracy by which the physical process has to be described. A realistic and popular approach to construct mathematical models of the circulatory system is the *geometric multiscale approach*, where the system is represented by a combination of 3D, 1D and lumped-parameter models, with appropriate matching conditions. For a complete review about 3D, 1D and 0D models as stand-alone and about the *geometric multiscale approach* for the numerical simulation of blood flow problems see [114], for example.

One of the main components of the circulatory system is given by the vascular networks of systemic arteries and veins, which are connected through the microcirculation. Most complete mathematical models for blood flow in compliant vessels consider coupled PDE systems describing fluid flow, wall mechanics and their interaction. The overall methodology falls within the field of 3D fluid-structure interaction (FSI) models. In these models, the 3D, time-dependent, incompressible Navier-Stokes equations describe the fluid dynamics within the vessel and are coupled to the equations of solid mechanics for the 3D structure, the deformable vessel wall. 3D-FSI models offer great level of detail and accurate description of relevant quantities, but their numerical discretization is very challenging and requires large computational resources. Hence, at the present time, it is still unrealistic to think of deploying 3D-FSI models for very large vascular networks and cardiovascular models, or even for the full human vasculature.

In this context, two families of simplified, reduced-order models can be derived departing from the 3D Navier-Stokes equations and exploiting specific features of blood flow, such as the basically cylindrical morphology of the vessels [51]: one-dimensional (1D) models and zero-dimensional (0D) or lumped-parameter models of blood flow, where 1D models are governed by time-dependent systems of partial differential equations (PDE), whereas lumped-parameter models by systems of ordinary differential equations (ODE). Even though these models are highly simplified with respect to the local 3D flow dynamics, they can provide reasonably good approximations of more complex 3D models and reliable numerical results at a much lower computational cost, see [116, 153, 22] for example. Moreover, a strong argument in favor of this simplified modeling perspective is the more straightforward connection with measurable physiological signals and clinical variables.

Let us first start with an overview about existing one-dimensional models of blood flow in single vessels and vascular networks and their validation. 1D blood flow models can be derived from the cross-sectional averaging of the full 3D Navier-Stokes equations [51] and nowadays represent a well-established and powerful approach to study hemodynamics. In a simplified FSI setting, they are able to accurately describe wave propagation phenomena and predict pressure and flow waveforms in large vessels, at a reasonable computational cost. Indeed, in the last years, several studies have shown the ability of the 1D blood flow models to capture the main features of pressure pulse conformation and flow rate distribution in large vessels and different vascular districts, when compared to both 3D-FSI numerical data [116, 153, 22, 3] and 3D-CFD results [95, 107, 62, 18, 56, 103, 54], as well as to *in-vivo* measurements [117, 118, 111, 99, 100, 144, 16] and *in-vitro* experiments [89, 5, 121], demonstrating that these models can be adopted to accurately simulate physiologically and clinically relevant problems at a reasonable computational cost. Hence, in the field of computational hemodynamics and mathematical modeling of the cardiovascular system, 1D models have become popular and widely used since the mid of the last century, to simulate and study wave propagation phenomena in arterial networks and also in the venous circulation. Key contributions in this field include the works of Aviolo [10], Stergiopulos *et al.* [131], Olufsen *et al.* [111], Formaggia *et al.* [50], Sherwin *et al.* [128], Mynard and Nithiarasu [107], Reymond *et al.* [117, 118], Liang *et al.* [85], and, more recently, the works of Müller and Toro [99, 100] then refined by Toro *et al.* [144], of Blanco *et al.* [17, 16] and Mynard and Smolich [108].

In several of the above mentioned works, the 1D models employed to describe the arterial and, in a few studies, venous networks are coupled to lumped-parameter models representing other components of the circulatory system, in a geometrically multiscale modeling framework. For instance, in the global, closed-loop mathematical model developed by Müller and Toro [99, 100] and recently extended in [144], 1D models are adopted for large vessels of both arterial and venous systemic networks, whereas the heart, the pulmonary circulation, the microcirculation, venous valves and Starling resistors are described using 0D models. Another relevant example is the model proposed by Mynard and Smolich [108], where arterial and venous networks for the systemic, coronary, cerebral and pulmonary circulations are described employing

1D models, while lumped-parameters models are used for the heart and the microvasculature beds.

Even if 0D models can not resolve wave propagation and the spatial variation of physical quantities of interest, they are cheaper than 3D and 1D models, representing simple mathematical objects with physical parameters that can be usually quantified from clinical measurements. This class of models can be used to describe different components of the cardiovascular system, from the heart and valves, to the microcirculation, to portions of vascular networks or even single vessels, depending on the specific problem, aim or application.

0D cardiovascular system representation and analysis started with the modeling of arterial flow using the well-known Windkessel model. The first and simplest 0D mono-compartment description is the famous two-element Windkessel model, which was first proposed by Stephen Hales in 1733, and later formulated mathematically by Otto Frank in 1899 [120]. The Windkessel model consists of two parallel elements, a capacitor C, describing the storage properties of large arteries, and a resistor R, that describes the dissipative nature of small peripheral vessels including arterioles and capillaries. Later on, this approach was expanded to cover the modeling of other cardiovascular components, such as the heart, heart valves and veins, with either mono-compartment or multi-compartment 0D models, to simulate the global haemodynamics in the whole circulation system, by considering and evolving in time, within any 0D component of the system, spatial averages of the fundamental variables, namely pressure, flow and volume. In the multi-compartment approach, suitable RLC models for a single vascular segment were then derived, as building blocks for constructing a vessel network model. In this regard, we refer to the works of Formaggia and Veneziani [52], Milišić and Quarteroni [91] and Formaggia *et al.* [51], where four typical compartment model configurations suited to the description of a vessel segment were derived, assuming that mean flow rate and pressure over the whole vessel are equivalent to either the input or the output values. In the work of Safaei *et al.* [119], a bond graph based lumped-parameter mathematical model was proposed for the cardiovascular system, where 0D models are adopted to describe the different system components and, in particular, each vessel segment is represented by a suitable combination of C, R and L-elements and vessels are coupled via $0-junctions$. Lumped-parameter models can also provide boundary conditions for 1D and local 3D models. For instance, in [2], the authors studied the effect of parameters of the 0D outflow models on the waveforms propagated in an arterial network, with the aim of providing appropriate outflow 0D models for patient-specific simulations. Finally, as pointed out above, 0D models can be coupled to 1D models and even more complex 3D models (see [21] for instance), in a multiscale approach for modeling the whole cardiovascular system.

It is well-known that the mechanics of the cardiovascular system can exhibit strong nonlinearities. These nonlinear effects include, for example, the contribution of the convective acceleration terms in the momentum equation, the nonlinear relationship between pressure and volume which is observed in real vessels [27, 60], the pressure-dependent vessel compliance, the collapse of vessels due to external pressure, *etc*. For a complete review on these nonlinear phenomena characterizing the cardiovascular system see [129], for instance. Among these nonlinearities, pressure-dependent constitutive equations and vessel properties represent an example of great interest. Indeed, in the 0D model description, the values of the different components C, L and R are generally taken to be constant parameters, defined in term of a reference baseline state. However, since they represent real physical parameters, they are subject to the same nonlinearities, such as nonlinear constitutive material relations, as any other description of vascular mechanics [129]. As the vessel diameter changes under changes of pressure, its compliance will change as will its resistance to flow. Furthermore, the vessel wall exhibits a nonlinear stress-strain curve [60], meaning that the compliance C is also a function of the luminal pressure. These effects are typically included in 1D models, but neglected in 0D models. In particular, since the diameter changes in the arterial system are relatively small and the range of arterial pressures over the cardiac cycle is such that the material tends to operate in a

relatively linear region of the stress-strain curve, it is a common practice to neglect the pressure dependence of the arterial properties [129]. This is not true for veins, at least when they enter a collapsed state. Several models based on *in-vivo* measurements or theoretical derivations have been proposed to describe the relation between cross-sectional area and internal pressure exhibited by vessels. Ursino *et al.* [147, 146] used an exponential curve to describe the nonlinear pressure-volume relationship in the peripheral and venous compartments in the simulation of carotid baro-regulation of pressure pulsation. Fogliardi *et al.* [49] compared the linear (*i.e.* incorporating a constant compliance) and nonlinear (*i.e.* including a nonlinear pressure-dependent compliance) formulation of the *RCR* Windkessel model, concluding that no additional physiological information was gained when a pressure-dependent compliance was incorporated. In contrast, Li *et al.* [82, 11] examined the consequences of incorporating a pressure-dependent compliance with exponential variation in a modified arterial system model given by a three-element *RCR* vessel model and concluded that a pressure-dependent compliance could more accurately reflect the behaviour of the arterial system. Cappello *et al.* [28] developed a one-step computational procedure for estimating the parameters of the nonlinear three-element Windkessel model of the arterial system incorporating a pressure-dependent compliance. In [148], the authors proposed a simple mathematical model of intracranial pressure dynamics, where the resistance in the the arterial-arteriolar cerebrovascular compartment was defined to be inversely proportional to the fourth power of the inner radius.
However, when dealing with 0D models suited to the representation of a single vascular segment [52, 91, 119], the nonlinearities characterizing the original 1D models have never been taken into account, assuming a linear relationship between the pressure and volume of the vascular compartment and constant parameters C, L and R, which are usually defined in terms of a reference state (A_0, P_0).

We also observe that, when adopting lumped-parameter models for blood flow in vessels and vascular networks, a common approach is to lump entire portions of a network into a single 0D model, a single-resistance or a *RCR* Windkessel element, for example. However, a few works are found in the literature where each vessel of a network is described by a single 0D model and 0D vessel elements are coupled together via suitable coupling conditions, so that the topology of the original network is fully preserved. In this context, we mention the work of Safaei *et al.* [119].

1.2.2 Computational efficiency of blood flow simulations

One-dimensional blood flow models have been extensively used in the past decades to study wave propagation phenomena in arteries and, more recently, this has been extended also the venous circulation. Relevant applications of 1D models include the study of basic physiology [4, 20, 127, 91, 53], as well as of pathological conditions [84]. In fact, a deep understanding of pressure and flow pulse wave propagation in the cardiovascular system and the impact of disease and anatomical variations on these propagation patterns may provide valuable information for clinical diagnosis and treatment [89, 13, 33, 59].

The complexity of vessel networks used in 1D blood flow models for the cardiovascular system has significantly increased over time. In the last years, more complex networks and models have been constructed in terms of enhanced anatomical detail, first of all by considering a larger number of arteries [117, 83]. A relevant example in terms of high anatomical detail of the human arterial network is the Anatomically Detailed Arterial Network (ADAN) model developed by Blanco *et al.* [17, 16], which is made of 2142 arteries, including 1598 arterial segments with a well-acknowledged name and 544 perforator arteries. In [19], the authors assessed the impact of vascular anatomy definition degree in the predictions of blood flow models of the arterial network, by systematically comparing results obtained with the above mentioned ADAN model and those obtained with an anatomically simplified network containing the main 86 vessels. Furthermore, in [15], the 1D ADAN network was coupled to cerebral arteriolar networks automatically

generated using the constrained constructive optimization (CCO) technique. On the other hand, the incorporation of a one-dimensional network for the venous system can also contribute to develop more complex and detailed networks and models. A distinctive feature of the global, closed-loop, multiscale mathematical model for the human circulation developed by Müller and Toro [99, 100], and recently extended in [144], is the detailed description of the venous system, particularly for intracranial and extracranial veins. In [108], Mynard and Smolich presented a model that accounts for wave propagation in anatomically realistic systemic (including coronary and cerebral) arterial/venous networks, pulmonary arterial/venous networks and portal veins.

In addition to the anatomically detailed description of arterial or venous networks, many other factors can contribute to the complexity of cardiovascular models and networks, such as the level at which biological mechanisms and mechanical characteristics of the cardiovascular system are modeled. For instance, when coupling the blood circulation to the CSF and brain dynamics, these two systems have very different temporal scales, as CSF absorption/generation is slow compared to blood flow and acts over longer time scales with respect to that of blood flow, thus strongly increasing the computational time and cost [144]. Control mechanisms, such as the baroreflex/chemoreflex controls and cerebral autoregulation, also act over long time scales if compared with the cardiac cycle duration [6, 20, 48], therefore requiring long simulation times which impact on computational cost and efficiency. Including the viscoelastic properties of vessel walls into the 1D blood flow models, to define more realistic and physically consistent models, also demands a considerably higher computational cost for solving the corresponding PDE system, with respect to the purely elastic case [102]. Modeling the cerebral microcirculation, via automatically generated peripheral microvasculature beds for instance, and integrating mechanisms like brain perfusion, waste clearance mechanisms and exchange of solutes between blood and various tissue beds may also contribute to the complexity of the designed models.

In light of the considerations made in the previous paragraphs, we come to the conclusion that the one-dimensional modeling of blood flow in anatomically detailed and complex vascular networks and models can result in computationally expensive simulations, where the high computational cost and execution time can be affected by the different aforementioned factors. Several strategies and methodologies have been proposed and developed to address such challenges, either by working on faster and more efficient solvers for the 1D models, or by introducing 0D models coupled with or in place of the 1D models, to improve the computational efficiency and optimize the topological complexity of the vascular networks.

In the first framework, it is worth to mention the work of Müller *et al.* [102], where the authors posed the need for accurate, robust and efficient numerical schemes to simulate 1D blood flow phenomena and able to produce results at a low computational cost. To address such issue, the authors proposed a high-order and robust fully local time-stepping (LTS) solver for 1D blood flow simulations in networks of elastic and viscoelastic vessels, comparing it to a global time-stepping (GTS) approach. When applied to the ADAN model, the GTS to LTS computational time ratios are 10.80 and 136.07, for the elastic and viscoelastic cases, respectively, demonstrating the benefits in terms of speed-up obtained by adopting an LTS over a GTS strategy.

In turn, several works concerning lumped-parameter/zero-dimensional models to simulate arterial blood flow are also found in the literature, which address the issues of computational efficiency and optimization of topological complexity. In [55], the authors presented a method to optimize the number of arterial segments included in 1D blood flow models and to find the model with the fewest number of necessary arteries for a given clinical application, by lumping distributed 1D segments into 0D Windkessel models, while preserving key features of flow and pressure waveforms. Similarly in [47], in the context of patient-specific 1D blood flow modeling, Epstein *et al.* investigated the effect of a reduction in the number of arterial segments in a given distributed 1D model on the shape of the simulated pressure and flow

waveforms, by systematically lumping peripheral 1D model branches into 0D (Windkessel) models that preserve the net resistance and total compliance of the original model. On the other hand, in [119], Safaei and collaborators proposed a bond graph based lumped-parameter mathematical model, which ensures mass and energy conservation, by preserving the topology of the original 1D network, to address the issue of execution time and the question of granularity in the context of modeling the cerebral circulation. This formulation was indeed applied to a model including arterial vessels with geometric and anatomical data based on the ADAN model [16]. Furthermore in [92], a distributed lumped-parameter (DLP) modeling framework was proposed to efficiently compute blood flow and pressure in vascular domains at a computational cost that is orders of magnitude lower than that of computational fluid dynamics (CFD) simulations.

1.2.3 Techniques for vascular networks generation and reconstruction

Given a tissue or an organ, such as the brain or the stomach, blood flow can be modeled and simulated in such domain, provided that vascular arterial and/or venous networks are available for the specific region, the first delivering blood to the tissue/organ and the second draining blood from it. The level of anatomical detail and complexity of the vascular network, as well as the spatial scales that are covered (from larger vessels to the microcirculation) can be different, depending on the specific problem of interest, the aim of the application in mind and, in particular, the available information/data about the network.

Then, the generation and reconstruction of vascular networks for blood flow modeling and computational simulations can be addressed employing two different families of techniques, either by automatically generating synthetic networks, or by extracting the real geometries of the vascular networks from clinical and medical data. The first class of methodologies aims indeed at generating vascular networks in an automatic manner, driven by physiological criteria and in compliance with a set of morphometric constraints and empirical laws. For instance, Constrained Constructive Optimization (CCO) algorithms are based on the sequential generation of the vessel network which is driven by the constrained minimization of a biologically-inspired cost functional [124, 125, 14, 88]. These methods allow to generate multi-scale vascular networks, from larger vessels up to the level of peripheral beds, offering a solution to circumvent the lack of information about the vascular architecture of these microvasculature beds, which, in many vascular territories, is not even accessible using high-resolution imaging techniques, in animal models and especially in humans [88].

On the other hand, the geometries of vascular networks can be extracted from clinical/medical imaging data acquired with different modalities, thus requiring suitable processing tools for segmentation, centerlines extraction and network reconstruction, depending mainly on the spatial scale and level of detail of the networks to be reconstructed. Segmentation of large vessels can be performed for instance using the open-source software ITK-SNAP [154, 74], which provides a user-friendly interface for a semi-automatic active contour evolution segmentation approach. Another relevant example is the open-source library Vascular Modeling ToolKit (VMTK) [7, 135], which offers a collection of libraries and tools for 3D segmentation and reconstruction and mesh generation for image-based modeling of blood vessels. However, when dealing with much smaller and denser vascular structures, such tools are not suited and more sophisticated and elaborate techniques and algorithms are required to extract, from the imaging data set, networks of vessels suitable to model and simulate blood flow.

Vessel enhancement filters, among which Frangi vesselness filter proposed by Frangi *et al.* [57], represent a gold standard to enhance vessel-like structures and to segment blood vessels. In the literature, several tools, softwares and algorithms are found which address these tasks and are based on different approaches. For instance, Qiber3D [75] is an open-source software package for the quantitative analysis of networks from 3D image stacks. Implemented as a Python package, it includes the essential image analysis

procedures required for image processing, from the raw image to the quantified data, among which image segmentation, network reconstruction and morphometric measurement of the reconstructed network. In Qiber3D, two reconstruction algorithms are available to compute the image skeleton: a thinning-based reconstruction which applies the medial axis Lee-Kashyap algorithm [81]; alternatively, the reconstruction with the TEASAR method [123], implemented in the Pyhton library kimimaro [79] and originally developed to skeletonize neurons. This toolkit can be indeed applied to a variety of structures, such as microvascular networks and neuronal structures. Another example in this framework is the modular software TiQuant [58, 64] for efficient quantification of biological tissues based on volume data obtained by biomedical image modalities. This tool includes techniques to segment central and portal veins, sinusoidal (type of capillary, very small blood vessels found in the liver) and bile canaliculi networks, to extract and analyze the network graph and to perform a number of morphological operations. With a completely different approach, in [134], a deep learning strategy, called DeepVesselNet, is presented to perform vessel segmentation, centerlines extraction and bifurcation detection tasks in 3D angiographic volumes. Here, different datasets, synthetic 3D vessel structures, real clinical data from human brain and experimental data from a rat brain, are used for training and testing the DeepVesselNet architecture. Along these lines, in [136] a deep learning-based framework, named VesSAP (Vessel Segmentation & Analysis Pipeline), is developed for the automated quantification and analysis of the entire mouse brain vasculature, using a convolutional neural network with a transfer learning approach. From the segmentation, centerlines extraction, based on a 3D thinning algorithm [81], detection of bifurcation points and calculation of vessel radii are addressed. Finally, in [40], Amira Software (Thermo Fisher Scientific) was adopted for the skeletonization of segmented blood vessels within a tumor microenvironment, which reconstructs the blood vessel networks in 3D graph format (nodes and connected segments, each with a radius corresponding to the size of the blood vessel). Similarly, the same software was employed in [133] to extract from a tumor image the corresponding tumor vascular network, which is skeletonized and segmented into a series of interconnected nodes and vessel segments with known diameters and lengths.

In the present thesis, the second approach id adopted. As it will be described in detail in Chapter 4, after an accurate review of existing tools and algorithms for vessel segmentation, centerlines extraction and network reconstruction, we decided to develop our customized processing pipeline to address such tasks, based on the specific features of our problem of interest and the aim of the application in mind. In particular, departing from *in-vivo* high-resolution MRI data in human brain, our ultimate goal is to reconstruct real arterio-venous cerebral networks suitable to perform blood flow simulations. For specific steps of the proposed processing pipeline we will exploit existing algorithms, routines or functions, in their original version or by introducing appropriate modifications or extensions.

1.3 Contributions of this thesis

The main contributions of this thesis regard: 1) the derivation of a family of *nonlinear* lumped-parameter models of blood flow, which preserves important nonlinear properties of the 1D blood flow equations we depart from; 2) the development of an efficient hybrid 1D-0D network solver to perform blood flow simulations in complex and large vascular networks; 3) the design of a processing pipeline to extract detailed arterio-venous cerebral networks from *in-vivo* MRI data and to calibrate and parametrize such networks, to perform blood flow simulations. These topics are addressed in the present thesis, according to the following organization:

- In Chapter 2, departing from a well-established 1D blood flow model, we derive a family of *nonlinear* lumped-parameter (0D) models for blood flow in deformable vessels, in a way to preserve important nonlinear properties of the original 1D equations. These properties include (i) the nonlinearity

in the tube law relating the internal pressure to the cross-sectional area, and (ii) the dependence of the parameters characterizing the 0D models, inductance L and resistance R, on the time-varying vessel cross-sectional area, to account for vessel cross-section changes under changes of pressure. By defining appropriate conditions to couple 0D vessels at junctions, we then apply the newly derived 0D models to construct networks of 0D vessels and simulate blood flow on such networks: each 1D vessel is replaced by a "0D vessel" by a per-segment 1D-to-0D mapping, so that the topology of the original 1D network is naturally preserved. The nonlinear 0D blood flow models are applied to reproduce several benchmark problems and the obtained computational results show their ability to produce reasonably good approximations of pressure and flow waveforms in all vessels of a network, when compared to the reference 1D solution. One of the main goals of this thesis is to develop an efficient modeling and computational approach for large networks of vessels. Hence, these 0D models will not be used as stand-alone tools, but we aim at combining the 1D model and this family of "cheaper" 0D models in a way to improve the computational efficiency of simulations in hybrid networks of 1D-0D vessels, as it will be described at the following point.

- In Chapter 3, we develop a hybrid 1D-0D network solver to perform efficient and accurate blood flow simulations in complex vascular networks. First, we propose an adaptive model selection approach to construct hybrid networks of 1D-0D vessels, which is based on (i) suitable coupling equations ensuring conservation principles; (ii) high-order numerical coupling strategies to solve 1D, 0D and hybrid junctions; (iii) model selection criteria to construct hybrid networks. With regard to the second point, the accurate numerical treatment of the coupling between 1D and 0D vessels is crucial, as it has to take into account the interaction between 1D and 0D vessels and ensure that the order of accuracy of the solution in the 1D vessels is preserved. Concerning the last point, to instantiate concrete hybrid networks, several *a-priori* model selection criteria are explored, to be used to determine the most suitable model, either 1D or 0D, for each vessel of a network. Our aim is to identify those criteria providing the best trade-off between the computational cost of the simulations in the resulting hybrid networks and a good level of accuracy in the predicted results. Here, the proposed hybrid network methodology is applied and tested on arterial networks of moderate complexity.

  Then, in the second part of Chapter 3, we extend this methodology from both modeling and numerical point of view, to be integrated into an already existing network solver coded in C++, developing an efficient hybrid network solver for very large and complex vascular models. The viscoelastic properties of vessel walls are included into both 1D and lumped-parameter blood flow descriptions; accordingly, 1D, 0D and hybrid coupling strategies are extended to account for viscoelasticity. In terms of computational improvements, we design an efficient strategy for solving very large and stiff ODE systems governing the blood flow dynamics in regions of 0D vessels, exploiting existing implicit ODE solvers, but also accounting for the specific features of the problem to be solved. Then, 0D regions must be coupled to 1D vessels, that are evolved in time according to fully explicit high-order numerical schemes. This task is addressed by deriving a suitable high-order numerical coupling strategy to solve hybrid junctions of 1D and 0D vessels. The local time-stepping (LTS) algorithm presented by Müller *et al.* [102] is also integrated in the solver.
  We apply the proposed modeling and computational framework to solve very complex and large vascular networks, namely the ADAN model [17, 16] and the same one coupled to CCO-generated cerebral arteriolar networks. We show how this hybrid network solver becomes crucial and absolutely necessary to gain computational efficiency when solving networks and models where the heterogeneity of spatial and/or temporal scales is relevant, still ensuring a good level of accuracy in the predicted results. In particular, when dealing with the ADAN model extended with the CCO peripheral beds,

a tremendous improvement is obtained in terms of computational efficiency of the simulations, with a speed-up of several orders of magnitude.

- In Chapter 4, we design a methodology for the reconstruction and calibration of detailed, real cerebral networks suited to perform blood flow simulations, departing from MRI data obtained from a novel *in-vivo* microvascular imaging technique of the human brain, the MICRO method, developed by Prof. E. Mark Haacke and his research group at Wayne State University [25, 24, 26], which allows to reveal very small cerebral vessels down to 100 μm of thickness in diameter. The proposed processing pipeline performs several steps. First, we extract detailed arterial and venous segmentations of specific cerebral districts in a way that the arterio-venous separation is addressed and the continuity and connectivity of the vascular structures is ensured. Next, equipped with these segmentations, we develop an algorithm to extract a network of vessels suitable to perform 1D/0D blood flow simulations. Here, we focus on the venous side, whose anatomy and patho-physiology is of great interest from both clinical and modeling points of view, given also the potential venous haemodynamic connection to some neurodegenerative diseases, as pointed out in Section 1.1. The networks of vessels generated are then calibrated and parametrized using perfusion data. Finally, we perform preliminary blood flow simulations on the reconstructed cerebral venous networks. The main purpose of these simulations is the validation of the proposed processing pipeline itself, to assess whether the obtained cerebral networks are reasonable from a physiological and fluid-dynamics point of view and suitable to perform blood flow simulations. By exploring the flow and pressure fields generated by the different venous networks, we investigate their ability to predict physiologically reasonable results in terms of pressure ranges in the corresponding vascular territories.

  Even if the proposed methodology has several limitations, open problems and aspects that need to be improved, this work represents a proof-of-concept study that it is possible to extract subject-specific cerebral networks from the MICRO imaging data and it sets the basis for detailed arterio-venous simulations of blood flow from patient-specific data, to explore, quantify and better characterize cerebral blood flow dynamics, with focus on venous blood drainage.

Chapter 2

Derivation of nonlinear lumped-parameter models for blood flow

2.1 Introduction

The mathematical model presented in this thesis includes both a one-dimensional (1D) and a lumped-parameter/zero-dimensional (0D) description of blood flow in compliant vessels, together with the equations that, based on conservation principles, allow to couple 1D and 0D vessels in a network. Departing from a well-established formulation of the 1D equations describing blood flow in a one-dimensional vascular domain, the main goal of this chapter is to derive a family of *nonlinear* lumped-parameter blood flow models which preserve certain important nonlinear properties of the original 1D model. By extending the traditional approach of deriving 0D models for blood flow in a vascular segment [52, 91, 51], the nonlinearity in the tube law relating the pressure to the cross-sectional area and pressure-dependent model parameters, inductance L and resistance R, are included in the resulting family of nonlinear lumped-parameter models. In this chapter, for both 1D and 0D models, we restrict to the case of a purely elastic tube law. Furthermore, the convective terms are not excluded *a-priori* from these nonlinear 0D models, but an exhaustive investigation of the contribution and relative importance of these terms in both 1D and 0D blood flow models is carried out. As the pressure term in the momentum balance equation results to play a more significant role with respect to the convective terms and given also that we aim at applying these 0D models to the smaller vessels of a network, where it is well-known that the convective contribution is negligible, we decide to neglect the convective terms in the family of nonlinear 0D models here derived.

To solve blood flow in vascular networks, 1D vessels can be coupled at junctions by defining a suitable set of coupling equations following the Riemann problem-based approach proposed by Toro and Siviglia [141]. Here, following the methodology presented by Safaei *et al.* [119], a 0D coupling strategy is also introduced, where 0D vessels are coupled through 0D junctions, at which mass conservation and continuity of pressure are satisfied. This coupling approach allows to construct networks of 0D vessels, where each 1D vessel of the original 1D network is replaced by a "0D vessel" by a per-segment 1D-to-0D mapping, so that the topology of such network is preserved.

In order to validate and test the newly derived 0D models, we reproduce several benchmark test cases proposed in [22]. We compare the 0D results obtained with the nonlinear 0D models against the original 1D model for different arterial networks, to assess the ability of such 0D models to produce reasonably good approximations of pressure and flow waveforms in all vessels of a network, with respect to the reference 1D solution. Furthermore, the nonlinear 0D results are also compared against the linear 0D results obtained with linear pressure-area relation and constant model parameters, to show that these 0D results are considerably improved when including certain nonlinearities in the lumped-parameter models. The relative

contributions of single nonlinear components (nonlinear pressure-area relation, nonlinear resistance and nonlinear inductance) in the 0D models in determining pressure and flow waveforms is also assessed.

The chapter proceeds as follows. In Section 2.2 we introduce the governing equations of 1D blood flow in compliant vessels and we perform a dimensional analysis of these equations. Then, in Section 2.3 a family of nonlinear lumped-parameter models is derived departing from the 1D model. Afterwards, in Section 2.4 we restrict to the linear case, namely to the standard 0D models with constant parameter, linear pressure-volume relation and without convective terms, to carry out a stability analysis of the corresponding ODE systems. Thereafter, in Section 2.5 we describe how to couple 0D vessels converging to a shared node (bifurcation/junction of vessels) and how to couple 0D vessels to RCR terminal models. Finally, in Section 2.7 numerical experiments are carried out and the obtained results are discussed in detail.

2.2 1D blood flow model

A well-established formulation of the 1D model describing blood flow in deformable vessels is given by the following time-dependent system of partial differential equations (PDEs), including the classical laws of conservation of mass and of balance of momentum

$$\begin{cases} \partial_t A + \partial_x q = 0, \\ \partial_t q + \partial_x \left(\alpha \dfrac{q^2}{A} \right) + \dfrac{A}{\rho} \partial_x p = f. \end{cases} \tag{2.1}$$

For a full derivation of the 1D model (2.1) see [51], for example. In system (2.1), $x \in [0, l]$ is the axial coordinate along the longitudinal axis of the vessel, with l being the vessel length, and $t > 0$ is time. The three problem unknowns are the cross-sectional area of the vessel $A(x,t)$, the flow rate $q(x,t)$, and the cross-sectional averaged internal pressure $p(x,t)$. In the balance of momentum equation, α is a momentum correction factor and $f(x,t) = -k_R \frac{q}{A}$ is the friction force per unit length, where $k_R > 0$ is the viscous resistance coefficient. Both parameters α and k_R depend on the assumed velocity profile. Here, the following axisymmetric velocity profile was prescribed

$$u_x(x, \xi, t) = u(x,t) s(\xi) = u(x,t) \frac{\zeta + 2}{\zeta} \left[1 - \left(\frac{\xi}{r} \right)^{\zeta} \right], \tag{2.2}$$

where $u_x(x, \xi, t)$ is the axial component of the fluid velocity, $u(x,t) := \frac{q}{A}$ is the average blood velocity on each cross-section, $s(\xi)$ is the assumed velocity profile, ξ is the vessel radial coordinate, $r(x,t)$ is the lumen radius and ζ is the velocity profile order. The viscous resistance per unit length of tube k_R is defined as a function of the velocity profile as

$$k_R = -\frac{\mu}{\rho} \int_{\partial S} \frac{\partial s}{\partial \vec{n}_{\partial S}} d\gamma, \tag{2.3}$$

where ∂S is the boundary of the vessel cross-section S and $\vec{n}_{\partial S}$ is the outward normal vector to ∂S, and which, for the velocity profile chosen in (2.2), becomes

$$k_R = 2(\zeta + 2)\pi \frac{\mu}{\rho}, \tag{2.4}$$

where ρ and μ are the constant blood density and viscosity, respectively. The momentum correction coefficient α is well-defined for unidirectional flow, namely

$$\alpha = \frac{\int_S u_x^2 \, d\sigma}{A u^2}, \tag{2.5}$$

from which we have that the momentum correction coefficient α and the velocity profile order ζ are related by $\alpha = \frac{\zeta+2}{\zeta+1}$. The value $\zeta = 9$ defines a blunt velocity profile, which is especially valid for large arteries [71],

while for a Poiseuille flow, the parabolic velocity profile is obtained by setting $\zeta = 2$. For the coefficient α, the choice $\alpha = 1$ (adopted throughout the entire thesis), which indicates a perfectly flat velocity profile, is commonly used since it simplifies the analysis of the resulting 1D model.

The system of PDEs (2.1) has more unknowns than equations; hence, an additional closure condition is required. Such extra condition, usually called *tube law*, links the internal pressure p to the vessel cross-sectional area A, to couple the internal blood flow distribution with the mechanical properties of the solid moving vessel wall, in a simplified fluid-structure interaction (FSI) setting. Different tube laws can be chosen, from purely elastic pressure-area relations to more complex viscoelastic tube laws, distinguishing between arterial and venous vessels. In [151], a comparative analysis of various mathematical descriptions of elastic properties of vessel walls in modern 1D models of haemodynamics was presented. The elastic description can be extended and improved by including the viscoelastic properties of vessel wall into both arteries and veins, as done for instance in [12, 117, 5, 108, 17, 16, 97, 144]. It is worth noting that the specific choice of the tube law determines not only the model sophistication at which the vessel wall mechanics is characterized and described, but also the nature of the resulting PDE system and, consequently, its numerical discretization. In this thesis, different tube laws will be adopted depending on the model and problem of interest. Each tube law will be introduced when necessary throughout the thesis, together with its parametrization and the modeling and numerical implications.

2.2.1 1D blood flow model with elastic tube law

In this section and throughout the entire Chapter 2, we consider a purely elastic tube law to close the 1D blood flow model (2.1). Under this assumption, pressure $p(x,t)$ can be described by the following algebraic relation

$$p(x,t) - p_{ext}(x,t) = \psi(A(x,t); A_0, K, m, n, P_0), \tag{2.6}$$

with

$$\psi(A(x,t); A_0, K, m, n, P_0) = K\left[\left(\frac{A(x,t)}{A_0}\right)^m - \left(\frac{A(x,t)}{A_0}\right)^n\right] + P_0, \tag{2.7}$$

where $p_{ext}(x,t)$ is the external pressure acting on the vessel and P_0 is the reference pressure at which $A = A_0$. We note that the tube law (2.6)-(2.7) is valid for both arteries and veins, under suitable choices of the parameters characterizing this relation; in this chapter, we will focus on the case of arterial vessels. The above relation describes the elastic deformation of the vessel wall with variations of the transmural pressure $p - p_{ext}$, assuming that dissipative (viscous) effects are negligible. Pressure $p(x,t)$ also depends on the reference cross-sectional area A_0, the vessel wall stiffness K, and the pair of parameters m and n, two real numbers to be specified. Normally, m and n are parameters derived from higher-order models or simply computed from experimental measurements; typical values for arteries are $m = 0.5$ and $n = 0$. In particular, if we assume geometric and mechanical vessel properties to be independent of x and we consider arterial vessels, then the factor $K > 0$ in (2.6) represents the arterial stiffness and it is modeled as in [137, 51] by

$$K \equiv K_a = \frac{\sqrt{\pi} h_0 E}{(1-\nu^2)\sqrt{A_0}}, \tag{2.8}$$

where h_0 is the vessel wall thickness, E is the Young's modulus and ν is the Poisson ratio. We adopt $\nu = 0.5$, which implies that the vessel wall is assumed to be incompressible.

We note that system (2.1) with elastic tube law (2.6) can be rewritten under the classical form of balance laws, that is

$$\partial_t \boldsymbol{Q} + \partial_x \boldsymbol{F}(\boldsymbol{Q}) = \boldsymbol{S}(\boldsymbol{Q}), \tag{2.9}$$

with $\boldsymbol{Q} = (A, q)^T$ being the vector of conserved variables and

$$\boldsymbol{F}(\boldsymbol{Q}) = \begin{pmatrix} q \\ \alpha \dfrac{q^2}{A} + \dfrac{KA}{\rho}\left[\dfrac{m}{m+1}\left(\dfrac{A}{A_0}\right)^m - \dfrac{n}{n+1}\left(\dfrac{A}{A_0}\right)^n\right] \end{pmatrix}, \quad \boldsymbol{S}(\boldsymbol{Q}) = \begin{pmatrix} 0 \\ -k_R \dfrac{q}{A} \end{pmatrix}, \tag{2.10}$$

where $\boldsymbol{F}$ is the physical flux function and $\boldsymbol{S}$ is the source term vector.
We introduce here also the wave speed, denoted by c, as follows

$$c = \sqrt{\frac{A}{\rho}\frac{\partial \psi}{\partial A}} \tag{2.11}$$

and the coefficient matrix $\boldsymbol{A}(\boldsymbol{Q})$ of system (2.9) as

$$\boldsymbol{A}(\boldsymbol{Q}) := \frac{\partial \boldsymbol{F}}{\partial \boldsymbol{Q}} = \begin{pmatrix} 0 & 1 \\ c^2 - u^2 & 2u \end{pmatrix}, \tag{2.12}$$

which allows us to rewrite (2.9) in quasi-linear form, that is

$$\partial_t \boldsymbol{Q} + \boldsymbol{A}(\boldsymbol{Q})\partial_x \boldsymbol{Q} = \boldsymbol{S}(\boldsymbol{Q}), \tag{2.13}$$

The eigenvalues of matrix $\boldsymbol{A}$ are $\lambda_1 = u - c$ and $\lambda_2 = u + c$, with corresponding right eigenvectors

$$\boldsymbol{R}_1 = \gamma_1 \begin{pmatrix} 1 \\ u - c \end{pmatrix}, \qquad \boldsymbol{R}_2 = \gamma_2 \begin{pmatrix} 1 \\ u + c \end{pmatrix}, \tag{2.14}$$

for arbitrary scaling factors $\gamma_1, \gamma_2 \in \mathbb{R}$. From this analysis, under the choice of the tube law (2.6) and under a suitable assumption for coefficients m and n, we have that system (2.9), or, equivalently, system (2.13), is always strictly hyperbolic. Furthermore, both λ_1- and λ_2-characteristic fields are genuinely nonlinear and, therefore, are associated with shocks and rarefaction waves. The generalized Riemann invariants (GRI) associated with the genuinely nonlinear fields are the following

$$\Gamma_1 = u + \int_{\widehat{A}}^{A} \frac{c(\xi)}{\xi} d\xi, \qquad \Gamma_2 = u - \int_{\widehat{A}}^{A} \frac{c(\xi)}{\xi} d\xi, \tag{2.15}$$

where $\widehat{A}$ is the cross-sectional area at a reference state. This eigenstructure analysis will be necessary for the construction of the numerical scheme adopted to solve the 1D blood flow model and to define suitable boundary conditions to be prescribed at the inlet/outlet of the vessel and coupling conditions to connect multiple 1D vascular domains.
We note that definition (2.11) of the wave speed c is valid for any choice of the tube law. Moreover, as the PDE system (2.9) can be written in conservative form, the coefficient matrix $\boldsymbol{A}$ represents the Jacobian matrix $\partial \boldsymbol{F}/\partial \boldsymbol{Q}$ of the physical flux $\boldsymbol{F}$. This is no longer true in the case where the system of PDEs does not admit a conservative form as the one in (2.9), as we will see in the next chapter of this thesis.

2.2.2 Dimensional analysis

In order to assess the relative importance of each term in the 1D blood flow model (2.1), especially of convective, pressure and friction terms in the momentum balance equation, we perform here a dimensional analysis, similar to the analysis performed in [61, 121]. For this purpose, we introduce the following nondimensional variables

$$t = T_0 \bar{t}, \quad x = L_0 \bar{x}, \quad A = A_0 \overline{A}, \quad q = Q_0 \overline{Q} = (A_0 U_0)\, \overline{Q}, \tag{2.16}$$

where the constants T_0, L_0, A_0 and U_0 are orders of magnitude of the dimensional variables, so that nondimensional variables $\bar{t}$, $\bar{x}$, $\overline{A}$ and $\overline{Q}$ are of order 1. In particular, T_0 is the time scale, L_0 is the longitudinal

spatial scale, A_0 is the reference cross-sectional area and U_0 is a reference flow velocity.
The nondimensional equation of conservation of mass reads

$$\frac{\partial \overline{A}}{\partial \overline{t}} + \left[\frac{T_0 U_0}{L_0}\right] \frac{\partial \overline{Q}}{\partial \overline{x}} = 0. \tag{2.17}$$

By rewriting the pressure gradient $\partial_x p$ in terms of the nondimensional variables (2.16), after straightforward calculations we get the following nondimensional momentum balance equation

$$\frac{\partial \overline{Q}}{\partial \overline{t}} + \gamma_C \frac{\partial}{\partial \overline{x}} \left(\alpha \frac{\overline{Q}^2}{\overline{A}} \right) + \gamma_P \frac{\partial \overline{A}}{\partial \overline{x}} = -\gamma_F \frac{\overline{Q}}{\overline{A}}, \tag{2.18}$$

where the three coefficients for the convective, pressure and friction terms have been introduced, respectively given by

$$\gamma_C := \frac{T_0 U_0}{L_0}, \quad \gamma_P := \frac{T_0}{L_0 U_0} c^2, \quad \gamma_F := \frac{k_R T_0}{A_0}. \tag{2.19}$$

The above coefficients are nondimensional quantities and their magnitudes indicate the relative importance of each of these terms in the momentum balance equation. In Section 2.7 we will exploit this kind of analysis to decide whether the convective terms can be neglected or not in the family of nonlinear 0D models we are going to derive in the next section.

Remark 2.1. We observe that the ratio γ_C / γ_F can be simply rewritten as

$$\frac{\gamma_C}{\gamma_F} = \frac{U_0^2}{c_0^2} = \left(\frac{U_0}{c_0} \right)^2 = Fr^2, \tag{2.20}$$

where Fr denotes the *Foude number* (or *Mach number*), a dimensionless number defined as the ratio of the particles velocity to the wave speed. Then, the following flow regimes can be defined:

- critical flow, if $Fr = 1$, that is $|U_0| = c_0$;
- sub-critical flow, if $Fr < 1$, namely $|U_0| < c_0$;
- super-critical flow, if $Fr > 1$, which implies $|U_0| > c_0$.

In Section 2.7, for different benchmark arterial networks we will show that $Fr \ll 1$, that is $|U_0| \ll c_0$, which implies that we are under strongly sub-critical flow conditions.

2.3 Derivation of lumped-parameter models for blood flow

Along with the 1D blood flow model described in Section 2.2, here we consider a family of nonlinear 0D or lumped-parameter models for blood flow in a compliant vessel. We extend the traditional approach of deriving lumped-parameter models for blood flow in a vascular segment [52, 91, 51], in a way to preserve certain properties (nonlinear characteristics) of the original 1D blood flow models. Such properties include the nonlinear pressure-area relation, derived from the original 1D tube law, and the pressure-dependent parameters characterizing the 0D models, *i.e.* the resistance R and the inductance L. The constant compliance C is replaced by the nonlinear pressure-area relation in which the mechanical properties of the vessel wall are embedded. Considering the parameters L and R defined in terms of a time-dependent average cross-sectional area, in order to account for vessel cross-section changes under changes of pressure is expected to be relevant especially when modeling large deviations from a baseline state, such as hypertension, an haemorrhage or a collapsed state. However, remarkable differences will be also observed when comparing results obtained with the standard linear and the newly derived nonlinear 0D models even in physiologically normal conditions. Indeed, as we will show throughout this chapter, by including these nonlinearities

we obtain more realistic and physically consistent 0D models, representing a powerful tool to improve the computational efficiency of blood flow simulations, while still preserving and well reproducing the main features of pressure and flow waveforms in networks of vessels.

The proposed strategy to do so will be extensively described in this section, where we first derive a family of 0D model for a simple vascular compartment formed by a single vessel and then, by application of appropriate matching conditions obtained from conservation principles, we couple different 0D models to build more complex networks of vessels.

2.3.1 Governing ODE system

First of all, given a vessel with $x \in [x_L, x_R]$ of length $l = |x_R - x_L|$, we introduce the integral averages of the physical quantities of interest over the vessel length, as follows

$$\begin{cases} \widehat{Q}(t) = \dfrac{1}{l}\displaystyle\int_{x_L}^{x_R} q(x,t)\,dx \ : \text{ mean (volumetric) flow rate,} \\ \widehat{A}(t) = \dfrac{1}{l}\displaystyle\int_{x_L}^{x_R} A(x,t)\,dx \ : \text{ mean cross-sectional area,} \end{cases} \tag{2.21}$$

and we define the volume $V(t)$ of the vascular compartment as

$$V(t) := \widehat{A}(t)\, l. \tag{2.22}$$

Integrating in space the continuity equation in (2.1) over the interval $[x_L, x_R]$ leads to the following ordinary differential equation (ODE) in time for the volume $V(t)$

$$\frac{d}{dt}V(t) + Q_R(t) - Q_L(t) = 0, \tag{2.23}$$

where we have used definition (2.22) to rewrite the mass conservation equation in terms of the volume $V(t)$ and we have set

$$Q_L(t) = q(x_L, t), \quad Q_R(t) = q(x_R, t), \tag{2.24}$$

to denote the flow at the inlet and outlet of the vessel, respectively.

When considering the momentum balance equation in (2.1), two simplifying assumptions are added in the standard approach of deriving 0D models [52, 91, 51, 119]: (i) the contribution of the convective term $\partial_x(\alpha q^2/A)$ is neglected, assuming this term to be small compared to the other terms; (ii) the variation of A with respect to x is small compared to that of p and q, replacing A in the momentum equation with a constant value for the area, generally assumed to be the area at rest A_0. Indeed, the first assumption is particularly suited to represent the peripheral circulation, where blood flow is in general quite slow, while the second assumption is reasonable when the axial average is carried out over short segments.
However, in order to preserve certain important properties of the original 1D models in deriving the 0D models, we start integrating in space the momentum equation in (2.1) over the interval $[x_L, x_R]$ without considering the above simplifying assumptions. By including the contribution of the convective term, straightforward calculations yield

$$\frac{d}{dt}\left(\frac{1}{l}\int_{x_L}^{x_R} q\,dx\right) + \frac{\alpha}{l}\left(\frac{Q_R(t)^2}{A_R(t)} - \frac{Q_L(t)^2}{A_L(t)}\right) + \frac{1}{l}\int_{x_L}^{x_R}\frac{A}{\rho}\partial_x p\,dx = -\frac{k_R}{l}\int_{x_L}^{x_R}\frac{q}{A}\,dx. \tag{2.25}$$

Observing that space integrals of the pressure gradient and the viscous force depend on the area $A(x,t)$, we approximate the variable A by its spatial average $\widehat{A}(t)$, rather than by a constant value A_0 as done in the traditional approach, and since this quantity is no longer space-dependent we can bring it outside of these integrals, to get

$$\frac{d}{dt}\widehat{Q}(t) + \frac{\alpha}{l}\left(\frac{Q_R(t)^2}{A_R(t)} - \frac{Q_L(t)^2}{A_L(t)}\right) + \frac{\widehat{A}(t)}{\rho l}\int_{x_L}^{x_R}\partial_x p\,dx = -\frac{k_R}{\widehat{A}(t)}\left(\frac{1}{l}\int_{x_L}^{x_R} q\,dx\right), \tag{2.26}$$

that is

$$\frac{d}{dt}\widehat{Q}(t) + \frac{k_R}{\widehat{A}(t)}\widehat{Q}(t) + \frac{\widehat{A}(t)}{\rho l}\left(P_R(t) - P_L(t)\right) + \frac{\alpha}{l}\left(\frac{Q_R(t)^2}{A_R(t)} - \frac{Q_L(t)^2}{A_L(t)}\right) = 0, \tag{2.27}$$

where, again, we have set:

$$P_L(t) = p(x_L, t), \quad A_L(t) = A(x_L, t), \quad P_R(t) = p(x_R, t), \quad A_R(t) = A(x_R, t), \tag{2.28}$$

to denote the upstream and downstream pressures and cross-sectional areas. We then introduce the following parameters

$$\begin{cases} L(\widehat{A}) := \dfrac{\rho l}{\widehat{A}} \ : \ \textit{nonlinear} \text{ inductance}, \\ R(\widehat{A}) := \dfrac{\rho k_R l}{\widehat{A}^2} \ : \ \textit{nonlinear} \text{ resistance}, \end{cases} \tag{2.29}$$

to obtain the final form of the 0D momentum equation

$$L(\widehat{A})\frac{d}{dt}\widehat{Q}(t) + R(\widehat{A})\widehat{Q}(t) + P_R(t) - P_L(t) + \frac{\alpha\rho}{\widehat{A}}\left(\frac{Q_R(t)^2}{A_R(t)} - \frac{Q_L(t)^2}{A_L(t)}\right) = 0. \tag{2.30}$$

Equations (2.23) and (2.30) are then collected together in the following system of ODEs

$$\begin{cases} \dfrac{d}{dt}V(t) + Q_R(t) - Q_L(t) = 0, \\ L(\widehat{A})\dfrac{d}{dt}\widehat{Q}(t) + R(\widehat{A})\widehat{Q}(t) + P_R(t) - P_L(t) + \dfrac{\alpha\rho}{\widehat{A}(t)}\left(\dfrac{Q_R(t)^2}{A_R(t)} - \dfrac{Q_L(t)^2}{A_L(t)}\right) = 0. \end{cases} \tag{2.31}$$

The problem state variables are the volume $V(t)$ of the vessel compartment and the mean flow rate $\widehat{Q}(t)$ over the vascular segment; the parameters characterizing the 0D model, defined in (2.29), are the resistance $R(\widehat{A})$, which represents the resistance induced to the flow by the blood viscosity and depends on the chosen velocity profile, and the inductance $L(\widehat{A})$, which represents the inertial term in the momentum equation. These parameters are said to be *nonlinear* in the sense that they do no longer depend on a constant reference cross-sectional area A_0, but on the time-dependent average cross-section $\widehat{A}(t)$, which in turn, as we will see in Section 2.3.2, will depend on the mean pressure $P(t)$ acting on the vessel in a nonlinear way. We point out that it is important to define these vessel properties in terms of a time-varying cross-sectional area $\widehat{A}$, in order to account also for possible deviations from the baseline state, such as those encountered when modeling hypertension, vessel collapse or postural changes. We also remark that if in definition (2.29) the time-dependent area $\widehat{A}(t)$ is replaced by the reference value A_0, then these parameters become constant and coincide with the constant parameters found in standard 0D models, namely

$$L_0 = L(A_0) = \frac{\rho l}{\pi r_0^2}, \quad R_0 = R(A_0) = \frac{\rho k_R l}{A_0^2} = \frac{2(\zeta+2)\mu l}{\pi r_0^4}. \tag{2.32}$$

The ODE system (2.31) also involves input and output quantities, Q_L, P_L and Q_R, P_R, respectively, that need to be defined along with the initial conditions to the ODE problem (2.31). As we will see in Section 2.3.3, depending on the different possible assumptions about the data prescribed at the inlet and at the outlet of the vessel, we will obtain four different configurations, all of them describing flow and volume/pressure dynamic in a single vascular segment. Note that these are not boundary conditions, since the continuous space dependence has been lost in the axial average.

2.3.2 Nonlinearity of the pressure-area relation

System (2.31) describes the temporal evolution of volume $V(t)$ and mean flow rate $\widehat{Q}(t)$. At this point, we are interested in relating the system state variables to another important physical quantity, the mean

pressure $\widehat{P}(t)$. Indeed, the nonlinear 0D model (2.31) is derived without making any assumptions about the pressure law relating the mean pressure $\widehat{P}(t)$ to the average cross-sectional area $\widehat{A}(t)$, or, equivalently, to the volume $V(t)$ and the 0D mass conservation equation is obtained for the volume, not for the pressure. Therefore, in the following, we are going to characterize the relation to compute the pressure $\widehat{P}(t)$ from the area $\widehat{A}(t)$.

In the original 1D blood flow model (2.1), the pressure $p(x,t)$ is related to the cross-sectional area $A(x,t)$ via a tube law. Here, the elastic tube law (2.6) for arterial vessels was adopted, which is a nonlinear relationship describing the behaviour of the vessel wall in response to changes in the transmural pressure. On the one hand, in the traditional approach of deriving 0D models, where the convective terms are neglected and the model parameters L_0 and R_0 are constant, pressure $\widehat{P}$ and volume V are linearly related via the constant compliance C_0, as follows

$$\widehat{P}(t) = P_0 + \frac{V(t) - V_0}{C_0} + P_{ext}(t), \tag{2.33}$$

with

$$C_0 := l \left(\frac{\partial A}{\partial p} \right) \Big|_{A=A_0} = l \frac{2A_0}{K} = \frac{3}{2} \frac{\pi r_0^3 l}{E h_0}, \tag{2.34}$$

where the last two expressions of C_0 are specific for arteries. Since coefficient C_0, which represents the mass storage capacity due to the compliance of the vessel, is constant, the nonlinearity of the 1D pressure-area relation is lost in the resulting 0D models. Indeed, in the traditional approach, the 0D mass conservation equation is derived for the pressure $\widehat{P}$, and not for the volume V, by integrating in space both the 1D continuity equation and the 1D tube law under suitable assumptions (for the complete derivation, see for instance [51]). This procedure leads to the linear pressure law stated in equation (2.33), where the nonlinearity of the original 1D pressure-area relation is completely lost.

Here we propose to directly compute the pressure $\widehat{P}$ from the average cross-sectional area $\widehat{A}$ via the nonlinear tube law (2.6), given by

$$\widehat{P}(t) - P_{ext}(t) = K \left[\left(\frac{\widehat{A}(t)}{A_0} \right)^m - \left(\frac{\widehat{A}(t)}{A_0} \right)^n \right] + P_0, \tag{2.35}$$

which in the case of arteries turns out to be

$$\widehat{P}(t) - P_{ext}(t) = \frac{K}{\sqrt{A_0}} \left[\sqrt{\widehat{A}(t)} - \sqrt{A_0} \right] + P_0, \tag{2.36}$$

so that the nonlinearity of the original 1D pressure-area relation of the vessel is fully preserved also in the family of derived 0D models. In particular, the 0D model (2.31) provides the temporal dynamic of volume V, from which the time-dependent average cross-sectional area $\widehat{A}$ can be easily computed as $\widehat{A}(t) = V(t)/l$, to get the mean pressure $\widehat{P}(t) \equiv \widehat{P}(\widehat{A}(t))$ via the nonlinear tube law (2.36). The derived family of 0D models is then said to be *nonlinear*, together with the fact that parameters L and R characterizing these 0D models depend on the time-dependent cross-section $\widehat{A}(t)$, rather than on the constant reference value A_0.
Rewriting the linear relation (2.33) in terms of the area $\widehat{A}$ and replacing the explicit expression for the constant compliance C_0 leads to

$$\widehat{A} = A_0 + \frac{C_0}{l} \left(\widehat{P} - P_0 - P_{ext} \right) = A_0 \left[1 + \frac{2}{K} \left(\widehat{P} - P_0 - P_{ext} \right) \right], \tag{2.37}$$

namely, the average cross-sectional area $\widehat{A}$ depends linearly on pressure $\widehat{P}$. In contrast, from the nonlinear tube law (2.36), this dependence is kept quadratic, as follows

$$\widehat{A} = A_0 \left[1 + \frac{\widehat{P} - P_0 - P_{ext}}{K} \right]^2 = A_0 \left[1 + \frac{2}{K} \left(\widehat{P} - P_0 - P_{ext} \right) + \frac{\left(\widehat{P} - P_0 - P_{ext} \right)^2}{K^2} \right]. \tag{2.38}$$

As a consequence, by adopting relation (2.33) or, equivalently, (2.37), we are neglecting the second-order term arising from the tube law (2.36) and thus the nonlinearity of the original 1D pressure-area relation is lost. This nonlinearity is then fully preserved if, in the derived 0D models, the pressure $\widehat{P}$ is computed from the area $\widehat{A}$ via the nonlinear tube law (2.36).

In conclusion, the ODE system (2.31) involves the mean flow rate $\widehat{Q}$, the volume V and the mean pressure $\widehat{P}$ over the entire vessel, where the pressure $\widehat{P}$ is related to the average cross-sectional area $\widehat{A}$, and thus to V, via the nonlinear tube law (2.36). For the sake of simplicity in the notation, from now on we will denote the flow rate $\widehat{Q}$ and pressure $\widehat{P}$ just by Q and P, respectively. Furthermore, system (2.31) also depends on the input and output quantities exchanged by the vessel at its inlet and outlet, namely P_L, Q_L, which from now on will be denoted by P_{in}, Q_{in}, and P_R, Q_R, that will be replaced by P_{out}, Q_{out}.

Remark 2.2. The nonlinear pressure-area relation (2.35), which for arterial vessels is reformulated as in (2.36), was derived from the specific nonlinear tube law selected for the 1D blood flow model (2.1), that is the elastic pressure law (2.6). In the next chapter of the thesis, we will show that this approach can be adopted for other choices of the original 1D tube law, to obtain the corresponding pressure-area relation to be used for the family of nonlinear 0D models. In particular, in Chapter 3 we will consider a different tube law for arteries, which also accounts for viscoelastic properties of the vessel wall, taken from [17]. The pressure-area relation (2.6) can also be extended to the viscoelastic tube law adopted in [144] for both arteries and veins, to incorporate the viscoelastic nature of the vessel wall mechanics.
In fact, the work presented in Chapter 2 and 3 of this thesis is focused on arteries. However, we expect that the derived family of nonlinear 0D models for blood flow is valid and can be applied not only to arteries, but also to veins, by appropriately changing the geometric and mechanical properties of vessels and the tube law parametrization.

2.3.3 0D vessel configurations

The ODE system (2.31) defines a family of nonlinear 0D models. Indeed, four different 0D models are obtained depending on the different possible assumptions about the data prescribed at the inlet and outlet of the vessel. These models determine all the possible configurations of the same 0D vessel, which are the (P_{in}, Q_{out}), (Q_{in}, P_{out}), (P_{in}, P_{out}) and (Q_{in}, Q_{out})-type 0D vessels, all of them describing flow and volume/pressure dynamic in a compliant vessel.
In the following, we will discard the contribution of the convective component in the momentum balance equation, originally included in the general formulation of the family of nonlinear 0D models (2.31). This choice, commonly adopted in the literature, will be fully justified in Section 2.7, where we will extensively discuss whether it is reasonable or not to incorporate the contribution of the convective terms in the 0D models, also observing that including these terms in the 0D models is not straightforward as one would expect. Table 2.1 summarizes the different 0D vessel configurations and the corresponding ODE systems, which will be described in detail throughout the remaining of this section.

2.3.3.1 (P_{in}, Q_{out})-type 0D vessel

Suppose that the data prescribed at the inlet and outlet of the vessel are $P_{in}(t)$ and $Q_{out}(t)$, respectively. This first 0D vessel type, the (P_{in}, Q_{out})-type vessel, is displayed in the first row of Table 2.1. Then, the temporal dynamic of the state variables Q and V, which are the unknowns under time derivative, is governed

by the following system of ODEs

$$\begin{cases} \dfrac{d}{dt}V(t) = Q(t) - Q_{out}(t), \\ \dfrac{d}{dt}Q(t) = \dfrac{1}{L(\widehat{A})}\left[P_{in}(t) - R(\widehat{A})Q(t) - P(t)\right], \end{cases} \tag{2.39}$$

where, in the above momentum balance equation, the mean pressure P depends on the time-dependent area $\widehat{A}$ via the nonlinear relation (2.36). Clearly, for this 0D model, we have $Q_{in} = Q$. Given the nonlinear resistance $R_{tot}(\widehat{A})$ of the entire vessel according to formula (2.29), this total resistance has been split and equally distributed into two resistances in series, R and R_d, in order to add the distal resistance $R_d = R_{tot}(\widehat{A})/2$ at the outlet of the vessel, as shown in Table 2.1. Then, the outlet pressure P_{out} is directly computed as

$$P_{out}(t) = P(t) - R_d Q_{out}(t). \tag{2.40}$$

The above value of the pressure P_{out} at the outlet of the vessel, obtained by splitting the total vessel resistance and adding a distal resistance to the vessel, can then be used to enforce the continuity of pressure either at 0D junctions, or in the coupling with terminal elements, as it will be described in Section 2.5.3. For the same motivation, a proximal resistance will be added to the (Q_{in}, P_{out})-type 0D vessel and both a proximal and a distal resistance will be introduced into the (Q_{in}, Q_{out})-type 0D vessel, as illustrated in the next paragraphs. We observe that this choice does not involve additional hypothesis on the flow since the total vessel resistance to flow is kept the same and it is just split into two (or more) resistances in series.

We also observe that, by adding the usual simplifying assumptions considered in the standard approach of deriving 0D models, namely that the model parameters L and R are constant, and pressure P and volume V are linearly related via the constant compliance C_0, then the well-established formulation of the *linear* 0D blood flow model is restored, as follows

$$\begin{cases} \dfrac{d}{dt}V(t) = Q(t) - Q_{out}(t), \\ \dfrac{d}{dt}Q(t) = \dfrac{1}{L_0}\left[P_{in}(t) - R_0 Q(t) - P(t)\right], \end{cases} \tag{2.41}$$

where, as discussed in Section 2.3.2, the following linear relation between P and V holds

$$P - P_{ext} = P_0 + \frac{V - V_0}{C_0}. \tag{2.42}$$

The representation of the (P_{in}, Q_{out})-type vessel shown in Table 2.1 is precisely valid for the linear system (2.41), where the model parameters are constant, the convective terms are neglected and the pressure P is linearly related to the volume V via the compliance C_0. However, this description can still be conveniently used also for the nonlinear 0D model (2.39): the model parameters L and R are nonlinear, while the compliance C is now replaced by the nonlinear tube law (2.36) relating the mean pressure P and the average cross-sectional area $\widehat{A}$, in which the mechanical properties of the vessel wall are embedded. In general, the C-element represents the elastic component of the vessel regardless of how pressure and area are related.

Formulation of the mass conservation equation. By computing the time derivative of both sides of the linear relation (2.42), the mass conservation equation can be rewritten in terms of pressure P, as follows

$$\frac{dP}{dt} = \frac{Q - Q_{out}}{C_0}. \tag{2.43}$$

Clearly, this equivalence between the two formulations of the 0D mass conservation equation, the one in (2.41) describing the dynamic of V and the other (2.43) the dynamic of P, is no longer true for the nonlinear 0D model (2.39), since now pressure P depends in a nonlinear fashion on the cross-sectional area $\widehat{A}$, and thus on volume V, via the tube law (2.36). Indeed, on the one hand, the continuity equation in system

(2.39), describing the time-variation of volume V, is an exact relation obtained by directly integrating the 1D equation $\partial_t A + \partial_x q = 0$ over the vessel length $l = |x_R - x_L|$. On the other hand, using the fact that

$$\frac{\partial A}{\partial t} = \frac{\partial A}{\partial p}\frac{\partial p}{\partial t},$$

the mass conservation equation in system (2.1) integrated along the axial direction can be rewritten as follows

$$\frac{1}{l}\int_{x_L}^{x_R} \frac{\partial A}{\partial p}\frac{\partial p}{\partial t}\, dx + \frac{1}{l}\left(Q_R(t) - Q_L(t)\right) = 0. \tag{2.44}$$

To compute the integral in the above equation, we assume $\partial A/\partial p$ to be evaluated at $A = \widehat{A}$, being $\widehat{A}(t)$ the time-dependent average cross-sectional area of the vessel, namely we introduce the following approximation

$$\frac{\partial A}{\partial p} \approx \left(\frac{\partial A}{\partial p}\right)\Big|_{A=\widehat{A}}, \tag{2.45}$$

so that this quantity is no longer space-dependent and can be brought outside of the integral, to get

$$\frac{1}{l}\left(\frac{\partial A}{\partial p}\right)\Big|_{A=\widehat{A}} \int_{x_L}^{x_R} \frac{\partial p}{\partial t}\, dx + \frac{1}{l}\left(Q_R(t) - Q_L(t)\right) = 0, \tag{2.46}$$

which can be finally rewritten as

$$C(\widehat{A})\frac{dP(t)}{dt} + Q_R(t) - Q_L(t) = 0, \tag{2.47}$$

where we have introduced the following nonlinear parameter

$$C(\widehat{A}) := l\left(\frac{\partial A}{\partial p}\right)\Big|_{A=\widehat{A}} : \textit{nonlinear} \text{ compliance}. \tag{2.48}$$

The parameter $C(\widehat{A})$ represents the vessel wall compliance and, like the parameters L and R defined in (2.29), is said to be *nonlinear*, in the sense that it depends on the time-dependent area $\widehat{A}(t)$. In the case of the (P_{in}, Q_{out})-type 0D vessel under study, the approximate equation (2.47) becomes

$$C(\widehat{A})\frac{dP}{dt} = Q - Q_{out}. \tag{2.49}$$

This equation strongly recalls equation (2.43) obtained in the linear case, but now, because of the approximation introduced in (2.45), it is no longer equivalent to the first exact formulation of the continuity equation in (2.39). For this reason, in the nonlinear 0D model, we will restrict ourselves to consider the mass conservation equation in terms of the volume V, as given in (2.39), which is exact, while the pressure P will be always computed from the nonlinear relation (2.36) in order to fully preserve the nonlinearity of the original 1D tube law.

2.3.3.2 (Q_{in}, P_{out})-type 0D vessel

Suppose now that the inflow $Q_{in}(t)$ and the outlet pressure $P_{out}(t)$ are given data. The 0D vessel configuration corresponding to these input data is displayed in the second row of Table 2.1 and the governing equations of the nonlinear 0D model for the (Q_{in}, P_{out})-type vessel read

$$\begin{cases} \dfrac{d}{dt}V(t) = Q_{in}(t) - Q(t), \\ \dfrac{d}{dt}Q(t) = \dfrac{1}{L(\widehat{A})}\left[P(t) - R(\widehat{A})Q(t) - P_{out}(t)\right]. \end{cases} \tag{2.50}$$

Here, we clearly have $Q_{out} = Q$. Furthermore, also for this 0D vessel type, the nonlinear resistance $R_{tot}(\widehat{A})$ of the entire vessel, given in formula (2.29), has been split into two equal resistances in series, R_p and R, in order to add the proximal resistance $R_p = R_{tot}(\widehat{A})/2$ at the inlet of the vessel and to explicitly compute the inlet pressure P_{in} as

$$P_{in}(t) = P(t) + R_p Q_{in}(t), \tag{2.51}$$

which will be used in the coupling procedure between 0D vessels at 0D junctions and in the coupling of a 0D vessel to terminal elements, in order to enforce the continuity of pressure.

2.3.3.3 (P_{in}, P_{out})-type 0D vessel

With the (P_{in}, Q_{out}) and (Q_{in}, P_{out})-type vessels at hand, the last two 0D vessel types can be easily constructed by connecting two basic 0D configurations described so far, as can be clearly seen from Table 2.1. Indeed, if pressure is prescribed at both inlet and outlet of the vessel, $P_{in}(t)$ and $P_{out}(t)$, respectively, the corresponding system can be modeled by connecting a (P_{in}, Q_{out})-type 0D vessel to a (Q_{in}, P_{out})-type 0D vessel, yielding the configuration illustrated in the third row of Table 2.1. Then, the nonlinear 0D model is governed by the following ODE system

$$\begin{cases} \dfrac{d}{dt}V(t) = Q(t) - Q_d(t), \\ \dfrac{d}{dt}Q(t) = \dfrac{1}{L(\widehat{A})}\left[P_{in}(t) - R(\widehat{A})Q(t) - P(t)\right], \\ \dfrac{d}{dt}Q_d(t) = \dfrac{1}{L_d(\widehat{A})}\left[P(t) - R_d(\widehat{A})Q_d(t) - P_{out}(t)\right], \end{cases} \tag{2.52}$$

where the quantities Q and Q_d define the flow rates through the first proximal and the second distal parts of the 0D vessel, respectively. By construction, the total resistance $R_{tot}(\widehat{A})$ and inductance $L_{tot}(\widehat{A})$, as defined in (2.29), are equally distributed between these two proximal and distal portions of the segment, namely into (R, L) and (R_d, L_d), as shown in Table 2.1.

2.3.3.4 (Q_{in}, Q_{out})-type 0D vessel

Finally, assuming that flow rate data are prescribed at both inlet and outlet of the vessel, $Q_{in}(t)$ and $Q_{out}(t)$, respectively, yields the last possible configuration, that is the (Q_{in}, Q_{out})-type 0D vessel, obtained by connecting a (Q_{in}, P_{out})-type 0D vessel to a (P_{in}, Q_{out})-type 0D vessel and displayed in the bottom row of Table 2.1. In this case, the resulting system of ODEs reads

$$\begin{cases} \dfrac{d}{dt}V(t) = Q_{in}(t) - Q(t), \\ \dfrac{d}{dt}Q(t) = \dfrac{1}{L(\widehat{A})}\left[P(t) - R(\widehat{A})Q(t) - P_d(t)\right], \\ \dfrac{d}{dt}V_d(t) = Q(t) - Q_{out}(t), \end{cases} \tag{2.53}$$

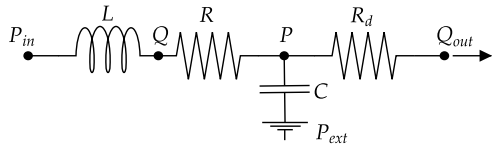
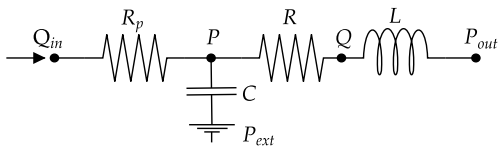
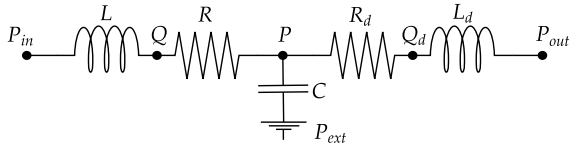
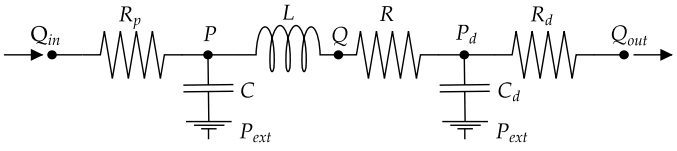
where the quantities V, P and V_d, P_d define volumes and pressures in the first proximal and in the second distal compartments of the vascular segment, respectively. The nonlinear resistance $R_{tot}(\widehat{A})$ over the entire vessel has been split into a proximal resistance R_p at the inlet of the vessel, a resistance R between the two capacitors and a distal resistance R_d at the outlet of the vessel, as shown in Table 2.1, so that the inlet and outlet pressures P_{in} and P_{out} are computed as

$$P_{in}(t) = P(t) + R_p Q_{in}(t), \qquad P_{out}(t) = P_d(t) - R_d Q_{out}(t). \tag{2.54}$$

Admissible choices are also to set either $R_d = 0$, so that we just have $P_{out} = P_d$, or $R_p = 0$, that implies $P_{in} = P$. Also for this 0D vessel configuration, the inlet and outlet pressures P_{in} and P_{out} will be used, as

described in Section 2.5.3, to couple 0D vessels in a network by enforcing the conservation of mass and the continuity of pressure.

TABLE 2.1: Summary of the four possible 0D vessel configurations depending on the different data prescribed at the inlet and outlet of the vessel: for each 0D vessel type, we report the associated governing ODE system (middle column) and display its representation in electric circuit notation (right column). In the linear case, the vessel wall compliance C is a constant parameter, as defined in (2.34); in the nonlinear case, C represents the mechanical properties of the vessel wall embedded in the nonlinear pressure-area relation (2.36).

0D vessel	ODE system	Representation
(P_{in}, Q_{out})	$\begin{cases} \frac{dV}{dt} = Q - Q_{out} \\ \frac{dQ}{dt} = \frac{1}{L(\widehat{A})}\left[P_{in} - R(\widehat{A})Q - P\right] \end{cases}$	 (A)
(Q_{in}, P_{out})	$\begin{cases} \frac{dV}{dt} = Q_{in} - Q \\ \frac{dQ}{dt} = \frac{1}{L(\widehat{A})}\left[P - R(\widehat{A})Q - P_{out}\right] \end{cases}$	 (B)
(P_{in}, P_{out})	$\begin{cases} \frac{dV}{dt} = Q - Q_d \\ \frac{dQ}{dt} = \frac{1}{L(\widehat{A})}\left[P_{in} - R(\widehat{A})Q - P\right] \\ \frac{dQ_d}{dt} = \frac{1}{L_d(\widehat{A})}\left[P - R_d(\widehat{A})Q_d - P_{out}\right] \end{cases}$	 (C)
(Q_{in}, Q_{out})	$\begin{cases} \frac{dV}{dt} = Q_{in} - Q \\ \frac{dQ}{dt} = \frac{1}{L(\widehat{A})}\left[P - R(\widehat{A})Q - P_d\right] \\ \frac{dV_d}{dt} = Q - Q_{out} \end{cases}$	 (D)

2.4 Stability analysis

In this section, we are interested in studying the stability properties of the systems of ODEs governing the 0D blood flow models. In particular, for each of the four different 0D vessel configurations presented in Section 2.3.3, we will perform the stability analysis of the corresponding linear ODE system with constant parameters C_0, R_0 and L_0, linear pressure-volume relation (2.42) and without convective terms. These systems of ODEs are linear and inhomogeneous, with periodic forcing terms. We point out that, to the best of our knowledge, such a stability analysis to investigate the behaviour of the exact solution of an ODE system arising from lumped-parameter models for blood flow has never been reported before, in the existing literature.

When including the convective part into the 0D models, even if the model parameters are still constant and the pressure-volume relation is kept linear, the convective terms introduce a nonlinear component in the corresponding ODE systems. It is well-known that the theory on the stability of systems of ODEs is strictly valid only in the case in which the ODE system is linear. Indeed, in the nonlinear case, the eigenvalues of the Jacobian matrix associated to the ODE system can not be used to describe the behaviour of the exact solution of the original problem. The analytical study of the stability properties of the complete ODE

systems including the convective terms turns out to be extremely complicated, if not impossible. Therefore, we limit our study to the linear case without convective terms. In Section 2.7, we also comment on numerical findings that suggest that the incorporation of convective terms has very strong implications on the stability of the resulting ODE global system, which in turn results in an extremely high computational cost and lack of robustness of its numerical treatment. On the other hand, concerning the nonlinearity of the pressure-area relation and of the parameters R and L, in general we observed that the stability results obtained here for the linear case are valid also for the nonlinear case, as confirmed by numerical experiments presented in Section 2.7.

We first consider the (P_{in}, Q_{out})-type 0D vessel displayed in the top row of Table 2.1 and, by adding the following assumptions:

- the model parameters L_0 and R_0 are constant,
- pressure P is linearly related to volume V via the constant compliance C_0 according to (2.42),

the resulting system of ODEs governing such a 0D vessel configuration reads

$$\begin{cases} \dfrac{dV}{dt} = Q - Q_{out}, \\ \dfrac{dQ}{dt} = \dfrac{1}{L_0}\left[P_{in} - R_0 Q - P\right], \end{cases} \tag{2.55}$$

where R_0 denotes the constant resistance between Q and P. The data prescribed at the inlet and outlet of the vessel, $P_{in} \equiv P_{in}(t)$ and $Q_{out} \equiv Q_{out}(t)$, respectively, are given time-dependent functions, that we assume to be periodic of a certain period $T_0 > 0$. By using relation (2.42), the momentum equation in (2.55) can be reformulated in terms of the state variable V as follows

$$\begin{cases} \dfrac{dV}{dt} = Q - Q_{out}, \\ \dfrac{dQ}{dt} = \dfrac{1}{L_0}\left[P_{in} - R_0 Q - \dfrac{V}{C_0}\right], \end{cases} \tag{2.56}$$

where, for the sake of simplicity in the notation, in (2.42) we have set $V_0 = P_0 = P_{ext} = 0$. Then, the above ODE system can be rewritten in matrix form as

$$\frac{d\boldsymbol{x}(t)}{dt} = \boldsymbol{A}\boldsymbol{x}(t) + \boldsymbol{b}(t), \tag{2.57}$$

where we have set

$$\boldsymbol{x}(t) = \begin{bmatrix} V(t) \\ Q(t) \end{bmatrix}, \quad \boldsymbol{A} = \begin{bmatrix} 0 & 1 \\ -\dfrac{1}{C_0 L_0} & -\dfrac{R_0}{L_0} \end{bmatrix}, \quad \boldsymbol{b}(t) = \begin{bmatrix} -Q_{out}(t) \\ \dfrac{P_{in}(t)}{L_0} \end{bmatrix}. \tag{2.58}$$

Namely, $\boldsymbol{x}(t)$ is the vector of unknowns, the model state variables V and Q, $\boldsymbol{A}$ is the constant coefficient matrix and $\boldsymbol{b}(t)$ is the time-dependent vector periodic forcing function, providing external data to the system. As the coefficient matrix $\boldsymbol{A}$ is constant, we have a non-homogeneous linear system of ODEs with constant coefficients.

The stability of the exact solution of the complete ODE system (2.57) is determined by the real part of the eigenvalues of the coefficient matrix $\boldsymbol{A}$. In particular, we are going to use the following two results:

(i) Given a linear homogeneous system of ODEs with constant coefficients, that is an ODE system of the form (2.57) with null forcing function $\boldsymbol{b}(t) \equiv 0$, a necessary and sufficient condition for this system to be *asymptotically stable* is that all eigenvalues of $\boldsymbol{A}$ have strictly negative real part.

(ii) If the forcing function $\boldsymbol{b}(t)$ is periodic and if the homogeneous part of system (2.57) is asymptotically stable, then the exact solution of the original inhomogeneous problem will converge to the periodic solution of system (2.57) as t increases, for any admissible choice of the initial condition.

These are well-known results [122, 63] and further details and proofs can be found in Appendix A.1.
The eigenvalues $\lambda_{1,2}$ associated to matrix $\boldsymbol{A}$ are the roots of the following second-degree characteristic polynomial

$$\lambda^2 + \frac{R_0}{L_0}\lambda + \frac{1}{C_0 L_0} = 0, \tag{2.59}$$

whose discriminant is

$$\Delta = \left(\frac{R_0}{L_0}\right)^2 - \frac{4}{C_0 L_0}. \tag{2.60}$$

At this point, we will show that, regardless of the sign of the above discriminant Δ, the eigenvalues associated to $\boldsymbol{A}$ have always strictly negative real part, condition that ensures the asymptotic stability of the homogeneous part of system (2.57). We distinguish and analyze the following three cases:

1. If $\Delta < 0$, then the eigenvalues $\lambda_{1,2}$ of matrix $\boldsymbol{A}$ are complex and conjugate, given by

$$\lambda_{1,2} = -\frac{R_0}{2L_0} \pm i\frac{1}{2}\sqrt{-\Delta} = -\frac{R_0}{2L_0} \pm i\frac{1}{2}\sqrt{\frac{4}{C_0 L_0} - \left(\frac{R_0}{L_0}\right)^2}, \tag{2.61}$$

   with strictly negative real part, that is

$$Re(\lambda_1) = Re(\lambda_2) = -\frac{R_0}{2L_0} < 0. \tag{2.62}$$

2. If $\Delta = 0$, then the two eigenvalues associated to matrix $\boldsymbol{A}$ are equal, real and strictly negative, namely with strictly negative real part, that is

$$\lambda_1 = \lambda_2 = -\frac{R_0}{2L_0} < 0. \tag{2.63}$$

3. If $\Delta > 0$, then the eigenvalues $\lambda_{1,2}$ of matrix $\boldsymbol{A}$ are distinct, real and both negative, given by

$$\lambda_1 = -\frac{1}{2}\left(\frac{R_0}{L_0} + \sqrt{\Delta}\right), \quad \lambda_2 = -\frac{1}{2}\left(\frac{R_0}{L_0} - \sqrt{\Delta}\right). \tag{2.64}$$

   From (2.64), the first eigenvalue λ_1 is clearly strictly negative, and it is straightforward to verify that the second eigenvalue λ_2 is also strictly negative. Indeed, the following chain of inequalities holds

$$0 < \Delta = \left(\frac{R_0}{L_0}\right)^2 - \frac{4}{C_0 L_0} < \left(\frac{R_0}{L_0}\right)^2 \quad \Longrightarrow \quad \sqrt{\Delta} = \sqrt{\left(\frac{R_0}{L_0}\right)^2 - \frac{4}{C_0 L_0}} < \frac{R_0}{L_0}, \tag{2.65}$$

   which implies $\lambda_2 < 0$.

In conclusion, the eigenvalues associated to the constant coefficient matrix $\boldsymbol{A}$ of system (2.57) have always strictly negative real part. Therefore, the homogeneous part of system (2.57) is asymptotically stable and, as a consequence, the complete ODE system (2.55) is stable, meaning that, for any choice of the initial condition, the exact solution will converge to the periodic solution.

Under the assumption that the forcing terms prescribed at the inlet and outlet of the vessel, $Q_{in} \equiv Q_{in}(t)$ and $P_{out} \equiv P_{out}(t)$, respectively, are periodic functions of t, the stability analysis of the (Q_{in}, P_{out})-type vessel is similar to that of the (P_{in}, Q_{out})-type vessel performed above. Indeed, it is straightforward to check

that the eigenvalues of the coefficient matrix $\boldsymbol{A}$ associated to the linear ODE system corresponding to the (Q_{in}, P_{out})-type 0D vessel are the same to those of the (P_{in}, Q_{out})-type 0D vessel, thus leading to the same stability properties of the exact solution of the ODE system.

Next, we move to the (P_{in}, P_{out})-type 0D vessel displayed in the third row of Table 2.1. The governing ODE system, of which we want to investigate the stability, reads

$$\begin{cases} \dfrac{dV}{dt} = Q - Q_d, \\ \dfrac{dQ}{dt} = \dfrac{1}{L_0/2}\left[P_{in} - \dfrac{R_0}{2}Q - P\right], \\ \dfrac{dQ_d}{dt} = \dfrac{1}{L_0/2}\left[P - \dfrac{R_0}{2}Q_d - P_{out}\right], \end{cases} \tag{2.66}$$

where, as usual, the pressure data prescribed at the inlet and outlet of the vessel, $P_{in} \equiv P_{in}(t)$ and $P_{out} \equiv P_{out}(t)$, respectively, are assumed to be time-dependent periodic functions of a certain period $T_0 > 0$. In this case, the eigenvalues associated to the constant coefficient matrix $\boldsymbol{A}$ of the homogeneous part of system (2.66) are given by

$$\lambda_1 = -\frac{R_0}{L_0}, \quad \lambda_{2,3} = \begin{cases} -\dfrac{R_0}{2L_0} \pm i\dfrac{1}{2}\sqrt{-\Delta}, & \text{if } \Delta = \left(\dfrac{R_0}{L_0}\right)^2 - \dfrac{16}{C_0 L_0} < 0, \\ -\dfrac{R_0}{2L_0}, & \text{if } \Delta = 0, \\ -\dfrac{R_0}{2L_0} \pm \dfrac{1}{2}\sqrt{\Delta}, & \text{if } \Delta > 0. \end{cases} \tag{2.67}$$

Therefore, we conclude that all the above eigenvalues have always strictly negative real part, meaning that the homogeneous part of system (2.66) is asymptotically stable. As a consequence, for any choice of the initial conditions, any solution of the inhomogeneous system (2.66) will converge to the periodic one.

We consider now the linear ODE system governing the last 0D vessel configuration, the (Q_{in}, Q_{out})-type 0D vessel depicted in the bottom row of Table 2.1, that is

$$\begin{cases} \dfrac{dV}{dt} = Q_{in} - Q, \\ \dfrac{dQ}{dt} = \dfrac{1}{L_0}\left[P - R_0 Q - P_d\right], \\ \dfrac{dV_d}{dt} = Q - Q_{out}, \end{cases} \tag{2.68}$$

where R_0 denotes the resistance element between P and P_d only. Algebraic manipulations yield the following eigenvalues associated to the constant coefficient matrix $\boldsymbol{A}$ of the homogeneous part of system (2.68)

$$\lambda_1 = 0, \quad \lambda_{2,3} = \begin{cases} -\dfrac{R_0}{2L_0} \pm i\dfrac{1}{2}\sqrt{-\Delta}, & \text{if } \Delta = \left(\dfrac{R_0}{L_0}\right)^2 - \dfrac{16}{C_0 L_0} < 0, \\ -\dfrac{R_0}{2L_0}, & \text{if } \Delta = 0, \\ -\dfrac{R_0}{2L_0} \pm \dfrac{1}{2}\sqrt{\Delta}, & \text{if } \Delta > 0. \end{cases} \tag{2.69}$$

The eigenvalues $\lambda_{2,3}$ have always strictly negative real part regardless the sign of the discriminant Δ, while the first eigenvalues λ_1 turns out to be equal to zero.
In the following, we are going to study the asymptotic properties of system (2.68) in order to find suitable assumptions on the periodic forcing functions $Q_{in}(t)$ and $Q_{out}(t)$ ensuring the stability of such ODE

system, for both cases $\Delta < 0$ and $\Delta > 0$. However, by analyzing the orders of magnitude of typical physiological values of all geometrical and physical parameters defining the elements R_0, L_0 and C_0, and thus the expression of Δ in (2.69), it is easy to check that we always have $\Delta < 0$. The above expression of Δ can be reformulated as follows

$$\begin{aligned}\Delta &= \left(\frac{R_0}{L_0}\right)^2 - \frac{16}{C_0 L_0} = \frac{1}{L_0}\left(\frac{R_0^2}{L_0} - \frac{16}{C_0}\right) \\ &= \frac{1}{L_0}\frac{4}{\pi r_0^3}\left[f_1 - f_2\right],\end{aligned} \tag{2.70}$$

with

$$f_1 = (\zeta+2)^2\frac{\mu^2 l}{\rho r_0^3}, \quad f_2 = \frac{8}{3}\frac{E h_0}{l}. \tag{2.71}$$

We consider the following order of magnitude ranges in arterial vessels for the variables defining the above factors f_1 and f_2

$$\begin{cases} \rho \sim 10^0 & [\text{g/cm}^3], \\ \mu \sim 10^{-2} & [\text{dyne}\cdot\,\text{s/cm}^2], \\ l \sim 10^0 - 10^1 & [\text{cm}], \\ r_0 \sim 10^{-1} - 10^0 & [\text{cm}], \\ h_0 \sim 10^{-2} - 10^{-1} & [\text{cm}], \\ E \sim 10^6 - 10^7 & [\text{dyne/cm}^2]. \end{cases} \tag{2.72}$$

Then, for the first term f_1, its order of magnitude approximately ranges between 10^{-3} and 10^2, while the order of magnitude of the second factor f_2 is estimated to vary between 10^4 and 10^6. Therefore, the second term f_2 is always the largest one, thus ensuring the negativity of Δ. These findings were also confirmed by computing exact values of f_1, f_2 and Δ for all vessels of all arterial networks considered in this paper and described in Section 2.7. Table 2.2 displays maximum and minimum values, mean value and corresponding standard deviation of the two factors f_1 and f_2 defined in (2.71), for the aortic bifurcation model (Section 2.7.3), the 37-artery network (Section 2.7.4) and the reduced ADAN56 model (Section 2.7.5). Even if there is high variability in the values of these two factors, we observe that the second factor f_2 is always orders of magnitude larger with respect to the first factor f_1, thus implying that the discriminant Δ corresponding to the (Q_{in}, Q_{out})-type 0D vessel and given in (2.70) is always strictly negative for all vessels of the three arterial networks considered. Then, our case of interest is the one corresponding to $\Delta < 0$.

TABLE 2.2: Quantitative assessment of the two factors f_1 and f_2 defining the discriminant Δ of the characteristic polynomial associated to the coefficient matrix $\boldsymbol{A}$ of the (Q_{in}, Q_{out})-type 0D vessel, for the vessels of the aortic bifurcation, the 37-artery network and ADAN56 model.

Network	max(f_1)	min(f_1)	mean(f_1)	std.dev(f_1)	max(f_2)	min(f_2)	mean(f_2)	std.dev(f_2)
Aortic bifurcation	7.19	2.47	5.61	2.72	160000.00	158117.65	158745.10	1086.78
37-artery network	315.26	7.30e-02	82.72	97.86	3076923.08	17777.78	227502.13	563787.17
ADAN56 model	1837.19	8.96e-03	113.44	313.31	1777910.46	5184.12	187403.52	354118.73

In general, if a linear homogeneous system of ODEs with constant coefficients has a null eigenvalue, then the coefficient matrix $\boldsymbol{A}$ is singular, with non-trivial null space, and any vector of the null space is an equilibrium point for the system. In other words, the homogeneous system (A.1) does not have a unique equilibrium point, but a line of equilibria, which can be either stable (but not asymptotically stable) or unstable, depending on the sign of the other eigenvalues. Hence, an homogeneous system of the form (A.1)

with coefficient matrix $\boldsymbol{A}$ having a zero eigenvalue is stable if all other eigenvalues of $\boldsymbol{A}$ have strictly negative real part, in the sense that it has an attractive line of equilibria and each equilibrium is stable, but not asymptotically stable.
However, the stability of the homogeneous system is not sufficient to ensure the stability of the corresponding inhomogeneous system (2.57), but an additional assumption on the periodic forcing function is needed in order to preserve the stability of ODE system, namely that any solution of (2.57) for any admissible choice of the initial condition will converge to the periodic one as $t \to +\infty$.

We state here only the obtained condition, but the full derivation of this assumption on the periodic forcing function $\boldsymbol{b}(t)$ is extensively provided in Appendix A.2, first in the scalar case of a single ODE, then for a system of ODEs, specifically focusing on system (2.68) governing the (Q_{in}, Q_{out})-type 0D vessel.
Given the inhomogeneous linear ODE system (2.68), whose coefficient matrix $\boldsymbol{A}$ has a null eigenvalue λ_1 and two eigenvalues $\lambda_{2,3}$ with strictly negative real part, the following condition on the periodic forcing function $\boldsymbol{b}(t)$ ensures the stability of the exact solution of the ODE system

$$\int_0^{T_0} \left[Q_{in}(s) - Q_{out}(s)\right] ds = 0 \quad \Longleftrightarrow \quad \int_0^{T_0} Q_{in}(s)\, ds = \int_0^{T_0} Q_{out}(s)\, ds. \tag{2.73}$$

Namely, under this assumption, the complete inhomogeneous system (2.53) is stable, in the sense that for any admissible choice of the initial condition the exact solution will converge to the periodic one. This is also a physically consistent condition: in order for the volume $V(t) + V_d(t)$ not to constantly increase/decrease and asymptotically diverge, the integral over a period $[0, T_0]$ of the inflow $Q_{in}(t)$ entering the vessel must equal the integral over the same period of the outflow $Q_{out}(t)$ leaving the vessel.

Remark 2.3. The stability analysis presented in this section for arterial vessels can be straightforwardly repeated also for veins, in order to study the stability properties of the corresponding ODE systems.

2.5 Junctions of vessels and coupling equations

Single 1D vessel domains can be coupled through 1D junction models to construct networks of vessels. The 1D-model-like vessel coupling is a well-established methodology and its validity has been extensively documented by works where 1D models have been validated against both *in-vitro* experimental models [89, 5] and more complex 3D-FSI models [153, 76], showing that it is reasonable to describe flow at junctions by means of a 1D model, especially when the focus is on reproducing wave propagation phenomena across a vascular network, with a good balance between accuracy and computational cost. The treatment of networks consisting of one-dimensional domains and its application to the modeling of the circulatory system have been widely addressed, where a crucial aspect is how to provide algebraic coupling conditions between 1D domains at junction nodes. Relevant contributions in this field include [50, 127, 89, 5, 16, 101, 99, 97].

In this section, we first describe the 1D coupling strategy adopted to define suitable coupling conditions to be prescribed at 1D junctions. Then, we consider the coupling between 0D vessels and we propose a first 0D coupling approach to construct networks of 0D vessels, where each 1D vessel is replaced by a 0D element by a per-segment 1D-to-0D mapping to preserve the geometry and topology of the original 1D network. Inspired by the 1D junction model, also here relevant conservation principles must be satisfied across the junction: the conservation of mass and the continuity of total pressure, or just pressure. This coupling strategy to couple 0D vessels together will be extended in the next chapter of the thesis, where the hybrid coupling between 1D and 0D vessels will be also addressed. The main focus of the study presented in this chapter is indeed to validate the newly derived family of nonlinear lumped-parameter models for blood flow, against the reference 1D blood flow model, and to assess whether these 0D models can be adopted

to construct cheaper 1D-0D hybrid models, to improve the computational efficiency of 1D-0D simulations, while still preserving a certain level of accuracy in the predicted results.

The approach proposed here to couple 0D vessels and construct 0D vascular networks is similar to the one presented in [119], with the main difference that our family of nonlinear 0D models includes a nonlinear pressure-area relation and the dependence of the 0D model parameters on the time-varying vessel cross-section.

2.5.1 1D coupling equations

If we have a junction J shared by N 1D vessels, a Riemann problem can be defined at the junction interface. Indeed, a junction between two or more 1D vessels defines a Riemann problem with discontinuous geometric and mechanical vessel properties. In the case of sub-critical flow, namely when $|u| < c$, this problem has been extensively studied and its exact solution has been derived in Toro and Siviglia [141] first and in Spilimbergo *et al.* [130] next. Also here, we will still restrict to sub-critical flow conditions. The Riemann problem formulated for N 1D vessels sharing vertex J reads

$$\begin{cases} \partial_t \boldsymbol{Q}_k + \boldsymbol{A}(\boldsymbol{Q}_k)\partial_x \boldsymbol{Q}_k = 0, \quad x \in \mathbb{R},\, t > 0, \\ \boldsymbol{Q}_k(x,0) = \boldsymbol{Q}_k^{1D}, \end{cases} \tag{2.74}$$

for $k = 1, \dots, N$, where we have dropped the vessel index k from the spatial coordinate x for the sake of simplicity in the notation. Then, the self-similar solution to the Riemann problem (2.74) consists of $2N$ constant states, the N initial condition states $\boldsymbol{Q}_k^{1D} = \left(A_k^{1D}, q_k^{1D}\right)^T$, with $k = 1, \dots, N$, provided by the 1D vessels, and the N unknown boundary states $\boldsymbol{Q}_k^{*} = \left(A_k^{*}, q_k^{*}\right)^T$, with $k = 1, \dots, N$, to be determined, which will provide the coupling variables for each one of the vessels converging to the junction J. By following the approach proposed in [141, 130], we can construct the Riemann problem solution and compute these unknown boundary states. First, under the assumption of adopting a two-rarefaction Riemann solver, which assumes that, at each boundary, the wave associated to the pertinent characteristic field traveling into the 1D domain is a rarefaction wave, the unknown boundary states $\boldsymbol{Q}_k^{*}$, with $k = 1, \dots, N$, are connected to the initial condition states $\boldsymbol{Q}_k^{1D}$, with $k = 1, \dots, N$, via the continuity of the generalized Riemann invariants (2.15), as follows

$$\frac{q_k^*}{A_k^*} - \frac{q_k^{1D}}{A_k^{1D}} + g_{1D}^k \int_{A_k^{1D}}^{A_k^*} \frac{c(\xi)}{\xi} d\xi = 0, \quad \text{for } k = 1, \dots, N, \tag{2.75}$$

where g_{1D}^k is the auxiliary function

$$g_{1D}^k = \begin{cases} -1, & \text{if } x_J^k = 0, \\ 1, & \text{if } x_J^k = l_k, \end{cases} \tag{2.76}$$

and x_J^k is the local coordinate of the k-th vessel, evaluated at vertex J. In this way, we obtain the first N nonlinear equations.

On the other hand, the state vectors $\boldsymbol{Q}_k^{*}$, with $k = 1, \dots, N$, are connected among themselves via the linearly degenerate stationary contact discontinuity generated by the discontinuous variation of geometric and mechanical properties of vessels converging at junction J. When considering the material and geometric parameters $K(x)$, $A_0(x)$ and $p_{ext}(x,t)$ as functions of distance x along the vessel length, system (2.1) can then be rewritten as an augmented system, where these parameters become actual variables of the PDE system which is extended with additional evolutionary equations for K, A_0 and p_{ext} (see Section 3.2.1 and [141, 130] for full details). From the eigenstructure analysis of the coefficient matrix of the augmented continuous problem, we obtain that, in addition to $u \pm c$, all the other eigenvalues of this matrix are null, whose

characteristic fields are linearly degenerate (LD) and associated with contact discontinuities. The following wave relations, derived from the GRI associated to the stationary contact discontinuity, are found

$$f_{MC}(q_1^*,\dots,q_N^*) = \sum_{k=1}^{N} g_{1D}^k q_k^* = 0 \tag{2.77}$$

and

$$p_{tot,1}^* - p_{tot,k}^* = 0 \quad \Longrightarrow \quad p(A_1^*) + \frac{1}{2}\rho\left(\frac{q_1^*}{A_1^*}\right)^2 - p(A_k^*) - \frac{1}{2}\rho\left(\frac{q_k^*}{A_k^*}\right)^2 = 0, \quad \text{for } k = 2,\dots,N. \tag{2.78}$$

Equation (2.77) enforces mass conservation at the junction; the other $N-1$ relations prescribe the continuity of total pressure p_{tot}^* between the vessels. In other words, the wave relations associated to the stationary contact discontinuity exactly coincide with those physically consistent conservation principles that we would expect to be satisfied at a junction. Full details on the derivation of wave relations in (2.77) and (2.78) are given in [141, 130].
In conclusion, we obtain a nonlinear system of $2N$ equations in $2N$ unknowns that can be numerically solved to compute the sought boundary states $\boldsymbol{Q}_k^*$, with $k = 1,\dots,N$.

2.5.2 Boundary conditions for 1D vessels

Given a vascular network of 1D domains, suitable boundary conditions must be prescribed at the inlet and outlet nodes of the network, together with coupling conditions between vessels. The GRI-based approach can be adopted also in this case. The idea is that, in the boundary state vector $\boldsymbol{Q}^* = (A^*, q^*)^T$ to be prescribed at the left/right boundary interface of a vessel, one of the two components is known/enforced or provided by an additional algebraic relation to be satisfied at the boundary. Then, the other component is determined by imposing the continuity of the generalized Riemann invariant Γ_2, if at the left boundary interface, or Γ_1, if at the right one, between $\boldsymbol{Q}^*$ and the corresponding initial condition state $\boldsymbol{Q}^{1D}$. For instance, a common choice for the boundary condition to be prescribed at the root/inlet node of an arterial network is to impose a time-varying inflow curve $q_{in}(t)$. In this case, we will have $q^* = q_{in}$, while the unknown cross-sectional area A^* will be the solution of the following nonlinear equation

$$\frac{q_{in}}{A^*} - \frac{q^{1D}}{A^{1D}} - \int_{A^{1D}}^{A^*} \frac{c(\xi)}{\xi} d\xi = 0. \tag{2.79}$$

On the other hand, terminal vessels of the network are usually coupled to single-resistance elements or RCR Windkessel models, as the one shown in Figure 2.3. At the boundary interface between the vessel and the attached terminal element, the following relation must hold

$$q^* = \frac{p(A^*) - P_T}{R_T}, \tag{2.80}$$

where (P_T, R_T) are either the outlet pressure and the total resistance of the resistive terminal element, or the pressure in the Windkessel model and its proximal resistance, respectively. The continuity of the GRI is then enforced to connect the unknown state $\boldsymbol{Q}^*$ to the given state $\boldsymbol{Q}^{1D}$ in the last computational cell of the vessel, as follows

$$\frac{q^*}{A^*} - \frac{q^{1D}}{A^{1D}} + \int_{A^{1D}}^{A^*} \frac{c(\xi)}{\xi} d\xi = 0. \tag{2.81}$$

Once again, by replacing expression (2.80) for q^*, we obtain a nonlinear equation to be solved in the only unknown A^*.

2.5.3 0D junctions and coupling equations

Equipped with the family of nonlinear 0D models for blood flow derived in Section 2.3 for a single vessel, we consider now the coupling of 0D vessels to construct more complex networks of vessels.
Two or more 0D vessels can be coupled through 0D junctions, which satisfy the conservation of mass and also impose a common pressure on all branches, to ensure the continuity of pressure throughout the 0D junction. We immediately note that, in contrast to 1D junctions between 1D vessels, where the total pressure continuity can be enforced, in junction between 0D vessels we enforce pressure continuity only. The choice of imposing pressure continuity at each 0D junction allows us to always solve a linear coupling problem, whereas it is well-known that the nonlinear problem to be solved at 1D junctions can become very computationally expensive. However, on the other hand, in order to arrange compatible segment types into a network, with inlets and outlets coupled appropriately, restrictions on admissible 0D vessel types are necessary for vessels converging at a 0D junction. In particular, input data to prescribe at the inlet and outlet of each vessel are defined by the state of their adjacent compartments, in order to ensure the conservation of mass and continuity of pressure. The coupling of 0D vessels without any restrictions on compatible 0D vessel configurations will be addressed in the next chapter, in Section 3.2.3, where hybrid junctions where 1D and 0D vessels are coupled together will be also introduced.
The simplest 0D junctions are two-vessel and three-vessel junctions, connecting two or three vessels, respectively, which can be generalized in a generic 0D junction attaching an arbitrary number of 0D vessels. In addition, in open-loop networks, terminal vessels can be coupled to single-resistance or RCR Windkessel elements to model the cumulative effects of all vessels distal to the terminal segments of the vessel network.

2.5.3.1 Two-vessel junction (J2)

To describe the coupling procedure adopted, let us consider, for instance, two (P_{in}, Q_{out})-type 0D vessels connected in a simple two-vessel junction, as displayed in Figure 2.1a. Coupling conditions are needed to determine, at the junction point, the flow rate Q^1_{out} at the outlet of the first (parent) vessel and the pressure P^2_{in} at the inlet of the second (daughter) vessel. By enforcing the conservation of mass, we obtain

$$Q^1_{out}(t) = Q^2(t),$$

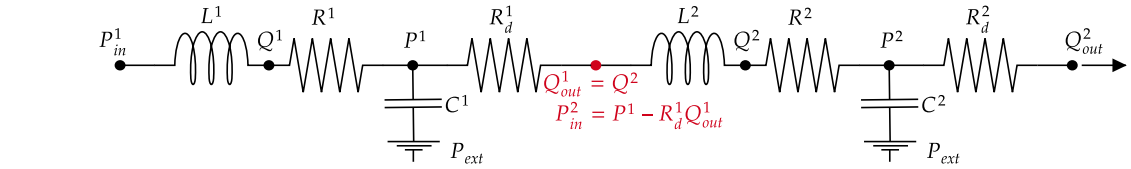
where Q^2 is the flow rate state variable in the second vessel; then, by imposing the continuity of pressure, we get

$$P^2_{in}(t) = P^1(t) - R^1_d Q^1_{out}(t) = P^1(t) - R^1_d Q^2(t),$$

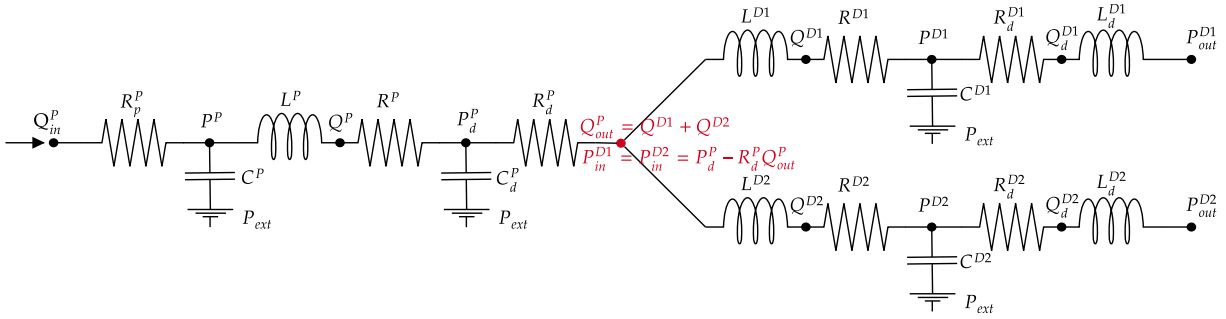
where P^1 is the pressure state variable in the parent vessel and R^1_d is the distal resistance at the outlet of the same vessel, as illustrated in Figure 2.1a. Note that in the case where $R^1_d = 0$, we simply obtain $P^2_{in} = P^1$.
From this test case, it is straightforward to conclude that all the possible pairs of vessel types that can be coupled to form a two-vessel 0D junction are such that the outlet of the parent vessel is of pressure type and the inlet of the daughter vessel is of flow type, or vice versa. All other configurations are not allowed, because no assumption would be made either on the flow rate Q or on the pressure P at the junction point between vessels.

Moreover, we observe that the two-vessel junction may be also used to represent a single 0D vessel with two 0D compartments of the same type coupled in series, either (P_{in}, Q_{out}) or (Q_{in}, P_{out}). Indeed, the per-segment mapping replaces each 1D vessel of a network by a 0D vessel, which, in turn, can be composed of just one or more 0D compartments.

FIGURE 2.1: (A) Example of a 0D representation for a two-vessel junction between two (P_{in}, Q_{out})-type 0D vessels. (B) Example of a 0D representation for a bifurcation branch (three-vessel splitting flow junction): (Q_{in}, Q_{out})-type 0D vessel for parent vessel and (P_{in}, P_{out})-type 0D vessels for daughter vessels.



(A) J2



(B) J3

2.5.3.2 Three-vessel junction (J3)

For the family of three-vessel junctions, we present here the coupling procedure adopted in the case of a *splitting flow* junction, where the 0D junction represents the branching point at which the end of the parent vessel is connected to the inlets of the two daughter vessels, but the coupling conditions to be imposed in a *merging flow* junctions, where the 0D junction represents the adjoining point at which the outlets of the two daughter vessels converge into the beginning of the parent vessel, can be easily derived in a similar way, as proposed in [119].

We consider, for instance, a (Q_{in}, Q_{out})-type 0D vessel for the parent vessel and (P_{in}, P_{out})-type 0D vessels for both daughter vessels. By imposing the mass conservation, we get that the flow rate Q^P_{out} at the outlet of the parent vessel must be equal to the sum of the two daughter branches' flows Q^{D1} and Q^{D2}, that is

$$Q^P_{out}(t) = Q^{D1}(t) + Q^{D2}(t).$$

Then, by enforcing the continuity of pressure, we have that the pressure at the inlet of both daughter vessels must be equal to the distal pressure in the parent vessel, namely

$$P^{D1}_{in}(t) = P^{D2}_{in}(t) = P^P_d(t) - R^P_d Q^P_{out}(t) = P^P_d(t) - R^P_d \left(Q^{D1}(t) + Q^{D2}(t)\right),$$

where the pressure P^P_d is the distal pressure state variable in the parent vessel and R^P_d is the distal resistance at the outlet of the same vessel, as depicted in Figure 2.1b. We observe that in the particular case where $R^P_d = 0$, the above condition of continuity of pressure becomes $P^{D1}_{in} = P^{D2}_{in} = P^P_d$.

From this test case, we can then derive the following restrictions on compatible segment types for vessels converging in a three-vessel splitting flow junction: the outlet of the parent vessel must be of flow type, while the inlets of both daughter vessels must be of pressure type.

2.5.3.3 Generic 0D junction

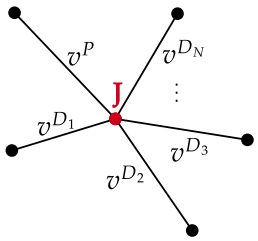
In the most general situation, a 0D junction connects an arbitrary number of 0D vessels, sharing their inlets or outlets at the junction point, as displayed in Figure 2.2. In order to couple appropriately all the 0D vessels converging at the junction, first of all, a single vessel has to be chosen as parent vessel (for instance, the vessel with the largest cross-sectional area), while all other vessels are classified as daughter vessels. As a consequence, the role of each vessel, either parent or daughter, will define the corresponding vessel type, depending on the inlet/outlet data to be prescribed at the junction point.
For the parent segment, at the vessel end shared at the junction a condition on the flow Q^P is prescribed, which is computed by imposing the conservation of mass. Indeed, at the junction, the flow rate in each daughter vessel is known and denoted by Q^{D_j}. For instance, if we refer to the configuration illustrated in Figure 2.2, the flow rate Q^P_{out} at the outlet of the chosen parent vessel is given by

$$Q^P_{out}(t) = \sum_{j=1}^{N} Q^{D_j}(t). \tag{2.82}$$

In equation (2.82), the flow direction in each vessel, namely if the blood stream enters or leaves the 0D junction, is taken into account by the sign of Q. On the other hand, for each daughter, at the vessel end shared at the junction a condition on the pressure P^{D_j} must be prescribed in order to enforce pressure continuity throughout the 0D junction. Then, this pressure must be equal to the pressure in the parent vessel, that is

$$P^{D_j}_{in/out}(t) = P^P(t) \quad j = 1, \dots, N. \tag{2.83}$$

FIGURE 2.2: Example of a generic 0D junction connecting $(N+1)$ 0D vessels: one vessel is chosen as parent vessel, while all other N segments are treated as daughter vessels.



2.5.3.4 Terminal vessels

In open-loop arterial networks, the cumulative effects of all distal vessels (small arteries, arterioles and capillaries) at ending locations of terminal arteries have to be taken into account. These effects can be modeled using either single-resistance or *RCR* Windkessel elements coupled to the terminal arteries.

In particular, a *RCR* Windkessel model is composed of a proximal terminal resistance R^1_{wk}, a terminal capacitor C_{wk} and a distal terminal resistance R^2_{wk}, as displayed in Figure 2.3. Pressure P_{wk} and flow rate Q_{wk} in this terminal element are governed by

$$\begin{cases} \dfrac{dP_{wk}}{dt} = \dfrac{Q - Q_{wk}}{C_{wk}}, \\ Q_{wk} = \dfrac{P_{wk} - P_v}{R^2_{wk}}, \end{cases} \tag{2.84}$$

where Q is the flow rate from the 0D vessel coupled to the *RCR* element and P_v is the constant outflow pressure.
Depending on the configuration of the 0D vessel coupled to the Windkessel model, either the flow rate Q_{out}

or the pressure P_{out} must be prescribed at the outlet of the vessel. For instance, in the case of a (P_{in}, Q_{out})-type 0D vessel, the flow rate Q_{out} has to be assigned at the outlet of the vascular segment, as illustrated in the top row of Table 2.1, which is computed from the coupling to the Windkessel element, as follows

$$Q_{out} = \frac{P - P_{wk}}{(R_d + R^1_{wk})}, \tag{2.85}$$

where P and R_d are pressure and (if present) distal resistance in the 0D vessel, respectively. On the other hand, if we consider, for example, a (Q_{in}, P_{out})-type 0D vessel, the pressure P_{out} to be enforced at the outlet of the vessel, as displayed in the second row of Table 2.1, can be calculated as

$$P_{out} = P_{wk} + R^1_{wk} Q, \tag{2.86}$$

where Q is the flow rate in the 0D vessel coupled to the RCR element.

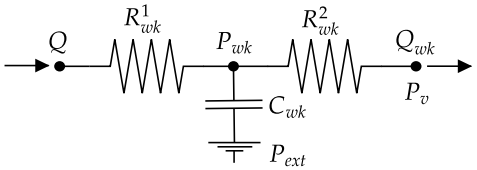
Alternatively, if terminal vessels are coupled to single-resistance terminal elements, we simply get

$$Q_{out} = \frac{P - P_v}{(R_d + R_{wk})} \qquad \text{or} \qquad P_{out} = P_v + R_{wk} Q, \tag{2.87}$$

where R_{wk} is now the only total peripheral resistance to the flow in the resistive terminal element.

We observe that, in general, RCR Windkessel models and single-resistance elements may be also coupled to the inlet of 0D vessels. In this case, the pressure P_{in} or the flow rate Q_{in} to be prescribed at the inlet of the 0D vessel can be computed in a similar way by the coupling to the terminal element, by modifying relations (2.85)-(2.86) or (2.87) accordingly.

FIGURE 2.3: Schematic representation of a RCR Windkessel terminal model.



2.6 Numerical methods

In this section, we present the numerical scheme used to numerically solve the hyperbolic PDE system (2.9) of 1D blood flow and the numerical coupling strategy employed to solve junctions of 1D vessels; we also describe the numerical method adopted to integrate the ODE system (2.31) governing blood flow in 0D vessels and networks.

2.6.1 Numerical scheme for 1D blood flow model

System (2.1) governing 1D blood flow is solved using a second-order MUSCL-Hancock numerical scheme [149], where MUSCL stands for Monotonic Upstream-Centred Scheme for Conservation Laws, with ENO (Essentially Non-Oscillatory) reconstruction [66, 67] and numerical source computed following the ADER (Arbitrary high-order DERivatives Riemann solver) approach [139, 138]. Since the original MUSCL-Hancock scheme was first formulated to deal only with conservation laws without source terms, the MUSCL-Hancock procedure was then extended to take into account also source terms via the ADER approach based on solution of the generalized Riemann Problem (GRP), formulated as in [30].

In order to approximate the solutions of system (2.1), we first discretize the one-dimensional space domain $[0, l]$ in $\overline{M}$ computational cells of constant mesh spacing $\Delta x = x_{i+\frac{1}{2}} - x_{i-\frac{1}{2}}$, where each cell $I_i = (x_{i-\frac{1}{2}}, x_{i+\frac{1}{2}})$ has center located in x_i, with $x_{i\pm\frac{1}{2}} = x_i \pm \frac{\Delta x}{2}$, for $i = 1, \ldots, \overline{M}$. The time domain $[0, t_{\text{End}}]$ is

also discretized into a discrete set of temporal levels with time step $\Delta t^n = t^{n+1} - t^n$ constrained by the usual Courant-Friedrichs-Lewy (CFL) stability condition. Then, if we consider system (2.1) written under the balance law form (2.9), given the approximate solution $\boldsymbol{Q}_i^n$ at time t^n in each cell I_i, we can evolve the numerical solution to time $t^{n+1} = t^n + \Delta t^n$ by using a finite volume method of the form

$$\boldsymbol{Q}_i^{n+1} = \boldsymbol{Q}_i^n - \frac{\Delta t^n}{\Delta x}\left[\boldsymbol{F}_{i+\frac{1}{2}} - \boldsymbol{F}_{i-\frac{1}{2}}\right] + \Delta t^n \boldsymbol{S}_i, \tag{2.88}$$

where $\boldsymbol{F}_{i+\frac{1}{2}}$ is the numerical flux that approximates the time-integral average over $[t^n, t^{n+1}]$ of the physical flux $\boldsymbol{F}$ at the cell interface $x = x_{i+\frac{1}{2}}$, while $\boldsymbol{S}_i$ is the numerical source in cell I_i that approximates the volume-integral average over $V_i^n = [x_{i-\frac{1}{2}}, x_{i+\frac{1}{2}}] \times [t^n, t^{n+1}]$ of the source term $\boldsymbol{S}$. Finite volume schemes (2.88) are indeed obtained by integrating the equations of system (2.9) on the control volume V_i^n and by introducing suitable approximations of the integral averages.
In the framework of Godunov-type schemes, the MUSCL-Hancock approach achieves second-order accuracy in space and time by computing the intercell flux $\boldsymbol{F}_{i+\frac{1}{2}}$ according to the following three steps:

(I) Data reconstruction and cell boundary values: based on the set of cell averages $\left\{\boldsymbol{Q}_i^n\right\}$, we obtain a first-degree reconstruction polynomial vector $\boldsymbol{\Phi}_i(x)$ for each cell I_i by finding a linear polynomial $\varphi_{l,i}(x)$ for each component of the vector of conserved variables, that is

$$\varphi_{l,i}(x) = w_{l,i}^n + (x - x_i)\Delta_{l,i}, \quad \text{for } l = 1, 2, \tag{2.89}$$

where $w_{l,i}^n$ is the l-th component of vector $\boldsymbol{Q}_i^n$ and $\Delta_{l,i}$ is the associated slope of its reconstruction polynomial $\varphi_{l,i}(x)$. Here, the slopes $\Delta_{l,i}$ for all components $w_{l,i}^n$ are computed by using the ENO criterion to preserve conservation and non-oscillatory properties. The boundary extrapolated values are then computed as follows

$$\boldsymbol{Q}_i^L = \boldsymbol{\Phi}_i(x_{i-\frac{1}{2}}), \quad \boldsymbol{Q}_i^R = \boldsymbol{\Phi}_i(x_{i+\frac{1}{2}}). \tag{2.90}$$

(II) Evolution of boundary extrapolated values by a time $\frac{\Delta t^n}{2}$ accounting for source term

$$\begin{cases} \overline{\boldsymbol{Q}}_i^L = \boldsymbol{Q}_i^L - \frac{1}{2}\frac{\Delta t^n}{\Delta x}\left[\boldsymbol{F}(\boldsymbol{Q}_i^R) - \boldsymbol{F}(\boldsymbol{Q}_i^L)\right] + \frac{\Delta t^n}{2}\boldsymbol{S}(\boldsymbol{Q}_i^L), \\ \overline{\boldsymbol{Q}}_i^R = \boldsymbol{Q}_i^R - \frac{1}{2}\frac{\Delta t^n}{\Delta x}\left[\boldsymbol{F}(\boldsymbol{Q}_i^R) - \boldsymbol{F}(\boldsymbol{Q}_i^L)\right] + \frac{\Delta t^n}{2}\boldsymbol{S}(\boldsymbol{Q}_i^R). \end{cases} \tag{2.91}$$

(III) Solution of a classical Riemann problem with piecewise constant data $\left(\overline{\boldsymbol{Q}}_i^R, \overline{\boldsymbol{Q}}_{i+1}^L\right)$ to obtain the similarity solution $\boldsymbol{Q}_{i+\frac{1}{2}}\left(\frac{x}{t}\right)$ and compute the intercell flux as

$$\boldsymbol{F}_{i+\frac{1}{2}} = \boldsymbol{F}\left(\boldsymbol{Q}_{i+\frac{1}{2}}(0)\right), \tag{2.92}$$

where $\boldsymbol{Q}_{i+\frac{1}{2}}(0)$ denotes the value of $\boldsymbol{Q}_{i+\frac{1}{2}}\left(\frac{x}{t}\right)$ at $\frac{x}{t} = 0$. Any approximate Riemann solver can be used to solve the Riemann problem. In this work, we adopt the HLL approximate Riemann solver [65, 138].

As last step, to compute the numerical source $\boldsymbol{S}_i$ we proceed by following the ADER approach [139] and we set

$$\boldsymbol{S}_i = \boldsymbol{S}\left(\boldsymbol{Q}_i^n + \frac{\Delta t^n}{2}\left[-\boldsymbol{A}(\boldsymbol{Q}_i^n)\Delta_i + \boldsymbol{S}(\boldsymbol{Q}_i^n)\right]\right), \tag{2.93}$$

which is obtained by approximating the volume-integral average of the source term $\boldsymbol{S}(\boldsymbol{Q}(x,t))$ by using the midpoint rule in space and time, where the midpoint value $\boldsymbol{Q}\left(x_i, \frac{\Delta t^n}{2}\right)$ is computed by performing a Taylor expansion in time and applying the Cauchy-Kowalewski method at point x_i.

2.6.2 1D numerical coupling strategy

In Section 2.5.1, we have described the 1D coupling approach adopted to join an arbitrary number of 1D vessels. In the simplest case, the initial condition states $\boldsymbol{Q}_k^{1D}$, with $k = 1, \dots, N$, provided by the 1D vessels to the Riemann problem (2.74), are given by the first-order cell-averaged solutions $\left\{ \boldsymbol{Q}_{k,i}^n \right\}$, with either $i = 1$ if $x_J^k = 0$, namely if the k-th vessel shares its left vertex with the junction, or $i = \overline{M}_k$ if $x_J^k = l_k$, that is if the k-th vessel shares its right vertex with the junction, where $\overline{M}_k$ is the number of computational cells of the k-th vessel, for $k = 1, \dots, N$. However, the resulting numerical coupling strategy to compute the unknown boundary states $\boldsymbol{Q}_k^*$, with $k = 1, \dots, N$, and evolve the solution from time t^n to time $t^{n+1} = t^n + \Delta t^n$ is clearly first-order accurate in space and time.

In general, high-order numerical coupling between 1D vessels can be achieved by following, for instance, the methodology presented in Müller and Blanco [96] or the approach introduced in Borsche and Kall [23]. Here, to obtain a 1D numerical coupling strategy that is second-order accurate in space and time and to preserve the global second-order accuracy over the entire 1D network, departing from the work of Müller and Blanco [96] we adopt a simplified approach, as follows. In the RP defined at the junction interface, it is sufficient to replace the cell-averaged values by the evolved boundary extrapolated values defined in step (II) of MUSCL-Hancock scheme, that is

$$\boldsymbol{Q}_k^{1D} = \begin{cases} \overline{\boldsymbol{Q}}_{k,1}^{L,n}, & \text{if } x_J^k = 0, \\ \overline{\boldsymbol{Q}}_{k,\overline{M}_k}^{R,n}, & \text{if } x_J^k = l_k. \end{cases} \tag{2.94}$$

In particular, if the k-th vessel shares its left vertex with the junction, that is $x_J^k = 0$, then we will consider the left evolved boundary extrapolated value in the first computational cell $\overline{\boldsymbol{Q}}_{k,1}^{L,n}$; whereas, if the vessel shares its right vertex with the junction, namely $x_J^k = l_k$, in this case the initial condition state $\boldsymbol{Q}_k^{1D}$ will be given by the right evolved boundary extrapolated value in the last computational cell $\overline{\boldsymbol{Q}}_{k,\overline{M}_k}^{R,n}$ of the vessel 1D domain.

Equipped with these initial condition states, the Riemann problem can be solved as illustrated in Section 2.5.1 to obtain the unknown boundary states $\boldsymbol{Q}_k^*$, with $k = 1, \dots, N$. By adopting the midpoint integration rule to approximate the time integral of the interface flux, the computed boundary state vectors are finally used to evaluate the boundary numerical fluxes in the finite volume formula (2.88) for the 1D vessels converging at the junction

$$\begin{cases} \boldsymbol{F}_{\frac{1}{2}}^k = \boldsymbol{F}(\boldsymbol{Q}_k^*) \approx \dfrac{1}{\Delta t^n} \displaystyle\int_{t^n}^{t^{n+1}} \boldsymbol{F}\left(\boldsymbol{Q}(x_{\frac{1}{2}}, t) \right) dt, & \text{if } x_J^k = 0, \\ \boldsymbol{F}_{\overline{M}_k + \frac{1}{2}}^k = \boldsymbol{F}(\boldsymbol{Q}_k^*) \approx \dfrac{1}{\Delta t^n} \displaystyle\int_{t^n}^{t^{n+1}} \boldsymbol{F}\left(\boldsymbol{Q}(x_{\overline{M}_k + \frac{1}{2}}, t) \right) dt, & \text{if } x_J^k = l_k, \end{cases} \tag{2.95}$$

for $k = 1, \dots, N$.

Clearly, the same choice of the initial condition state $\boldsymbol{Q}^{1D}$ is also adopted to compute boundary conditions, such as a prescribed inflow boundary condition and the coupling of terminal vessels to *RCR* Windkessel or single-resistance terminal elements. In fact, using a lower-order coupling approach to treat boundary conditions may affect the global order of accuracy of the solution in the 1D vessel.

2.6.3 Numerical scheme for 0D blood flow models

Along with the 1D discretization considered so far, a vascular network can also be entirely modeled by using 0D vessels. In particular, as discussed in Section 2.5.3, in order to arrange compatible segment types into a structure, the 0D configuration to be used for each vessel of the network has to be chosen so that inlets and outlets of vessels converging at the 0D junctions are all coupled appropriately. Hence, we end up

with just one system of ODEs describing the dynamics of the entire network, where the single subsystems corresponding to each vessel are not isolated, but are connected to each other via the variables prescribed at the inlets and outlets of vessels. Indeed, pressures and/or flow rates imposed at the inlets and outlets of vessels converging at 0D junctions are defined by the state of the adjacent vessels, in order to ensure the conservation of mass and continuity of pressure across each junction. Clearly, appropriate boundary conditions are prescribed at those inlets and outlets that do not converge to 0D junctions.
The resulting ODE system can be written in compact form as follows

$$\frac{d}{dt}\boldsymbol{Y}(t) = \boldsymbol{B}(t, \boldsymbol{Y}(t), \boldsymbol{Y}^D(t)), \quad \boldsymbol{Y}(t=0) = \boldsymbol{Y}_0, \tag{2.96}$$

where $\boldsymbol{Y} \in \mathbb{R}^{N_S}$ is the global unknown vector composed of the state variables sub-vectors $\boldsymbol{y}_i$, $i = 1, \dots, N$, of the N vessels of the network, with N_S being the total number of the system state variables. $\boldsymbol{Y}_0$ is the initial condition vector, $\boldsymbol{B}$ is the nonlinear vector function on the right-hand side of the ODE system and $\boldsymbol{Y}^D \in \mathbb{R}^{N_D}$ is the vector of the data prescribed at inlets and outlets of vessels that do not converge at 0D junctions, whose size N_D is determined by the number of conditions prescribed at such inlets and outlets. Specifically, for a (P_{in}, Q_{out})- or (Q_{in}, P_{out})-type 0D vessel we have $\boldsymbol{y}_i = (V_i(t), Q_i(t))$; for a (P_{in}, P_{out})-type 0D vessel the associated state vector is given by $\boldsymbol{y}_i = (V_i(t), Q_i(t), Q_{d,i}(t))$; while $\boldsymbol{y}_i = (V_i(t), Q_i(t), V_{d,i}(t))$ is the vector of state variables for a (Q_{in}, Q_{out})-type 0D vessel. Coupling conditions at junctions between 0D vessels are incorporated into $\boldsymbol{B}$ via $\boldsymbol{Y}$, as they only depend on the state variables of the 0D vessels coupled together. On the other hand, the vector $\boldsymbol{Y}^D$ can include conditions coming from the coupling of a 0D vessel to a single-resistance or a RCR terminal model, as well as external sources $f_{ext}(t)$ to the vessels, such as a prescribed inflow at the inlet of the aorta.
Then, the global ODE system (2.96) is solved using the four-step explicit fourth-order Runge-Kutta (RK4) method, where the coupling conditions between 0D vessels and any other conditions to be prescribed at the borders of the 0D network are computed and updated at each intermediate step of RK4 method.

2.7 Numerical experiments

In this section, we validate the ability of the derived nonlinear 0D models to reproduce the essential blood flow distribution and the main features of pressure and flow waveforms in networks of deformable vessels with respect to the well-known and widely used 1D blood flow model (2.1), at a much lower computational cost.
We reproduce several benchmark problems proposed in [22]. First, we consider a simple test case: a model of blood flow in the aortic bifurcation (Section 2.7.3). Then, we assess the results in two different arterial networks: the 37-artery network of the aorta and the largest central system arteries constructed in [89], for which *in-vitro* pressure and flow waveforms were acquired in [89] (Section 2.7.4), and a reduced version of the ADAN model developed by Blanco *et al.* [17, 16], which contains the largest 56 systemic arteries of the human circulation (Section 2.7.5), referred to as ADAN56. For each test case, 0D results of pressure and flow rate in each vessel of the network are qualitatively and quantitatively compared to the 1D results obtained from the 1D model (2.1). Furthermore, in order to assess the properties of the newly derived nonlinear 0D models, we also compare the results from the nonlinear and the linear 0D models, where in the latter the convective terms are neglected *a-priori*, the model parameters are constant and the pressure-volume relation is linear. For each test case, we provide graphical comparisons supported by error tables.
The relative error metrics for pressure P and flow rate Q are introduced in Section 2.7.1. Before performing the 0D simulations and compare 0D results to 1D results, a detailed analysis of the contribution and relative importance of the convective component within the momentum equation is carried out in Section 2.7.2, to decide whether it is reasonable or not to neglect the convective terms in the 0D models.

The number of computational cells used in the j-th vessel of each 1D network is defined as

$$\overline{M}_j = \max\left\{\left\lceil \frac{l_j}{\Delta x_{\max}} \right\rceil, 2\right\}, \tag{2.97}$$

where l_j is the length of vessel j and $\Delta x_{\max}$ is the maximum mesh size. For all numerical experiments, before setting the maximum mesh size $\Delta x_{\max}$, a mesh convergence study of the 1D solution was first carried out in order to select a reference sufficiently accurate 1D solution for the comparison with the 0D results. The values of $\Delta x_{\max}$, which ensure a 1D mesh-independent solution, used in the different benchmark problems are displayed, together with all other computational parameters for the 1D/0D simulations, in Table 2.3.

The time step adopted to integrate in time the ODE system (2.96) for each 0D network using RK4 method is also chosen such that the stability of the explicit numerical scheme and the mesh independence of the solution are guaranteed. The time steps selected for each arterial network are reported in Table 2.3. Furthermore, it is worth also noting that numerical experiments have shown that the restrictions on the allowable time step ensuring the stability of RK4 method to solve the different arterial networks are the same when using linear and nonlinear 0D models. Indeed, as can be observed from Table 2.3, for each arterial network we adopt the same time step Δt to solve both the linear and nonlinear fully 0D network configurations. Then, our numerical results lead us to the conclusion that the coupling between several nonlinear 0D models is not affecting the numerical stability of the discretized model.

TABLE 2.3: Computational parameters adopted in the 1D/0D numerical simulations for the three arterial networks.

Parameter	**Aortic bif.**	**37-artery network**	**ADAN56 model**
Max mesh size, $\Delta x_{\max}$	2 mm	1 mm	1 mm
CFL number, CFL	0.9	0.9	0.9
RK4 time step, Δt	10^{-3} s	10^{-4} s	10^{-4} s
Cardiac cycle, T_0	1.1 s	0.827 s	1.0 s
Final time, t_{End}	29.7 s	24.81 s	15.0 s

2.7.1 Error calculations

To provide a quantitative assessment of the predicted waveforms compared with the reference 1D solution and to measure the benefit, if any, that we get by preserving certain nonlinearities of the original 1D model in the newly derived 0D models, we introduce the following relative error metrics for pressure P and flow rate Q

$$\begin{aligned}
\varepsilon_P^{\text{RMS}} &= \sqrt{\frac{1}{n}\sum_{i=1}^{n}\left(\frac{P_i^{0D}-P_i^{1D}}{P_i^{1D}}\right)^2}, & \varepsilon_Q^{\text{RMS}} &= \sqrt{\frac{1}{n}\sum_{i=1}^{n}\left(\frac{Q_i^{0D}-Q_i^{1D}}{\max_j\left(Q_j^{1D}\right)}\right)^2}, \\
\varepsilon_P^{\text{SYS}} &= \frac{\max_i\left(P_i^{0D}\right)-\max_i\left(P_i^{1D}\right)}{\max_i\left(P_i^{1D}\right)}, & \varepsilon_Q^{\text{SYS}} &= \frac{\max_i\left(Q_i^{0D}\right)-\max_i\left(Q_i^{1D}\right)}{\max_i\left(Q_i^{1D}\right)}, \\
\varepsilon_P^{\text{DIAS}} &= \frac{\min_i\left(P_i^{0D}\right)-\min_i\left(P_i^{1D}\right)}{\min_i\left(P_i^{1D}\right)}, & \varepsilon_Q^{\text{DIAS}} &= \frac{\min_i\left(Q_i^{0D}\right)-\min_i\left(Q_i^{1D}\right)}{\max_i\left(Q_i^{1D}\right)},
\end{aligned} \tag{2.98}$$

where $i = 1, \ldots, n$ are time points over the cardiac cycle at which the solution is sampled, P^{0D} and Q^{0D} are 0D pressure and flow, either from the nonlinear or the linear 0D models, and P^{1D} and Q^{1D} are 1D pressure and flow at the midpoint of the vessel. We compare the solution obtained using 1D models sampled at this location since this is a commonly observed variable in this research field. Other choices are possible (like, for example, averaged quantities over the 1D domain) and would not affect the conclusions of this work (results not reported here).

All error metrics are calculated over a single cardiac cycle, once the numerical results are in the periodic regime. Periodicity is defined as the distance in L^∞-norm between the normalized solutions over two consecutive cardiac cycles to be smaller than a threshold of 10^{-3} (pressure and cross-sectional area are normalized by the mean pressure and mean cross-sectional area, respectively, over the cardiac cycle; flow rate is normalized by the maximum flow over the cardiac cycle).

2.7.2 Analysis of relative contribution of convective terms

We note that we have made no assumptions yet about the contribution of the convective terms in the family of nonlinear 0D models governed by the system of ODEs (2.31). A first insight into the role of the convective term in the momentum balance equation of the 1D blood flow model (2.1) and its relative importance especially with respect to the pressure term is given by the dimensional analysis of the 1D equations carried out in Section 2.2.2 and, in the following, applied to the different arterial networks considered. The coefficients γ_C and γ_P characterizing the convective and pressure terms, respectively, in the nondimensional momentum balance equation (2.18) are defined in terms of the average flow velocity U_0. Since for all the arterial networks of interest 1D simulations of blood flow have been performed to obtain 1D mesh-independent solutions, the average flow velocity U_{1D}^{mean} and the maximum flow velocity U_{1D}^{max} can be computed from the 1D results for each vessel of each network. Then, from the estimated velocities, we are able to quantify the nondimensional coefficients (2.19) and to assess the contribution and relative importance of the convective, pressure and friction terms within the momentum equation. Values of the ratios γ_C/γ_P and γ_F/γ_P are displayed for the aortic bifurcation, some vessels of both the 37-artery network and ADAN56 model in Table 2.4. Furthermore, for the 37-artery network maximum and mean values of the ratio γ_C/γ_P are

$$(\gamma_C/\gamma_P)_{\text{max}}^{\text{net37}} = \begin{cases} 0.00259 & \text{if } U_0 = U_{1D}^{\text{mean}}, \\ 0.00947 & \text{if } U_0 = U_{1D}^{\text{max}}, \end{cases} \qquad (\gamma_C/\gamma_P)_{\text{mean}}^{\text{net37}} = \begin{cases} 4.801\text{e-}04 & \text{if } U_0 = U_{1D}^{\text{mean}}, \\ 0.00223 & \text{if } U_0 = U_{1D}^{\text{max}}, \end{cases} \tag{2.99}$$

where the two maximum values of γ_C/γ_P are found in the left anterior tibial and in the left iliac-femoral III arteries, respectively, while for the reduced ADAN56 model we have

$$(\gamma_C/\gamma_P)_{\text{max}}^{\text{adan56}} = \begin{cases} 0.00791 & \text{if } U_0 = U_{1D}^{\text{mean}}, \\ 0.09804 & \text{if } U_0 = U_{1D}^{\text{max}}, \end{cases} \qquad (\gamma_C/\gamma_P)_{\text{mean}}^{\text{adan56}} = \begin{cases} 0.00195 & \text{if } U_0 = U_{1D}^{\text{mean}}, \\ 0.02233 & \text{if } U_0 = U_{1D}^{\text{max}}. \end{cases} \tag{2.100}$$

where the two maximum values of γ_C/γ_P are both achieved in the thoracic aorta VI.
The magnitude of these coefficient ratios clearly suggests that the pressure gradient is the dominating term in the momentum balance equation in (2.1), with respect to the convective and the friction terms. In particular, from Table 2.4 we observe that, on the one hand, the frictional losses become more and more important as we consider vessels of consecutive generations of bifurcations more distant from the aortic trunk, while, on the other hand, the pressure term is always significantly dominating over the convective component. As expected, the pressure gradient represents the main term in the momentum balance equation, while the contribution of the convective term turns out to be consistently smaller in all vessels of the three arterial networks. In addition, this analysis shows that overall the ratio γ_C/γ_P is larger in ADAN56 model than in the 37-artery network, suggesting that in ADAN56 model the contribution of the convective term is of greater importance.
Moreover, the result $\gamma_C/\gamma_P \ll 1$ found for these arterial networks implies $Fr \ll 1$, that is $|U_0| \ll c_0$, thus concluding that we are under strongly sub-critical flow conditions.

Equipped with these findings, we conclude that the convective terms can be neglected in the family of nonlinear 0D models derived in Section 2.3 according to the following two main motivations:

TABLE 2.4: Quantitative assessment of the relative importance of the convective, pressure and friction terms within the momentum balance equation, by computing the ratio between coefficients γ_C and γ_P and between coefficients γ_F and γ_P, for the vessels of the aortic bifurcation, the 37-artery network and ADAN56 model.

		$U_0 = U_{1D}^{\text{mean}}$		$U_0 = U_{1D}^{\text{max}}$	
Test case	**Vessel**	γ_C/γ_P	γ_F/γ_P	γ_C/γ_P	γ_F/γ_P
Aortic bifurcation	Aorta	2.537e-05	7.915e-05	0.00233	7.584e-04
	Iliac artery	2.027e-05	1.214e-04	9.479e-04	8.303e-04
37-artery network	Aortic arch II	1.047e-04	2.085e-05	0.00266	1.050e-04
	Thoracic aorta II	1.071e-04	7.530e-05	0.00273	3.802e-04
	L subclavian I	2.199e-04	0.00174	0.00195	0.00518
	R iliac-femoral II	3.344e-04	0.00393	0.00327	0.01227
	L ulnar	5.963e-04	0.00734	0.00120	0.01041
	R anterior tibial	7.988e-04	0.01186	0.00200	0.01878
	R ulnar	6.389e-04	0.00603	0.00105	0.00775
	Splenic	0.00121	0.01436	0.00223	0.01948
ADAN56 model	Aortic arch I	0.00106	8.842e-05	0.02354	4.168e-04
	Thoracic aorta III	0.00249	5.660e-05	0.03793	2.209e-04
	Abdominal aorta V	0.00228	3.677e-04	0.04167	0.00157
	R common carotid	7.868e-04	9.420e-04	0.01311	0.00384
	R renal	0.00453	0.00157	0.01482	0.00284
	R common iliac	0.00224	0.00126	0.03577	0.00505
	R internal carotid	0.00106	0.00324	0.00994	0.00993
	R radial	0.00256	0.03949	0.01074	0.08010
	R internal iliac	0.00189	0.00230	0.01100	0.00555
	R posterior interosseous	0.00135	0.08253	0.00329	0.12892
	R femoral II	1.271e-04	0.00247	0.03294	0.03983
	R anterior tibial	0.00102	0.04334	0.01833	0.18414

- the dimensional analysis performed so far shows that the pressure gradient is significantly larger with respect to the convective term in the 1D momentum balance equation;
- the ultimate goal of our work is to apply this family of nonlinear 0D models to larger and more complex networks of vessels, such as the global, closed-loop, multiscale model of Müller and Toro [99, 100] and the complete ADAN model developed by Blanco *et al.* [17, 16], in order to construct hybrid 1D-0D networks in the attempt of facing the issues of computational efficiency and execution time. These newly derived 0D models would then be applied not to all vessels of the network, but to small vessels where it is well-known that the convective terms are negligible.

Finally, it is worthy to note that numerical experiments (not reported) have shown that including the convective terms into the 0D models is not a straightforward operation. Indeed, numerical difficulties arise in solving the resulting 0D models even by using implicit methods and ODE solvers for stiff problems. We claim that these numerical issues are not related to the instability or stiffness of the ODE systems to be solved, but that the source of these problems lies in the fact that, according to the coupling approach described in Section 2.5.3, the input data to be prescribed at the inlet/outlet of the vessels converging at the 0D junction are defined by the state of their adjacent compartments, but in each 0D vessel no interaction between the input data and internal vessel state is enforced. This coupling procedure is indeed different from the approach usually adopted for 1D junctions, where in the Riemann problem to be solved at the 1D junction the unknown boundary state vectors are connected not only among themselves, but also to the vessel initial condition states via non-linear waves. As a consequence, this produces ambiguity in determining which are the correct flow rates Q_L, Q_R and cross-sections A_L, A_R to be used in the convective terms difference originally included in (2.31).

In conclusion, dealing with convective terms in 0D blood flow models is clearly an open problem which, to the best of our knowledge, has never been addressed in previous scientific works. Indeed, in the standard derivation of 0D blood flow models, convective terms are commonly neglected under the assumption that the contribution of the convective terms difference is small compared to the other terms in the momentum balance equation and can thus be discarded. No further discussion is found in the literature about this topic, which remains to be further investigated.

2.7.3 Aortic bifurcation model

We simulate the abdominal aorta branching into the two iliac arteries using a single bifurcation model, consisting of a three-vessel junction, as reported in [22]. Both iliac arteries are coupled to *RCR* Windkessel terminal models of the rest of the systemic circulation. The geometrical and mechanical properties of this model are taken from [22] and summarized in Table 2.5. 1D/0D initial areas $A(x,0)/\widehat{A}(0)$ are computed using the tube law (2.6) with $P_0 = P_d$ and $A_0 = A_d$, where A_d is the vessel cross-sectional area at diastolic pressure P_d. The inflow boundary condition $q_{in}(t)$ prescribed at the inlet of the abdominal aorta is an *in-vivo* signal taken from [153] and available in the Supporting Information of [22]. For the 0D simulations, the abdominal aorta (parent vessel) is discretized using a (Q_{in}, Q_{out})-type 0D vessel, while both iliac arteries (daughter vessels) are represented as (P_{in}, P_{out})-type 0D vessels. Flow rate Q_{in} at the inlet of the parent vessel is given by the periodic inflow boundary condition; flow rate Q_{out} at the outlet of the aorta and pressure P_{in} at the inlet of both iliac arteries are determined by imposing the coupling conditions at a 0D junction; pressure P_{out} at the outlet of both parent vessels is defined by the adjacent *RCR* Windkessel terminal element. The computational parameters of the 1D/0D simulations are chosen according to Table 2.3.

Figure 2.4 shows a qualitative comparison of pressure and flow waveforms for the aortic bifurcation model. We can observe that, compared to the reference 1D results, the amplitude and the shape of these waveforms are well-captured by both the nonlinear and linear 0D results, with differences between the two 0D models that can not be appreciated in the scale of the figures. However, the 0D solution becomes less accurate when using the linear pressure-volume relation and constant parameters C_0, R_0 and L_0 in the 0D simulations. This is evident in the systolic phase of the pressure waveform, where the systolic peak corresponding to the linear 0D results is higher with respect to the reference 1D results, while the pressure peak is perfectly captured by the nonlinear 0D model. These observations are confirmed also by the quantitative assessment. Relative errors were determined with respect to the 1D solution and are displayed in Table 2.6. Relative errors for pressure and flow rate are consistently very small, relative root mean square errors are all smaller than 0.5% for the pressure and smaller than 1% for the flow rate. Furthermore, relative errors in the nonlinear 0D results are in general smaller than the corresponding relative errors in the linear 0D results.

2.7.4 37-artery network

We consider the arterial network presented in [89, 5], for which *in-vitro* pressure and flow measurements were acquired at multiple locations. This arterial tree is made up of 37 silicone vessels representing the largest central systemic arteries of the human vascular system. A schematic representation of the 37-artery network is shown in Figure 2.5. For the detailed topology of the network, the reader is referred to [89]. At the inlet of the ascending aorta (vessel 1 in Fig. 2.5), the flow rate measured *in-vitro* is prescribed as a periodic inflow boundary condition $q_{in}(t)$. Outflow boundary conditions are prescribed by coupling terminal vessels to single-resistance models, characterizing the peripheral resistance to the flow. In all vessels, initial 1D/0D cross-sectional areas $A(x,0)/\widehat{A}(0)$, corresponding to the zero initial pressure prescribed, are

TABLE 2.5: Geometrical and mechanical properties of the aortic bifurcation model from [22].

Property	**Value**	
Blood density, ρ	1.060 g/cm^3	
Blood viscosity, μ	0.04 dyne·s/cm^2	
Velocity profile order, ζ	9	
Diastolic pressure, P_d	$9.4\hat{6}\cdot10^4$ dyne/cm^2	
External pressure, p_{ext}	0	
	Aorta	**Iliac**
Length, l	8.6 cm	8.5 cm
Radius at diastolic pressure, r_d	0.86 cm	0.60 cm
Area at diastolic pressure, A_d	2.3235 cm^2	1.1310 cm^2
Wall thickness, h	1.032 mm	0.72 mm
Young's modulus, E	$5.0\cdot10^6$ dyne/cm^2	$7.0\cdot10^6$ dyne/cm^2
WK resistance, R_1	-	$6.8123\cdot10^2$ dyne·s/cm^5
WK compliance, C	-	$3.6664\cdot10^{-5}$ cm^5/dyne
WK resistance, R_2	-	$3.1013\cdot10^4$ dyne·s/cm^5
Outflow pressure, P_{out}	-	0
Initial cross-sectional area, $A(x,0)/\widehat{A}(0)$	1.8062 cm^2	0.94789 cm^2
Initial velocity, $u(x,0)/U(0)$	0	0
Initial pressure, $p(x,0)/P(0)$	0	0

TABLE 2.6: Aortic bifurcation. Relative errors (in %) for pressure and flow between for both nonlinear (0D-NL) and linear (0D-L) 0D results with respect to the 1D results (1D) at the midpoint of the vessel, computed according to the relative error metrics (2.98).

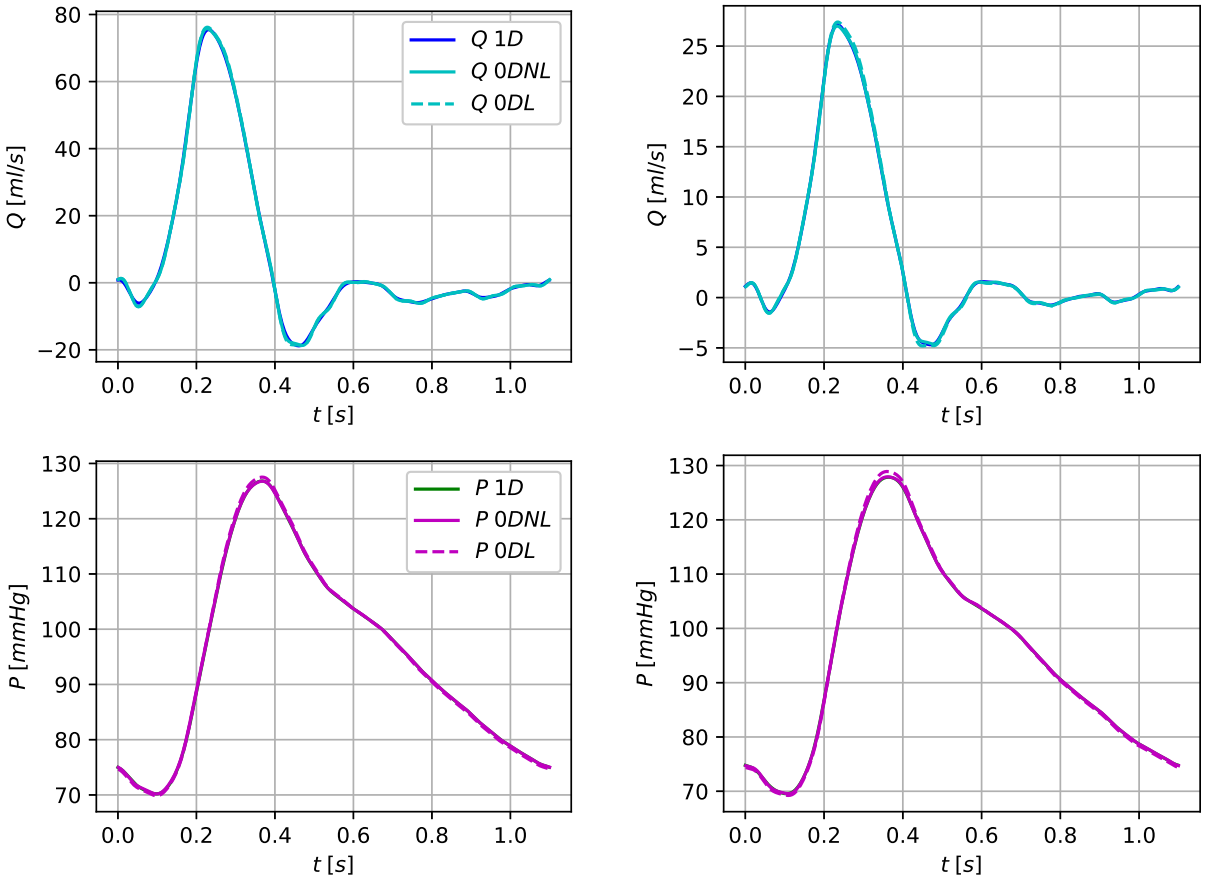
Vessel	**0D model**	$\varepsilon_P^{\text{RMS}}(\%)$	$\varepsilon_Q^{\text{RMS}}(\%)$	$\varepsilon_P^{\text{SYS}}(\%)$	$\varepsilon_Q^{\text{SYS}}(\%)$	$\varepsilon_P^{\text{DIAS}}(\%)$	$\varepsilon_Q^{\text{DIAS}}(\%)$
Abdominal aorta	0D-NL	0.231	0.620	-0.027	0.424	-0.013	0.127
	0D-L	0.437	0.680	0.551	0.970	-0.482	0.092
Iliac arteries	0D-NL	0.149	0.406	0.051	-0.484	0.010	0.212
	0D-L	0.462	0.695	0.823	1.010	-0.458	-0.445

computed using the tube law (2.6) with reference pressure $P_0 = P_d = 0$ and cross-sectional area $A_0 = A_d$. General parameters of this arterial network are given in Table 2.7. For a complete set of parameters, we refer the reader to [89, 5] and to the Supplementary Information of [22]. We note that, differently from the just cited works, the 1D results we present here do not include vessel tapering. For each vessel, the reference constant radius r_0, from which the reference cross-sectional area A_0 is computed, is obtained as the mean value between the cross-sectional radii at the inlet and outlet of the vessel, r_{in} and r_{out} respectively, given in [89, 22]. We point out that this is a limitation of this study that will be addressed in next part of the thesis.

For the 0D simulations, the first vessel of the arterial network, the ascending aorta, is discretized using a (Q_{in}, Q_{out})-type 0D vessel, terminal vessels, which are coupled to single-resistance terminal elements, are represented as (P_{in}, P_{out})-type 0D vessels, while all other vessels, which are not at the extremities of the network, are modeled as two-split (P_{in}, Q_{out})-type 0D vessels. Results are shown for two aortic segments (aortic arch II and thoracic aorta II), two vessels of the first generation of bifurcations (left subclavian I and right iliac-femoral II), two of the second generation (left ulnar and right anterior tibial) and two of the third generation (right ulnar and splenic). Qualitative comparisons between nonlinear 0D, linear 0D and reference 1D solutions are shown in Figure 2.6 for the aortic segments and in Figures 2.7-2.9 for the vessels of first, second and third generations, respectively. Table 2.8 displays the relative errors computed for both nonlinear and linear 0D results with respect to 1D results.

As expected, when we move to a more complex network, the differences between 0D and 1D results become

FIGURE 2.4: Aortic bifurcation. Comparison between 1D, nonlinear 0D and linear 0D results in the abdominal aorta (A) and in the iliac arteries (B). 1D/Q 1D: 1D numerical solution at the midpoint of the vessel; P 0DNL/Q 0DNL: 0D numerical solution from the nonlinear 0D models; P 0DL/Q 0DL: 0D numerical solution from the linear 0D models.



(A) Abdominal aorta

(B) Iliac arteries

more significant, even when adopting the nonlinear 0D models. In Figures 2.6-2.9 we observe that, especially in the flow waveforms, some oscillations are amplified, while other oscillations are not captured by the 0D models with respect to the reference 1D solution. However, if we focus on the nonlinear 0D results, we can conclude that they are quite satisfactory: overall, the predicted pressure and flow waveforms are in good agreement with the 1D results and, given the complexity of the flow to be simulated, the essential features, shape and amplitude, of these waves are well-captured. Furthermore, from this benchmark problem we clearly see how the nonlinearity included in the 0D models, through the nonlinear pressure-area relation and the nonlinear parameters, strongly improves the 0D results, especially the pressure waveforms: in general, the linear 0D solution overestimates the systolic peak in pressure, while the pressure peak reproduced by the nonlinear 0D results is much more in agreement with the reference 1D results.

All these observations are confirmed also by the quantitative assessment presented in Table 2.8. Relative errors in the nonlinear 0D results are overall smaller than the corresponding relative errors in the linear 0D results. Indeed, when moving from the linear to the nonlinear 0D models, the RMS relative errors decrease and, in particular, the systolic relative errors in pressure are significantly reduced, suggesting that overall the proposed family of nonlinear 0D models is able to better reproduce pressure and flow waveforms and to capture their essential features, such as the systolic peak of the pressure wave. Indeed, since the nonlinearity mostly enters in the evaluation of the pressure via the nonlinear pressure-area relation, this

improvement is mainly reflected on the pressure waveforms, as expected. For the nonlinear 0D results, RMS relative errors are all smaller than 6.0% for the pressure and smaller than 15.0% for the flow rate; systolic relative errors are all smaller than 4.0% for the pressure and smaller than 6.0% for the flow rate, with an exception in the right iliac-femoral II artery, where the systolic peak in the flow rate seems to be slightly overestimated.

FIGURE 2.5: Schematic representation of the 37-artery network reported in [5]. Figure reproduced with permission [5].

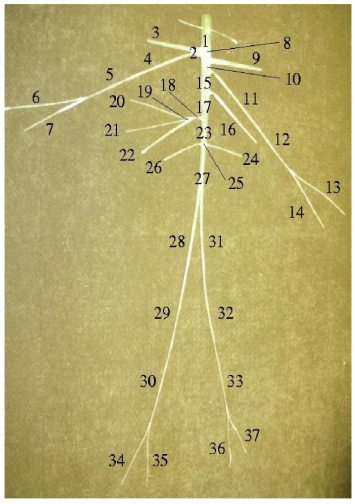


TABLE 2.7: General model parameters of the 37-artery network.

Property	Value
Blood density, ρ	1.050 g/cm^3
Blood viscosity, μ	0.025 dyne·s/cm^2
Velocity profile order, ζ	9
Young's modulus, E	1.2·10^7 dyne/cm^2
Diastolic pressure, P_d	0
External pressure, p_{ext}	0
Outflow pressure, P_{out}	4.2663·10^3 dyne/cm^2 (≈3.2 mmHg)
Initial velocity, $u(x,0)/U(0)$	0
Initial pressure, $p(x,0)/P(0)$	0

2.7.5 Reduced ADAN56 model

The last benchmark model considered is a reduced version of the anatomically detailed arterial network model developed by Blanco *et al.* [17, 16]. This model, hereafter referred to as ADAN56 model, was presented in Reference [22] and contains the largest 56 vessels of the human arterial system. A schematic representation of ADAN56 model is displayed in Figure 2.10. General properties of this arterial model are reported in Table 2.9, while for the topology of the network and a complete set of parameters, we refer the reader to [22]. The periodic inflow boundary condition $q_{in}(t)$ prescribed at the inlet of the aorta (vessel 1 in Fig. 2.10), inspired from one of the inflow signals reported in [104], is taken from [22]. Terminal vessels are coupled to RCR Windkessel models. In the tube law (2.6), we set $P_0 = P_d = 10^5$ dyne/cm^2 (≈75 mmHg) and $A_0 = A_d$, from which the 1D/0D initial cross-sectional areas $A(x,0)/\widehat{A}(0)$ corresponding to the prescribed initial pressure are computed in all vessels. The vessel wall thickness is computed using the

TABLE 2.8: 37-artery network. Relative errors (in %) for pressure and flow between for both nonlinear (0DNL) and linear (0DL) 0D results with respect to the 1D results (1D) at the midpoint of the vessel, computed according to the relative error metrics (2.98).

Vessel	**0D model**	$\varepsilon_P^{\mathrm{RMS}}(\%)$	$\varepsilon_Q^{\mathrm{RMS}}(\%)$	$\varepsilon_P^{\mathrm{SYS}}(\%)$	$\varepsilon_Q^{\mathrm{SYS}}(\%)$	$\varepsilon_P^{\mathrm{DIAS}}(\%)$	$\varepsilon_Q^{\mathrm{DIAS}}(\%)$
Aortic arch II	0D-NL	0.638	6.218	-0.205	5.532	0.983	7.135
	0D-L	2.780	7.641	4.958	5.443	-1.568	7.967
Thoracic aorta II	0D-NL	0.868	7.803	0.308	2.543	-0.161	-6.772
	0D-L	3.028	10.085	5.438	2.576	-2.150	5.367
L subclavian I	0D-NL	1.193	10.638	0.251	-4.304	0.369	-13.605
	0D-L	3.114	12.584	5.610	-6.796	-2.372	-16.745
R iliac-femoral II	0D-NL	2.560	13.841	1.786	10.405	-2.846	-6.015
	0D-L	6.286	20.628	8.489	11.780	-3.264	-10.194
L ulnar	0D-NL	2.839	7.199	2.401	-2.167	-1.141	-1.025
	0D-L	4.653	9.115	5.924	-3.247	-4.483	-2.019
R anterior tibial	0D-NL	5.291	7.785	3.600	-1.957	-2.675	4.733
	0D-L	10.635	11.526	7.854	-2.466	-8.565	0.104
R ulnar	0D-NL	2.766	8.322	1.855	0.160	-1.248	-2.766
	0D-L	3.829	8.849	4.992	4.683	-3.301	-0.366
Splenic	0D-NL	1.748	4.970	0.805	-0.422	-0.584	2.417
	0D-L	3.571	7.517	4.717	-0.519	-2.388	-0.251

empirical relation adopted for the complete ADAN model [17, 16] and obtained by curve fitting of the data about lumen radius r_0 and wall thickness h reported for a large number of arterial vessels in [10], that is

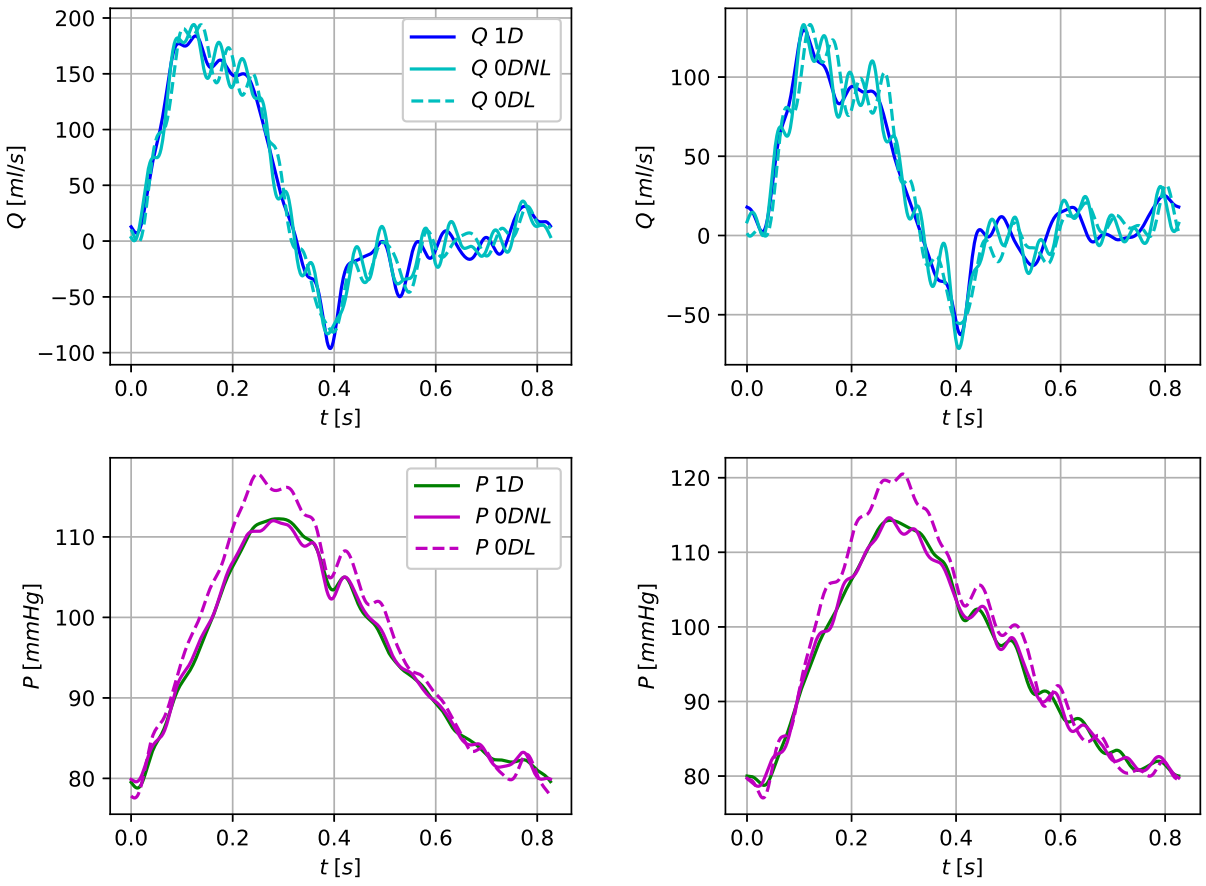
$$h = r_0 \left[\widetilde{a} \exp(\widetilde{b} r_0) + \widetilde{c} \exp(\widetilde{d} r_0) \right], \tag{2.101}$$

where r_0 is the vessel reference radius, related to A_0, $\widetilde{a} = 0.2802$, $\widetilde{b} = -5.053$ cm^{-1}, $\widetilde{c} = 0.1324$ and $\widetilde{d} = -0.1114$ cm^{-1}. As for the 37-artery network, also here we do not consider vessel tapering, but we assume all vessels to have a constant reference cross-sectional area A_0, related to the constant reference radius r_0 computed as the mean value between the proximal and distal radii given in [22].

For the 0D simulations, the choice of the 0D vessel configurations is the same as that for the 37-artery network: the first vessel of the arterial model, that is the first portion of the aortic arch, is of (Q_{in}, Q_{out})-type; terminal vessels are of (P_{in}, P_{out})-type and coupled to *RCR* Windkessel terminal elements; all other vessels of the network are modeled as two-split (P_{in}, Q_{out})-type 0D vessels. Results are shown for three aortic segments (aortic arch I, thoracic aorta III and abdominal aorta V), three first-generation vessels (right common carotid, right renal and right common iliac), three second-generation vessels (right internal carotid, right radial and right internal iliac) and three third-/fourth-generation vessels (right posterior interosseous, right femoral and right anterior tibial). Qualitative comparisons between nonlinear 0D, linear 0D and reference 1D solutions are illustrated in Figure 2.11 for the aortic segments and in Figures 2.12-2.14 for the vessels of first, second and third/fourth generations, respectively. Table 2.10 summarizes the relative errors computed for both nonlinear and linear 0D results with respect to 1D results.

As for the 37-artery network considered in Section 2.7.4, for this arterial model we also observe that, even if some oscillations in the pressure and flow waveforms are amplified, there is globally a good agreement between the nonlinear 0D predicted results and the reference 1D results. Overall, pressure and flow profiles are reproduced with a reasonably good level of accuracy; the main features, shape and amplitude, of the waveforms are well-captured by the nonlinear 0D models, even if the differences between 1D and 0D results are not negligible. For instance, in Figure 2.14, we note that for these vessels of third and fourth generations of bifurcations the 0D waveforms are slightly delayed to the right with respect to the 1D waves.

FIGURE 2.6: 37-artery network. Comparison between 1D (at vessel midpoint), nonlinear 0D and linear 0D results in two aortic segments.



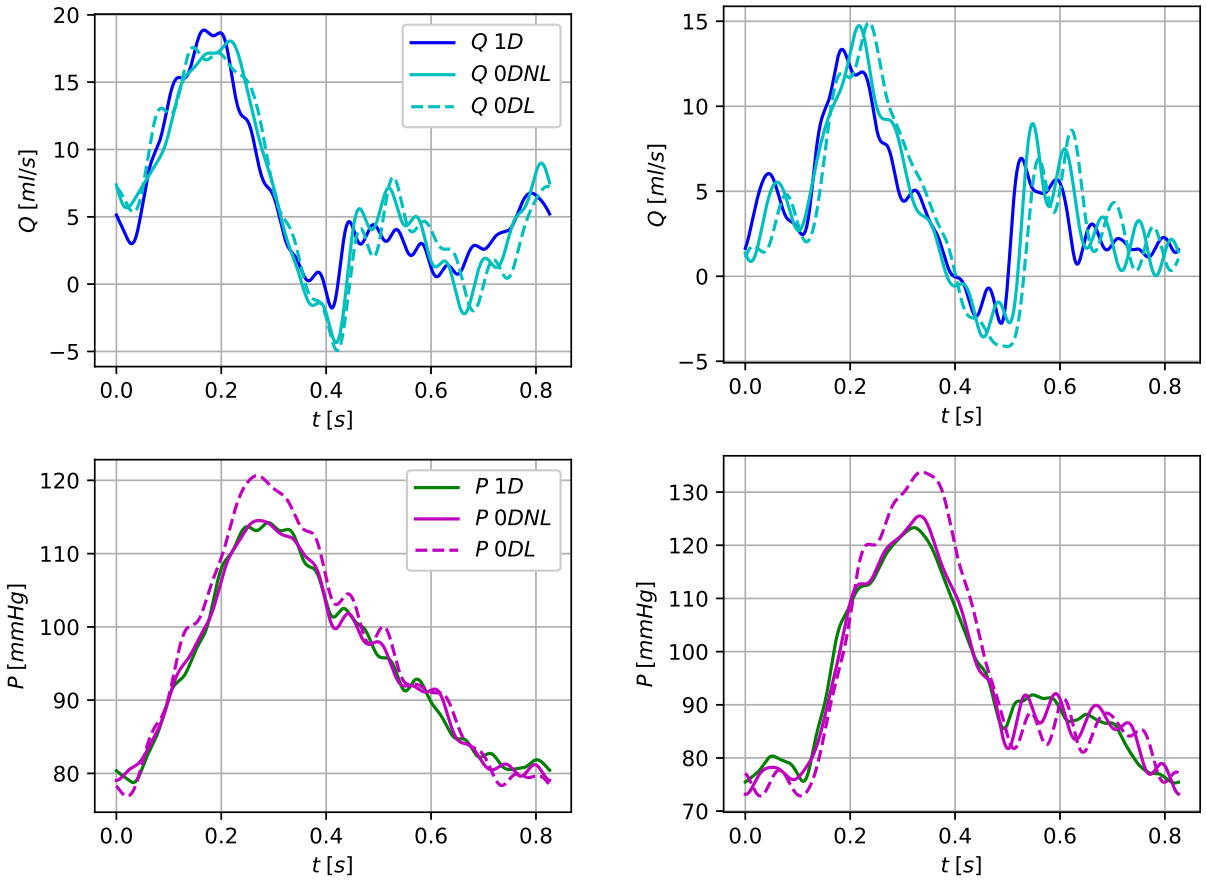
(A) Aortic arch II

(B) Thoracic aorta II

However, once again, we note that generally, by preserving in the 0D models adopted the nonlinearity of the original 1D model, the 0D results are strongly improved with respect to the linear case also for this benchmark arterial network. This is quite evident in the pressure waves, where the systolic pressure is well-reproduced by the nonlinear 0D models. There are only few isolated cases where the linear 0D results seem to be better than the nonlinear ones, as, for example, in the right radial artery, where from Figure 2.13b we can observe the systolic peak in pressure to be approximated better by the linear 0D solution, rather than by the nonlinear 0D solution.

The quantitative assessment presented in Table 2.10 supports all these observations. From the linear to the nonlinear 0D results, the RMS relative errors computed with respect to the reference 1D results are reduced, suggesting that the nonlinear 0D models are able to better reproduce the overall dynamics of pressure and flow rate in all vessels. Furthermore, also in this case, the systolic relative errors for pressure are confirmed to be, in general, significantly smaller in the nonlinear 0D results with respect to the linear ones, illustrating the ability of the nonlinear 0D models to capture and reproduced the essential features of pressure and flow waveforms. For the nonlinear 0D results, RMS relative errors are all smaller than 12.0% for the pressure and smaller than 18.0% for the flow rate; systolic relative errors are all smaller than 4.0% for the pressure and smaller than 10.0% for the flow rate, with an exception in the right anterior tibial artery, where the peak in the flow rate waveform seems to be underestimated, as confirmed by Figure 2.14c.

FIGURE 2.7: 37-artery network. Comparison between 1D (at vessel midpoint), nonlinear 0D and linear 0D results in two first-generation vessels.



(A) Left subclavian I

(B) Right iliac-femoral II

TABLE 2.9: General parameters of the reduced ADAN56 model.

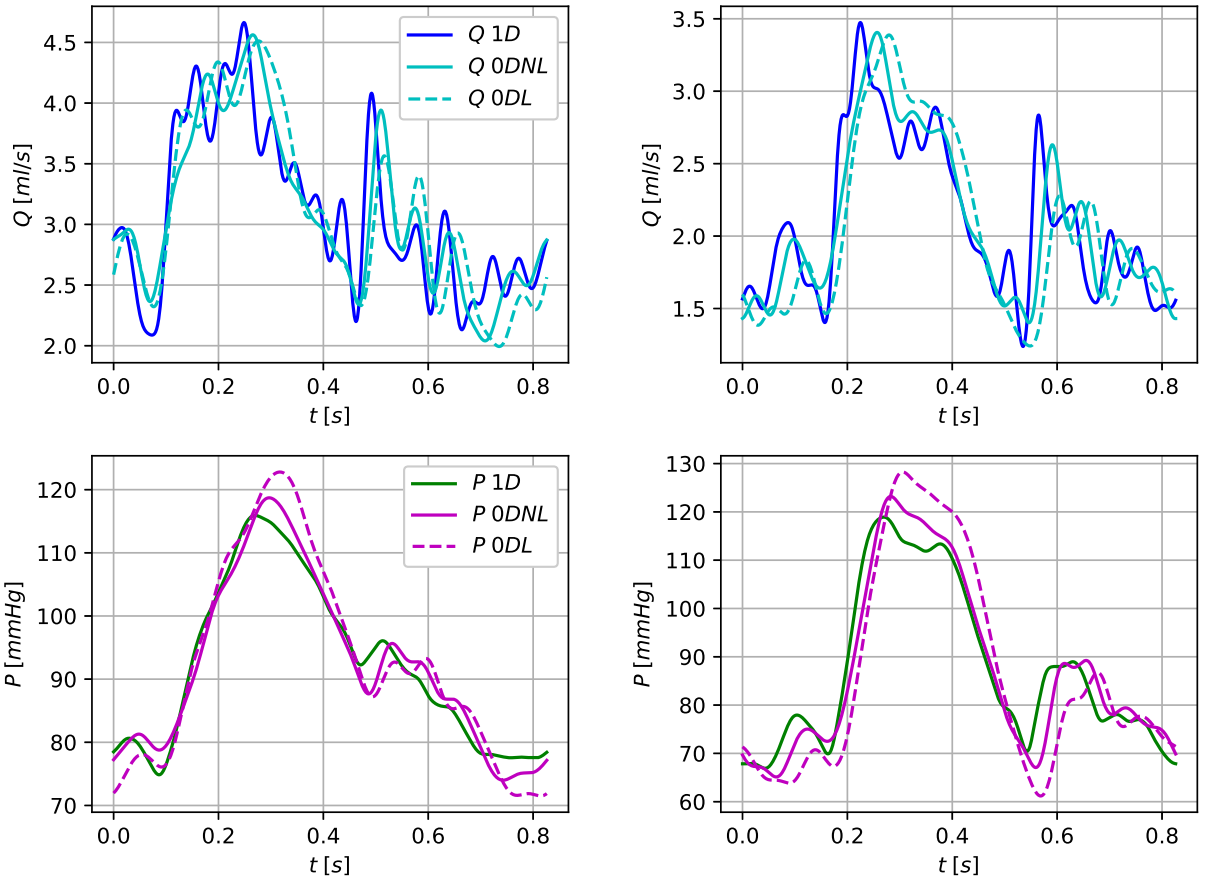
Property	**Value**
Blood density, ρ	1.040 g/cm^3
Blood viscosity, μ	0.04 dyne·s/cm^2
Velocity profile order, ζ	2
Young's modulus, E	2.25·10^6 dyne/cm^2
Diastolic pressure, P_d	10^5 dyne/cm^2 (≈75 mmHg)
External pressure, p_{ext}	0
Outflow pressure, P_{out}	0
Initial velocity, $u(x,0)/U(0)$	0
Initial pressure, $p(x,0)/P(0)$	P_d

2.7.6 CPU times

With this work, by constructing nonlinear 0D blood flow models to replace the original 1D model in not necessarily all, but in certain vessels of a network (according to some *a-priori* model selection criteria), we aim at obtaining cheap simulations of blood flow in large and highly complex vascular networks, by drastically reducing their computational cost and execution time, while still preserving a good level of details in the results.

In Table 2.11 we compare the mean CPU times per cardiac cycle measured to perform the fully 1D and fully

FIGURE 2.8: 37-artery network. Comparison between 1D (at vessel midpoint), nonlinear 0D and linear 0D results in two second-generation vessels.

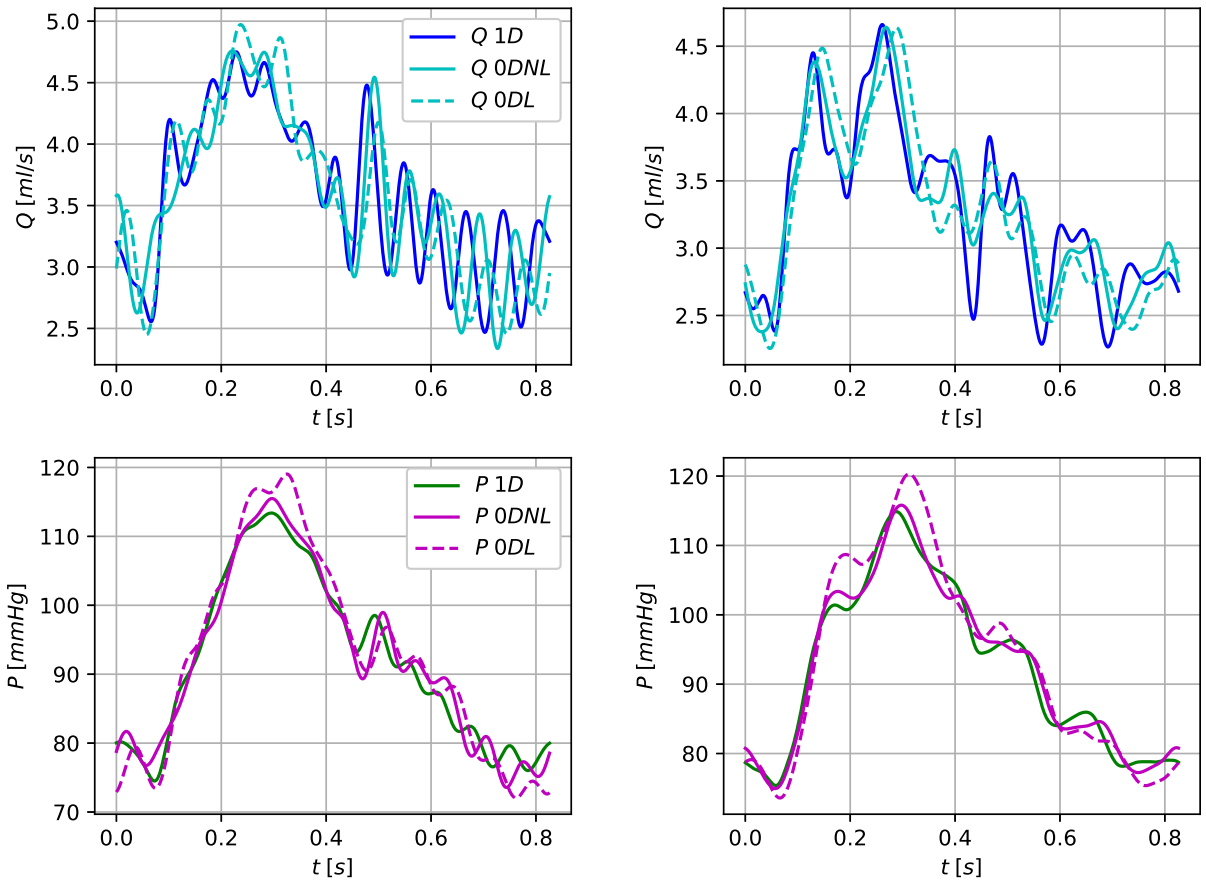


(A) Left ulnar

(B) Right anterior tibial

0D (nonlinear and linear) simulations for the three arterial networks. 1D and 0D simulations were executed in Python, running on a Linux Ubuntu 18.04 machine with Gold Intel Xeon 6130 processor (2.1 GHz, 3.7 GHz Turbo, 16C/32T, 10,4 GT/s 2UPI, 22 MB Cache). From Table 2.11, we first observe that the CPU time gradually increases with increasing network complexity. We note that, in the fully 1D simulations, the mean CPU times needed to solve the 37-artery network and ADAN56 model are approximately comparable, even if the second arterial network is larger than the first one. This observation can be justified by the fact that, because of the very fine mesh we are using to perform the 1D mesh-independent simulations, the time step Δt, computed according to the CFL condition, results to be smaller in the 37-artery network ($\Delta t \approxeq$ 6.05e-05 s) than in the ADAN56 model ($\Delta t \approxeq$ 1.3e-04 s), thus increasing the CPU time demanded to solve the first network. Furthermore, most importantly, the computational cost of the 0D simulations in all arterial networks is strongly reduced by orders of magnitude with respect to the corresponding 1D simulation, while the difference between the CPU times of nonlinear and linear 0D simulations is negligible. In Table 2.11, in the columns of the CPU times corresponding to the 0D simulations, the speed-up gained when passing from the fully 1D simulation to the fully 0D simulation (either linear or nonlinear) is also indicated between brackets, measured as the ratio CPUtime1D/CPUtime0D. For the 37-artery network, the mean CPU time required to perform the fully 1D simulation with mesh-independent results is about 6245.1 s, while the CPU time demanded for the nonlinear, fully 0D simulation is significantly reduced to approximately 27.0 s, with a speed-up in the simulation of more than 230 times. Similarly, for the reduced ADAN56 model, the fully 1D simulation with mesh-independent results is performed with a mean CPU

FIGURE 2.9: 37-artery network. Comparison between 1D (at vessel midpoint), nonlinear 0D and linear 0D results in two third-generation vessels.



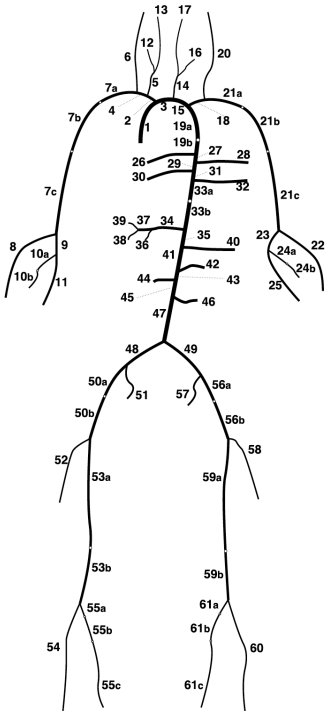
(A) Right ulnar

(B) Splenic

time of about 6492.7 s, while the CPU time demanded for the nonlinear, fully 0D simulation is decreased to approximately 84.9 s, with a speed-up in the simulation of more than 75 times. These results prove that the derived family of nonlinear 0D models may represent a powerful tool to improve the computational efficiency of blood flow simulations, while still preserving and well reproducing the main features of pressure and flow waveforms in networks of vessels. Of course, we expect this to be even more pronounced when this methodology will be applied to more complex networks, such as the global, closed-loop, multiscale cardiovascular model developed by Müller and Toro [99, 100], the ADAN model presented by Blanco *et al.* [17, 16] and the comprehensive 1D model of the entire adult cardiovascular system reported by Mynard and Smolich [108]. Indeed, in these networks, the number of vessels and spatial scales change drastically and, since we expect to always use 1D models for the larger vessels, the agreement in the results and the gain in terms of computational efficiency and execution time will be strongly improved by using hybrid 1D-0D networks.

We observe that, in many practical situations and applications, the mesh-independence of the 1D solution may not be necessary and cheaper 1D models may be employed. In this case, the computational cost of the fully 1D simulations would be considerably reduced with respect to that of the 1D mesh-independent model and thus, also the speed-up obtained by adopting the 0D models would be not as relevant. However, our main goal here is to investigate and assess the ability of the newly derived nonlinear 0D models to reproduce the physics and physical properties of blood flow through the vessel, when compared to the original 1D model. For this reason, it is important to have mesh-independent 1D results, to ensure that the

FIGURE 2.10: Schematic representation of the reduced ADAN56 model presented in [22]. Figure reproduced with permission [22].



physics of the problem is reproduced by the 1D model as accurately as possible. In addition, as pointed out above, we expect really impressive improvements in terms of computational efficiency when this methodology will be applied to much more complex networks and models, where the heterogeneity of spatial and/or temporal scales is relevant and also non mesh-independent simulations are really expensive.

Finally, we remark that the CPU time analysis presented in this section represents a preliminary study to provide a first insight and estimate of the impact of using 0D models on the computational cost and efficiency of the simulations. More than the single CPU time values, the 1D/0D CPU time ratios are more relevant and informative about the speed-up obtained with respect to the reference 1D simulations. This analysis was performed using Python as programming language. We believe that what may drastically increment/decrement the speeds-up reported in this work is how efficiently 1D and 0D model discretizations are implemented, rather than the specific choice of the programming language. Indeed, in the case of serial code, we expect these ratios/speeds-up to be approximately maintained also when moving to another programming language (like C++), even if this would not be necessarily true in the case of a parallel code implementation.

2.7.7 Analysis of relative contributions of single nonlinear terms

In this section, we analyze the relative contributions of considering as nonlinear single components of the 0D models (resistance, inductance and pressure-area relation) in determining pressure and flow waveforms and in producing more accurate 0D results. Indeed, in Sections 2.7.4 and 2.7.5, we found that, for both the 37-artery network and ADAN56 model, overall considering nonlinear pressure-area relation and nonlinear parameters L and R in the 0D blood flow models strongly improves their ability of accurately predict pressure and flow waveforms, which are in good agreement with the reference 1D results. Here, we want to investigate and assess the contribution to the 0D model accuracy obtained by including only a single component as nonlinear and to compare these different possible scenarios with the previously

TABLE 2.10: ADAN56 model. Relative errors (in %) for pressure and flow between for both nonlinear (0DNL) and linear (0DL) 0D results with respect to the 1D results (1D) at the midpoint of the vessel, computed according to the relative error metrics (2.98).

Vessel	0D model	$\varepsilon_P^{\mathrm{RMS}}(\%)$	$\varepsilon_Q^{\mathrm{RMS}}(\%)$	$\varepsilon_P^{\mathrm{SYS}}(\%)$	$\varepsilon_Q^{\mathrm{SYS}}(\%)$	$\varepsilon_P^{\mathrm{DIAS}}(\%)$	$\varepsilon_Q^{\mathrm{DIAS}}(\%)$
Aortic arch I	0D-NL	1.010	3.230	0.479	1.331	-0.361	0.808
	0D-L	1.790	4.147	1.210	0.955	-1.075	-3.114
Thoracic aorta III	0D-NL	1.200	4.131	0.649	2.303	-1.332	5.122
	0D-L	2.198	6.403	3.011	2.788	-1.412	8.198
Abdominal aorta V	0D-NL	1.735	9.719	1.740	-7.392	0.732	13.722
	0D-L	3.447	12.800	5.656	-7.777	-0.319	16.683
R common carotid	0D-NL	1.111	6.857	1.272	6.378	-0.926	0.372
	0D-L	2.081	9.335	4.937	7.623	-0.694	-1.530
R renal	0D-NL	1.281	3.211	1.230	0.118	0.398	-0.780
	0D-L	2.765	5.940	4.733	3.339	-0.429	-2.143
R common iliac	0D-NL	2.119	9.885	1.522	-7.062	2.242	8.388
	0D-L	3.718	13.111	5.680	-5.566	1.030	9.935
R internal carotid	0D-NL	2.268	5.845	3.489	3.459	-0.712	4.082
	0D-L	3.552	8.918	7.456	5.690	-1.081	2.035
R radial	0D-NL	3.324	4.985	1.529	-3.377	0.453	11.274
	0D-L	3.586	5.514	-0.319	-7.678	-0.358	13.079
R internal iliac	0D-NL	2.620	6.387	-0.204	-8.080	2.152	10.220
	0D-L	4.012	8.659	3.104	-7.054	1.711	7.333
R post. inteross.	0D-NL	3.275	4.132	0.134	-1.734	0.998	-0.9951
	0D-L	3.801	4.737	-2.797	-4.547	0.469	-0.155
R femoral II	0D-NL	4.888	16.954	-2.224	-7.812	6.997	-0.868
	0D-L	7.103	21.109	1.012	-15.742	7.955	0.225
R anterior tibial	0D-NL	11.454	14.681	-1.044	-19.454	5.643	3.510
	0D-L	14.342	17.424	-0.949	-27.568	6.699	3.128

TABLE 2.11: Comparison between mean CPU times per cardiac cycle (in seconds) of the 1D, nonlinear 0D (0D-NL) and linear 0D (0D-L) simulations for the aortic bifurcation model, the 37-artery network and ADAN56 model. The speed-up gained in the 0D simulation (either linear or nonlinear) with respect to the 1D simulation is also reported between brackets, measured as the ratio CPUtime1D/CPUtime0D.

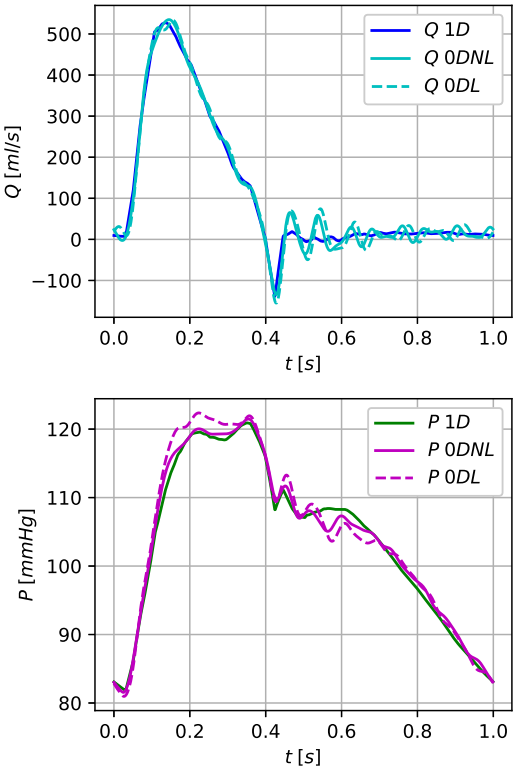
	CPU time per card.cycle [s]		
Test case	**1D sim.**	**0D-NL sim. (speed-up)**	**0D-L sim. (speed-up)**
Aortic bifurcation	51.251	0.400 (128.096)	0.332 (154.179)
37-artery network	6245.066	27.010 (231.215)	19.923 (313.455)
ADAN56 model	6492.655	84.887 (76.486)	78.486 (82.724)

considered ones where all components are either linear or nonlinear.

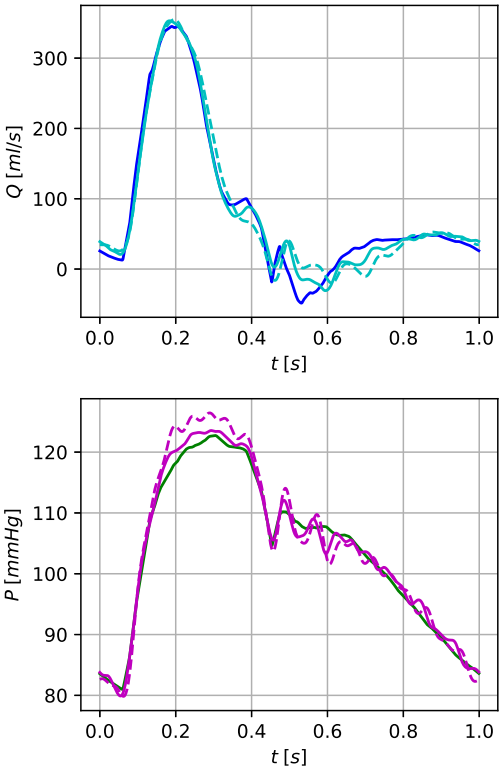
To this aim, we performed, for both the 37-artery network and ADAN56 model, a new set of fully 0D simulations, where in each simulation a single nonlinear term is activated in the 0D models (either the resistance R, the inductance L or the pressure-area relation), while all the other components are kept linear. The obtained 0D results are then compared to the available fully-linear and fully-nonlinear 0D results.

Figures 2.15 and 2.16 display the error analysis carried out for the 37-artery network and ADAN56 model, respectively. For each type of 0D model (fully-linear, with nonlinear resistance, with nonlinear inductance, with nonlinear pressure-area relation and fully-nonlinear), the errors in the predicted 0D results are computed with respect to the reference 1D results in the different relative error metrics (2.98). In each

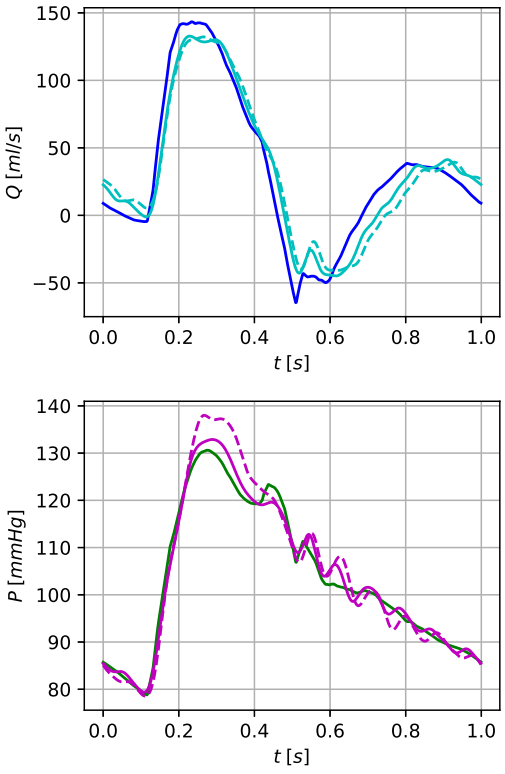
FIGURE 2.11: ADAN56 model. Comparison between 1D (at vessel midpoint), nonlinear 0D and linear 0D results in three aortic segments.



(A) Aortic arch I

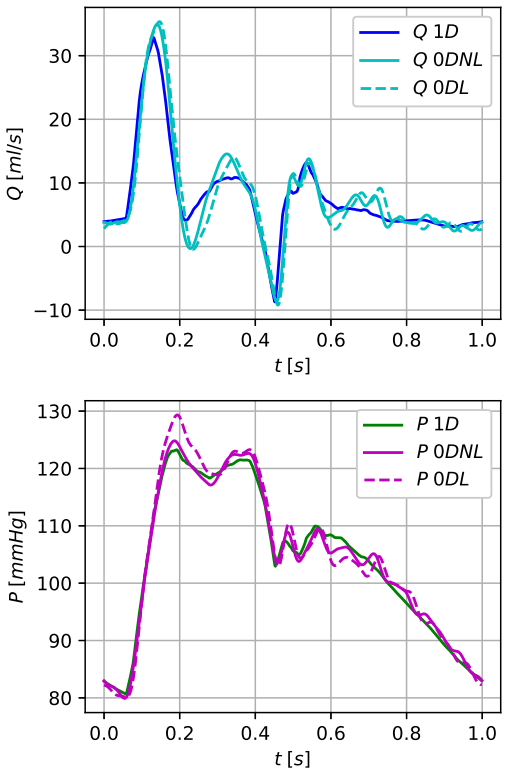


(B) Thoracic aorta III

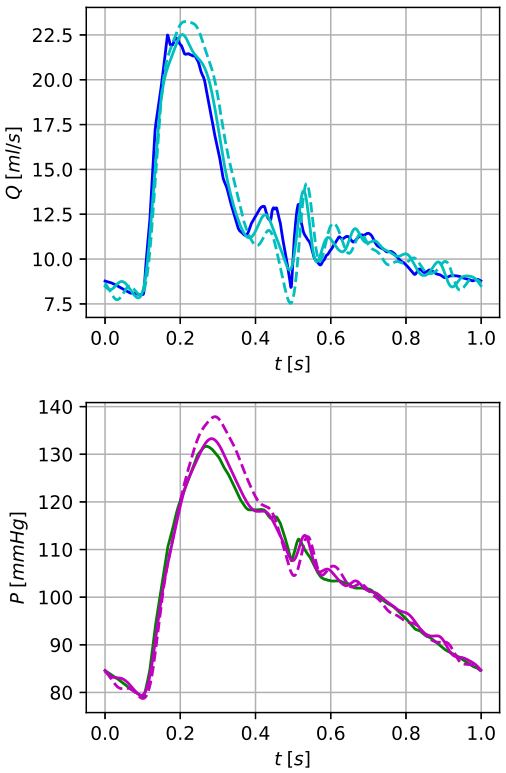


(C) Abdominal aorta V

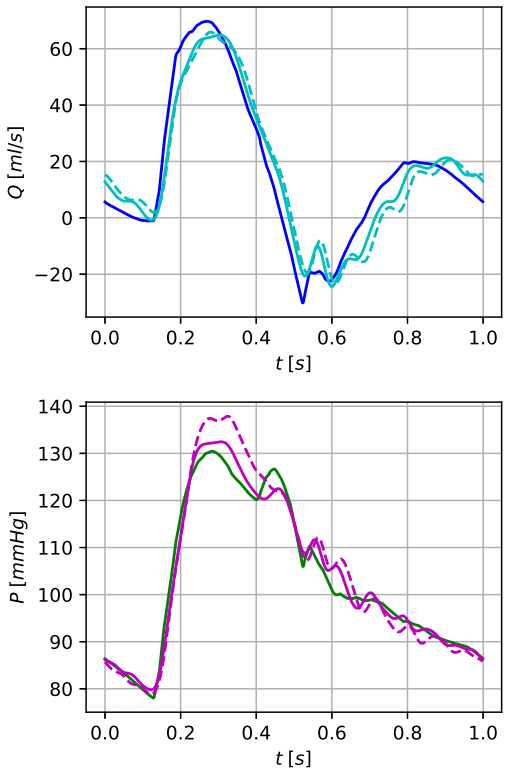
FIGURE 2.12: ADAN56 model. Comparison between 1D (at vessel midpoint), nonlinear 0D and linear 0D results in three first-generation vessels.



(A) Right common carotid

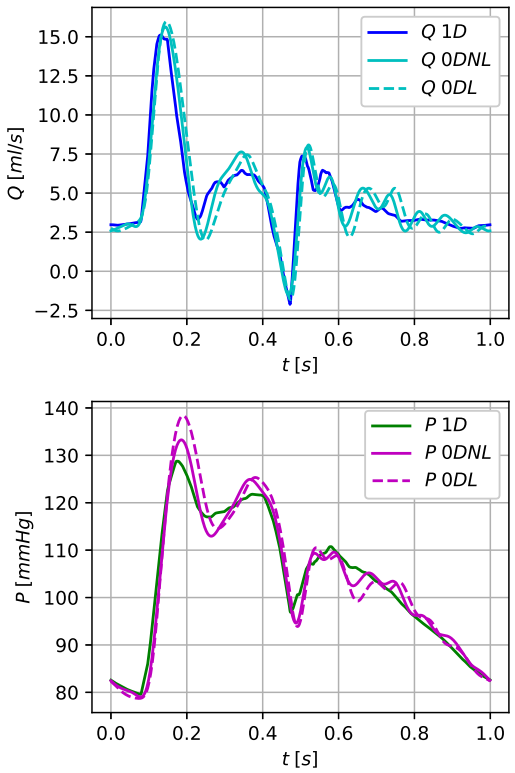


(B) Right renal

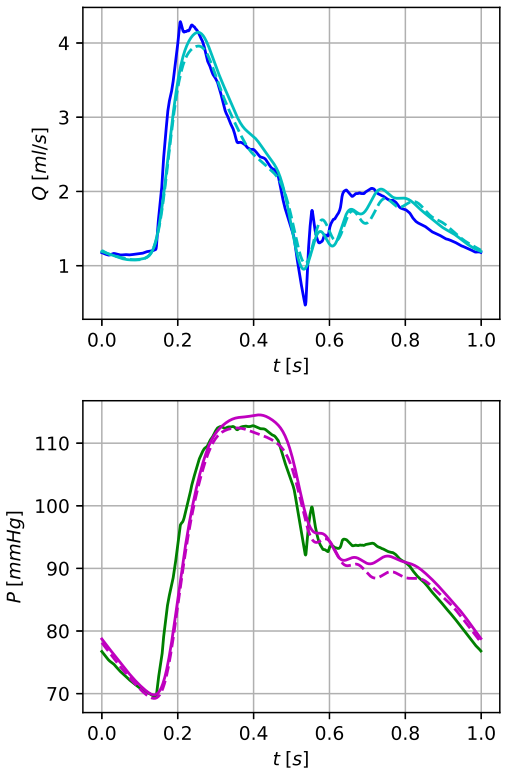


(C) Right common iliac

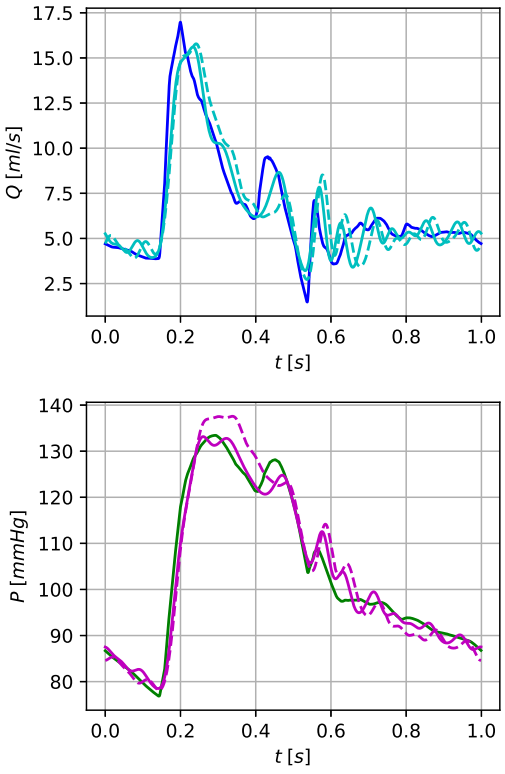
FIGURE 2.13: ADAN56 model. Comparison between 1D (at vessel midpoint), nonlinear 0D and linear 0D results in three second-generation vessels.



(A) Right internal carotid

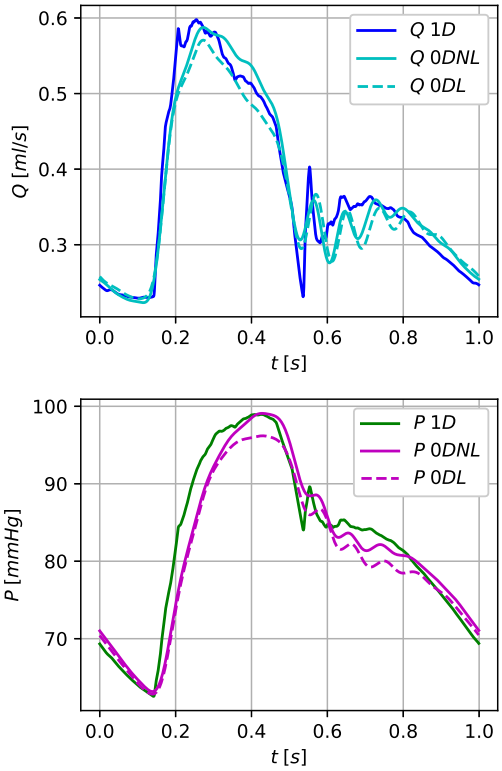


(B) Right radial

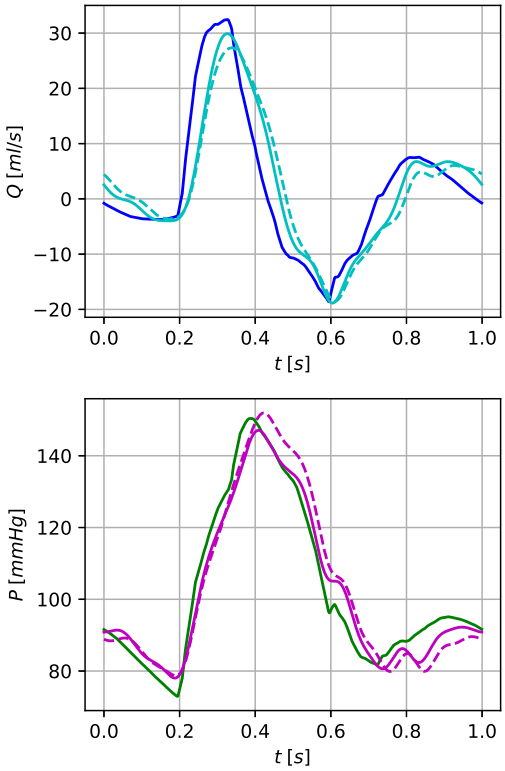


(C) Right internal iliac

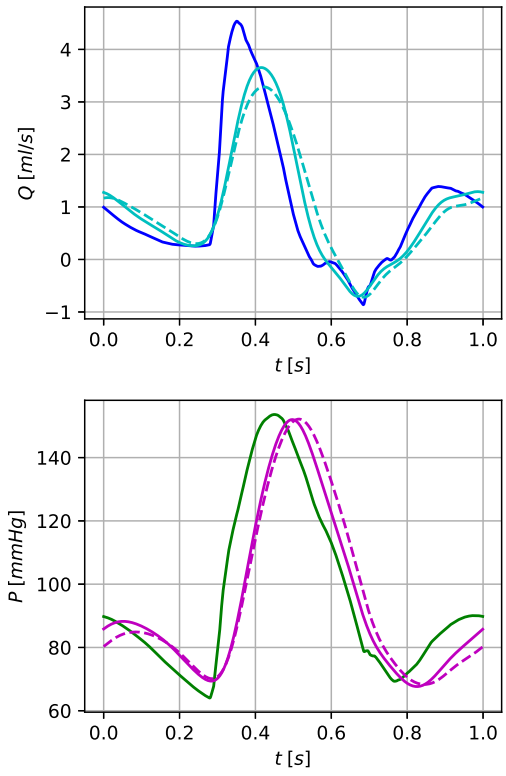
FIGURE 2.14: ADAN56 model. Comparison between 1D (at vessel midpoint), nonlinear 0D and linear 0D results in three third- and fourth-generation vessels.



(A) Right posterior interosseous



(B) Right femoral II



(C) Right anterior tibial

boxplot, errors are compared over the entire network and in several specific vascular regions, namely the aorta, right arm and right leg, to examine whether specific features of the performance of the different 0D models emerge in any of the vascular districts considered. In all boxplots, for all error metrics, 0D model types and vascular regions, we report the median value, the interquartile range (IQR) and the minimum and maximum values of the error data. The IQR is computed as the difference between the 75th (upper) and 25th (lower) quartiles of each error dataset.

From this error analysis, several observations and outcomes are worthy to be pointed out. Overall, the fully-nonlinear scenario improves the performance of the corresponding 0D blood flow models and the accuracy of the predicted results with respect to the fully-linear scenario; in few isolated cases, the fully-nonlinear and fully-linear results are comparable, with no significant gain obtained when all the nonlinearities are included in the 0D models, but also with no relevant worsening. Furthermore, when activating single nonlinear terms in the 0D models, the nonlinear inductance L results to be the most determining nonlinear component which brings the major benefits to these models in terms of reduction of errors with respect to the reference 1D solution. Indeed, the contribution of this nonlinear parameter alone is significant in accurately defining both pressure and flow waveforms, with errors having small median values and small variability (small-sized IQR). The nonlinear pressure-area relation also plays a considerable role in defining more accurate pressure results. This fact is evident when looking at the boxplots for the relative systolic errors, for both arterial networks considered. Finally, it is worth mentioning that the main motivation for the introduction of nonlinear components, especially the pressure-area relation, regards the application of these 0D models to situations in which large deviations from a baseline state are modeled, such as hypertension, an haemorrhage, a collapsed state or postural changes. Indeed, in these non physiological conditions, the combined contribution of the nonlinear pressure-area relation and of the nonlinear pressure-dependent parameters is expected to play an important role in accurately predicting the corresponding haemodynamic states.

FIGURE 2.15: 37-artery network. Boxplots comparing the errors computed in the different relative error metrics (2.98) with respect to the reference 1D results for (in each boxplot, from left to right): fully-linear 0D results (all-LIN), 0D results with nonlinear resistance (NL-R), 0D results with nonlinear inductance (NL-L), 0D results with nonlinear pressure-area relation (NL-Tl) and fully-nonlinear 0D results (all-NL). In each boxplot, errors are compared over the entire network (yellow) and in several specific vascular regions: aorta (blue), right arm (green) and right leg (red). Relative errors for pressure P are shown in the top row boxplots (from left to right boxplots: RMS, systolic and diastolic errors), while relative errors for flow rate Q are reported in the bottom row boxplots. In each box, the box mid-line represents the median value, the box itself corresponds to the interquartile range (IQR), while the lines (whiskers) extending from the box indicate the minimum and maximum values.

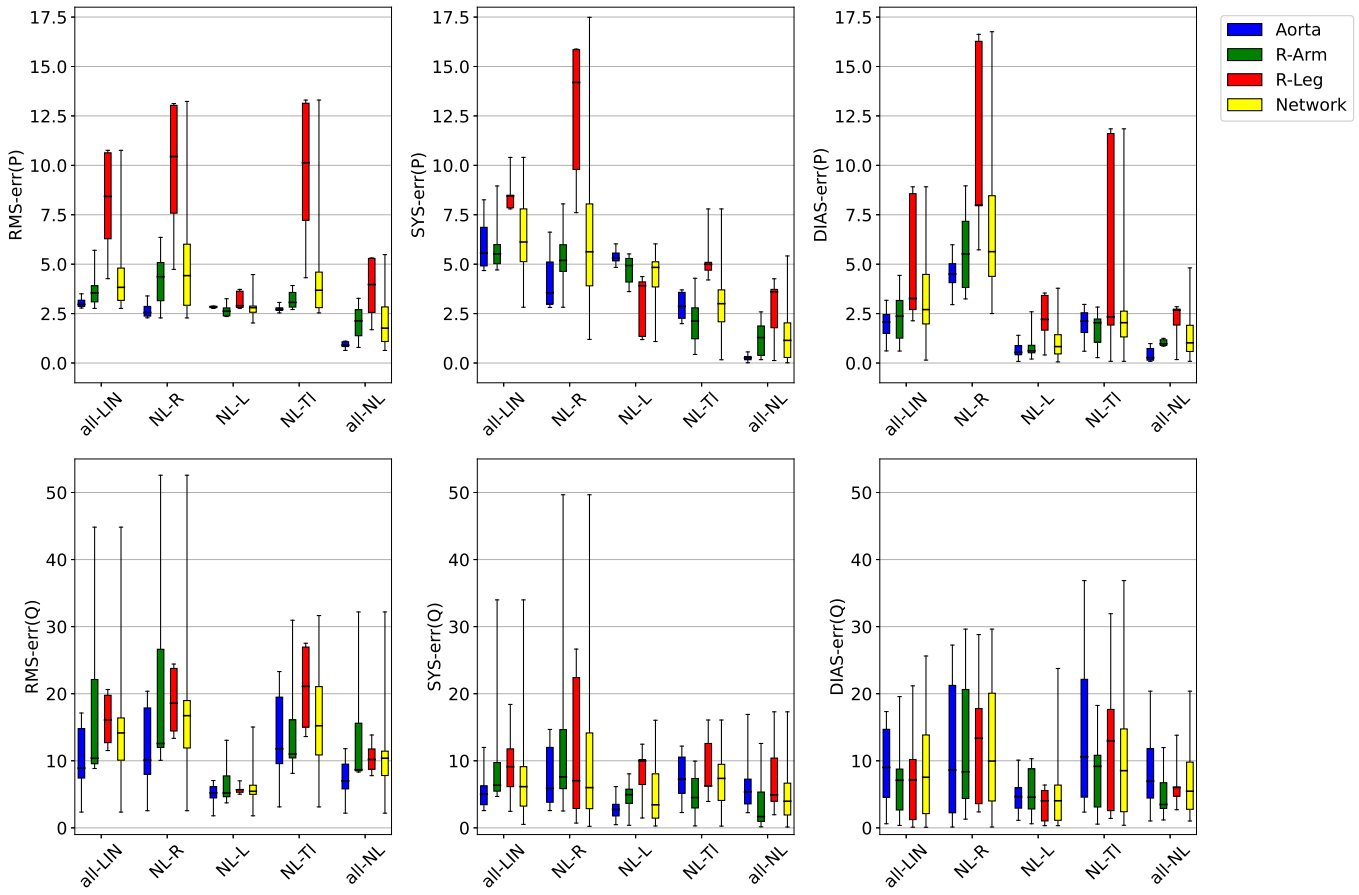
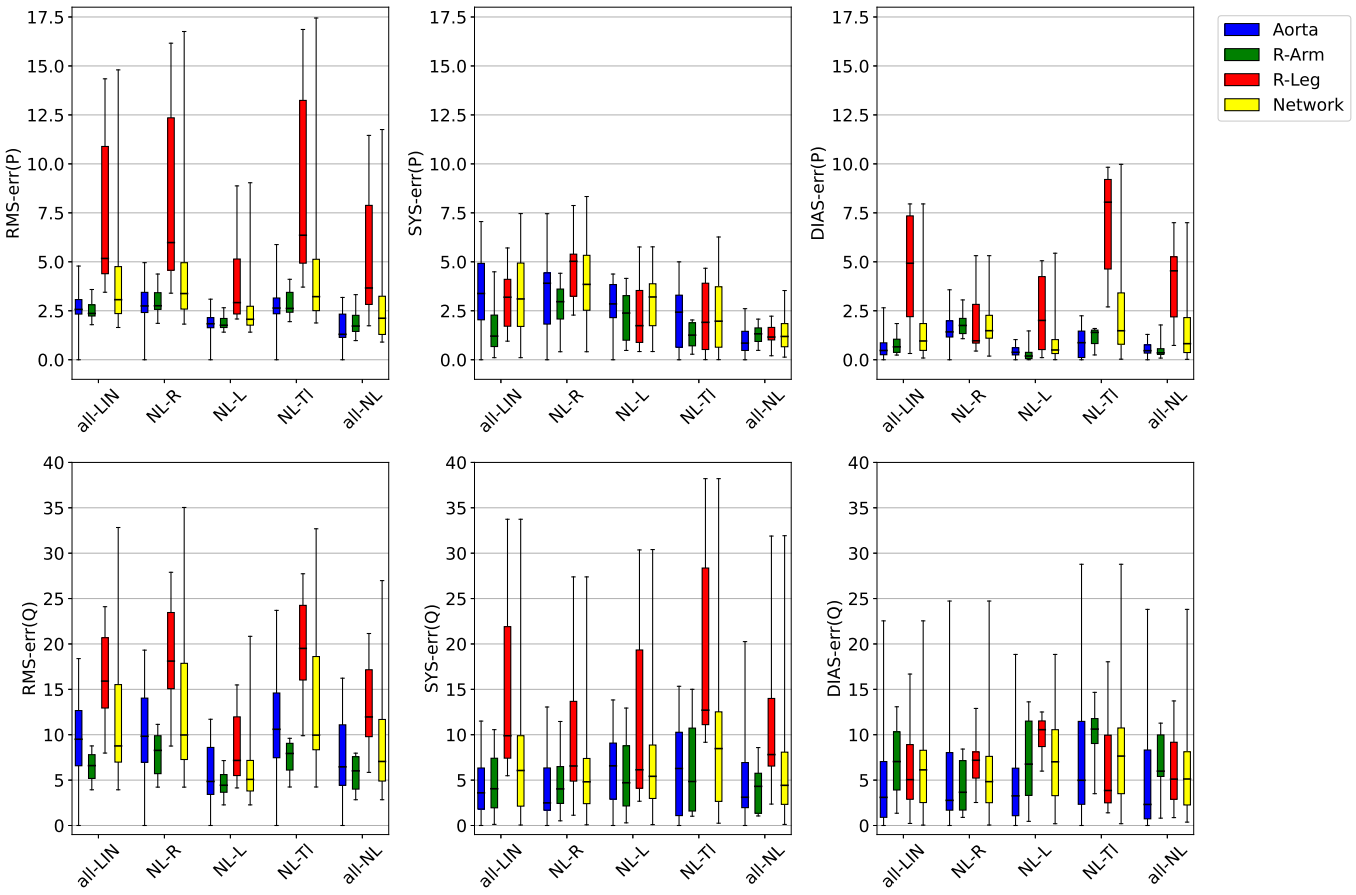


FIGURE 2.16: ADAN56 model. Boxplots comparing the errors computed in the different relative error metrics (2.98) with respect to the reference 1D results for (in each boxplot, from left to right): fully-linear 0D results (all-LIN), 0D results with nonlinear resistance (NL-R), 0D results with nonlinear inductance (NL-L), 0D results with nonlinear pressure-area relation (NL-Tl) and fully-nonlinear 0D results (all-NL). In each boxplot, errors are compared in the entire network (yellow) and in several specific vascular regions: aorta (blue), right arm (green) and right leg (red). Relative errors for pressure P are shown in the top row boxplots (from left to right boxplots: RMS, systolic and diastolic errors), while relative errors for flow rate Q are reported in the bottom row boxplots. In each box, the box mid-line represents the median value, the box itself corresponds to the interquartile range (IQR), while the lines (whiskers) extending from the box indicate the minimum and maximum values.



Chapter 3

A hybrid 1D-0D solver for efficient blood flow simulations in complex vascular networks

3.1 Introduction

Equipped with both the 1D blood flow model introduced in Chapter 2 and the family of *nonlinear* lumped-parameter models of blood flow derived and validated in the same chapter, the main goal of the present chapter is the development of a hybrid 1D-0D network solver to perform computationally efficient and accurate blood flow simulations in complex vascular networks. In fact, one-dimensional modeling of blood flow in large and complex vascular models and networks can result in computationally expensive simulations, posing the need for extremely efficient numerical methods and solvers.

As briefly reviewed in Section 1.2.2, several methods and approaches have been proposed in the literature, which consider the coupling of 1D models to lumped-parameter models to simulate blood flow in networks of vessels, to address the issues of computational cost, execution time and optimization of topological complexity. However, here we propose a hybrid network methodology which presents some main essential aspects that were never found combined together in the works mentioned in Section 1.2.2. First, when constructing both 0D and hybrid network configurations, the topology of the original 1D network is preserved, so that blood flow and pressure distribution and waveforms can be reproduced and analyzed in each 1D/0D vessel of the original network. Second, even if they are simpler than the 1D models, the adopted nonlinear 0D blood flow models preserve important nonlinear properties of the original 1D description, which strongly improve their ability to reproduce good approximations of flow and pressure waveforms with respect to the reference 1D results. In this chapter, the family of nonlinear lumped-parameter models derived in Section 2.3 will be further extended to account for the viscoelastic properties of vessel wall. Lastly, the numerical coupling strategy designed to couple 1D and 0D vessels at junctions, which evolve with their own time marching schemes, preserves the order of accuracy of the solution in 1D vessels. In this way, 1D and 0D vessels are coupled together via hybrid junctions to construct hybrid networks, where vessels or regions of vessels where higher accuracy is required are modeled as 1D, while the remaining vessels are described using 0D models, to gain computational efficiency in the resulting simulations.

This chapter consists of three main parts. First, in Section 3.2 we focus on the mathematical models. In particular, the viscoelastic properties of vessel walls are included into both 1D and 0D blood flow descriptions, by adopting a viscoelastic tube law; 1D and 0D coupling strategies introduced in Section 2.5 are also extended to the viscoelastic case. In this section, a suitable hybrid coupling strategy to couple 1D and 0D vessels together in hybrid 1D-0D networks is also proposed, for both elastic and viscoelastic scenarios,

where, once again, the conservation of mass and the continuity of total pressure are ensured across each hybrid junction.

Afterwards, in Section 3.3, a hybrid network methodology is first developed in a simplified modeling and computational setting. We propose an adaptive model selection approach to construct hybrid networks of 1D-0D vessels, which is based on appropriate *a-priori* model selection criteria employed to convert 1D segments into the corresponding 0D counterparts. Here, both 1D and 0D blood flow models are still coupled to the elastic tube laws (2.6) and (2.35), respectively. In order to design accurate and efficient numerical schemes to solve hybrid networks of vessels, the high-order hybrid numerical coupling of 1D and 0D vessels is addressed. The proposed numerical technique takes into account the mutual interaction between 1D and 0D vessels at each time step and ensures that the desired accuracy of the solution in the 1D vessels is preserved and not affected by the coupling with 0D vessels. To instantiate concrete hybrid networks an adaptive model selection strategy is then developed. This methodology is based on relevant *a-priori* model selection criteria, defined in terms of geometrical and mechanical vessel properties or of flow distribution information. Given any generic vascular network, these criteria are used to determine, *a-priori*, the most suitable model, either 1D or 0D, to adopt for each vessel. In particular, our aim here is to identify those criteria providing the best trade-off between the computational cost of the simulations in the resulting hybrid networks and a good level of accuracy in the predicted results with respect to the reference 1D solution. The improvement in the computational efficiency must not come at the expense of a significant loss in terms of accuracy of the solution, in both 1D and 0D vessels, but a good balance between these two essential computational and modeling aspects is needed. In this section, the proposed methodology, implemented using Python as programming language, is applied and tested on arterial networks of moderate complexity.

Finally, in Section 3.4, the hybrid network methodology proposed in Section 3.3 is extended from both modeling and numerical point of view, to be integrated into an already existing network solver coded in C++. The main goal here is to develop an efficient hybrid network solver which allows to perform blood flow simulations in highly complex vascular models and networks. The viscoelastic nature of the vessel wall mechanics is now incorporated in the 1D blood flow model, as well as in the family of nonlinear 0D models. On the other hand, the computational improvements mainly concern (i) the development of an efficient strategy for solving very large and stiff ODE systems governing the blood flow dynamics in regions of 0D vessels, exploiting existing implicit ODE solvers, but also accounting for the specific features of the problem to be solved; and (ii) the derivation of a suitable numerical coupling strategy for the accurate numerical treatment of hybrid junctions of 1D and 0D vessels. Furthermore, together with a standard global time-stepping (GTS) strategy, the hybrid network solver also integrates the high-order local time-stepping (LTS) algorithm proposed by Müller *et al.* [102] for further computational efficiency in the solution of the one-dimensional part of hybrid 1D-0D networks. By applying this modeling and computational framework to solve very complex and large vascular models, we will show how the proposed hybrid network solver becomes crucial to gain computational efficiency when solving networks and models where the heterogeneity of spatial and/or temporal scales is relevant, still ensuring a good level of accuracy in the predicted results.

3.2 Mathematical models

In this section, we start back from the one-dimensional and zero-dimensional descriptions of blood flow in compliant vessels presented in the previous chapter, in Sections 2.2 and 2.3, respectively, under the assumptions of adopting a purely elastic tube law (further restricted to the case of arterial vessels) and of considering, in the 1D model, constant geometric and mechanical vessel properties, *i.e.* independent

of the axial coordinate x along the vessel length. Suitable 1D and 0D coupling strategies have also been introduced in Sections 2.5.1 and 2.5.3, respectively, to couple 1D vessels or 0D vessels via elastic junctions.

The aim of this section is then to extend both 1D and 0D models for blood flow and the proposed coupling strategies. In particular, the viscoelastic properties of vessel walls will be included into both 1D and 0D blood flow descriptions, by adopting a viscoelastic tube law. In addition, in the 1D model (2.1), material and geometric vessel parameters will be regarded no longer as constant parameters, but as general functions of the axial coordinate x.

The 1D coupling strategy is extended to the case of viscoelastic vessels. The improvement proposed for the 0D coupling approach is twofold: first, the coupling procedure presented in Section 2.5.3 is generalized in order to couple 0D vessels without any restrictions on the admissible 0D vessel types converging at a junction; next, this coupling approach is also extended to account for viscoelasticity. Finally, a hybrid coupling strategy is developed that allows us to arbitrarily couple 1D and 0D vessels together and to constrict hybrid 1D-0D networks.

3.2.1 1D blood flow model for viscoelastic vessels

Let us consider the 1D blood flow model (2.1) introduced in Section 2.2. In the first part of this chapter, specifically in Section 3.3, we will still adopt this model coupled to the purely elastic tube law (2.6), focusing on the case of arterial vessels, under the assumption of constant material and geometric vessel properties, that is parameters K, A_0 and p_{ext} are independent of the axial coordinate x. We recall that the resulting system of hyperbolic PDEs can be written in conservative form as given in (2.9).
Then, in the second part of this chapter, throughout Section 3.4, an improved version of the 1D model (2.1) will be adopted, such that

- the material and geometric vessel parameters are in general functions of the axial coordinate x along the vessel length;
- a viscoelastic tube law accounting for the viscoelastic properties of the vessel wall is employed.

This section is devoted to review the 1D blood flow model obtained under the above assumptions, together with the chosen viscoelastic pressure law, and its mathematical reformulation.

First, system (2.1) is closed by considering the following viscoelastic tube law taken from [17]

$$p(x,t) = \zeta(x,t) + p_r(x,t), \tag{3.1}$$

with $p_r(x,t) = P_0 + p_{ext}(x,t)$ and

$$\zeta(x,t) = \frac{\pi r_0 h_0}{A_d}\left[E_e\varepsilon(A) + E_c\epsilon_r \ln\left(e^{\chi(A)}+1\right) + \frac{K_m}{2\sqrt{A_0 A}}\partial_t A\right], \tag{3.2}$$

where

$$\varepsilon(A) = \sqrt{\frac{A}{A_0}} - 1, \qquad \chi(A) = \frac{\varepsilon(A)-\varepsilon_0}{\epsilon_r}. \tag{3.3}$$

Here, $r_0 = r_0(x)$ is the vessel radius at reference state, clearly related to the reference cross-sectional area $A_0 = A_0(x)$, and $h_0 = h_0(x)$ is the vessel wall thickness at reference state; P_0 is the reference pressure and p_{ext} is the external pressure. The constitutive arterial wall equation (3.1) accounts for elastin, collagen and smooth muscle contributions [8, 145]: $E_e = E_e(x)$ is the effective elastic modulus of elastin, $E_c = E_c(x)$ is the effective elastic modulus of collagen and K_m is the effective viscoelastic parameter. $\varepsilon = \varepsilon(A)$ is the current deformation state; ε_0 and ϵ_r characterize the recruitment of fibers, with ε_0 being the deformation state for which 50% of collagen fibers have been activated and ϵ_r the standard deviation of the fiber activation state distribution. A_d could be taken as $A_d = 3/4A_0$ yielding a widely used constitutive law, when $E_c = K_m = 0$

in (3.2), [89, 5, 50, 128]. Following [152, 17, 16], here we set $A_d = A$, which results in a tube law that considers the incompressibility of the vessel wall and, consequently, the reduction of wall thickness as the vessel wall is stretched.
The last term in (3.2) is the viscoelastic term of the tube law and depends on the time partial derivative of the cross-sectional area of the vessel.

3.2.1.1 Variable material properties and augmented equations

As pointed out above, here we assume that the material and geometric vessel parameters are in general functions of distance x along the vessel length, that is $A_0 = A_0(x)$, $h_0 = h_0(x)$, $E_e = E_e(x)$, $E_c = E_c(x)$ and $p_{ext} = p_{ext}(x,t)$. Spatially varying coefficients in ζ (3.2) generate the so-called *geometric source terms* in the momentum balance equation of system (2.1).

Making use of the mass conservation equation in (2.1), the time derivative of A in (3.2) can be replaced by the spatial derivative of the flow q, that is

$$\partial_t A(x,t) = -\partial_x q(x,t) \quad \Longrightarrow \quad \zeta(x,t) = \frac{\pi r_0 h_0}{A_d}\left[E_e\varepsilon(A) + E_c\epsilon_r \ln\left(e^{\chi(A)}+1\right) - \frac{K_m}{2\sqrt{A_0 A}}\partial_x q\right]. \tag{3.4}$$

Then, the spatial derivative of pressure $p(x,t)$ reads

$$\begin{aligned}\partial_x p &= \partial_x \zeta + \partial_x p_r \\ &= \zeta_A \partial_x A + \zeta_{A_0}\partial_x A_0 + \zeta_{h_0}\partial_x h_0 + \zeta_{E_e}\partial_x E_e + \zeta_{E_c}\partial_x E_c + \zeta_{\partial_x q}\partial_x^{(2)} q + \partial_x p_r,\end{aligned} \tag{3.5}$$

where $\zeta_\tau = \partial_\tau \zeta$, with $\tau = A, A_0, h_0, E_e, E_c, \partial_x q$. The accurate numerical treatment of geometric source terms is crucial when designing explicit numerical schemes, in order to correctly compute solutions to time-dependent problems with this type of source terms. Here, we follow the approach proposed by Toro and Siviglia [141], which consists in (i) first, reformulating the 1D model by considering the spatially varying parameters as additional problem unknowns to incorporate the problematic geometric source terms into the eigenstructure of the system, and (ii) then, constructing a suitable numerical scheme for the obtained augmented system. This approach has been applied to system (2.1) with tube law (3.1)-(3.2) in [97, 102]. Following these works and the early work by Toro and Siviglia [141], we get the following extended 7×7 system

$$\begin{cases} \partial_t A + \partial_x q = 0, \\ \partial_t q + \partial_x\left(\alpha\dfrac{q^2}{A}\right) = -\dfrac{A}{\rho}\zeta_A\partial_x A - \dfrac{A}{\rho}\zeta_{\partial_x q}\partial_x^{(2)} q \\ \qquad\qquad - \dfrac{A}{\rho}\left(\zeta_{A_0}\partial_x A_0 + \zeta_{h_0}\partial_x h_0 + \zeta_{E_e}\partial_x E_e + \zeta_{E_c}\partial_x E_c + \partial_x p_r\right) + f, \\ \partial_t A_0 = 0, \\ \partial_t h_0 = 0, \\ \partial_t E_e = 0, \\ \partial_t E_c = 0, \\ \partial_t p_r = F(x,t), \end{cases} \tag{3.6}$$

with $F(x,t)$ prescribed. In (3.6), the momentum balance equation includes the term $\frac{A}{\rho}\zeta_{\partial_x q}\partial_x^{(2)} q$, which is a higher-order differential term arising from the viscoelastic part of the tube law (3.2). Because of this differential term, we get a system of advection–diffusion–reaction equations which defines a parabolic problem, no longer hyperbolic, as in the case of a purely elastic tube law (see Section 2.2.1).

3.2.1.2 Mathematical reformulation: hyperbolic approximation

The time-dependent parabolic system (3.6) can be approximated by a hyperbolic system with stiff source terms by adopting the method proposed by Toro and Montecinos [140, 94], which is an extension of the Cattaneo relaxation approach [31]. In [93], Montecinos and coworkers applied this procedure to a network of arterial blood vessels, which has then be extended to the global, closed-loop circulation model developed by Toro *et al.* [144], including both arteries and veins. The hyperbolic approximation of system (3.6) with viscoelastic tube law (3.1)-(3.2) has been applied in [97, 102] and we refer the reader to all the above mentioned works for full details.

In order to retrieve a first-order PDE system, we introduce the auxiliary variable θ and a relaxation time $T > 0$. The spatial gradient of the flow variable $\partial_x q$ in (3.6) is then replaced by the new variable θ, which is in turn constrained to satisfy the following evolution equation, that is the constitutive Cattaneo's law

$$\partial_t \theta = \frac{1}{T}\left(\partial_x q - \theta\right). \tag{3.7}$$

From (3.7), it holds that

$$\theta \to \partial_x q \quad \text{as} \quad T \to 0. \tag{3.8}$$

We then obtain an augmented 8×8 system

$$\partial_t \boldsymbol{Q} + \boldsymbol{A}(\boldsymbol{Q})\partial_x \boldsymbol{Q} = \boldsymbol{S}(\boldsymbol{Q}), \tag{3.9}$$

for which the vector of unknowns $\boldsymbol{Q}$, the coefficient matrix $\boldsymbol{A}$ and the source term vector $\boldsymbol{S}$ are given by

$$\boldsymbol{Q} = \left(A, q, \theta, A_0, h_0, E_e, E_c, p_r\right)^T, \tag{3.10}$$

$$\boldsymbol{A}(\boldsymbol{Q}) = \begin{pmatrix} 0 & 1 & 0 & 0 & 0 & 0 & 0 & 0 \\ c^2 - u^2 & 2u & \frac{A}{\rho}\zeta_\theta & \frac{A}{\rho}\zeta_{A_0} & \frac{A}{\rho}\zeta_{h_0} & \frac{A}{\rho}\zeta_{E_e} & \frac{A}{\rho}\zeta_{E_c} & \frac{A}{\rho} \\ 0 & -\frac{1}{T} & 0 & 0 & 0 & 0 & 0 & 0 \\ 0 & 0 & 0 & 0 & 0 & 0 & 0 & 0 \\ 0 & 0 & 0 & 0 & 0 & 0 & 0 & 0 \\ 0 & 0 & 0 & 0 & 0 & 0 & 0 & 0 \\ 0 & 0 & 0 & 0 & 0 & 0 & 0 & 0 \\ 0 & 0 & 0 & 0 & 0 & 0 & 0 & 0 \end{pmatrix} \tag{3.11}$$

and

$$\boldsymbol{S}(\boldsymbol{Q}) = \left(0, f, -\frac{\theta}{T}, 0, 0, 0, 0, F\right)^T, \tag{3.12}$$

respectively, with $c = \sqrt{\frac{A}{\rho}\zeta_A}$.

The complete eigenstructure analysis of system (3.9) is carried out in detail in [97]. Here, we report essential results for the construction of the numerical schemes and the definition of the coupling conditions to be prescribed at a junction of viscoelastic vessels (to extend the 1D coupling strategy presented in Section 2.5.1 in the case of elastic vessels).

System (3.9) with coefficient matrix (3.11) is hyperbolic if the following condition holds

$$\zeta_A - \frac{\zeta_\theta}{T} > 0, \tag{3.13}$$

with eigenvalues

$$\lambda_1 = u - c_T, \quad \lambda_2 = \lambda_3 = \lambda_4 = \lambda_5 = \lambda_6 = \lambda_7 = 0, \quad \lambda_8 = u + c_T, \tag{3.14}$$

where

$$c_T = \sqrt{c^2 - \frac{A}{\rho}\frac{\zeta_\theta}{T}} = \sqrt{\frac{A}{\rho}\left(\zeta_A - \frac{\zeta_\theta}{T}\right)}, \tag{3.15}$$

and linearly independent right eigenvectors

$$\begin{aligned}
&\boldsymbol{R}_1 = \gamma_1 \begin{pmatrix} 1 \\ u - c_T \\ -\frac{1}{T} \\ 0 \\ 0 \\ 0 \\ 0 \\ 0 \end{pmatrix}, \quad \boldsymbol{R}_2 = \gamma_2 \begin{pmatrix} 0 \\ 0 \\ 0 \\ 1 \\ 0 \\ 0 \\ 0 \\ -\zeta_{A_0} \end{pmatrix}, \quad \boldsymbol{R}_3 = \gamma_3 \begin{pmatrix} 0 \\ 0 \\ 0 \\ 0 \\ 1 \\ 0 \\ 0 \\ -\zeta_{h_0} \end{pmatrix}, \quad \boldsymbol{R}_4 = \gamma_4 \begin{pmatrix} 0 \\ 0 \\ 0 \\ 0 \\ 0 \\ 1 \\ 0 \\ -\zeta_{E_e} \end{pmatrix}, \\
&\boldsymbol{R}_5 = \gamma_5 \begin{pmatrix} 0 \\ 0 \\ 0 \\ 0 \\ 0 \\ 0 \\ 1 \\ -\zeta_{E_c} \end{pmatrix}, \quad \boldsymbol{R}_6 = \gamma_6 \begin{pmatrix} 1 \\ 0 \\ 0 \\ 0 \\ 0 \\ 0 \\ 0 \\ \frac{\rho(u^2 - c^2)}{A} \end{pmatrix}, \quad \boldsymbol{R}_7 = \gamma_7 \begin{pmatrix} 0 \\ 0 \\ 1 \\ 0 \\ 0 \\ 0 \\ 0 \\ -\zeta_\theta \end{pmatrix}, \quad \boldsymbol{R}_8 = \gamma_8 \begin{pmatrix} 1 \\ u + c_T \\ -\frac{1}{T} \\ 0 \\ 0 \\ 0 \\ 0 \\ 0 \end{pmatrix},
\end{aligned} \tag{3.16}$$

where γ_i, for $i = 1, \dots, 8$, are arbitrary scaling factors.

We now consider two fundamental properties of system (3.9), namely the nature of the characteristic fields and the generalized Riemann invariants. For parameters and states in physiological ranges, it has been shown that the characteristic fields associated to eigenvalues λ_1 and λ_8 are genuinely nonlinear [97], while the remaining characteristic fields associated to eigenvalues λ_i, for $i = 2, \dots, 7$, are linearly degenerate (LD). The generalized Riemann invariants for the λ_1-characteristic field are

$$\begin{aligned}
&\Gamma_1^1 = u + \int_{\widehat{A}}^{A} \frac{\widetilde{c}_T(\xi)}{\xi} d\xi, \quad \Gamma_1^2 = \theta + \frac{A}{T}, \\
&\Gamma_1^3 = A_0, \quad \Gamma_1^4 = h_0, \quad \Gamma_1^5 = E_e, \quad \Gamma_1^6 = E_c, \quad \Gamma_1^7 = p_r,
\end{aligned} \tag{3.17}$$

with

$$\widetilde{c}_T(A) = c_T\left(A, \widetilde{\theta}(A)\right), \qquad \widetilde{\theta}(A) = \widehat{\theta} + \frac{\widehat{A} - A}{T}, \tag{3.18}$$

where $\widehat{A}$ and $\widehat{\theta}$ are reference values. Similarly, the generalized Riemann invariants associated to the λ_8-characteristic field are the following

$$\begin{aligned}
&\Gamma_8^1 = u - \int_{\widehat{A}}^{A} \frac{\widetilde{c}_T(\xi)}{\xi} d\xi, \quad \Gamma_8^2 = \theta + \frac{A}{T}, \\
&\Gamma_8^3 = A_0, \quad \Gamma_8^4 = h_0, \quad \Gamma_8^5 = E_e, \quad \Gamma_8^6 = E_c, \quad \Gamma_8^7 = p_r.
\end{aligned} \tag{3.19}$$

As regards the linearly degenerate fields associated to λ_i, for $i = 2, \dots, 7$, they are related to a stationary contact discontinuity and the generalized Riemann invariants for these fields are

$$\Gamma_{LD}^1 = q = constant, \qquad \Gamma_{LD}^2 = p + \frac{1}{2}\rho u^2 = constant. \tag{3.20}$$

Remark 3.1. As reported in [97], to ensure that the formulation error is smaller than the discretization error, the following relation must hold

$$\triangle := \frac{T}{(\Delta x)^p} \frac{1 - 2^{-\frac{1}{2}}}{2^{p-\frac{1}{2}} - 1} = O(1), \tag{3.21}$$

where p is the order of accuracy of the numerical scheme and Δx is the characteristic size of the computational cells.

Remark 3.2. It is worth noting that the hyperbolization procedure adopted has two main implications from the numerical point of view. First, as the relaxation time T appears in (3.15), this results in larger values of the celerity with respect to the elastic case. Furthermore, the parameter T can be small, so the third component of the source term vector (3.12) may then be stiff. Therefore, the numerical scheme selected to solve system (3.9) must be able to deal with this type of source terms.

Remark 3.3. System (3.9) is written in non-conservative form. As a consequence, to solve this system it is not possible to employ conservative numerical schemes of the form (2.88). In this case, we will adopt the path-conservative framework to compute the numerical fluctuations, the analogues of the numerical fluxes for conservative methods, as will be detailed in Section 3.4.1.

3.2.2 0D blood flow models with viscoelastic pressure-area relation

Let us consider the family of nonlinear lumped-parameter models for blood flow presented in Section 2.3. As already pointed out, this family of 0D blood flow models has been derived by extending the traditional approach of constructing lumped-parameter models for blood flow in a vascular segment, in a way to preserve certain nonlinear properties of the original 1D models. First, the nonlinear model parameters, the inductance L and the resistance R defined in (2.29), are no longer constant, bu they depend on the time-dependent average cross-sectional area $\widehat{A}(t)$, which, in turn, is related to the mean pressure $P(t)$. Second, pressure $P(t)$ is directly computed from the cross-sectional area $\widehat{A}(t)$, via a nonlinear pressure-area relation preserving the nonlinearity of the original 1D tube law.

In this section, in order to construct more realistic and reliable 0D models for blood flow, we will extend the family of nonlinear lumped-parameter models governed by the first-order ODE system (2.31) by adopting a viscoelastic tube law. As for the 1D blood flow model, throughout Section 3.3 we will still consider the nonlinear 0D models (2.31) coupled to the elastic pressure-area relation (2.35), focusing on the case of arterial vessels. Then, in the second part of this chapter, specifically in Section 3.4, a viscoelastic tube law will be adopted to relate pressure and area in these 0D models accounting for viscoelastic properties of the vessel wall.

Here, we first formulate the generic expression of a lumped-parameter viscoelastic tube law, which will be then specialized to the case of the viscoelastic pressure law (3.1) introduced for the 1D blood flow model in Section 3.2.1.

We define a generic viscoelastic tube law, relating the mean pressure $P(t)$ to the time-dependent average cross-sectional area $\widehat{A}(t)$ as follows

$$P(t) = P_0 + P_{El}(\widehat{A}; \Theta_{El}) + P_{Visco} + P_{ext}(t), \tag{3.22}$$

where P_0 is the reference pressure, P_{ext} is the external pressure, P_{El} is the elastic component, while P_{Visco} represents the viscoelastic term. Note that for now no dependencies have been specified for P_{Visco}, as the viscoelastic term has still to be characterized; on the other hand, the elastic component P_{El} depends on the time-dependent area $\widehat{A}(t)$, possibly in a nonlinear way, and on the set Θ_{El} of geometric and mechanical vessel parameters.

The 1D viscoelastic tube law (3.1)-(3.3) belongs to a very specific type of viscoelastic models, the Voigt-type viscoelastic models [5], for which the viscoelastic term of the tube law depends on the time partial derivative of the cross-sectional area of the vessel. However, we note that other classes of viscoelastic models can have very different terms. Here, in the derivation of a suitable viscoelastic pressure-area relation for the 0D blood flow models, we also restrict to the family of Voigt-type viscoelastic models. In the lumped-parameter case, the area $\widehat{A}(t)$ depends on time only, thus the partial derivative can be replaced by the total derivative, as follows

$$\partial_t \widehat{A} \equiv \frac{d\widehat{A}}{dt} = \frac{1}{l}\frac{d(l\widehat{A})}{dt} = \frac{1}{l}\frac{dV}{dt}, \tag{3.23}$$

which, by making use of the mass conservation equation in (2.31), can be rewritten as

$$\frac{1}{l}\frac{dV}{dt} = \frac{1}{l}\left(Q_{in} - Q_{out}\right). \tag{3.24}$$

At this point, we are ready to define the viscoelastic term P_{Visco} included in the tube law (3.22) as follows

$$P_{Visco} \equiv P_{Visco}(\widehat{A}, Q_{in}, Q_{out}; \Theta_{Visco}) = \frac{\Gamma(\widehat{A}; \Theta_{Visco})}{l}\left(Q_{in} - Q_{out}\right), \tag{3.25}$$

where Γ is the *nonlinear* viscoelastic coefficient, which depends on the time-dependent area $\widehat{A}(t)$ and on the set of geometric and mechanical vessel properties Θ_{Visco}. Inlet and outlet flow rates Q_{in} and Q_{out}, respectively, clearly depend on the specific 0D vessel configuration considered. In the case of a (P_{in}, Q_{out})-type 0D vessel, the viscoelastic term (3.25) becomes

$$P_{Visco} \equiv P_{Visco}(\widehat{A}, Q, Q_{out}; \Theta_{Visco}) = \frac{\Gamma(\widehat{A}; \Theta_{Visco})}{l}\left(Q - Q_{out}\right), \tag{3.26}$$

as the flow rate Q_{in} at the inlet of the 0D vessel coincides with the state variable Q. On the other hand, for a (Q_{in}, P_{out})-type 0D vessel, we have

$$P_{Visco} \equiv P_{Visco}(\widehat{A}, Q_{in}, Q; \Theta_{Visco}) = \frac{\Gamma(\widehat{A}; \Theta_{Visco})}{l}\left(Q_{in} - Q\right), \tag{3.27}$$

as in this case the flow rate Q_{out} at the outlet of the 0D vessel coincides with the state variable Q. Similarly, the viscoelastic term (3.25) for a (P_{in}, P_{out})-type 0D vessel is given by

$$P_{Visco} \equiv P_{Visco}(\widehat{A}, Q, Q_d; \Theta_{Visco}) = \frac{\Gamma(\widehat{A}; \Theta_{Visco})}{l}\left(Q - Q_d\right) \tag{3.28}$$

and, at last, as the (Q_{in}, Q_{out})-type 0D vessel is characterized by both a proximal and distal pressure variables, $P(t)$ and $P_d(t)$, respectively, the corresponding viscoelastic terms are defined as follows

$$P_{Visco} \equiv P_{Visco}(\widehat{A}, Q_{in}, Q; \Theta_{Visco}) = \frac{\Gamma(\widehat{A}; \Theta_{Visco})}{l/2}\left(Q_{in} - Q\right) \tag{3.29}$$

and

$$P_{d,Visco} \equiv P_{d,Visco}(\widehat{A}_d, Q, Q_{out}; \Theta_{d,Visco}) = \frac{\Gamma(\widehat{A}_d; \Theta_{d,Visco})}{l/2}\left(Q - Q_{out}\right). \tag{3.30}$$

Then, by replacing the viscoelastic term (3.25) into relation (3.22), we get the following lumped-parameter viscoelastic tube law

$$P(t) = P_0 + P_{El}(\widehat{A}; \Theta_{El}) + \frac{\Gamma(\widehat{A}; \Theta_{Visco})}{l}\left(Q_{in}(t) - Q_{out}(t)\right) + P_{ext}(t). \tag{3.31}$$

If the 0D vessel configuration considered includes more than one pressure state variable (*i.e.*, in the electric circuit notation employed in Table 2.1 to represent the different 0D vessel types, we have more than one capacitor), the same viscoelastic pressure law (3.31) is adopted for each one of the pressure variables, as

in the case of the (Q_{in}, Q_{out})-type 0D vessel illustrated above, where l will be replaced by a fraction of the entire vessel length and inlet and outlet flow rates Q_{in} and Q_{out} will be chosen appropriately.

From the general viscoelastic pressure law (3.31), the 0D counterpart of the 1D viscoelastic constitutive arterial wall equation (3.1)-(3.3) can be obtained by choosing

$$\begin{cases} P_{El}(\widehat{A};\Theta_{El}) = \dfrac{\pi r_0 h_0}{\widehat{A}}\left[E_e\varepsilon(\widehat{A}) + E_c\epsilon_r \ln\left(e^{\chi(\widehat{A})}+1\right)\right], & \text{with } \Theta_{El} = \{A_0, h_0, E_e, E_c, \varepsilon_0, \epsilon_r\}, \\ \Gamma(\widehat{A};\Theta_{Visco}) = \dfrac{\pi r_0 h_0}{\widehat{A}}\dfrac{K_m}{2\sqrt{A_0\widehat{A}}}, & \text{with } \Theta_{Visco} = \{A_0, h_0, K_m\}, \end{cases} \tag{3.32}$$

under the assumption that $A_d = A$ in (3.2). Clearly, in this case all the geometric and mechanical parameters defining both elastic and viscoelastic terms of the tube law, embedded in the sets Θ_{El} and Θ_{Visco}, respectively, are constant parameters.

In Section 3.4, we will adopt the family of nonlinear lumped-parameter blood flow models (2.31) coupled to the viscoelastic tube law (3.31)-(3.32).

Remark 3.4. We observe that choosing $\Theta_{El} = \{A_0, K, m, n\}$,

$$P_{El}(\widehat{A};\Theta_{El}) = K\left[\left(\frac{\widehat{A}(t)}{A_0}\right)^m - \left(\frac{\widehat{A}(t)}{A_0}\right)^n\right] \tag{3.33}$$

and $\Gamma(\widehat{A}) \equiv 0$ yields the purely elastic tube law adopted in Section 2.3.2.

3.2.3 Coupling equations

Given a generic vascular network, each vessel can be modeled either as a 1D domain or as a 0D compartment. In the first case, its physics will be described by the 1D blood flow model (2.1). In the latter case, the vessel will be represented according to one of the four possible 0D vessel configurations presented in Section 2.3.3 and its dynamics will governed by the corresponding ODE system reported in Table 2.1. Our aim is to, departing from a network of vessels, allow for any possible combination of 1D and 0D vessels to be considered. In this way, hybrid network configurations can be constructed, including both 1D and 0D vessels, where three different types of junction/coupling can be found: 1D coupling, 0D coupling and hybrid coupling. In this section, we illustrate the adopted coupling approach and derive the coupling equations that must be satisfied for each junction type. Indeed, a crucial aspect for constructing consistent networks of vessels is how to provide boundary conditions at terminal vertexes and algebraic coupling conditions between 1D and 0D domains at internal vertexes.

The coupling approach is based on conservation principles. Indeed, the coupling of two or more vessels at a junction must satisfy the following properties: (i) the conservation of mass, and (ii) the continuity of total pressure (or some approximation). Furthermore, only in the 1D and hybrid couplings, additional relations are obtained by imposing the continuity of the Riemann invariants in each 1D vessel.

3.2.3.1 1D coupling equations

In the case of purely elastic tube law (2.6), the 1D coupling approach to define the coupling conditions to be prescribed at a junction of 1D elastic vessels is the same as the one introduced in the previous chapter, in Section 2.5.1. Here, this methodology is extended to the case of a 1D junction of viscoelastic vessels.

Given a junction J shared by N 1D viscoelastic vessels, the same Riemann problem (2.74) with discontinuous geometric and mechanical vessel properties can be defined at the junction interface, as for the elastic case. Once again, the self-similar solution to the Riemann problem (2.74) consists of $2N$ constant states, the N initial condition states $\boldsymbol{Q}_k^{1D} = \left(A_k^{1D}, q_k^{1D}, \theta_k^{1D}\right)^T$, with $k = 1, \dots, N$, provided by the 1D vessels, and the N unknown boundary states $\boldsymbol{Q}_k^* = \left(A_k^*, q_k^*, \theta_k^*\right)^T$, with $k = 1, \dots, N$, to be determined. The unknowns of the

junction problem are now $3N$, not $2N$ as in the elastic case, because of the additional variable θ obtained from the hyperbolization procedure.

By following [97], the unknown state vectors $\boldsymbol{Q}_k^*$, with $k = 1, \dots, N$, are computed by solving the following nonlinear system of $3N$ equations

$$\begin{cases} \sum_{k=1}^{N} g_{1D}^k q_k^* = 0, \\ p(A_1^*, \theta_1^*) + \frac{1}{2}\rho \left(\frac{q_1^*}{A_1^*}\right)^2 - p(A_k^*, \theta_k^*) - \frac{1}{2}\rho \left(\frac{q_k^*}{A_k^*}\right)^2 = 0, \quad \text{for } k = 2, \dots, N, \\ \frac{q_k^*}{A_k^*} - \frac{q_k^{1D}}{A_k^{1D}} + g_{1D}^k \int_{A_k^{1D}}^{A_k^*} \frac{\widetilde{c}_T(\xi)}{\xi} d\xi = 0, \quad \text{for } k = 1, \dots, N, \\ \theta_k^* + \frac{A_k^*}{T_k} - \theta_k^{1D} - \frac{A_k^{1D}}{T_k} = 0, \quad \text{for } k = 1, \dots, N, \end{cases} \tag{3.34}$$

where g_{1D}^k is the auxiliary function defined as in (2.76). As in the elastic case, we are still imposing the conservation of mass and the continuity of total pressure across the junction, while the relations in the last two rows of system (3.34) enforce the continuity of the generalized Riemann invariants obtained from the eigenstructure analysis of the PDE system (3.9).

The relaxation time T is allowed to be different for each vessel, but it is assumed to be constant within each vessel, thus the eigenstructure analysis reported in Section 3.2.1.2 is not altered.

3.2.3.2 0D coupling equations

To couple 0D vessels at a junction, we extend the coupling procedure presented in the previous chapter, in Section 2.5.3, where the coupling conditions defined between 0D vessels ensure the conservation of flow and also impose a common pressure on all branches, to guarantee the continuity of pressure across the junction. By enforcing pressure continuity only, instead of total pressure continuity as in the 1D coupling, the problem to be solved at the junction is linear. However, in order to arrange compatible 0D vessel types into a network, with inlets and outlets coupled appropriately, restrictions on admissible 0D vessel configurations are necessary for vessels converging at the junction. Here, we extend this approach in order to find appropriate coupling conditions between 0D vessels that do not require any restrictions on the admissible 0D vessel types converging at a junction, but still ensuring the linearity of the coupling problem to be solved. Otherwise, the computational cost of solving a 0D coupling problem would increase and become comparable to the one required to solve a 1D nonlinear coupling problem.

The coupling conditions to be prescribed at a junction of 0D vessels are first defined in the elastic case, where mean pressure P and time-dependent average cross-sectional area $\widehat{A}$ are related via the nonlinear elastic tube law (2.35), for instance. The proposed 0D coupling approach is then extended to the viscoelastic case, where the family of nonlinear 0D blood flow models (2.31) is coupled to a viscoelastic tube law of the form (3.31).

Here, it is important to observe that, in the case of a purely elastic tube law, such as the elastic pressure-area relation (2.35) introduced in Section 2.3.2, the mean pressure $P(t)$ is a function of the time-dependent average cross-sectional area $\widehat{A}(t)$, or, equivalently, of the volume $V(t)$, only. On the other hand, if a viscoelastic tube law of the form (3.31) is adopted, then we have that the mean pressure $P(t)$ depends not only on $\widehat{A}(t)$, but also on the flow rates Q_{in} and Q_{out} at the inlet and outlet of the 0D vessel, respectively. This implies that, depending on the 0D vessel configuration of interest, the viscoelastic pressure $P(t)$ may be also a function of the flow rate state variable Q and/or of the flow rates Q_{in}/Q_{out} prescribed at the inlet/outlet of the vessel via suitable coupling conditions or boundary conditions. This fact will be taken into account when extending the 0D coupling approach presented in this section from the elastic to the viscoelastic case.

Elastic case. Suppose to have a junction connecting an arbitrary number M of 0D elastic vessels, sharing their inlets or outlets at the junction point. Then, the input and output quantities to be prescribed at the inlets and outlets of these vessels, P_{in}/Q_{in} and P_{out}/Q_{out}, respectively, depending on the configuration of each vessel, need to be determined in a way to ensure mass conservation and continuity of total pressure. This is done by prescribing to all inlets and outlets converging at the junction a common pressure P^*, which represents an approximation of the total pressure P^*_{tot} and is computed by enforcing the conservation of mass, that is

$$f_{MC}(P^*) = \sum_{j=1}^{M} g^j_{0D} Q^*_j = 0, \tag{3.35}$$

where g^j_{0D} is the auxiliary function similar to the one defined in (2.76) for the 1D coupling problem

$$g^j_{0D} = \begin{cases} -1, & \text{if } v^j \text{ shares its inlet,} \\ 1, & \text{if } v^j \text{ shares its outlet,} \end{cases} \tag{3.36}$$

and

$$Q^*_j = \begin{cases} Q^j, & \text{if } v^j \text{ shares } P\text{-type inlet/outlet,} \\ Q^j_{in}(P^*) = \dfrac{P^* - P^j}{R^j_p}, & \text{if } v^j \text{ shares } Q\text{-type inlet,} \\ Q^j_{out}(P^*) = \dfrac{P^j - P^*}{R^j_d}, & \text{if } v^j \text{ shares } Q\text{-type outlet,} \end{cases} \tag{3.37}$$

for $j = 1, \dots, M$. Note that the flow rates Q^*_j leaving or entering each 0D vessel can be either known (and given by the state variable Q – or Q_d – of the corresponding ODE system), or unknown and defined in terms of the pressure P^* (as a pressure difference over the vessel resistance), depending on the 0D vessel configuration.

The function f_{MC} in (3.35) is linear in the pressure unknown P^* and, once the value of P^* has been computed, in the j-th 0D vessel v^j we prescribe either a condition on the pressure, that is $P^j_{in} = P^*$ or $P^j_{out} = P^*$, or a condition on the flow rate, that is $Q^j_{in}(P^*)$ or $Q^j_{out}(P^*)$ given by the relations in (3.37), depending on the 0D vessel configuration. Equation (3.35) is solved exactly with an analytical formula to calculate P^*, thus no significant additional computational cost is required to solve the 0D elastic coupling problem.

Remark 3.5. We point out that, in the proposed 0D linear coupling procedure, only one configuration is not admitted, that is the one where all the inlets and outlets of the 0D vessels converging at the junction are of pressure type (P-type). Indeed, in this case, it is easy to see that in the mass conservation function f_{MC} defined in (3.35) only known quantities occur, that are the flow rates Q^j, $j = 1, \dots, M$, across the 0D vessels, and thus, there is no dependency on the common pressure P^*. As a consequence, both mass conservation and continuity of total pressure would be lost in this configuration.

Extension of the 0D coupling strategy to the viscoelastic case. Here, we extend the 0D elastic coupling strategy proposed above to the viscoelastic case. It is convenient to introduce the following notation: M denotes the total number of viscoelastic 0D vessels converging at the junction, with $M = M_P + M_Q$, where M_P is the number of 0D vessels sharing an inlet/outlet of P-type and M_Q is the number of 0D vessels sharing an inlet/outlet of Q-type. We also assume, without loss of generality, that the M 0D vessels can be reordered such that the first M_Q vessels are those sharing a Q-type inlet/outlet, for $j = 1, \dots, M_Q$, while the remaining M_P vessels are those sharing a P-type inlet/outlet, for $j = M_Q + 1, \dots, M$.
Then, the treatment of inlets/outlets of P-type converging at the 0D viscoelastic junction is the same as the

one applied in the elastic case; whereas, more care is required to deal with inlets/outlets of Q-type, as we will describe in the following.

Let us start from an example. Suppose to have a (Q_{in}, P_{out})-type 0D vessel sharing its inlet of flow-type at a 0D junction. The flow rate Q_{in} to be prescribed at the inlet of the vessel can be defined as

$$Q_{in} = \frac{P^* - P}{R_p}, \tag{3.38}$$

where P^* is the unknown common pressure across the junction, to be determined, P is the viscoelastic pressure in the 0D vessel and R_p is the proximal resistance of the vascular segment. Differently from the elastic case, now the pressure P is not known as it depends on the coupling condition Q_{in} itself entering in the viscoelastic term (3.27), that is

$$P = P_0 + P_{El}(\widehat{A}) + \frac{\Gamma(\widehat{A})}{l}(Q_{in} - Q) + P_{ext}, \tag{3.39}$$

where we have dropped the dependence from the geometric and mechanical parameters for the sake of simplicity in the notation. To address this issue, we propose to consider the pressure P in the 0D vessel as an additional unknown of the 0D viscoelastic junction problem, which must then satisfy the following additional equation

$$P - \left[P_0 + P_{El}(\widehat{A}) + \frac{\Gamma(\widehat{A})}{l}(Q_{in} - Q) + P_{ext}\right] = 0, \tag{3.40}$$

which, by making use of expression (3.38) for the inlet flow rate Q_{in}, can be rewritten as

$$P - \left[P_0 + P_{El}(\widehat{A}) + \frac{\Gamma(\widehat{A})}{l}\left(\frac{P^* - P}{R_p} - Q\right) + P_{ext}\right] = 0. \tag{3.41}$$

Clearly, this can be done for each one of the M_Q 0D vessels converging at the 0D junction with an inlet or outlet of Q-type: the pressure P^j, for $j = 1, \dots, M_Q$, becomes an additional problem unknown and an equation of the form (3.41) can be provided for the unknown pressure P^j, modified accordingly depending if the the 0D vessels shares either its inlet, Q_{in}, or its outlet Q_{out}.

At this point, we can generalize the proposed procedure and state the, still linear, coupling problem to be solved at a junction of 0D viscoelastic vessels. Given a junction connecting an arbitrary number M of 0D viscoelastic vessels, with $M = M_P + M_Q$, we define the following linear junction problem of $M_Q + 1$ equations in $M_Q + 1$ unknowns

$$\begin{cases} f_{MC}(P^*, P_1^*, \dots, P_{M_Q}^*) = \displaystyle\sum_{j=1}^{M_Q} g_{0D}^j Q_j^* + \sum_{h=M_Q+1}^{M} g_{0D}^h Q^h = 0, \\ P_j^* - \begin{cases} \left[P_0 + P_{El}(\widehat{A}^j) + \dfrac{\Gamma(\widehat{A}^j)}{l_j}\left(Q_j^* - Q^j\right) + P_{ext}\right] = 0, & \text{if } v^j \text{ shares } Q\text{-type inlet,} \\ \left[P_0 + P_{El}(\widehat{A}^j) + \dfrac{\Gamma(\widehat{A}^j)}{l_j}\left(Q^j - Q_j^*\right) + P_{ext}\right] = 0, & \text{if } v^j \text{ shares } Q\text{-type outlet,} \end{cases} \\ \qquad\qquad\qquad\qquad\qquad\qquad\qquad\qquad\qquad\qquad\qquad\qquad\qquad\qquad \text{for } j = 1, \dots, M_Q, \end{cases} \tag{3.42}$$

where

$$Q_j^*(P^*, P_j^*) = \begin{cases} Q_{in}^j(P^*, P_j^*) = \dfrac{P^* - P_j^*}{R_p^j}, & \text{if } v^j \text{ shares } Q\text{-type inlet,} \\ Q_{out}^j(P^*, P_j^*) = \dfrac{P_j^* - P^*}{R_d^j}, & \text{if } v^j \text{ shares } Q\text{-type outlet,} \end{cases} \qquad \text{for } j = 1, \dots, M_Q. \tag{3.43}$$

The first equation in (3.42) guarantees mass conservation across the junction. The $M_Q + 1$ unknowns are: the common pressure P^* prescribed at the junction point to ensure the continuity of (total) pressure; the

pressures P_j^*, for $j = 1, \dots, M_Q$, in each 0D vessel sharing an inlet or outlet of Q-type to the junction. We note that, as in the elastic case, the augmented viscoelastic junction problem (3.42) is still linear, thus no iterative procedure is required for its resolution.

Once the pressure unknowns have been computed, the corresponding condition on the flow rate, that is $Q_{in}^j(P^*, P_j^*)$ or $Q_{out}^j(P^*, P_j^*)$ given by the relations in (3.43), for $j = 1, \dots, M_Q$, or on the pressure, that is $P_{in}^j = P^*$ or $P_{out}^j = P^*$, for $j = M_Q + 1, \dots, M$, can be prescribed to each 0D vessel converging at the junction, depending on its configuration.

Remark 3.6. The proposed 0D viscoelastic coupling approach can be also adopted to solve other types of boundary conditions, such as the coupling of a 0D vessel to a *RCR* Windkessel or a single-resistance terminal model. In particular, if to be coupled to the terminal element is a 0D vessel inlet or outlet of Q-type, then the coupling conditions between the vessel and the terminal model presented in Section 2.5.3.4 can be augmented by considering the viscoelastic pressure P in the 0D vessel as an additional unknown and the corresponding linear equation to be satisfied by P.

Remark 3.7. It is worth noting that, in the viscoelastic case, solving the junction problem (3.42), or any other boundary condition problems (if the 0D vessel is coupled to a *RCR* Windkessel terminal model, for instance) allows us to compute the coupling conditions to be prescribed at the inlet/outlet of the 0D vessels converging at the junction, but also the viscoelastic pressure P in those vessels that share an inlet or outlet of Q-type at the junction. In fact, the quantities P_j^*, for $j = 1, \dots, M_Q$, obtained by solving system (3.42) represent the viscoelastic pressures in such vessels.

3.2.3.3 Hybrid coupling equations

The most general coupling of vessels at junctions is the one where both 1D and 0D vessels are coupled together, which allows us to construct hybrid networks of 1D-0D vessels. However, a hybrid coupling approach that ensures mass conservation and continuity of total pressure can be easily obtained by appropriately merging the 1D and 0D coupling procedures described in Sections 3.2.3.1 and 3.2.3.2, respectively, for both the elastic and viscoelastic cases.

Elastic case. Suppose to have a junction connecting N 1D elastic vessels and M 0D elastic vessels. For each 1D vessel, we have to compute the unknown boundary state vector $\boldsymbol{Q}_k^* = (A_k^*, q_k^*)$, with $k = 1, \dots, N$, whereas for each 0D vessel the input/output quantity to be prescribed at its inlet/outlet, that is P_{in}^j / Q_{in}^j or P_{out}^j / Q_{out}^j, with $j = 1, \dots, M$, has to be determined.

The hybrid coupling problem is governed by the following nonlinear system

$$\begin{cases} f_{MC}(q_1^*, \dots, q_N^*, p_{tot}^*) = \displaystyle\sum_{k=1}^{N} g_{1D}^k q_k^* + \sum_{j=1}^{M} g_{0D}^j Q_j^* = 0, \\ p(A_1^*) + \dfrac{1}{2}\rho \left(\dfrac{q_1^*}{A_1^*}\right)^2 - p(A_k^*) - \dfrac{1}{2}\rho \left(\dfrac{q_k^*}{A_k^*}\right)^2 = 0, \quad \text{for } k = 2, \dots, N, \\ \dfrac{q_k^*}{A_k^*} - \dfrac{q_k^{1D}}{A_k^{1D}} + g_{1D}^k \displaystyle\int_{A_k^{1D}}^{A_k^*} \frac{c(\xi)}{\xi} d\xi = 0, \quad \text{for } k = 1, \dots, N, \end{cases} \tag{3.44}$$

where

$$Q_j^* = \begin{cases} Q^j, & \text{if } v^j \text{ shares } P\text{-type inlet/outlet}, \\ Q_{in}^j(p_{tot}^*) = \dfrac{p_{tot}^* - P^j}{R_p^j}, & \text{if } v^j \text{ shares } Q\text{-type inlet}, \\ Q_{out}^j(p_{tot}^*) = \dfrac{P^j - p_{tot}^*}{R_d^j}, & \text{if } v^j \text{ shares } Q\text{-type outlet}, \end{cases} \qquad \text{for } j = 1, \dots, M. \tag{3.45}$$

The first relation in system (3.44) enforces mass conservation at the junction, taking into account the contribution of all vessels, both 1D and 0D. In particular, the 0D flow rates Q_j^*, with $j = 1, \dots, M$, given in (3.45), entering or leaving the 0D vessels converging at the junction, are defined in the same way as in (3.37) for the 0D coupling, with the only difference here that the approximate pressure P^* has now been replaced by the exact value of the total pressure p_{tot}^*, to be determined. Hence, the remaining equations in system (3.44) prescribe the continuity of the total pressure p_{tot}^* between the 1D vessels and the constancy of the generalized Riemann invariants in each 1D vessel. The idea is that we can still define and solve a Riemann problem at the junction interface between the 1D vessels, but when constructing its solution the presence of 0D vessels and their contribution to the flow balance through the junction have to be taken into account, as expressed in system (3.44).

System (3.44) includes $2N$ nonlinear equations in $2N$ unknowns, that are $A_1^*, \dots, A_N^*$ and $q_1^*, \dots, q_N^*$. By solving numerically this algebraic problem, we obtain the 1D boundary states $\boldsymbol{Q}_k^*$, for $k = 1, \dots, N$, and thus the common total pressure p_{tot}^*. The computed value of p_{tot}^* is then used to enforce in each 0D vessel either a condition on the pressure, that is $P_{in}^j = p_{tot}^*$ or $P_{out}^j = p_{tot}^*$, or a condition on the flow rate, that is $Q_{in}^j(p_{tot}^*)$ or $Q_{out}^j(p_{tot}^*)$ as defined in (3.45), for $j = 1, \dots, M$, depending on each 0D vessel configuration.

Remark 3.8. At hybrid junctions, 0D vessels are coupled via the total pressure p_{tot}^*. This choice is reasonable if we assume the kinetic term $\left(\frac{1}{2}\rho u^2\right)$ to be small compared to the pressure term, as will be demonstrated in Section 3.3.4.3 devoted to the validation of the adopted 1D junction model.
However, a possible improvement of the proposed hybrid coupling strategy may be to use, at the inlet/outlet of each 0D vessel converging at the hybrid junction, a pressure P_j^* obtained as the difference between the total pressure p_{tot}^* and the kinetic term in that vessel, as follows

$$P_j^* = p_{tot}^* - \frac{1}{2}\rho \left(\frac{Q_j^*}{\widehat{A}(P_j^*)} \right)^2, \tag{3.46}$$

for $j = 1, \dots, M$, where $\widehat{A}(P_j^*)$ is the average cross-sectional area corresponding to the pressure P_j^* via the nonlinear pressure-area relation (2.35). A nonlinear equation of the form (3.46) should then be added to the junction problem (3.44) for each 0D vessel converging at the junction, with P_j^* becoming an additional unknown of the augmented nonlinear problem to be solved.
This approach would allow us to still ensure the continuity of the total pressure across the junction, but prescribing the following coupling conditions for 0D vessels: $P_{in}^j = P_j^*$ or $P_{out}^j = P_j^*$, if the j-th vessel shares a P-type inlet/outlet; $Q_{in}^j(P_j^*)$ or $Q_{out}^j(P_j^*)$ as defined in (3.45), where p_{tot}^* has been replaced by P_j^*, if the j-th vessel shares a Q-type inlet/outlet.
This improvement has not been considered in this thesis, but it will be kept in mind for future work.

Extension of the hybrid coupling strategy to the viscoelastic case. At this point, we can easily extend the hybrid coupling strategy proposed above to the viscoelastic case. Let us consider a viscoelastic junction connecting N 1D vessels and M 0D vessels, with $M = M_P + M_Q$, under the same notation assumptions introduced before for the 0D viscoelastic coupling. For each 1D vessel, the unknown boundary state vector $\boldsymbol{Q}_k^* = \left(A_k^*, q_k^*, \theta_k^*\right)$, with $k = 1, \dots, N$, has to be determined, whereas for each 0D vessel the input/output quantity to be prescribed at its inlet/outlet, that is P_{in}^j / Q_{in}^j or P_{out}^j / Q_{out}^j, with $j = 1, \dots, M$, has to be computed. Furthermore, the viscoelastic pressure P_j^*, with $j = 1, \dots, M_Q$, in each 0D vessel sharing an inlet or outlet of Q-type is an additional unknown of the junction problem.

Then, the hybrid coupling problem is governed by the following nonlinear system

$$\begin{cases} f_{MC}(q_1^*,\dots,q_N^*,p_{tot}^*,P_1^*,\dots,P_{M_Q}^*) = \sum_{k=1}^{N} g_{1D}^k q_k^* + \sum_{j=1}^{M_Q} g_{0D}^j Q_j^* + \sum_{h=M_Q+1}^{M} g_{0D}^h Q_h = 0, \\ p(A_1^*,\theta_1^*) + \frac{1}{2}\rho\left(\frac{q_1^*}{A_1^*}\right)^2 - p(A_k^*,\theta_k^*) - \frac{1}{2}\rho\left(\frac{q_k^*}{A_k^*}\right)^2 = 0, \quad \text{for } k=2,\dots,N, \\ \frac{q_k^*}{A_k^*} - \frac{q_k^{1D}}{A_k^{1D}} + g_{1D}^k \int_{A_k^{1D}}^{A_k^*} \frac{\widetilde{c}_T(\xi)}{\xi} d\xi = 0, \quad \text{for } k=1,\dots,N, \\ \theta_k^* + \frac{A_k^*}{T_k} - \theta_k^{1D} - \frac{A_k^{1D}}{T_k} = 0, \quad \text{for } k=1,\dots,N, \\ P_j^* - \begin{cases} \left[P_0 + P_{El}(\widehat{A}^j) + \frac{\Gamma(\widehat{A}^j)}{l_j}\left(Q_j^* - Q^j\right) + P_{ext}\right] = 0, & \text{if } v^j \text{ shares } Q\text{-type inlet}, \\ \left[P_0 + P_{El}(\widehat{A}^j) + \frac{\Gamma(\widehat{A}^j)}{l_j}\left(Q^j - Q_j^*\right) + P_{ext}\right] = 0, & \text{if } v^j \text{ shares } Q\text{-type outlet}, \end{cases} \quad \text{for } j=1,\dots,M_Q, \end{cases} \tag{3.47}$$

where

$$Q_j^*(p_{tot}^*,P_j^*) = \begin{cases} Q_{in}^j(p_{tot}^*,P_j^*) = \dfrac{p_{tot}^* - P_j^*}{R_p^j}, & \text{if } v^j \text{ shares } Q\text{-type inlet}, \\ Q_{out}^j(p_{tot}^*,P_j^*) = \dfrac{P_j^* - p_{tot}^*}{R_d^j}, & \text{if } v^j \text{ shares } Q\text{-type outlet}, \end{cases} \quad \text{for } j=1,\dots,M_Q. \tag{3.48}$$

System (3.47) includes $3N+M_Q$ nonlinear equations in $3N+M_Q$ unknowns, that are $A_1^*,\dots,A_N^*$, $q_1^*,\dots,q_N^*$, $\theta_1^*,\dots,\theta_N^*$ and $P_1^*,\dots,P_{M_Q}^*$. By solving numerically this algebraic nonlinear problem, we obtain the 1D boundary states $\boldsymbol{Q}_k^*$, for $k=1,\dots,N$, the data to be prescribed at the inlet/outlet of the M 0D vessels and the viscoelastic pressures P_j^*, for $j=1,\dots,M_Q$, in those 0D vessels that share an inlet or outlet of Q-type at the hybrid junction.

Remark 3.9. With respect to the elastic case, the nonlinear hybrid coupling problem (3.47) defined for a viscoelastic hybrid junction includes an additional equation in the unknown pressure P_j^*, for $j=1,\dots,M_Q$, for each 0D vessel sharing an inlet or outlet of flow type at the junction. On the other hand, if all inlets and outlets are of pressure type, no extra equations are added to the nonlinear coupling problem to be solved.
When performing numerical simulations on the ADAN model [17, 16] by applying the proposed hybrid coupling strategy, we encountered some stability issues in certain hybrid network configurations where 0D vessels were coupled to 1D vessels at hybrid junctions with inlets/outlets of Q-type. These issues were not reported when the "problematic" hybrid networks were modified in order to avoid hybrid junction configurations with 0D vessel's inlets/outlets of Q-type. Since the source of such instability is still unclear, for viscoelastic hybrid junctions only, in this work we will restrict to consider junction configurations where inlets and outlets of 0D vessels are always of P-type. We note that this restriction does not limit the hybrid configurations that can be constructed for a network, but just the 0D element type to be used for those 0D vessels converging at hybrid junction, in the viscoelastic case.
Future work will include the design a more robust hybrid coupling strategy for viscoelastic junctions.

3.3 Hybrid networks and *a-priori* model selection criteria

In this section, we present a methodology proposed to construct and solve hybrid networks of 1D-0D vessels coupled together, focusing on the development and validation of a high-order numerical coupling strategy to treat hybrid junctions and on the identification of *a-priori* model selection criteria to be used to construct hybrid models, which provide a good trade-off between computational cost of the simulations

and accuracy in the predicted results. We point out that, to the best of our knowledge, a methodology to construct hybrid networks of 1D-0D vessels based on some model selection criteria and to perform blood flow simulations in such networks has never been reported before, in the existing literature. In this section, the hybrid network methodology is first developed in a simplified modeling and computational setting, and applied to several benchmark arterial networks of moderate complexity to be tested and validate. In particular, for both 1D and 0D blood flow models we still consider (i) purely elastic tube laws (2.6) and (2.35), respectively, and (ii) constant geometric and mechanical properties in 1D vessels. Hence, 1D and 0D vessels are coupled via the 1D, 0D and hybrid coupling strategies defined in Section 3.2.3 for the elastic case.

In particular, in Section 3.3.1.1 we first recall the numerical methods adopted to solve the 1D and 0D blood flow models, already introduced in the previous chapter of the thesis. Next, in Section 3.3.2 the high-order numerical coupling procedures proposed to solve the 0D and hybrid coupling of vessels are illustrated, while the numerical treatment of 1D junctions is the same as the one described and adopted in the previous chapter, in Section 2.6.2. In fact, when using high-order numerical schemes to approximate the solutions of the 1D blood flow model (2.1) and of the lumped-parameter models (2.31), high-order coupling strategies are also needed in order to preserve the space and time accuracy of the original schemes over the entire network. Afterwards, in Section 3.3.3, we develop an adaptive model selection approach based on *a-priori* model selection criteria to construct hybrid networks of 1D-0D vessels. Our aim is to find relevant criteria, based on vessel geometrical and mechanical properties or on flow distribution information, that enable us to choose the most suitable model to be used for each vessel of a network, ensuring the correct trade-off between the accuracy of the predicted results and the computational cost of the simulations, with respect to the 1D network. Finally, in Section 3.3.4, we perform a series of numerical experiments and discuss the obtained results. In particular, a set of convergence rate studies is first carried out and then, the proposed adaptive model selection strategy built upon several different *a-priori* model selection criteria is tested and applied to two arterial networks. The numerical experiments section is closed by presenting a quantitative study of a simple bifurcation model where 1D simulation results are compared against 3D results to validate the adopted 1D junction model and assess its ability to describe and reproduce flow splitting and wave propagation at junctions.

3.3.1 Numerical methods

3.3.1.1 Numerical schemes for 1D and 0D blood flow models

Under the assumption of constant material and geometric vessels properties and the choice of the elastic tube law (2.6), the PDE system (2.1) governing 1D blood flow is written in conservative form (2.9) and, also here, is discretized using the second-order MUSCL-Hancock numerical scheme, with ENO reconstruction and numerical source computed following the ADER approach. We refer to Section 2.6.1 for full details about the numerical method.

In the previous chapter, fully 0D network configurations were solved numerically by constructing a global system of ODEs, describing the dynamics of the entire network. On the other hand, here each 0D vessel of either a fully 0D or a hybrid network model is evolved separately and connected to the neighboring 1D/0D vessels via coupling conditions at each time level.

We proceed as follows. Each 0D vessel configuration describing blood flow in a 0D vascular segment is governed by a system of first-order, nonlinear ODEs obtained from (2.31), which can be rewritten in compact form as

$$\frac{d}{dt}\boldsymbol{Y}_j(t) = \boldsymbol{B}_j(t, \boldsymbol{Y}_j(t), \boldsymbol{Y}_j^D(t)), \quad \boldsymbol{Y}_j(0) = \boldsymbol{Y}_j^0, \tag{3.49}$$

where $\boldsymbol{Y}_j \in \mathbb{R}^{N_{S,j}}$ is the state variable vector of 0D vessel v^j, with $N_{S,j}$ being the number of state variables of v^j, and $\boldsymbol{Y}_j^0$ is the initial condition vector. The nonlinear vector function $\boldsymbol{B}_j$ on the right-hand side of the system depends on $\boldsymbol{Y}_j(t)$ directly and on the vector $\boldsymbol{Y}_j^D(t)$ of the data prescribed at the inlet and outlet of the j-th vessel, with $\boldsymbol{Y}_j^D \in \mathbb{R}^{N_{D,j}}$, being $N_{D,j}$ the number of conditions to be prescribed to the j-th vessel. These prescribed data can include coupling conditions at internal junctions, coupling conditions to either single-resistance or RCR Windkessel elements for terminal vessels, and also external sources $f_{ext}(t)$ to the vessel, such as a prescribed inflow at the inlet of the aorta. In particular, if a 0D vessel shares its inlet and/or outlet at junctions, then the vector $\boldsymbol{Y}_j^D(t)$ will be defined also by the state of its adjacent 1D/0D vessels, according to the different coupling approaches introduced in Section 3.2.3.
Then, for each 0D vessel, the corresponding ODE system of the form (3.49) is solved using RK4 method with appropriate time step to guarantee the stability of the scheme and the mesh independence of the solution.

3.3.2 High-order numerical couplings

In general, given a generic hybrid network of elastic vessels, where 1D and 0D vessels are coupled via the proposed 1D, 0D and hybrid coupling strategies, all vessels will be evolved by using the same global time step Δt^n, given by

$$\Delta t^n = \min_{k=1,\dots,N_{1D}} \Delta t_k^{n,CFL}, \tag{3.50}$$

for $n \geq 0$, where N_{1D} is the total number of 1D vessels of the network and $\Delta t_k^{n,CFL}$ is the time step corresponding to the k-th 1D vessel at the time level n, computed according to the CFL stability condition. This choice of the global time step Δt^n (3.50) clearly ensures the stability of the adopted numerical method in all 1D vessels. However, on the other hand, this time step may not be sufficiently small to guarantee also the stability of the explicit numerical scheme used to solve the ODE systems corresponding to the 0D vessels of the network. If that is the case, the global time stepping procedure can be replaced by a local time stepping technique, so that 1D and 0D vessels are evolved with two different time steps, Δt^n and Δt^{m_n}, respectively, each one ensuring the stability of the corresponding numerical method. Given the 1D time step Δt^n computed as in formula (3.50), we define a 0D local time step Δt^{m_n} by dividing the time step Δt^n in a finite number n_{step} of subintervals, as

$$\Delta t^{m_n} = \frac{\Delta t^n}{n_{step}}, \tag{3.51}$$

where the subscript n to the index m in Δt^{m_n} emphasizes that the 0D time step Δt^m clearly depends on the 1D time step Δt^n at the time level n.
In this way, 0D vessels will evolve with reduced local time step Δt^{m_n} from time t^m to time $t^{m+1} = t^m + \Delta t^{m_n}$, $m \geq 0$, while 1D vessels will evolved with time step Δt^n from time t^n to time $t^n + 1 = t^n + \Delta t^n$, $n \geq 0$, only when $t^{n+1} \equiv t^{m+1}$, that is when the 1D and 0D time levels are synchronized. For full details on the local time stepping (LTS) methodology see [102]. We also emphasize that the choice of the number of subintervals n_{step} may depend on the specific problem and the network characteristics.

When dealing with networks of vessels, a very important aspect to be addressed is the accurate numerical treatment of junctions. In fact, the order of accuracy of the numerical schemes adopted to solve the 1D and 0D models for a single vessel must be preserved also by the different coupling procedures, at the level of junctions, in order to globally ensure the desired accuracy of the solutions. In particular, when constructing hybrid networks of vessels, the idea is that we can adopt a 1D model for those vessels in which we need higher accuracy, while vessels that are less relevant for the specific problem/application can be modeled as 0D elements. As a consequence, it is crucial for the numerical coupling strategy adopted to solve hybrid junction of 1D and 0D vessels to preserve the accuracy of the solution in the 1D vessels, which must not be affected by the coupling with 0D vessels.

In the following of this section, we will describe the different methodologies adopted to achieve high-order numerical coupling for the different types of junctions. 1D junctions are solved using the numerical coupling approach presented in Section 2.6.2. Hence, in this section, we will focus on the coupling techniques proposed to solve 0D and hybrid junction. In Section 3.3.4.1, a systematic convergence rate study will be carried out in order to verify that the expected order of accuracy of the proposed numerical coupling strategies is actually attained.

3.3.2.1 0D coupling

In the case of 0D coupling, it is straightforward to preserve the fourth-order accuracy in time of the RK4 method also at the level of junctions, in the 0D coupling procedure. The RK4 scheme, adopted to solve the ODE systems associated to the different 0D vessel configurations and reported in the Supporting Information, is a four-step method. The approximate solution at the next time level $t^{m+1} = t^m + \Delta t^m$ is obtained by summing to the approximate solution at the present time level t^m the product between the weighted average of four increments, $\{K_s\}_{s=1,\dots,4}$, and the size of the time interval Δt^m.

Given a junction connecting M 0D vessels, even if each 0D vessel is evolved separately according to the corresponding ODE system governing its dynamics, these vessels are not isolated, but are interacting with each other via the coupling conditions (pressures/flow rates) prescribed at their inlets and outlets converging at the junction. As a consequence, to evolve from time t^m to time t^{m+1} the solution in each 0D vessel according to RK4 method (B.1), the coupling conditions between these vessels must be updated at each of the four intermediate steps of the scheme, namely the 0D coupling problem must be solved at each RK4 intermediate step. This is clear also from the RK4 method's formulae (B.1), where each of the four increments, K_s, for $s = 1, \dots, 4$, is computed by using the intermediate updated RK4 solution and prescribed data, contained in vector $\boldsymbol{Y}^D$, corresponding to each intermediate step. The outline of the algorithm is given in Appendix B.

3.3.2.2 Hybrid coupling

We deal now with the case of hybrid coupling between 1D and 0D vessels. In particular, 1D vessels are evolved using the second-order MUSCL-Hancock scheme and 0D vessels are solved adopting the explicit RK4 method, either with a global time step Δt^n or with two different local time steps, Δt^n for the 1D vessels and Δt^{m_n} for the 0D vessels, as explained at the beginning of this section. Here, we propose a numerical strategy that allows to achieve high-order hybrid coupling, to preserve second-order accuracy in space and time in the 1D vessels and the second-order accuracy in time in the 0D vessels.

Let us start from the case of global time step, namely the case where all 1D and 0D vessels converging at a hybrid junction have the same time step Δt^n. Suppose to have a junction at which N 1D vessels and M 0D vessels join, and that all these vessels are evolved with the same global time step Δt^n computed as in (3.50). To evolve the solution in all vessels from time t^n to time $t^{n+1} = t^n + \Delta t^n$, the 1D-0D coupling conditions must be updated at each one of the four intermediate steps of RK4 method (B.1). To be precise, at step s of RK4 scheme, for $s = 1, \dots, 4$, the nonlinear coupling problem defined in Section 3.2.3.3 for a hybrid junction must be solved, to compute the corresponding coupling conditions between vessels, by considering:

- in the 0D vessels, the RK4 intermediate solution obtained at step s of the method to compute the increment K_s, in the same way as illustrated in Section 3.3.2.1 for 0D coupling;

- in the 1D vessels, the MUSCL boundary extrapolated values $\boldsymbol{Q}_{k,1}^{L,n}$ / $\boldsymbol{Q}_{k,\overline{M}_k}^{R,n}$, with $k = 1, \dots, N$, evolved by a fraction of the time step Δt^n equal to that used at the intermediate step s of RK4 method, that is

$$\begin{cases} \overline{\boldsymbol{Q}}_{k,1}^{L,n+H_s} = \boldsymbol{Q}_{k,1}^{L,n} - \dfrac{H_s \Delta t^n}{\Delta x_k} \left[\boldsymbol{F}(\boldsymbol{Q}_{k,1}^{R,n}) - \boldsymbol{F}(\boldsymbol{Q}_{k,1}^{L,n}) \right] + H_s \Delta t^n \boldsymbol{S}(\boldsymbol{Q}_{k,1}^{L,n}), & \text{if } x_J^k = 0, \\ \overline{\boldsymbol{Q}}_{k,\overline{M}_k}^{R,n+H_s} = \boldsymbol{Q}_{k,\overline{M}_k}^{R,n} - \dfrac{H_s \Delta t^n}{\Delta x_k} \left[\boldsymbol{F}(\boldsymbol{Q}_{k,\overline{M}_k}^{R,n}) - \boldsymbol{F}(\boldsymbol{Q}_{k,\overline{M}_k}^{L,n}) \right] + H_s \Delta t^n \boldsymbol{S}(\boldsymbol{Q}_{k,\overline{M}_k}^{R,n}), & \text{if } x_J^k = l_k, \end{cases} \tag{3.52}$$

  for $s = 1, \dots, 4$ and $k = 1, \dots, N$. $H = \left\{0, \frac{1}{2}, \frac{1}{2}, 1\right\}$ is the vector containing the time step fractions to be used to evolve the 1D boundary extrapolated values in the four RK4 intermediate steps. In particular, at step $s = 1$ of RK4 method, we have no evolution of the MUSCL reconstructed variables, at steps $s = 2, 3$ of the scheme the boundary extrapolated values are evolved by a half Δt^n, and at step $s = 4$ we will have the evolution of a complete time step Δt^n.

Then, by solving the hybrid coupling problem, at each step of RK4 method we get:

- the 0D coupling conditions $P_{in/out}^{j,s}$ / $Q_{in/out}^{j,s}$, for $j = 1, \dots, M$, namely pressures and flow rates to be prescribed at the inlets and outlets of the 0D vessels converging at the hybrid junction;
- the 1D boundary state vectors $\boldsymbol{Q}_k^{*,s}$, for $k = 1, \dots, N$, for the 1D vessels.

Once the four intermediate steps of RK4 method are completed, 0D vessels are simply evolved according to RK4 formula. On the other hand, in each 1D vessel, the time integral of the boundary flux, needed to evolve the 1D solution from time t^n to time t^{n+1} according to the finite volume formula (2.88), is approximated using a quadrature formula with nodes over the interval $[t^n, t^{n+1}]$ given by the four times corresponding to the four steps of RK4 and the same weights of the four RK4 increments, as follows

$$\begin{cases} \text{nodes:} & \{t_s^n = t^n + H_s \Delta t^n\}_{s=1,\dots,4}, \\ \text{weights:} & \{\omega_s\}_{s=1,\dots,4} = \left\{\frac{1}{6}, \frac{1}{3}, \frac{1}{3}, \frac{1}{6}\right\}, \end{cases} \tag{3.53}$$

to get

$$\begin{cases} \boldsymbol{F}_{\frac{1}{2}}^k = \displaystyle\sum_{s=1}^{4} \omega_s \boldsymbol{F}(\boldsymbol{Q}_k^{*,s}) \approx \frac{1}{\Delta t^n} \int_{t^n}^{t^{n+1}} \boldsymbol{F}\left(\boldsymbol{Q}(x_{\frac{1}{2}}, t)\right) dt, & \text{if } x_J^k = 0, \\ \boldsymbol{F}_{\overline{M}_k + \frac{1}{2}}^k = \displaystyle\sum_{s=1}^{4} \omega_s \boldsymbol{F}(\boldsymbol{Q}_k^{*,s}) \approx \frac{1}{\Delta t^n} \int_{t^n}^{t^{n+1}} \boldsymbol{F}\left(\boldsymbol{Q}(x_{\overline{M}_k + \frac{1}{2}}, t)\right) dt, & \text{if } x_J^k = l_k, \end{cases} \tag{3.54}$$

for $k = 1, \dots, N$.

With this methodology, 1D and 0D vessels converging at the hybrid junction are evolved with their own time-marching schemes, but their mutual interaction is taken into account at each intermediate step of RK4 method and we achieve the second-order accuracy of the coupling.

Remark 3.10. It is clear that adopting the four-step RK4 method to solve the ODE systems governing blood flow in the 0D vessels and the proposed numerical hybrid coupling strategy requires that, at each time step, the hybrid coupling problem must be solved four times at each junction of 1D-0D vessels to preserve the desired second-order accuracy in the solution. Since in the 1D domain we use a second-order accurate numerical scheme, it would be reasonable to employ a second-order method also for the 0D domain, so that each time step would demand to solve the hybrid coupling just two times, thus reducing the computational effort and time of the simulations. However, our choice of using the fourth-order Runge-Kutta scheme is justified by the fact that this method has better stability properties than other possible second-order, explicit numerical schemes for ODE systems. Indeed, as we will see in Section 3.3.4 devoted to numerical experiments, when using a sufficiently fine 1D mesh size, the 1D time step obtained according

to the CFL condition can be used for both 1D and 0D vessels as global time step, also ensuring the stability of RK4 method and the accuracy of the predicted 0D results. On the other hand, numerical experiments (not reported here) have shown that second-order, explicit schemes, like Heun's method and the midpoint method, are not as stable as the RK4 scheme, thus requiring a significantly smaller time step than the 1D time step computed via the CFL condition. In this case, a "local time stepping procedure", as the one described at the beginning of Section 3.3.2, could be implemented, but, because of the very small 0D time step, the number of times to solve the hybrid coupling would increase even more in order to synchronize 1D and 0D vessels converging at the same junction.

The proposed strategy can be easily extended also to the case of local time steps Δt^n for 1D vessels, defined as in (3.50), and Δt^{m_n} for 0D vessels, computed as in (3.51). From the definitions of these local time steps, we clearly have $\Delta t^n = n_{step}\Delta t^{m_n}$. Hence, starting from time t^n, the numerical procedure illustrated above is performed over each time interval of the form $[t^n + (r-1)\Delta t^{m_n}, t^n + r\Delta t^{m_n}]$, for $r = 1, \dots, n_{step}$, to update the solution in the 0D vessels and to compute the 1D boundary vector states $\left\{\boldsymbol{Q}_k^{*,rs}\right\}_{s=1,\dots,4}$, for $r = 1, \dots, n_{step}$ and $k = 1, \dots, N$. Then, the boundary numerical fluxes in the 1D vessels are obtained by approximating the time integral of the interface flux over the entire interval $[t^n, t^{n+1}]$, with $t^{n+1} = t^n + \Delta t^n = t^n + n_{step}\Delta t^{m_n}$, as

$$\left.\begin{array}{ll} \text{if } x_J^k = 0, & \boldsymbol{F}_{\frac{1}{2}}^k \\ \text{if } x_J^k = l_k, & \boldsymbol{F}_{M_k+\frac{1}{2}}^k \end{array}\right\} = \frac{1}{n_{step}} \sum_{r=1}^{n_{step}} \sum_{s=1}^{4} \omega_s \boldsymbol{F}(\boldsymbol{Q}_k^{*,rs}), \tag{3.55}$$

for $k = 1, \dots, N$. These boundary flux vectors are finally used to evolve the solution in the 1D vessels from time t^n to time t^{n+1} according to the finite volume formula (2.88).

In the case in which a 1D vessel is coupled to a *RCR* Windkessel model, the same hybrid coupling strategy can be adopted to solve the "hybrid junction" between the vessel and the *RCR* element, where the RK4 method is applied to evolve the ODE governing the temporal dynamics of the pressure $P_{wk}(t)$ in the Windkessel.

3.3.3 Adaptivity and *a-priori* model selection criteria

At this point, equipped with both 1D and 0D blood flow models and with suitable numerical coupling strategies, we need an effective methodology to construct hybrid networks of vessels. In particular, we want to identify relevant *a-priori* model selection criteria that, given any network of vessels of which geometrical and mechanical properties are known, allow us to determine the most suitable model, either 1D or 0D, to be used for each vessel of the network.

One of the main goals of the present work is to address the issues of computational cost and efficiency related to the modeling and simulation of blood flow in highly complex networks. Therefore, we look for model selection criteria able to provide the best trade-off between (i) computational cost of the simulations in the resulting hybrid networks, and (ii) accuracy in the predicted results with respect to the reference, computationally expensive 1D results. The starting point is a 1D network, namely a network where all vessels are represented as coupled 1D domains. Then, we explore different model selection criteria to be used to determine the vessels that can be turned into 0D models. The analysis carried out allows us to identify those parameters that generate hybrid network configurations where, on the one hand, the computational cost of the simulations is strongly reduced and, on the other hand, pressure and flow waveforms are reproduced with a good level of accuracy throughout the entire network.

We have proposed and tested the following *a-priori* model selection criteria: vessel length l; vessel radius r_0; intravascular volume $V_0 = (\pi r_0^2)l$; vessel compliance $C_0 := l\left(\frac{\partial A}{\partial p}\right)\Big|_{A=A_0}$; mean flow rate $\overline{Q}$ through the

vessel; r_0^3, which is an (inverse) indicator of wall shear stress; r_0^4, which is an (inverse) indicator of resistance; Reynolds number $Re = \frac{\rho D \overline{U}}{\mu}$, where D is the vessel diameter and $\overline{U}$ is the mean blood velocity.

In the following, we are going to illustrate the methodology adopted to assess the performance of these criteria, to identify the most suitable ones to construct hybrid networks of 1D-0D vessels. This adaptive model selection strategy will be then applied in Section 3.3.4.2 to two different arterial networks, the 37-artery network presented in [89] and the reduced ADAN56 model reported in [22].

Before starting, we point out that most of the criteria considered above are defined in terms of known geometrical and mechanical vessel properties. However, the mean flow rate $\overline{Q}$ through the vessel, as well as the average flow velocity $\overline{U}$, characterizing the nondimensional Reynolds number Re, are not known *a-priori* in all vessels of any generic network. In the present work, for both arterial networks to which this methodology is to be applied in Section 3.3.4.2, the 37-artery network and ADAN56 model, these quantities are computed for all vessels from the available reference solution, that is the 1D results. However, in general, this approach may not be feasible, especially for highly complex and large networks where computational results are not available *a-priori*.

Suppose to have an arterial network with N_{tot} vessels. First of all, for each parameter defining a criterion $\mathcal{C}$, with $\mathcal{C} \in \{l, r_0, V_0, C_0, \overline{Q}, r_0^3, r_0^4, Re\}$, we consider different 1D-0D thresholds $\gamma_1^{\mathcal{C}}, \dots, \gamma_p^{\mathcal{C}}$. To determine these thresholds, we look at the distribution of the parameters of the vessels defining the different criteria: for each parameter, we choose a set of 1D-0D thresholds such that, when moving from a threshold $\gamma_h^{\mathcal{C}}$ to the consecutive one $\gamma_{h+1}^{\mathcal{C}}$, for $h = 1, \dots, p-1$, the number of 1D vessels that become 0D is sufficiently uniform. We do not require always the same number of vessels to be changed from 1D to 0D, but at least a certain regularity in the sampling procedure. Then, for each criterion $\mathcal{C}$ and each criterion threshold $\gamma_h^{\mathcal{C}}$, with $h = 1, \dots, p$, the corresponding hybrid network is constructed as follows

$$v^j = \begin{cases} \text{0D}, & \text{if } \mathcal{C}_j < \gamma_h^{\mathcal{C}}, \\ \text{1D}, & \text{otherwise}, \end{cases} \qquad \text{for } j = 1, \dots, N_{tot}, \tag{3.56}$$

where $\mathcal{C}_j$ denotes the value of the parameter defining the criterion $\mathcal{C}$ in the j-th vessel.

In addition, recalling the dimensional analysis performed in Section 2.2.2 for the 1D blood flow equations (2.1), we have identified the following nondimensional coefficient (denoted by γ_P in Section 2.2.2), which characterizes the pressure term in the corresponding nondimensional momentum balance equation and may also be used as model selection criterion

$$\Gamma_P = \frac{T_0}{l\overline{U}} c^2, \tag{3.57}$$

where T_0 is the time scale, l is the longitudinal spatial scale (*i.e.*, the vessel length), $\overline{U}$ is the average flow velocity and c is the wave speed. In particular, if we replace the wave speed c by a constant reference value c_0, the above nondimensional parameter Γ_P can be rewritten in terms of the intravascular volume V_0 and the compliance C_0, as follows

$$\Gamma_P = \frac{T_0}{\rho l \overline{U}} \frac{V_0}{C_0}. \tag{3.58}$$

As for the Reynolds number Re, calculating the value of the nondimensional pressure coefficient Γ_P in each vessel of a network also depends on available *a-priori* estimates of the average flow velocity $\overline{U}$, as discussed above.

In expression (3.58) defining Γ_P, the volume V_0 is at the numerator, which means that smaller values of V_0 correspond to smaller values of Γ_P, while, since the compliance C_0 is at the denominator of the definition of Γ_P, we have that smaller values of C_0 give larger values of the nondimensional coefficient Γ_P. Therefore, given a network of vessels and chosen a set of thresholds for the parameter Γ_P, this specific model selection criterion will be tested "in both directions". Namely, for each threshold, two corresponding hybrid

networks are constructed, according to both the rule defined in (3.56) (this criterion will be called Γ_P "from below") and the following one (this criterion will be referred to as Γ_P "from above")

$$v^j = \begin{cases} \text{1D}, & \text{if } \mathcal{C}_j < \gamma_h^{\mathcal{C}}, \\ \text{0D}, & \text{otherwise}, \end{cases} \qquad \text{for } j = 1, \dots, N_{tot}, \tag{3.59}$$

with $\mathcal{C} = \Gamma_P$.

For each hybrid network available, the CPU time required by the simulation is recorded and the root mean square (RMS) relative errors in the predicted results are computed with respect to the reference 1D results, as follows

$$\varepsilon_P^{RMS} = \sqrt{\frac{1}{n}\sum_{i=1}^{n}\left(\frac{P_i - P_i^{ref}}{P_i^{ref}}\right)^2}, \qquad \varepsilon_Q^{RMS} = \sqrt{\frac{1}{n}\sum_{i=1}^{n}\left(\frac{Q_i - Q_i^{ref}}{\max_j\left(Q_j^{ref}\right)}\right)^2}, \tag{3.60}$$

where $i = 1, \dots, n$ are time points over the cardiac cycle at which the solution is sampled, P and Q are pressure and flow results from the hybrid network, while P^{ref} and Q^{ref} are reference pressure and flow results from the 1D network. In both configurations, in the 1D vessels the solution is sampled at the midpoint of the vessel. Other choices are possible (like, for example, averaged quantities over the 1D domain) and would not affect the conclusions of this work (results not reported here).

Hence, CPU time and errors distributions, as well as efficiency plots can be generated and analyzed for each criterion and compared between different criteria, in order to identify the model selection criteria providing the best trade-off between errors and computational cost.

We emphasize that out goal here is to identify suitable *a-priori* model selection criteria to construct hybrid networks of vessels. However, the choice of the specific threshold to be used for each parameter is not addressed, since it may depend on problem-specific characteristics, the aim of the application in mind and thus the level of accuracy required by the scientific question under consideration.

3.3.4 Numerical experiments

In this section we perform and discuss a series of numerical experiments to validate the proposed coupling approaches, verify their accuracy and test the adaptive model selection strategy devised in Section 3.3.3.

First, in Section 3.3.4.1 a family of convergence rate studies is carried out to check that the expected theoretical order of accuracy of the 1D and hybrid numerical couplings, presented in Section 2.6.2 and Section 3.3.2.2, respectively, is achieved. In particular, we want to verify that the coupling to 0D vessels, as well as any type of boundary conditions, such as the coupling to terminal Windkessel elements, do not affect and harm the expected order of accuracy in the 1D vessels. Next, in Section 3.3.4.2 the adaptive model selection strategy described in Section 3.3.3 to construct hybrid networks of vessels is applied to two different arterial models. We explore the proposed methodology on the 37-artery network presented in [89] and the reduced ADAN56 model reported in [22]. Finally, in Section 3.3.4.3 the validity of the 1D junction model presented in Section 2.5.1 is carefully assessed by comparing 1D simulation results for a simple bifurcation model to data obtained from a more complex 3D model [76]. Numerical predictions of flow rate, pressure and changes in luminal radius are compared at several sites between the 1D and 3D models. In particular, total pressure variation and energy dissipation are evaluated across the bifurcation, to validate the proposed 1D coupling approach and prove its ability to correctly describe flow splitting and reproduce wave propagation for the considered problem, while ensuring mass conservation and continuity of total pressure.

3.3.4.1 Convergence rate studies

We carry out a set of convergence rate studies in order to verify that the expected order of accuracy of the adopted numerical schemes and, especially, of the proposed numerical coupling strategies is actually attained. We will also show that the problem-specific choice of the boundary conditions to be prescribed at initial and terminal branches of a network does not affect such order of accuracy. In particular, we have to check that both the 1D and the hybrid couplings preserve the expected, global second-order of accuracy, in both space and time, in the 1D vessels.

To this end, by applying the method of manufactured solutions, we first construct three different test problems for a modified nonlinear system of equations that is a perturbation of the original PDE system via a source term vector. In this way, the modified non-homogeneous nonlinear system has a smooth, exact solution which can be used to assess the convergence rates of the numerical solution. Then, a convergence rate study is performed on different hybrid configurations of an aortic bifurcation model.

In the first three test problems performed by adopting the method of manufactured solutions, the exact solution is known, whereas, in the convergence rate study on the aortic bifurcation model, the exact solution is not known and replaced by a numerical reference solution. In the 1D vessels, the error at the output time between the numerical and the exact/reference solutions of each variable $\{A, q\}$ is measured in L^1-, L^2- and L^∞-norms. The numerical solution is first reconstructed over each computational cell by applying the ENO reconstruction procedure. Then, by following the approach described in [42], the integrals defining the error in the continuous L^1- and L^2-norms are approximated using a suitable quadrature formula over each computational cell: in the first three tests where the exact solution is known, we simply use the midpoint rule; for the aortic bifurcation model where a reference solution is available, we adopt the Gauss-Lobatto quadrature formula with 7 integration points. In both cases, the error in L^∞-norm is obtained by taking the maximum error arising in any of the integration points in any of the cells.

Single vessel. We consider a single 1D vessel and the following smooth vector function $\widehat{\boldsymbol{Q}}(x,t)$

$$\widehat{\boldsymbol{Q}}(x,t) = \begin{pmatrix} \widehat{A}(x,t) \\ \widehat{q}(x,t) \end{pmatrix} = \begin{pmatrix} A^c + \delta_A A^c \sin\left(\dfrac{2\pi}{l}x\right)\cos\left(\dfrac{2\pi}{T_0}t\right) \\ q^c - \delta_A A^c \dfrac{l}{T_0}\cos\left(\dfrac{2\pi}{l}x\right)\sin\left(\dfrac{2\pi}{T_0}t\right) \end{pmatrix}, \tag{3.61}$$

where the quantities A^c and q^c are average values, while the term δ_A represents the fluctuation around the average. The smooth function $\widehat{\boldsymbol{Q}}(x,t)$ does not necessarily satisfy the original 1D blood flow system (2.9) or, equivalently, (2.13), but by inserting (3.61) into (2.13) we obtain the following new inhomogeneous nonlinear system

$$\partial_t \boldsymbol{Q} + \boldsymbol{A}(\boldsymbol{Q})\partial_x \boldsymbol{Q} = \boldsymbol{S}(\boldsymbol{Q}) + \widehat{\boldsymbol{S}}(x,t), \tag{3.62}$$

which represents a perturbation of the original system (2.13) and of which the function $\widehat{\boldsymbol{Q}}(x,t)$ is a smooth, exact solution. The new source term vector $\widehat{\boldsymbol{S}}(x,t)$, which depends on space x and time t only, arises from the fact that (3.61) is not a solution of the original system (2.9) and its explicit expression can be calculated using algebraic manipulators (not reported here).

Geometrical and mechanical vessel properties are: $r_0 = 1.4$ cm, $h = 0.5$ mm, $\rho = 1.060$ g/cm^3, $\mu = 0$ dyne·s/cm^2, $E = 1.2 \cdot 10^7$ dyne/cm^2, $P_0 = p_{ext} = 0$ dyne/cm^2. Furthermore, we set: $l = 10^2$ cm, $T_0 = 1.0$ s, $A^c = A_0 = \pi r_0^2$, $\delta_A = 0.1$ and $q^c = 100$ ml/s. To perform the convergence rate study, we start from the coarsest mesh with $\overline{M} = 4$ computational cells and at each mesh refinement step we double the number of cells of the previous step. The output time of the simulations is $t_{\text{End}} = 0.5$ s and the time step is computed according to the CFL stability condition with $CFL = 0.9$. The initial condition is given by the smooth function (3.61) evaluated at $t = 0$, the 1D vessel is evolved by using the second-order MUSCL-Hancock

scheme presented in Section 2.6.1 and the same test problem is solved by prescribing two different sets of boundary conditions. In the first case, periodic boundary conditions are assigned at both left and right extremities of the vessel; instead, in the second case, at each boundary interface the value of one of the two variables, either cross-sectional area or flow rate, is prescribed to be equal to the corresponding variable of the exact solution, while the other variable is computed by imposing the continuity of the generalized Riemann invariants across the boundary interface, following the approach presented in Section 2.5.1. Here, we will show results obtained by prescribing the value of the flow rate q at the left interface and the value of the cross-sectional area A at the right boundary, but other choices are also possible.

Errors between the numerical solution and the exact solution and empirical convergence rates are computed in norms L^1, L^2 and L^∞ and are reported in Table 3.1. The expected convergence rates are reached in both variables, A and q, for all norms and regardless the choice of the prescribed boundary conditions. Indeed, from Table 3.1 we conclude that errors are decreasing and the numerical solution is converging to the exact one with the correct and expected order of accuracy also in the case where boundary conditions are assigned via the continuity of the Riemann invariants.

TABLE 3.1: Errors and empirical convergence rates obtained with the method of manufactured solutions for the single vessel test problem, with both periodic boundary conditions and prescribed variable boundary conditions with Riemann invariants. In this last case, the flow rate q is prescribed at the left interface and the value of the cross-sectional area A is enforced at the right boundary.

Test	$\overline{M}$	L^1		L^2		L^∞		$O(L^1)$		$O(L^2)$		$O(L^\infty)$	
		A [cm^2]	q [ml/s]	A	q	A	q	A	q	A	q	A	q
Single vessel	4	4.93e+00	8.74e+03	5.52e-01	8.78e+02	8.32e-02	1.00e+02	-	-	-	-	-	-
+ periodic BCs	8	1.48e+00	1.20e+03	1.80e-01	1.24e+02	3.20e-02	1.66e+01	1.74	2.86	1.62	2.82	1.38	2.59
	16	4.32e-01	2.82e+02	4.94e-02	2.99e+01	7.73e-03	5.09e+00	1.77	2.09	1.86	2.05	2.05	1.70
	32	1.11e-01	6.94e+01	1.24e-02	7.50e+00	1.95e-03	1.51e+00	1.96	2.02	2.0	2.00	1.99	1.75
	64	2.70e-02	1.71e+01	3.00e-03	1.86e+00	4.65e-04	2.66e-01	2.04	2.02	2.04	2.01	2.07	2.51
	128	6.72e-03	4.26e+00	7.52e-04	4.64e-01	1.16e-04	7.44e-02	2.01	2.01	2.00	2.00	2.00	1.84
Single vessel	4	8.39e+00	1.06e+04	9.63e-01	1.25e+03	1.42e-01	1.74e+02	-	-	-	-	-	-
+ Riemann inv. BCs	8	4.48e+00	1.87e+03	4.75e-01	2.37e+02	7.48e-02	4.43e+01	0.90	2.50	1.02	2.40	0.93	1.97
	16	1.27e+00	4.46e+02	1.39e-01	5.42e+01	2.28e-02	1.23e+01	1.82	2.07	1.77	2.13	1.71	1.84
	32	3.18e-01	1.09e+02	3.56e-02	1.32e+01	6.51e-03	3.30e+00	1.99	2.03	1.97	2.04	1.81	1.90
	64	7.99e-02	2.70e+01	9.07e-03	3.19e+00	1.64e-03	7.02e-01	1.99	2.01	1.97	2.05	1.99	2.23
	128	2.00e-02	6.71e+00	2.27e-03	7.93e-01	4.05e-04	1.75e-01	2.00	2.01	2.00	2.01	2.02	2.01

Single vessel coupled to a Windkessel model. In this section, we extend the method of manufactured solutions described and adopted in the previous convergence study of a single 1D vessel to the case of a 1D vessel coupled to an *RCR* Windkessel (WK) terminal model. Indeed, we want to verify that the coupling between the 1D vessel and the three-element lumped-parameter model does not affect and penalize the expected convergence rate in the 1D vessel.

The time evolution of the pressure $P_{wk}(t)$ in the Windkessel is governed by the following linear ODE

$$\begin{cases} \dfrac{d}{dt}P_{wk}(t) = \dfrac{Q_{in}(t) - Q_{wk}(t)}{C}, \\ Q_{wk}(t) = \dfrac{P_{wk}(t) - P_{out}}{R_2} \end{cases} \quad \Longrightarrow \quad \frac{d}{dt}P_{wk}(t) = \frac{1}{C}\left[Q_{in}(t) - \frac{P_{wk}(t) - P_{out}}{R_2}\right], \tag{3.63}$$

where $Q_{wk}(t)$ is the flow rate through the Windkessel model, the parameters C and R_2 denote the compliance and the distal resistance of the *RCR* model, respectively, $Q_{in}(t)$ is the time-dependent inflow prescribed at the inlet of the Windkessel and P_{out} is a constant outflow pressure assigned at its outlet. In particular, if in the 1D vessel we still prescribe the following smooth, exact function for the flow rate $\widehat{q}(x,t)$

$$\widehat{q}(x,t) = q^c - \delta_A A^c \frac{l}{T_0}\cos\left(\frac{2\pi}{l}x\right)\sin\left(\frac{2\pi}{T_0}t\right), \tag{3.64}$$

then, for the mass conservation principle, the inflow $Q_{in}(t)$ to the Windkessel model will be given by the flow rate leaving the 1D vessel, that is

$$Q_{in}(t) = \widehat{q}(x = l, t) = q^c - \delta_A A^c \frac{l}{T_0} \sin\left(\frac{2\pi}{T_0} t\right), \quad t \geq 0. \tag{3.65}$$

Equipped with the explicit expression (3.65) of $Q_{in}(t)$, by inserting (3.65) into the ODE (3.63) and integrating in time such equation, with the help of the integrating factor $e^{\int \frac{1}{R_2 C} dt} = e^{\frac{t}{R_2 C}}$ it is possible to derive the analytical solution of the three-element lumped-parameter model with prescribed time-dependent inflow $Q_{in}(t)$ and constant output pressure P_{out}. After straightforward calculations, we get

$$\widehat{P}_{wk}(t) = P_{out} + \widetilde{\gamma} e^{-\frac{t}{R_2 C}} + R_2 \left\{ q^c - \frac{\delta_A A^c l}{T_0^2 + (2\pi R_2 C)^2} \left[T_0 \sin\left(\frac{2\pi}{T_0} t\right) - 2\pi R_2 C \cos\left(\frac{2\pi}{T_0} t\right) \right] \right\}, \tag{3.66}$$

where $\widetilde{\gamma}$ is the integration constant obtained by imposing the initial condition $\widehat{P}_{wk}(t = 0) = P_{wk,0}$ and given by

$$\widetilde{\gamma} = P_{wk,0} - P_{out} - R_2 \left[q^c + \frac{(\delta_A A^c l)(2\pi R_2 C)}{T_0^2 + (2\pi R_2 C)^2} \right]. \tag{3.67}$$

Together with the conservation of flow, we also want the continuity of pressure to be ensured at the vessel-Windkessel coupling interface. Therefore, the exact, smooth function for the vessel cross-sectional area $\widehat{A}(x, t)$ must be chosen such that

$$p(\widehat{A}(x = l, t)) = P_{in,wk}(t) = \widehat{P}_{wk}(t) + R_1 Q_{in}(t) = \widehat{P}_{wk}(t) + R_1 \widehat{q}(x = l, t), \quad t \geq 0, \tag{3.68}$$

where R_1 is the proximal resistance of the Windkessel model. Then, the smooth function for $\widehat{A}(x, t)$ proposed in (3.61) can be appropriately modified as follows, so that condition (3.68) is satisfied for any $t \geq 0$

$$\widehat{A}(x, t) = A_0 \left[1 + \frac{1}{K} \left(\widehat{P}_{wk}(t) + R_1 \widehat{q}(x = l, t) - P_0 \right) \right]^2 + \delta_A A^c \sin\left(\frac{2\pi}{l} x\right) \cos\left(\frac{2\pi}{T_0} t\right), \tag{3.69}$$

where the first term in (3.69) is the inverse of the tube law (2.6)–(2.7) (with $m = 0.5$, $n = 0$ and $p_{ext} = 0$) evaluated at $P_{in,wk}(t)$ as given in (3.68) and replaces the constant average quantity A^c. It easy to check that, for any $t \geq 0$, the proposed function (3.69) for $\widehat{A}(x, t)$ satisfies the pressure continuity condition (3.68).

Hence, the smooth functions (3.69) and (3.64) constitute the analytical solution to the modified nonlinear blood flow system of the form (3.62), while the function (3.66) is the exact solution to the *RCR* Windkessel model governed by equation (3.63). These functions have been constructed in a way that the coupling conditions between the two models, namely conservation of mass and continuity of pressure, are exactly verified.

This test problem is applied to the upper thoracic aorta model reported in [22], where the thoracic aorta from the aortic root to the descending aorta is simulated as a single vessel with uniform properties coupled to a three-element lumped parameter model of the rest of the systemic circulation. Geometrical and mechanical properties of both the vessel and the Windkessel are taken from [22] and summarized in Table 3.2. The tube law (2.6) is adopted with $P_0 = P_d$ and $A_0 = A_d$, where P_d and A_d are the diastolic pressure and the corresponding vessel cross-section. Furthermore, we set: $T_0 = 1.0$ s, $A^c = A_d$, $\delta_A = 0.1$, $q^c = 0$ ml/s and $P_{wk,0} = 0$ dyne/cm^2. To perform the convergence rate study, we refine the mesh size in the 1D vessel by a factor of 2. The output time of the simulations is $t_{\text{End}} = 0.5$ s and the time step is computed according to the CFL stability condition with $CFL = 0.9$. The 1D vessel is solved by using the second-order MUSCL-Hancock scheme, while the Windkessel model is evolved using RK4 method with the same time step of the 1D vessel. At the left vessel boundary, we prescribe the flow rate and compute the cross-sectional area from the continuity of the generalized Riemann invariant; at the right boundary

interface, which is coupled to the *RCR* Windkessel model, we compute the vessel unknown boundary state $\boldsymbol{Q}^* = (A^*, q^*)$ by employing the strategy described at the end of Section 2.5.1. Once $\boldsymbol{Q}^*$ has been calculated, we prescribe the inflow to the Windkessel element as $Q_{in} = q^*$. Since equation (3.63) for the pressure P_{wk} in the Windkessel, equipped with the initial condition $P_{wk}(t = 0) = P_{wk,0}$, is solved numerically by using RK4 method, the coupling conditions between the 1D vessel and the terminal Windkessel model are updated at each one of the four intermediate steps of RK4 scheme and the time integral of the boundary flux in the 1D vessel is approximated with a procedure analogous to the one proposed in Section 3.3.2.2 for the hybrid coupling between 1D and 0D vessels.

Errors between the numerical solution and the exact solution and empirical convergence rates for this convergence study are summarized in Table 3.3. We observe that the numerical solution converges with the expected order in all norms, proving that the coupling between the 1D vessel and the Windkessel model is able to preserve the correct order of accuracy in the 1D vessel.

TABLE 3.2: Geometrical and mechanical properties of the model of the upper thoracic aorta coupled to an *RCR* Windkessel element.

Property	**Value**
Length, l	24.137 cm
Radius at diastolic pressure, r_d	1.2 cm
Area at diastolic pressure, A_d	πr_d^2 =4.5 cm^2
Wall thickness, h	1.2 mm
Blood density, ρ	1.060 g/cm^3
Blood viscosity, μ	0.04 dyne·s/cm^2
Velocity profile order, ζ	9
Young's modulus, E	4.0·10^6 dyne/cm^2
Diastolic pressure, P_d	9.4$\hat{6}$ ·10^4 dyne/cm^2
External pressure, p_{ext}	0
Outflow pressure, P_{out}	0
WK resistance, R_1	1.1752·10^2 dyne·s/cm^5
WK compliance, C	1.0163·10^{-3} cm^5/dyne
WK resistance, R_2	1.1167·10^3 dyne·s/cm^5

TABLE 3.3: Errors and empirical convergence rates obtained with the method of manufactured solutions for the test problem consisting of a single 1D vessel coupled to an *RCR* Windkessel element.

Test	$\overline{M}$	L^1		L^2		L^∞		$O(L^1)$		$O(L^2)$		$O(L^\infty)$	
		A [cm^2]	q [ml/s]	A	q	A	q	A	q	A	q	A	q
Single vessel	4	1.70e+00	1.28e+03	3.84e-01	2.62e+02	1.22e-01	6.14e+01	-	-	-	-	-	-
+ WK element	8	5.54e-01	1.69e+02	1.17e-01	3.49e+01	2.97e-02	8.80e+00	1.62	2.92	1.71	2.91	2.04	2.80
	16	1.41e-01	2.88e+01	3.05e-02	7.33e+00	8.62e-03	2.68e+00	1.97	2.55	1.94	2.25	1.78	1.71
	32	3.64e-02	5.40e+00	8.17e-03	1.16e+00	2.40e-03	3.71e-01	1.96	2.41	1.90	2.66	1.84	2.86
	64	9.14e-03	1.17e+00	2.04e-03	2.67e-01	6.26e-04	1.16e-01	1.99	2.20	2.00	2.12	1.94	1.68
	128	2.29e-03	2.72e-01	5.13e-04	6.42e-02	1.58e-04	3.59e-02	2.00	2.11	2.00	2.06	1.99	1.69

Closed-loop two-vessel network. Here we reproduce the convergence test proposed by Müller and Blanco in [96], which is performed over a network of two 1D vessels connected at both extremities, thus forming a closed loop where each connection represents a 1D coupling problem.

The method of manufactured solutions is adopted: the smooth, exact function $\widehat{\boldsymbol{Q}}(x, t)$, all geometrical and mechanical properties for both vessels and the other parameters, the simulation setup for the convergence study are the same as the ones used in the first convergence test for the single vessel.

Table 3.4 displays the errors between the numerical solution and the exact solution measured in the norms L^1, L^2 and L^∞ and the corresponding empirical convergence rates, for one of the two vessels of the

closed-loop network. Also in this test problem, the expected convergence rates are reached for all norms, thus demonstrating that the adopted 1D numerical coupling strategy is second-order accurate.

TABLE 3.4: Errors and empirical convergence rates obtained with the method of manufactured solutions for the test problem consisting of a closed-loop network of two 1D vessels connected at both extremities.

Test	$\overline{M}$	L^1		L^2		L^∞		$O(L^1)$		$O(L^2)$		$O(L^\infty)$	
		A [cm^2]	q [ml/s]	A	q	A	q	A	q	A	q	A	q
Two-vessel	4	5.16e+00	8.49e+03	6.04e-01	8.59e+02	9.54e-02	1.03e+02	-	-	-	-	-	-
network	8	1.48e+00	1.20e+03	1.81e-01	1.24e+02	3.22e-02	1.66e+01	1.80	2.82	1.74	2.79	1.57	2.63
	16	4.32e-01	2.82e+02	4.94e-02	2.99e+01	7.73e-03	5.09e+00	1.78	2.09	1.87	2.05	2.06	1.70
	32	1.11e-01	6.94e+01	1.24e-02	7.50e+00	1.95e-03	1.51e+00	1.96	2.02	2.00	2.00	1.99	1.75
	64	2.70e-02	1.71e+01	3.00e-03	1.86e+00	4.65e-04	2.66e-01	2.04	2.02	2.04	2.01	2.07	2.51
	128	6.72e-03	4.26e+00	7.52e-04	4.64e-01	1.16e-04	7.44e-02	2.01	2.01	2.00	2.00	2.00	1.84

Aortic bifurcation model. We consider the aortic bifurcation model reported in [22], which consists of a parent vessel, the abdominal aorta, branching into two daughter vessels, the iliac arteries. The 1D and different hybrid configurations of this bifurcation model are constructed, to verify that the expected convergence rates are always achieved by the proposed numerical schemes:

Test 1 All vessels: 1D;

Test 2 Aorta: 1D; L iliac: 0D, two-split (P_{in}, Q_{out})-type; R iliac: 0D, (P_{in}, P_{out})-type;

Test 3 Aorta: 0D, (Q_{in}, Q_{out})-type; L iliac: 1D; R iliac: 0D, two-split (P_{in}, Q_{out})-type;

Test 4 Aorta: 1D; L iliac: 1D; R iliac: 0D, (P_{in}, P_{out})-type.

In the first test, the three coupled 1D vessels define a 1D coupling problem; in Tests 2 and 3, we have two different arrangements of a junction connecting one 1D vessel and two 0D vessels; in the last test, a hybrid coupling problem between two 1D vessels and one 0D vessel is to be solved.

For the model parametrization, geometric and mechanical parameters of vessels, boundary conditions and initial conditions see Section 2.7.3 and Table 2.5. Both iliac arteries are coupled to RCR Windkessel terminal models, with a methodology similar to the one described and adopted in the convergence study for the single 1D vessel coupled to a Windkessel model.

To perform the convergence rate study, in all tests we set the maximum mesh size for the coarsest mesh to $\Delta x_{\max} = 2$ cm. In each vessel of the bifurcation model, the number of computational cells corresponding to the mesh size $\Delta x_{\max}$ is computed according to formula (2.97), which gives $\overline{M}_1 = 5$ in both parent and daughter vessels. Then, the number of cells used in each mesh refinement step in each one of the vessels is always obtained by doubling the number of cells used in the previous step. For each configuration, the exact solution is replaced by a reference solution computed on a very fine mesh with $\overline{M}_{\text{ref}} = \overline{M}_1 \cdot 2^8 = 1280$ computational cells. For all tests, the output time is taken as $t_{\text{End}} = 20T_0$, with $T_0 = 1.1$ s, which ensures that the periodic regime has been reached in all vessels of the network; a global time step is used and computed as in (3.50), with CFL number $CFL = 0.9$.

We point out that, since 1D mesh size Δx and time step Δt are related via the CFL stability condition and since we use the same global time step for all 1D and 0D vessels, in the hybrid configurations (Test 2-4) the space refinement in the 1D vessels also implies a refinement of the time resolution in the 0D vessels.

Tables 3.5–3.8 display the computed errors and empirical convergence rates corresponding to the four configurations considered of the aortic bifurcation model, for both cross-sectional area and flow rate and in all the three norms, L^1, L^2 and L^∞. For the 1D configuration, Table 3.5 shows that the errors decrease and the numerical solution converges with the expected order in all vessels and for all norms, even with reduced

number of computational cells discretizing the domain. Hence, these results suggest once again that the 1D numerical coupling presented in Section 2.6.2 is second-order accurate in space and time and preserves the expected order in all 1D vessels joining at the junction. In the same way, for all the three different hybrid configurations assessed, we conclude that the expected convergence rates are achieved in all 1D vessels of each test and for all norms, as demonstrated in Tables 3.6–3.8. The hybrid numerical coupling proposed in Section 3.3.2.2 is then proved to be second-order accurate, in both space and time, in solving the 1D vessels of the junction. In particular, these results show that, by adopting the methodology proposed in Section 3.3.2.2 to solve the hybrid coupling at junctions of 1D and 0D vessels, the accuracy of the solution in the 1D vessels is not affected by the coupling with 0D vessels.

In conclusion, this convergence study demonstrates that the expected convergence rates are achieved by both the 1D and hybrid numerical coupling procedures adopted to solve networks of vessels.

TABLE 3.5: Test 1: Errors and empirical convergence rates obtained for the 1D configuration of the aortic bifurcation model.

Vessel	$\overline{M}$	L^1		L^2		L^∞		$O(L^1)$		$O(L^2)$		$O(L^\infty)$	
		A [cm^2]	q [ml/s]	A	q	A	q	A	q	A	q	A	q
Aorta (1D)	5	1.31e-04	9.09e-02	5.44e-05	3.92e-02	5.63e-05	5.02e-02	-	-	-	-	-	-
	10	3.48e-05	2.14e-02	1.49e-05	8.97e-03	1.71e-05	1.13e-02	1.91	2.09	1.87	2.13	1.72	2.16
	20	8.77e-06	5.44e-03	3.82e-06	2.29e-03	4.36e-06	2.68e-03	1.99	1.98	1.96	1.97	1.97	2.07
	40	2.26e-06	1.42e-03	1.01e-06	6.21e-04	1.06e-06	7.04e-04	1.96	1.93	1.92	1.88	2.03	1.93
	80	5.81e-07	3.65e-04	2.75e-07	1.68e-04	3.98e-07	2.39e-04	1.96	1.97	1.88	1.89	1.42	1.56
L/R iliac (1D)	5	1.36e-05	1.09e-02	5.75e-06	4.22e-03	5.54e-06	3.48e-03	-	-	-	-	-	-
	10	2.95e-06	2.71e-03	1.29e-06	1.06e-03	1.52e-06	9.47e-04	2.21	2.01	2.16	1.99	1.86	1.88
	20	6.90e-07	6.60e-04	3.01e-07	2.53e-04	3.84e-07	2.23e-04	2.09	2.04	2.10	2.07	1.99	2.08
	40	1.71e-07	1.61e-04	7.51e-08	6.31e-05	1.02e-07	6.17e-05	2.01	2.03	2.00	2.00	1.91	1.86
	80	4.68e-08	4.00e-05	2.05e-08	1.59e-05	2.75e-08	1.99e-05	1.87	2.01	1.88	1.99	1.89	1.63

TABLE 3.6: Test 2: Errors and empirical convergence rates obtained for a hybrid configuration of the aortic bifurcation model.

Vessel	$\overline{M}$	L^1		L^2		L^∞		$O(L^1)$		$O(L^2)$		$O(L^\infty)$	
		A [cm^2]	q [ml/s]	A	q	A	q	A	q	A	q	A	q
Aorta (1D)	5	1.52e-04	6.75e-02	6.12e-05	2.87e-02	5.82e-05	3.52e-02	-	-	-	-	-	-
	10	3.75e-05	1.75e-02	1.55e-05	7.36e-03	1.69e-05	9.22e-03	2.02	1.95	1.98	1.96	1.78	1.93
	20	1.02e-05	6.00e-03	4.43e-06	2.67e-03	5.23e-06	2.73e-03	1.88	1.54	1.81	1.46	1.69	1.76
	40	2.66e-06	1.36e-03	1.10e-06	6.04e-04	1.21e-06	6.16e-04	1.94	2.15	2.01	2.14	2.12	2.15
	80	6.43e-07	3.55e-04	2.67e-07	1.57e-04	2.90e-07	2.03e-04	2.05	1.93	2.04	1.95	2.06	1.60

TABLE 3.7: Test 3: Errors and empirical convergence rates obtained for a hybrid configuration of the aortic bifurcation model.

Vessel	$\overline{M}$	L^1		L^2		L^∞		$O(L^1)$		$O(L^2)$		$O(L^\infty)$	
		A [cm^2]	q [ml/s]	A	q	A	q	A	q	A	q	A	q
L iliac (1D)	5	1.42e-05	8.32e-03	6.57e-06	3.33e-03	5.39e-06	3.28e-03	-	-	-	-	-	-
	10	3.51e-06	1.74e-03	1.56e-06	7.93e-04	1.61e-06	1.14e-03	2.02	2.25	2.07	2.07	1.74	1.52
	20	8.51e-07	4.43e-04	3.76e-07	2.01e-04	4.09e-07	2.72e-04	2.04	1.98	2.05	1.98	1.98	2.07
	40	2.12e-07	1.10e-04	9.40e-08	5.08e-05	1.15e-07	7.48e-05	2.01	2.01	2.00	1.98	1.84	1.86
	80	5.18e-08	2.77e-05	2.32e-08	1.29e-05	2.91e-08	2.06e-05	2.03	1.99	2.02	1.98	1.98	1.86

TABLE 3.8: Test 4: Errors and empirical convergence rates obtained for a hybrid configuration of the aortic bifurcation model.

Vessel	$\overline{M}$	L^1		L^2		L^∞		$O(L^1)$		$O(L^2)$		$O(L^\infty)$	
		A [cm^2]	q [ml/s]	A	q	A	q	A	q	A	q	A	q
Aorta (1D)	5	1.45e-04	9.74e-02	6.04e-05	4.16e-02	6.18e-05	5.20e-02	-	-	-	-	-	-
	10	3.77e-05	2.28e-02	1.62e-05	9.67e-03	2.05e-05	1.15e-02	1.94	2.10	1.90	2.11	1.59	2.17
	20	9.63e-06	5.76e-03	4.20e-06	2.46e-03	5.23e-06	2.69e-03	1.97	1.98	1.95	1.97	1.97	2.10
	40	2.47e-06	1.49e-03	1.12e-06	6.64e-04	1.37e-06	7.36e-04	1.96	1.95	1.91	1.89	1.94	1.87
	80	6.22e-07	3.81e-04	2.92e-07	1.76e-04	4.06e-07	2.42e-04	1.99	1.97	1.94	1.92	1.75	1.61
L iliac (1D)	5	1.26e-05	8.87e-03	5.45e-06	3.56e-03	5.70e-06	3.73e-03	-	-	-	-	-	-
	10	2.88e-06	2.68e-03	1.27e-06	1.02e-03	1.32e-06	8.02e-04	2.13	1.73	2.10	1.80	2.11	2.22
	20	7.01e-07	6.61e-04	3.05e-07	2.61e-04	3.33e-07	1.91e-04	2.04	2.02	2.06	1.96	1.98	2.07
	40	1.82e-07	1.69e-04	7.68e-08	6.80e-05	8.47e-08	6.10e-05	1.94	1.96	1.99	1.94	1.98	1.65
	80	4.50e-08	4.28e-05	1.90e-08	1.75e-05	2.22e-08	1.97e-05	2.02	1.98	2.01	1.96	1.93	1.63

3.3.4.2 Application of the adaptive model selection strategy

Here we apply the adaptive model selection strategy proposed and described in Section 3.3.3 to two different arterial models, the 37-artery network presented in [89] and the reduced ADAN56 model reported in [22]. Among all the *a-priori* model selection criteria considered, we want to identify the ones with the best performance, namely those criteria that, when employed to determine the most suitable model (1D/0D) to be used for each vessel of a network, provide the best trade-off between computational cost and accuracy in the resulting hybrid network configurations.

We proceed as follows. For each arterial model, we look at the distribution of the parameters of the vessels defining the different criteria, in order to choose, for each criterion, a set of 1D-0D thresholds to be used to construct the corresponding hybrid configurations to test. As discussed in Section 3.3.3, these sets of 1D-0D thresholds are selected in a way to ensure that, for each criterion, the number of 1D vessels that become 0D when moving from a threshold to the consecutive one is kept quite uniform and regular. For the numerical experiments performed in this section, the specific thresholds adopted to test the different *a-priori* model selection criteria are reported in Tables 3.9 and 3.10 for the 37-artery network, in Tables 3.11 and 3.12 for ADAN56 model.

Both arterial networks, the 37-artery network and the ADAN56 model, were already presented in the previous chapter, in Sections 2.7.4 and 2.7.5, respectively. For full details about each network parametrization, geometric and mechanical parameters of vessels, boundary conditions and initial conditions see Section 2.7.4 and Table 2.7 for the 37-artery network, Section 2.7.5 and Table 2.9 for ADAN56 model. Also in this study and for both arterial models, 1D vascular segments do not include vessel tapering, but the reference constant radius r_0 is computed as the mean value between the cross-sectional radii at the inlet and outlet of the vessel, r_{in} and r_{out}, respectively.

For both the 37-artery network and ADAN56 model, the characteristic mesh spacing for 1D vessels is $\Delta x_{\max} = 1$ mm, with all vessels discretized by at least two computational cells. The CFL number is set to 0.9 for all simulations and, at each time level n, a global time step Δt^n is used and computed as in (3.50). For the 0D simulations, the time step is constant and set to $\Delta t^m = 10^{-4}$ s, which ensures the stability of the adopted numerical method to solve 0D vessels and the mesh independence of the solution, for both the 37-artery network and ADAN56 model. The output time t_{End} is not fixed, but each simulation is run until periodic regime is reached in all vessels of the network, where periodicity is defined as the L^∞-distance between the normalized solutions over two consecutive cardiac cycles to be smaller than a tolerance of 10^{-3}. In the 0D and hybrid configurations of both arterial models, the 0D vessel type to assign to each 0D vessel is chosen as follows: (Q_{in}, Q_{out})-type if the 0D vessel is the first vessel at the inlet of the network; (P_{in}, P_{out})-type if

the 0D vessel is a terminal vessel, coupled either to a single-resistance or to an *RCR* Windkessel model; two-split (P_{in}, Q_{out})-type 0D vessel otherwise.
For each criterion $\mathcal{C}$ and each criterion threshold $\gamma_h^{\mathcal{C}}$, $h = 1, \dots, p$, the root mean square (RMS) relative errors between the computational results obtained from the hybrid network configuration and the reference 1D results are computed as explained in Section 3.3.3 according to formulae (3.60).

All simulations were executed in Python, running on a Linux Ubuntu 18.04 machine with AMD® Ryzen™ Threadripper™ 3990X Processor (Base Clock: 2.9 GHz, Max. Boost Clock: up to 4.3 GHz, 64 CPU Cores/128 Threads, Total L3 Cache: 256 MB). In particular, to retrieve the CPU times, each simulation was run over a single cardiac cycle for five consecutive times, the CPU time of each execution was recorded and then the mean CPU time was computed by taking the average between the different values obtained. Furthermore, the coefficient of variation, defined as the ratio of the standard deviation to the mean CPU time, was computed for each set of five CPU times to verify that the variability of the sample in relation to the mean CPU time value was negligible (results not reported).

37-arteries network. We first consider the 37-artery network presented by Matthys *et al.* [89] and described in Section 2.7.4. Figure 3.1 displays the efficiency plots obtained for the 37-artery network showing CPU times, on the x-axis, versus mean and maximum RMS relative errors, on the y-axis, in both pressure and flow rate. In each plot, each curve of a different color corresponds to a different criterion tested, while, on each curve, each marker corresponds to a different 1D-0D threshold considered for that parameter. The CPU time axis is inverted: all efficiency curves arise form the common left lower spot, which corresponds to the 1D simulation, for which we have zero errors and maximum CPU time, and merge into the common right upper spot, which corresponds to the 0D simulation, for which we obtain the largest errors and the smallest computational cost. As we move from the 1D to the 0D network, passing through different sets of hybrid configurations, the number of 1D vessels in the network decreases, and so does the total number of 1D computational cells, resulting in an increasing reduction in the computational cost of the simulations and, on the other hand, a progressive increase in pressure and flow errors.
By looking at the efficiency plots corresponding to the mean RMS errors (top row of Figure 3.1), we conclude that, at least for this arterial network, the intravascular volume V_0 (in green) and the vessel compliance C_0 (in violet) can be identified as the the most suitable *a-priori* model selection criteria to construct hybrid networks of 1D-0D vessels, since they provide the best trade-off between computational cost of the simulations and accuracy of the results. Indeed, for several thresholds, at least the first 3/4 thresholds for both volume V_0 and compliance C_0, as the CPU times decrease, errors in both pressure and flow rate are not increasing too much, but remain within a reasonable range, still ensuring a good level of accuracy in the predicted results. Volume and compliance efficiency curves are considerably below the curves obtained for all the other model selection criteria, for which the reduction in terms of computational cost is always associated to a more significant increase in the errors magnitude. Mean RMS errors are relevant since they give a general overview of the entire network performance. Moreover, these observations are also confirmed by the efficiency plots corresponding to the maximum RMS errors (bottom row of Figure 3.1), where intravascular volume and vessel compliance stand again as the most convenient model selection criteria. Since we are looking at the maximum RMS errors over the entire arterial model, the error magnitude is quite higher, especially in the flow rate results, than the mean RMS errors, but the obtained curve trend is very similar to that just described for the mean RMS errors efficiency plots.

The sets of 1D-0D thresholds used for the different *a-priori* model selection criteria and the features of each hybrid network configuration constructed (total 1D length and total number of 1D computational cells) are reported in Table 3.9. For each model selection criterion and each criterion threshold, these tables also summarize precise values of: average CPU time per cardiac cycle and speed-up with respect to the 1D simulation, measured as the ratio between the CPU times of the 1D and hybrid simulations; mean and

maximum RMS relative errors (in percent) in the predicted pressure and flow results, with respect to the reference 1D solution, with indication also of the standard deviation for mean RMS errors. CPU time and error values presented in Table 3.9 support the analysis and observations from the efficiency plots in Figure 3.1 discussed above.

Results for the nondimensional coefficient Γ_P, tested as model selection criterion both "from below" and "from above", are reported in Table 3.10 and efficiency plots corresponding to this parameter are shown in Figure 3.2 compared to that of the vessel compliance and the intravascular volume. These efficiency plots demonstrate that the nondimensional coefficient Γ_P does not represent a valid and good model selection criterion to construct hybrid networks of vessels, as confirmed also by precise values of CPU times and RMS relative errors detailed in Table 3.10. Indeed, when adopting this criterion both "from below" and "from above" to create a hybrid configuration of the 37-artery network, its performance is clearly not as good as that of the vessel compliance C_0 and the intravascular volume V_0. In particular, if we look at the mean RMS errors, we observe a steep increase in both pressure and flow errors even with the first thresholds, meaning that also a small gain in terms of CPU time would come at the cost of a significant loss in terms of accuracy. In addition, since according to its definition (3.58) Γ_P is directly related to volume V_0, but inversely related to the compliance C_0, neither the criterion Γ_P "from below" nor the criterion Γ_P "from above" can provide a unified model selection criterion in which both volume and compliance are embedded.

For this arterial network, the vessel compliance C_0 and the intravascular volume V_0 have been identified as the best *a-priori* model selection criteria to be adopted to construct hybrid network configurations, where a good balance between computational efficiency and accuracy is accomplished. Thus, we look now at some qualitative comparisons between results obtained from the 1D and 0D models and some hybrid configurations of the 37-artery network, generated by using some 1D-0D thresholds either for C_0 or for V_0.

Figure 3.3 illustrates the computational results obtained for a hybrid configuration of the 37-artery network constructed using the intravascular volume V_0 as model selection criterion with a 1D-0D threshold of $V_0 = 6$ cm^3. The total 1D length of this hybrid configuration, given by the sum of the lengths of the 1D vessels, is reduced from 524.9 cm (the total 1D length of the 1D network) to 177.7 cm; the CPU time required to perform the 1D simulation with mesh-independent results is about 5246.76 s, while the CPU time demanded for the hybrid simulation is considerably reduced to 983.01 s, with a speed-up of about 5.3. Clearly, the highest speed-up is obtained with the 0D configuration, which is simulated with a CPU time per cardiac cycle of about 73.92 s, corresponding to a speed-up of 71 times with respect to the 1D simulation, but with a much more significant loss in terms of accuracy of the solution. Indeed, in the results for the hybrid configuration, mean RMS errors are around 1.3% for pressure and 5.7% for flow rate, while, in the 0D network, they are almost doubled with values around 2.3% for pressure and 10.5% for flow rate; similarly, maximum RMS errors remain smaller than 3.5% for pressure and smaller than 10% for flow rate in the hybrid network configuration, while, for the 0D results, maximum errors rise up to almost 5.5% for pressure and 32% for flow rate. In Figure 3.3, computational results obtained from the 1D, 0D and hybrid configurations of the 37-artery network are compared for two vessels: the left iliac-femoral I (vess. 31), which is a 1D vessel in the hybrid network, and the left ulnar (vess. 14), which is a 0D vessel in the hybrid network.

The computational results displayed in Figure 3.4 are obtained from a hybrid network configuration constructed using the vessel compliance C_0 a model selection criterion with a 1D-0D threshold of $C_0 = 1.5 \cdot 10^{-5}$ cm^5/dyne. Here, the total 1D length of the hybrid configuration is 158.2 cm and the CPU time demanded to perform the simulation is about 877.42 s, with a speed-up of 6 times with respect to the 1D simulation. As expected, the improvement in terms of computational cost is not as relevant as for the 0D network, but this is balanced by the good level of accuracy preserved in the predicted results: in the results for the hybrid network, mean RMS errors are around 1.3% for pressure and 5.9% for flow rate, maximum

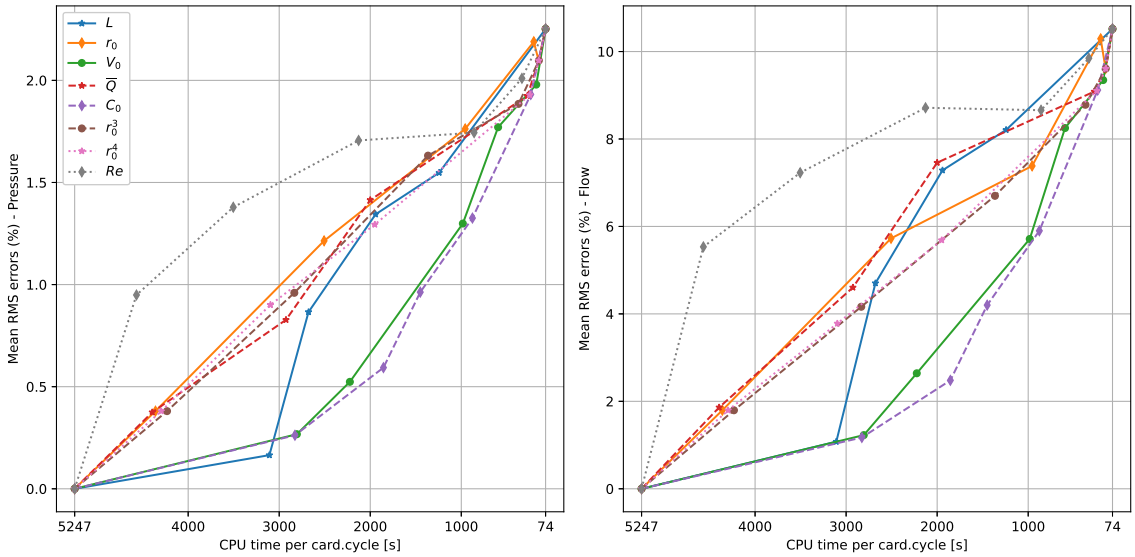
RMS errors are smaller than 3.5% for pressure and smaller than 13.5% for flow rate. In Figure 3.4, the computational results obtained from this hybrid configuration of the 37-artery network are compared to 1D and 0D results for two vessels: the abdominal aorta I (vess. 23), which is a 1D vessel in the hybrid network, and the right anterior tibial (vess. 34), which is a 0D vessel in the hybrid network.

As confirmed by the computed CPU times and errors, Figures 3.3 and 3.4 show that both hybrid configurations are still able to produce good approximations of pressure and flow waveforms and that the essential features, shape and amplitude, of these waves are well-captured, including the systolic pressure peak. Even if some accuracy is lost with respect to the 1D results, a great improvement is obtained with respect to the 0D results. In fact, when compared to the reference 1D results, in the 0D results we frequently observe oscillations that are amplified and/or delayed, curve peaks that are under-/over-estimated in both pressure and flow waveforms. These phenomena are significantly reduced and corrected in the results produced by the hybrid network configuration. This analysis is valid for both 1D and 0D vessels of the two hybrid networks; in particular, the nonlinearity included in the 0D models, through the nonlinear pressure-area relation and the nonlinear parameters L and R, as demonstrated in the study presented in the previous Chapter, strongly improves the ability of these 0D models to approximate pressure and flow waveforms in 0D vessels. Overall, even if the differences are not negligible, there is good agreement between the results predicted by the hybrid network and the reference 1D results, and the reasonable loss in terms of accuracy is balanced by the considerable improvement in terms of computational efficiency.

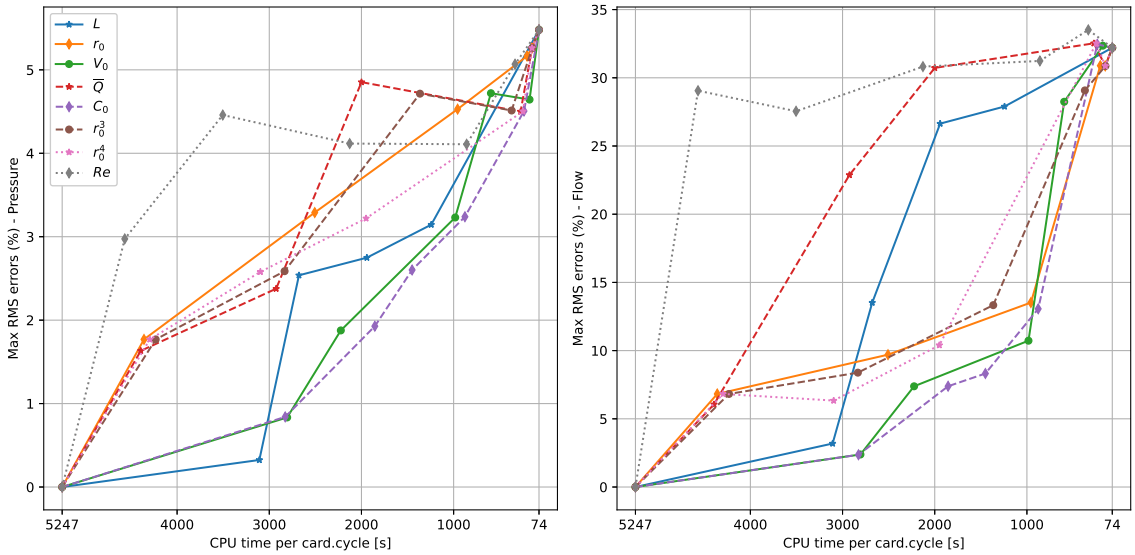
We observe that, in both the hybrid networks considered, the one obtained with the volume threshold of $V_0 = 6$ cm^3 and the other constructed with the compliance threshold of $C_0 = 1.5 \cdot 10^{-5}$ cm^5/dyne, the entire aorta is 1D, except for just one very short aortic segment, the abdominal aorta III, which is 0D. Hence, the very good agreement of these results with the reference, 1D results is likely ensured also by the fact that, with these model selection criteria and these specific 1D-0D thresholds, the main aortic vessels are kept 1D and thus, pressure and flow distributions in these vessels are still reproduced with a very good level of accuracy. When applying this methodology to more complex networks of vessels, specific vessels or portions of the network, like the aortic trunk, could be enforced to be 1D and the chosen *a-priori* model selection criteria would be then applied to all the other vessels. This was not done here, in order to blindly test the performance of the different model selection criteria.

Reduced ADAN56 model. The second arterial network to which we apply the proposed adaptive model selection strategy is the reduced ADAN56 model reported in Boileau *et al.* [22] and here already introduced in Section 2.7.5. Figure 3.5 shows the efficiency plots obtained for the ADAN56 model displaying CPU times, on the inverted x-axis, versus mean and maximum RMS relative errors, on the y-axis, in both pressure and flow rate results. By examining the efficiency plots corresponding to the mean RMS errors (top row of Figure 3.5), we conclude that, as for the 37-artery network, also for this arterial model the intravascular volume V_0 (in green) and the vessel compliance C_0 (in violet) provide a very good trade-off between computational cost of the simulations and errors in the predicted results, thus supporting the choice of these two criteria as the most suitable *a-priori* model selection criteria to construct hybrid networks of vessels. Volume and compliance efficiency curves show that several increasing 1D-0D thresholds of both parameters produce hybrid configurations of ADAN56 model which can be simulated at a lower computational cost, but still preserving a good level of accuracy in the solution and with small RMS errors. These observations are also confirmed by the efficiency plots corresponding to the maximum RMS errors (bottom row of Figure 3.5), where, even if not as clearly as for the 37-artery network, volume V_0 and compliance C_0 can still be distinguished among the other criteria for their quite satisfactory job. It is interesting to note that, for this arterial network, also the vessel radius r_0 and its third and fourth power, r_0^3 and r_0^4, respectively, turn out to be good model selection criteria, in the sense that their performance in terms of trade-off between computational efficiency and accuracy is comparable to that of V_0 and C_0. This was not observed for the 37-artery network,

FIGURE 3.1: Efficiency plots generated for the 37-artery network with CPU time per cardiac cycle versus (A) mean and (B) maximum RMS relative errors for both pressure and flow rate, to assess and compare the performance of the different *a-priori* model selection criteria tested.



(A) Efficiency plots: CPU time vs Mean RMS relative errors



(B) Efficiency plots: CPU time vs Maximum RMS relative errors

and this is not surprising given that they are two very different networks, especially with ADAN56 model based on solid geometric and anatomic considerations. On the other hand, length, mean flow rate and Reynolds number appear to be the criteria with the worst performance, since the gain obtained in terms of computational efficiency comes always with a significant loss in terms of accuracy of the solution, with errors that considerably increase in both flow rate and pressure. However, since we are looking for general criteria that can be applied to any network of vessels, we conclude that the intravascular volume V_0 and vessel compliance C_0 can be chosen as *a-priori* model selection criteria defining the adaptive model selection strategy proposed in Section 3.3.3 to construct hybrid networks of 1D-0D vessels.

The sets of 1D-0D thresholds used for the different *a-priori* model selection criteria and the features of each hybrid network configuration constructed (total 1D length and total number of 1D computational cells) are summarized in Table 3.11, together with precise values of average CPU times per cardiac cycle,

TABLE 3.9: Results obtained by applying the proposed adaptive model selection strategy to the 37-artery network. For each *a-priori* model selection criterion $\mathcal{C}$ tested, the different 1D-0D thresholds $\gamma_1^{\mathcal{C}}, \ldots, \gamma_p^{\mathcal{C}}$ considered for this arterial model are listed in column 2. For each criterion and each criterion threshold, we report precise values of: total 1D length and total number of 1D computational cells of the hybrid network configuration; mean CPU time per cardiac cycle of the simulation and speed-up with respect to the 1D simulation; mean (with standard deviation between brackets) and maximum RMS relative errors (in %) in both pressure and flow rate in the predicted results with respect to the reference 1D solution.

Criterion $\mathcal{C}$	Thresh. $\gamma^{\mathcal{C}}$	Tot.1D length [cm]	Tot.1D cells	Mean CPU time [s]	Speed-up wrt 1D	Mean ε_P^{RMS} (%) (std.dev)	Mean ε_Q^{RMS} (%) (std.dev)	Max ε_P^{RMS}(%)	Max ε_Q^{RMS}(%)
1D	-	524.9	5250	5246.76	-	-	-	-	-
0D	-	0.0	0	73.92	71.0	2.25 (1.40)	1.05e+01 (5.15)	5.48	3.22e+01
Length l [cm]	5.0	507.7	5077	3107.76	1.7	1.65e-01 (6.93e-02)	1.08 (5.34e-01)	3.24e-01	3.19
	13.0	441.9	4419	2678.07	2.0	8.66e-01 (5.58e-01)	4.70 (2.19)	2.54	1.35e+01
	18.0	311.6	3116	1941.23	2.7	1.34 (7.15e-01)	7.28 (4.87)	2.75	2.66e+01
	20.0	196.0	1960	1242.85	4.2	1.55 (7.98e-01)	8.21 (5.09)	3.14	2.79e+01
Radius r_0 [cm]	0.2	427.1	4272	4359.05	1.2	3.80e-01 (3.46e-01)	1.80 (1.53)	1.77	6.82
	0.3	236.1	2362	2506.87	2.1	1.21 (8.83e-01)	5.73 (1.79)	3.29	9.70
	0.4	75.1	752	956.91	5.5	1.76 (1.25)	7.38 (2.52)	4.53	1.35e+01
	0.7	31.1	312	203.63	25.8	2.19 (1.30)	1.03e+01 (4.89)	5.17	3.09e+01
	1.0	21.4	215	150.23	34.9	2.10 (1.41)	9.61 (5.22)	5.26	3.09e+01
Volume V_0 [cm^3]	2.0	460.2	4603	2805.93	1.9	2.67e-01 (2.18e-01)	1.23 (5.49e-01)	8.34e-01	2.38
	3.0	360.7	3608	2223.83	2.4	5.24e-01 (3.91e-01)	2.64 (1.84)	1.88	7.38
	6.0	177.7	1778	983.01	5.3	1.30 (8.98e-01)	5.71 (2.14)	3.23	1.07e+01
	10.0	100.3	1004	595.47	8.8	1.77 (1.27)	8.25 (4.87)	4.72	2.82e+01
	15.0	26.8	268	176.51	29.7	1.98 (1.22)	9.35 (5.43)	4.64	3.24e+01
Compl. C_0 [cm^5/dyne]	3.0e-06	464.7	4648	2827.20	1.9	2.62e-01 (2.20e-01)	1.17 (5.26e-01)	8.40e-01	2.37
	4.5e-06	351.0	3511	1854.93	2.8	5.93e-01 (4.66e-01)	2.48 (1.18)	1.9	7.39
	1.0e-05	271.4	2715	1450.35	3.6	9.63e-01 (6.82e-01)	4.20 (1.61)	2.60	8.32
	1.5e-05	158.2	1583	877.42	6.0	1.33 (8.94e-01)	5.90 (2.50)	3.24	1.31e+01
	2.5e-05	38.0	381	236.65	22.2	1.93 (1.23)	9.12 (5.56)	4.51	3.25e+01
Mean flow $\overline{Q}$ [ml/s]	3.0	435.3	4354	4394.34	1.2	3.75e-01 (3.41e-01)	1.86 (1.42)	1.63	6.06
	4.0	282.1	2822	2925.38	1.8	8.27e-01 (4.99e-01)	4.60 (3.85)	2.38	2.29e+01
	5.0	185.4	1855	1999.65	2.6	1.41 (1.11)	7.46 (5.75)	4.85	3.07e+01
	7.0	45.3	454	273.68	19.2	1.92 (1.23)	9.09 (5.55)	4.50	3.25e+01
	20.0	21.4	215	149.47	35.1	2.10 (1.41)	9.61 (5.22)	5.26	3.09e+01
r_0^3 [cm^3]	8.0e-03	427.1	4272	4232.07	1.2	3.80e-01 (3.46e-01)	1.80 (1.53)	1.80	6.82
	2.0e-02	277.2	2773	2833.90	1.9	9.60e-01 (6.78e-01)	4.16 (1.57)	2.59	8.38
	5.0e-02	123.4	1235	1365.26	3.8	1.63 (1.30)	6.70 (2.69)	4.71	1.33e+01
	1.0e-01	59.3	594	371.07	14.1	1.88 (1.22)	8.78 (4.72)	4.51	2.91e+01
	1.0	21.4	215	147.70	35.5	2.10 (1.41)	9.61 (5.22)	5.26	3.09e+01
r_0^4 [cm^4]	1.5e-03	427.1	4272	4296.30	1.2	3.80e-01 (3.46e-01)	1.80 (1.53)	1.80	6.82
	3.0e-03	301.0	3011	3096.38	1.7	9.01e-01 (6.77e-01)	3.78 (1.24)	2.58	6.34
	1.0e-02	183.5	1836	1949.93	2.7	1.29 (8.92e-01)	5.69 (2.09)	3.22	1.04e+01
	5.0e-02	41.5	416	247.34	21.2	1.93 (1.23)	9.11 (5.56)	4.50	3.25e+01
	1.0	21.4	215	149.38	35.1	2.10 (1.41)	9.61 (5.22)	5.26	3.09e+01
Reynolds number Re	250	450.7	4508	4567.84	1.1	9.49e-01 (6.63e-01)	5.53 (5.70)	2.97	2.91e+01
	300	340.5	3406	3504,47	1.5	1.38 (1.04)	7.23 (5.40)	4.46	2.75e+01
	350	198.7	1988	2127.82	2.5	1.71 (1.02)	8.71 (5.38)	4.12	3.08e+01
	400	132.6	1327	859.06	6.1	1.74 (1.00)	8.66 (5.49)	4.11	3.12e+01
	450	51.3	514	333.92	15.7	2.01 (1.22)	9.85 (5.54)	5.07	3.35e+01

mean (with standard deviation) and maximum RMS relative errors (in percent). Once again, also for this arterial model, CPU time and error values reported in Table 3.11 validate the observations and outcomes from the efficiency plots presented in Figure 3.5 discussed above.

TABLE 3.10: Results obtained by applying the proposed adaptive model selection strategy to the 37-artery network. Continuation of Table 3.9.

Criterion $\mathcal{C}$	Thresh. $\gamma^{\mathcal{C}}$	Tot.1D length [cm]	Tot.1D cells	Mean CPU time [s]	Speed-up wrt 1D	Mean ε_P^{RMS} (%) (std.dev)	Mean ε_Q^{RMS} (%) (std.dev)	Max ε_P^{RMS}(%)	Max ε_Q^{RMS}(%)
Γ_P "from below"	1.2e+03	393.2	3933	3995.64	1.3	6.96e-01 (7.19e-01)	3.25 (1.69)	3.33	7.13
	1.5e+03	259.9	2600	2709.32	1.9	1.16 (8.71e-01)	5.18 (1.58)	3.29	8.07
	2.5e+03	129.0	1291	1420.85	3.7	1.68 (1.29)	6.86 (2.19)	4.54	1.10e+01
	5.5e+03	46.6	467	660.61	7.9	1.92 (1.23)	9.08 (5.5)	4.50	3.25e+01
	1.0e+04	13.4	135	305.64	17.2	2.23 (1.41)	1.05e+01 (5.36)	5.46	3.32e+01
Γ_P "from above"	1.0e+04	511.5	5115	3089.11	1.7	1.50e-01 (6.52e-02)	9.27e-01 (4.86e-01)	3.07e-01	3.07
	5.5e+03	478.3	4783	2903.13	1.8	7.80e-01 (5.18e-01)	4.34 (1.99)	1.97	1.18e+01
	2.5e+03	395.9	3959	2363.64	2.2	1.21 (6.82e-01)	6.90 (5.11)	2.71	2.61e+01
	1.5e+03	265.0	2650	1617.22	3.2	1.67 (7.47e-01)	9.19 (5.51)	3.22	3.17e+01
	1.2e+03	131.7	1317	723.17	7.3	1.99 (1.13)	9.86 (5.36)	5.16	3.22e+01

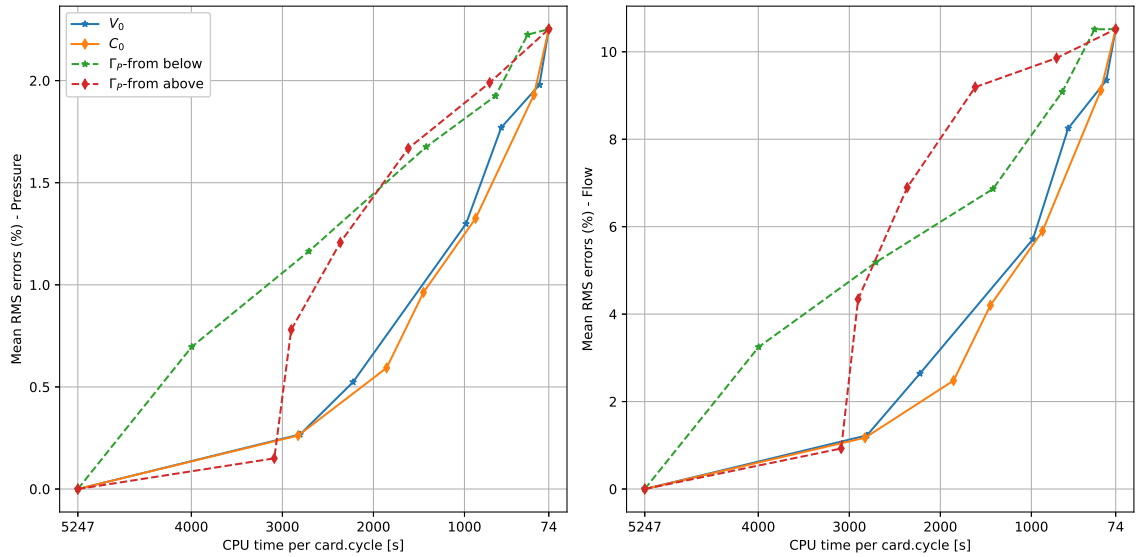
Results and efficiency plots for the nondimensional coefficient Γ_P, tested as model selection criterion both "from below" and "from above", are presented in Table 3.12) and in Figure 3.6, respectively. Analysis and considerations on the performance of the parameter Γ_P and its use as *a-priori* model selection criterion "from below" and/or "from above" are the same as for the 37-artery network.

Figures 3.7 and 3.8 depict the computational results obtained for a hybrid configuration of ADAN56 model constructed using the intravascular volume V_0 as model selection criterion with a 1D-0D threshold of $V_0 = 3.5$ cm^3. The total 1D length of the 1D network is 888.874 cm and in the hybrid configuration is reduced to 161.583 cm. The CPU times demanded to perform the 1D and 0D simulations are about 5382.75 s and 201.17 s, respectively, with a 1D to 0D computational time ratio of about 26.8; on the other hand, the CPU time required by the hybrid network configuration is around 935.63 s, with a speed-up of almost 6 times, which is a quite remarkable improvement. A good level of accuracy of the solution is also preserved: in the results for the hybrid configuration, mean RMS errors are around 1.6% for pressure and 4.7% for flow rate, while, in the 0D network, they are doubled with values around 3.2% for pressure and 9.5% for flow rate. Similarly, maximum RMS errors remain smaller than 6% for pressure and smaller than 16% for flow rate in the hybrid network configuration, while, for the 0D results, maximum errors jump up to almost 12% for pressure and 38% for flow rate. Computational results obtained from the 1D, 0D and hybrid configurations of ADAN56 model are compared in Figure 3.7 for the aortic arch IV (vess. 19a) and the abdominal aorta V (vess. 47), which are both 1D vessels in the hybrid network, and in Figure 3.8 for the right internal iliac (vess. 51) and the right posterior tibial (vess. 55c), which are both 0D vessels in the hybrid network.

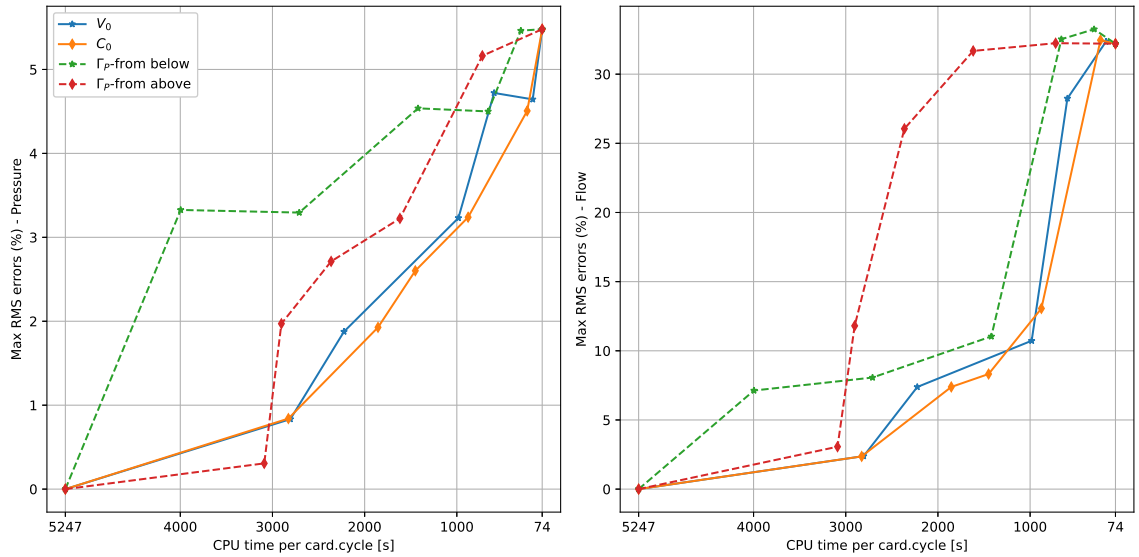
The computational results displayed in Figures 3.9 and 3.10 are obtained from a hybrid network configuration constructed using the vessel compliance C_0 a model selection criterion with a 1D-0D threshold of $C_0 = 7 \cdot 10^{-6}$ cm^5/dyne. The total 1D length of the hybrid configuration is 337.697 cm and the CPU time required by the simulation is about 1957.06 s, with a speed-up of around 2.8 times with respect to the 1D simulation. Here, the speed-up is moderate with respect to the previous hybrid configuration, but still the accuracy preserved in the predicted results is quite satisfactory: in the results for the hybrid network, mean RMS errors are around 1.3% for pressure and 3.8% for flow rate, while maximum RMS errors are smaller than 4.5% for pressure and smaller than 16.5% for flow rate. Results produced by the different network configurations are compared in Figure 3.9 for the abdominal aorta III (vess. 43) and the left popliteal I (vess. 59 b), which are both 1D vessels in the hybrid network, and in Figure 3.10 for the right radial (vess. 8) and the right anterior tibial (vess. 4), which are both 0D vessels in the hybrid network.

In accordance with computed CPU times and errors, from Figures 3.7–3.10 we conclude that, in the two hybrid configurations of ADAN56 model considered, pressure and flow profiles are reproduced with

FIGURE 3.2: Efficiency plots generated for the 37-artery network with CPU time per cardiac cycle versus (A) mean and (B) maximum RMS relative errors for both pressure and flow rate, to assess the performance of the two *a-priori* model selection criteria based on the nondimensional coefficient Γ_P and compare them to the results obtained from the volume and compliance criteria.



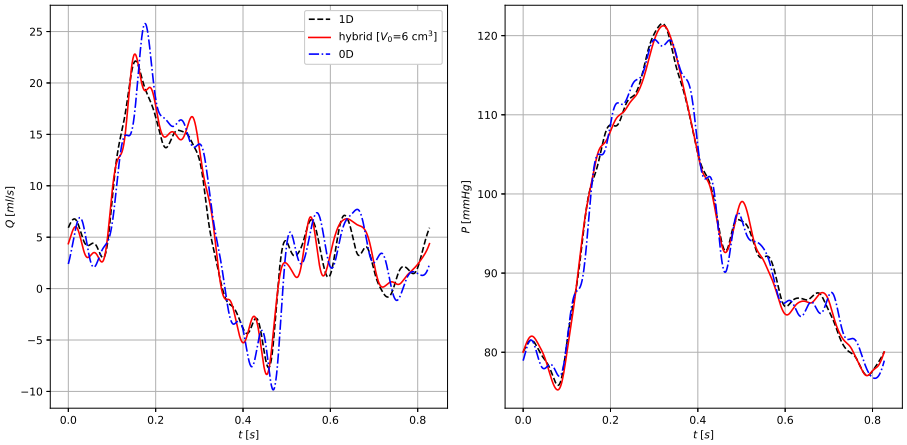
(A) Efficiency plots: CPU time vs Mean RMS relative errors



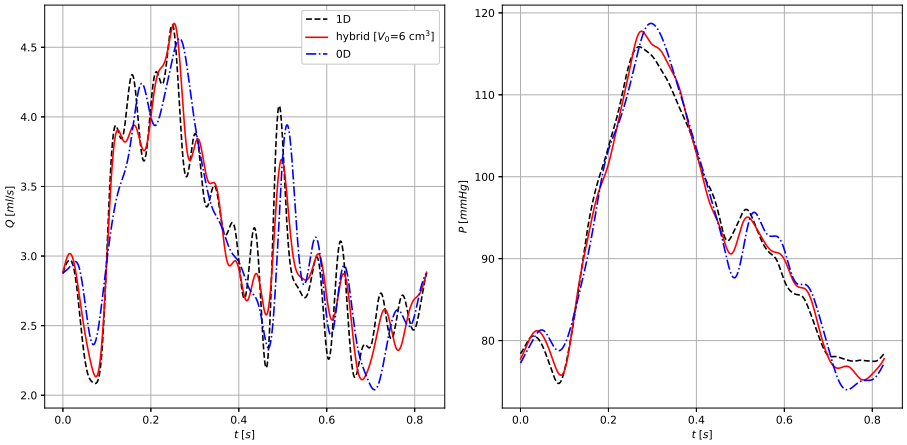
(B) Efficiency plots: CPU time vs Maximum RMS relative errors

a very good level of accuracy and agreement with the reference 1D results, in both 1D and 0D vessels. Overall, shape and amplitude of pressure and flow waveforms are well-approximated, preserving all their characteristic features. The evident delay of both pressure and flow waveforms, observed in certain 0D vessels of the 0D configuration, with respect to the 1D reference waves, is almost absent in the results obtained using the hybrid configuration (right anterior tibial in Fig. 3.8, left popliteal I in Fig. 3.9, right anterior tibial in Fig. 3.10, for instance). In these results, flow and pressure systolic peaks are very well-captured also in the 0D vessels, with a considerable improvement with respect to the 0D results, which, in general, present larger over-/under-estimated systolic peaks (abdominal aorta V in Fig. 3.7, right radial and right anterior tibial in Fig. 3.10, for instance). Furthermore, amplified or shifted wave oscillations are observed in the 0D results when compared to those obtained from the hybrid network, with respect to

FIGURE 3.3: Qualitative comparison between computational results for flow rate and pressure obtained from the 1D (dashed black line), the 0D (blue dashed-dotted line) and a hybrid (red continuous line) configuration of the 37-artery network, where the last is constructed using the volume V_0 as model selection criterion, with a 1D-0D threshold of $V_0 = 6$ cm^3.



(A) Left iliac-femoral I (1D)



(B) Left ulnar (0D)

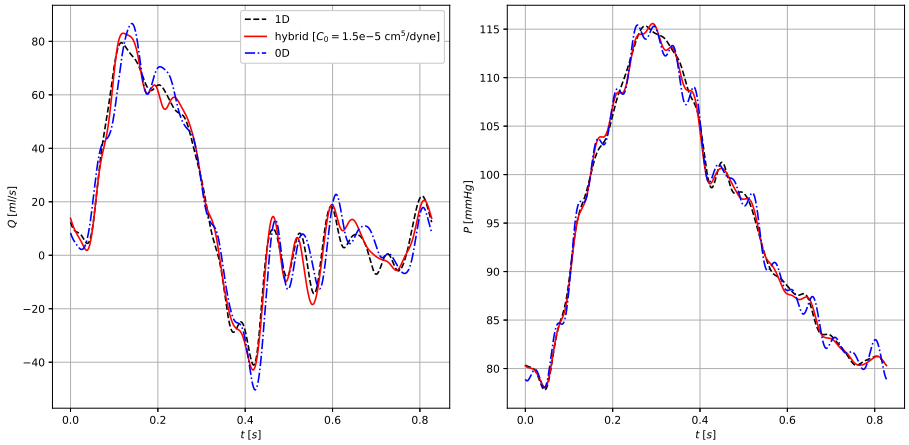
the reference 1D solution (aortic arch IV and abdominal aorta V in Fig. 3.7, right internal iliac in Fig. 3.8, abdominal aorta III in Fig. 3.9, for instance).

Remark 3.11. A feature of ADAN model is that, in the purely elastic case where viscoelastic properties of vessel walls are neglected, when refining the mesh to obtain mesh-independent results, very small new waves arise in the solutions, in the pressure and flow waveforms, which are not spurious oscillations. In the hybrid network configurations of ADAN56 model considered so far, the new small waves that are observed may be also generated by the wave reflection due to the strong interaction between 1D and 0D models.

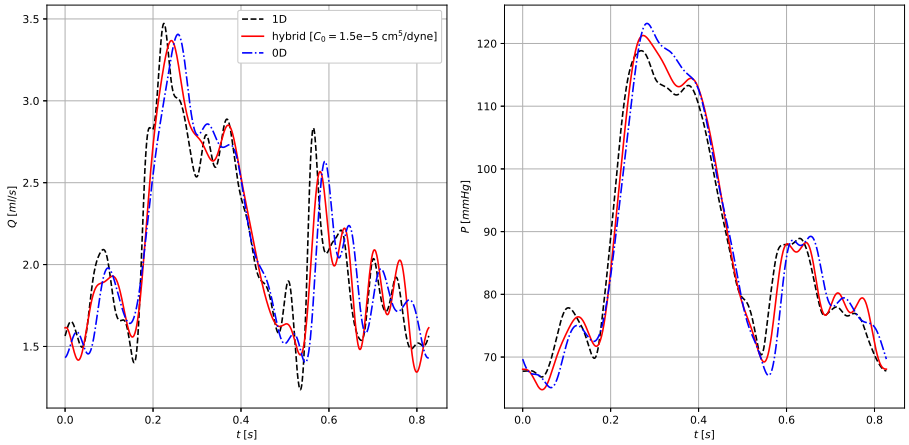
Remark 3.12. For both arterial models considered, the characteristic mesh spacing for 1D vessels was set to $\Delta x_{\max} = 1$ mm, to ensure the mesh independence of the 1D results. The very fine mesh size also restricts the global time step used to solve the entire network, thus contributing to increase the computational cost of the simulations.

In conclusion, by applying the proposed strategy to different arterial networks of moderate complexity, the vessel compliance C_0 and the intravascular volume V_0 has been identified as the most suitable model selection criteria to construct hybrid networks of vessels, providing the best trade-off between computational cost and accuracy. As we will show in Section 3.4, this methodology is expected to be significantly more effective when applied to much more complex networks and models where the heterogeneity of spatial

FIGURE 3.4: Qualitative comparison between computational results for flow rate and pressure obtained from the 1D (dashed black line), the 0D (blue dashed-dotted line) and a hybrid (red continuous line) configuration of the 37-artery network, where the last is constructed using the compliance C_0 as model selection criterion, with a 1D-0D threshold of $C_0 = 1.5 \cdot 10^{-5}$ cm^5/dyne.



(A) Abdominal aorta I (1D)



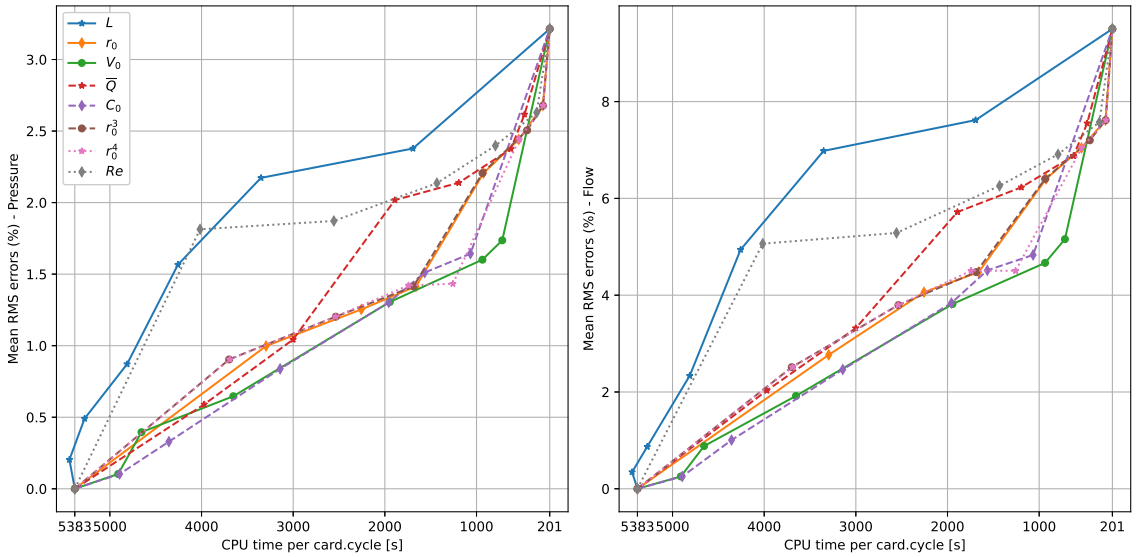
(B) Right anterior tibial (0D)

and/or temporal scales is relevant, such as the ADAN model developed by Blanco *et al.* [17, 16], possibly coupled to automatically generated cerebral arteriolar networks. We observe that, depending on problem-specific characteristics and the aim of the application in mind, different model selection criteria could be adopted to select 1D and 0D vessels of a network, based on the improvement in terms of computational efficiency to be achieved or the level of accuracy to be preserved in certain vessels or vascular regions of interest.

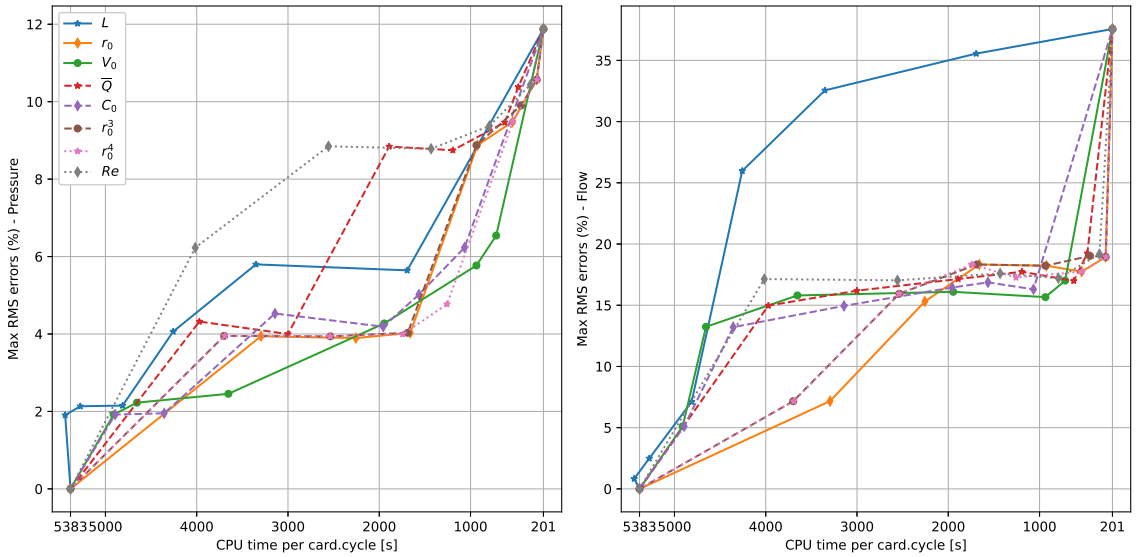
3.3.4.3 On the validity of 1D junction/bifurcation models

The flow at a junction/bifurcation of two or more vessels is intrinsically three-dimensional and local flow details can be reproduced only using a local 3D description of flow. However, in the present work, as well as, more generally, in the one-dimensional blood flow modeling framework, the focus is on (i) correctly describing flow splitting and wave propagation and (ii) preserving relevant quantities, such as mass and total pressure, at each junction of a network, rather than resolving the local 3D flow dynamics. In fact, by adopting a 1D junction model as the one illustrated in Section 3.2.3.1, the 1D coupling of vessels is modeled and solved in a way that mass and total pressure are preserved at each junction and wave propagation phenomena are reproduced throughout the entire network, even if the local flow dynamics is simplified.

FIGURE 3.5: Efficiency plots generated for ADAN56 model with CPU time per cardiac cycle versus (A) mean and (B) maximum RMS relative errors for both pressure and flow rate, to assess and compare the performance of the different *a-priori* model selection criteria tested.



(A) Efficiency plots: CPU time vs Mean RMS relative errors

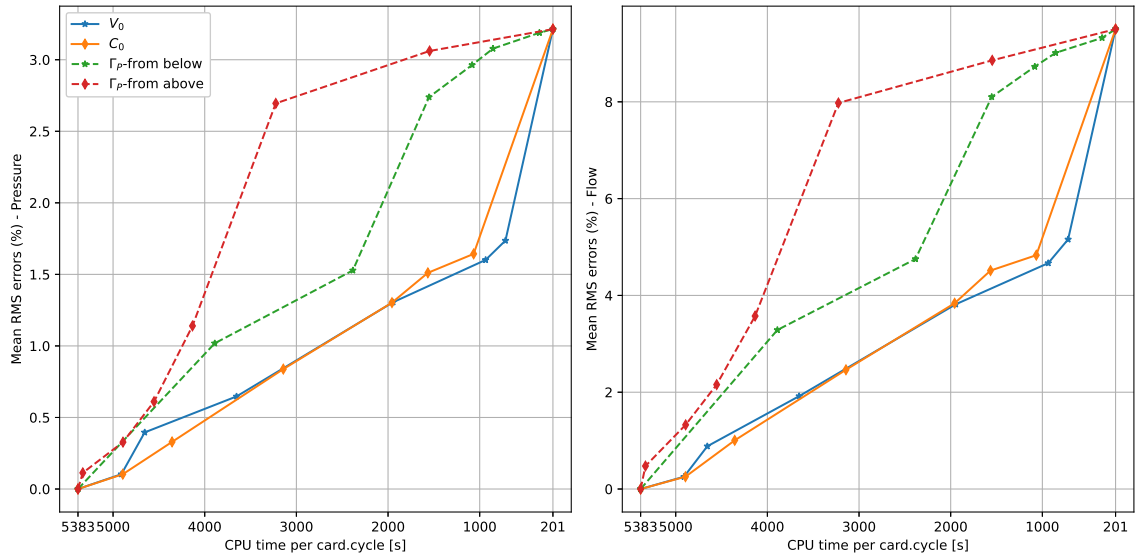


(B) Efficiency plots: CPU time vs Maximum RMS relative errors

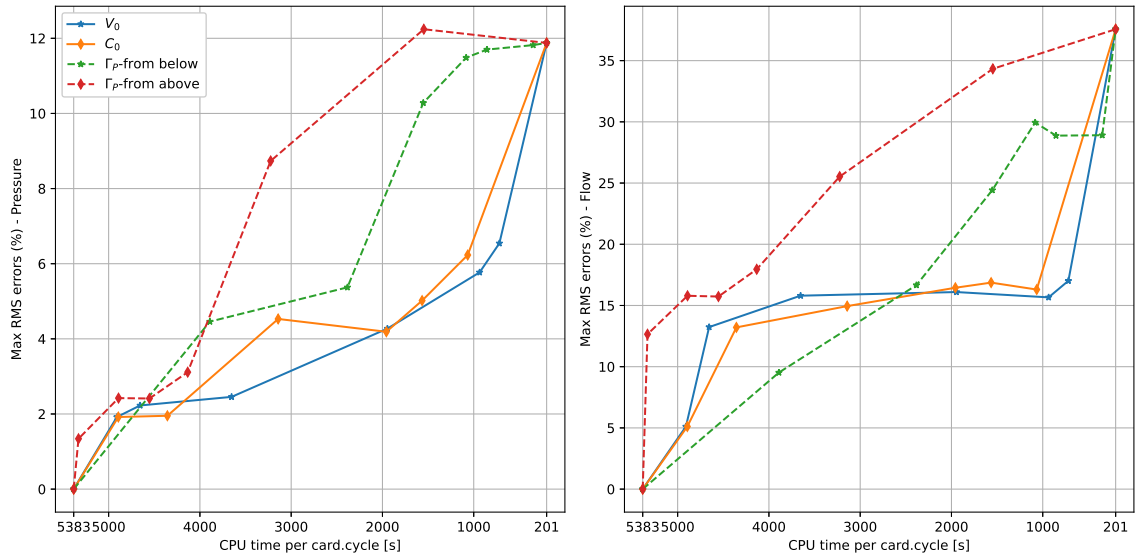
This approach is suitable when the local 3D flow details at junctions are less relevant than accounting for wave propagation phenomena across the vascular network, Furthermore, it is worth noting that adopting 3D models for representing the entire networks, and even using a local 3D approach at junctions only, would result in an intractable mathematical problem due to its complexity and computational cost when applied to realistic vascular networks.

In 1D junction models, the real geometric structure of a junction of vessels is simplified by imposing that the junction is lumped at one point and by neglecting the effect of the angles between the vessels. Under these assumptions, a domain splitting technique is adopted to cast the global coupling problem into a set of 1D problems, where each vessel is associated with its own intrinsic coordinate system and suitable interface/coupling conditions are required, to appropriately couple the 1D domains converging at the junction point. In this work, this framework has been extended also to junctions of 0D vessels and

FIGURE 3.6: Efficiency plots generated for ADAN56 model with CPU time per cardiac cycle versus (A) mean and (B) maximum RMS relative errors for both pressure and flow rate, to assess the performance of the two *a-priori* model selection criteria based on the nondimensional coefficient Γ_P and compare them to the results obtained from the volume and compliance criteria.



(A) Efficiency plots: CPU time vs Mean RMS relative errors



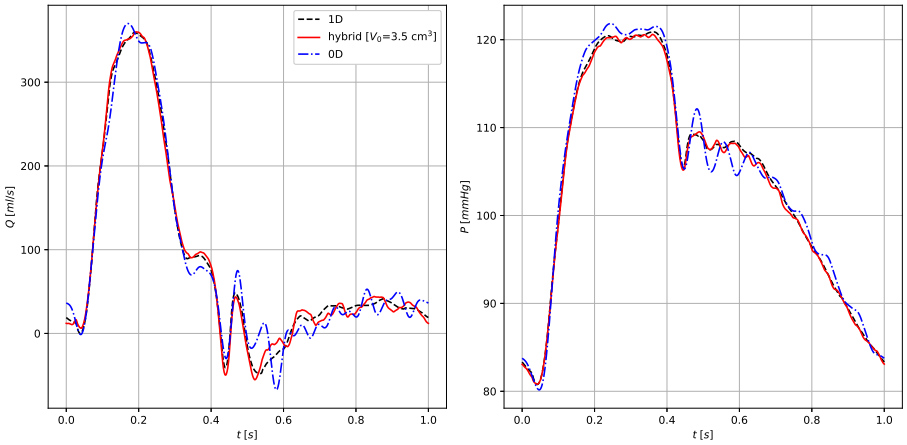
(B) Efficiency plots: CPU time vs Maximum RMS relative errors

junctions where 1D and 0D vessels are coupled together.

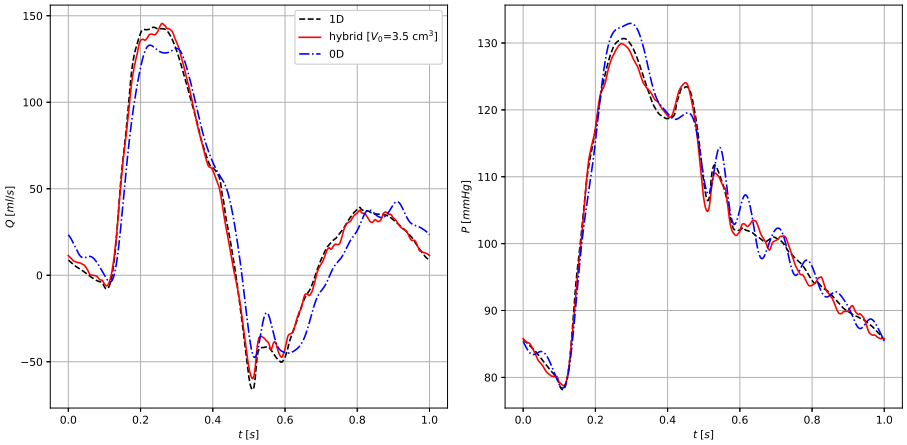
The pure 1D-model-like vessel coupling is a well-established methodology and its validity has been widely documented by works where 1D models have been validated against both *in-vitro* experimental models [89, 5] and more complex 3D-FSI models [153, 76], showing that it is reasonable to describe flow at junctions by means of a 1D model, especially when the focus is on reproducing flow rate variation along time, pressure wave propagation and average velocities in vascular networks with a good balance between accuracy and computational cost.

In blood flow in networks, flow splitting at junctions is primarily governed by peripheral resistance (resistances at terminal points of the 1D network representing the downstream vasculature), while its dependence upon the flow characteristics at junctions is negligible. This fact explains why flow is reasonably

FIGURE 3.7: Qualitative comparison between computational results for flow rate and pressure obtained from the 1D (dashed black line), the 0D (blue dashed-dotted line) and a hybrid (red continuous line) configuration of ADAN56 model, where the last is constructed using the volume V_0 as model selection criterion, with a 1D-0D threshold of $V_0 = 3.5$ cm^3.



(A) Aortic arch IV (1D)



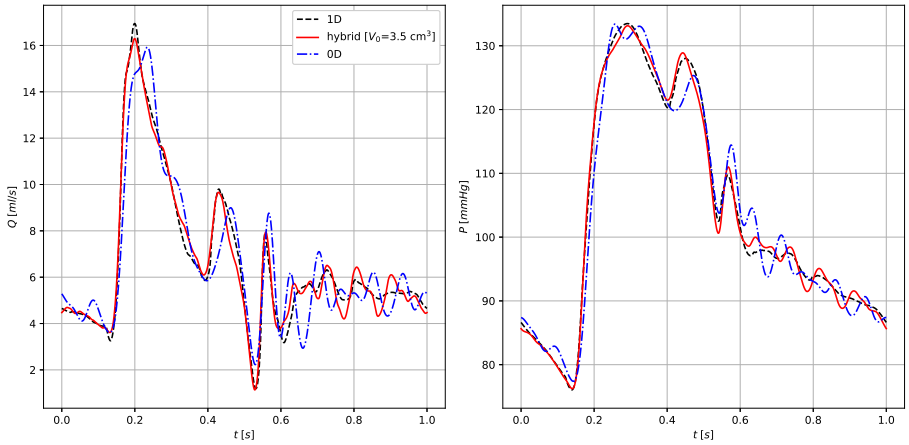
(B) Abdominal aorta V (1D)

well-captured by 1D and 0D models. The peripheral resistance is indeed orders of magnitude larger than any disturbance in the resistance that a junction can introduce, thus making the contribution of junction losses almost negligible, as largely demonstrated in the previously cited validation studies. For instance, in [89] the authors model energy losses at bifurcations by adding a loss coefficient into the continuity of the total pressure $\left(p + \frac{1}{2}\rho u^2\right)$, which takes into account the branching angles and the flow and area ratios of the vessels joining at the bifurcation. They observe that the addition of these loss coefficients in the simulations does not have a significant effect on pressure and flow waveforms, but energy losses at bifurcations have a secondary, thus negligible, effect on blood flow in large arteries.

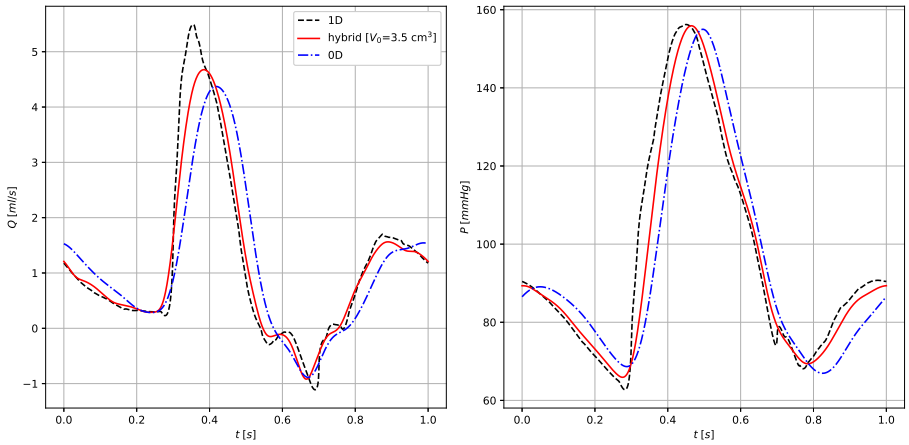
At least for arteries, in $\left(p + \frac{1}{2}\rho u^2 + losses\right)$, the pressure term p is indeed the dominant one, making the total pressure $\left(p + \frac{1}{2}\rho u^2\right)$, or even the pressure p alone (because of the relatively low flow velocities), a suitable coupling condition. Once again, this depends on the fact that peripheral resistance is larger than junction resistance and plays a dominant role in flow splitting at junctions.

The quantitative study performed on the aortic bifurcation model and proposed in the following aims at

FIGURE 3.8: Qualitative comparison between computational results for flow rate and pressure obtained from the 1D (dashed black line), the 0D (blue dashed-dotted line) and a hybrid (red continuous line) configuration of ADAN56 model, where the last is constructed using the volume V_0 as model selection criterion, with a 1D-0D threshold of $V_0 = 3.5$ cm^3.



(A) Right internal iliac (0D)

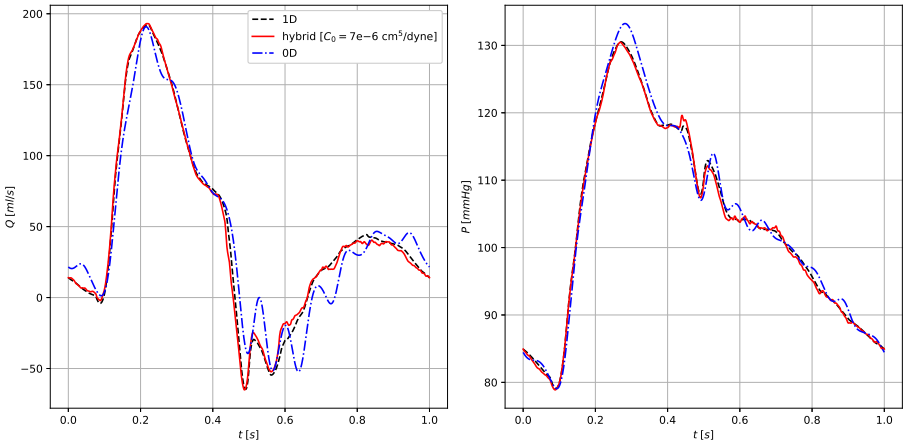


(B) Right posterior tibial (0D)

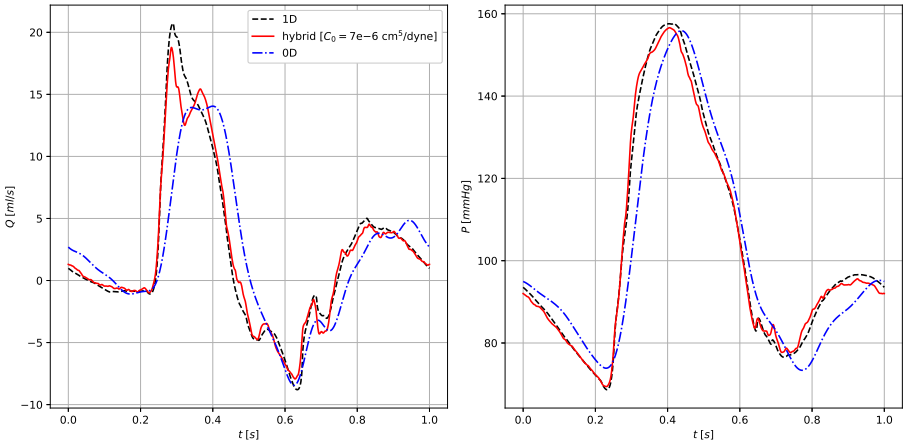
validating the 1D modeling approach for blood flow in vascular networks with 3D-FSI data and at demonstrating the validity and ability of the 1D formulation to correctly describe flow splitting and wave propagation across junctions of vessels.

We consider the aortic bifurcation model already adopted in Section 2.7.3 and in the convergence rate study presented in Section 3.3.4.1, but with several geometrical and mechanical vessel properties modified according to [76] and reported in Table 3.13. 3D-FSI data used for comparison and validation of our 1D model were kindly made available to us by the authors of [76] and we refer the reader to this work for further details about the 3D model formulation and resolution. 3D and 1D data are sampled in time at different spatial locations, namely at the mid and end points of the aorta and at the inlet and mid point of the iliac arteries, for pressure, flow rate and radius. In the 1D problem set-up, the diastolic pressure P_d is no longer set to the same values for all vessels, but the diastolic pressure to be prescribed in each 1D vessel is obtained from the corresponding 3D solution at the vessel midpoint as the pressure P^{3D} at which $\Delta R^{3D} = R^{3D} - r_d = 0$, being r_d the vessel radius at diastolic pressure. For both 1D and 3D simulations the output time is taken as $t_{\text{End}} = 30T_0$, with $T_0 = 1.1$. The 1D aortic bifurcation model is solved adopting the numerical methods illustrated in Section 2.6.1, with $\Delta x_{\max} = 1$ mm and $CFL = 0.9$.

FIGURE 3.9: Qualitative comparison between computational results for flow rate and pressure obtained from the 1D (dashed black line), the 0D (blue dashed-dotted line) and a hybrid (red continuous line) configuration of ADAN56 model, where the last is constructed using the compliance C_0 as model selection criterion, with a 1D-0D threshold of $C_0 = 7 \cdot 10^{-6}$ cm^5/dyne.



(A) Abdominal aorta III (1D)



(B) Left popliteal I (1D)

First of all, the 1D numerical solution is compared to the 3D data using the following relative error metrics

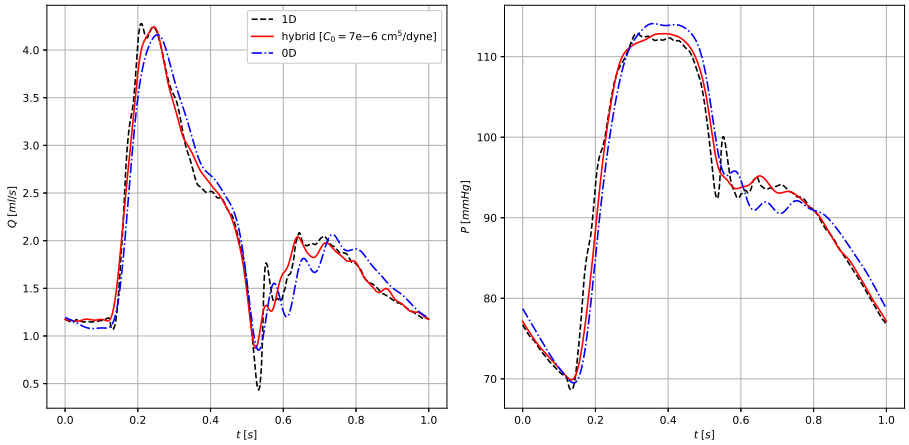
$$\begin{aligned}
\varepsilon_X^{\text{RMS}} &= \sqrt{\frac{1}{n}\sum_{i=1}^{n}\left(\frac{X_i^{1D}-X_i^{3D}}{X_i^{3D}}\right)^2}, & \varepsilon_Q^{\text{RMS}} &= \sqrt{\frac{1}{n}\sum_{i=1}^{n}\left(\frac{Q_i^{1D}-Q_i^{3D}}{\max_j\left(Q_j^{3D}\right)}\right)^2},\\
\varepsilon_X^{\text{MAX}} &= \max_i\left|\frac{X_i^{1D}-X_i^{3D}}{X_i^{3D}}\right|, & \varepsilon_Q^{\text{MAX}} &= \max_i\left|\frac{Q_i^{1D}-Q_i^{3D}}{\max_j\left(Q_j^{3D}\right)}\right|,\\
\varepsilon_X^{\text{SYS}} &= \frac{\max_i\left(X_i^{1D}\right)-\max_i\left(X_i^{3D}\right)}{\max_i\left(X_i^{3D}\right)}, & \varepsilon_Q^{\text{SYS}} &= \frac{\max_i\left(Q_i^{1D}\right)-\max_i\left(Q_i^{3D}\right)}{\max_i\left(Q_i^{3D}\right)},\\
\varepsilon_X^{\text{DIAS}} &= \frac{\min_i\left(X_i^{1D}\right)-\min_i\left(X_i^{3D}\right)}{\min_i\left(X_i^{3D}\right)}, & \varepsilon_Q^{\text{DIAS}} &= \frac{\min_i\left(Q_i^{1D}\right)-\min_i\left(Q_i^{3D}\right)}{\max_i\left(Q_i^{3D}\right)},
\end{aligned} \tag{3.70}$$

for flow rate Q and for $X = P$ (pressure), R (radius), P_{tot} (total pressure), with

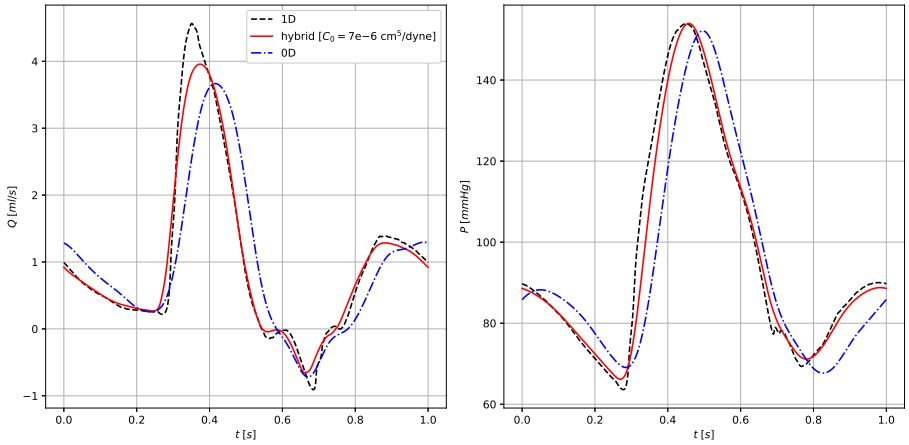
$$P_{tot} = P + \frac{1}{2}\rho U^2, \qquad U := \frac{Q}{A} = \frac{Q}{\pi R^2}. \tag{3.71}$$

In (3.70), $i = 1, \dots, n$ are time points over the cardiac cycle at which the 1D/3D solution is sampled, the superscript "$1D$" denotes the results at each time point i from the 1D simulation at a single spatial location,

FIGURE 3.10: Qualitative comparison between computational results for flow rate and pressure obtained from the 1D (dashed black line), the 0D (blue dashed-dotted line) and a hybrid (red continuous line) configuration of ADAN56 model, where the last is constructed using the compliance C_0 as model selection criterion, with a 1D-0D threshold of $C_0 = 7 \cdot 10^{-6}$ cm^5/dyne.



(A) Right radial (0D)



(B) Right anterior tibial (0D)

while the superscript "$3D$" denotes the cross-sectional averaged results at each time point i from the 3D model at a single cross-section.

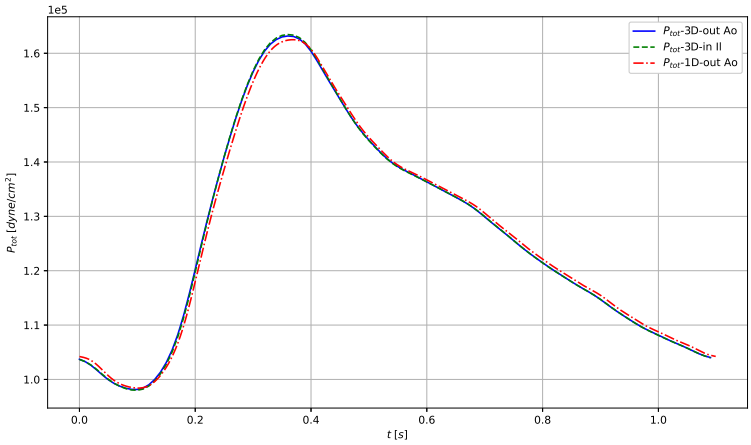
Relative errors between 1D and 3D data are summarized in Table 3.14. From this table, we can observe that there is a very good agreement between the results predicted by the two models, with errors consistently small in all metrics, variables and vessel locations considered, illustrating that the 1D formulation is able to correctly capture the multiple wave reflections generated at the junction, which contribute to shape pressure, flow and area waveforms in these vessels.

One of the coupling conditions prescribed in the 1D junction model proposed in Section 2.5.1 is the continuity of total pressure. The total pressure variation across the junction from the aorta outlet point to the iliac inlet point is evaluated for both 1D and 3D models according to the following relative error metrics

$$\begin{aligned}
\varepsilon_X^{\mathrm{RMS},*} &= \sqrt{\frac{1}{n}\sum_{i=1}^{n}\left(\frac{X_i^{out,Ao} - X_i^{in,Il}}{X_i^{out,Ao}}\right)^2}, \qquad \varepsilon_X^{\mathrm{MAX},*} = \max_i \left|\frac{X_i^{out,Ao} - X_i^{in,Il}}{X_i^{out,Ao}}\right|, \\
\varepsilon_X^{\mathrm{SYS},*} &= \frac{\max_i\left(X_i^{out,Ao}\right) - \max_i\left(X_i^{in,Il}\right)}{\max_i\left(X_i^{out,Ao}\right)}, \qquad \varepsilon_X^{\mathrm{DIAS},*} = \frac{\min_i\left(X_i^{out,Ao}\right) - \min_i\left(X_i^{in,Il}\right)}{\min_i\left(X_i^{out,Ao}\right)},
\end{aligned} \tag{3.72}$$

for $X = P_{tot}$, where the superscript "out, Ao" denotes the 1D/3D solution at the outlet point of the aorta, while the superscript "in, Il" denotes the 1D/3D solution at the inlet point of the iliac artery.
Relative errors for both 1D and 3D aortic bifurcation models are shown and compared in Table 3.15. From this table, we can see that there is no variation in total pressure across the 1D junction model, as expected. Furthermore, we observe that the total pressure variation across the 3D junction is also extremely small, with a maximum relative error below 0.5%. These observations are confirmed by the total pressure ratios reported in the same Table 3.15, which are very close to 1.0 for both 1D and 3D models. Hence, the very little, almost negligible, change in total pressure across the 3D junction suggests that the continuity of total pressure represents a consistent and suitable coupling condition to be prescribed in this kind of reduced-order junction models. Figure 3.11 displays the total pressure curves at the outlet point of the aorta and at inlet point of the iliac in the 3D model, and at the outlet point of the aorta in the 1D model. The two total pressure profiles from the 3D model are almost perfectly overlapped and the total pressure curve from the 1D model also shows an excellent agreement with the 3D results.

FIGURE 3.11: Qualitative comparison between total pressure profiles at the outlet point of the aorta (blue continuous line) and at the inlet point of the iliac (green dashed line) of the 3D model, and at the outlet point of the aorta (red dashed-dotted line) of the 1D model.



Next, we analyze the relative contributions of single terms in the total pressure by defining the following coefficients

$$\gamma_P = \frac{P}{P_{tot}}, \qquad \gamma_K = \frac{\frac{1}{2}\rho U^2}{P_{tot}}, \tag{3.73}$$

for the pressure term P and the kinetic term $\frac{1}{2}\rho U^2$, respectively.
Mean and maximum values of the coefficients γ_P and γ_K at several sites are reported in Table 3.16 for both 1D and 3D models. These results clearly show that the pressure term is the dominant term in the total pressure, while the contribution of the kinetic term is almost negligible (at least in arteries, thanks to the relatively low flow velocities). Once again, this suggests the total pressure, or even the pressure alone, to be a suitable coupling condition for vessels at junctions and this depends on the fact that peripheral resistance is larger than junction resistance, playing a dominant role in flow splitting at junctions.

Next, we define the time integral of the energy flux $(Q \cdot P_{tot})$ as follows

$$E := \int_0^{T_0} \left(Q(t) \cdot P_{tot}(t)\right)\, dt, \tag{3.74}$$

to quantify the amount of energy associated to a specific vessel location over a complete cycle $[0, T_0]$. This integral is approximated adopting the composite trapezoidal rule and evaluated using the available 1D and 3D numerical solutions at several sites. By taking the outlet point of the aorta as the reference point, the

energy dissipation by the junction and by the Windkessel models is estimated by computing the difference of the energy flux time integrals at the aorta reference point and at a selected point along the iliac arteries, normalized with respect to the time integral of the energy flux at the aorta end point. For instance, the energy dissipation by the junction only is computed as

$$E^J_{diss} = \frac{E_{out,Ao} - 2E_{in,Il}}{E_{out,Ao}}. \tag{3.75}$$

We point out that formula (3.74) is exact for 1D quantities, while, when applied to the 3D results, it represents only an estimate as it is computed using 1D-like, cross-sectional averaged, quantities. The correct and equivalent formula for 3D signals should make use of the full 3D velocity and pressure fields, which were not available for the present study. As a consequence, here we apply formula (3.74) also to the cross-sectional averaged 3D results to show that energy in the 1D model behaves like (at least a first-order estimate of) the energy in the 3D model.

Table 3.17 summarizes and compares the results obtained for both 1D and 3D models corresponding to: (i) values of the energy flux time integral computed at several sites of the aorta and iliac arteries; (ii) estimates of energy dissipation (in %) by the junction and the Windkessel elements. From this table, we observe that there in no energy dissipation by the 1D junction, up to convergence errors introduced by the numerical resolution of the nonlinear junction problem, thus concluding that the 1D junction model is energy-preserving. On the other hand, the energy dissipation by the 3D junction is also very small, of about 0.25% of the total energy estimated at the outlet point of the aorta. Indeed, we can clearly see that the energy is almost entirely dissipated by the Windkessel models: about 99.7% and 98.9% of the total energy at the reference end point of the aorta is dissipated by the Windkessel terminal elements in the 1D and 3D models, respectively. In conclusion, the energy in the 1D model behaves like (at least a first-order estimate of) the energy in the 3D model and the energy dissipated in the 1D model is negligible compared to that of the Windkessel model. This is again determined by the fact that peripheral resistance is significantly larger than junction resistance.

To conclude, it is worth noting that the analysis and results presented in this section are valid for physiological situations, while this might not be true in pathological cases, as, for example, in the presence of a stenosis across a junction.

TABLE 3.11: Results obtained by applying the proposed adaptive model selection strategy to the ADAN56 model. For each $\mathcal{C}$, the different 1D-0D thresholds $\gamma_1^{\mathcal{C}}, \ldots, \gamma_p^{\mathcal{C}}$ considered for this arterial model are listed in column 2. For each criterion and each criterion threshold, we report precise values of: total 1D length and total number of 1D computational cells of the hybrid network configuration; mean CPU time per cardiac cycle of the simulation and speed-up with respect to the 1D simulation; mean (with standard deviation between brackets) and maximum RMS relative errors (in %) in both pressure and flow rate in the predicted results with respect to the reference 1D solution.

Criterion $\mathcal{C}$	Thresh. $\gamma^{\mathcal{C}}$	Tot.1D length [cm]	Tot.1D cells	Mean CPU time [s]	Speed-up wrt 1D	Mean ε_P^{RMS} (%) (std.dev)	Mean ε_Q^{RMS} (%) (std.dev)	Max ε_P^{RMS}(%)	Max ε_Q^{RMS}(%)
1D	-	888.874	8931	5382.75	-	-	-	-	-
0D	-	0.0	0	201.17	26.8	3.21 (2.72)	9.50 (5.81)	1.19e+01	3.76e+01
Length l [cm]	1.0	881.994	8859	5441.23	1.0	2.04e-01 (2.68e-01)	3.45e-01 (1.98e-01)	1.90	8.27e-01
	4.0	845.875	8492	5275.82	1.0	4.91e-01 (4.38e-01)	8.70e-01 (5.84e-01)	2.13	2.49
	7.0	788.765	7914	4812.49	1.1	8.71e-01 (5.49e-01)	2.34 (1.08)	2.15	7.11
	12.0	704.901	7069	4257.26	1.3	1.57 (1.03)	4.94 (3.12)	4.06	2.60e+01
	20.0	547.776	5489	3351.54	1.6	2.17 (1.46)	6.98 (4.29)	5.80	3.26e+01
	30.0	278.854	2792	1693.60	3.2	2.38 (1.37)	7.62 (4.50)	5.64	3.56e+01
Radius r_0 [cm]	0.14	583.651	5873	3295.85	1.6	9.98e-01 (9.07e-01)	2.77 (1.49)	3.94	7.17
	0.2	399.774	4028	2256.57	2.4	1.25 (9.29e-01)	4.06 (2.97)	3.89	1.53e+01
	0.25	291.064	2934	1660.08	3.2	1.41 (1.03)	4.48 (3.35)	4.03	1.83e+01
	0.3	146.926	1485	924.05	5.8	2.21 (2.05)	6.40 (4.04)	8.88	1.82e+01
	0.4	68.706	697	538.6	10.0	2.44 (2.18)	7.04 (4.14)	9.48	1.77e+01
	0.8	29.427	298	276.03	19.5	2.68 (2.43)	7.62 (4.61)	1.06e+01	1.89e+01
Volume V_0 [cm^3]	0.5	831.403	8353	4909.36	1.1	1.03e-01 (3.32e-01)	2.54e-01 (8.50e-01)	1.92	5.11
	1.0	785.323	7887	4655.03	1.2	3.96e-01 (4.93e-01)	8.83e-01 (1.65)	2.23	1.32e+01
	1.5	618.008	6206	3653.06	1.5	6.47e-01 (5.65e-01)	1.92 (2.85)	2.46	1.58e+01
	2.0	335.966	3379	1945.62	2.8	1.31 (9.22e-01)	3.82 (3.02)	4.27	1.61e+01
	3.5	161.583	1626	935.63	5.8	1.60 (1.20)	4.67 (3.30)	5.77	1.57e+01
	6.0	119.544	1201	719.10	7.5	1.74 (1.33)	5.16 (3.44)	6.54	1.70e+01
Compl. C_0 [cm^5/dyne]	1.0e-06	831.403	8353	4893.75	1.1	1.03e-01 (3.32e-01)	2.54e-01 (8.50e-01)	1.92	5.11
	3.0e-06	733.734	7371	4356.27	1.2	3.29e-01 (3.99e-01)	1.01 (2.07)	1.95	1.32e+01
	4.0e-06	530.066	5326	3142.61	1.7	8.38e-01 (8.31e-01)	2.46 (3.06)	4.53	1.49e+01
	7.0e-06	337.697	3397	1957.06	2.8	1.30 (9.21e-01)	3.84 (3.02)	4.19	1.64e+01
	1.2e-05	185.900	1871	1065.98	5.0	1.51 (1.08)	4.51 (3.32)	5.02	1.69e+01
	2.0e-05	138.415	1392	820.45	6.6	1.64 (1.28)	4.83 (3.35)	6.23	1.63e+01
Mean flow $\overline{Q}$ [ml/s]	1.0	676.814	6804	3971.03	1.4	5.90e-01 (7.94e-01)	2.03 (3.10)	4.32	1.50e+01
	2.0	517.434	5205	3000.82	1.8	1.04 (9.35e-01)	3.32 (3.09)	4.00	1.62e+01
	3.0	323.937	3265	1891.16	2.8	2.02 (2.06)	5.72 (4.08)	8.84	1.71e+01
	7.0	192.820	1944	1193.76	4.5	2.14 (2.03)	6.23 (3.99)	8.75	1.77e+01
	12.0	91.472	925	625.26	8.6	2.37 (2.20)	6.88 (4.10)	9.46	1.70e+01
	40.0	32.781	333	348.00	15.5	2.62 (2.39)	7.55 (4.57)	1.04e+01	1.92e+01
r_0^3 [cm^3]	2.5e-03	644.828	6485	3699.25	1.5	9.04e-01 (9.29e-01)	2.51 (1.63)	3.95	7.16
	5.0e-03	444.396	4476	2535.65	2.1	1.20 (9.27e-01)	3.80 (2.94)	3.94	1.59e+01
	1.5e-02	291.064	2934	1687.63	3.2	1.41 (1.03)	4.48 (3.35)	4.03	1.83e+01
	2.5e-02	146.926	1485	935.12	5.8	2.21 (2.05)	6.40 (4.04)	8.88	1.82e+01
	8.0e-02	48.721	495	447.38	12.0	2.51 (2.28)	7.20 (4.35)	9.90	1.90e+01
	5.0e-01	29.427	298	274.40	19.7	2.68 (2.43)	7.62 (4.61)	1.06e+01	1.89e+01
r_0^4 [cm^4]	3.5e-04	644.828	6485	3691.79	1.5	9.04e-01 (9.29e-01)	2.51 (1.63)	3.95	7.16
	6.0e-04	444.396	4476	2537.48	2.1	1.20 (9.27e-01)	3.80 (2.94)	3.94	1.59e+01
	3.0e-03	300.056	3026	1742.58	3.1	1.42 (1.03)	4.51 (3.36)	3.99	1.83e+01
	7.0e-03	210.784	2125	1257.52	4.3	1.43 (1.04)	4.50 (3.31)	4.80	1.73e+01
	3.0e-02	68.706	697	536.05	10.0	2.44 (2.18)	7.04 (4.14)	9.48	1.77e+01
	5.0e-01	29.427	298	271.89	19.8	2.68 (2.43)	7.62 (4.61)	1.06e+01	1.89e+01
Reynolds number Re	100	672.184	6755	4016.17	1.3	1.81 (1.80)	5.06 (3.86)	6.23	1.71e+01
	200	428.294	4309	2556.33	2.1	1.87 (2.11)	5.29 (4.31)	8.85	1.70e+01
	300	233.790	2355	1432.08	3.8	2.14 (2.02)	6.26 (3.94)	8.78	1.76e+01
	500	112.775	1138	793.73	6.8	2.40 (2.14)	6.91 (4.07)	9.37	1.72e+01
	900	31.583	321	343.46	15.7	2.63 (2.41)	7.57 (4.58)	1.04e+01	1.92e+01

TABLE 3.12: Results obtained by applying the proposed adaptive model selection strategy to the ADAN56 model. Continuation of Table 3.11.

Criterion $\mathcal{C}$	Thresh. $\gamma^{\mathcal{C}}$	Tot.1D length [cm]	Tot.1D cells	Mean CPU time [s]	Speed-up wrt 1D	Mean ε_P^{RMS} (%) (std.dev)	Mean ε_Q^{RMS} (%) (std.dev)	Max ε_P^{RMS}(%)	Max ε_Q^{RMS}(%)
Γ_P "from below"	5.0e+02	637.180	6410	3890.71	1.4	1.02 (8.79e-01)	3.29 (2.17)	4.46	9.52
	1.2e+03	368.513	3714	2383.80	2.3	1.53 (1.11)	4.75 (2.49)	5.37	1.67e+01
	1.8e+03	216.016	2181	1552.66	3.5	2.74 (2.32)	8.10 (4.35)	1.03e+01	2.44e+01
	4.0e+03	137.147	1385	1082.76	5.0	2.96 (2.67)	8.73 (5.04)	1.15e+01	2.99e+01
	1.0e+04	103.401	1043	855.10	6.3	3.08 (2.71)	9.01 (5.08)	1.17e+01	2.89e+01
	1.6e+04	24.199	246	348.43	15.5	3.19 (2.70)	9.32 (5.31)	1.18e+01	2.89e+01
Γ_P "from above"	1.6e+04	864.675	8685	5330.20	1.0	1.13e-01 (1.77e-01)	4.75e-01 (1.44)	1.34	1.27e+01
	1.0e+04	785.473	7888	4891.78	1.1	3.28e-01 (4.88e-01)	1.33 (3.17)	2.42	1.58e+01
	4.0e+03	751.727	7546	4553.05	1.2	6.11e-01 (4.37e-01)	2.16 (3.06)	2.41	1.57e+01
	1.8e+03	672.858	6750	4133.75	1.3	1.14 (8.40e-01)	3.57 (3.42)	3.11	1.80e+01
	1.2e+03	520.362	5217	3224.80	1.7	2.70 (2.33)	7.98 (4.76)	8.74	2.55e+01
	5.0e+02	251.694	2521	1546.75	3.5	3.06 (2.73)	8.86 (5.44)	1.22e+01	3.43e+01

TABLE 3.13: Geometrical and mechanical properties of the aortic bifurcation model from [76].

Property	**Value**	
Blood density, ρ	1.060 g/cm^3	
Blood viscosity, μ	0.04 dyne·s/cm^2	
Velocity profile order, ζ	9	
External pressure, p_{ext}	0	
	Aorta	**Iliac**
Length, l	12.0 cm	12.0 cm
Radius at diastolic pressure, r_d	0.86 cm	0.60 cm
Wall thickness, h	0.876 mm	0.876 mm
Young's modulus, E	$6.0{\cdot}10^6$ dyne/cm^2	$6.0{\cdot}10^6$ dyne/cm^2
WK resistance, R_1	-	$6.8123{\cdot}10^2$ dyne·s/cm^5
WK compliance, C	-	$3.6664{\cdot}10^{-5}$ cm^5/dyne
WK resistance, R_2	-	$3.1013{\cdot}10^4$ dyne·s/cm^5
Outflow pressure, P_{out}	-	0

TABLE 3.14: Relative errors (in %) in the 1D solution with respect to the 3D solution as defined in (3.70) evaluated at several spatial location: the midpoint and outlet point of the aorta (parent vessel) and the inlet point and midpoint of the iliac artery (daughter vessel).

Relative errors (%)	**Midpoint Ao**	**Outlet Ao**	**Inlet Il**	**Midpoint Il**
ε_Q^{RMS}	0.799	1.479	1.169	1.235
ε_P^{RMS}	0.784	0.754	0.728	0.761
ε_R^{RMS}	0.104	0.132	0.496	4.871e-02
$\varepsilon_{P_{tot}}^{RMS}$	0.786	0.757	0.725	0.760
ε_Q^{MAX}	2.616	4.179	3.433	3.256
ε_P^{MAX}	1.992	1.860	1.674	1.730
ε_R^{MAX}	0.186	0.229	1.003	0.113
$\varepsilon_{P_{tot}}^{MAX}$	2.000	1.875	1.665	1.730
ε_Q^{SYS}	-1.109	-1.394	3.143	2.256
ε_P^{SYS}	-5.673e-03	-0.413	-0.574	-0.715
ε_R^{SYS}	-4.712e-02	-8.167e-02	-1.003	-0.109
$\varepsilon_{P_{tot}}^{SYS}$	-1.358e-02	-0.418	-0.579	-0.714
ε_Q^{DIAS}	0.967	1.690	-0.222	8.514e-02
ε_P^{DIAS}	0.406	0.259	0.409	0.306
ε_R^{DIAS}	-1.370e-02	-0.128	9.585e-02	3.960e-02
$\varepsilon_{P_{tot}}^{DIAS}$	0.407	0.259	0.409	0.306

TABLE 3.15: Comparison between 1D and 3D total pressure variation across the junction. Relative errors (in %) in the total pressure at the inlet point of the iliac artery with respect to the total pressure at the outlet point of the aorta are computed as in (3.72). Mean and maximum values of the total pressure ratio $P_{tot}^{in,Il}/P_{tot}^{out,Ao}$ are also reported for both 1D and 3D aortic bifurcation models.

Relative errors (%)	**1D**	**3D**
$\varepsilon_{P_{tot}}^{RMS,*}$	0.000	0.125
$\varepsilon_{P_{tot}}^{MAX,*}$	0.000	0.410
$\varepsilon_{P_{tot}}^{SYS,*}$	0.000	-0.162
$\varepsilon_{P_{tot}}^{DIAS,*}$	0.000	0.149
$\text{mean}\left(\frac{P_{tot}^{in,Il}}{P_{tot}^{out,Ao}}\right)$	1.000000	0.999843
$\max\left(\frac{P_{tot}^{in,Il}}{P_{tot}^{out,Ao}}\right)$	1.000000	1.001766

TABLE 3.16: Analysis of relative contributions of single terms, pressure and kinetic terms, in the total pressure, estimated according to the coefficients γ_P and γ_K defined in (3.73) and evaluated at four different locations: mid and outlet point of the aorta, inlet and mid point of the iliac artery, for both 1D and 3D models.

	1D				**3D**			
	Midpoint Ao	**Outlet Ao**	**Inlet Il**	**Midpoint Il**	**Midpoint Ao**	**Outlet Ao**	**Inlet Il**	**Midpoint Il**
mean(γ_P)	0.9996	0.9997	0.9997	0.9998	0.9996	0.9997	0.9997	0.9998
max(γ_P)	1.000	1.000	1.000	1.000	1.000	1.000	1.000	1.000
mean(γ_K)	4.049e-04	2.608e-04	2.874e-04	2.004e-04	4.164e-04	2.745e-04	2.689e-04	1.947e-04
max(γ_K)	3.728e-03	2.520e-03	2.761e-03	1.923e-03	3.737e-03	2.554e-03	2.500e-03	1.791e-03

TABLE 3.17: Analysis of energy dissipation for both 1D and 3D aortic bifurcation models. Values of the time integral of the energy flux defined in (3.74) at different locations arranged from the midpoint of the aorta to the outlet point of the Windkessel model are reported, together with estimates of the energy dissipation (in %) by the junction (due to the junction resistance) and the Windkessel elements (due to the peripheral resistance).

Time integral of energy flux [g· cm^2/s^2]	**1D**	**3D**
$E_{mid,Ao}$	1194378.136	1216388.680
$E_{out,Ao}$	1192772.882	1203724.804
$E_{in,Il}$	596387.071	600369.322
$E_{mid,Il}$	595231.962	597595.398
$E_{out,il}$	594422.133	595446.895
$E_{out,WK}$	0.000	0.000
Energy dissipation (%)	**1D**	**3D**
$(E_{out,Ao} - 2E_{in,Il})/E_{out,Ao}$	0.000	0.248
$(E_{out,Ao} - 2E_{mid,Il})/E_{out,Ao}$	0.194	0.709
$(E_{out,Ao} - 2E_{out,Il})/E_{out,Ao}$	0.329	1.066
$(E_{out,Ao} - 2E_{out,WK})/E_{out,Ao}$	100.000	100.000
$2(E_{out,Il} - E_{out,WK})/E_{out,Ao}$	99.671	98.934

3.4 An efficient hybrid network solver and its application to complex vascular models

In this section, the hybrid network methodology proposed in Section 3.3 is extended from both modeling and numerical point of view, to be integrated into an already existing network solver coded in C++. This solver allows to solve complex cardiovascular models and networks, such as the global, closed-loop, multiscale mathematical model for the entire human circulation developed by Müller and Toro [99, 100] and extended in Toro *et al.* [144], or the Anatomically Detailed Arterial Network (ADAN) model proposed by Blanco *et al.* [17, 16]. However, in the already existing version of the solver, these large and complex networks of arteries and, in the global model, of veins can only be modeled and simulated via fully 1D models. In the global, closed-loop model of the circulatory system, which in its most recent extension [144] is also coupled to a refined description of the CSF dynamics in the craniospinal cavity, several other components of the cardiovascular system (heart, pulmonary circulation, microcirculation) and of the CSF circulation are modeled as lumped-parameter compartments, but the vascular networks of systemic arteries and veins are fully one-dimensional.

As already pointed out, performing fully 1D simulations in such, or even more complex and large vascular networks and models can become extremely expensive in terms of computational cost. For this reason, our goal here is the integration of the proposed hybrid network methodology into such network solver, in order to allow to perform not only fully 1D simulations, but also simulations on fully 0D and hybrid network configurations, in order to gain computational efficiency when dealing with very complex networks and models.

In terms of modeling improvements, the viscoelastic properties of vessel walls are now included into both one-dimensional and lumped-parameter blood flow descriptions, as described in Section 3.2. We consider the hyperbolic system (3.9) governing blood flow in a one-dimensional domain, with variable geometric and mechanical vessel properties and viscoelastic tube law (3.1)-(3.3), resulting from the hyperbolic approximation illustrated in Section 3.2.1.2 to deal with the higher-order differential term arising from the viscoelastic part of the tube law. The 1D coupling strategy adopted to couple 1D viscoelastic vessels at junctions has been presented in Section 3.2.3.1, extending the elastic case introduced in the previous chapter, in Section 2.5.1. On the other hand, the viscoelastic nature of the vessel wall mechanics is also incorporated in the family of nonlinear 0D models (2.31), via the lumped-parameter viscoelastic tube law (3.32) derived in Section 3.2.2. Hence, as illustrated in Sections 3.2.3.2 and 3.2.3.3, a set of suitable coupling equations is defined to couple viscoelastic vessels at 0D and hybrid junctions, respectively. Once again, the proposed viscoelastic 0D and hybrid coupling strategies extend the coupling approaches introduced for the elastic case in the same sections. As we will see in Section 3.4.3 devoted to numerical experiments, including the viscoelastic properties of vessel wall also in the nonlinear 0D models allows us to construct more realistic and reliable lumped-parameter models, able to produce good approximations of flow and pressure waveforms with respect to the reference 1D results.

Then, the methodology developed in Section 3.3 is improved and extended also from a numerical and computational point of view. Such computational improvements mainly concern (i) the development of an efficient strategy for solving very large and stiff ODE systems governing the blood flow dynamics in regions of 0D vessels, exploiting specific features of the problem to be solved, as will be described in detail in Section 3.4.1; and (ii) the derivation of a suitable numerical coupling strategy for the accurate numerical treatment of hybrid junctions of 1D and 0D vessels, as will be illustrated in Section 3.4.2. As 1D vessels are evolved using a fully explicit path-conservative scheme, in the ADER high-order numerical framework [139], while 0D vessels are advanced in time using an implicit ODE solver, particular care is required to solve the hybrid coupling between 1D and 0D vessels. We refer to the next section for full details.

Finally, in Section 3.4.3 the proposed modeling and computational framework is applied to solve very complex and large vascular models, namely the ADAN model and the same arterial model coupled to CCO-generated cerebral arteriolar networks. We will show how the proposed hybrid network solver becomes crucial to gain computational efficiency when solving networks and models where the heterogeneity of spatial and/or temporal scales is relevant, still ensuring a good level of accuracy in the predicted results. In particular, when dealing with the ADAN model extended with the CCO peripheral beds, a tremendous improvement is obtained in terms of computational efficiency of the simulations, with a speed-up of several orders of magnitude.

3.4.1 Numerical methods

In this section, we present the numerical scheme adopted to solve the hyperbolic system (3.9) governing blood flow within each one-dimensional vascular domain, the numerical methodology employed to solve regions of 0D vessels, where each lumped-parameter domain evolves according to the nonlinear ODE system (2.31), as well as the numerical treatment proposed for the different types of junctions, to couple 1D and/or 0D vessels together. The numerical methodology introduced in this section extends the one presented in Section 3.3, to account for the viscoelasticity of vessel walls into both 1D and 0D blood flow formulations and to construct an efficient network solver to solve much more complex and large cardiovascular models and networks.

In addition to the standard global time stepping (GTS) strategy, where all the 1D vessels of a network are evolved with the same global minimum time step, here the high-order local time stepping (LTS) solver developed by Müller *et al.* [102] is employed to evolve the 1D vessels in both fully 1D and hybrid networks. Hence, in Section 3.4.1.1, together with the path-conservative scheme employed to solve the 1D blood flow model, the high-order LTS technique proposed in [102] to couple vessels at 1D junctions is described. We remark that, with this thesis, we did not contribute to the derivation of the 1D numerical methodology, which is presented here for the sake of completeness in the exposition, together with relevant references.

On the other hand, the main contributions of this part of the thesis concern the development of an efficient ODE solver to solve very large and stiff systems of ODEs governing whole regions of 0D vessels included in fully 0D and hybrid network configurations and the derivation of a hybrid numerical coupling strategy to solve junctions of 1D-0D elastic or viscoelastic vessels, where 1D vessels are evolved using a fully explicit numerical scheme, while 0D vessels adopting an implicit ODE solver. The proposed implicit solver for stiff ODE problems is described in Section 3.4.1.3, while the hybrid numerical coupling strategy is presented in Section 3.4.2.

3.4.1.1 Path-conservative numerical scheme for PDE system

The hyperbolic PDE system (3.9) governing blood flow in a one-dimensional domain is solved numerically using the ADER high-order numerical framework [139], where a key ingredient of the ADER method is the solution of the generalized Riemann problem (GRP). System (3.9), resulting from the hyperbolic approximation procedure introduced in Section 3.2.1.2 to deal with the higher-order differential term arising from the viscoelastic part of the tube law (3.2), is written in non-conservative form and can not be recast in conservative form, as done for the 1D blood flow model with purely elastic tube law (2.9). As a consequence, the path-conservative framework proposed by Parés [112] is employed to compute the numerical fluctuations, the analogue of the numerical fluxes for conservative methods. Specifically, the path-conservative numerical scheme adopted here was first proposed in [41] for conservative systems, the Dumbser-Enaux-Toro (DET) GRP solver, and then extended to non-conservative systems in [45, 46].

System (3.9) is integrated in space and time over the control volume $V_i^n = [x_{i-\frac{1}{2}}, x_{i+\frac{1}{2}}] \times [t^n, t^{n+1}]$, to get

$$\boldsymbol{Q}_i^{n+1} = \boldsymbol{Q}_i^n - \frac{1}{\Delta x} \int_{t^n}^{t^{n+1}} \int_{x_{i-\frac{1}{2}}}^{x_{i+\frac{1}{2}}} \boldsymbol{A}(\boldsymbol{Q}) \partial_x \boldsymbol{Q} \, dx dt - \frac{\Delta t^n}{\Delta x} \left[\boldsymbol{D}_{i+\frac{1}{2}}^- + \boldsymbol{D}_{i-\frac{1}{2}}^+ \right] + \Delta t^n \boldsymbol{S}_i, \tag{3.76}$$

where

$$\boldsymbol{Q}_i^n = \frac{1}{\Delta x} \int_{x_{i-\frac{1}{2}}}^{x_{i+\frac{1}{2}}} \boldsymbol{Q}(x, t^n) \, dx, \tag{3.77}$$

$$\boldsymbol{S}_i = \frac{1}{\Delta t^n \Delta x} \int_{t^n}^{t^{n+1}} \int_{x_{i-\frac{1}{2}}}^{x_{i+\frac{1}{2}}} \boldsymbol{S}(\boldsymbol{Q}(x,t)) \, dx dt \tag{3.78}$$

and

$$\boldsymbol{D}_{i+\frac{1}{2}}^{\pm} = \frac{1}{\Delta t^n} \int_{t^n}^{t^{n+1}} \mathcal{D}_{i+\frac{1}{2}}^{\pm} \left(\boldsymbol{Q}_{i+\frac{1}{2}}^-(t), \boldsymbol{Q}_{i+\frac{1}{2}}^+(t), \boldsymbol{\Psi} \left(\boldsymbol{Q}_{i+\frac{1}{2}}^-(t), \boldsymbol{Q}_{i+\frac{1}{2}}^+(t), s \right) \right) dt. \tag{3.79}$$

In (3.79), $\boldsymbol{Q}_{i+\frac{1}{2}}^{\pm}(t)$ are locally evolved data at the cell interface $x_{i+\frac{1}{2}}$, which define the left and right limiting states arising in the GRP for system (3.9) at $x_{i+\frac{1}{2}}$; $\mathcal{D}_{i+\frac{1}{2}}^{\pm}$ are fluctuations, *i.e.* the equivalent of numerical fluxes in finite volume methods for conservative systems, which depend on the integration path $\boldsymbol{\Psi}(\boldsymbol{Q}_{i+\frac{1}{2}}^-(t), \boldsymbol{Q}_{i+\frac{1}{2}}^+(t), s)$, to be defined.

Clearly, to obtain a high-order numerical scheme, the integrals in formula (3.76) have to be approximated with the corresponding accuracy. The numerical scheme adopted here at each time step performs the following three substeps:

- piecewise polynomial spatial reconstruction using current time data, $\boldsymbol{Q}_i^n \rightarrow \boldsymbol{w}^i(x, t^n)$;
- local space-time prediction, $\boldsymbol{w}^i(x, t^n) \rightarrow \boldsymbol{Q}_i^{ST}(x, t)$;
- explicit data evolution, $\boldsymbol{Q}_i^n \rightarrow \boldsymbol{Q}_i^{n+1}$.

Each one of the three steps will be briefly described in the following. For full details about the high-order path-conservative numerical scheme the reader is referred to [102] and references therein.

First-order fluctuations. The fluctuations in integral (3.79) arise from the solution of a Riemann problem at each cell interfaces. We consider a modified version of the Dumbser–Osher–Toro (DOT) Riemann solver [43, 44], proposed in [98, 101]. In these works, the original DOT Riemann solver is modified to construct well-balanced fluctuations for a first-order non-oscillatory scheme in the framework of path-conservative schemes.

Fluctuations in the DOT solver [43] are computed as

$$\mathcal{D}_{i+\frac{1}{2}}^{\pm} = \frac{1}{2} \int_0^1 \left[\boldsymbol{A} \left(\boldsymbol{\Psi} \left(\boldsymbol{Q}_{i+\frac{1}{2}}^-(t), \boldsymbol{Q}_{i+\frac{1}{2}}^+(t), s \right) \right) \pm \left| \boldsymbol{A} \left(\boldsymbol{\Psi} \left(\boldsymbol{Q}_{i+\frac{1}{2}}^-(t), \boldsymbol{Q}_{i+\frac{1}{2}}^+(t), s \right) \right) \right| \right] \frac{\partial \boldsymbol{\Psi}}{\partial s} \, ds, \tag{3.80}$$

where the absolute value operator of a matrix applies as follows

$$|\boldsymbol{A}| = \boldsymbol{R} |\boldsymbol{\Lambda}| \boldsymbol{R}^{-1}, \quad |\boldsymbol{\Lambda}| = \mathrm{diag}(|\lambda_1|, |\lambda_2|, \ldots, |\lambda_N|), \tag{3.81}$$

where $\boldsymbol{R}$ is the matrix of right eigenvectors of $\boldsymbol{A}$, $\boldsymbol{R}^{-1}$ is its inverse matrix and $|\boldsymbol{\Lambda}|$ is the diagonal matrix of eigenvalues of $\boldsymbol{A}$ in absolute value, with N being the number of state variables of the PDE system. The path $\boldsymbol{\Psi} = \boldsymbol{\Psi}(\boldsymbol{Q}_{i+\frac{1}{2}}^-(t), \boldsymbol{Q}_{i+\frac{1}{2}}^+(t), s)$, with $0 \leq s \leq 1$, connects the left state $\boldsymbol{Q}_{i+\frac{1}{2}}^-$ to the right state $\boldsymbol{Q}_{i+\frac{1}{2}}^+$ in phase-space and is a Lipschitz continuous function such that

$$\boldsymbol{\Psi}(\boldsymbol{Q}_{i+\frac{1}{2}}^-, \boldsymbol{Q}_{i+\frac{1}{2}}^+, 0) = \boldsymbol{Q}_{i+\frac{1}{2}}^-, \quad \boldsymbol{\Psi}(\boldsymbol{Q}_{i+\frac{1}{2}}^-, \boldsymbol{Q}_{i+\frac{1}{2}}^+, 1) = \boldsymbol{Q}_{i+\frac{1}{2}}^+. \tag{3.82}$$

In [43], the simple *segment*, or *canonical*, *path* is proposed

$$\boldsymbol{\Psi}(\boldsymbol{Q}^-_{i+\frac{1}{2}}, \boldsymbol{Q}^+_{i+\frac{1}{2}}, s) = \boldsymbol{Q}^-_{i+\frac{1}{2}} + s\left(\boldsymbol{Q}^+_{i+\frac{1}{2}} - \boldsymbol{Q}^-_{i+\frac{1}{2}}\right). \tag{3.83}$$

However, in [101], it was shown that the path (3.83) must be better characterized in order to obtain a well-balanced scheme able to correctly reproduce steady states. In fact, the segment path (3.83) does not preserve steady solutions, not even stationary ones. Then, the path proposed in [101] uses the segment path (3.83) for all variables, except for the cross-sectional area A, where in this case the resulting path is a parametrization of the integral curve connecting two states that are located at each side a the stationary contact discontinuity. For full details about this path and its derivation, see [101].

The integral in (3.80) for the DOT Riemann solver with the chosen path is performed numerically, as follows

$$\mathcal{D}^{\pm}_{i+\frac{1}{2}} = \frac{1}{2}\left(\sum_{p=1}^{n_{GP}} \omega_p \left\{\left[\boldsymbol{A}\left(\boldsymbol{\Psi}\left(\boldsymbol{Q}^-_{i+\frac{1}{2}}, \boldsymbol{Q}^+_{i+\frac{1}{2}}, s_p\right)\right) \pm \left|\boldsymbol{A}\left(\boldsymbol{\Psi}\left(\boldsymbol{Q}^-_{i+\frac{1}{2}}, \boldsymbol{Q}^+_{i+\frac{1}{2}}, s_p\right)\right)\right|\right] \frac{\partial \boldsymbol{\Psi}}{\partial s}\bigg|_{s_p}\right\}\right), \tag{3.84}$$

where ω_p and s_p, for $p = 1, \ldots, n_{GP}$, are the weights and nodes of a Gaussian quadrature rule with n_{GP} points.

Piecewise polynomial spatial reconstruction. High-order nonlinear spatial reconstruction of the cell averages is obtained using the weighted essentially non-oscillatory (WENO) method [42]. We denote by $\boldsymbol{w}^n_h$ the generic reconstruction polynomial in the reference coordinate $0 \leq \xi \leq 1$ given by $x = x_{i-\frac{1}{2}} + \xi \Delta x_i$, instead of considering the specific polynomial $\boldsymbol{w}^n_i$. For a scheme of order k, at each time level t^n, we consider element-wise polynomials of the type

$$\boldsymbol{w}^n_h = \boldsymbol{w}_h(\xi, t^n) = \sum_{j=1}^{M+1} \psi_j(\xi)\widehat{\boldsymbol{w}}_j(t^n) := \psi_j(\xi)\widehat{\boldsymbol{w}}_j(t^n), \tag{3.85}$$

where $M = k - 1$ is the polynomial degree of the spatial reconstruction, ψ_j, for $j = 1, \ldots, M+1$, are the corresponding basis functions and $\widehat{\boldsymbol{w}}_j$, for $j = 1, \ldots, M+1$, are the expansion coefficients at time $t = t^n$. Note that, in the last expression of (3.85), the Einstein summation convention has been introduced.

The spatial reconstruction is performed for each element on a reconstruction stencil given by the union of the element T_i and its neighbors T_e, defined as follows

$$\mathcal{S}^s_i = \bigcup_{e=i-L}^{i+R} T_e, \tag{3.86}$$

where $T_i = [x_{i-\frac{1}{2}}, x_{i+\frac{1}{2}}]$, $L = L(M, s)$ and $R = R(M, s)$ are the stencil extents to the left and to the right, respectively, with respect to the central element T_i. The reconstructed polynomial $\boldsymbol{w}_h(\xi, t^n)$ for element T_i is computed by requiring integral conservation for all elements T_e within the stencil $\mathcal{S}^s_i$, that is

$$\int_{T_e} \boldsymbol{w}^s_h(\xi, t^n)\, d\xi = \widehat{\boldsymbol{w}}^s_j(t^n) \int_{T_e} \psi_j(\xi)\, d\xi = \boldsymbol{Q}^n_e, \quad \forall T_e \in \mathcal{S}^s_i. \tag{3.87}$$

Relation (3.87) results in a linear system in the unknown coefficients $\widehat{\boldsymbol{w}}^s_j(t^n)$, from which the coefficients $\widehat{\boldsymbol{w}}_j(t^n)$ can then be computed as follows

$$\widehat{\boldsymbol{w}}_j(t^n) = \sum_{s=1}^{N_s} \omega_s \widehat{\boldsymbol{w}}^s_j(t^n), \tag{3.88}$$

where N_s is the number of stencils used and ω_s, for $s = 1, \ldots, N_s$, are nonlinear weights. For full details about the choice of the stencils and of the nonlinear weights ω_s and related parameters, see [102].

Finally, the spatial reconstruction must preserve the the well-balanced property of the numerical scheme. As proposed in [98], this is achieved by performing a spatial reconstruction on deviations around a hypothetical stationary solution.

Local space-time predictor: DET solver. Equipped with the spatial reconstruction, the following generalized Riemann problem (GRP) can be defined at cell interface $x_{i+\frac{1}{2}}$ (locally at $x = 0$)

$$\begin{cases} \partial_t \boldsymbol{Q} + \boldsymbol{A}(\boldsymbol{Q})\partial_x \boldsymbol{Q} = 0, \quad x \in \mathbb{R},\, t > t^n, \\ \boldsymbol{Q}(x,0) = \begin{cases} \boldsymbol{w}_i(x,t^n), & \text{if } x < 0, \\ \boldsymbol{w}_{i+1}(x,t^n), & \text{if } x > 0, \end{cases} \end{cases} \tag{3.89}$$

where $\boldsymbol{w}_i(x,t^n)$ and $\boldsymbol{w}_{i+1}(x,t^n)$ are piecewise polynomials at left and right sides of the cell interface, respectively. Then, by solving the GRP (3.89), we obtain a time-dependent solution at the interface to be used to evaluate the integrals in (3.79).

The Dumbser–Enaux–Toro (DET) GRP solver [41] is adopted to solve (3.89). This solver performs a local temporal evolution of the reconstruction polynomials at both sides of the cell interface in order to obtain space-time predictions, $\boldsymbol{w}_h \rightarrow \boldsymbol{Q}_h^{ST}$. In the original ENO scheme of Harten *et al.* [67] and in the ADER high-order numerical framework [139], this time evolution is achieved via a Taylor series expansion, by applying the so-called Cauchy–Kovalewski procedure. However, this approach is not able to handle stiff source terms, such as the ones resulting from the hyperbolic approximation of the parabolic system incorporating the viscoelastic properties of the vessel wall. The novel and distinct feature of the DET solver [41] is that the time evolution of the initial data left and right of the interface is performed by a local space-time discontinuous Galerkin (DG) predictor. This locally implicit method is able to handle stiff source terms and provides a local space-time polynomial $\boldsymbol{Q}_i^{ST}$ to be used in (3.79).

Then, the solution to the GRP (3.89) at time $t \in [t^n, t^{n+1}]$ is found by solving a classical Riemann problem using the space-time reconstructed states extrapolated to both sides of the cell interface, at points along $\frac{x}{t} = 0$ where the GRP solution is required. Normally, the GRP solution is required at quadrature points for the computation of integrals in (3.79) and of the space-time average of the source term (3.78) and of the non-conservative product in (3.76).

Full details about the DET local space-time predictor can be found in [41, 102] and are not reported here. Following [102], for reconstructed polynomials $\boldsymbol{w}_h$ and space-time polynomials $\boldsymbol{Q}_h^{ST}$, a nodal basis function is adopted, where space and space-time nodes are given by Gaussian quadrature points and space and space-time basis functions are the Lagrange interpolation polynomials passing through these points.

3.4.1.2 1D temporal discretization strategies: GTS and LTS solvers

As we use a fully explicit numerical scheme, the CFL stability condition must be satisfied in every computational cell of each one-dimensional domain of a network, that is

$$\Delta t^{n,CFL} = CFL \frac{\Delta x}{S_{\max}^n} \tag{3.90}$$

where CFL is the CFL number, Δx is the size of the computational cell and $S_{\max}^n$ is an estimate of the largest wave speed present at time level t^n.

A standard temporal discretization strategy consists in evolving, at each time level, all the 1D vessels according to the same time step determined as the minimum time step between all the vessels, namely

$$\Delta t^n = \min_{k=1,\dots,N_{1D}} \Delta t_k^{n,CFL}, \tag{3.91}$$

where N_{1D} is the total number of 1D vessels in the network and $\Delta t_k^{n,CFL}$ if the time step of the k-th vessel, for $k = 1, \dots, N_{1D}$, computed according to the CFL condition (3.90). In principle, this network can be either fully 1D or hybrid, but for the moment we will focus on the 1D part, while the temporal discretization of the 0D part will be addressed later, in Section 3.4.1.4. Throughout this section, we will refer to this approach as global time-stepping (GTS) strategy.

The GTS technique is convenient to use when the time step distribution among the 1D vessels of the network is homogeneous. However, when dealing with very large vascular networks, where the heterogeneity of spatial and temporal scales is relevant and vessels are characterized by time steps that differ of orders of magnitude, the GTS strategy is not efficient. Indeed, all the vessels of the network may be restricted to evolve with a very small global time step, thus performing, in those vessels with a larger CFL time step, much more vessel updates than those required and considerably increasing the computational cost of the simulations. This is more accentuated when viscoelastic vessel walls are considered, as the vessel length has an impact on the allowed time step because of the accuracy criteria (3.21).

To address this issue, in [102] the authors proposed a high-order and robust local time-stepping (LTS) solver, which allows each 1D vessel of a network to evolve in time according to a local time step given by its local stability criterion. This fully LTS scheme is applied in a vessel-wise manner, where all vessels have a common synchronization time and the coupling among neighboring vessels is performed locally at the corresponding time step for each junction. As shown in [102], this LTS strategy improves the computational efficiency of simulations in complex vascular networks by orders of magnitude.

In this work, the LTS solver proposed by Müller *et al.* [102] is adopted. In the following, the LTS methodology is briefly illustrated, focusing on the high-order LTS coupling strategy to couple vessels at 1D junctions and compute fluctuations along these junctions. For a complete description of the LTS algorithm we refer the reader to the work of Müller *et al.* [102]. Afterwards, in Section 3.4.2, this high-order LTS coupling strategy will be extended to the case of hybrid junctions, accounting for the fact that 1D vessels converging at the hybrid junction evolve via a fully explicit scheme, while the 0D vessels are advanced in time using an implicit ODE solver. Once again, as pointed out in the previous section, the accurate numerical treatment of junctions is crucial. In particular, the numerical coupling strategy adopted to solve hybrid junctions of 1D and 0D vessels must preserve the accuracy of the solution in the 1D vessels.

We observe that the LTS solver [102] represents a powerful tool for efficient simulations in complex networks. By applying the LTS methodology to the ADAN model developed by Blanco *et al.* [17, 16], in [102] the authors showed the benefits in terms of speed-up obtained by adopting an LTS over a GTS strategy; a benefit that becomes larger as the heterogeneity of time steps in the network increases. However, when dealing with even more complex vascular networks, such as the ADAN model coupled to cerebral arteriolar networks generated using a CCO technique, further computational efficiency may be needed. Hence, as it will be shown in Section 3.4.3 devoted to numerical experiments, the hybrid network solver developed in this thesis is expected to be crucial to gain computational efficiency in such framework, where 1D models can be adopted in regions where higher accuracy is needed, while 0D models can be employed in the other portions of the network.
Moreover, the complexity of the LTS solver algorithm is considerably higher than the one of the GTS solver, thus requiring more effort for its implementation. The implementation differences between the two methods regard only the management of the time marching algorithm, while no additional resources are required by the LTS with respect to the GTS solver. As a consequence, if a GTS network solver is already available, in order to make it more efficient to solve very complex and large vascular networks, the first step could be to integrate the hybrid network methodology proposed here in the GTS solver, allowing to perform cheaper, but still accurate, simulations in hybrid 1D-0D networks, rather than to adapt the GTS solver to the LTS algorithm.

Local time-stepping algorithm. Let us assume to have a network of N_{1D} one-dimensional vessels, with no 0D vessels. In Section 3.4.2, this methodology will be extended also to the case of hybrid networks, where 1D vessels are coupled to 0D vessels via hybrid junctions.

At the beginning of the simulation, the local time step for the j-th vessel is set to be

$$\Delta t_j^0 = \frac{\Delta t_{\max}}{k_j^0}, \tag{3.92}$$

with

$$k_j^0 = \left\lceil \frac{\log\left(\Delta t_{\max}/\widetilde{\Delta t}_j^0\right)}{\log(2)} \right\rceil, \tag{3.93}$$

where $\widetilde{\Delta t}_j^0$ is the vessel time step at t_j^0 given by the CFL condition at the current vessel state; $\Delta t_{\max}$ is a common synchronization time between all vessels defined by the maximum time step allowed by the LTS procedure, fixed by the user or adaptively changed during the simulation. Then, the local time step $\Delta t_j^{n_j}$ for the j-th vessel at the time iteration n_j is updated according to Algorithm 1 in [102], that we briefly present in the following and we refer the reader to the work of Müller *et al.* [102] for full details.

In general, the time step $\widetilde{\Delta t}_j^{n_j}$ for the j-th vessel at time level n_j is computed as in (3.90), that is

$$\widetilde{\Delta t}_j^{n_j} = CFL \frac{\Delta x_j}{\widetilde{S}_j^{n_j}}, \tag{3.94}$$

with

$$\widetilde{S}_j^{n_j} = \max_{i=1,\dots,\overline{M}_j} \left\{ |u_{j,i}^{n_j}| + c_T(A_{j,i}^{n_j}, \theta_{j,i}^{n_j}) \right\}, \tag{3.95}$$

where $\overline{M}_j$ is the number of computational cells of vessel j. From $\widetilde{\Delta t}_j^{n_j}$ in (3.94), we can then calculate

$$\Delta t_j^{n_j} = \frac{\Delta t_{\max}}{k_j^{n_j}}, \tag{3.96}$$

with

$$k_j^{n_j} = \left\lceil \frac{\log\left(\Delta t_{\max}/\widetilde{\Delta t}_j^{n_j}\right)}{\log(2)} \right\rceil, \tag{3.97}$$

Once we get $\Delta t_j^{n_j}$, the last step consists in verifying that the global CFL stability condition is fulfilled by the obtained time step. The following local variables are first introduced

$$CFL_{\text{loc}} = \widetilde{S}_j^{n_j} \frac{\Delta t_j^{n_j}}{\Delta x_j}, \qquad \Delta t_{\text{loc}} = \Delta t_j^{n_j}, \qquad k_{\text{loc}} = k_j^{n_j}. \tag{3.98}$$

If the local CFL number CFL_{loc} exceeds the user-defined value CFL, then the local time step is reduced; on the other hand, if CFL_{loc} is lower than the user-defined value, the local time step might be increased. In the first case, if $CFL_{\text{loc}} > CFL$, we iterate to change CFL_{loc} and reduce Δt_{loc} until we get $CFL_{\text{loc}} \leq CFL$, as follows

$$k_{\text{loc}} = k_{\text{loc}} + 1, \qquad \Delta t_{\text{loc}} = \min\left\{ \Delta t_{\max}, \frac{\Delta t_{\max}}{2^{k_{\text{loc}}}} \right\}, \qquad CFL_{\text{loc}} = \widetilde{S}_j^{n_j} \frac{\Delta t_{\text{loc}}}{\Delta x_j}. \tag{3.99}$$

Once the iteration is terminated, we set

$$\Delta t_j^{n_j} = \Delta t_{\text{loc}}, \qquad k_j^{n_j} = k_{\text{loc}}. \tag{3.100}$$

On the other hand, if $CFL_{\text{loc}} < CFL$, we iterate to change CFL_{loc} and increase Δt_{loc} while $CFL_{\text{loc}} < CFL$. Here, particular attention is required, as increasing the local time step is allowed only if the new time level is a multiple of $\Delta t_{\max}$, so that the synchronization of the solution at junctions is ensured. We perform the following iteration until we get $CFL_{\text{loc}} \geq CFL$

$$k_{\text{loc}} = k_{\text{loc}} - 1, \qquad \Delta t_{\text{loc}} = \min\left\{ \Delta t_{\max}, \frac{\Delta t_{\max}}{2^{k_{\text{loc}}}} \right\}, \qquad CFL_{\text{loc}} = \widetilde{S}_j^{n_j} \frac{\Delta t_{\text{loc}}}{\Delta x_j}, \tag{3.101}$$

after which we assign

$$k_{\text{loc}} = k_{\text{loc}} + 1, \qquad \Delta t_{\text{loc}} = \min\left\{\Delta t_{\text{max}}, \frac{\Delta t_{\text{max}}}{2^{k_{\text{loc}}}}\right\}. \tag{3.102}$$

Finally, if the new time level $t_j^{n_j} + \Delta t_{\text{loc}}$ is a multiple of Δt_{max}, namely if $\mod\left(t_j^{n_j} + \Delta t_{\text{loc}}, \Delta t_{\text{max}}\right) = 0$, we set

$$\Delta t_j^{n_j} = \Delta t_{\text{loc}}, \qquad k_j^{n_j} = k_{\text{loc}}; \tag{3.103}$$

otherwise, the time step $\Delta t_j^{n_j}$ is calculated using (3.92).

The LTS algorithm illustrated above ensures that the j-th vessel, for $j = 1, \dots, N_{1D}$, will evolve with its local time step, but taking into account the synchronization criteria of the solution at junctions. If we denote by $N_{j,\text{neigh}}$ the set of vessels that share a 1D junction with the j-th vessel, then the j-th vessel can evolve from time $t_j^{n_j}$ to time $t_j^{n_j+1} = t_j^{n_j} + \Delta t_j^{n_j}$ if the following update criterion is satisfied

$$t_j^{n_j} + \Delta t_j^{n_j} \leq \min_{m=1,\dots,N_{j,\text{neigh}}} \left\{t_m^{n_m} + \Delta t_m^{n_m}\right\}. \tag{3.104}$$

In fact, relation (3.104) ensures that the information needed to compute integrals (3.79) at the boundary interfaces of the j-th vessel is available through its entire time step, as we will see in the next part of this section.

Computation of fluctuations along junctions. If we consider internal cell interfaces, within the one-dimensional space domain of a vessel, integrals in (3.79) are approximated by solving classical Riemann problems at appropriate quadrature points, where the initial conditions for these Riemann problems are provided by the space-time predictions at both sides of the cell interface, computed as described in Section 3.4.1.1. On the other hand, in the case of boundary cell interfaces at junctions, the space-time polynomials are available only at one side of the interface. In this last case, fluctuations are computed as follows

$$\boldsymbol{D}^{+}_{j,1-\frac{1}{2}} = \frac{1}{\Delta t_j^{n_j}} \int_{t_j^{n_j}}^{t_j^{n_j+1}} \mathcal{D}^{+}_{j,1-\frac{1}{2}}\left(\boldsymbol{Q}^{*}_{j,1-\frac{1}{2}}(t), \boldsymbol{Q}^{ST}_{j,1}(x=0,t), \boldsymbol{\Psi}\right) dt, \tag{3.105}$$

for a boundary cell interface at $x_j = 0$, and

$$\boldsymbol{D}^{-}_{j,\overline{M}_j+\frac{1}{2}} = \frac{1}{\Delta t_j^{n_j}} \int_{t_j^{n_j}}^{t_j^{n_j+1}} \mathcal{D}^{-}_{j,\overline{M}_j+\frac{1}{2}}\left(\boldsymbol{Q}^{ST}_{j,\overline{M}_j}(x=l_j,t), \boldsymbol{Q}^{*}_{j,\overline{M}_j+\frac{1}{2}}(t), \boldsymbol{\Psi}\right) dt, \tag{3.106}$$

for a boundary cell interface located at $x_j = l_j$, with l_j being the length of the j-th vessel. $\boldsymbol{Q}^{ST}_{j,1}(0,t)$ and $\boldsymbol{Q}^{ST}_{j,\overline{M}_j}(l_j,t)$ are the space-time polynomials predicted by the DET solver for cell $i = 1$ and cell $i = N_j$, respectively; $\boldsymbol{Q}^{*}_{j,1-\frac{1}{2}}(t)$ and $\boldsymbol{Q}^{*}_{j,\overline{M}_j+\frac{1}{2}}(t)$ are the unknown boundary states obtained by solving the nonlinear coupling problem (3.34) defined in Section 3.2.3.1 for a given junction of 1D viscoelastic vessels, as explained in the following.

As we are using a LTS technique and each vessel converging at a 1D junction is evolving in time with its own local time step, integrals in (3.105) and (3.106) have to be computed as the sum of partial time integrals. Each integral is approximated using a Gauss-Lobatto quadrature rule. Similarly to the Riemann problem (2.74) defined at a 1D junction interface in the GTS case, also here, at each quadrature node t_p, the following Riemann problem can be formulated for N 1D vessels sharing a junction J

$$\begin{cases} \partial_t \boldsymbol{Q}_k + \boldsymbol{A}(\boldsymbol{Q}_k)\partial_x \boldsymbol{Q}_k = 0, \quad x \in \mathbb{R},\ t > t_p, \\ \boldsymbol{Q}_k(t_p) = \boldsymbol{Q}^{ST}_{k,\hat{i}_k}(x_k^J, t_p), \end{cases} \tag{3.107}$$

for $k = 1, \dots, N$. The initial condition states $\boldsymbol{Q}^{ST}_{k,\hat{i}_k}(x^J_k, t_p)$, for $k = 1, \dots, N$, are provided by the predicted space-time polynomials evaluated at time point t_p and at the vessel boundary interface x^J_k shared with the junction. Specifically, $x^J_k = 0$ and $\hat{i}_k = 1$, if the k-th vessel shares its left vertex with the junction; $x^J_k = l_k$ and $\hat{i}_k = \overline{M}_k$, if the vessel shares its right vertex with the junction, for $k = 1, \dots, N$.

The self-similar solution to the Riemann problem (3.107) is constructed as described in Section 3.2.3.1. Then, if space-time predictions for all N vessels sharing a junction J are available at time t_p, the unknown boundary state vectors $\boldsymbol{Q}^*_{k,\tilde{i}_k}(t_p)$, with $k = 1, \dots, N$, are computed by solving the nonlinear system (3.34), with $\tilde{i}_k = 1 - \frac{1}{2}$ if $x^J_k = 0$, or $\tilde{i}_k = \overline{M}_k + \frac{1}{2}$ if $x^J_k = l_k$. These states are used to evaluate the first-order fluctuations at specified quadrature nodes in (3.105) and (3.106).

In system (3.9), the first equation of mass conservation is written in conservative form. Following [43], to ensure mass conservation also at the discrete level, the first component of the integrands in (3.105) and (3.106) is replaced by the following expressions

$$\begin{cases} \mathcal{D}^+_{j,1-\frac{1}{2}}\left(\boldsymbol{Q}^*_{j,1-\frac{1}{2}}(t_p), \boldsymbol{Q}^{ST}_{j,1}(0,t_p), \boldsymbol{\Psi}\right)[1] = q^{ST}_{k,\hat{i}_k}(0,t_p) - q^*_{k,\tilde{i}_k}(t_p), \\ \mathcal{D}^-_{j,\overline{M}_j+\frac{1}{2}}\left(\boldsymbol{Q}^{ST}_{j,\overline{M}_j}(l_j,t_p), \boldsymbol{Q}^*_{j,\overline{M}_j+\frac{1}{2}}(t_p), \boldsymbol{\Psi}\right)[1] = q^*_{k,\tilde{i}_k}(t_p) - q^{ST}_{k,\hat{i}_k}(l_k,t_p). \end{cases} \tag{3.108}$$

Note that this is done only for boundary interfaces, not at internal cell interfaces.

Remark 3.13. The LTS algorithm incorporates the GTS solver, as a particular case. In fact, when the GTS procedure is adopted, all the 1D vessels sharing a junction vertex J are evolved with the same time step Δt^n, therefore at each time level the synchronization criterion for the solution at junctions is always satisfied and the information needed to compute integrals (3.79) at the boundary interfaces is available in all vessels converging at each junction for the entire time step. As a consequence, integrals in (3.105) and (3.106) can be performed numerically between time levels t^n and $t^{n+1} = t^n + \Delta t^n$ using the appropriate integration rule, as described above.

Ghost cell filling for spatial reconstruction. When performing the WENO reconstruction procedure, the spatial reconstruction stencil $\mathcal{S}^s_i$ includes computational cells at both sides of the i-th cell where the reconstruction is being applied. Then, in the case of cells at, or sufficiently close to boundaries, the stencil will fall outside the one-dimensional spatial domain of the vessel. In particular, in each vessel, the value of the state variables is required at M ghost cells at each side of the 1D domain.

Following the methodology introduced in [97, 96] and employed in [102], an approximation of the solution outside the 1D domain, to be used to compute cell averages at ghost cells, is extrapolated by performing a Taylor series expansion around the vertex J shared by the j-th vessel

$$\boldsymbol{Q}^{\text{ex}}_j(\varepsilon, t^{n_j}_j) = \boldsymbol{Q}^*_{j,\tilde{i}_j}(t^{n_j-1}_j + \Delta t^{n_j-1}_j) + \sum_{r=1}^{M} \frac{1}{r!} \partial^{(r)}_x \boldsymbol{Q}^*_{j,\tilde{i}_j}(t^{n_j-1}_j + \Delta t^{n_j-1}_j)\varepsilon^r, \tag{3.109}$$

where ε is a local spatial coordinate with origin located at the vertex J and $\boldsymbol{Q}^*_{j,\tilde{i}_j}(t^{n_j-1}_j + \Delta t^{n_j-1}_j)$ is the solution of the Riemann problem at the junction J obtained at the previous time step.
Then, the spatial derivatives needed in the Taylor expansion (3.109) are computed by solving a linearized Riemann problem, obtained from a linearized version of the original PDE system, involving the spatial gradients of the predicted space-time polynomials of all vessels sharing the junction J and evaluated at the time $t^{n_j-1}_j + \Delta t^{n_j-1}_j$. This procedure is inspired in the Titarev–Toro GRP solver [142] and full details, not reported here, can be found in [97, 96, 102].

3.4.1.3 An efficient strategy for solving large and stiff ODE systems

Differently from the previous section, where, in both fully 0D and hybrid networks, each 0D vessel was evolved separately by numerically integrating the ODE system governing its temporal dynamics and

connected to the neighboring 1D/0D vessels via coupling conditions at each time level, here we consider a different approach based on the construction of regions of connected 0D vessels. Then, an efficient strategy to solve the ODE system governing blood flow in each 0D region is developed, exploiting existing implicit ODE solvers, but also accounting for the specific features of the problem to be solved. We proceed through the following steps:

- First, we identify the regions of connected 0D vessels included in a hybrid network and we define the global ODE system governing blood flow in each 0D region;
- The numerical integration of each ODE system is then performed adopting standard implicit ODE solvers (implicit Euler scheme or Crank-Nicolson method), where implicit methods are required to resolve the stiffness problem;
- The nonlinear system associated to the implicit ODE method is solved using Broyden's method, so that the Jacobian matrix of the nonlinear system is computed only at the first iteration of the algorithm;
- Such Jacobian matrix is represented and calculated exploiting its highly sparse structure;
- The system of linear equations associated to Broyden's method is solved employing a specific set of routines suited to efficiently solve sparse linear systems.

Each one of these steps is described in detail in the following.

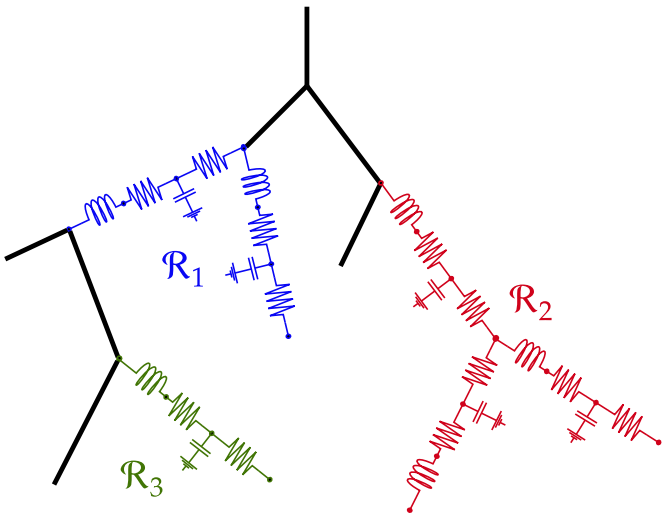
Construction of regions of 0D vessels. Clearly, if we consider a fully 0D network configuration, then we will have just one 0D region corresponding to the entire network itself. On the other hand, given a hybrid network of 1D-0D vessels and given the set of all its 1D/0D vessels and their connectivity, a 0D region can be defined as a subset of 0D vessels all connected among themselves, but not connected to any of the 0D vessels not included in this subset, where connections are made through 0D and hybrid junctions.

To identify a region of connected 0D vessels, we (arbitrarily) select a 0D vessel not yet assigned to any already defined 0D regions and we initialize the new 0D region with this vessel. Then, we start an iterative procedure where, at each iteration, we loop over all the 0D vessels included in the 0D region and we check whether the selected 0D vessel is connected to any other 0D vessels: if one or more 0D vessels connected to such vessel are found and if these 0D vessels are not already included into the 0D region, they are added to it. The iterative process is terminated when the size (*i.e.* the number of 0D vessels) of the 0D region at the current and at the previous iteration is the same, namely no new 0D vessels have been added to the 0D region.
0D vessels within the same 0D region are "internally" connected via 0D junctions; 0D vessels "at the borders" of the 0D region can be either terminal vessels of the network or be connected to 1D vessels via hybrid junctions. We note that if terminal vessels are coupled to *RCR* Windkessel models, these terminal elements are included in the 0D region as well. Figure 3.12 displays a schematic representation of a simple hybrid network of 1D-0D vessels, with three 0D regions, highlighted with blue, red and green colors, which are connected to the 1D vessels of the network (black segments) via hybrid junctions.

Once all the 0D regions contained in the hybrid network configuration are identified, we denote by N_R the number of 0D regions of the network, by $\mathcal{R}_j$ the subset of 0D vessels and, possibly, *RCR* elements belonging to the j-th 0D region and by $N_{R,j} = N_{R,j}^V + N_{R,j}^{RCR}$ the total number of 0D elements, 0D vessels ($N_{R,j}^V$) and *RCR* elements ($N_{R,j}^{RCR}$) of the j-th 0D region, for $j = 1, \dots, N_R$. Then, for each 0D region, we can construct the ODE system governing its temporal dynamics, as follows

$$\frac{d}{dt}\boldsymbol{Y}_j(t) = \boldsymbol{B}_j(t, \boldsymbol{Y}_j(t), \boldsymbol{Y}_j^D(t)), \quad \boldsymbol{Y}_j(0) = \boldsymbol{Y}_j^0, \tag{3.110}$$

FIGURE 3.12: Schematic representation of a hybrid network of 1D-0D vessels. The hybrid network has three 0D regions, $\mathcal{R}_1$ in blue, $\mathcal{R}_2$ in red and $\mathcal{R}_3$ in green, which are connected to the 1D vessels, depicted as black segments, via hybrid junctions.



for $j = 1, \dots, N_R$. $\boldsymbol{Y}_j(t)$ is the global vector of unknowns of the j-th 0D region, which is composed of the state variables sub-vectors $\boldsymbol{y}_{j,i}$, $i = 1, \dots, N_{R,j}$, of the $N_{R,j}^V$ 0D vessels and $N_{R,j}^{RCR}$ Windkessel elements of the 0D region, and $\boldsymbol{Y}_j^0$ is the vector of initial conditions. The nonlinear vector function $\boldsymbol{B}_j$ on the right-hand side of the ODE system depends not only on $\boldsymbol{Y}_j(t)$, but also on the vector $\boldsymbol{Y}_j^D(t)$ of the data to be prescribed "at the borders" of the j-th 0D region. These prescribed data can include (i) coupling conditions to 1D vessels at hybrid junctions and/or (ii) "boundary conditions", different from the coupling to a *RCR* Windkessel model, enforced at the inlet/outlet of 0D vessels at the borders of the 0D region. $\boldsymbol{Y}_j^D \in \mathbb{R}^{N_{D,j}}$, where $N_{D,j}$ is the number of such conditions to be prescribed to the j-th 0D region. Coupling conditions at 0D junctions and between 0D vessels and *RCR* elements are indeed embedded into $\boldsymbol{B}_j$ via $\boldsymbol{Y}_j$, as they only depend on the state variables of the 0D vessels and *RCR* elements coupled together.

Implicit ODE solvers for stiff ODE problems. So far, in Chapter 2 and in Section 3.3 of the present chapter, an explicit numerical method was always adopted to numerically integrate the ODE systems governing the 0D blood flow models, specifically the four-step explicit Runge-Kutta (RK4) method, and all the numerical experiments were performed on vascular networks of moderate complexity, the 37-artery network and ADAN56 model. To be precise, when carrying out fully 0D simulations, we were always able to select a not too restrictive time step Δt^{0D} ensuring the stability of the numerical scheme; while, when performing simulations on hybrid network configurations, the 1D time step obtained according to the CFL condition was used for both 1D and 0D vessels, also guaranteeing the stability of RK4 method. However, we were not able to adopt lower-order schemes than RK4 method, such as explicit Euler scheme or Heun's method, as stability issues were encountered with these explicit ODE solvers.

Then, when moving to much more complex and large vascular models, such as the ADAN model developed by Blanco *et al.* [17, 16] (which will be presented in detail in Section 3.4.3), we observed that explicit solvers, even higher-order ones, could not be adopted, requiring prohibitively small time steps, as when considering very large systems of ODEs or many ODE systems coupled together the problem to be solved becomes extremely stiff.

As a consequence, to resolve the stiffness problem, here we employ implicit ODE solvers. In particular, the ODE system (3.110) associated to a fully 0D network or to each 0D region of a hybrid network configuration

is solved by using θ-*methods* of the following form

$$\boldsymbol{Y}^{n+1} = \boldsymbol{Y}^n + \Delta t^n \left[\theta \boldsymbol{B}^n + (1-\theta)\boldsymbol{B}^{n+1}\right], \qquad \theta \in [0,1), \tag{3.111}$$

where Δt^n is the time step of the 0D region, $\boldsymbol{Y}^n$ denotes the numerical solution at the current time t^n and $\boldsymbol{Y}^{n+1}$ is the numerical solution at the next time level $t^{n+1} = t^n + \Delta t^n$, to be determined, $\boldsymbol{B}^n = \boldsymbol{B}(t^n, \boldsymbol{Y}^n, \boldsymbol{Y}^{D,n})$ and $\boldsymbol{B}^{n+1} = \boldsymbol{B}(t^{n+1}, \boldsymbol{Y}^{n+1}, \boldsymbol{Y}^{D,n+1})$. Here, the index j of the 0D region has been dropped to simplify the notation. For $\theta \in [0,1)$, the θ-method (3.111) is implicit and here we will consider the following choices of the parameter:

- $\theta = 0$, which corresponds to the first-order implicit Euler scheme;
- $\theta = 0.5$, for which we have the second-order Crank-Nicolson method (or trapezoidal rule).

However, implicit solvers come at the cost of having to solve the associated nonlinear system $\boldsymbol{G}(\boldsymbol{Y}^{n+1}) = 0$ to compute the sought solution $\boldsymbol{Y}^{n+1}$, which in the case of the θ-method (3.111) reads

$$\boldsymbol{G}(\boldsymbol{Y}^{n+1}) = \boldsymbol{Y}^{n+1} - \boldsymbol{Y}^n - \Delta t^n \left[\theta \boldsymbol{B}^n + (1-\theta)\boldsymbol{B}^{n+1}\right]. \tag{3.112}$$

Iterative algorithms, such as Newton's method or Broyden's method, can be adopted, requiring to compute, at each iteration of the algorithm, the Jacobian matrix $\boldsymbol{J}_{\boldsymbol{G}}$ of the vector function $\boldsymbol{G}$, or some approximation of it, and to solve a linear system. When dealing with very large ODE problems, of several thousands of equations, the evaluation of the Jacobian matrix, as well as the resolution of the associated linear problem can become prohibitively expensive operations, making unfeasible to employ the resulting implicit ODE solver, as these operations must be performed at each time step, for several iterations, until convergence of the iterative procedure.

Therefore, in the next part of this section, we will describe the steps performed to develop, departing from standard implicit ODE solvers, such as implicit Euler scheme and Crank-Nicolson method, an efficient strategy to solve potentially very large and stiff ODE systems. This strategy will be optimized also by exploiting specific features of the ODE problems we are interested to solve, such as the high sparsity of the Jacobian matrix associated to the nonlinear system (3.112).

Broyden's method. Given the numerical solution in a 0D region at time t^n, $\boldsymbol{Y}^n$, the numerical solution $\boldsymbol{Y}^{n+1}$ at the next time level $t^{n+1} = t^n + \Delta t^n$ is computed by adopting the θ-method (3.111), with $\theta \in [0,1)$. The solution of the nonlinear system (3.112) associated to the implicit solver, that is the updated vector of state variables $\boldsymbol{Y}^{n+1}$, can be approximated by using, for instance, Newton's method.
Given an initial guess $\boldsymbol{X}^{(0)}$ for $\boldsymbol{Y}^{n+1}$, Newton's method for a system of nonlinear equations $\boldsymbol{G}(\boldsymbol{Y}^{n+1}) = 0$ reads

$$\boldsymbol{X}^{(k+1)} = \boldsymbol{X}^{(k)} - \boldsymbol{DX}^{(k)}, \tag{3.113}$$

where the increment $\boldsymbol{DX}^{(k)}$ is given by the solution of the following system of linear equations

$$\boldsymbol{J}_{\boldsymbol{G}}(\boldsymbol{X}^{(k)})\boldsymbol{DX}^{(k)} = \boldsymbol{G}(\boldsymbol{X}^{(k)}), \tag{3.114}$$

for $k = 0, \dots, N_{max}$, where N_{max} is the maximum number of iterations. First of all, we note that at each iteration Newton's method requires the evaluation of the Jacobian matrix $\boldsymbol{J}_{\boldsymbol{G}}$, which, for a very large system, can become extremely expensive. In addition, the linear system (3.114) to compute the increment $\boldsymbol{DX}^{(k)}$ to be added to $\boldsymbol{X}^{(k)}$ to obtain the solution at the next iteration $\boldsymbol{X}^{(k+1)}$ has to be solved. Once again, solving a very large linear system of thousands of equations is not a trivial and cheap operation, which must be preformed by accounting for specific features of the linear problem to be solved.
The increment $\boldsymbol{DX}^{(k)}$ can also be used to define a stopping criterion for the iterative procedure (3.113). In

our implementation, the iterative algorithm is stopped when the absolute value of all the components of the increment vector $\boldsymbol{DX}^{(k)}$ relative to a reference vector $\boldsymbol{X}_{ref}$ are smaller than a fixed threshold $tol = 10^{-7}$. The vector $\boldsymbol{X}_{ref}$ consists of reference values depending on the corresponding type of variable: the reference vessel volume V_0 for each volume variable; a reference value Q_0 for the average flow rate in each vessel, estimated from a target wall shear stress, for each flow variable; a reference pressure P_0 for each pressure variable.

As just observed, since computing the Jacobian matrix at each iteration of Newton's algorithm is a very expensive and difficult operation, here Netwon's method (3.113) is replaced by Broyden's method, where the idea is that the whole Jacobian matrix $\boldsymbol{J_G}$ is computed only at the first iteration of the algorithm, while at each subsequent iteration the Jacobian matrix is approximated using that of the previous iteration, according to the following formula

$$\boldsymbol{J}_{\boldsymbol{G}}^{(k)} = \boldsymbol{J}_{\boldsymbol{G}}^{(k-1)} + \frac{\Delta \boldsymbol{G}^{(k)} - \boldsymbol{J}_{\boldsymbol{G}}^{(k-1)} \Delta \boldsymbol{X}^{(k)}}{\|\Delta \boldsymbol{X}^{(k)}\|^2} \left(\Delta \boldsymbol{X}^{(k)}\right)^T, \tag{3.115}$$

where $\Delta \boldsymbol{X}^{(k)} = \boldsymbol{X}^{(k)} - \boldsymbol{X}^{(k-1)}$ and $\Delta \boldsymbol{G}^{(k)} = \boldsymbol{G}^{(k)} - \boldsymbol{G}^{(k-1)}$, $\boldsymbol{G}^{(k)} = \boldsymbol{G}(\boldsymbol{X}^{(k)})$ and $\boldsymbol{J}_{\boldsymbol{G}}^{(k)} = \boldsymbol{J}_{\boldsymbol{G}}(\boldsymbol{X}^{(k)})$. In this way, at each time step, the whole Jacobian matrix is computed just once, at the first iteration of Broyden's method, to significantly reduce the cost of the iterative algorithm.

Calculation of the sparse Jacobian matrix. Let us now focus of the actual calculation of the Jacobian matrix $\boldsymbol{J_G}$ and on the resolution of the associated linear system (3.114). First of all, the Jacobian matrix $\boldsymbol{J_G}$ can be rewritten in terms of the Jacobian matrix $\boldsymbol{J_B}$ of the vector function $\boldsymbol{B}$ defining the right-hand side of the ODE system governing a 0D region, as follows

$$\boldsymbol{J_G} = \boldsymbol{I}_N - \Delta t(1-\theta)\boldsymbol{J_B}, \tag{3.116}$$

where $\boldsymbol{I}_N$ denotes the $N \times N$ identity matrix, being N the number of components of the state vector $\boldsymbol{Y}$ of the 0D region. The Jacobian matrix $\boldsymbol{J_G}$ is highly sparse, as the number of non-zero elements is much smaller than the total number of elements of the matrix. In fact, each equation of the nonlinear system (3.112) corresponds to the right-hand side of an equation of the ODE system governing the dynamics of a vessel of the 0D region. Hence, such nonlinear equation will only depend on the state variables of the vessel and of the neighboring 0D vessels and/or RCR element to which it is connected. Furthermore, when initializing the 0D region, its global state vector $\boldsymbol{Y}$ can be re-ordered such that the resulting Jacobian matrix will be a band matrix, whose non-zero entries are confined to a diagonal band. Then, since the structure of the Jacobian matrix $\boldsymbol{J_G}$ associated to a 0D region is fixed, this matrix is not defined and initialized as a dense matrix, but using a sparse matrix representation, storing only the row-column indexes of the elements where the matrix contains non-zero values along with those values. We denote by N_{NZ} the number of non-zero elements of the Jacobian matrix $\boldsymbol{J_G}$, by $\mathcal{I}_{row}$, $\mathcal{I}_{col}$ and $\mathcal{I}_{elem}$ the N_{NZ}-tuples containing the row indexes, the column indexes and the values of the non-zero elements of $\boldsymbol{J_G}$, where the i-th value in $\mathcal{I}_{elem}$ corresponds to the non-zero entry with row index given by the i-th index in $\mathcal{I}_{row}$ and column index given by the i-th index in $\mathcal{I}_{col}$. Hence, only the non-zero elements of $\boldsymbol{J_G}$ are approximated using central differences, as follows

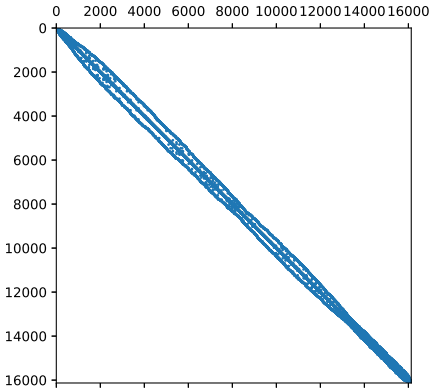
$$\begin{aligned} \mathcal{I}_{elem}^i = (\boldsymbol{J_G})_{r,c} &= \frac{\partial G_r(\boldsymbol{X})}{\partial X_c} \\ &\approx \frac{G_r(X_1, \dots, X_{c-1}, X_c + h_c, X_{c+1}, \dots, X_N) - G_r(X_1, \dots, X_{c-1}, X_c - h_c, X_{c+1}, \dots, X_N)}{2h_c}, \end{aligned} \tag{3.117}$$

with $r = \mathcal{I}_{row}^i$ and $c = \mathcal{I}_{col}^i$, for $i = 1, \dots, N_{NZ}$, where $\mathcal{I}_{_}^i$ denoted the i-th component of the tuple $\mathcal{I}_{_}$, and $h_c > 0$ sufficiently small. Note that the increment h_c used to approximate the derivative in (3.117) is not the same for all variables in $\boldsymbol{X}$, but it is given by $h_j = \delta \cdot X_{ref,j}$, for $j = 1, \dots, N$, where $X_{ref,j}$ is the j-th

component of the reference vector $\boldsymbol{X}_{ref}$ defined above and $\delta = 10^{-8}$. Figure 3.13 displays an example of structure of the sparse Jacobian matrix $\boldsymbol{J}_G$ corresponding to a fully 0D configuration of the ADAN model, showing its highly sparse nature.

Then, the linear system (3.114) to be solved is a sparse linear system. In order to exploit the high sparsity of the system to efficiently compute its solution, we employ the UMFPACK library.

FIGURE 3.13: Visualization of the structure of the sparse Jacobian matrix $\boldsymbol{J}_G$ corresponding to a fully 0D configuration of the ADAN model, where blue dots represent non-zero elements of the matrix.



Solution of the sparse linear system using the UMFPACK library. The UMFPACK library, written by Timothy Davis [35, 36], is part of the SuiteSparse package, available at [132], and is a set of routines for solving unsymmetric sparse linear systems of the form $\boldsymbol{Ax} = \boldsymbol{b}$, when $\boldsymbol{A}$ is sparse and unsymmetric, using the Unsymmetric MultiFrontal method [38, 37] and direct sparse LU factorization.

First of all, UMFPACK requires the sparse matrix to be stored in a common format known as "compressed column (CC) format", which is a compact compressed column data structure simplifying the UMFPACK routines that operate on the sparse matrix $\boldsymbol{A}$. Given the number of non-zero element N_{NZ} in the "standard triplet (ST) format" introduced above, with tuples $\mathcal{I}_{row}$ and $\mathcal{I}_{col}$ of row and columns indexes of non-zero elements, respectively, the CC indexes are created from the ST data and stored in two array, the array $\mathcal{I}_{CC}$ of the CC rows of size N_{CC}, where N_{CC} is the number of CC elements, and the array $\mathcal{C}_{CC}$ of the compressed CC columns of size N, where N is the number of columns in the matrix. A third array $\mathcal{V}_{CC}$ of size N_{CC} is also generated to store the numerical values of the non-zero matrix entries. The row indexes of non-zero entries in column i are stored in $\mathcal{I}_{CC}[\mathcal{C}_{CC}[i] \dots \mathcal{C}_{CC}[i+1]-1]$, the corresponding numerical values are stored in $\mathcal{V}_{CC}[\mathcal{C}_{CC}[i] \dots \mathcal{C}_{CC}[i+1]-1]$.

Then, five primary UMFPACK routines are used to factorize the sparse matrix $\boldsymbol{A}$ and solve the associated sparse linear system $\boldsymbol{Ax} = \boldsymbol{b}$. First, given the non-zero pattern of $\boldsymbol{A}$ in CC format, the routine `umfpack_di_symbolic` performs a column pre-ordering and a symbolic factorization. This routine returns a `Symbolic` object as a `void *` pointer, containing the symbolic analysis needed for the numeric factorization. Next, given the computed symbolic factorization, the routine `umfpack_di_numeric` performs the numerical factorization, $\boldsymbol{PAQ} = \boldsymbol{LU}$ for instance, where $\boldsymbol{P}$ and $\boldsymbol{Q}$ are permutation matrices, $\boldsymbol{L}$ is unit-lower triangular and $\boldsymbol{U}$ is upper triangular. This routine returns a `Numeric` object as a `void *` pointer. We note that, if the non-zero pattern of the matrix does not change, `umfpack_di_numeric` can be called multiple times for each call to `umfpack_di_symbolic`. The `Symbolic` object is computed once and re-used for subsequent matrices with identical non-zero pattern. Afterwards, given the LU factors of matrix $\boldsymbol{A}$ computed in the numerical factorization and the right-hand side $\boldsymbol{b}$, the sparse linear system is solved using the routine `umfpack_di_solve` to

find its solution $\boldsymbol{x}$. The routines `umfpack_di_free_symbolic` and `umfpack_di_free_numeric` can then be used to free the `Symbolic` and `Numeric` objects created, respectively, when they are no longer needed.

To summarize, given a fully 0D or hybrid network configuration, the ODE system (3.110) governing each 0D region is solved using a stiff, implicit ODE solver of the form (3.111). To evolve the numerical solution from time t^n, $\boldsymbol{Y}^n$, to time $t^{n+1} = t^n + \Delta t^n$, $\boldsymbol{Y}^{n+1}$, the nonlinear system associated to the implicit ODE solver is solved using Broyden's method, where the whole Jacobian matrix $\boldsymbol{J_G}$ is computed only at the first iteration of the algorithm (its non-zero elements, as this matrix is highly sparse), while at each subsequent iteration the Jacobian matrix is approximated using that of the previous iteration. At each iteration of Broyden's method, the sparse linear system (3.114) is then solved by using the routines of the UMFPACK library. At convergence of the iterative algorithm, the new numerical solution $\boldsymbol{Y}^{n+1}$ is obtained and the state variables sub-vectors of the 0D vessels and *RCR* Windkessel elements of the 0D region are also updated.

3.4.1.4 0D temporal discretization strategy

In the case of a fully 0D network, thus a single 0D region given by the entire network itself, we set a constant time step Δt^{0D} to evolve the 0D region. As we are employing implicit numerical methods to integrate in time the ODE systems governing blood flow in regions of 0D vessels, the allowable time step is not as restrictive as in the case of explicit schemes, provided that the mesh independence of the solution is ensured.

On the other hand, when considering hybrid network configurations, where one or more 0D regions are coupled to 1D vessels via hybrid junctions, the time step of each 0D region of the hybrid network is determined as follows. The temporal discretization strategy we consider is similar to the one adopted in Section 3.3.2, to compute the global time step of a hybrid network used to evolve all its vessels, both 1D and 0D. Here, the time step of a 0D region is determined as the minimum time step between all the 1D vessels connected/attached to that 0D region. If we denote by $\mathcal{R}_j^{1D}$ the set of 1D vessels which are coupled to the j-th 0D region via hybrid junctions, then the 0D time step $\Delta t_j^{0D,n_j}$ of region j is calculated as follows

$$\Delta t_j^{0D,n_j} = \min_{k \in \mathcal{R}_j^{1D}} \Delta t_k^{n_k}, \tag{3.118}$$

for $j = 1, \ldots, N_R$, where $\Delta t_k^{n_k}$ denotes the time step of the k-th 1D vessel, computed according to either the GTS or the LTS temporal discretization strategies introduced for 1D vessels in Section 3.4.1.2. Especially when considering viscoelasticity of vessel walls, the time step of 1D vessels can become very small. Hence, the main disadvantage of this strategy is clearly that the time step of a 0D region is restricted by the minimum time step of the 1D vessels to which it is attached, thus making the 0D region to be evolved with the chosen implicit ODE solver with a time step possibly much smaller than the one required by the numerical method, which may not be efficient.

We are aware of this limitation and future work will include to design a more efficient 0D temporal discretization strategy and thus, numerical hybrid coupling strategy, where 0D regions are allowed to evolve with their own time step, not restricted by that of the 1D vessels they are connected to.

Equipped with both 1D and 0D temporal discretization strategies, as well as the numerical schemes introduced to solve 1D vessels and regions of 0D vessels, the last key ingredient of the proposed hybrid network solver is a high-order numerical coupling strategy to solve hybrid junctions of 1D and 0D vessels coupled together, which is presented in the next section.

3.4.2 High-order numerical hybrid coupling strategy

In this section, we present the hybrid numerical coupling strategy developed to solve hybrid junctions and couple 1D and 0D vessels, where 1D vessels are evolved using a fully explicit numerical scheme, while 0D vessels belong to 0D regions that are advanced in time adopting an implicit ODE solver. As already pointed out, the accurate numerical treatment of the hybrid coupling between 0D regions and 1D vessels is crucial, to ensure the accuracy of the solution, especially in 1D vessels, also at the level of junctions and thus, throughout the entire network.

The numerical coupling strategy proposed here extends the one derived in Section 3.3.2.2, with the difference that the boundary numerical fluxes are now replaced by the numerical fluctuations (3.79) that need to be appropriately approximated at the boundary cell interfaces along hybrid junctions, as done for 1D junctions. In addition, two other important aspects have to be taken into account. First, the numerical method employed for integrating the ODE systems governing regions of 0D vessels is no longer explicit, but an implicit ODE solver is adopted to resolve the problem of stiffness. Second, differently from the hybrid coupling strategy developed in Section 3.3.2.2, in addition to the GTS solver, here the LTS algorithm can also be used. Therefore, each 1D/0D vessel converging at a hybrid junction can evolve with its local time step (which, in the case of 0D vessels, is the time step of the 0D region they belong to) and an update criterion similar to the one in (3.104) is then required.

We describe here the proposed numerical hybrid coupling strategy in the case where the LTS algorithm is employed. The same numerical coupling approach can be easily applied also in the case of a global time step used for the entire hybrid network, as a particular case of the procedure presented in the following. Let us assume to have a hybrid junction J connecting together N 1D vessels and M 0D vessels, with $N, M > 0$. Clearly, the M 0D vessels belongs to the same j-th 0D region, so they are evolved together with the same time step. We denote by t_j^{0D,n_j} and $\Delta t_j^{0D,n_j}$ the current time level and the time step of the j-th 0D region, respectively, common to all the M 0D vessels converging at junction J. On the other hand, each one of the N 1D vessels sharing the same hybrid junction J can advance in time with its local time step. We denote by $t_k^{n_k}$ the current time level and by $\Delta t_k^{n_k}$ the local time step of the k-th 1D vessel, respectively, for $k = 1, \dots, N$. We observe that $\Delta t_j^{0D,n_j}$ may be different from any of the 1D time steps $\Delta t_k^{n_k}$, for $k = 1, \dots, N$, as it is computed according to formula (3.118) as the minimum time step between all the 1D vessels the j-th 0D region it is connected to. As a consequence, the j-th 0D region can always advance in time from the current time level $\Delta t_j^{0D,n_j}$ to the next time level $t_j^{0D,n_j+1} = t_j^{0D,n_j} + \Delta t_j^{0D,n_j}$, while the k-th 1D vessel converging at the hybrid junction can evolve from time $t_k^{n_k}$ to time $t_k^{n_k+1} = t_k^{n_k} + \Delta t_k^{n_k}$ only if the following updating criterion is satisfied

$$t_k^{n_k} + \Delta t_k^{n_k} \leq t_j^{0D,n_j} + \Delta t_j^{0D,n_j}, \tag{3.119}$$

for $k = 1, \dots, N$. Relation (3.119) ensures that the information needed to compute integrals (3.79) at the boundary interfaces of the k-th 1D vessel is available through its entire time step, information that depends on the other 1D vessels converging at the hybrid junction and also on the 0D vessels of the j-th 0D region sharing their inlets/outlets with this junction, as explained in the following.

First, the j-th 0D region is updated in time implicitly from t_j^{0D,n_j} to t_j^{0D,n_j+1} using the implicit ODE solver presented in Section 3.4.1.3, which is based on a θ-method of the form (3.111). Here, we set either $\theta = 0$ to adopt the implicit Euler scheme, or $\theta = 0.5$ to employ the second-order Crank-Nicolson method. Then, depending on the chosen numerical method, the hybrid junction J, joining the N 1D vessels and the M 0D vessels belonging to the j-th 0D region, must be solved at the different time points required by the scheme. Specifically, implicit Euler scheme requires the evaluation of the vector function $\boldsymbol{B}$ at the new time level only, that is t_j^{0D,n_j+1}, so the hybrid junction is solved iteratively with the entire 0D region using Broyden's method. On the other hand, Crank-Nicolson scheme uses the evaluation of the vector

function $\boldsymbol{B}$ at both current and new time levels, so the hybrid junction must be solved first at time t_j^{0D,n_j} and then within Broyden's algorithm to compute the updated coupling conditions at time t_j^{0D,n_j+1}. Solving the hybrid junction means that the nonlinear hybrid coupling problem (3.47) is solved, where the initial conditions states $\boldsymbol{Q}_k^{1D}$ are provided by the predicted space-time polynomials evaluated at the appropriate time point t_p and at the vessel boundary interface x_k^J shared with the hybrid junction, that is $\boldsymbol{Q}_{k,\hat{i}_k}^{ST}(t_p, x_k^J)$, for $k = 1, \dots, N$. $x_k^J = 0$ and $\hat{i}_k = 1$, if the k-th vessel shares its left vertex with the junction; $x_k^J = l_k$ and $\hat{i}_k = \overline{M}_k$, if the vessel shares its right vertex with the junction, for $k = 1, \dots, N$. For the time points $\{t_p\}_{p=1,\dots,N_p}$, clearly we will have

$$\{t_p\}_{p=1,\dots,N_p} = \begin{cases} \left\{ t_j^{0D,n_j} + \Delta t_j^{0D,n_j} \right\}, & N_p = 1, \quad \text{if implicit Euler scheme,} \\ \left\{ t_j^{0D,n_j}, t_j^{0D,n_j} + \Delta t_j^{0D,n_j} \right\}, & N_p = 2, \quad \text{if Crank-Nicolson scheme.} \end{cases} \tag{3.120}$$

Then, at time point t_p, the solution of the nonlinear coupling problem (3.47) will provide:

- the 0D coupling conditions $P_{in/out}^{i_j}(t_p)/Q_{in/out}^{i_j}(t_p)$, for $i_j = 1, \dots, M$, namely pressures and flow rates to be prescribed at the inlets and outlets of the 0D vessels converging at the hybrid junction;
- the 1D boundary state vectors $\boldsymbol{Q}_{k,\tilde{i}_k}^*(t_p)$, for $k = 1, \dots, N$, for the 1D vessels, where $\tilde{i}_k = 1 - \frac{1}{2}$ if $x_k^J = 0$, or $\tilde{i}_k = \overline{M}_k + \frac{1}{2}$ if $x_k^J = l_k$.

Once the j-th 0D region is advanced in time, to the new time level $t_j^{0D,n_j} + \Delta t_j^{0D,n_j}$, and thus the M 0D vessels converging at the hybrid junction J, we can deal with the N 1D vessels sharing the same vertex J. For the 1D vessels, the fluctuations at the boundary cell interfaces along the hybrid junction must be computed as in (3.105) and (3.106). Because of the updating criterion (3.119), also in this case the integrals in (3.105) and (3.106) have to be computed as the sum of partial time integrals. In particular, instead of using a Gauss-Lobatto quadrature rule as done in the LTS algorithm for 1D junctions in Section 3.4.1.2, each partial integral is now approximated using an integration rule with quadrature nodes given by the time points of the ODE numerical method adopted to solve the 0D region, that is the time points $\{t_p\}$ defined in (3.120), and corresponding weights $\{\omega_p\}$. Specifically, for implicit Euler scheme we have $\{\omega_p\}_{p=1} = \{1.0\}$; while for Crank-Nicolson method we set $\{\omega_p\}_{p=1,2} = \{0.5, 0.5\}$.
In this way, at each integration point t_p, the integrand in (3.105) and (3.106) is calculated by considering the predicted space-time polynomial evaluated at t_p and at the vessel boundary interface x_k^J, that is $\boldsymbol{Q}_{k,\hat{i}_k}^{ST}(t_p, x_k^J)$, and the boundary state vector $\boldsymbol{Q}_{k,\tilde{i}_k}^*(t_p)$ previously computed by solving the nonlinear hybrid coupling problem at time point t_p.

We note that the integration rule adopted to compute the integrals in (3.105) and (3.106) of fluctuations along hybrid junctions can be different from the quadrature rule employed to approximate the same integrals along fully 1D junctions and the integrals in (3.79) of fluctuations at internal cell interfaces, depending on the implicit ODE solver used to evolve the 0D regions.

To conclude, we point out two relevant aspects of the numerical coupling procedure proposed to solve hybrid junctions. First, it can be shown that this coupling strategy enforces mass and also energy conservation across the hybrid junction. Second, the desired order of accuracy of the solution in 1D vessels can be preserved by choosing an ODE method with the same order of accuracy, in time, of the numerical scheme used for the 1D domains. For instance, if we employ the second-order path-conservative numerical scheme introduced in Section 3.4.1.1, then the second-order accuracy in space and time is expected to be preserved in the 1D solution also at the level of hybrid junctions when the second-order Crank-Nicolson method (*i.e.* method (3.111) with $\theta = 0.5$) is used for integrating in time the ODE systems governing the 0D regions to which the 1D vessels are connected to. To achieve higher-order accuracy in 1D vessels, then a suitable higher-order implicit ODE solver should be selected accordingly, but this is not done in the present work.

3.4.3 Numerical experiments

As a challenging example of a complex vascular network, we consider the Anatomically Detailed Arterial Network (ADAN) computational haemodynamics model introduced by Blanco *et al.* [17, 16]. The ADAN model was developed in compliance with classical descriptive anatomy textbooks [34, 110], for the case of an average young healthy male. Almost every single arterial vessel with a well-established name according to the International Anatomical Terminology [34] was included in the model. An overview of this model of the human arterial system is shown in Figure 3.14: it comprises 2142 arterial vessels (4041 one-dimensional segments), reaching an unprecedented level of detail in the anatomical description of the human arterial vasculature; 1598 vessels are arterial segments with a well-acknowledged name, while 544 are perforator arteries, *i.e.* pre-arteriolar vessels feeding certain vascular territories. The arterial vasculature supplies blood to 28 specific organs (brain, heart, glands, liver, *etc*) and 116 vascular territories which constitute distributed organs (skin, nerves, muscles and bones). Terminal vessels are connected to *RCR* lumped-parameter models and an inflow curve is prescribed at the inlet of the aortic arch. For a detailed description of the model, the model parameters and the criteria used to define blood flow distribution among organs and vascular territories, the reader is referred to the works by Blanco *et al.* [17, 16]. Figure 3.14 displays the complete ADAN model with a zoom on the vasculature of the head.

The ADAN model includes a wide range of vessel radii, from 3.552×10^{-3} cm to 1.533 cm, and lengths, from 3.286×10^{-2} cm to 36.654 cm. Figure 3.16a shows histograms of radius and length distributions in the ADAN model. In addition, the heterogeneity in the spatial scale is considerably accentuated when viscoelastic properties of vessel walls are considered, as the vessel length has an impact on the allowed time step by the accuracy criteria (3.21). Hence, the ADAN model represents the perfect scenario where to test the hybrid 1D-0D network solver proposed in this thesis. In fact, the arterial network models considered so far, *i.e.* the 37-artery network and the reduced ADAN56 model, have much less heterogeneity in terms of spatial (vessel lengths and radii) and temporal scales, and by applying the proposed methodology to these vascular models we would only partially demonstrate the potential of this hybrid network solver. In this section, this methodology is then applied and tested to much more complex networks and models, where the heterogeneity of spatial and/or temporal scales is relevant, such as the ADAN model.

Furthermore, we consider the cerebral arteriolar networks reported in Blanco *et al.* [15] and automatically generated using an optimization technique (constrained constructive optimization (CCO) technique) which follows well-defined morphometric and functional rules [14, 124]. These arteriolar trees were constructed for two specific peripheral sites, namely the peripheral bed of the lenticulostriate artery and the peripheral bed of the posterior parietal branch of the middle cerebral artery (MCA). The arteriolar networks are coupled to the ADAN model at corresponding cerebral arteries, to generate an even more complex and heterogeneous arterial model, from the larger systemic arteries to the level of arterioles in the brain. Figure 3.15 shows detail of the two CCO-generated peripheral beds. Radius and length distributions in the ADAN model coupled to each one of the cerebral arteriolar networks are displayed in Figures 3.16b and 3.16c, showing that the heterogeneity in the spatial scales is further increased with respect to the ADAN model, towards considerably smaller scales for both radius and length.
Terminal vessels of the arteriolar networks are coupled to purely resistive elements, to model the microcirculation, where terminal resistances are set up in a way to ensure that the average flow rate is the same for all the outlets of the network.

The blood rheology in small vessels, specifically the blood viscosity μ, is modeled as suggested by Pries *et al.* [113], in order to account for viscosity variation as function of the vessel radius. In particular, the fluid viscosity μ is characterized by the following constitutive relation, an *in-vivo* empirical description proposed

by Pries *et al.* [113],

$$\mu_{rel} = \left[1 + (\mu^*_{0.45} - 1)\,\frac{(1-H_D)^C - 1}{(1-0.45)^C - 1}\left(\frac{D}{D-1.1}\right)^2\right]\left(\frac{D}{D-1.1}\right)^2, \tag{3.121}$$

with

$$\mu^*_{0.45} = 6e^{-0.085D} + 3.2 - 2.44e^{-0.06D^{0.645}} \tag{3.122}$$

and

$$C = \left(0.8 + e^{-0.075D}\right)\left(-1 + \frac{1}{1+10^{-11}D^{12}}\right) + \frac{1}{1+10^{-11}D^{12}}, \tag{3.123}$$

where $D = 2R_0$, with $R_0 = \sqrt{A_0/\pi}$, is the vessel diameter (in μm) and we have assumed $H_D = 0.5$ to be the value of the hematocrit. Since the quantity μ_{rel} calculated according to (3.124) represents the relative blood viscosity with respect to that of plasma, the effective viscosity μ is then obtained as

$$\mu = \mu_{rel} \cdot \mu_{plasma}, \tag{3.124}$$

with $\mu_{plasma} = 0.011$.

As for large arteries, arterioles are also considered as deformable vessels, so the same 1D and 0D mathematical models for blood flow, the PDE system (3.9) with viscoelastic tube law (3.1)-(3.3) and the ODE system (2.31) coupled to the viscoelastic pressure law (3.31)-(3.32), respectively, are adopted for both ADAN model and the cerebral arteriolar networks. The viscoelastic tube law introduced in Section 3.2 is employed: the wall thickness in each vessel is estimated using relation (2.101) taken from [10]; the complete set of material parameters characterizing the viscoelastic tube law (3.1)-(3.3) and its 0D counterpart (3.31)-(3.32) can be found in [17]. General parameters of the ADAN model and of the CCO-generated cerebral arteriolar networks are summarized in Table 3.18; the blood viscosity μ in the arteriolar vessels of the peripheral beds is not taken equal to the value reported in Table 3.18, but it is computed in each vessel according to formula (3.121).

Computational parameters for all the simulations, 1D, 0D and hybrid, presented in Sections 3.4.3.3 and 3.4.3.2 are listed in Table 3.18.

All simulations were run on a Linux Ubuntu 18.04 machine with AMD® Ryzen™ Threadripper™ 3990X Processor (Base Clock: 2.9 GHz, Max. Boost Clock: up to 4.3 GHz, 64 CPU Cores/128 Threads, Total L3 Cache: 256 MB).

TABLE 3.18: General parameters of the ADAN model and of the CCO-generated cerebral arteriolar networks.

Property	**Value**
Blood density, ρ	1.040 g/cm^3
Blood viscosity, μ	0.04 dyne·s/cm^2
Blood viscosity - perforator, μ_{perf}	0.01 dyne·s/cm^2
Velocity profile order, ζ	2
Reference pressure, P_0	10^5 dyne/cm^2
External pressure, p_{ext}	0
Outflow pressure, P_{out}	0

3.4.3.1 Region-based hybrid networks

In Section 3.3, we have developed a modeling and computational methodology to construct hybrid networks of 1D-0D vessels and perform blood flow simulations in such networks that provide a good trade-off between computational efficiency and accuracy in the results. In particular, by carrying out error

FIGURE 3.14: Anatomically Detailed Arterial Network (ADAN) model with detail of the vasculature in the head. It includes over 2000 arterial vessels, with 162 cerebral vessels forming the intracranial vasculature.

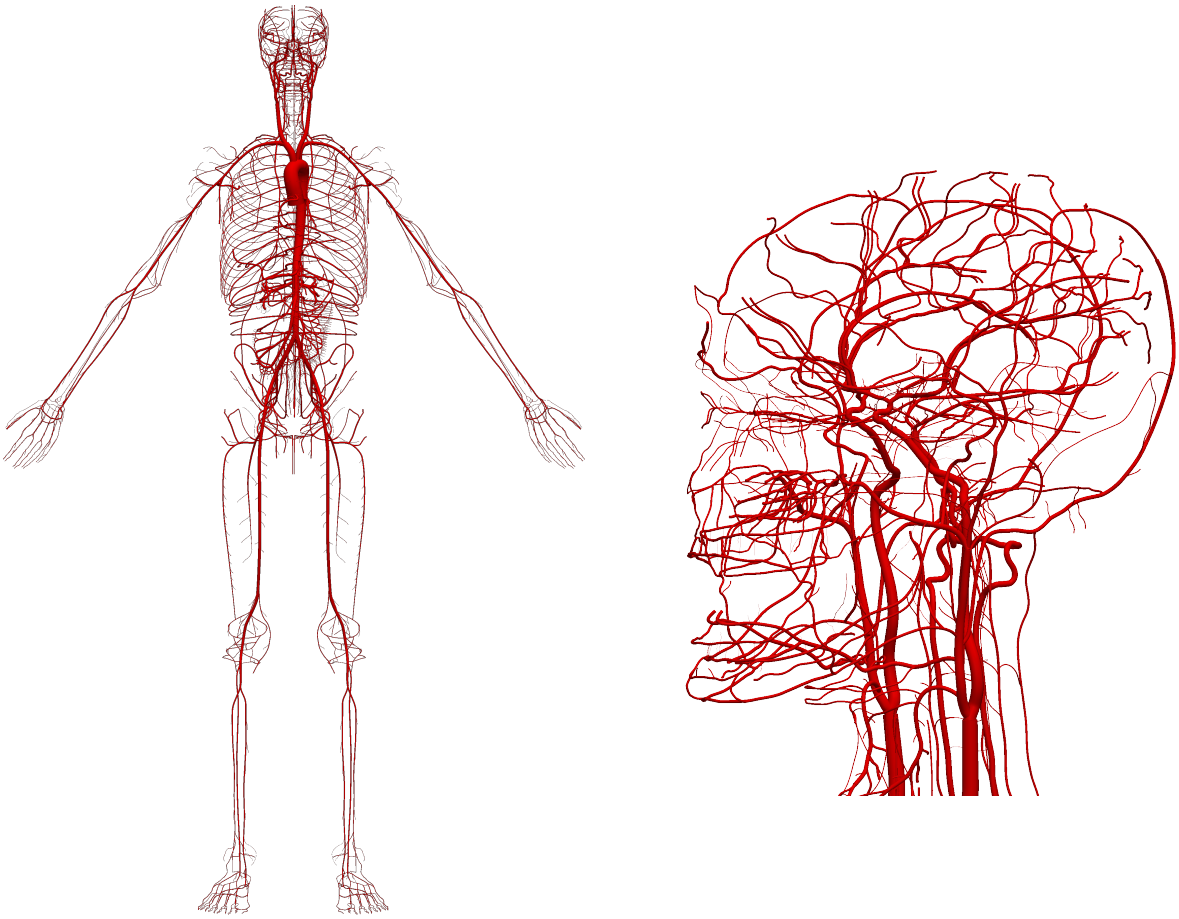
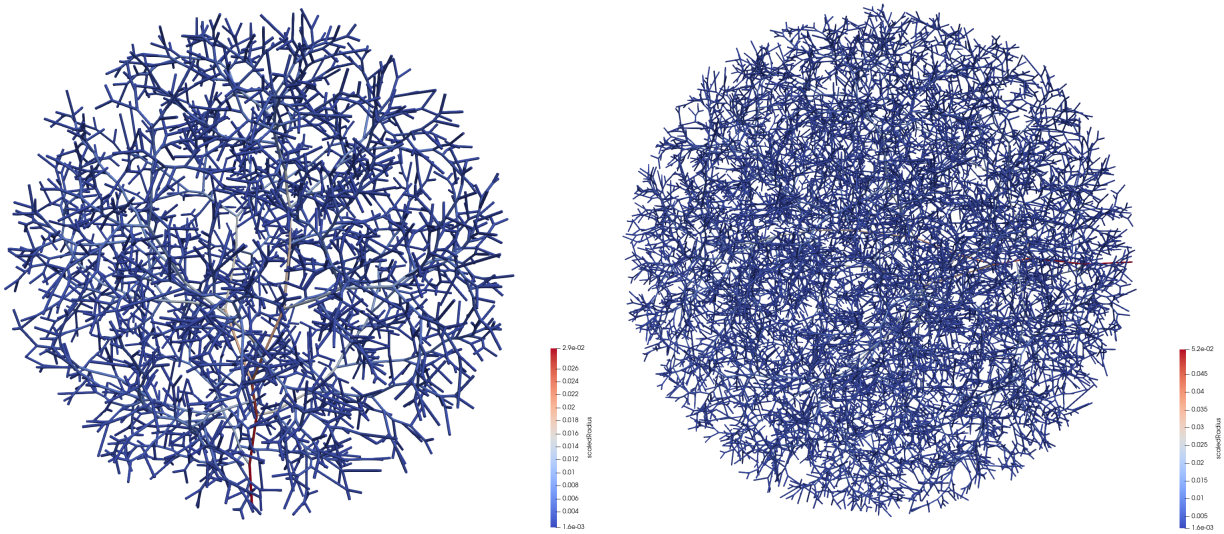


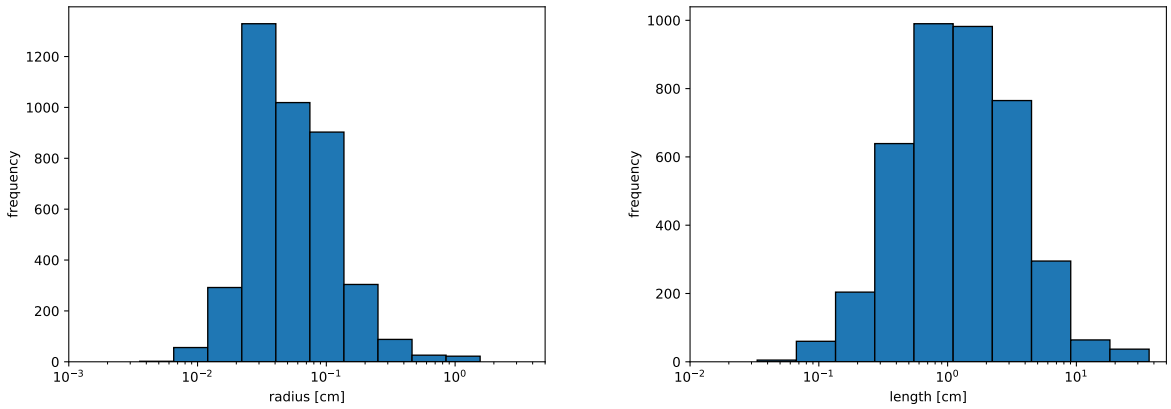
FIGURE 3.15: Detail of the CCO-generated cerebral peripheral beds corresponding (A) to the lenticulostriate artery and (B) to the posterior parietal branch of the middle cerebral artery. The color map is scaled with respect to the vessel radius in centimeters.



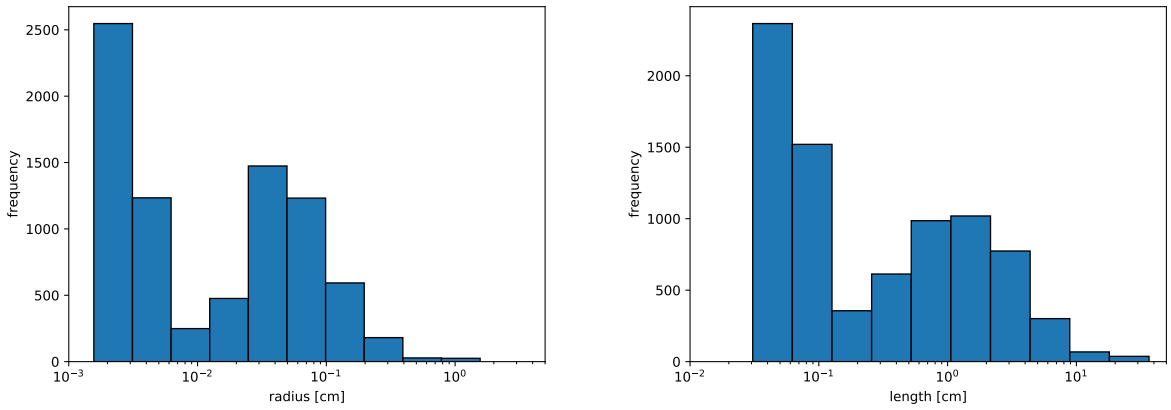
(A) (B)

and efficiency analyses on selected arterial networks of moderate complexity, some *a-priori* model selection criteria have been identified: the intravascular volume V_0 and the vessel compliance C_0.

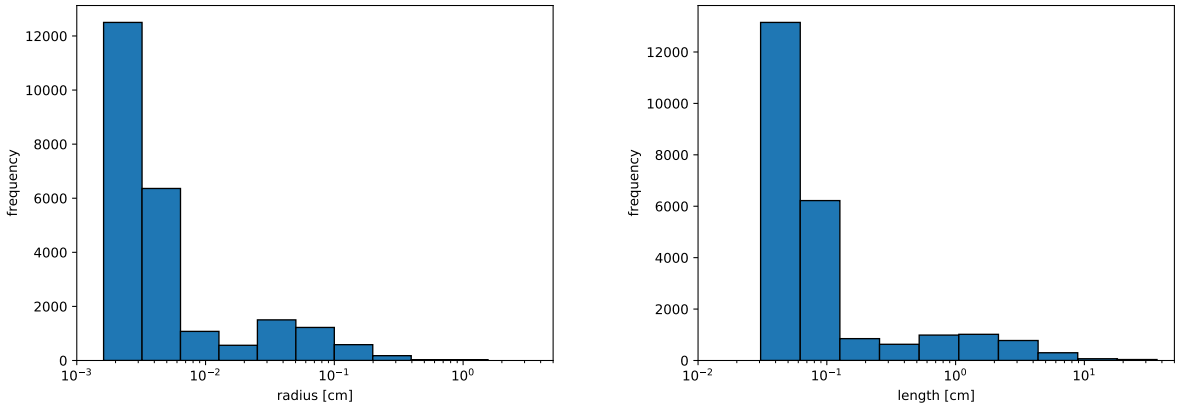
FIGURE 3.16: Radius and length distributions for the ADAN model (top row), the ADAN model coupled to the CCO network of the lenticulostriate artery (mid row) and the ADAN model coupled to the peripheral bed of the posterior parietal branch of the MCA (bottom row).



(A) ADAN model



(B) ADAN model + peripheral bed of lenticulostriate artery



(C) ADAN model + peripheral bed of posterior parietal branch of MCA

Given now a new network, the ADAN model for instance, we do not have to re-perform the same full analysis of all the different model selection criteria, since we already know which are the most suitable parameters to be used to generate the corresponding hybrid network configuration, *i.e.* V_0 and C_0. On the other hand, since we do not know the specific value of the 1D-0D threshold to set for each parameter, an

TABLE 3.19: Computational parameters adopted in the simulations for the ADAN model and for the ADAN model coupled to the CCO-generated cerebral arteriolar networks.

Parameter	**ADAN model**	**ADAN model + CCO**
Max mesh size, $\Delta x_{\max}$	1 cm	1 cm
CFL number, CFL	0.9	0.9
Time step - 0D sim., Δt^{0D}	10^{-3} s	10^{-3} s
Cardiac cycle, T_0	1.0 s	1.0 s
Final time, t_{End}	$15T_0$	$10T_0$

ad hoc analysis targeted to identify these specific thresholds could be carried out. The choice of the 1D-0D thresholds may depend on problem-specific characteristics, the aim of the application in mind and thus the required level of accuracy by which the physical process has to be described. Two different hybrid configurations of the same network may be obtained if the network would be adopted in two different contexts and for different applications: less or more restrictive 1D-0D thresholds may be chosen depending on the improvement in terms of computational efficiency to be achieved and/or the level of accuracy to be preserved.

However, for the more complex vascular models considered in this section, we suggest a new model selection criterion, that is the anatomical region classification. The main reason of this choice stands in the fact that here 0D regions are evolved adopting an implicit ODE solver and the time step of these 0D regions is constrained by that of the 1D vessels they are connected to. As a consequence, we want to construct hybrid network configurations with uniform regions of 1D and 0D vessels. The proposed C++-coded hybrid network solver will be applied to region-based hybrid configurations of the ADAN model and its extended version coupled to the CCO-generated arteriolar networks, where a hybrid configuration is obtained by selecting the regions to keep 1D and the ones that can be made 0D, based on the anatomical region classification of the vessels. In this way, the resulting hybrid network configuration will consist of uniform regions of either 1D/0D vessels, coupled together via hybrid junctions. In fact, this approach could be adopted also in many applications where one or a few vascular regions of interest, where higher accuracy is required, are modeled as 1D regions, while the remaining regions of the vascular model can be turned into 0D regions, with a considerable gain in terms of the computational efficiency of the resulting hybrid simulations.
The anatomical regions of the ADAN model are listed in Table 3.20 and will be used in the next section to construct and test different hybrid configurations of this arterial model.

3.4.3.2 ADAN model

We simulate the ADAN model considering a fully 1D and a fully 0D network configuration, and the three hybrid model configurations reported in Table 3.21. These hybrid configurations are constructed adopting the region-based criterion introduced in Section 3.4.3.1. A schematic representation of the different hybrid model configurations considered is also illustrated in Figure 3.17, with color-coded 1D (in red) and 0D (in blue) regions. In the first configuration (Test 1), the entire aorta is 1D, while all the other vessels are 0D; in the second hybrid model (Test 2), the aorta, the left and right shoulders and arms are 1D, whereas all the other vessels are 0D; in the last hybrid network configuration (Test 3), the aorta and all the vessels of neck and head are 1D, while all the remaining vessels are 0D. These are just three representative hybrid configurations used to test the proposed hybrid network solver and to explore its performance and capabilities, in terms of computational efficiency of the simulations, but also of accuracy of the predicted results. Depending on the specific problem and the aim of the application in mind, many other hybrid

TABLE 3.20: Anatomical regions of ADAN model. Each region is identified by its region ID. Each arterial vessel of the ADAN model is assigned to one of the listed anatomical regions.

Region ID	Region name	Region ID	Region name
1	head	32	right suprarenal
2	encephalon	33	left suprarenal
3	brain	34	liver
4	cerebellum	35	stomach
5	pons	36	spleen
6	duramater	37	pancreas
7	scalp	38	right kidney
8	face	39	left kidney
9	neck	40	intestine
10	right upper limb	41	dorsum
11	right shoulder	42	spinal
12	right arm	43	spinal cord
13	right forearm	44	cervical spinal cord
14	right hand	45	thoracic spinal cord
15	left upper limb	46	lumbar spinal cord
16	left shoulder	47	lumbar
17	left arm	48	cauda equina
18	left forearm	49	pelvis
19	left hand	50	right lower limb
20	trunk	51	right gluteal region
21	aorta	52	right hip tight
22	aortic arch	53	right knee
23	thoracic aorta	54	right leg
24	abdominal aorta	55	right foot
25	chest	56	left lower limb
26	coronaries	57	left gluteal region
27	right coronaries	58	left hip tight
28	left coronaries	59	left knee
29	sternum	60	left leg
30	abdomen	61	left foot
31	diaphragm		

models could be designed departing from the fully 1D one, where one or a few vascular regions of interest, where higher accuracy is required, are modeled as 1D, while the remaining regions can be described as 0D.

Even if we are mostly interested in the viscoelastic case, for the ADAN model only we present and discuss also the results obtained from the elastic simulations for the fully 1D, the fully 0D and the Test 3-hybrid network configurations. In the elastic case, we set $K_m = 0$ in the viscoelastic tube laws (3.2) and (3.32) for 1D and 0D vessels, respectively.

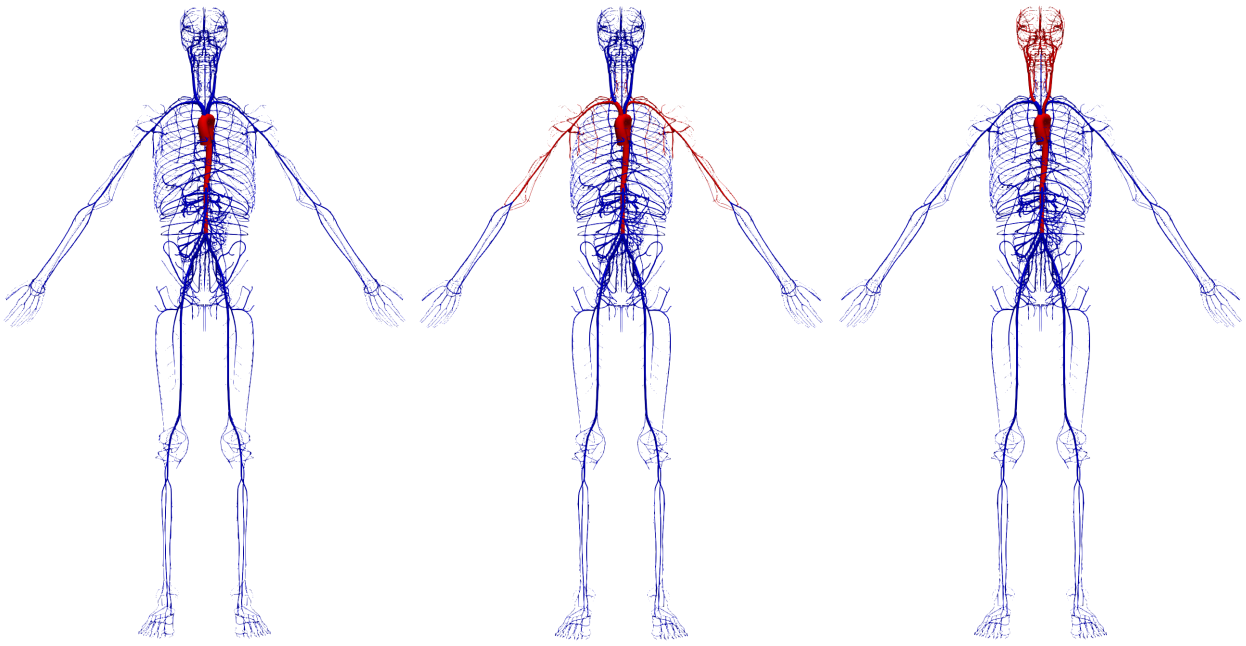
For 1D and hybrid simulations, the network solver is tested using both GTS and LTS strategies for the 1D part. In fact, even if we have a LTS solver available, which has been proved to be a very powerful tool to gain computational efficiency when dealing with complex vascular networks and models [102], its complexity is considerably higher than the one of a GTS solver, thus requiring more effort for its implementation. Therefore, departing from a GTS solver for one-dimensional networks only, in order to make it more efficient, it would be more convenient and straightforward to first integrate the hybrid network methodology proposed here in the GTS solver, allowing to perform cheaper, but still accurate, simulations in hybrid 1D-0D networks.

Code profiling. First of all, for the fully 0D simulation of the elastic ADAN model, the profiling of the code relevant to the 0D solver is carried out, to estimate the cost of the single operations performed by the implicit ODE solver developed in Section 3.4.1.3. The code profiling output is shown in Table 3.22. We note that for the fully 0D ADAN model we have just one 0D region which corresponds to the entire network itself, including both vessels and *RCR* models attached to the terminal vessels. Hence, the ODE system to be

TABLE 3.21: Region-based hybrid configurations of ADAN model. For each test reported in the table, the corresponding hybrid network configuration is constructed by making 1D all the vessels belonging to the anatomical regions listed in the second column "1D regions", according to the anatomical region classification introduced in Table 3.20, while all other vessels are modeled as 0D. N_R: number of 0D regions of the network; N_V^{1D}: total number of 1D vessels of the network.

Test	**1D regions**	N_R	N_V^{1D}
Test 1	22,23,24	13	47
Test 2	22,23,24,11,12,16,17	15	375
Test 3	22,23,24,9,2,3,4,5,7,8	18	974

FIGURE 3.17: Schematic representation of the different region-based hybrid network configurations of the ADAN model. In each configuration, 1D regions are in red, while 0D regions are in blue. For specific IDs of 1D/0D regions in each configuration, refer to Table 3.21; for the complete anatomical region classification of ADAN model, refer to Table 3.20.



(A) Hybrid Test 1 (B) Hybrid Test 2 (C) Hybrid Test 3

solved to evolve the 0D region is very large and the Jacobian matrix of the nonlinear system associated to the implicit ODE method is highly sparse, as displayed in Figure 3.13. From Table 3.22, we can observe that the most expensive operation is the calculation of the Jacobian matrix $\boldsymbol{J_G}$, according to the central differences approximation (3.117). However, by making use of Broyden's method, rather than Newton's method, at each time step the Jacobian matrix is computed only at the first iteration of the algorithm, while at each subsequent iteration $\boldsymbol{J_G}$ is approximated using that of the previous iteration, which requires a significantly lower computational effort. On the other hand, from this table we can see that the resolution of the linear system (3.114) associated to Broyden's method is performed in a reasonably low computational time. In fact, operations from 4 to 7 in Table 3.22 are executed in about 0.4 s. This is achieved thanks to the use of the UMFPACK library, suited to efficiently solve sparse linear systems.

Speed-up analysis. Tables 3.23 and 3.24 show the CPU times needed to simulate a cardiac cycle for the elastic and viscoelastic ADAN models, respectively, for the different network configurations considered, using both the GTS and the LTS strategies to solve the 1D vessels of the fully 1D and hybrid model configurations. From these tables, we can observe that the fully 0D simulations are extremely fast, in both elastic and viscoelastic cases. In the first case (see Table 3.23), the speed-up with respect to the 1D simulation with

TABLE 3.22: Code profiling output for the fully 0D simulation of the elastic ADAN model: cost of the single operations performed by the implicit ODE solver to evolve the 0D network of a time step $\Delta t^{0D} = 10^{-3}$ s.

Operation	**CPU time** $[s]$
1-Calculation of ODE system RHS $\boldsymbol{B}$	1.0608e-01
2-Calculation of nonlinear vector function $\boldsymbol{G}$	7.1022e-04
3-Calculation of Jacobian matrix $\boldsymbol{J_G}$	1.6168
4-Conversion of $\boldsymbol{J_G}$ from ST to CC format	1.4425e-02
5-Numeric factorization of $\boldsymbol{J_G}$	3.5829e-01
6-Resolution of linear system (3.114)	3.8177e-02
7-Freeing of numeric factorization	5.7280e-05

GTS is of 60 times, while, when the LTS solver is adopted in the reference 1D simulation, we have a 1D to 0D computational time ratio of about 5, which is still a reasonably good speed-up. On the other hand, from Table 3.24 we can see that, in the viscoelastic case, with the fully 0D simulation we get a tremendous improvement in terms of computational efficiency when compared to the fully 1D model solved with both GTS and LTS strategies, with speed-ups of almost 8740 times and of about 68 times, respectively.
A different scenario is obtained when considering the simulations performed on the hybrid configurations of ADAN model, where the results mainly depend on the 1D temporal discretization strategy adopted, either GTS or LTS. From Table 3.23 we have that, in the elastic case, the CPU time required by the hybrid network configuration solved with GTS is still reduced by a factor of 7, while when the LTS solver is adopted there is basically no speed-up with respect to the 1D simulation. Similarly, Table 3.24 shows that, in the viscoelastic case, the hybrid network solver is crucial to gain computational efficiency for all the different hybrid model configurations tested when adopting the GTS strategy, with CPU times of the simulations that are reduced of one to two orders of magnitude. On the other hand, when the same hybrid configurations of ADAN model are solved employing the LTS algorithm, there is no computational improvement in the simulations, which become slightly more expensive than the reference 1D one (see last column in Table 3.24, for the last group of hybrid simulations). The main reason of this fact stands in the temporal discretization strategy adopted for the 0D regions. Indeed, as illustrated in Section 3.4.1.4, the time step of a 0D region is determined as the minimum time step between all the 1D vessels connected to that 0D region via hybrid junctions. As in the viscoelastic case the time step of 1D vessels can become very small, order of magnitude smaller than in the elastic case, this implies that 0D regions may be coupled to 1D vessels with very restrictive time steps, which in turn will restrict the time step of the 0D regions. As a consequence, if a 0D region is very large, including thousands of 0D vessels, evolving the associated ODE system using the implicit ODE solver proposed in Section 3.4.1.3 with a very small time step can become expensive and not efficient. Clearly, this depends on the specific hybrid configuration considered, especially on which vessels of the network are 1D and which are the characteristic time steps of these 1D vessels.

Therefore, from this analysis, the following conclusions can be drawn. First, the fully 0D simulations allow to achieve excellent speed-ups, especially in the viscoelastic case. 0D simulations could then be exploited to generate results to be used as initial conditions for the corresponding 1D simulations, in order to initialize the 1D simulation with a solution sufficiently close to the expected solution at periodic regime and, consequently, to significantly reduce the number of cardiac cycles needed to reach the periodicity in the 1D solution. Second, when adopting the GTS strategy, the proposed hybrid network solver strongly improves the computational efficiency of the simulations, in the elastic and, even more, in the viscoelastic case. On the other hand, as observed above, when employing the LTS strategy in the simulations of the different hybrid configurations of the viscoelastic ADAN model, we do not have any speed-up with respect to the reference fully 1D simulation, when employing the LTS strategy. However, when dealing with even more complex vascular models and networks than the ADAN model, such as those considered in the next

section, the LTS solver proposed by Müller *et al.* [102] may not be sufficient to efficiently solve such networks; the hybrid network solver developed in this thesis integrated with the LTS is expected to be more effective and to be crucial to gain computational efficiency in such framework, where the heterogeneity of spatial and temporal scales is even more accentuated.

TABLE 3.23: CPU times needed to simulate a cardiac cycle ($T_0 = 1.0\,s$) for the elastic ADAN model: comparison between 1D, 0D and hybrid simulations. The speed-up in all simulations is computed with respect to the reference CPU time $t_{CPU}^{Ref,X}$, with $X = GTS, LTS$, corresponding to the 1D simulation performed with GTS or LTS, respectively. To record CPU times for longer simulations, only a fraction of the cardiac cycle T_0 is simulated, assuming that the computational cost is uniform over the entire cycle. On the other hand, to obtain the computational results, selected simulations were run for 15 cardiac cycles, with $t_{\text{End}} = 15T_0$, until periodic regime was reached. PCo2: second-order path-conservative scheme; IE: implicit Euler method; CN: Crank-Nicolson method.

Config.	Model	Methods	Time step	t_{CPU} [s, h : m : s]	$t_{CPU}^{Ref,GTS}/t_{CPU}$	$t_{CPU}^{Ref,LTS}/t_{CPU}$
1D	elastic	PCo2	LTS	303.53 ≈ 00:05:04	12.13	1.0
1D	elastic	PCo2	GTS	3682.15 ≈ 01:01:22	1.0	0.082
0D	elastic	IE	$\Delta t^{0D} = 10^{-3}s$	61.14 ≈ 00:01:01	60.22	4.96
Hybrid - Test 3	elastic	PCo2+CN	GTS	523.82 ≈ 00:08:44	7.03	0.579
Hybrid - Test 3	elastic	PCo2+CN	LTS	198.23 ≈ 00:03:18	18.58	1.53

TABLE 3.24: CPU times needed to simulate a cardiac cycle ($T_0 = 1.0\,s$) for the viscoelastic ADAN model: comparison between 1D, 0D and hybrid simulations. The speed-up in all simulations is computed with respect to the reference CPU time $t_{CPU}^{Ref,X}$, with $X = GTS, LTS$, corresponding to the 1D simulation performed with GTS or LTS, respectively. To record CPU times for longer simulations, only a fraction of the cardiac cycle T_0 is simulated, assuming that the computational cost is uniform over the entire cycle. On the other hand, to obtain the computational results, selected simulations were run for 15 cardiac cycles, with $t_{\text{End}} = 15T_0$, until periodic regime was reached. PCo2: second-order path-conservative scheme; IE: implicit Euler method; CN: Crank-Nicolson method.

Config.	Model	Methods	Time step	t_{CPU} [s, h : m : s]	$t_{CPU}^{Ref,GTS}/t_{CPU}$	$t_{CPU}^{Ref,LTS}/t_{CPU}$
1D	visco	PCo2	LTS	6555.74 ≈ 01:49:16	128.15	1.0
1D	visco	PCo2	GTS	840087.00 ≈ 233:21:27	1.0	0.008
0D	visco	IE	$\Delta t^{0D} = 10^{-3}s$	96.16 ≈ 00:01:36	8736.09	68.17
Hybrid - Test 1	visco	PCo2+CN	GTS	7096.19 ≈ 01:58:16	118.39	0.924
Hybrid - Test 2	visco	PCo2+CN	GTS	10642.21 ≈ 02:57:22	78.94	0.616
Hybrid - Test 3	visco	PCo2+CN	GTS	42916.06 ≈ 11:55:16	19.58	0.153
Hybrid - Test 1	visco	PCo2+CN	LTS	8232.49 ≈ 02:17:12	102.05	0.796
Hybrid - Test 2	visco	PCo2+CN	LTS	6969.90 ≈ 01:56:10	120.53	0.941
Hybrid - Test 3	visco	PCo2+CN	LTS	7319.25 ≈ 02:01:59	114.78	0.896

Error and waveform analysis. Relative errors in the results obtained from both the fully 0D and the hybrid network configurations of the elastic/viscoelastic ADAN model are computed with respect to the reference elastic/viscoelastic 1D solution, in selected vessels. Relative root mean square (RMS), systolic (SYS) and diastolic (DIAS) errors are calculated according to the relative error metrics (2.98), adapted not only to compute the 0D *vs* 1D errors, but also to the hybrid *vs* 1D errors. Such errors are computed for both pressure and flow rate results sampled in time over a complete cardiac cycle, where the solution in the 1D vessels is

sampled at the midpoint of the vascular segment. For each hybrid model configuration, we compute errors both in vessels that are 1D and in vessels that are 0D in the hybrid network.

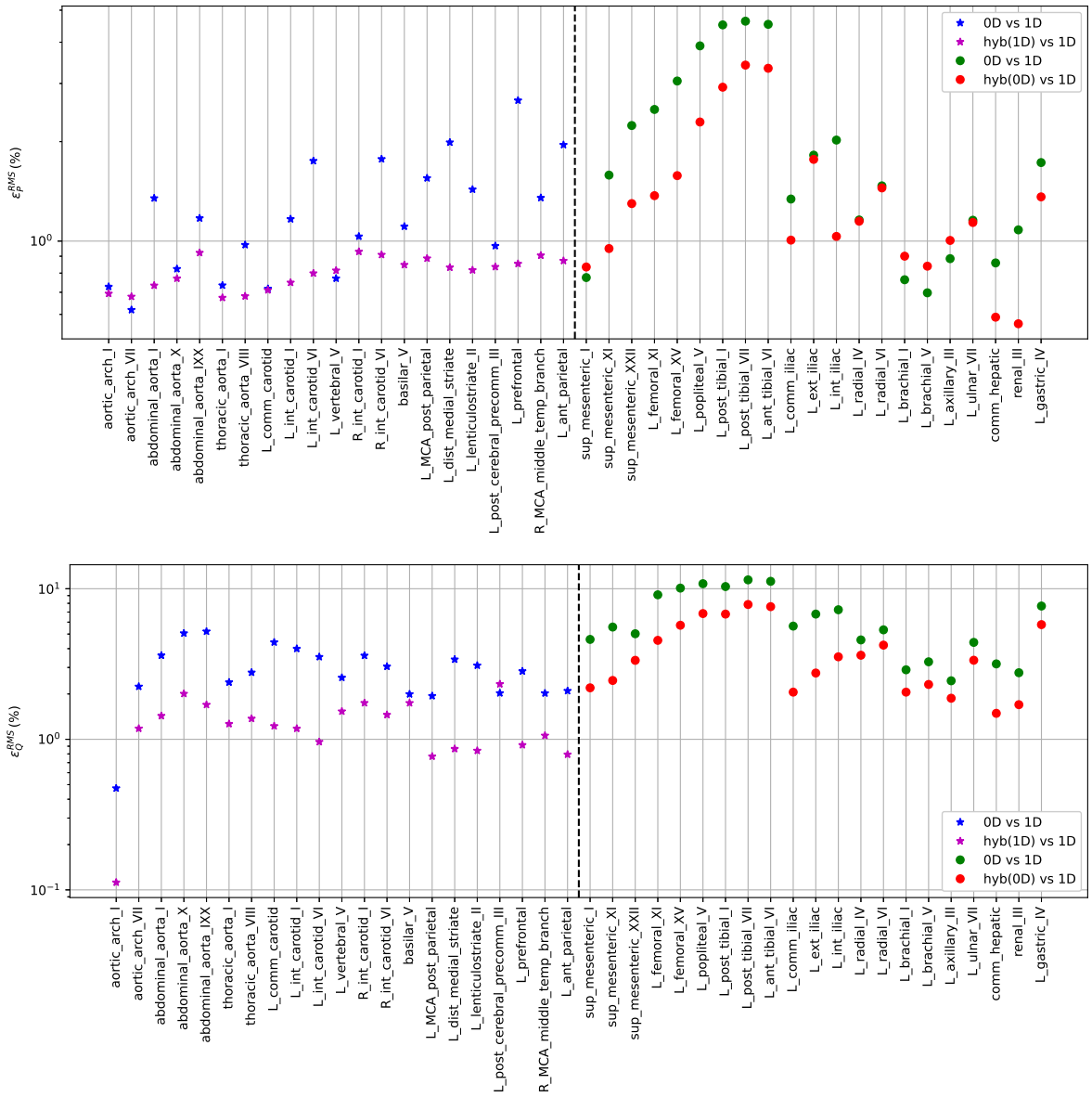
Let us start by analyzing the elastic case. The distribution of root mean square and systolic errors in the results from the 0D and hybrid configurations of the elastic ADAN model is displayed in Figures 3.18 and 3.19, respectively. In these figures, vessels are divided into two groups, visually separated by the vertical black dashed line, depending if in the hybrid configuration they are 1D (left group) or 0D (right group). In addition, precise errors values for a smaller group of vessels are provided in Table C.1 in Appendix C. From both Figures 3.18 and 3.19 and from Table C.1, we can observe that, in general, errors in the 0D results are larger than the errors in the results from the hybrid model configuration, for both 1D and 0D vessels, and that overall these errors are reasonably small. In the fully 0D model, larger RMS errors in both pressure and flow rate are found in the vessels of the lower limb (common iliac, femoral, posterior tibial arteries), with peaks around 5% for pressure and 10% for flow rate (see green dots in Fig. 3.18 and Table C.1); in the abdominal aorta we record a RMS error in the flow rate of about 5%, while the prefrontal artery in the head has a relative error in the pressure of about 2.7% (see blue stars in Fig. 3.18 and Table C.1). In all other vessels considered, RMS erros are significantly reduced. Similar outcomes are obtained for relative systolic errors displayed in Figure 3.19. Peaks around 2.5% are registered for systolic errors in the pressure for the right internal carotid artery and the superior mesenteric artery (see top plot in Fig. 3.19), while in the flow rate we have systolic errors around 9/10% in some vessels of the lower limb and around 7% in the radial artery (see bottom plot in Fig. 3.19). Systolic errors in all other vessels are much lower. Considering that this a fully 0D simulation, these errors are very satisfactory.

Regarding the results obtained from the hybrid network configuration, from Figure 3.18 it is evident that, in general, RMS errors are decreased with respect to errors in the fully 0D model, in both pressure and flow rate, for both 1D and 0D vessels in the hybrid configurations. In a few cases, errors in the 0D and hybrid results are comparable or, even, the errors from the fully 0D model are slightly smaller than those from the hybrid one (see, for instance, aortic arch and brachial artery in Fig. 3.18 and in Table C.1). However, these are isolated vessels, where, in any case, these RMS errors remain reasonably small in both 0D and hybrid model configurations. For vessels that are 1D in the hybrid model configuration, RMS errors are below 1% for pressure and 2.5% for flow rate (see magenta stars in Fig. 3.18); for the 0D vessels, we have RMS errors below 1% for pressure and 7% for flow rate (see red dots in Fig. 3.18). A very similar scenario is observed also in Figure 3.19 when comparing systolic errors between the fully 0D and the hybrid models and supported by Table C.1. In fact, from Figure 3.19 we can see that overall the hybrid network configuration reduces the systolic errors in both pressure and flow rate results, for both 1D and 0D vessels. In some cases, the improvement obtained is really good: for instance, in the right internal carotid (which is 1D in the hybrid model) the systolic error in the pressure is reduced from about 2.2% in the fully 0D model to 0.1% in the hybrid one (see top plot in Fig. 3.19); in the brachial artery (which is still 0D in the hybrid model) the systolic error in the flow rate is reduced almost by a factor of 10, from about 3% in the fully 0D model to 0.3% in the hybrid one (see bottom plot in Fig. 3.19).

Qualitative comparisons between solutions obtained from the 1D, 0D and hybrid model configurations of the elastic ADAN model are displayed for selected vessels in Figure 3.20. These pictures confirm what observed from the quantitative error analysis presented above. In fact, we can see that, in both 0D and hybrid model configurations, pressure and flow profiles are reproduced with a very good level of accuracy and agreement with the reference 1D results. In particular, the results from the hybrid network show overall an excellent agreement with the reference 1D solution and are considerably improved when compared to the results from the fully 0D model. In the hybrid configuration, shape and amplitude of pressure and flow waveforms are well-approximated, preserving all their characteristic features; the systolic peak is generally well-captured in both pressure and flow waves. These observations are valid for both 1D and 0D vessels

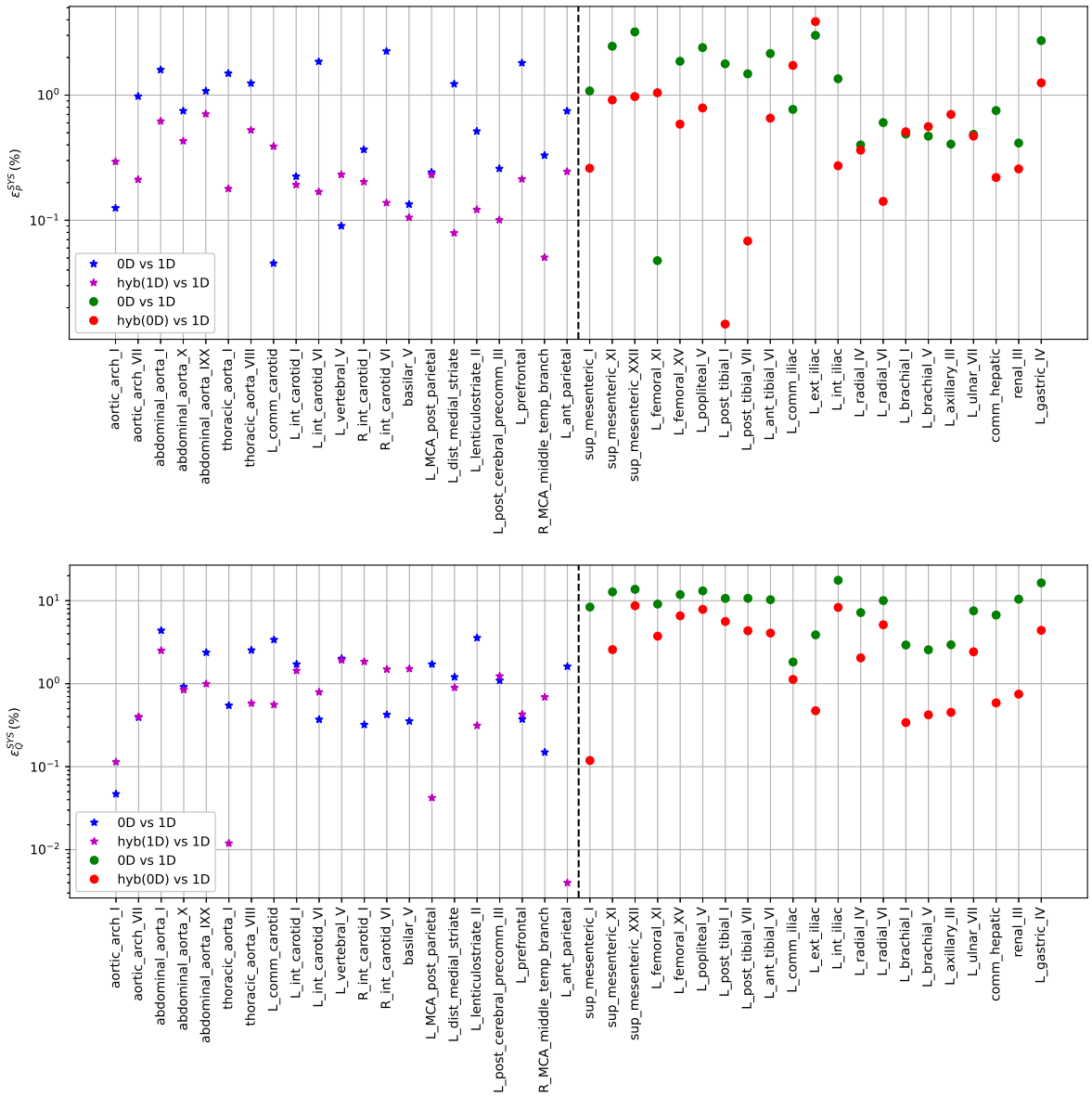
in the hybrid model. As a consequence, this implies that the benefits in terms of accuracy of considering a hybrid network configuration over a fully 0D one have an impact not only on the vessels that are 1D in the hybrid model, but also on the 0D vessels, especially the ones that are closer to these 1D vessels (see, for instance, the superior mesenteric artery in Fig. 3.20).

FIGURE 3.18: Elastic ADAN model. Distribution of relative root mean square errors (in %) for (A) pressure and (B) flow results, obtained from the fully 0D and the Test 3-hybrid model configurations with respect to the reference 1D results, in selected vessels. The vessels are divided into two groups, left and right of the vertical black dashed line, depending if in the hybrid network configuration are 1D or 0D, respectively. The y-axis is in logarithmic scale.



Let us move now to the viscoelastic case. Here, three different hybrid network configurations have been considered (see Table 3.21), together with the fully 1D and fully 0D ones. Distributions of root mean square and systolic errors in the results obtained from the 0D and each hybrid network configuration of the viscoelastic ADAN model are displayed in Figures 3.21 and 3.22 for the hybrid Test 1, in Figures 3.24 and 3.25 for the hybrid Test 2, and in Figures 3.27 and 3.28 for the hybrid Test 3. Relative errors are computed with respect to the reference viscoelastic 1D solution, in selected vessels. Once again, for each hybrid model

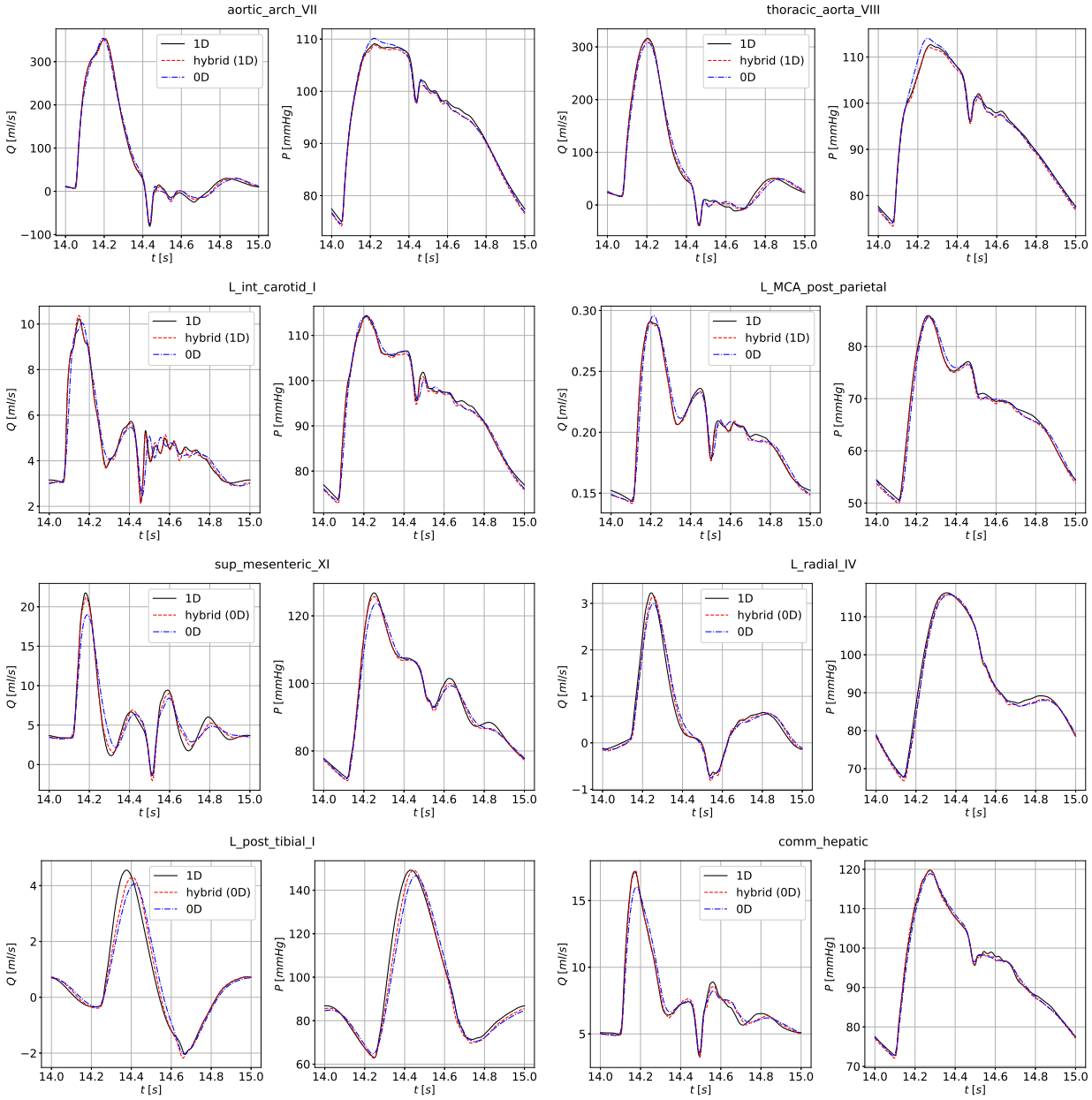
FIGURE 3.19: Elastic ADAN model. Distribution of relative systolic errors (in %) for (A) pressure and (B) flow results, obtained from the fully 0D and the Test 3-hybrid model configurations with respect to the reference 1D results, in selected vessels. The vessels are divided into two groups, left and right of the vertical black dashed line, depending if in the hybrid network configuration are 1D or 0D, respectively. Systolic errors are plotted in absolute value, we logarithmic scale on the y-axis.



configuration, we calculate errors both in vessels that are 1D and in vessels that are 0D in the hybrid network. Furthermore, precise values of root mean square, systolic and diastolic errors for a smaller group of vessels are provided in Table C.2 for the hybrid Test 1, in Table C.3 for the hybrid Test 2, and in Table C.4 for the hybrid Test 3, in Appendix C. In each plot and table, together with relative errors in the corresponding hybrid network model, errors in the fully 0D model are always reported for comparison. In general, the relative error distribution plots, comparing errors between the fully 0D model and each hybrid network configuration, show a similar trend to that observed in the elastic case, with RMS and systolic errors being overall reasonably small and errors in the 0D results being larger than the errors in the results from the hybrid model, even if here a more accurate analysis is required.

For the fully 0D viscoelastic ADAN model, larger RMS errors are found in vessels of the lower limb, with peaks around 4.5% in the pressure and 10% in the flow rate (see green dots in Fig. 3.21 and Table C.2).

FIGURE 3.20: Elastic ADAN model. Qualitative comparison between computational results for flow rate and pressure obtained from the 1D (black line), 0D (blue dashed-dotted line) and Test3-hybrid (red dashed line) configurations. Vessels in the first and second rows belong to the aorta, head and neck regions, so in the hybrid network configuration are 1D vessels; while vessels in the last two rows belong to 0D regions of the hybrid model.



If in Figure 3.21 we focus on the green dots corresponding to the vessels of the lower limb, we can note how the RMS error in the pressure gradually increases as we move downstream, further from the aorta. Similarly, higher systolic errors for both pressure and flow rate are still recorded in the vessels of the lower limb and in a few other vessels (see Fig. 3.22 and Table C.2); for instance, both internal carotid arteries present a systolic error in the pressure around 2%, while femoral and posterior tibial arteries have systolic errors in the flow rate of about 11% and 13%, respectively. Given the fact that this is a fully 0D simulation, we can conclude that errors in the 0D results with respect to the reference 1D solution are relatively small, as they overall remain within reasonable ranges of percent deviation from the 1D results and do not increase too much.

In the hybrid Test 1, the entire aorta is 1D, while all other vessels of the ADAN model are 0D. Figure 3.21 shows that, when moving from the fully 0D to this hybrid model configuration, RMS errors in both pressure and flow rate are reduced in many, but not all vessels. For instance, in several tracts of the aorta, RMS errors in the flow rate are significantly decreased (see magenta stars in bottom plot of Fig. 3.21), while the errors in the pressure are slightly larger in the hybrid model than in the fully 0D one (see magenta stars in top plot of Fig. 3.21), even if these are 1D vessels in the hybrid network configuration. However, we do not consider this to be an issue, as the differences between these errors are not negligible, but still very small. In the aortic arch, for example, the RMS errors in the pressure for the results from the 0D and the hybrid models are of about 0.65% and 0.84%, respectively (see Table C.2). For the vessels of the aorta, which are 1D in the hybrid model of Test 1, the same trend is observed also in the systolic errors for the pressure, as shown in the top plot of Figure 3.22. The same analysis is valid also for the vessels that are 0D in the hybrid network configuration. In fact, from both Figures 3.21 and 3.22, we can see that, when moving from the fully 0D (green dots) to the hybrid model configuration (red dots), RMS and systolic errors in both pressure and flow rate decrease in certain vessels and increase in others. For instance, in the vessels of the lower limb, relative errors are reduced, suggesting that modeling the aorta only as 1D has also an impact on other vessels that receive blood from it. On the other hand, in the vessels of head and neck, no benefit is observed when considering the 1D aorta in the hybrid model, as in many cerebral arteries RMS and systolic errors are comparable to or larger than those corresponding to the fully 0D model (see Fig. 3.21 and 3.22). However, in general, these errors do not differ of orders of magnitude; furthermore, this is less surprising than for the 1D vessels of the hybrid model, as these vessels are still 0D also in the hybrid network configuration. Then, the relevant conclusion here is that the results obtained from both the fully 0D viscoelastic ADAN model and the Test 1-hybrid network configuration are characterized by reasonably small errors, in both pressure and flow rate. In particular, including the 1D aorta in the hybrid model has a positive impact in terms of accuracy of the predicted results not only on the vessels of the aorta itself, but also on other 0D vessels, such as those of the lower limb.

All these observations are supported also by the qualitative comparisons between solutions obtained from the 1D, 0D and Test1-hybrid model configurations of the viscoelastic ADAN model, displayed in Figure 3.23 for selected vessels. Pressure and flow waveforms predicted by both 0D and hybrid model configurations are in very good agreement with the reference 1D solution. In most vessels, the results from the hybrid model (red dashed line) are improved with respect to those from the 0D one (blue dashed-dotted line), in both 1D and 0D vessels of the hybrid network, when compared to the 1D solution (black line). In the thoracic aorta, superior mesenteric, internal iliac and femoral arteries, the systolic peak is better captured and estimated by the hybrid model, in both pressure and flow waves (see Fig. 3.23). On the other hand, in line with the error analysis carried out above, in some vessels, such as the vertebral artery in Figure 3.23, the 0D solution is better than that obtained from the hybrid model. We note also that incorporating the viscoelastic properties of vessel walls in the tube law damps the oscillations present in the elastic solution of 1D vessels, as expected, but also of 0D vessels.

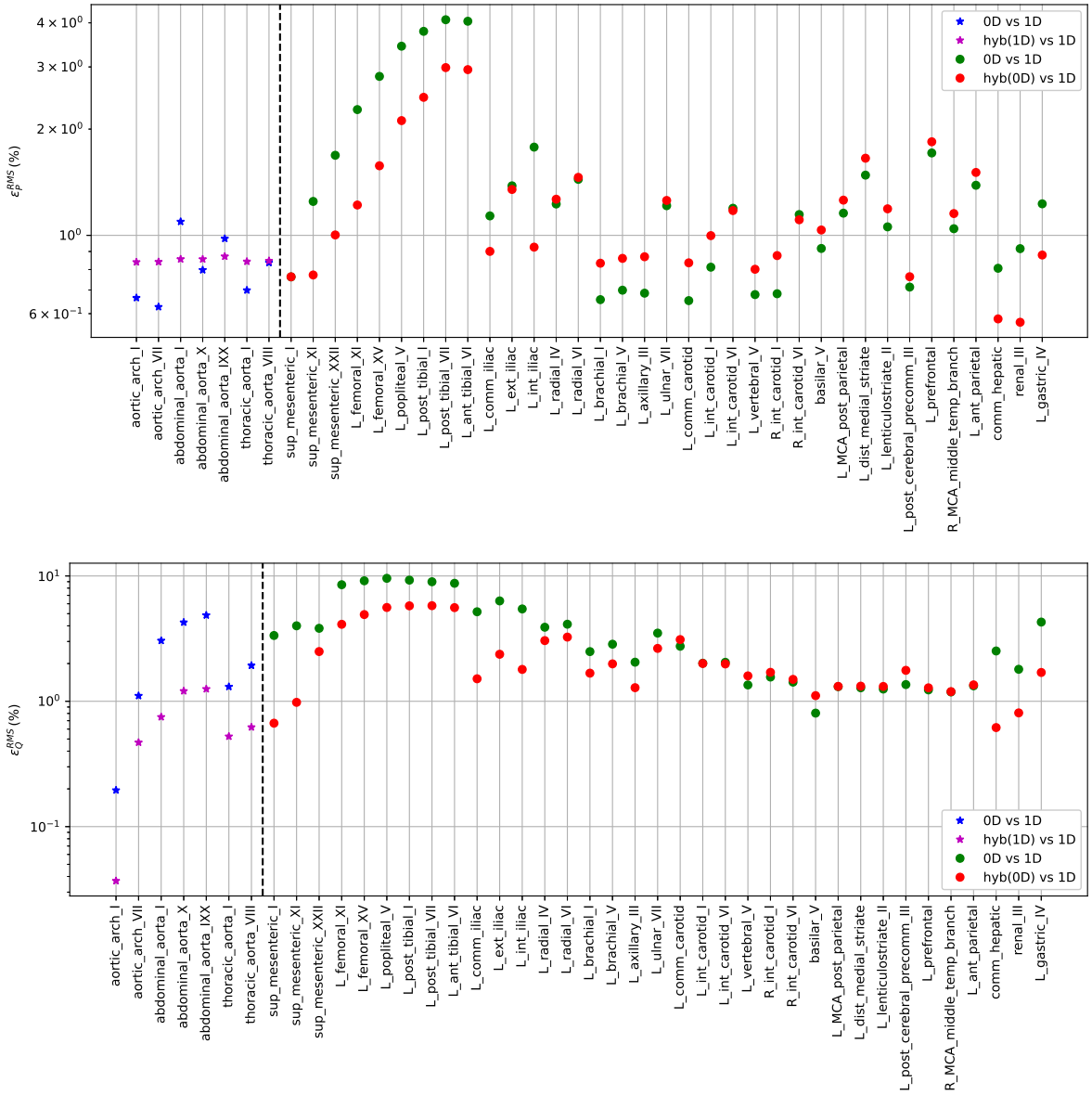
In the hybrid Test 2, the aorta, left and right shoulders and arms regions are 1D, while all the remaining vessels are 0D. The results from the fully 0D model used for comparison with the results from each hybrid network configuration are always the same, so we refer to the paragraph above devoted to the analysis of the 0D results. Concerning the results obtained from this hybrid model, the analysis and considerations made for the hybrid Test 1 perfectly apply also here. In fact, from Figures 3.24 and 3.25, we observe that, for the 1D vessels of the hybrid model configuration, RMS and systolic errors in the flow rate are considerably reduced with respect to the errors in the same vessels in the 0D model (see bottom plots in Fig. 3.24 and Fig. 3.25), while RMS and systolic errors in the pressure are decreased in some vessels, but increased in others (see, for instance, aortic arch, brachial and axillary arteries in the top plots in Fig. 3.24 and Fig.

3.25). Similarly to the previous test, the behaviour in the relative errors for the 0D vessels of the hybrid network is very heterogeneous, especially in the vessels of head and neck. However, overall these errors are reasonably small, with RMS errors below 3% in the pressure and 6% in the flow rate (see red dots in Fig. 3.24 and Table C.3), thus ensuring that pressure and flow waveforms are still predicted with a good level of accuracy by the hybrid network model, in both 1D ans 0D vessels.
These observations are supported also by the computational results presented in Figure 3.26, where solutions from the 1D, 0D and Test2-hybrid model configurations of the viscoelastic ADAN model are compared for selected vessels.

Let us know consider the last hybrid network configuration of the viscoelastic ADAN model, corresponding to Test 3, where the aorta and vessels of head and neck are 1D, while all other regions are 0D, that is the same hybrid configuration tested in the elastic case. Figures 3.27 and 3.28, together with specific error values in Table C.4, show that, in general, when moving from the fully 0D to this hybrid model, relative errors are decreased in both pressure and flow rate, for both 1D and 0D vessels in the hybrid configuration. Also in this case, there are vessels in which RMS and systolic errors increase, especially in the pressure results. This is observed in some tracts of the aorta and in certain vessels of head and neck, which are 1D vessels in the hybrid model (see magenta *vs* blue stars in the top plots of Fig. 3.27 and Fig. 3.28). For instance, in the common carotid artery, the RMS errors in the pressure for the results from the 0D and the hybrid models are of about 0.65% and 0.82%, respectively, and of about 0.68% and 0.85% in the first tract of the right internal carotid artery (see also Table C.4). As already pointed out, the differences between the error values corresponding to the fully 0D and hybrid models are very small, thus not affecting the accuracy of the solution in these 1D vessels. Overall, for vessels that are 1D in the hybrid network configuration, RMS errors are below 1% for pressure and 1.5% for flow rate; whereas systolic errors are below 1% for pressure and 3% for flow rate (see magenta stars in Fig. 3.27 and Fig 3.28, respectively, and Table C.4). For the 0D vessels, we have RMS errors below 3% for pressure and 6% for flow rate; while systolic errors are below 3% for pressure and 8% for flow rate (see red dots in Fig. 3.27 and Fig 3.28).
Qualitative comparisons between results obtained from the 1D, 0D and Test3-hybrid model configurations of the viscoelastic ADAN model are displayed in Figure 3.29 for selected 1D vessels of aorta, head and neck, and in Figure 3.30 for some 0D vessels of other regions. Once again, these pictures confirm what observed from the quantitative error analysis presented above. Indeed, in both 0D and hybrid model configurations, pressure and flow waveforms are reproduced with a very good level of accuracy and agreement with the reference 1D results, the main features of these waves are preserved and the systolic peak is generally well-captured in both pressure and flow profiles (see both Fig. 3.29 and Fig. 3.30). The results obtained from the hybrid model for the 1D vessels of the aorta, neck and head illustrated in Figure 3.29 are very satisfactory in terms of accuracy and agreement with the reference 1D solution. On the other hand, as we can see from Figure 3.30, using a hybrid model rather than a fully 0D one has a strong impact not only on the vessels that are 1D, but also on the vessels that remain 0D in the hybrid network configuration, especially the ones that are closer to the 1D vessels. For instance, the results obtained from this hybrid model (red dashed line) for the superior mesenteric, common hepatic and common iliac arteries, displayed in Figure 3.30, show indeed a great improvement with respect to the results from the fully 0D network (blue dashed-dotted line), especially in the approximation of the systolic peak for both pressure and flow waveforms.

To conclude, we remark that all error tables also report relative diastolic errors in both pressure and flow results. In the above discussion, these errors were not analyzed as in detail as done for root mean square and systolic errors, as they are less informative than the other two error metrics. Interestingly, we note that in general, relative diastolic errors are smaller in the fully 0D models, than in the hybrid ones, for both pressure and flow rate results.

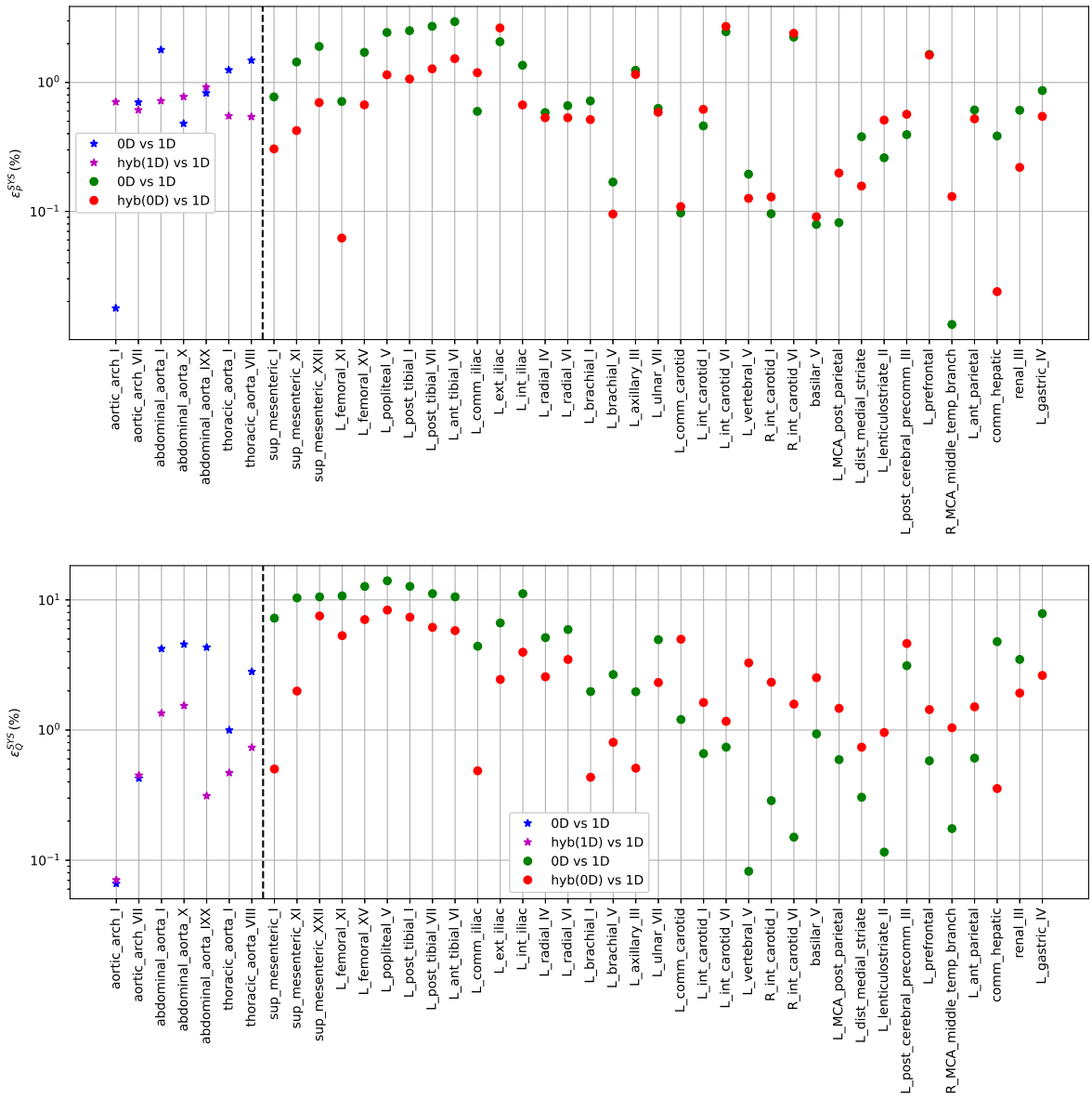
FIGURE 3.21: Viscoelastic ADAN model. Distribution of relative root mean square errors (in %) for (A) pressure and (B) flow results, obtained from the fully 0D and the Test 1-hybrid model configurations with respect to the reference 1D results, in selected vessels. The vessels are divided into two groups, left and right of the vertical black dashed line, depending if in the hybrid network configuration are 1D or 0D, respectively. The y-axis is in logarithmic scale.



3.4.3.3 ADAN model coupled to CCO cerebral networks

We simulate the ADAN model coupled to two different CCO-generated cerebral arteriolar networks: the peripheral bed of the lenticulostriate artery and the peripheral bed of the posterior parietal branch of the MCA. These arteriolar networks include 3999 and 19999 vascular segments, respectively. Radius and length distributions in the ADAN model coupled to each one of the peripheral beds are displayed in Figures 3.16b and 3.16c. The "root" of the first arteriolar network is connected to the left lenticulostriate artery of the ADAN model via a two-vessel junction; while in the case of the peripheral bed of the posterior parietal branch of the MCA, this CCO network is attached to the corresponding branch of the left MCA of the ADAN model, still via a two-vessel junction. For both resulting models, we consider the fully 1D and fully 0D configurations, and a hybrid network configuration where the original ADAN model is 1D,

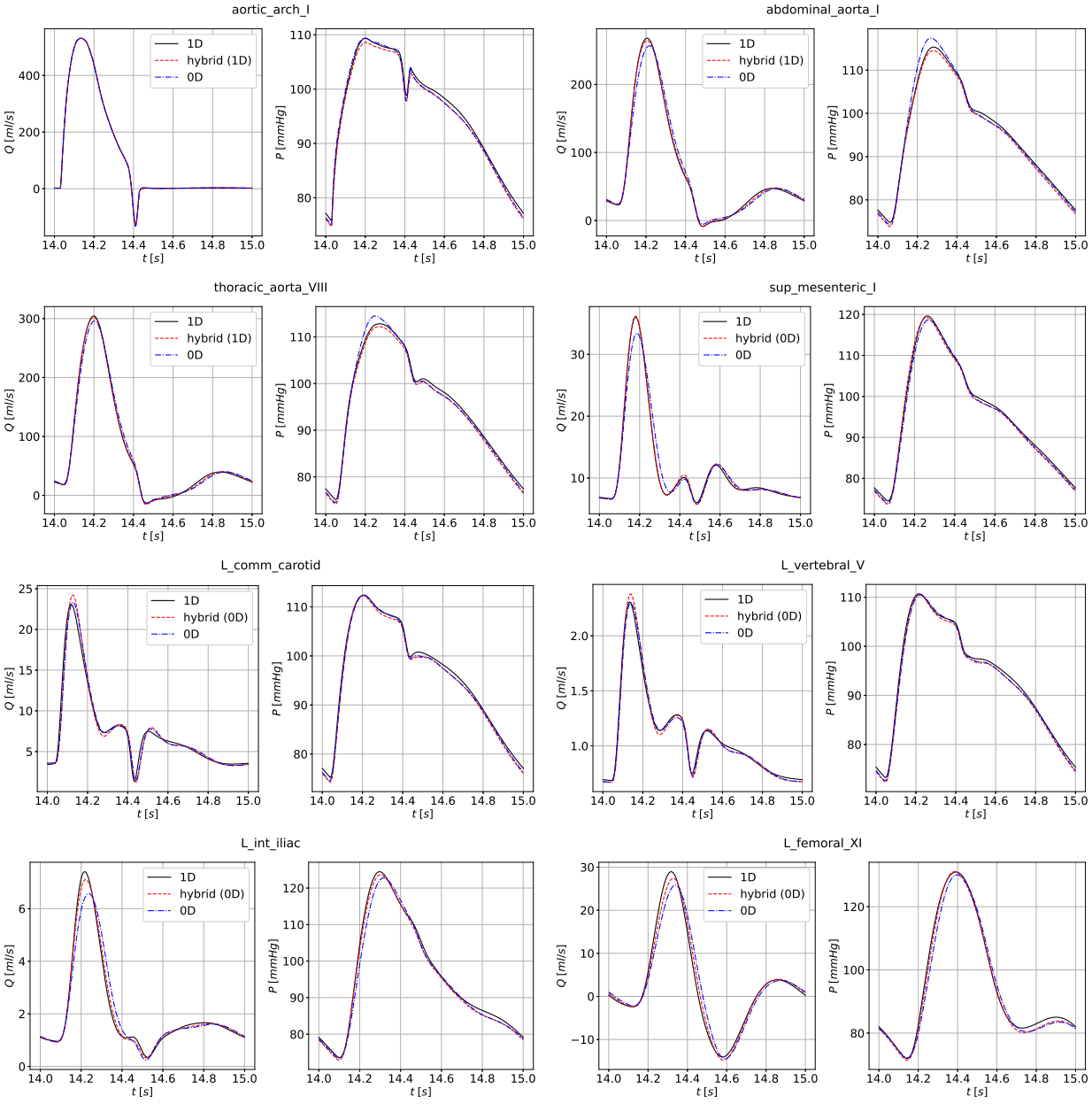
FIGURE 3.22: Viscoelastic ADAN model. Distribution of relative systolic errors (in %) for (A) pressure and (B) flow results, obtained from the fully 0D and the Test 1-hybrid model configurations with respect to the reference 1D results, in selected vessels. The vessels are divided into two groups, left and right of the vertical black dashed line, depending if in the hybrid network configuration are 1D or 0D, respectively. Systolic errors are plotted in absolute value, we logarithmic scale on the y-axis.



whereas the entire CCO network is 0D. Therefore, each hybrid model contains only one hybrid junction, making the connection between the peripheral bed and the corresponding vessel of the ADAN model.

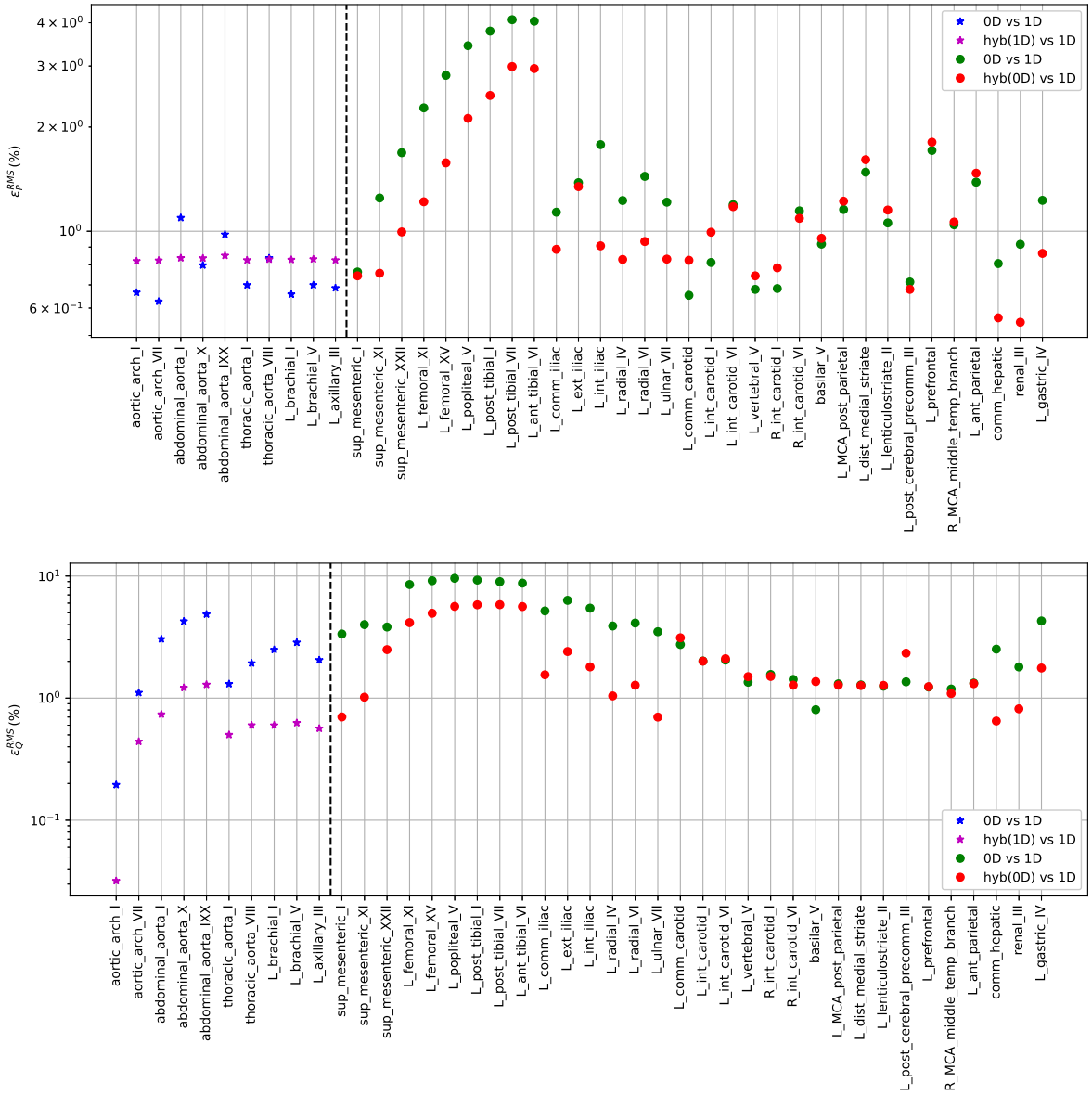
Speed-up analysis. Tables 3.25 and 3.26 display the CPU times needed to simulate a cardiac cycle for the viscoelastic ADAN model coupled to the CCO-generated peripheral beds of the lenticulostriate artery and of the posterior parietal branch of the MCA, respectively, with LTS strategy used to solve the 1D vessels of the fully 1D and hybrid model configurations. First of all, from these tables we can observe that the fully 1D simulations are extremely costly, The situation becomes more severe as the complexity and size of the CCO cerebral network coupled to the ADAN model increase, requiring enormous resources to perform such simulations. Employing the GTS strategy would be completely unfeasible. Then, in this framework, the use of the proposed hybrid network solver becomes absolutely necessary to improve the computational

FIGURE 3.23: Viscoelastic ADAN model. Qualitative comparison between computational results for flow rate and pressure obtained from the 1D (black line), 0D (blue dashed-dotted line) and Test1-hybrid (red dashed line) configurations. In the hybrid network configuration, the segments of the aorta are 1D vessels; while all other vessels displayed belong to 0D regions of the hybrid model.



efficiency of blood flow simulations in such complex vascular networks. The fully 0D simulation for the ADAN model coupled to the peripheral bed of the lenticulostriate artery is executed in 3 minutes, with a speed-up of more than 2280 times with respect to the reference 1D simulation (see Table 3.25). The CPU time demanded to perform the hybrid simulation, where the ADAN model is 1D and the CCO network is 0D, is also considerably reduced, with a speed-up of almost 30 times. As we can appreciate form Table 3.26, these speed-ups are further improved when considering the ADAN model coupled to the second, more complex arteriolar network. Here, the 1D to 0D computational time ratio is about 4480 and the fully 0D simulation is executed in less than 10 minutes; whereas the simulation in the hybrid model configuration achieves a speed-up of 145 times, reducing the CPU time required for simulating a single cardiac cycle from 27 days to less than 5 hours.

FIGURE 3.24: Viscoelastic ADAN model. Distribution of relative root mean square errors (in %) for (A) pressure and (B) flow results, obtained from the fully 0D and the Test 2-hybrid model configurations with respect to the reference 1D results, in selected vessels. The vessels are divided into two groups, left and right of the vertical black dashed line, depending if in the hybrid network configuration are 1D or 0D, respectively. The y-axis is in logarithmic scale.



Hence, the proposed hybrid network solver, possibly integrated with the high-order LTS algorithm developed by Müller *et al.* [102], is shown to be an effective and powerful tool for the solution of highly complex networks of 1D and 0D vessels, where the benefits of adopting this methodology become larger as the complexity of the vascular networks and the heterogeneity of spatial and temporal scales in such networks increase.

FIGURE 3.25: Viscoelastic ADAN model. Distribution of relative systolic errors (in %) for (A) pressure and (B) flow results, obtained from the fully 0D and the Test 2-hybrid model configurations with respect to the reference 1D results, in selected vessels. The vessels are divided into two groups, left and right of the vertical black dashed line, depending if in the hybrid network configuration are 1D or 0D, respectively. Systolic errors are plotted in absolute value, we logarithmic scale on the y-axis.

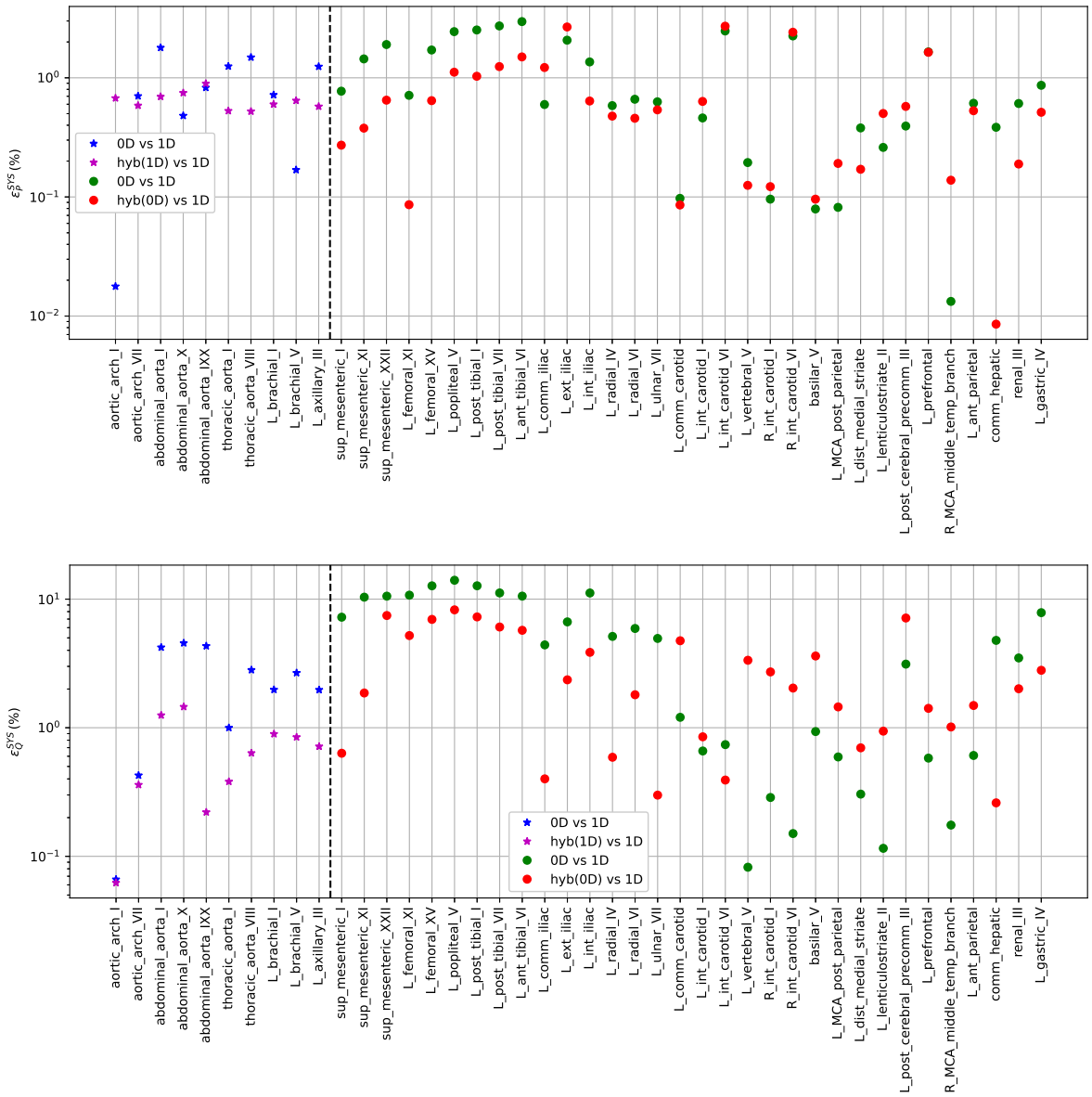


TABLE 3.25: CPU times needed to simulate a cardiac cycle ($T_0 = 1.0\,s$) for the viscoelastic ADAN model coupled to the CCO-generated peripheral bed of the lenticulostriate artery: comparison between 1D, 0D and hybrid simulations, where in the last case the ADAN model is 1D and the CCO network is 0D. The speed-up in all simulations is computed with respect to the reference CPU time t_{CPU}^{Ref} of the 1D simulation. To record CPU times for longer simulations, only a fraction of the cardiac cycle T_0 is simulated, assuming that the computational cost is uniform over the entire cycle. On the other hand, to obtain the computational results, selected simulations were run for 10 cardiac cycles, with $t_{\text{End}} = 10T_0$, until periodic regime was reached. PCo2: second-order path-conservative scheme; IE: implicit Euler method; CN: Crank-Nicolson method.

Config.	**Model**	**Methods**	**Time step**	$t_{CPU}\,[s, h:m:s]$	t_{CPU}^{Ref}/t_{CPU}
1D	visco	PCo2	LTS	407568.66 ≈ 113:12:49	1.0
0D	visco	IE	$\Delta t^{0D} = 10^{-3}s$	178.50 ≈ 00:02:58	2283.2978
Hybrid	visco	PCo2+CN	LTS	14951.01 ≈ 04:09:11	27.2603

FIGURE 3.26: Viscoelastic ADAN model. Qualitative comparison between computational results for flow rate and pressure obtained from the 1D (black line), 0D (blue dashed-dotted line) and Test2-hybrid (red dashed line) configurations. Vessels in the first and second rows belong to the aorta, shoulders and arms regions, so in the hybrid network configuration are 1D vessels; while vessels in the last two rows belong to 0D regions of the hybrid model.

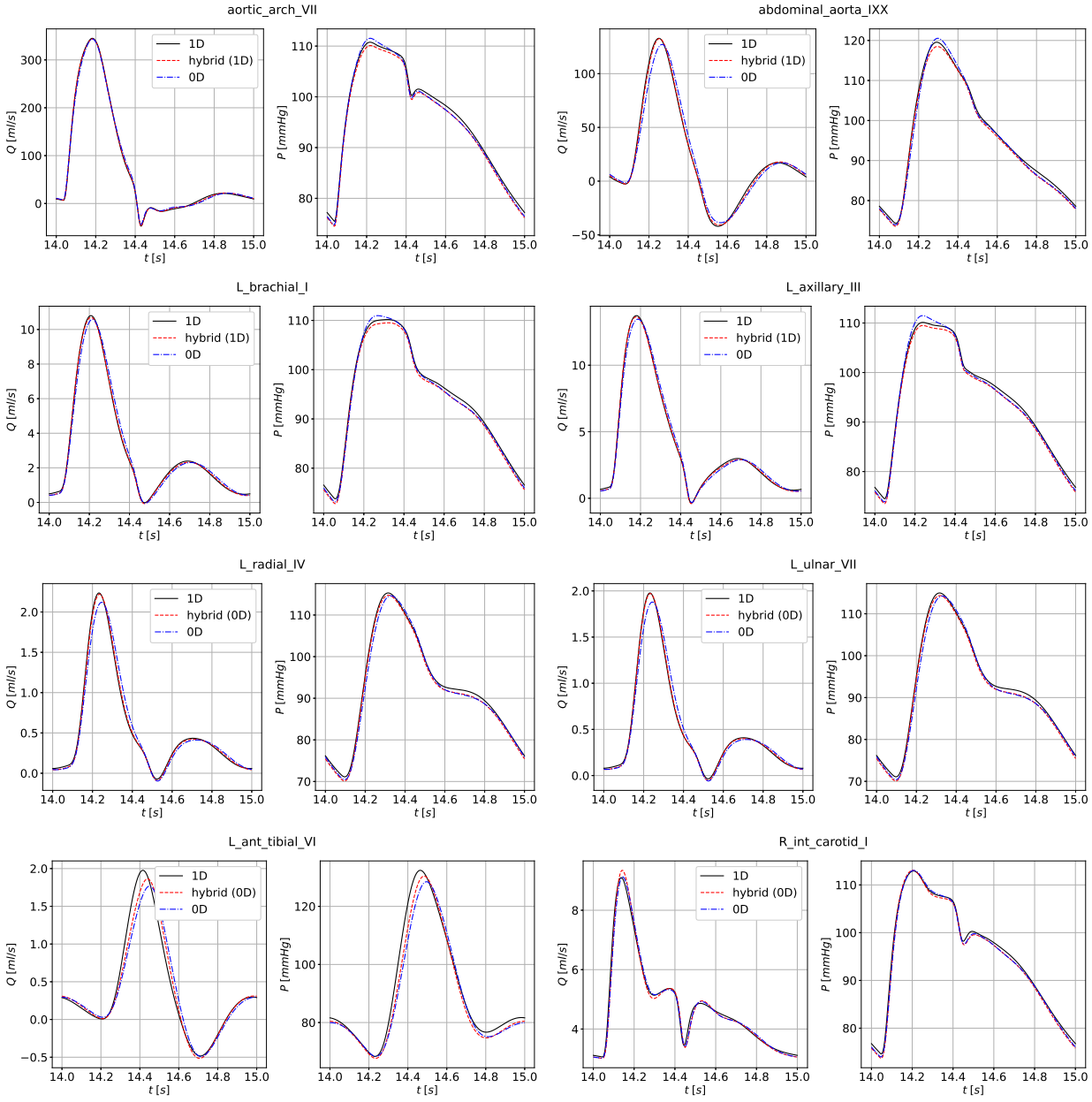
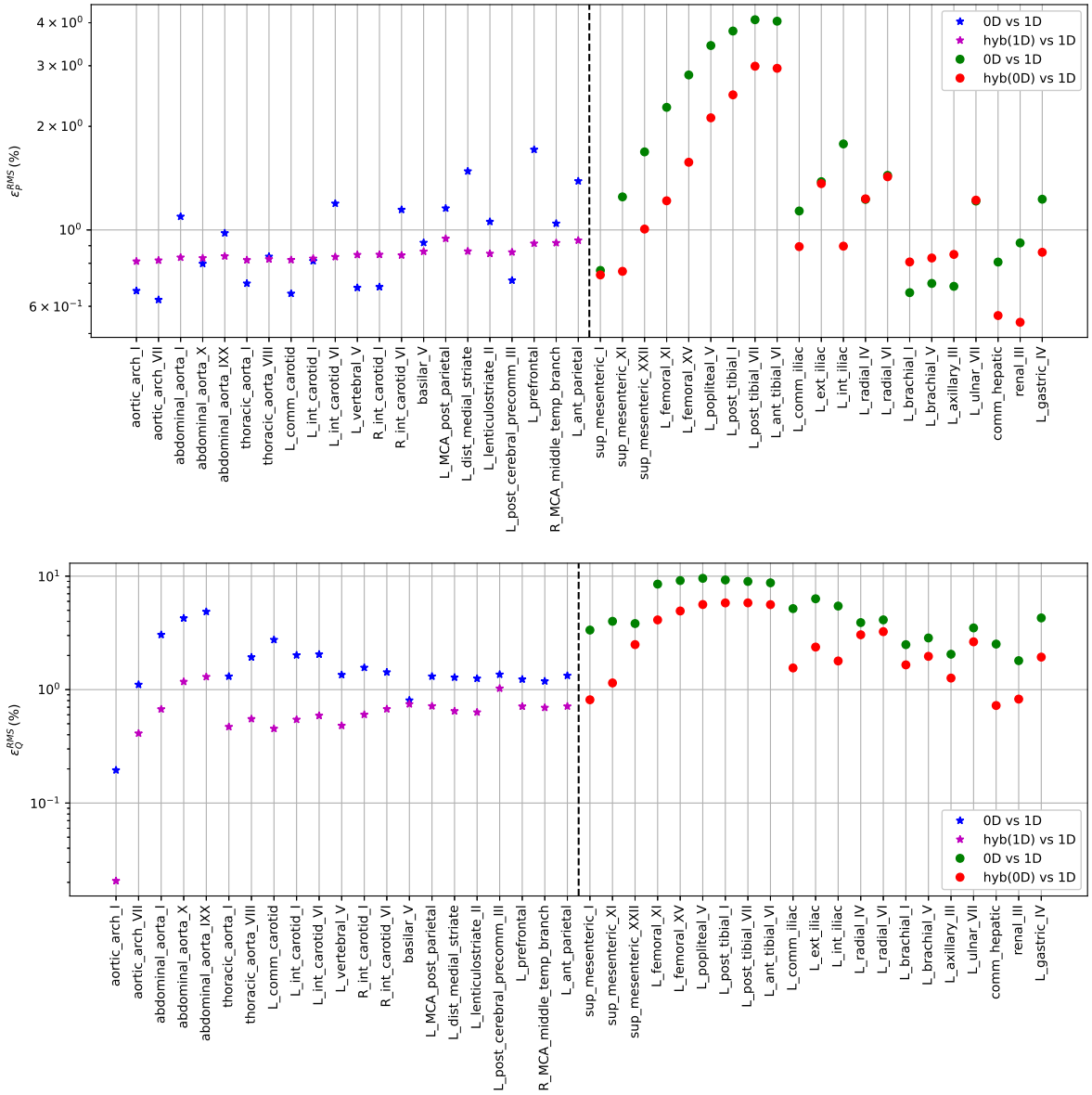


TABLE 3.26: CPU times needed to simulate a cardiac cycle ($T_0 = 1.0\,s$) for the viscoelastic ADAN model coupled to the CCO-generated peripheral bed of the MCA's posterior parietal branch: comparison between 1D, 0D and hybrid simulations, where in the last case the ADAN model is 1D and the CCO network is 0D. The speed-up in all simulations is computed with respect to the reference CPU time t_{CPU}^{Ref} of the 1D simulation. To record CPU times for longer simulations, only a fraction of the cardiac cycle T_0 is simulated, assuming that the computational cost is uniform over the entire cycle. PCo2: second-order path-conservative scheme; IE: implicit Euler method; CN: Crank-Nicolson method.

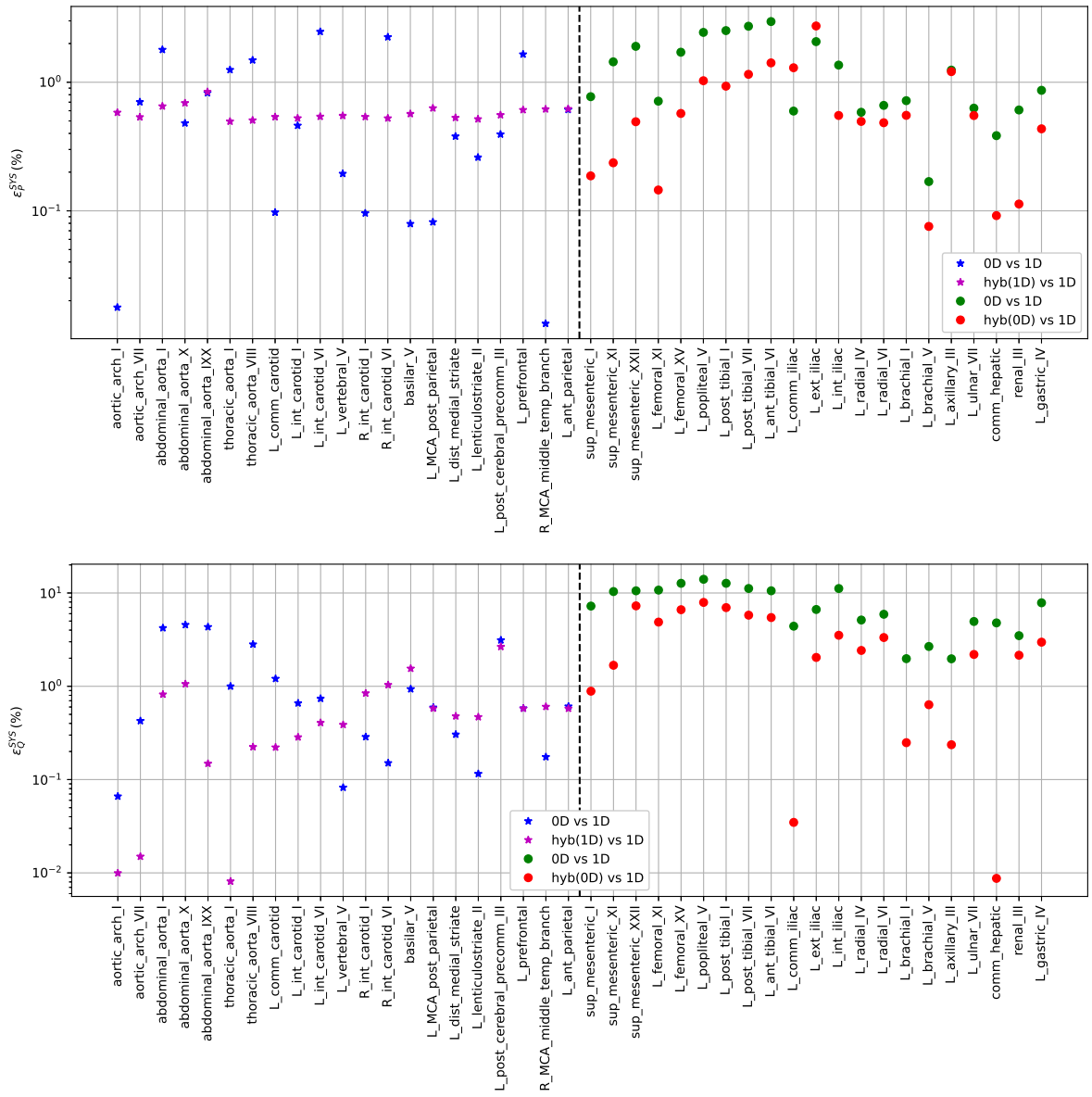
Config.	**Model**	**Methods**	**Time step**	$t_{CPU}\,[s, h:m:s]$	t_{CPU}^{Ref}/t_{CPU}
1D	visco	PCo2	LTS	2328564.28 ≈ 646:49:24 (≈ 27 days)	1.0
0D	visco	IE	$\Delta t^{0D} = 10^{-3}s$	519.99 ≈ 00:08:40	4478.0943
Hybrid	visco	PCo2+CN	LTS	16104.51 ≈ 04:28:25	144.59082

FIGURE 3.27: Viscoelastic ADAN model. Distribution of relative root mean square errors (in %) for (A) pressure and (B) flow results, obtained from the fully 0D and the Test 3-hybrid model configurations with respect to the reference 1D results, in selected vessels. The vessels are divided into two groups, left and right of the vertical black dashed line, depending if in the hybrid network configuration are 1D or 0D, respectively. The y-axis is in logarithmic scale.



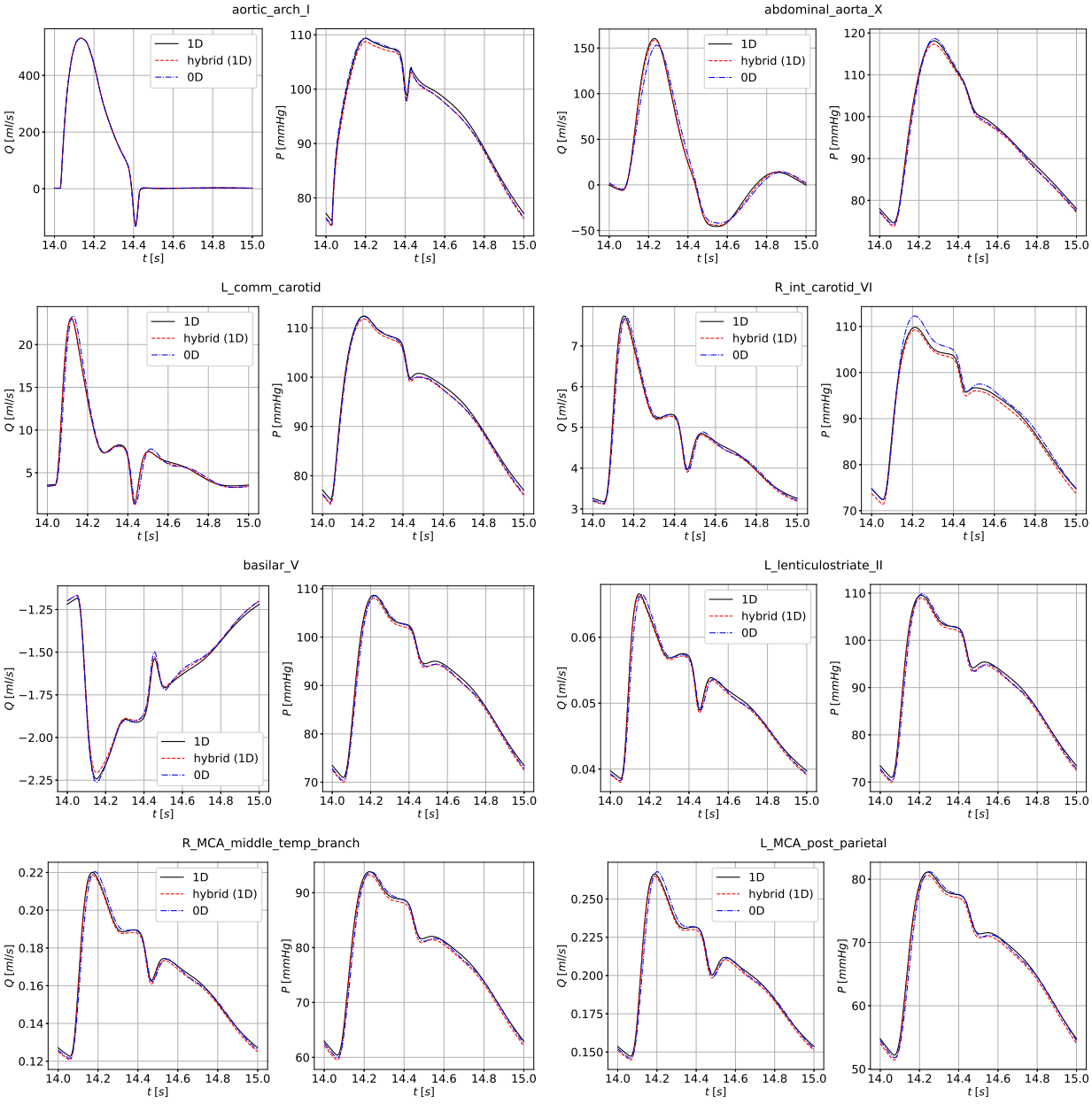
Error and waveform analysis. We present here and discuss the computational results obtained for the viscoelastic ADAN model coupled to the CCO-generated peripheral bed of the lenticulostriate artery. The distribution of relative root mean square and systolic errors in the results from the 0D and hybrid network configurations, computed with respect to the reference 1D solution, is displayed in Figures 3.31 and 3.32, respectively, for a group of selected vessels. Once again, for the hybrid model configuration, we calculate errors both in vessels of the ADAN model and of the CCO network, that are, respectively, 1D and 0D in the hybrid configuration considered. In addition, precise values of root mean square, systolic and diastolic relative errors are reported in Table C.5 in Appendix C. Here, the focus is on the vessels of head and neck, as the CCO network is connected to a cerebral artery, so that we can assess the impact of using different model configurations on the vessels of these regions. From the error distribution plots shown in Figures 3.31 and 3.32, we can first see that errors in the 0D results are overall reasonably small. RMS errors in the

FIGURE 3.28: Viscoelastic ADAN model. Distribution of relative systolic errors (in %) for (A) pressure and (B) flow results, obtained from the fully 0D and the Test 3-hybrid model configurations with respect to the reference 1D results, in selected vessels. The vessels are divided into two groups, left and right of the vertical black dashed line, depending if in the hybrid network configuration are 1D or 0D, respectively. Systolic errors are plotted in absolute value, we logarithmic scale on the y-axis.



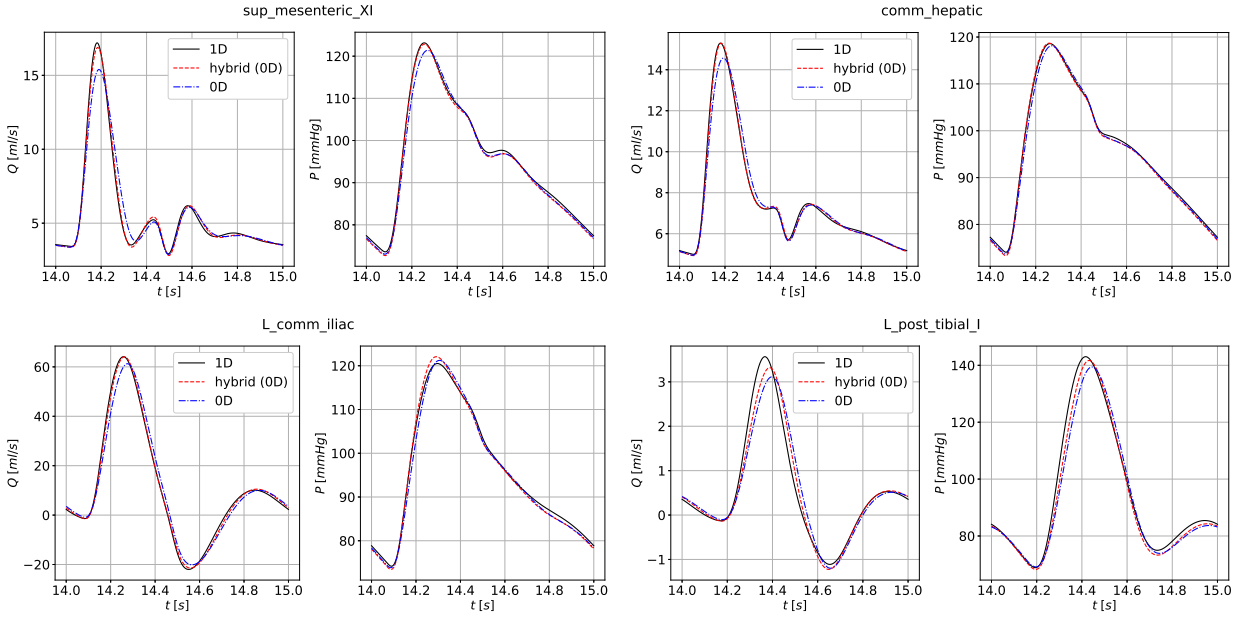
pressure are below 2% in all vessels displayed, while RMS errors in the flow rate are bounded within 5% (see Fig. 3.31 and Table C.5). Similarly, systolic errors in pressure and flow rate have peak values of about 2% and 4%, respectively (see Fig. 3.32 and Table C.5). The very interesting outcome is that, in the hybrid network configuration, both RMS and systolic errors are significantly reduced, in the 1D vessels of ADAN model (see magenta stars in Fig. 3.31-3.32), but also in the 0D vessels of the CCO network (see red dots in Fig. 3.31-3.32). Overall, relative errors in the 1D vessels are of the order of magnitude of $10^{-5}/10^{-6}$, for both pressure and flow rate results, which are extremely small. As we can note from Table C.5, the only 1D vessel with larger errors, but still of the order of $10^{-1}/10^{-2}$, is the lenticulostriate artery, which is indeed the vessel to which the CCO network is attached. Relative errors are considerably decreased also in the 0D vessels: RMS errors in both pressure and flow rate are overall reduced by a factor of 10 to 100 (see Fig. 3.31 and Table C.5).

FIGURE 3.29: Viscoelastic ADAN model. Qualitative comparison between computational results for flow rate and pressure obtained from the 1D (black line), 0D (blue dashed-dotted line) and Test3-hybrid (red dashed line) configurations. All vessels displayed belong to the aorta, head and neck regions, so in the hybrid network configuration are 1D vessels.



These observations are also supported by the qualitative comparisons between solutions obtained from the 1D, 0D and hybrid model configurations presented in Figures 3.33 and 3.34, for selected vessels of the ADAN model and of the arteriolar network, respectively. For the vessels of the ADAN model, from Figure 3.33 we conclude that the results from the hybrid network configuration (red dashed line) are in very good agreement with the reference 1D solution (black line), being almost indistinguishable. The 0D results (blue dashed-dotted line) clearly present more evident differences with respect to the 1D results, but overall we still get reasonably good and accurate approximations of pressure and flow waveforms in all the displayed vessels. A very similar scenario is obtained for the vessels of the CCO-generated peripheral bed. In particular, from Figure 3.34 we can observe that the results from the hybrid model are still in good agreement with the reference 1D solution, with an almost negligible loss in terms of accuracy of the predicted results.

FIGURE 3.30: Viscoelastic ADAN model. Qualitative comparison between computational results for flow rate and pressure obtained from the 1D (black line), 0D (blue dashed-dotted line) and Test3-hybrid (red dashed line) configurations. All vessels displayed are 0D vessels in the hybrid network configuration.

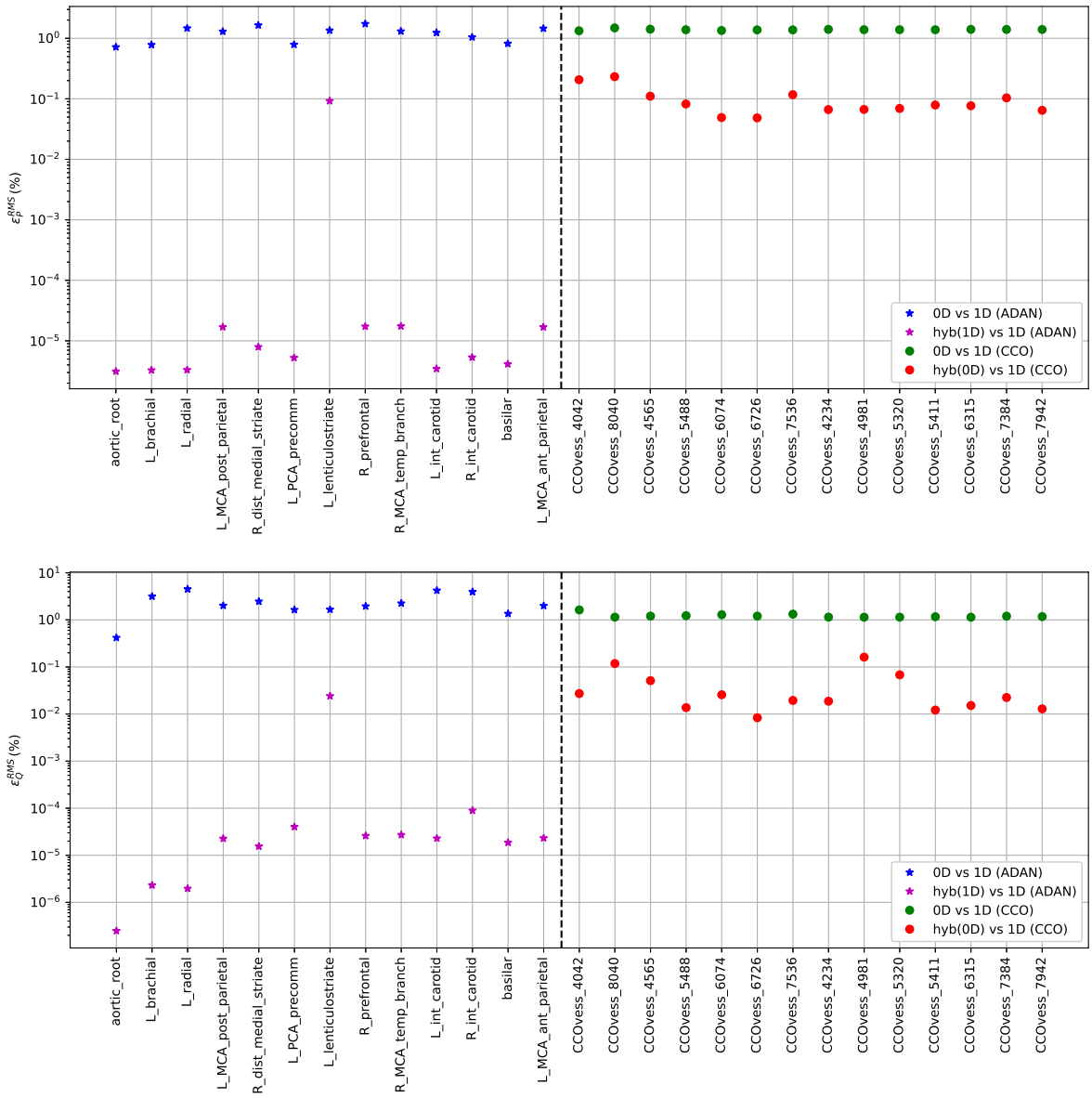


Pressure and flow waveforms and their essential features, shape, amplitude and systolic peak, are very well-reproduced by the hybrid model configuration, also in the 0D vessels of the CCO network (see Fig. 3.34). This suggests that the larger vessels of the ADAN model have a strong impact in determining and shaping pressure and flow waveforms also in the smaller vessels of the CCO network. As we can appreciate from Figure 3.34, also the results from the fully 0D model are satisfactory, where, clearly, a much more significant gain in terms of computational efficiency of the corresponding fully 0D simulation comes at the cost of a larger loss in terms of accuracy of the results.

3.4.3.4 Concluding remarks

From the speed-up, error and waveform analyses performed on the results obtained by applying the proposed hybrid network solver to the ADAN model and the ADAN model coupled to CCO-generated cerebral arteriolar networks, we conclude that this methodology represents an effective and powerful tool to perform efficient and accurate blood flow simulations on large and complex vascular networks and models. Such complexity does not only depend on the anatomical detail by which a network is described, but also on the level at which physiological mechanisms and mechanical characteristics of the cardiovascular system are modeled, such as the viscoelasticity of vessel walls. A strong improvement in terms of computational efficiency is obtained when applying the hybrid network solver with GTS strategy to the ADAN model. When dealing with more complex vascular networks where the heterogeneity of spatial and temporal scales is even more relevant, adopting the hybrid network solver also integrated to the LTS algorithm becomes crucial and absolutely necessary to gain computational efficiency, as demonstrated by the speed-ups of orders of magnitude obtained for the viscoelastic ADAN model coupled to the CCO-generated arteriolar networks. On the other hand, we have shown that this hybrid network solver is also able to preserve a good level of accuracy in the predicted results, reproducing good approximations of pressure and flow waveforms in both 1D and 0D vessels of a hybrid network, when compared to the reference 1D results. Therefore, this solver is able to ensure the correct trade-off between computational cost of the simulations

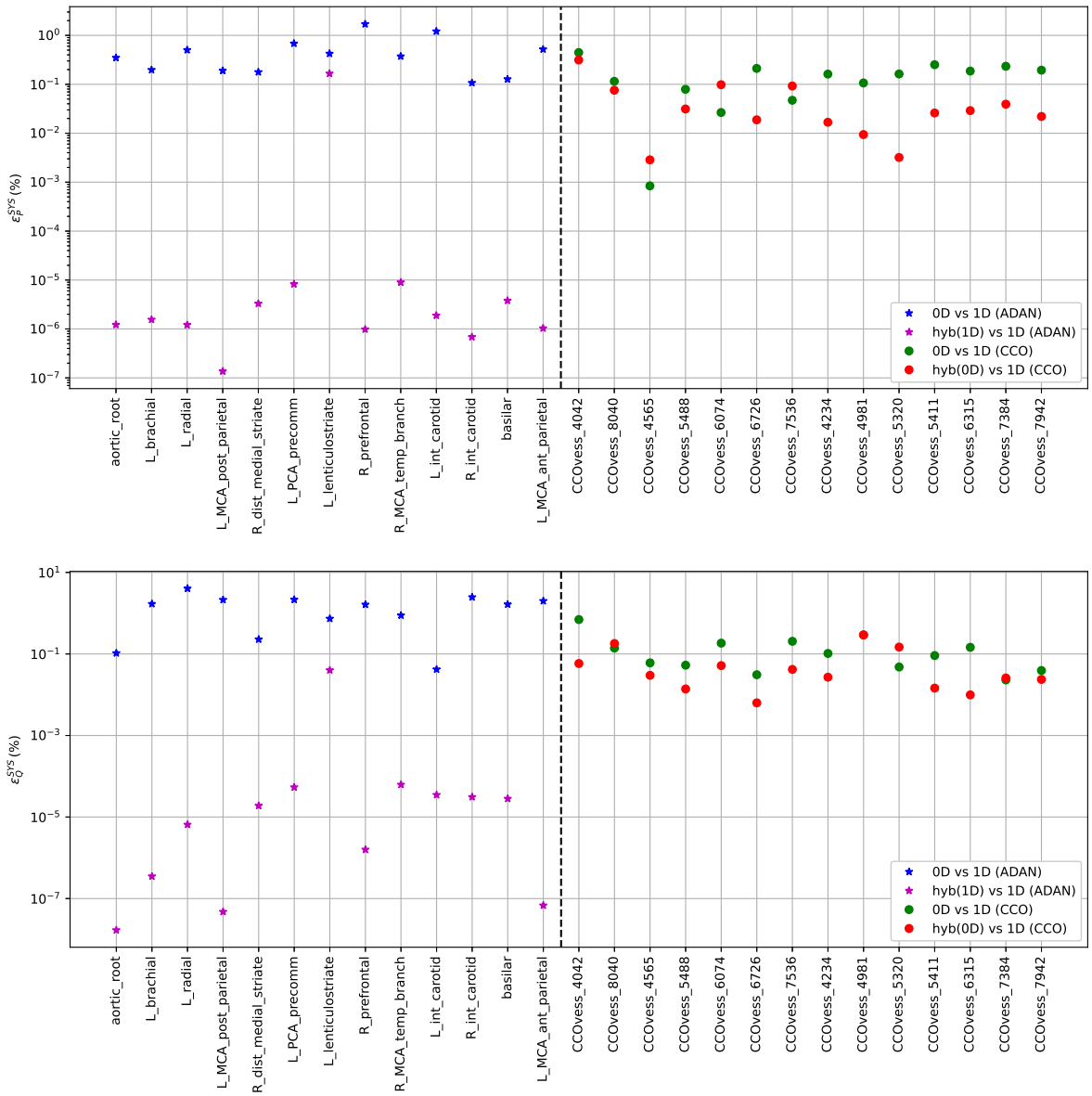
FIGURE 3.31: Viscoelastic ADAN model coupled to the CCO cerebral network of the lenticulostriate artery. Distribution of relative root mean square errors (in %) for (A) pressure and (B) flow results, obtained from the fully 0D and the hybrid model configurations with respect to the reference 1D results, in selected vessels. The vessels are divided into two groups, left and right of the vertical black dashed line, depending if in the hybrid network configuration are 1D or 0D, respectively. The y-axis is in logarithmic scale.



and accuracy in the results, representing a first step towards the definition of a high-performance modeling and computational framework for the solution of highly complex networks of 1D-0D vessels.

The LTS technique developed by Müller *et al.* [102], here integrated to the proposed hybrid network solver, is already a powerful tool to gain computational efficiency when solving highly complex one-dimensional networks. In fact, we have observed that, for the viscoelastic ADAN model, our hybrid network solver is not competitive with the LTS algorithm, as there is no speed-up in the simulations of the hybrid network configurations with respect to the fully 1D simulation performed by adopting the LTS strategy. However, the LTS technique is a very sophisticated and complex algorithm, which, in general, may not be available or ready and easy to implement in standard GTS network solvers. As a consequence, the methodology developed in this thesis may represent a very good alternative: the integration of this

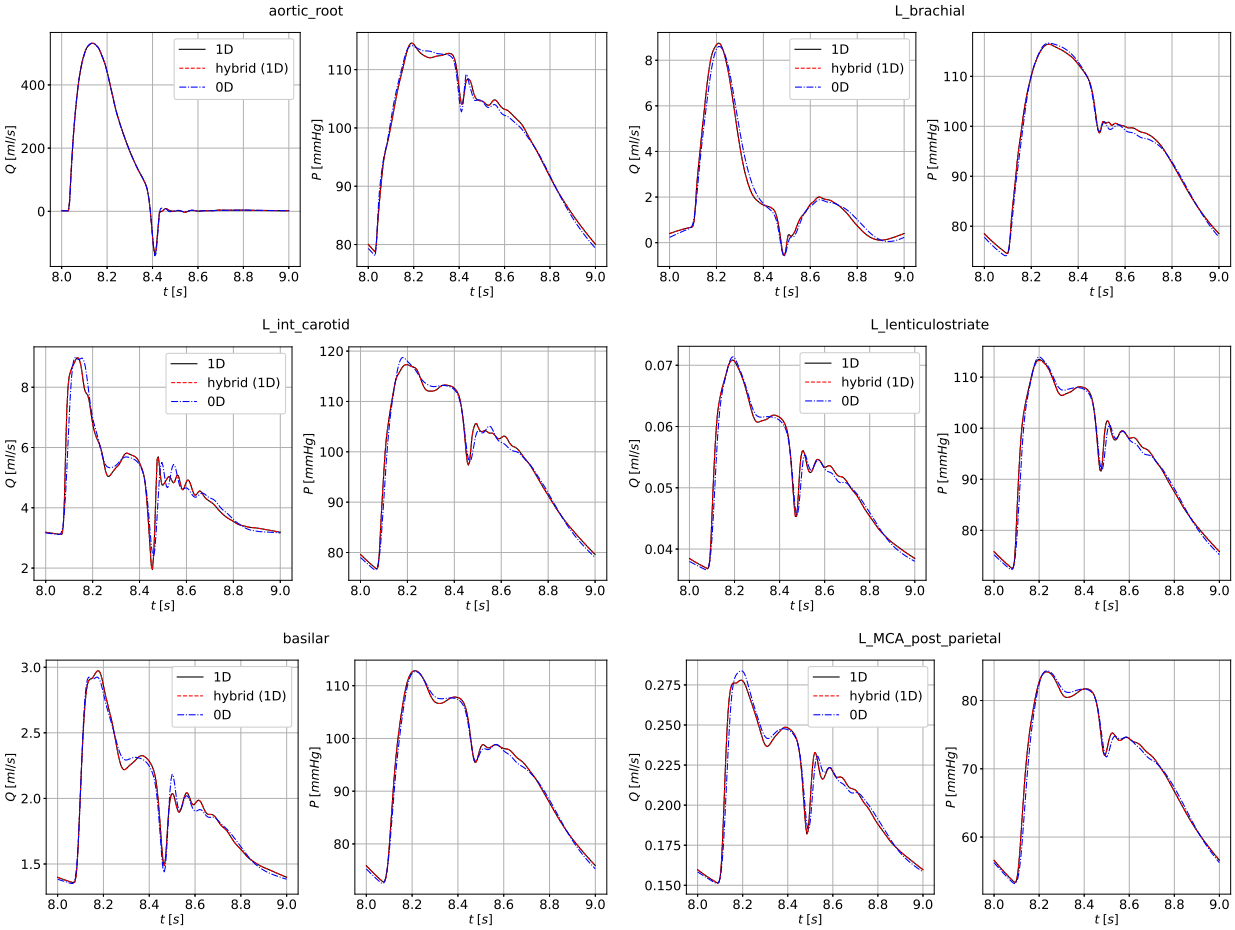
FIGURE 3.32: Viscoelastic ADAN model coupled to the CCO cerebral network of the lenticulostriate artery. Distribution of relative systolic errors (in %) for (A) pressure and (B) flow results, obtained from the fully 0D and the hybrid model configurations with respect to the reference 1D results, in selected vessels. The vessels are divided into two groups, left and right of the vertical black dashed line, depending if in the hybrid network configuration are 1D or 0D, respectively. Systolic errors are plotted in absolute value, we logarithmic scale on the y-axis.



hybrid network solver into an already existing solver for one-dimensional networks based on a GTS strategy may be crucial to make such solver significantly more efficient, but still accurate, when solving very complex and large vascular networks, as demonstrated here. Indeed, when adopting the GTS strategy, the proposed hybrid network solver strongly improves the computational efficiency of the simulations also for the ADAN model.

This work has some limitations as well. First of all, as already pointed out, the temporal discretization strategy proposed to determine the time step of 0D regions in hybrid networks is not always efficient, as it restricts each 0D region to evolve with the minimum time step of the 1D vessels it is connected to. Currently, we are already working to develop a more efficient hybrid coupling strategy, which allows to evolve 0D regions with their own time step, not constrained by that of the neighboring 1D vessels. In fact,

FIGURE 3.33: Viscoelastic ADAN model coupled to the CCO cerebral network of the lenticulostriate artery. Qualitative comparison between computational results for flow rate and pressure obtained from the 1D (black line), 0D (blue dashed-dotted line) and hybrid (red dashed line) configurations. All these vessels belong to the ADAN model, so in the hybrid network configuration are 1D vessels.

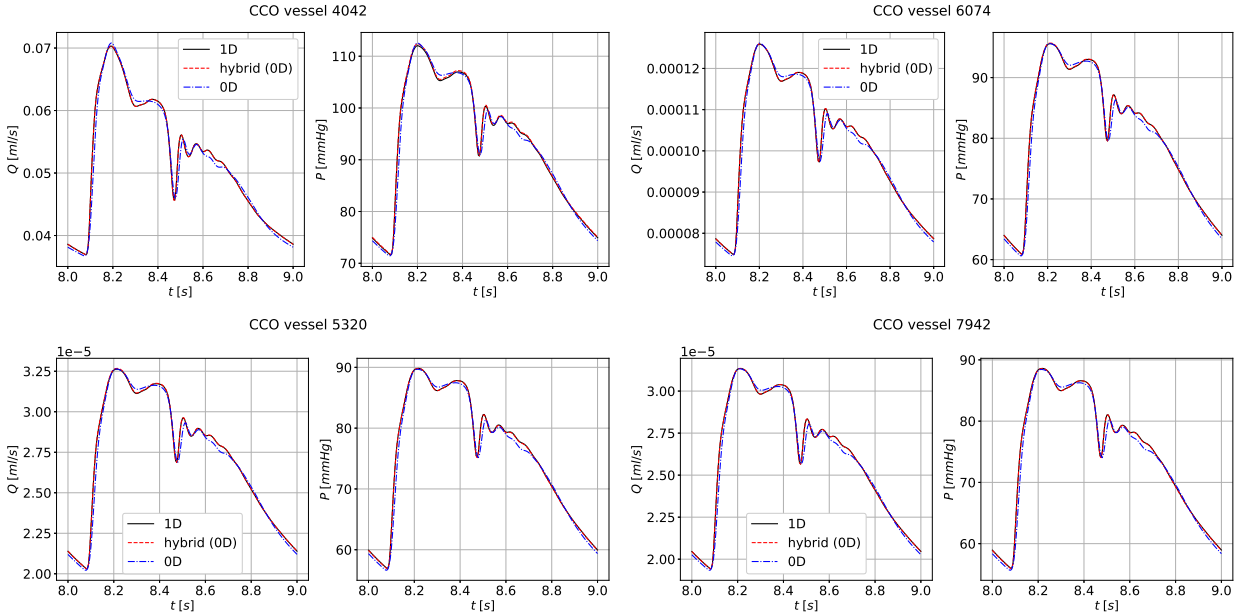


by using a larger time step for 0D regions, such strategy would significantly reduce the number of updates to be performed for each 0D regions using the implicit ODE solver, making the overall hybrid network methodology much more efficient. However, we note that special care is required to design this hybrid coupling strategy, as 1D and 0D vessels converging at a hybrid junction are evolved using a fully explicit and an implicit numerical scheme, respectively, possibly with different time steps, and the conservation of mass and energy must be ensured across the junction.

Second, the comparison here performed between results obtained from the 1D, 0D and hybrid network configurations of the different arterial models focuses on the solution over time at a certain point in space for the 1D vessels (*i.e.* the midpoint of the vessel). From this comparison, we have obtained that 0D and hybrid models' results are, in general, in very good agreement with the reference 1D solution. However, we did not explore and assess spatial resolution, which in 0D vessels would be just given by points. In fact, there are other aspects that could be investigated, such as pulse wave velocity and wave intensity analyses, or the propagation of the pressure wave along space, over the network or over a certain path. This is a major limitation of the analysis carried out in this study and further investigation will be addressed in the future.

Finally, we note that the 1D solver we departed from is parallelized and the fully 1D simulations performed in this work could be already parallelized. Hence, we plan to extend the proposed hybrid network

FIGURE 3.34: Viscoelastic ADAN model coupled to the CCO network of the lenticulostriate artery. Qualitative comparison between computational results for flow rate and pressure obtained from the 1D (black line), 0D (blue dashed-dotted line) and hybrid (red dashed line) configurations. All these vessels belong to the peripheral bed of the lenticulostriate artery, so in the hybrid network configuration are 0D vessels.



solver (the 0D part and the 1D-0D coupling) to parallel code implementation as well, for further computational improvement.

Chapter 4

Reconstruction of MRI-derived *in-vivo* human cerebral networks for blood flow simulations

4.1 Introduction

As pointed out in Section 1.1, current evidence links the dynamics of interacting fluid compartments of the CNS to the CNS fluid physiology and pathology of a number of neurological disorders, including neurodegenerative diseases associated with misaccumulation of waste products in the brain. However, even if CSF flow is acknowledged to play a primary role for the elimination of metabolic products, mechanisms and routes of waste clearance from the brain are still unclear and controversial [1, 69, 70]. Recent medical research [155] has also established a strong association between extracranial venous anomalies, such as stenoses, and a range of diseases with no cure and unknown cause, affecting the CNS, such as Multiple Sclerosis, bringing attention also to the blood flow circulation, especially the venous one. In this complex scenario, mathematical models and fluid dynamics simulations may contribute to the definition of a quantitative and comprehensive approach for the description of the interaction of intracranial fluids, including arterial and venous blood, CSF and interstitial fluid, allowing to study flow and transport in the brain parenchyma and also to explore current hypotheses about brain waste clearance.

Motivated by this, in the second part of this thesis, we focus on the modeling of one of the main components of this interacting cerebral fluids dynamics, blood flow, with emphasis on modeling and simulating the venous haemodynamics in MRI-reconstructed detailed cerebral networks. Indeed, modeling blood flow in such cerebral networks may contribute to investigate and quantify cerebral blood flow, potentially providing some insights into its complex dynamics and mechanisms.

The main goal of this chapter is to develop a methodology that, departing from *in-vivo* high-resolution MRI data in human brain, allows to reconstruct and calibrate subject-specific arterial and venous networks of specific cerebral districts, which are suitable to perform blood flow simulations. The imaging technique used to acquire the MRI data, the MICRO method, that will be briefly presented in Section 4.1.1, allows to visualize and extract *in-vivo* very small cerebral vessels, both arteries and veins, down to 100 μm of thickness in diameter, that previously could not be seen with standard *in-vivo* imaging methods. Then, the proposed processing pipeline consists of several steps, which allow to generate, from the acquired MRI data, networks of vessels with their geometry and connectivity, that, after calibration and parametrization, can be employed to perform blood flow simulations. We note that the high-resolution MRI data employed here, acquired using the novel MICRO imaging method in human brain developed by Prof. E. Mark Haacke and his research group (Wayne State University, Detroit, MI, USA), were never used before to extract networks of vessels and to perform blood flow simulations. This is the first time that a methodology to create

vascular networks for blood flow simulations from the MICRO imaging data is proposed. Hence, this work represents a proof-of-concept study that it is possible to extract subject-specific cerebral networks from these MRI data. We consider this work a first step towards the definition of an effective processing pipeline for the extraction and parametrization of real cerebral networks and blood flow simulations from subject-specific data, to explore, quantify and better characterize cerebral blood flow dynamics, with focus on venous blood drainage.

First, in Section 4.2, we extract detailed segmentations of arteries and veins of specific cerebral districts from the MICRO imaging data, in a way that (i) the arterio-venous separation is addressed, namely, the differentiation, in each vascular territories, between arterial and venous vessels, and (ii) the continuity and connectivity of the vascular structures is ensured. In fact, from a modeling point of view, it is important to generate arterial and venous segmentations, and thus vascular models and networks where the vessels are all well-connected. Especially in the venous side, these segmentations will include very small cerebral vessels (of a few hundreds of microns in diameter), micro-veins draining into the larger ones, always ensuring that all vessels are well-connected. Equipped with these segmentations, in Section 4.3 we then propose an algorithm to extract a network of vessels suited to perform 1D/0D blood flow simulations. Indeed, to solve blood flow in real cerebral networks using the 1D and 0D models introduced in the previous chapters, from the obtained 3D segmentations a one-dimensional network description has to be generated, with connectivity between vessels and geometric information. Here, we focus on the venous side, whose anatomy and patho-physiology is of great interest from both clinical and modeling points of view, given also the potential venous haemodynamic connection to some neurodegenerative diseases, as pointed out in Section 1.1. Afterwards, in Section 4.4, the MRI-reconstructed cerebral networks are parametrized and calibrated using perfusion data acquired for the same subject. Finally, in Section 4.5 preliminary blood flow simulations on the reconstructed venous networks are performed. As we will illustrate in Section 4.5, the main purpose of these simulations is the validation of the proposed processing pipeline itself, to assess whether the obtained cerebral networks are reasonable from a physiological and fluid-dynamics point of view and whether they are able to predict physiologically reasonable results in terms of pressure ranges in the corresponding vascular territories. In fact, through the simulations performed and the results obtained, we can identify limitations, weak points and aspects that need to be improved of the methodology developed.

4.1.1 The MICRO method

The "Microvascular In-vivo Contrast Revealed Origins (MICRO)" method is a novel *in-vivo* microvascular imaging approach in human brain recently developed by Prof. E. Mark Haacke and his research group at Wayne State University (Detroit, MI, USA) [87, 126, 25, 24, 26]. MICRO imaging takes advantage of susceptibility weighted imaging (SWI) sequence, which exploits the magnetic susceptibility differences between tissues and uses the phase image to detect these differences. SWI is a powerful tool to image sub-voxel veins, but it is insensitive to arteries in their natural form. Because of the very low level of deoxygenated hemoglobin in arterial blood, there is no susceptibility contrast between arteries and surrounding tissue. The innovative aspect of the MICRO method is that it uses an ultra-small superparamagnetic iron oxide (USPIO) contrast agent, Ferumoxytol, to induce a non-zero susceptibility into blood, in both small arteries and small veins (in veins, increased susceptibility in addition to that caused by deoxyhemoglobin). This imaging technique employs multiple high-resolution dual-echo SWI sequences, acquired with a gradual increase in Ferumoxytol concentration. The magnetic susceptibility in blood is drastically increased due to the superparamagnetic property of Ferumoxytol, even at a low-dose of 4 mg/kg. Hence, with the increase in susceptibility-related contrast comes the potential to make small sub-voxel vessels visible, which previously could not be seen through standard *in-vivo* imaging methods, but only in cadaver brain studies.

Indeed, with a sufficiently high resolution, the human brain microvasculature can be revealed and extracted *in-vivo*, with the smallest detectable vessel size being of 100 μm at 3T, and of even 50 μm at 7T.

The potential of MICRO method has been demonstrated in several studies published by Prof. Haacke's group. In [26], the authors used the high-resolution SWI data with low-dose Ferumoxytol to map the intra-hippocampal microvasculature, segment its subfields and measure the fractional vessel density of each subfield in healthy subjects. Hippocampal vessels are small ($<$ 1 mm) and difficult to visualize through *in-vivo* imaging methods, restricting their examination so far to cadaver studies. Buch *et al.* [24] focused on the application of high-resolution MICRO imaging in enhancing the vascular contrast and mapping the microvascular nature of Multiple Sclerosis (MS) lesions. The authors showed that this imaging technique reveals small arteries and veins not only in healthy tissue, but also in MS plaques and that the proposed approach has the potential to monitor the venous vasculature present in MS lesions, catalog their characteristics and compare spatially the vascular structures to the presence of lesions. Finally, in [25], the MICRO imaging protocol was adopted to study the anatomy and microvasculature of the midbrain in healthy volunteers, with an eye towards future work in studying vascular abnormalities in diseases such as Parkinson's disease.

In this thesis, with the help of MICRO imaging, our goal is to extract detailed segmentations of the arterio-venous cerebral vasculature of districts of interest, from which networks of vessels can then be generated, parametrized and calibrated, to perform blood flow simulations from subject-specific data, to better characterize and quantify cerebral blood flow dynamics.

Remark 4.1. Conventional MRI techniques can reveal vessels down to 500 μm of thickness in diameter. In research only, but not in clinical practice, this limit can be pushed up to 250 μm. However, with standard *in-vivo* imaging methods very small vessels below this limit can not be seen.
The novel MICRO imaging method allows to visualize vessels down to 100 μm of thickness in diameter at 3T (50 μm at 7T), revealing the entire human brain microvasculature. In fact, anything below 100/50 μm can be regarded as capillaries, while small vessels above this limit can be considered as microvasculature (arterioles and venules). At present, the MICRO method is not able to detect the capillaries only.

4.2 Reconstruction of arterio-venous segmentations of specific vascular territories

In this thesis, we used the high-resolution MICRO imaging data acquired from a healthy-control subject and kindly provided by Prof. E. Mark Haacke and Dr. Sagar Buch. Data were acquired with institutional review board approval at Wayne State University (Detroit, MI, USA) and the subject signed an informed consent form.
The subject was imaged on a 3T MRI scanner with a 32-channel head coil. The imaging protocol included: T1W magnetization prepared rapid gradient echo and dual-echo SWI sequences, both acquired pre and post Ferumoxytol administration. The subject was scanned with the dual echo SWI sequence at four time points: the first was acquired pre-contrast (Fe_0) and the remaining three (Fe_1, Fe_2 and Fe_3) were acquired post-contrast at intervals of 11 minutes during a gradual increase in dose. The final Ferumoxytol dose (4 mg/kg) was diluted with 60 mL of 0.9% sodium chloride (or normal saline) solution. The contrast administration was initiated at the start of the first post-contrast scan and the entire contrast dose was administered to the subject before starting the last post-contrast scan (Fe_3).
The MR imaging parameters for the MICRO protocol were the following: TE1/TE2/TR = 7.5/15/27 ms, bandwidth = 180 Hz/pixel, number of slices = 96, flip angle = 15° (Fe_0 and Fe_3) and 20° (Fe_1 and Fe_2), voxel size = $0.22\times0.44\times1$ mm^3 (interpolated in k-space to $0.22\times0.22\times1$ mm^3), acquisition time for each sequence = 11 mins, GRAPPA = 2/36, final Ferumoxytol dose = 4 mg/kg, dose delivery time = 21-23 mins.

Then, the SWI images were generated, by SWI data processing using both original phase and magnitude images. In particular, the SWI data for the Fe_2 and Fe_3, SWI_{Fe2} and SWI_{Fe3} respectively, were obtained and averaged to generate an improved SWI data set, $SWI_{avg,2,3}$, with higher signal-to-noise ratio. For full details about the post-processing of SWI data we refer the reader to [26] and reference therein.

The departing point for the extraction of detailed segmentations of arteries and veins of cerebral regions of interest from the high-resolution MICRO imaging data are the major arteries and major veins masks obtained from the pre-contrast data, and the mask of the entire human brain microvasculature revealed by the MICRO method generated from the post-contrast data.

Both masks of major arteries and major veins were extracted from the pre-contrast data. A MR angiogram (MRA) of the major arteries was obtained using a nonlinear subtraction, MRA_{nl}, of the long Echo Time (TE) from the short TE of the pre-contrast magnitude data, with a subtraction constant of 1.5. Then, the standard deviation $\sigma_{MRA_{nl}}$ over the map MRA_{nl} was computed and a threshold of $3 \times \sigma_{MRA_{nl}}$ was applied, to discard all the pixels with values below this threshold and keep the pixels with values above the same threshold as corresponding to arterial vessels. The final arterial segmentation was obtained by removing the islands with connectivity equal or smaller than 10 voxels in 3D, in the binarized thresholded image.

On the other hand, three representations of major veins were generated: pre-contrast quantitative susceptibility mapping (QSM), R_2^* map and T_1-enhancement map. The R_2^* map was calculated from the pre-contrast short and long TE magnitude data, while the T_1-map was obtained by dividing the short TE Fe_1 magnitude data by the short TE Fe_0 magnitude data. The three venous maps were then normalized to values between 0 and 1 and averaged to produce a high-quality MR venogram, denoted by MRV_{avg}. The obtained venous map MRV_{avg} includes all the major veins, but also a lot of background noise and surrounding tissue. To suppress everything outside the veins, the algorithm for vessel segmentation developed by Descoteaux *et al.* [39] was adopted (by setting the constants α, β and c to 0.5, 0.5 and 500, respectively, to compute the vesselness measures and by using the vessel size range of 1 to 10 voxels, incrementing the scale by 1). The mask generated by the algorithm was then applied to the original venous map MRV_{avg} to obtain the final binarized venous segmentation.

Figure 4.1 shows a comparison between pre-contrast MRA_{nl}, which displays all the major arteries, pre-contrast SWI data, which shows all the major veins, and MICRO imaging data (*i.e.* post-contrast SWI data), which reveals the entire human brain microvasculature, down to 100 μm thick vessels. First of all, this comparison demonstrates how well the MICRO method works in enhancing the cerebral vessels, especially the smaller ones, which are not included neither in the arterial map, nor in the venous map. Furthermore, from these pictures we can confirm that the MICRO imaging data shows both arteries and veins. On the pre-contrast SWI data in Figure 4.1b, major cerebral veins, such as the internal cerebral veins (ICV) (yellow arrows in Fig. 4.1b) and the septal veins draining into the ICV (green arrows in Fig. 4.1b), can be easily identified; hence, on the post-contrast SWI data in Figure 4.1c, all the small vessels draining/converging into these main veins can be classified as venous vessels as well. Similarly, the major arteries shown on the MRA_{nl} map in Figure 4.1a are also present on the MICRO imaging data in Figure 4.1c and, therefore, small vessels branching/generating from these main cerebral arteries can be considered as arterial vessels (transmedullary arteries, penetrating arteries/arterioles).

The segmentation of the entire human brain microvasculature (including also major arteries and veins) revealed by the MICRO method, the *all-vessels mask*, was obtained departing from the SWI_{Fe3} data, corresponding to the SWI processing of the final post-contrast data at time point Fe_3. To generate the segmentation of the cerebral microvasculature revealed by the MICRO method, no vessel enhancement filter was applied. Instead, manual vessel tracing and labeling was performed on the SWI_{Fe3} data, to enhance and extract all the small cerebral vessels. In particular, this operation was carried out by taking advantage of the reduced signal in correspondence of a vessel on the SWI_{Fe3} data. The minimum intensity projection

(mIP) over three slices (3 mm of thickness) was also used to make sure that each new label added was connected to a vessel: on a single slice, the labeled vessel appears like a dot, while the mIP shows the labels in continuity with each other and the vessel that is forming. Major arteries and major veins were first labeled by using the corresponding masks, and then the all-vessels mask was manually extended with the smaller vessels. The final microvasculature map/mask generated via manual vessel labeling, by including all the manually labeled small cerebral vessels, was denoted by MVM. Figure 4.2 shows selected slices from the maximum intensity projection (MIP) of the *all-vessels mask* over four slices (4 mm of thickness).

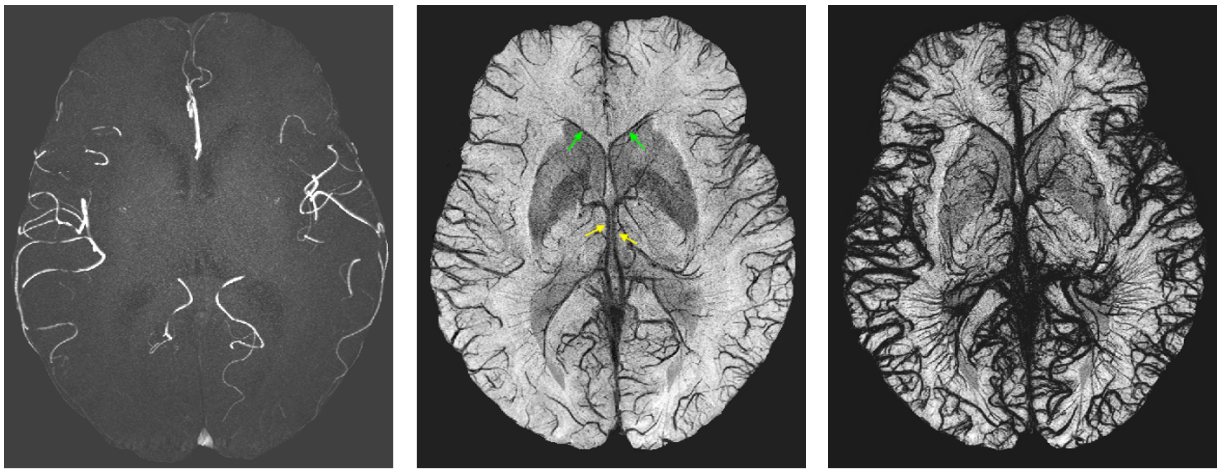
The segmentations of major arteries and major veins, as well as the *all-vessels mask* MVM of the entire human brain microvasculature were generated, as described above, by Dr. Sagar Buch. These segmentations represent the departing point of the methodology presented in the following sections to (i) extract detailed arterio-venous segmentations of cerebral districts of interest; (ii) reconstruct networks of vessels from such segmentations; (iii) calibrate and parametrize the MRI-reconstructed cerebral networks to perform blood flow simulations.

Remark 4.2 (*Vessel enhancement filters*). Frangi vesselness filter is a vesselness measure developed by Frangi *et al.* [57], obtained on the basis of all eigenvalues of the multiscale second-order local structure of an image, the Hessian matrix, to compute the likeliness of an image region to contain vessels. The vesselness measure allows to map the geometric features into probability estimates of vesselness using the three eigenvalues of the Hessian matrix, in order to differentiate the blood vessels (regarded as tubular structures) from other structures and the surrounding tissue. The vesselness function proposed by Frangi *et al.* depends on the choice of the constants α, β and c (Eq. (13) of [57]). This vesselness measure is analyzed at different scales, s, and the response of the line filter will be maximum at a scale that approximately matches the size of the vessel to be detected (Eq. (14) of [57]). The algorithm for vessel segmentation developed by Descoteaux *et al.* [39], employed to generate the major veins segmentation, is an extension, an improved version of Frangi filter. The idea is that Frangi vesselness measure is first applied to find putative centerlines of tubular structures along with their estimated radii, and then this measure is distributed to create a vector field which allows the flux maximizing flow algorithm of Vasilevskiy and Siddiqi [150] to be applied to recover vessel boundaries. The main advantage of Descoteaux algorithm with respect to Frangi vesselness filter is that it reduces discontinuities between vessels.

As pointed out above, no vessel enhancement filter was applied to obtain the *all-vessels mask* MVM, which was generated by manual vessel tracing and labeling on the post-contrast SWI_{Fe3} data. The main reason of this choice is that the goal standard in vessel segmentation is still manual labeling, especially when dealing with small vessels. Of course, manual vessel labeling is exposed to human error and Frangi filter may enhance vessels that can not be seen by visual/manual tracing. However, on the other hand, the vessel enhancement filter has also some limitations: it could miss small vessels which run very close or parallel to each other, or which are not considered as "tube-like" structures; it could introduce discontinuity errors and segment broken vessels. Moreover, Frangi filter detects also noise: for instance, in regions containing cerebrospinal fluid (CSF), just CSF can be enhanced by the vesselness filter even if no vessels are present, only because there is noise. As a consequence, even if Frangi vesselness filter is commonly adopted for vessel segmentation, for this specific subject our choice was to perform manual vessel labeling to generate the microvasculature map MVM.

Frangi filter had some issues also when applied to the arterial map MRA_{nl}, creating vessels not present on the map and missing others. For this reason, the major arteries mask was generated by adopting a thresholding procedure, as described above.

FIGURE 4.1: Comparison between (A) pre-contrast MRA (TE = 7.5 ms), which displays all the major arteries; (B) pre-contrast SWI data (TE = 22.5 ms), which shows the major veins; (C) MICRO imaging data (*i.e.* post-constrast SWI data, at TE = 15 ms), which reveals all the vessels, both arteries and veins, down to 100 μm. These images were acquired with a resolution of 0.22 x 0.44 x 1 mm^3 at 3T and are minimum intensity projections (mIP) over 15 slices (15 mm of thickness each). Yellow and green arrows on the pre-contrast SWI data, in panel (B), indicate the internal cerebral veins and the septal veins draining into the ICV, respectively. Pictures kindly provided by Dr. Sagar Buch.



(A) MRA_{nl} (B) Pre-contrast SWI (C) Post-contrast SWI

4.2.1 Arterio-venous separation and Vessel Tracking (VT) algorithm

Both the post-contrast SWI data displayed in Figure 4.1c and the *all-vessels mask* MVM shown in Figure 4.2 clearly demonstrate the ability of the MICRO method to reveal and extract the human brain microvasculature, small cerebral vessels down to 100 μm of thickness in diameter. In fact, by making use of Ferumoxytol contrast agent, both small arteries and small veins are enhanced by this imaging technique. As a consequence, one of the main difficulties of extracting detailed segmentations of arteries and veins down to the scale of these small vessels, even when restricting to specific cerebral districts of interest, is the separation, differentiation between arterial and venous vessels, as in many regions arteries and veins run very close, even parallel to each other, being very challenging to be distinguished.

To deal with this issue, we develop a vessel tracking (VT) algorithm, implemented in Matlab, in a way that the arterio-venous separation is addressed and the connectivity and continuity of the vascular structures is ensured for a specific cerebral district of interest. The idea is that, departing from a larger vessel that we know to be a vein (or an artery) from the major veins (major arteries) mask, we can track all the smaller veins (or smaller arteries) draining into/branching from the main vessel and belonging to a specific cerebral region. We proceed as follows:

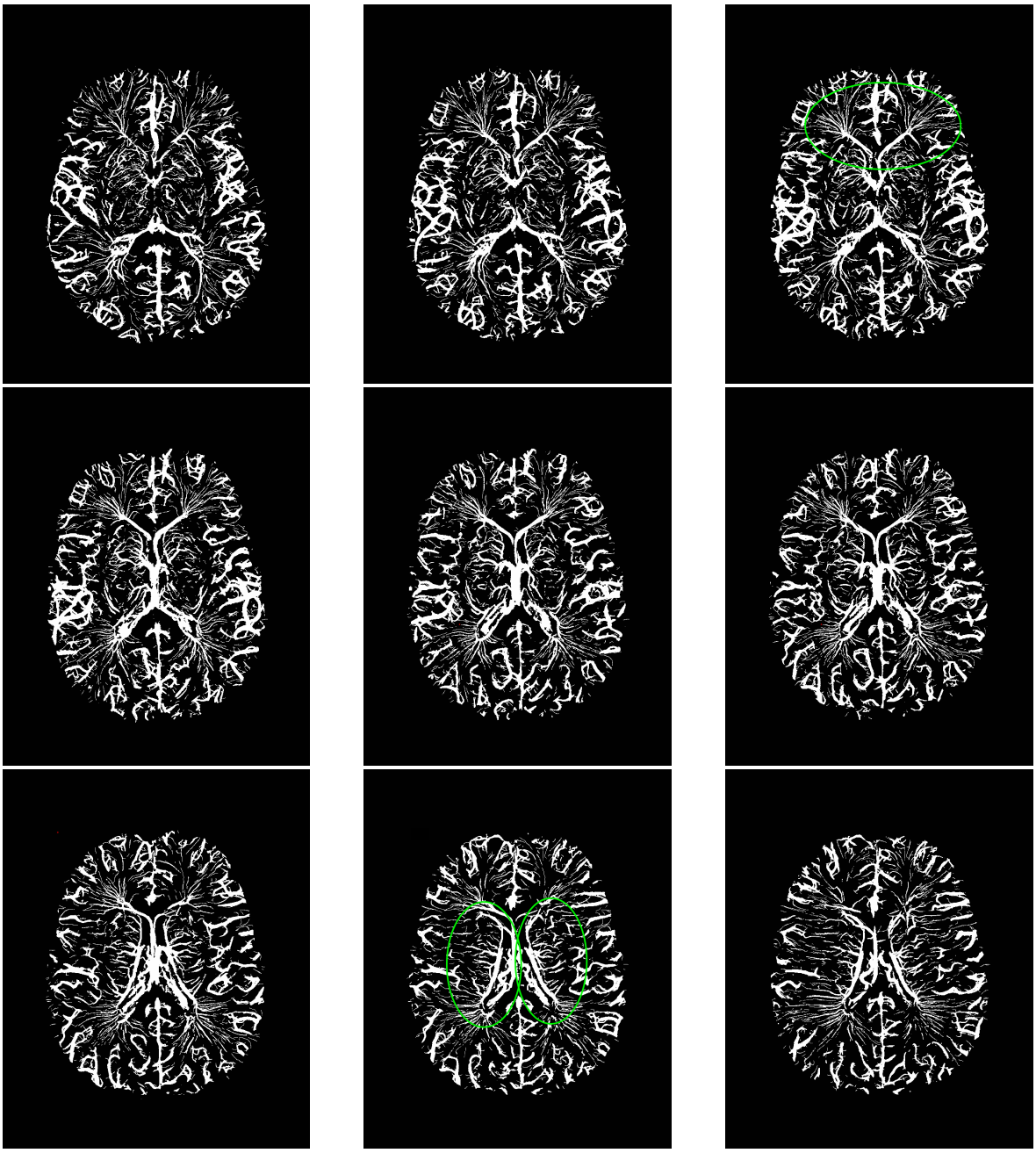
1. On the original all-vessels mask MVM, the region (or, better, volume)-of-interest (ROI) is selected, which includes the entire vascular territory or cerebral region to be tracked and extracted.

2. The original all-vessels mask is cropped using the ROI defined at point 1.

3. [Optional] Pre-vessel tracking correction of the cropped mask: if unwanted artery-vein connections are visually identified, they are manually removed, to prevent unwanted arteries to be tracked when extracting a small-veins mask and vice versa.

4. The vessel tracking of veins (arteries) on the cropped mask is performed, by placing a seed point on a large vein (artery) and selecting the connectivity C (usually $C = 3, 4$). The connectivity C defines the neighboring region of $C \times C \times C$ pixels to be tracked around a pixel.

FIGURE 4.2: Selected slices from the MIP of the final *all-vessels mask* MVM over 4 slices (4 mm of thickness). The green circles identify the venous vascular territories addressed of left/right septal veins (top right image) and left/right longitudinal ependymal veins (bottom central image), to extract the micro-veins masks first, and the corresponding small-arteries masks next.



4.a Initialization of the algorithm: the input data to the VT algorithm are the cropped mask, the seed point(s) to initialize the algorithm, the connectivity C;

4.b Iterative procedure: at the first iteration, the connectivity C defines the neighboring region to be tracked around the seed point(s). At each subsequent iteration, the next neighboring region around the already tracked pixels is evaluated using the same connectivity C;

4.c Termination criterion: the iterative algorithm is stopped if the structural similarity between the current and previous iteration results (tracked masks) is > 0.9999999.

In general, the VT algorithm ensures that we are primarily tracking either the venous or the arterial

network with possibly different neighboring connectivities. Mainly, pre-VT corrections, if necessary, and VT iterations with different connectivities guarantee that either the vein-only or artery-only network is tracked for a specific vascular region.

We point out that the proposed vessel tracking algorithm addresses the separation between arteries and veins, but also ensures the connectivity and continuity of the vascular structures and of the vessels that are tracked. Indeed, all this work is based on vessel tracking, as it is fundamental to generate arterial and venous segmentations, and thus vascular models and networks where the vessels are all well-connected. With vessel tracking, we may not be able to track and include all the vessels, separating between arteries and veins, in the final arterial and venous masks. However, this is expected, because our main goal is not just to include in our masks and vascular models as many vessels as possible, but to include vessels that are well-connected and generate well-connected vascular models and networks, even if this comes at the cost of losing some other vessels. In conclusion, this is achieved by finding a good trade-off to include as many (small) vessels as possible, but ensuring the connectivity and continuity between theses vessels.

The VT algorithm is the departing point for the extraction of micro-veins and small-arteries masks of specific cerebral districts from the *all-vessels mask* MVM, as will be described in Section 4.2.4 and Section 4.2.6, respectively. In Sections 4.2.2 and 4.2.3, the VT algorithm will be also first applied to major veins and major arteries masks, respectively. In fact, even if these segmentations are already vein-only and artery-only masks, the vessel tracking will ensure that all arteries and veins included in the final masks are well-connected.

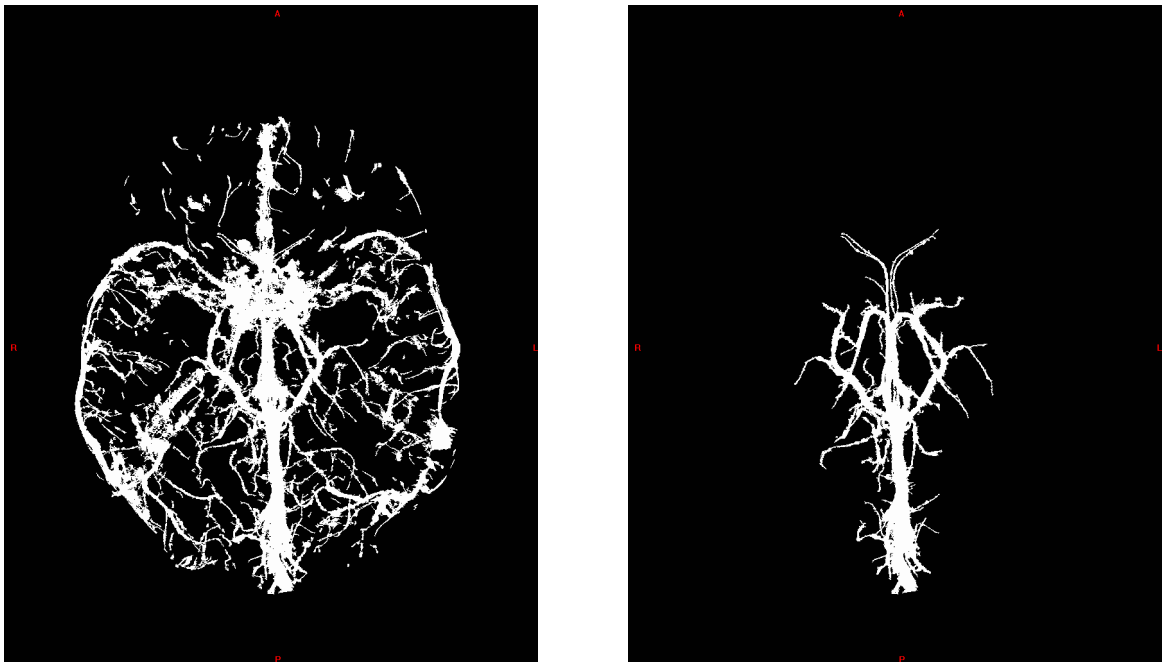
4.2.2 Major-veins mask

The major veins mask was generated from the MR venogram MRV_{avg}, as described at the beginning of Section 4.2. The MIP of the original binarized venous segmentation, over the entire brain thickness, is displayed in Figure 4.3a. Clearly, no arterio-venous separation is needed here, as this is a vein-only segmentation of main cerebral veins and venous sinuses. However, from this image we can observe that this venous mask includes many broken and unconnected branches and also noisy regions of pixels, which need to be removed. As pointed out above, the main goal here is not just to create segmentations including as many vessels as possible, but rather to generate vascular models where the connectivity and continuity between vessels is ensured, even if some unconnected vessels or broken branches are lost. In addition, in this particular case, extracting the cortical edges of this segmentation, namely the transverse sinuses and related veins, is more difficult and challenging with respect to the other venous vessels included in the mask.

In view of these considerations, we decide to include in the final major veins mask the following vessels: superior sagittal sinus (SSS), straight sinus and inferior sagittal sinus (ISS), great vein of Galen, basal veins of Rosenthal and internal cerebral veins (ICV), thalamostriate veins (with possible segments of the longitudinal ependymal veins), septal veins draining into the ICV and other branches of these main cerebral veins and venous sinuses. By appropriately selecting the ROI to be applied to the venous mask, some of the veins to be removed are simply cut out from the region of interest; while other veins will be discarded by the vessel tracking algorithm. The final venous segmentation is indeed obtained by applying the VT algorithm described in Section 4.2.1 to the major veins mask shown in Figure 4.3a, first cropped via the selected ROI, by placing a seed point on one of the two ICV and with connectivity of $C = 3$. To further improve the venous mask, manual correction is also performed pre- and post-vessel tracking on the binarized image. Before applying the VT algorithm, if connections to noisy regions of pixels or to unwanted vessels are visually detected, then these connections are manually removed, so that these structures will not be tracked by the tracking algorithm. Similarly, the output mask obtained from the vessel tracking algorithm is carefully inspected and refined by manually removing any unwanted structures left in the segmentation.

The MIP of the final, corrected and tracked, output venous mask is displayed in Figure 4.3b, while Figure 4.4a shows the 3D volume rendering of this mask. From these pictures, we can observe that, thanks to the use of the vessel tracking algorithm, all the vessels included in the final major veins mask are well-connected. However, from Figure 4.4a, we can see that the initial portion of the SSS draining into the confluence of sinuses is missing, not well-defined. This mainly depends on the imaging protocol used to acquire the high-resolution SWI data. As this may be an issue when extracting the corresponding network of vessels from this segmentation, the T_1-weighted post-contrast data are exploited to improve the major-veins mask by manually adding the missing connection for the SSS and both transverse sinuses that we were not able to include from the original MR venogram. The obtained mask is displayed in Figure 4.4b, which is considerably improved compared to the venous model in Figure 4.4a: both transverse sinuses are now included, the SSS is well-connected to the confluence of sinuses and, in general, the entire SSS is more regular, smooth and well-delineated; in addition, the "enlarged" vessel observed in between the SSS and the straight sinus on the venous mask in Figure 4.4a has now been removed.

FIGURE 4.3: MIP over the entire mask thickness of the major veins segmentation. Comparison between (A) the original venous segmentation generated from the MR venogram MRV_{avg}; (B) the final processed venous mask, obtained after vessel tracking and manual correction.



(A) Original venous segmentation

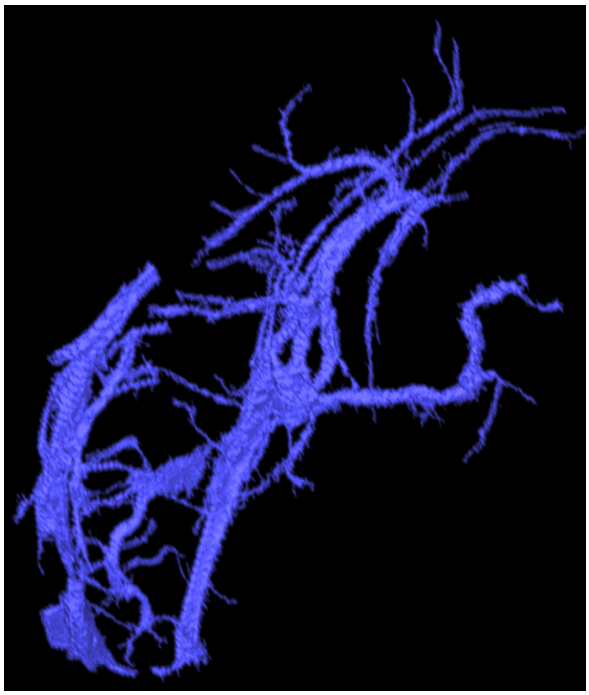
(B) Final processed major veins mask

4.2.3 Major-arteries mask

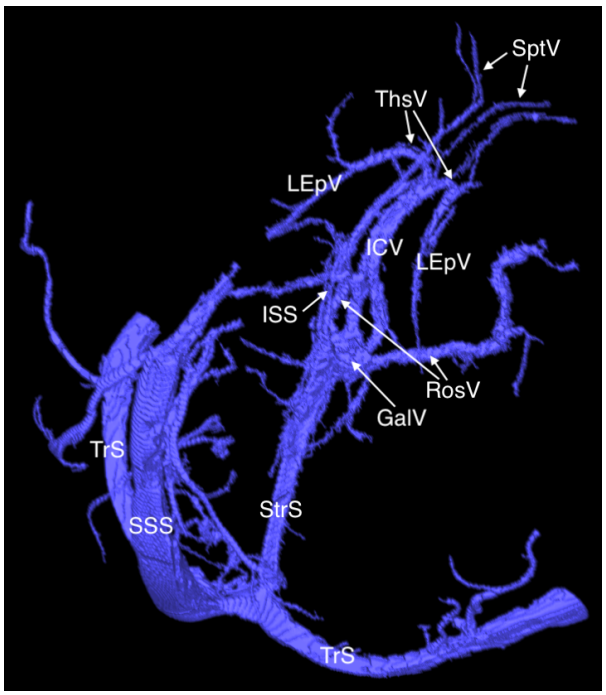
The major arteries mask was generated from the arterial map MRA_{nl}, as illustrated at the beginning of Section 4.2. The MIP of the original binarized arterial mask, over the entire brain thickness, is displayed in Figure 4.5a.

As done in Section 4.2.2 for the major veins mask, also here we first apply the vessel tracking algorithm to the arterial mask shown in Figure 4.5a, by placing a seed point on one of the two anterior cerebral arteries (ACA) and with connectivity of $C = 4$, to validate and asses the connectivity between the arterial vessels included in this segmentation. The MIP of the output mask obtained from the vessel tracking algorithm is shown in Figure 4.5b. From this picture, we can clearly see that some main arteries and arterial branches are lost when performing the vessel tracking, because of missing connections. In particular, the left posterior

FIGURE 4.4: 3D volume rendering of the obtained main cerebral veins mask. (A) The venous mask generated from the VT algorithm includes: SSS, straight sinus (StrS) and ISS, great vein of Galen (GalV), basal veins of Rosenthal (RosV) and ICV. Thalamostriate veins (ThsV) and longitudinal ependymal veins (LEpV), as well as septal veins (SptV) are also extracted and included in this segmentation, to which the reconstructed micro-veins masks will be connected. (B) Extended venous mask, obtained by manually improving the venous mask in (A) using the T_1-weighted post-contrast data: the missing connection for the SSS and both transverse sinuses (TrS) are added; the enlarged vein in between the SSS and the straight sinus is removed.



(A) Main cerebral veins mask



(B) Manually corrected main cerebral veins mask

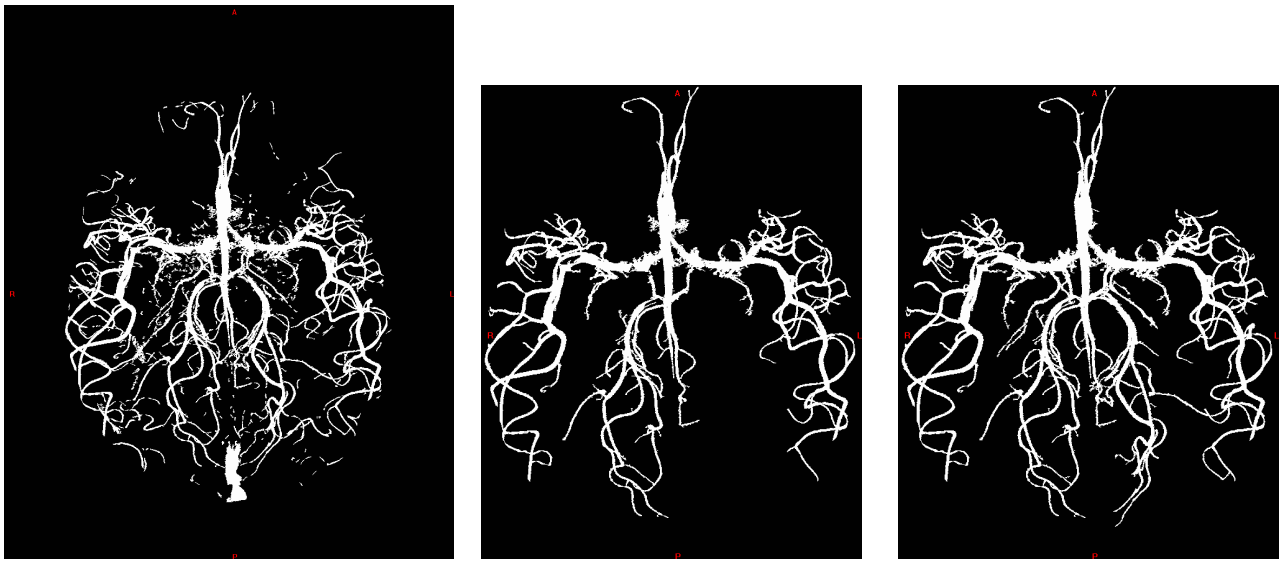
cerebral artery (PCA) and all its branches are not included in the tracked arterial mask because of the missing connection to the corresponding posterior communicating artery (PCoA); both anterior choroidal arteries (AChA) are also left out from the output arterial mask. In addition, by examining more in detail the original arterial mask, it can be observed that the connections of both PCoA to the corresponding ACA need also to be strengthened and improved.

Hence, we go back to the original arterial mask, shown in Figure 4.5a, which is manually improved and corrected using the pre-contrast short TE magnitude data to create the missing connections. The VT algorithm is then applied to the manually corrected arterial mask, with seed point on one of the two ACA and with connectivity of $C = 4$. The MIP of the final, corrected and tracked, major arteries mask is displayed in Figure 4.5c, showing that all the main cerebral arteries and their many branches are now included in the segmentation and are well-connected. This is demonstrated also by the 3D volume rendering of the final arterial mask illustrated in Figure 4.6.

4.2.4 Micro-veins masks

In the previous sections, segmentations of major cerebral veins and arteries have been generated and processed to ensure the connectivity and continuity between vessels in the resulting arterial and venous vascular models. However, the potential of the MICRO method is that it allows to reveal and extract *in-vivo* the human brain's microvasculature, very small cerebral vessels down to 100 μm in diameter, that previously could only be seen in cadaver brain studies, but were difficult to visualize with standard *in-vivo* imaging methods. Then, by making use of the MICRO imaging data, the main goal here the extraction of

FIGURE 4.5: MIP over the entire mask thickness of the major arteries segmentation. Comparison between (A) the original arterial segmentation generated from the arterial map MRA_{nl}; (B) the processed arterial mask, obtained after vessel tracking without manual correction; (B) the final processed major arteries mask, obtained after manual correction and vessel tracking.



(A) Original arterial segmentation

(B) Processed major arteries mask without manual correction

(C) Final processed major arteries mask with manual correction

FIGURE 4.6: 3D volume rendering of the obtained main cerebral arteries mask. The final, tracked and manually corrected, arterial segmentation includes all major cerebral arteries: ACA, MCA, PCoA, PCA, AChA and many arterial branches arising from the main arteries.



detailed arterio-venous segmentations of cerebral districts of interest, where arteries and veins are separated and the connectivity between vessels is ensured.

In this section, the extraction of micro-veins masks of selected venous vascular territories is addressed. We first address veins rather than arteries for reasons that will be explained in the following; then, in Section 4.2.6, small-arteries masks matching the venous models extracted here will be also reconstructed.

In particular, the following vascular territories are targeted, which are highlighted in Figure 4.2 with green circles:

- Medullary veins of white matter (WM) draining into the left/right septal veins, which then drain into the ICV. These vascular regions will be briefly denoted by LSV and RSV, respectively.
- Medullary veins of WM draining into the left/right longitudinal ependymal veins, which are connected to the ICV via the thalamostriate veins. These vascular territories will be referred to as LLEV and RLEV, respectively.

Since in WM the vein-to-artery ratio is approximately 4:1 and since the susceptibility is much stronger in veins than in arteries, the use of Ferumoxytol allows to reveal and, thus, extract much more small veins and venous branches draining into larger veins, rather than small arteries. However, the choice of the venous vascular territories to address has been also very important. In fact, some regions like the midbrain are very difficult to be processed because of small arteries and veins running very close to each other and, in some cases, appearing as a single larger vessel. On the other hand, by comparing the major arteries and major veins masks with the *all-vessels mask* MVM and the post-contrast SWI data, the vascular territories listed above were selected as we expected the arterio-venous separation to work much better and produce good results in these regions. In fact, even if there are small arteries and veins running close or parallel to each other, these vessels were observed to be sufficiently distant to be distinguished by the vessel tracking algorithm.

The extraction of these micro-veins masks is based on the vessel tracking algorithm presented in Section 4.2.1. For each venous cerebral district of interest, the corresponding ROI ((x, y)-coordinates and range of slices in the z-direction) is selected in a way to enclose all the small veins we want to be included in the final tracked mask. The *all-vessels mask* MVM is then cropped using this ROI and the VT algorithm is applied to the cropped mask, by placing a seed point on a larger vein to track all the smaller venules and veins draining into the larger ones. Here, the function of the vessel tracking algorithm is twofold: first, it addresses the arterio-venous separation, as it ensures that we are primarily tracking the venous network, while arterial vessels are not tracked; second, as vessels are tracked using a selected neighboring connectivity, the VT algorithm also guarantees the connectivity and continuity between these vessels.
If necessary, a manual correction step can be performed priori to applying the vessel tracking algorithm: if unwanted artery-vein connections are detected on the cropped mask to be tracked, these connections can be manually removed, so that no arteries will be tracked by the algorithm as connected to the veins.

All venous masks are extracted with a connectivity of $C = 3$, by placing a seed point on the left/right longitudinal ependymal vein for LLEV and RLEV territories, and on a left/right septal vein for LSV and RSV venous territories. The pre-vessel tracking correction step was performed for the LSV and RSV masks only, to remove some unwanted connections between small arteries and veins. In fact, in these regions, we observed that there are some small arteries branching from larger cortical arteries that are very close to, in contact with small veins to be tracked. On the other hand, no post-VT correction was needed for any of the final, tracked micro-veins masks.

The MIPs of the four output micro-veins masks are displayed in Figures 4.7a, 4.7c, 4.7e and 4.7g. However, as explained in the following section, these are not the final segmentations yet, as a thinning algorithm has to be applied to correct the "enlarging effect" caused by the Ferumoxytol contrast agent on the post-contrast SWI data.

4.2.5 Thinning algorithm

Because of the presence of Ferumoxytol contrast agent, the small vessels on the post-contrast SWI data, both arteries and veins, appear slightly enlarged, swelled, with respect to their true size on the pre-contrast

data. To correct this effect and restore, as much as possible, the true size of small arteries and veins, a thinning algorithm is implemented and applied to the *all-vessels mask* MVM generated from the post-contrast Ferumoxytol-enhanced SWI data. We proceed as follows:

1. The Matlab function `bwmorph(mask, operation='thin')` is applied three consecutive times to the manually labeled mask MVM, where the morphological operation 'thin' acts by removing pixels from the boundary of the object. We denote this first output mask by tMVM_1.

2. A modified Frangi vesselness filter, *i.e.* customized to enhance the smaller vessels rather than the larger ones, is applied to the original averaged $\text{SWI}_{\text{avg,2,3}}$ data. In particular, at each voxel, the vesselness is computed using the vessel size range of $s_{min} = 0.2$ to $s_{max} = 1.2$ voxels, incrementing the scale by 0.1 (by setting the constants α, β and c to 0.5, 0.5 and 500, respectively, to compute the vesselness measures), and the maximum vesselness response along its scale is selected. In fact, s_{min} and s_{max} define the minimum and maximum scales at which relevant structures are expected to be found and can be chosen so that they cover the desired range of vessel widths [57]. Frangi vesselness filtering is then followed by setting a vesselness threshold of 2×10^{-4} to discard the unwanted background noise and by removing the islands with connectivity equal or smaller than 8 voxels in 3D, in the binarized vesselness image. Next, the Matlab function `bwmorph(mask, operation='thin')` is applied one time only to the obtained Frangi data. We denote this second output mask by tMVM_2.

3. The final *thinned all-vessels mask* tMVM is obtained by merging the masks tMVM_1 and tMVM_2. In this way, we ensure that all small vessels enhanced and extracted by both the manual vessel labeling operation and the Frangi vesselness filter are included and preserved in the thinned mask.

For each micro-veins mask extracted in Section 4.2.4, the corresponding thinned micro-veins mask is obtained by multiplying the original tracked micro-veins mask and the thinned all-vessels mask. By doing so, the 'interior' part of each tracked vessel is preserved and its true size is restored, while additional vessels included in the thinned mask are discarded. The MIPs of the four final, thinned micro-veins segmentations are displayed in Figures 4.7b, 4.7d, 4.7f and 4.7h, compared to the pre-thinning masks. The 3D volume rendering of the micro-veins masks obtained by means of the vessel tracking and thinning algorithms for the four different venous vascular territories, RSV, LSV, RLEV and LLEV, are shown in Figure 4.9. In all the four selected districts, the VT algorithm worked very well and was able to track most of the small veins and venous branches present on the original *all-vassels mask*, while discarding all the arterial vessels. In particular, we can observe the incredible detail that is preserved in the micro-veins models corresponding to both right and left septal veins (see Figures 4.9a and 4.9b, respectively).

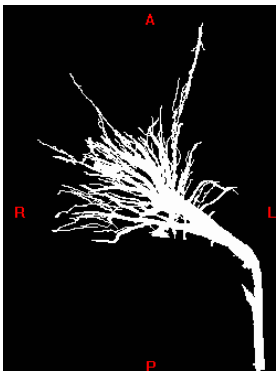
On the other hand, the thinned microvasculature mask tMVM is directly used in the extraction process of the small-arteries masks as described in the following section.

4.2.6 Small-arteries masks

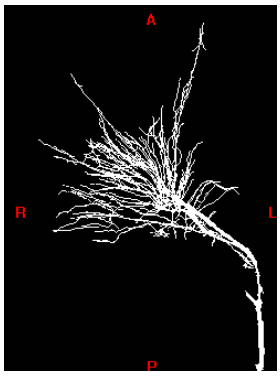
In order to close our MRI-reconstructed arterio-venous model, the last step needed is to extract the arterial network counterpart corresponding to each one of the micro-veins masks obtained for the different venous vascular territories addressed in Section 4.2.6.

As already pointed out, the 4:1 vein-to-artery ratio in WM and the much stronger susceptibility in veins than in arteries explain why, in the post-contrast SWI data, much more smaller veins and connection between small venous branches are revealed, with respect to the arterial side, where not as many smaller arteries and connections can be visualized branching from the major arteries. However, even if we do not expect to reconstruct small-arteries masks with the same level of detail as for the venous side, our goal here is to extract arterial segmentations including as many small arteries as possible generating from the larger

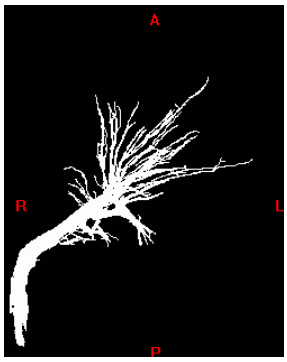
FIGURE 4.7: MIPs over the entire mask thickness of the extracted micro-veins masks for the different cerebral districts of interest. For each venous territory, we compare the segmentation obtained pre- and post-thinning algorithm.



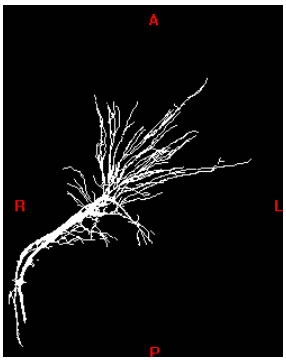
(A) Pre-thinning RSV micro-veins mask



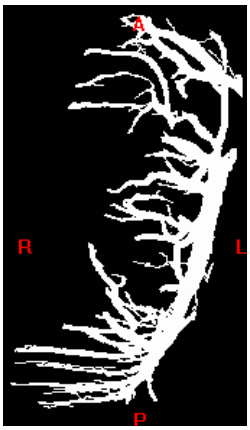
(B) Post-thinning RSV micro-veins mask



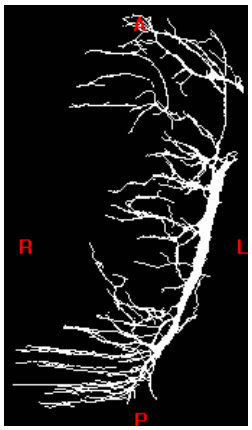
(C) Pre-thinning LSV micro-veins mask



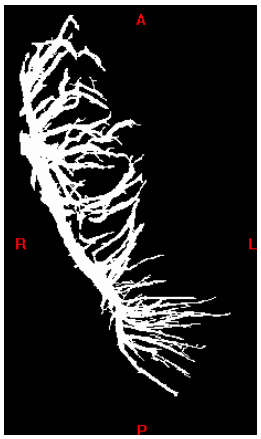
(D) Post-thinning LSV micro-veins mask



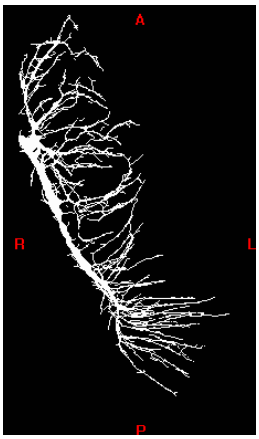
(E) Pre-thinning RLEV micro-veins mask



(F) Post-thinning RLEV micro-veins mask



(G) Pre-thinning LLEV micro-veins mask



(H) Post-thinning LLEV micro-veins mask

cortical arteries and branches of the main cerebral arteries, still ensuring the connectivity and continuity between these vessels.

We tested different strategies for the extraction of the small-arteries masks, comparing their performance (results not reported here). The following methodology was selected and it is applied to the different cerebral regions, as the results obtained were very satisfactory. Differently from the venous side, the starting point of the extraction process of the small-arteries segmentations is already the *thinned all-vessels mask* tMVM. For a specific vascular territory, we perform the following steps:

1. The original major-veins mask is dilated using the Matlab function `imdilate(vmask,ones(n,n,n))`, with dilation factor $n = 5$. Here, we consider the original major veins mask shown in Figure 4.3a, not the processed mask obtained in Section 4.2.2, as it includes also cortical veins.

2. The dilated major-veins mask is subtracted to the thinned all-vessels mask tMVM. We denote the resulting subtraction mask by $\text{tMVM}_{\text{subt}}$.

3. The original ROI used to extract the corresponding small-veins mask is shifted in the (x, y)-plane towards the arterial region, so that all the arteries to be included in the arterial segmentation are enclosed in the ROI; the range of slices in the z-direction is also increase.

4. The subtraction mask $\text{tMVM}_{\text{subt}}$ obtained at point 2 is cropped using the selected arterial ROI.

5. The original major arteries mask generated from the arterial map MRA_{nl} is also cropped, using the same arterial ROI. Also here, we consider the original major arteries mask displayed in Figure 4.5a, not the processed mask obtained in Section 4.2.3.

6. The vessel tracking algorithm is applied to the cropped mask $tMVM_{subt}$, by using the cropped major arteries mask as the seed points (+ a few manually added seed points, if necessary) and with connectivity of $C = 3$.

   Remark 4.3. Manually-added extra seed points may be needed if there are some regions of the arterial mask to be tracked that do not include any seed points from the major arteries masks and, if not well-connected to other main branches, would be lost and not included by the vessel tracking. In this case, these seed points must be carefully placed on arteries, not on veins, as there are also cortical veins running in the same arterial regions.

7. The venous mask obtained by merging the tracked major veins mask, created in Section 4.2.2, and the non-thinned micro-veins masks, generated in Section 4.2.4, is subtracted to the tracked arterial mask obtained at point 6.

   Remark 4.4. This additional subtraction step is performed to remove any unwanted veins still included in the arterial mask by the vessel tracking algorithm, because of the proximity between small arteries and veins. We observe that the subtraction is performed using the non-thinned micro-veins masks. In this way, similarly to the dilation of the major veins mask applied at point 1, since the veins are larger, we expect to have a higher probability to discard unwanted veins and small venous branches, to remove small artery-vein connections still included in the arterial mask.

8. The original major arteries mask is merged to the final, tracked small-arteries mask obtained at point 7, so that major arteries possibly broken by the subtraction with the venous masks are restored and the connectivity and continuity between small arteries and the main arterial branches they are generated from is ensured.

9. [Optional] If, by visually inspecting the arterial segmentation obtained at point 8, any unwanted artery-vein connections are still detected, they can be removed by manual correction.

10. [Optional] The vessel tracking algorithm is applied a second time to the arterial mask obtained at point 9, with connectivity of $C = 3$ and by using all the same seed points used at point 6. If all connections between the small arteries and veins were successfully removed at point 9, the final arterial mask will only include the arteries of the selected region and their smaller branches (cerebral arteries and penetrating arteries/arterioles).

We conclude this section with some considerations. First, we note that the methodology proposed to extract segmentations of small arteries requires several steps and it appears to be more challenging and complicated than the one developed to extract the corresponding small-veins masks. The main reason of this is the completely different structures of the arterial and venous networks. As can be seen from Figure 4.9, on the venous side, for each cerebral region considered, all the smaller venules and veins drain, converge into one or a few larger veins. By placing a seed point on one of these larger draining veins, the entire network is then easily tracked by the VT algorithm. On the other hand, on the arterial side, the smaller arteries and branches are not generated from one or a few larger arteries: the small arteries may come form different arterial branches of the main cerebral arteries, which, as a consequence, on each small-arteries mask may not appear all well-connected between each other, as they are connected to the main arteries included in the major arteries mask.

The arterial vessels extracted from the *all-vessels mask* can be classified as cortical/pial arteries to penetrating arteries and arterioles. In fact, the reconstructed small-arteries masks have the following hierarchical

structure: a large cerebral artery (MCA, for instance) gives rise to its main branches which are still quite large (and, in the case of the MCA, can be defined as cortical/pial arteries running along the surface of the brain); then, these branches generate the arteries and arterioles penetrating into the substance of the brain that we can classify as penetrating/perforating arteries (and arterioles).

This methodology, from point 1 to point 10, is not fully automatic, as well as all the extraction procedures described for major veins, major arteries and micro-veins masks. For instance, the choice of the ROI and the manual correction to remove unwanted connections between arteries and veins are operations performed by the user and could be clearly exposed to human error. However, all other steps could be implemented into a processing pipeline that could then be applied to any other subject's MICRO imaging data set, by making this methodology as much automatic as possible, requiring the user's action only for specific operations.

4.2.6.1 Extraction of superficial/cortical arteries

In order to complete the arterial vascular model and make sure that all arteries extracted so far, from large to small, are well-connected, with no missing connections or broken vessels, a last step is needed. Namely, we extract the superficial/cortical arteries running along the surface of the brain from a different arterial map and we include such arteries in the major arteries segmentation and small-arteries masks generated in Sections 4.2.3 and 4.2.6, respectively. In fact, even if these arterial vessels should be already present on the segmentation of main cerebral arteries, some portions or segments or connections at the edges of the brain may be missing. We considering a new arterial map generated as follows:

1. The first echo time is characterized by a large Time-of-flight effect for arteries, but also for the surrounding tissue and structures (mostly white matter and gray matter). Hence, to suppress the surrounding structures, the subtraction between the first TE and the second TE is performed.

2. By taking advantage of the different intensities of arteries and veins on this subtraction map (lower intensity of veins versus higher intensity of arteries), the new arterial map is obtained by thresholding and island removal:

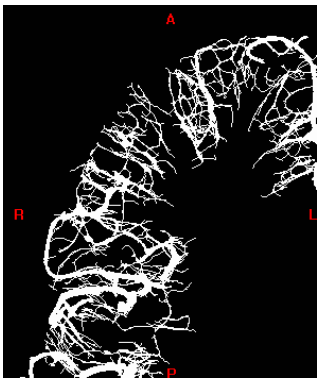
   - First, the arterial map is thresholded (with a selected threshold of 100799 – neither too large, thus with the risk of losing arteries, nor too small, thus with the risk of including also veins);
   - Next, the Matlab function `bwareaopen(amap, P=50)` is applied to the thresholded arterial map for island removal, to remove all connected components that have fewer than $P = 50$ pixels.

As in the case of the arterial map MRA_{nl}, the thresholding-based procedure adopted to generate this new arterial map performs much better than applying the Frangi vesselness filter to the subtraction map (as, in this case, also veins would be enhanced by the filter).

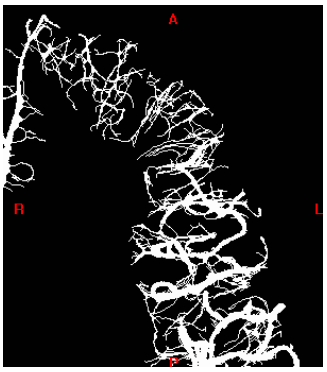
A surface mask is applied to the thresholded arterial map to get only the surface region of interest, which is then merged to the major arteries mask extracted in Section 4.2.3 and to the small-arteries masks generated in Section 4.2.6, to include also the cortical/superficial arteries in these segmentations.
In particular, in the case of the small-arteries masks reconstructed for the different vascular territories of interest (LSV, RSV, LLEV and RLEV), the VT algorithm is applied to each mask obtained after merging to assess and validate the connectivity of the obtained superficial-small-arteries mask.

The MIPs of the four final small-arteries masks are displayed in Figure 4.8. The 3D volume rendering of these segmentations is shown in Figure 4.9, where, for each of the four arterio-venous vascular territories addressed, the extracted micro-veins mask is represented with its matching small-arteries mask.

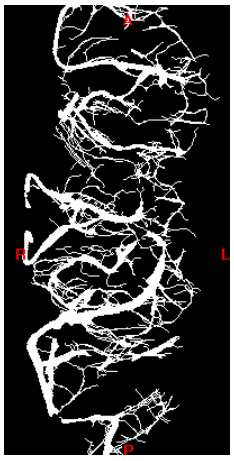
FIGURE 4.8: MIPs over the entire mask thickness of the extracted small-arteries masks for the different cerebral districts of interest, where each arterial mask is the arterial network counterpart corresponding to each one of the extracted micro-veins masks for the (A) RSV, (B) LSV, (C) RLEV and (D) LLEV vascular territories.



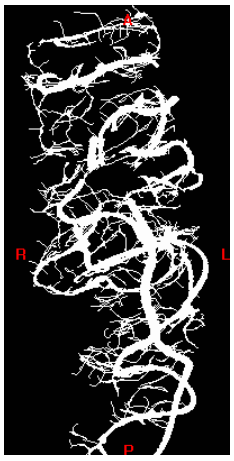
(A) RSV small-arteries mask



(B) LSV small-arteries mask



(C) RLEV small-arteries mask



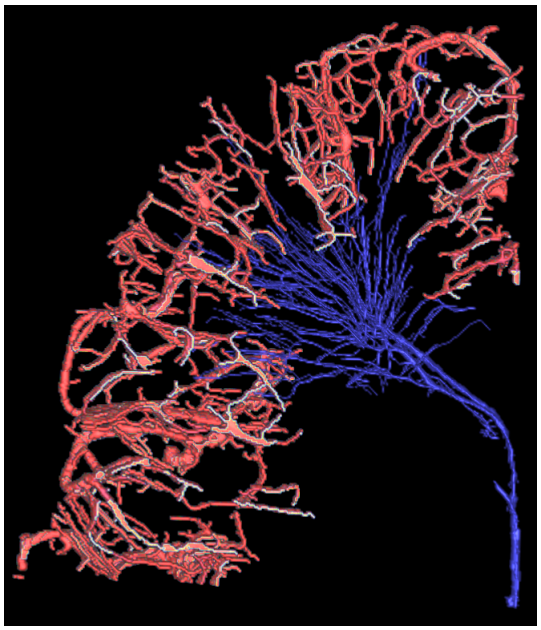
(D) LLEV small-arteries mask

4.2.7 A high-resolution map of the human brain's vasculature

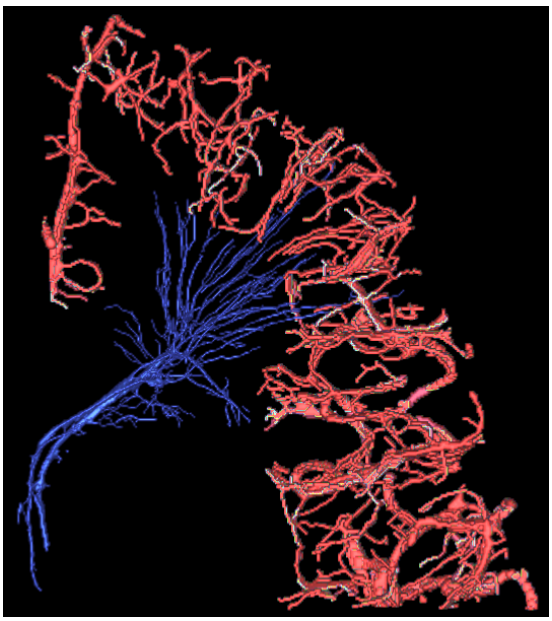
Equipped with both major veins and micro-veins masks and both major arteries and small-arteries masks, all these segmentations are merged together to generate a high-resolution map of the human brain's vasculature. The obtained arterio-venous vascular model is displayed in Figure 4.10. We remark that this vasculature map is not complete, as only selected cerebral vascular districts of arteries and veins were extracted from the MICRO imaging data. However, this work may contribute to the definition of a high-resolution subject-specific map of the human brain's vasculature using the MICRO imaging data, which could then be used in several applications, such as stroke and other vascular diseases where flow quantification and detailed vascular information is required to better diagnose the disease. Furthermore, as we will illustrate in the next sections of this chapter, from a computational modeling point of view, this arterio-venous vascular model represents the departing point to extract refined cerebral networks of arteries and veins on which simulations of the cerebral blood flow dynamics can be performed, on a subject-specific basis.

Here, generating the model shown in Figure 4.10 is also a crucial step to validate the connectivity between the small-vessels masks of the different vascular territories to the masks of the major arteries and veins. From Figure 4.10, we can observe that all the different micro-veins networks are well-connected to the corresponding main draining veins in the major veins segmentation, with longitudinal ependymal veins (via thalamostriate veins) and septal veins draining into the ICV. The small-arteries networks are also well-connected to the corresponding main feeding cerebral arteries.

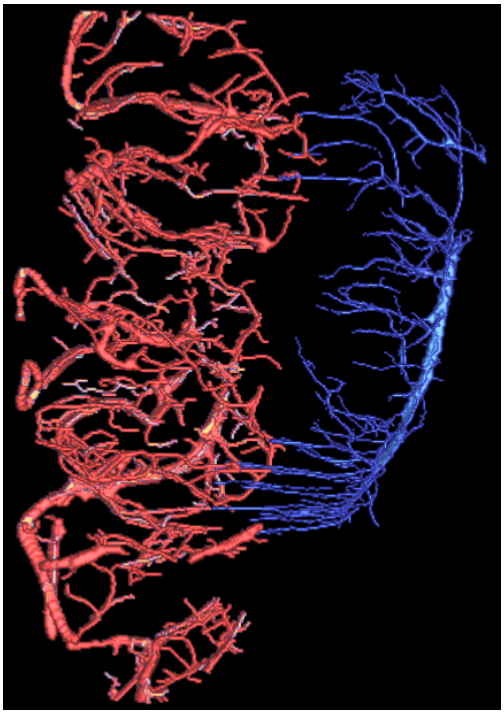
FIGURE 4.9: 3D volume rendering of the small-veins and small-arteries masks extracted for each of the four vascular territories of interest: left/right septal veins (LSV/RSV) and left/right longitudinal ependymal veins (LLEV/RLEV) vascular territories. Small draining veins territories are shown in blue, where we can see all the smaller veins draining into the larger ones. Matching arterial districts of cortical arteries, branching into penetrating arteries/arterioles, are shown in red. As the small-arteries masks were tracked by using the major arteries mask as the seed points for the VT algorithm, the connectivity between main arteries and small-arteries masks is ensured. Thalamostriate and longitudinal ependymal veins, as well as septal veins were included in the major veins segmentation, to which the reconstructed micro-veins masks will be connected.



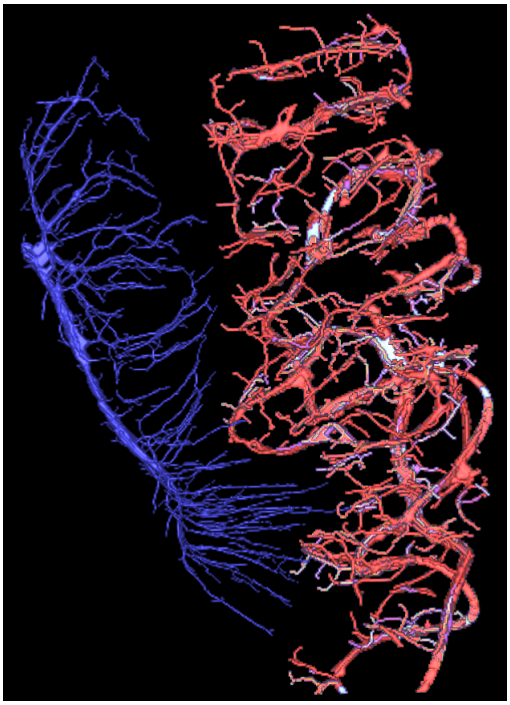
(A) RSV arterio-venous mask



(B) LSV arterio-venous mask



(C) RLEV arterio-venous mask



(D) LLEV arterio-venous mask

Before moving to the next part of this work, focused on the extraction of actual networks of vessels from the reconstructed arterio-venous segmentations, we conclude this section with some final remarks and observations.

As already pointed out, this work is based on vessel tracking, as it is fundamental to generate arterial and venous segmentations, and thus vascular models and networks, where the vessels are all well-connected. Therefore, here arterial and venous masks are extracted in a way to ensure the connectivity between vessels, even if this comes at the cost of losing others. Our main concern is indeed about the connectivity, rather than the accuracy of including as many vessels as possible but with missing connections and discontinuities.

In this work, only selected cerebral districts have been addressed to extract the corresponding small-veins and small-arteries networks. The idea is that, for the venous side, we chose those vascular territories where we were completely sure about the venous origin, where we were able to identify the major draining vein(s) of the region, into which smaller veins and venous branches drain. On the other hand, for the arterial side, it was even more difficult and complex, since for a specific vascular territory it is not possible to identify just one or few major arteries from which all the smaller arterial vessels generate from. Clearly, a possible extension of this work would be to explore other districts of the brain, such as the midbrain, where the arterio-venous separation would be much more challenging.

MATLAB was used for all processing steps. Manual correction of the binary masks was performed using SPIN-Research software developed by Prof. Haacke's research team (SpinTech MRI, Bingham Farms, MI 48025, USA). VolView (VolView 3.4, Kitware) was used for 3D rendering of the vascular networks.

FIGURE 4.10: 3D volume rendering of the human brain's arterio-venous vasculature map reconstructed from the MICRO data. Small veins are shown in dark blue, major veins are displayed un lighter blue, major to small arteries are labeled using a color map from red to green. Figure kindly provided by Dr. Sagar Buch.



4.3 Extraction of a network of vessels

In order to model and simulate cerebral blood flow in the MRI-extracted arterial and venous vascular territories, a network of vessels has to be reconstructed from each 3D segmentation. The network description must provide the connectivity between individual segments (vessels) and geometric information suitable to perform 1D/0D blood flow simulations on such reconstructed cerebral networks. To address this task, in this section we develop an algorithm, implemented in Python programming language, which, given a 3D segmentation of arteries or veins, builds the corresponding network of vessels, extracts its connectivity and computes shape-related features of vessels, such as length and radius.

The designed methodology is then applied to reconstruct the vascular networks corresponding to the segmentations of: (i) main cerebral arteries; (ii) main cerebral veins and venous sinuses; (iii) small-veins cerebral districts (of left/right septal veins and left/right longitudinal ependymal veins). With regard to the small-vessels masks of veins and arteries extracted in Sections 4.2.4 and 4.2.6, respectively, in this work we focus on the venous side for two main reasons. First, the anatomy and patho-physiology of the venous side are of great interest from both clinical and modeling points of view, given also the potential venous haemodynamic connection to some neurodegenerative diseases, as pointed out in Section 1.1. Second, it is worth noting that the extraction of a network of vessels has been a complicated and challenging process and we encountered several difficulties in addressing this task, even though departing from good and detailed segmentations, due to the high complexity of these cerebral vascular networks. Therefore, we decide to first address the venous side, as these small-veins networks have a more defined structure, with all smaller veins draining into one or a few larger vessels (the septal veins or the longitudinal ependymal veins); whereas the small-arteries territories include arteries and arterioles arising from different cortical branches and main cerebral arteries. This difference in the structure of arterial and venous networks can be clearly observed from Figure 4.9. However, the arterial side will be also tackled in the future.

The starting point of the algorithm is the original segmentation (binary mask). The Python package for multidimensional image processing `scipy.ndimage` and the module `morphology` of the Python package `scikit-image` for image processing are used. The algorithm performs the following steps in the specified order:

1. The input segmentation is pre-processed by performing the binary closing of the mask and by filling holes on both the 3D binary mask and slice by slice, on each 2D binary image, to remove possible holes in the original segmentation.
   - The function `scipy.ndimage.binary_closing` performs multidimensional binary closing with a given structuring element; the closing of an input image by a structuring element consists in the erosion of the dilation of the image by the structuring element. Here, no structuring element is provided, so an element with a square connectivity equal to one is generated by default (*i.e.*, only nearest neighbors are connected to the center, while diagonally-connected elements are not considered neighbors).
   - The function `scipy.ndimage.binary_fill_holes` fills the holes in the input 2D/3D binary object.
2. Because of the anisotropic voxel size of the original segmentation, ($0.22\times0.22\times1$ mm^3), the 3D binary mask is interpolated to get approximately isotropic voxel size in the three-space dimensions ($0.22\times0.22\times0.25$ mm^3). The function `scipy.ndimage.zoom` is adopted, which zooms the input array according to the zoom factor provided along each axis, using spline interpolation of the requested order. Here, a zoom factor of 1 is set for both x- and y-axes (no interpolation), while a zoom factor of 4 is chosen in the z-direction with spline interpolation of order 3.

3. The interpolated segmentation is processed as described at point 1.

4. The skeletonization of the interpolated segmentation is performed using the function `skimage.morphology.skeletonize_3d`. This function computes the skeleton of the input binary image, where a thinning algorithm is used to reduce each connected component in the binary image to a single-pixel wide skeleton. The Python routine implements the method proposed by Lee *et al.* [81], which uses an octree data structure to examine a $3\times3\times3$ neighborhood of a pixel. The algorithm proceeds by iteratively sweeping over the image, and removing pixels at each iteration until the image stops changing. Each iteration consists of two steps: (i) a list of candidates for removal is assembled; (ii) then, pixels from this list are rechecked sequentially, to better preserve connectivity of the image.

5. In the skeleton obtained at point 4 there are very small segments, which are likely not true vessels, but artificial segments created by the skeletonization process. In Matlab, these small segments (spurs) can be removed by using the function `bwskel(skeleton,'MinBranchLength',N)` applied to the obtained skeleton. This Matlab function removes all branches shorter than the specified minimum branch length N, where the length of the segment is calculated as the number of pixels in a branch using 8-connectivity for 2D and 26-connectivity for 3D. As we did not find an equivalent function in Python, this step of the algorithm is performed in Matlab, to apply the Matlab function `bwskel` to the centerlines mask. The choice of the minimum branch length N is not unique and it should be selected in a way that, in the best scenario, only spurious segments are removed, while all segments corresponding to true vessels are preserved in the skeleton. Here, we set different values of N for the different segmentations of arteries and veins, which will be specified afterwards.

6. The "pruned" skeleton obtained at point 5 is processed as described at point 1.

7. The skeletonization is re-computed on the skeleton obtained at point 6 to get the final centerlines mask.

At this point of the algorithm, we have the final skeleton/centerlines mask derived from the input binary mask, which defines the voxels corresponding to the vessels and from which a network of vessels will be generated according to the following next steps. First, we observe that, in Python, the image skeleton (as well as the original image segmentation) is represented and stored as a 3D array of size $N_x \times N_y \times N_z$, where each element is uniquely identified by its set of indexes (i, j, k) and has either value 1 if it corresponds to a voxel of the skeleton (segmentation), or value 0 if it is a background voxel. On the other hand, by knowing the voxel size (v_x, v_y, v_z) and the original image origin (x_O, y_O, z_O) in the 3D Euclidean space, each point/voxel of the skeleton can be also represented by the 3D coordinates (x, y, z) of its barycenter, with $x = x_O + 0.5v_x + iv_x$, for $i = 0, \ldots, N_x - 1$, $y = y_O + 0.5v_y + jv_y$, for $j = 0, \ldots, N_y - 1$, and $z = z_O + 0.5v_z + kv_z$, for $k = 0, \ldots, N_z - 1$.

8. The minimum radius of the vessel section surrounding each centerlines point is computed. The Python function `scipy.ndimage.distance_transform_edt` is adopted to get the index of the closest background element to each segmented (foreground) voxel: it calculates the Euclidean distance transform for every segmented pixel to the closest background pixel. By knowing the indexes of each centerlines voxel V and of the corresponding closest background voxel B, the 3D coordinates of the two barycenters can be obtained and the radius around the centerlines point V can be computed exactly as the length of the segment connecting V and B minus the length of the portion of segment $\overline{VB}$ lying within the background voxel, as illustrated in Figure 4.11.

9. Centerlines voxels are classified into endpoints, internal vessel points and branchpoints/bifurcation points. A voxel with only one neighbor voxel is considered as an endpoint and endpoints will define

inlet and outlet nodes of the network; a voxel with two neighbor voxels is labeled as an internal vessel point; lastly, a voxel with more than two neighbors is marked as a branchpoint and branchpoints will determine junction nodes of the network connecting two or more segments. We also note that multiple neighbor branchpoints can be found, forming a *cluster* of branchpoints.

10. Individual segments are extracted, where each segment is defined by its set of points, with the first and last points being branchpoints or endpoints. We observe that what we usually refer to as a single vessel here may be broken down into multiple connected segments, if, for instance, other vessels branch out along its length, creating intermediate branchpoints which split the vessel into different segments. From this, the network connectivity naturally follows: segments with the first or last point being an endpoint will be terminal vessels; segments sharing the same branchpoint will be connected via that junction point.

11. There are cases in which, for a given arterial or venous segmentation, the skeletonization process breaks the connectivity of the vascular structures, thus obtaining two or more disconnected regions in the centerlines mask. Regions of connected centerlines/segments are extracted and classified, according to the total region length and volume. Usually, we observe that there is a main, larger region and a few smaller regions which are not well-connected to the major one.

12. If the skeleton includes multiple regions as described at point 11, disconnected regions are connected according to some criteria based on proximity, radius similarity and point type, by proceeding as follows.

    (S1) Select a region to be connected, which is denoted by $\mathcal{R}_1$.

    (S2) Find one or more possible connections for region $\mathcal{R}_1$ at the same minimum distance $d_{\min} = dist(P_1, P_2)$, with point $P_1 \in \mathcal{R}_1$ and point $P_2 \in \mathcal{R}_2$, being $(P_2, \mathcal{R}_2)$ a point and corresponding region to make the connection with $(P_1, \mathcal{R}_1)$.

    (S2.a) If only one pair of points $(P_1, \mathcal{R}_1)$ and $(P_2, \mathcal{R}_2)$ is found for the connection based on the proximity criterion, then move to point (S3);

    (S2.b) Otherwise, select just one connection pair such that the radii r_1, r_2 of the two points P_1, P_2 to be connected have the highest similarity.

    (S2.b.i) If only one pair of points $(P_1, \mathcal{R}_1)$ and $(P_2, \mathcal{R}_2)$ is selected for the connection based on the radius similarity criterion, then move to point (S3);

    (S2.b.ii) Otherwise, if there are still multiple possible connections, select one according to the type of the two points to be connected, by favoring first a pair where one or both points are endpoints. Then move to point (S3).

    (S3) Make the connection between the two selected points P_1, P_2 depending on the type (end, branch or internal) of the points to be connected and merge the two regions $\mathcal{R}_1$, $\mathcal{R}_2$.

13. Single-vessel loops are identified and removed. A single-segment loop consists of one individual segment whose first (inlet) and last (outlet) points coincide, either being the same branchpoint or belonging to the same cluster of branchpoints. Once the loop is removed, the node type is changed accordingly: the point remains a branchpoint if still two or more segments converge to it; the point becomes an endpoint if only one segment includes it.

14. Each cluster of branchpoints is merged into a single bifurcation point, located at the barycenter between all the branchpoints of the cluster and with radius given by the average radius between all the branchpoints of the original cluster.

15. Then, for each segment we compute: mean radius r_{mean}; as the average radius between all the points defining the segment; segment length l, by summing up the Euclidean distance between the barycenters of two adjacent points; segment volume V; as follows

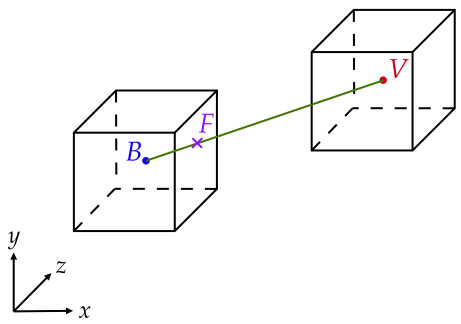
$$\begin{cases} r_{mean,i} = \frac{1}{n_{P,i}} \sum_{j=0}^{n_{P,i}-1} r_{i,j}, \\ l_i = \sum_{j=0}^{n_{P,i}-2} l_{i,j} = \sum_{j=0}^{n_{P,i}-2} \sqrt{(x_{i,j} - x_{i,j+1})^2 + (y_{i,j} - y_{i,j+1})^2 + (z_{i,j} - z_{i,j+1})^2}, \\ V_i = \sum_{j=0}^{n_{P,i}-2} l_{i,j} \pi \left(\frac{r_{i,j} + r_{i,j+1}}{2} \right)^2, \end{cases} \tag{4.1}$$

for the i-th segment, where $n_{P,i}$ denotes the number of points in the segment. The total length l_{tot} and volume V_{tot} of the entire network can then be easily calculated by knowing lengths and volumes of single segments.

16. Lastly, the vtk file corresponding to the reconstructed network is generated, with point data, cell (*i.e.* segment/vessel) data and connectivity. From the vtk file, the mesh and input files to perform simulations on such network are generated, where each segment is defined by it left node and right node, its radius and length, while nodes represent locations at which vessels bifurcate or end and define the connectivity of the network.

The skeletonization procedure based on the 3D thinning algorithm proposed by Lee *et al.* [81] using the Python function `skeletonize_3d` and the classification of the centerlines points into end, branch and internal points performed at point 9 of the algorithm were implemented by following the feature extraction algorithm included in the deep learning-based method VesSAP [136]. On the other hand, differently from the VesSAP methodology, where the Python routine `distance_transform_edt` was directly employed to compute the radius of segments, here this Python function was adopted only to get the index of the closest background element to each segmented voxel, whereas, by knowing such voxel indexes, we proposed a different approach for the calculation of the radius, as explained at point 8 of the algorithm and illustrated in Figure 4.11.

FIGURE 4.11: Schematic representation of how the proposed algorithm calculates the minimum radius of the vessel section surrounding each centerlines point. If V is the barycenter of a pixel of the computed skeleton and B is the barycenter of its closest background voxel, then the radius of the vessel section around the centerlines point V is calculate as $r_V = dist(V, B) - dist(B, F)$, where "$dist(\cdot, \cdot)$" denotes the Euclidean distance between two points, while F is the intersection point between the segment $\overline{VB}$ and the "face" of the background voxel.



The main arteries and main veins networks obtained by applying the proposed algorithm are shown in Figures 4.12 and 4.13, respectively, generated from the corresponding arterial and venous segmentations extracted in Section 4.2 and displayed in Figures 4.6 and 4.4b, respectively. From Figure 4.6, but also from

the MIP shown in Figure 4.5c, we can see that in the major arteries mask the region around the middle cerebral arteries is very noisy, with vessels not well-delineated and surrounded by spurious pixels. In order to correct this effect, the binary closing with spherical kernel was first applied to this region of the arterial mask only, before performing the skeletonization and network reconstruction procedure.

The venous networks extracted for the four small-veins cerebral districts are displayed in Figure 4.14. In this case, a manual correction was introduced before applying the network reconstruction algorithm to the LSV small-veins mask, to separate the two septal veins that, running parallel and very close to each other, were attached in some points on the original segmentation extracted (Figure 4.9b).

The tube rendering of the reconstructed cerebral networks, scaled by the estimated point radius, is illustrated in Figures 4.15, 4.16 and 4.17. From Figures 4.17a and 4.17b showing RSV and LSV venous networks, respectively, we can clearly see that the estimated radii for the larger septal veins are not consistent. In particular, these vessels present narrowing and dilation, thus resulting in a discontinuous variation in the radius. Also in the main cerebral veins network, displayed in Figure 4.16, some vessels report the same issue in the diameter estimation, such as the transverse sinuses. This aspect will be further investigated and discussed in Section 4.5 where blood flow simulations performed on the small-veins cerebral networks will allow us to validate the proposed processing pipeline and, specifically, the estimated diameter distribution for each venous network. This problem may be related to the procedure adopted to calculate the radius of the segments of a network, but also to specific characteristics of the original segmentations, that should then be improved.

Finally, Table 4.1 reports the main characteristics and geometric features for each network.

TABLE 4.1: Morphological properties and geometric features of the reconstructed cerebral networks. For each network we report: number of segments, total length and volume of the network, average (with standard deviation), minimum and maximum network radii. We can observe that the minimum detectable radius is related to/restricted by image resolution, by the voxel size, as r_{min} is exactly half of the voxel size in the x-/y-directions. The value of the minimum branch length N adopted for each network to prune the small segments is also specified in the last column of the table.

Network	**Number of segments**	l_{tot} [mm]	V_{tot} [mm^3]	r_{mean} [mm] (std.dev.)	r_{min} [mm]	r_{max} [mm]	N
Main arteries	482	$\approx$ 5256.7	$\approx$ 2724.9	0.33793 (0.22749)	0.109375	1.96442	16
Main veins	350	$\approx$ 2716.5	$\approx$ 5742.8	0.61612 (0.53577)	0.109375	2.75593	20
LSV veins	188	$\approx$ 818.9	$\approx$ 43.8	0.12026 (0.04679)	0.109375	0.53238	8
RSV veins	264	$\approx$ 1262.7	$\approx$ 71.3	0.12283 (0.05307)	0.109375	0.54688	10
LLEV veins	325	$\approx$ 1367.8	$\approx$ 163.9	0.14454 (0.12399)	0.109375	1.16148	8
RLEV veins	269	$\approx$ 992.3	$\approx$ 121.3	0.14863 (0.12385)	0.109375	1.02639	8

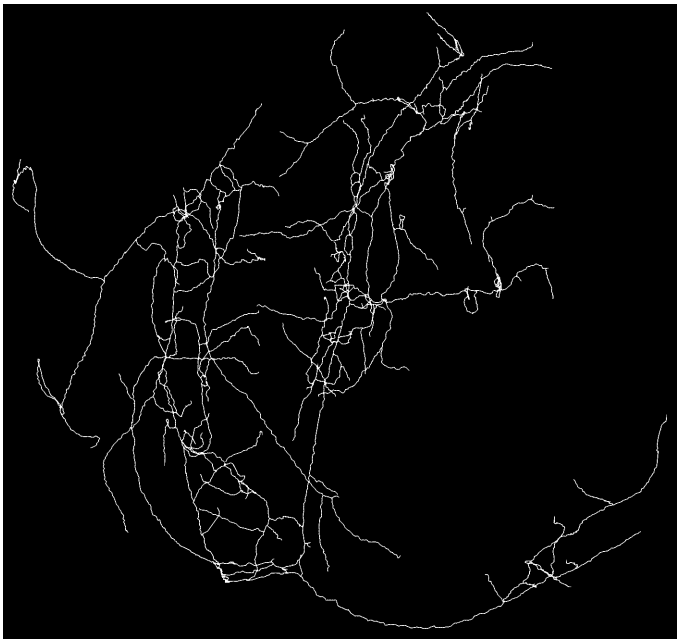
Remark 4.5. Based on the proposed algorithm and the obtained results, we conclude this section with some final considerations:

- The criteria employed to connect disconnected regions of centerlines (point 12 of the algorithm) could be improved by considering additional constraints to ensure that we are creating connections between vessels and branches that are consistent and reasonable from a "physiological/morphological" point of view.
- The reconstructed networks include not only single-vessel loops, but also multiple-segments loops. The present algorithm removes loops made of a single segment (point 13), but it does not deal with loops of multiples segments or similar structures.
- In the different cerebral networks reconstructed, centerlines and segments appear very tortuous, because of the skeletonization procedure. This problem could be solved by applying, for instance, s spline interpolation to smoothen the obtained centerlines. However, this is not addressed in the present work.

FIGURE 4.12: Main cerebral arteries network.

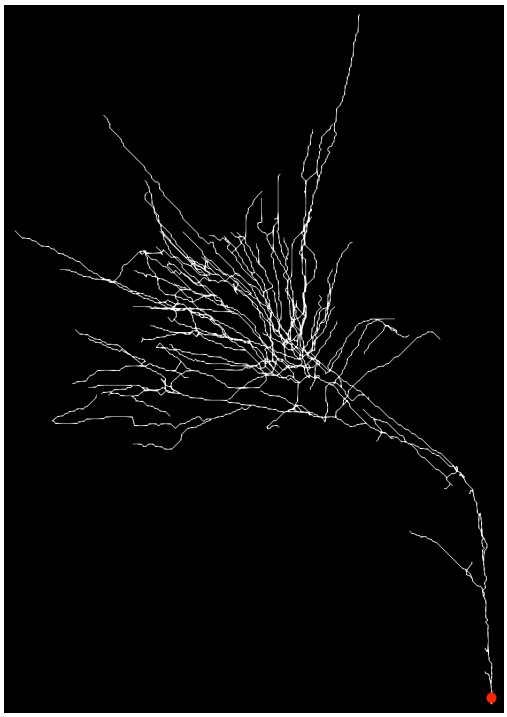


FIGURE 4.13: Main cerebral veins and venous sinuses network.

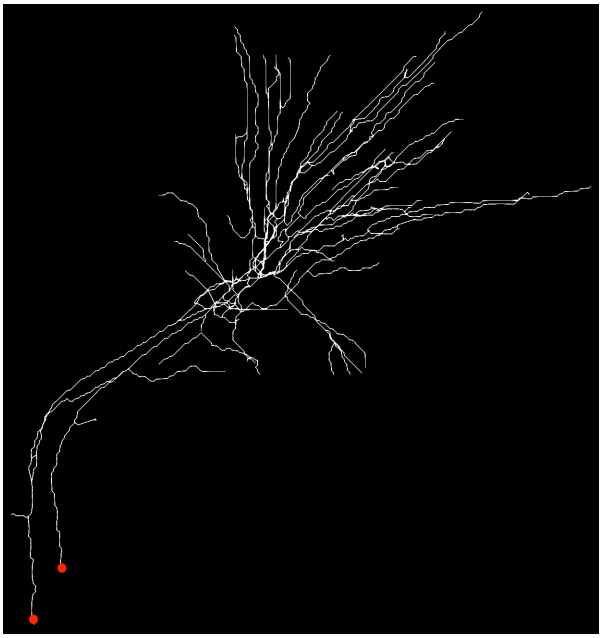


- Finally, as already pointed out, from the networks representation displayed in Figures 4.15-4.17, we can observe that the radius variation over each network, from larger to smaller vessels, is not uniform, but many vessels present narrowing, constrictions and a discontinuous variation in their radius, especially in the RSV and LSV venous networks (see Fig. 4.17a and Fig. 4.17b, respectively). This aspect will be extensively considered in Section 4.5, to discuss the effect of a wrong or imprecise estimate of the vessel radii on the outcomes of the blood flow simulations. We stress that this is a strong limitation of the proposed algorithm and a more robust method to estimate the radius of vessels needs to be developed.

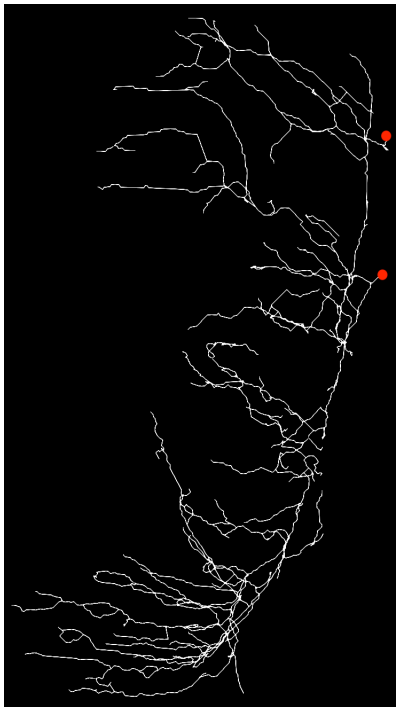
FIGURE 4.14: Cerebral venous networks reconstructed for the four small-veins vascular territories. Red dots on each venous network identify the outlet nodes; all other terminal points of each network can be regarded as inlet nodes.



(A) RSV venous network



(B) LSV venous network



(C) RLEV venous network



(D) LLEV venous network

FIGURE 4.15: Tube rendering of the main cerebral arteries network, scaled by the calculated radius. The centerlines points defining each segment can have different radius values, so each segment can have a space-varying radius. This space-varying radius may be replaced by a constant average radius over the segment. In the scale bar, radius values are in millimeters.

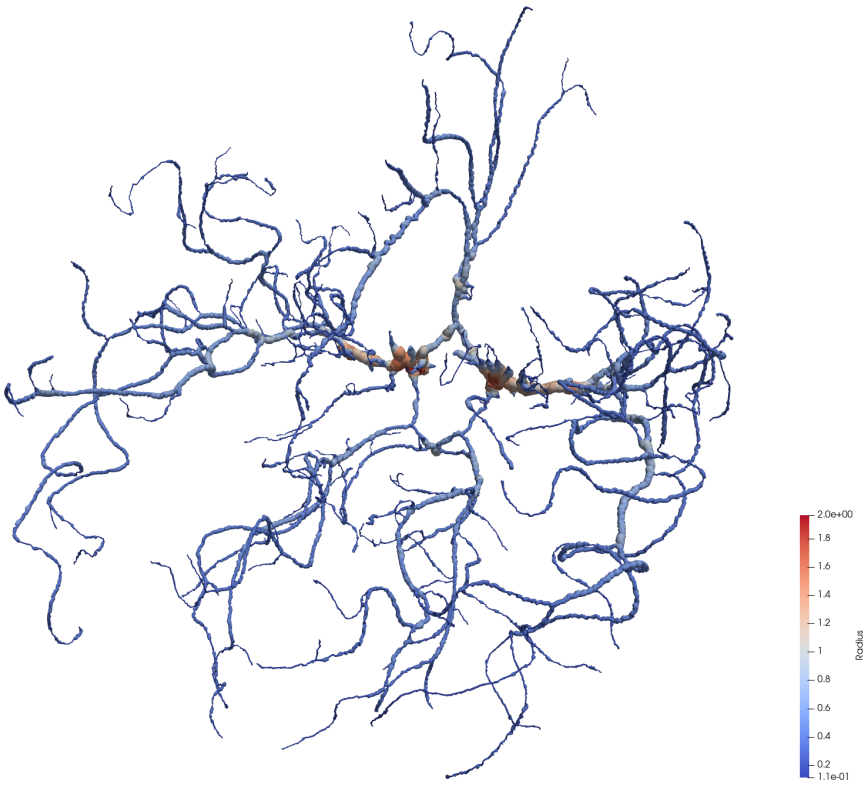


FIGURE 4.16: Tube rendering of the main cerebral veins network, scaled by the calculated radius. The centerlines points defining each segment can have different radius values, so each segment can have a space-varying radius. This space-varying radius may be replaced by a constant average radius over the segment. In the scale bar, radius values are in millimeters.

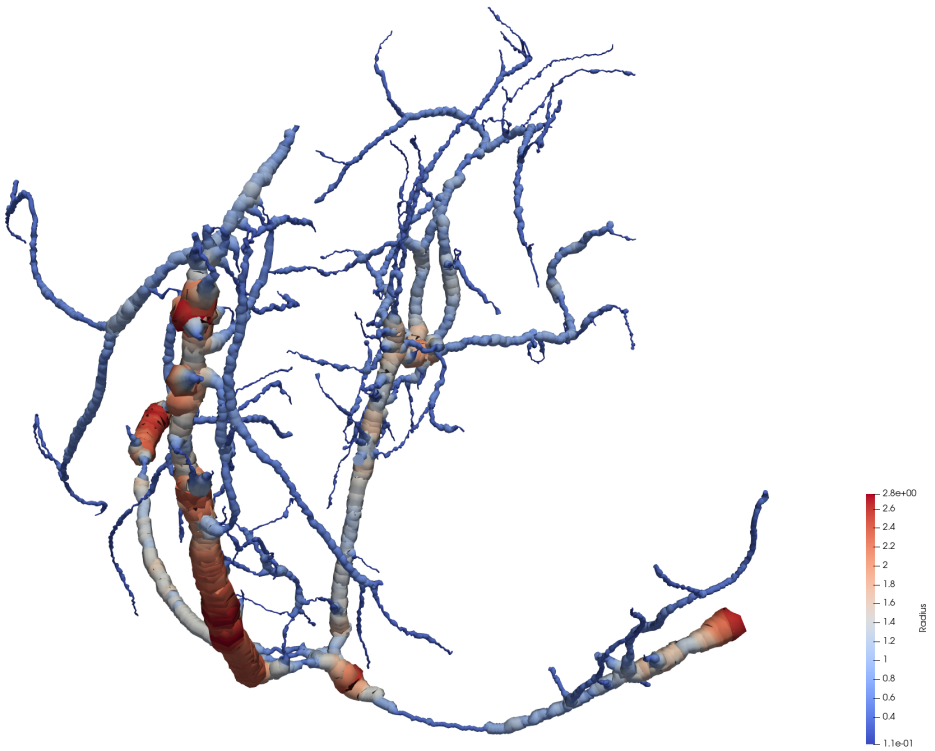
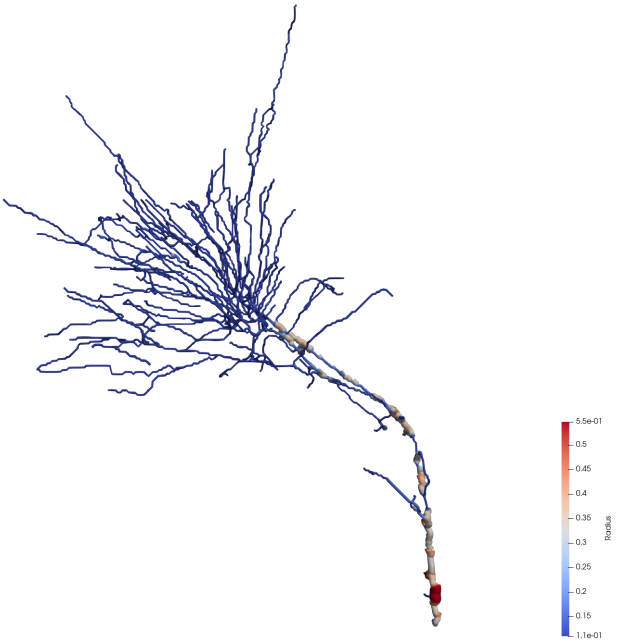
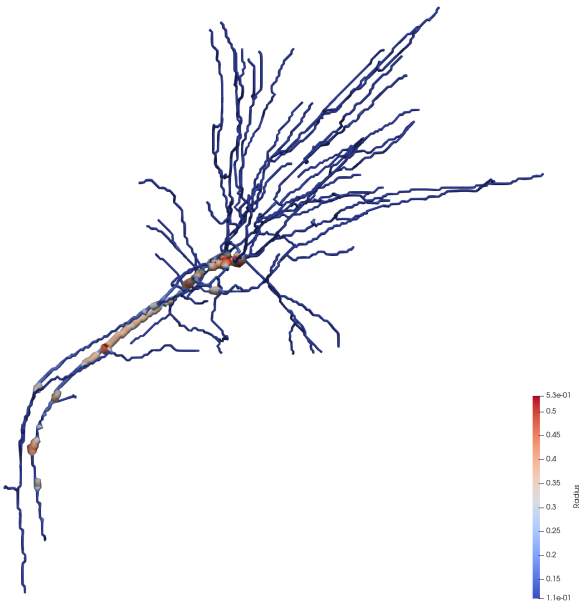


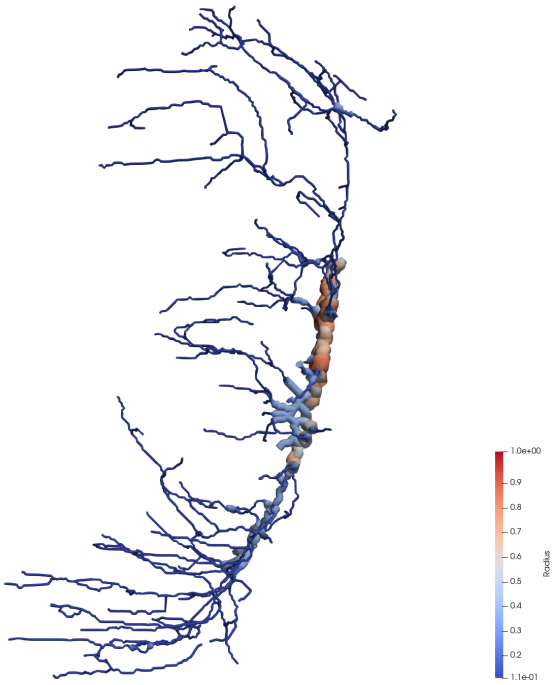
FIGURE 4.17: Tube rendering of the cerebral venous networks reconstructed for the four small-veins vascular territories, scaled by the calculated radius. The centerlines points defining each segment can have different radius values, so each segment can have a space-varying radius. This space-varying radius may be replaced by a constant average radius over the segment. In the scale bar, radius values are in millimeters.



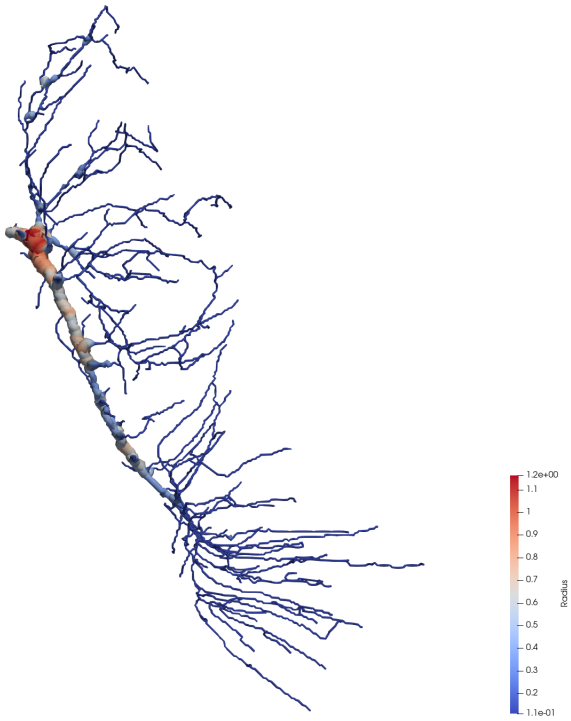
(A) RSV venous network



(B) LSV venous network



(C) RLEV venous network



(D) LLEV venous network

4.4 Networks calibration and parametrization

Pseudo-Continuous Arterial Spin Labeling (pCASL) perfusion MRI data and corresponding brain perfusion/cerebral blood flow (CBF) maps were also available, for the same subject of the MICRO data used to reconstruct the arterio-venous cerebral networks. From these CBF maps we can estimate subject-specific and region-specific perfusion rate and total flow into/out of a certain tissue, region or vascular district. Here, this information will be used to calibrate and parametrize the extracted cerebral networks and provide suitable boundary conditions to perform preliminary blood flow simulations on such networks. In this section, we present the procedure adopted for the calibration and parametrization of the MRI-reconstructed cerebral networks from the available CBF maps, focusing on the venous networks of left and right septal veins and of left and right longitudinal ependymal veins. In Section 4.5, we will then perform preliminary blood flow simulations on these venous networks.

Arterial Spin Labeling (ASL) is a MR imaging technique adopted to assess cerebral blood flow noninvasively (no contrast agent is used). ASL is based on the principle of magnetically labeling inflowing arterial blood protons prior to their entry into the tissue of interest. As such, it can be viewed as a tracer technique, with water acting as the natural endogenous tracer to estimate tissue perfusion. The label is created by applying radiofrequency pulses to invert the bulk magnetization of the blood water protons. Then, images are acquired after the labeling and inflow period, by using rapid acquisition techniques. A pair of images is always acquired: a labeled image, in which the blood water magnetization is inverted, and a control image, in which the blood water magnetization is not inverted. The signal difference between labeled and control images is proportional to the amount of magnetization inverted and delivered to the tissue. Therefore, if all the labeled blood has arrived at the imaging voxel at the time of image acquisition, the signal difference will be proportional to cerebral blood flow CBF, typically measured in mL/100 g of tissue/minute.
One of the main implementations of ASL is pseudo-Continuous ASL (pCASL), where a long labeling period (1–2 s) is made up of a train of very short ($\approx$ 1 ms) pulses. This train of short pulses is designed to invert the inflowing blood magnetization in an adiabatic or pseudo steady-state manner.
As described above, ASL measures brain perfusion at the tissue level, at the level of capillaries. ASL measures the tissue perfusion by the inflowing arterial blood and, as perfusion takes place at the capillary level, we can assume that the blood delivered to the tissue from the arterial side is then drained by the corresponding venous side and that the perfusion measurements are also valid for regions of venules and small veins. For this reason, the acquired CBF map can be used to quantify the perfusion rate for regions/territories of small arteries and small veins, but not for the larger vessels (both large arteries and veins), where the CBF would be very high and overestimated.

The pCASL sequence was acquired with the following imaging parameters: TR/TE = 3500/22.76 ms, flip angle = 180°, bandwidth = 2003 Hz/pixel, voxel resolution = 3.5 mm isotropic, with 30 measurements at 3T. The acquired perfusion data were then processed in Matlab, to generate the corresponding CBF map. The co-registration of functional (CBF map) and anatomical (MICRO data) images was also performed, in particular by co-registering the CBF map to the same matrix of the high-resolution SWI data. We observe that, from the perfusion data, we get the cerebral blood flow as a perfusion rate (volume/mass/time), rather than the actual blood flow (volume/time) coming to the brain or to a specific region of the brain. The idea is that, if we know the average brain perfusion and the mass of the perfused brain volume, then we can estimate the blood flow rate as volume/time.

Remark 4.6. The main drawback of using co-registered data is that registration is based on interpolation, which can cause a loss of precision in the perfusion map and underestimation of the CBF values. We are aware of this limitation, but, on the other hand, using the original, non-registered CBF data would have

the disadvantage that we can only approximately select the region of interest corresponding to any of the reconstructed cerebral networks of which we want to estimate the (average) CBF/perfusion values.

We depart from the cerebral venous networks reconstructed in Section 4.3 for the four venous vascular territories of interest and displayed in Figure 4.14. The vascular network corresponding to each of these small-veins districts is parametrized and calibrated and boundary conditions are provided as follows:

1. Given the set of nodes, inlet/outlet nodes and junction nodes, defining the network of vessels, as described in Section 4.3, each node provided with its 3D spatial coordinates, the smallest convex hull $\mathcal{C}$ including the entire network is computed using the Python library `scipy.spatial` for spatial data structures and algorithms. The volume of the convex hull $\mathcal{C}$ is calculated, denoted by $V_{\mathcal{C}}$, which can be regarded as an estimate of the brain volume perfused by the vascular region of interest.

2. Assuming a constant brain density $\rho_{br} = 1.040\,\mathrm{g/cm^3}$, the corresponding brain mass can be calculated as $m_{\mathcal{C}} = d_{br} V_{\mathcal{C}}$.

3. The computed convex hull $\mathcal{C}$ is overlaid on the co-registered CBF map and the average perfusion rate CBF_{avg} corresponding to the brain vascular territory is estimated as the mean CBF value between all the voxels of the perfusion map falling into $\mathcal{C}$. In particular, given the set of equations defining $\mathcal{C}$, a point is in the hull if and only if, for every equation (describing the hull facets), the scalar (dot) product between the point and the facet normal vector plus the offset is less than or equal to zero. For reasons related to numerical precision, we do not compare to zero, but to a small, positive constant $tol = 10^{-12}$. For each facet, the pair [normal, offset] forming the hyperplane equation of the facet is provided.

4. The total blood flow Q_{tot} flowing to the vascular territory is then obtained as $Q_{tot} = CBF_{avg} m_{\mathcal{C}}$.

5. Terminal nodes of the network are classified into inlet and outlet nodes: one or a few outlet nodes are located at the outflow points of the larger draining veins (septal veins or longitudinal ependymal veins); all other terminal nodes are classified as inlet nodes, which drain venous blood into the network. We note that the selected outlet nodes will be also the points of connection to the major veins network, where the septal veins drain into the left and right internal cerebral veins and the longitudinal ependymal veins converge also into the ICV via the thalamostriate veins.

6. For each segment of the network we consider a constant in space average radius given by the formula in (4.1).

7. Outlet nodes: a time-varying venous pressure curve $P_{dist}(t)$ is prescribed as distal pressure to each outlet node. This pressure curve is taken from the simulation results obtained from a global, closed-loop model of the human circulation [144], in the cerebral vein which is the closest to the outlet vessels of our cerebral venous networks, that is the left/right ICV.

8. Inlet nodes: the total blood flow Q_{tot} estimated at point 4 is distributed among all the inlet nodes using Murray's law [106, 105] and assuming that the flow rate Q is proportional to the radius cubed r^3, as follows

$$Q_{in,j} = \frac{r_j^3}{\sum_{i=1}^{N_{inlets}} r_i^3} Q_{tot}, \tag{4.2}$$

where N_{inlets} is the number of inlet nodes of the network, r_j is the radius of the j-th inlet node (corresponding to the radius of the segment to which the node belongs) and $Q_{in,j}$ is the estimated inflow to the j-th inlet node. Then, the j-th inlet node, for $j = 1, \ldots, N_{inlets}$, is attached to a RCR terminal model,

as displayed in Figure 4.18, whose proximal and distal resistances $R_{p,j}$ and $R_{d,j}$, respectively, and compliance C_j are calibrated as follows. The total terminal resistance $R_{tot,j} = R_{p,j} + R_{d,j}$ is calculated as

$$R_{tot,j} = \frac{P_{CP} - P_j}{Q_{in,j}}, \tag{4.3}$$

where $Q_{in,j}$ are P_j are the estimated inflow and a prescribed physiological pressure to the j-th node, respectively, and P_{CP} is a constant capillary pressure, here set to 25 mmHg. For the pressures P_j, for $j = 1, \dots, N_{inlets}$, we assume the same pressure in all inlet nodes, given by $P_j = \text{mean}(P_{dist})$. The proximal terminal resistance $R_{p,j}$ is set equal to the characteristic impedance Z_0 of the vessel, that is

$$R_{p,j} \equiv Z_{0,j}, \quad \text{with } Z_0 = \frac{\rho c_0}{A_0}, \tag{4.4}$$

and, in turn, the distal terminal resistance $R_{d,j}$ is obtained as

$$R_{d,j} = R_{tot,j} - R_{p,j} = R_{tot,j} - Z_{0,j}. \tag{4.5}$$

On the other hand, for estimating the compliance C_j of the RCR terminal model, for $j = 1, \dots, N_{inlets}$, we consider a total systemic venous compliance $C_{sys,ven} = 146$ mL/mmHg [32] and cardiac output $CO = 100$ mL/s. Then, the total compliance of the venous vascular network under consideration is computed as

$$C_{ven} = \frac{Q_{tot}}{CO} C_{sys,ven}. \tag{4.6}$$

The total venous compliance C_{ven} of the network includes the contribution of both the (1D) compliance of the vessels of the network and the (0D) compliance of the RCR terminal elements. Hence, the compliance $C_{ven,0D}$ to be distributed among the RCR terminal models attached to the inlet nodes of the network is computed as follows

$$C_{ven,0D} = C_{ven,sys} - C_{ven,1D} = C_{ven,sys} - \sum_{i=1}^{N_S} C_{1D,i} \tag{4.7}$$

where N_S is the number of segments in the network and $C_{1D,i}$ is the compliance of the i-th segment, calculated according to the following formula

$$C_{1D} = l \left(\frac{\partial A}{\partial p} \right) \Big|_{A=A_0} = \frac{l A_0}{\rho c_0^2}. \tag{4.8}$$

Finally, the terminal venous compliance of the network is distributed among the RCR models attached to the inlet nodes, using Murray's law and assuming that $C \propto Q \propto r^3$, namely

$$C_j = \frac{Q_{in,j}}{Q_{tot}} C_{ven,0D}, \tag{4.9}$$

for $j = 1, \dots, N_{inlets}$.

We note that, the convex hull $\mathcal{C}$ computed for each vascular network perfectly encloses the network itself. However, the territory perfused by such network is expected to be more extended around it. For this reason, once the convex hull $\mathcal{C}$ and its barycenter $B_{\mathcal{C}}$ are calculated for a given network, the convex hull should be expanded, for instance by moving away each point of the hull surface along the direction defined with the

barycenter of a certain distance, to slightly enlarge the brain region perfused by the vascular network. This improvement is not addressed in the present thesis, but it will be kept in mind for future work.

Table 4.2 summarizes the main features of the topology of each venous network, while Table 4.3 reports the calibration results obtained for the four different small-veins cerebral networks.

The time-varying pressure curve prescribed at the outlet nodes of each network, which corresponds to the pressure waveform in the ICV, is displayed in Figure 4.19 (left plot), together with the time-varying curve for the capillary pressure, which is also taken from the simulation results of the global mathematical model proposed by Toro *et al.* [144] and will be applied as the inlet pressure to the *RCR* terminal models in the transient simulations performed in the next section.

FIGURE 4.18: Schematic representation of the coupling between the inlet node n_{in} of a vessel and a *RCR* terminal model. The black arrow indicates the expected direction of flow, for our choice of the boundary conditions prescribed to the network, as venous blood is drained from the inlet nodes of the network towards the outflow nodes.

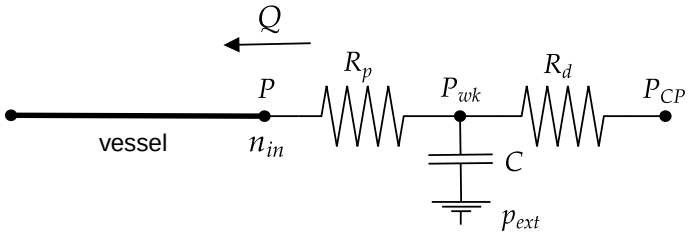


TABLE 4.2: Main features of the topology of the MRI-reconstructed small-veins cerebral networks. For each network we report: number of segments N_S, number of outlet nodes $N_{outlets}$, inlet nodes N_{inlet} and junction nodes N_{junc}.

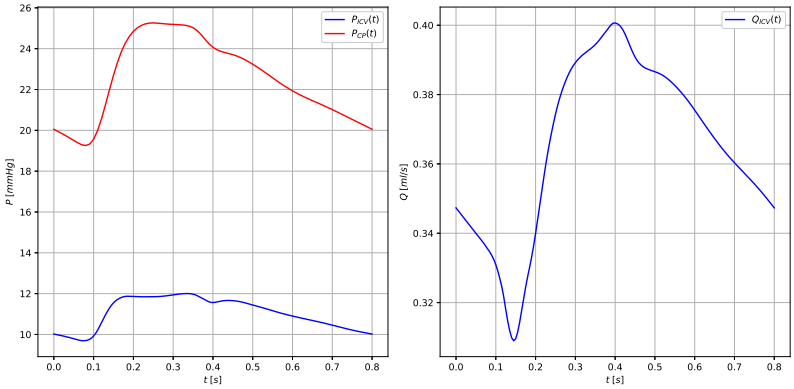
Network	N_S	$N_{outlets}$	N_{inlets}	N_{junc}
LSV veins	188	2	62	97
RSV veins	264	1	94	139
LLEV veins	325	1	116	169
RLEV veins	269	2	88	141

TABLE 4.3: Calibration results for the MRI-reconstructed small-veins cerebral networks. For each network we report: volume $V_{\mathcal{C}}$ of the smallest complex hull $\mathcal{C}$ including the network of vessel, corresponding brain mass $m_{\mathcal{C}}$, estimated average CBF of the vascular territory CBF_{avg} and standard deviation, computed total blood flow Q_{tot} flowing to the network, maximum and minimum inflow values to a single inlet node $Q_{in,j}$, maximum and minimum values of the estimated total resistance $R_{tot,j}$ and compliance C_j of the *RCR* terminal models attached to the inlet nodes. Here the pressure to all inlet nodes is set to $P_j = \text{mean}(P_{dist}) = 11.0576$ mmHg, for $j = 1, \ldots, N_{inlets}$, where the prescribed venous pressure curve $P_{dist}(t)$ is shown in Figure 4.19 (left plot).

Network	$V_{\mathcal{C}}$ [cm^3]	$m_{\mathcal{C}}$ [g]	CBF_{avg} (std.dev.) [mL/100 g tissue/min]	Q_{tot} [mL/s]	max($Q_{in,j}$) [mL/s]	min($Q_{in,j}$) [mL/s]	max($R_{tot,j}$) [dyne·s/cm^5]	min($R_{tot,j}$) [dyne·s/cm^5]	max(C_j) [cm^5/dyne]	min(C_j) [cm^5/dyne]
LSV veins	11.490	11.950	29.011 (8.981)	5.778e-02	7.695e-03	7.116e-04	2.612e+07	2.416e+06	4.849e-09	4.484e-10
RSV veins	20.961	21.799	32.468 (9.783)	1.180e-01	1.250e-02	7.295e-04	2.548e+07	1.487e+06	1.609e-08	9.393e-10
LLEV veins	15.226	15.835	24.356 (6.771)	6.428e-02	2.227e-02	1.272e-04	1.462e+08	8.348e+05	1.546e-08	8.832e-11
RLEV veins	12.353	12.847	23.819 (5.530)	5.100e-02	1.184e-02	8.977e-05	2.071e+08	1.570e+06	6.532e-09	4.953e-11

The blood viscosity μ is characterized by the constitutive relation (3.121)-(3.124) proposed by Pries *et al.* [113]. As regards the pressure-area relation and its parametrization, we consider the same tube law adopted for the one-dimensional networks of major arteries and major veins in the global model for the full human

FIGURE 4.19: (Left plot) Time-varying pressure curves prescribed as boundary conditions to the cerebral venous network, taken from the simulation results of the global, closed-loop model of the human circulation proposed by [144]: $P_{dist}(t) \equiv P_{ICV}(t)$ (blue line) is the pressure curve in the ICV, imposed at the outlet nodes of each network; $P_{CP}(t)$ (red line) is the capillary pressure curve prescribed at the inlet of the RCR terminal models attached to the inlet nodes of each network. (Right plot) Corresponding flow waveform in the ICV.



circulatory system [144]. The tube law employed in [144] accounts also for the viscoelastic properties of vessel wall; however, here we restrict to the elastic case, that is

$$p(x,t) = \psi(A(x,t); A_0(x), K(x), P_0) + p_{ext}(x,t), \tag{4.10}$$

with

$$\psi(A(x,t); A_0(x), K(x), P_0) = K(x)\left[\left(\frac{A(x,t)}{A_0(x)}\right)^m - \left(\frac{A(x,t)}{A_0(x)}\right)^n\right] + P_0. \tag{4.11}$$

The elastic term ψ depends on the reference pressure P_0, the space-varying reference cross-sectional area $A_0(x)$ and the vessel wall stiffness $K(x)$; p_{ext} is, as usual, the external pressure acting on the vessel. Suitable choices of geometric and mechanical parameters in the tube law allow to parametrize the pressure-area relation (4.10) differently for arteries and veins. We note that the elastic tube law (4.10) corresponds with the tube law adopted in Chapter 2 and in the first part of Chapter 3, in Section 3.3. However, in these previous chapters, such tube law was applied to solve arterial networks, whereas here we consider venous vessels. For veins, we set $m = 10$ and $n = -1.5$. Following [99, 144], the positive function $K(x)$ is obtained from the reference wave speed c_0 assumed for each vessel, as follows

$$K = \frac{\rho c_0^2}{(m-n)}, \tag{4.12}$$

where the venous reference wave speed c_0 is estimate as

$$c_0 = c_{0,max} - (c_{0,max} - c_{0,min})\left(\frac{r_0 - r_{min}}{r_{max} - r_{min}}\right)^{\frac{1}{2}}, \tag{4.13}$$

where $r_0(x)$ is the reference radius corresponding to $A_0(x)$. We set: $c_{0,max} = 400$ cm/s, $c_{0,min} = 150$ cm/s, $r_{max} = 0.8$ cm and $r_{max} = 0.08$ cm, taken from [144]. For full details about the tube law parametrization for veins (and arteries), we refer to [99, 144]. We observe that the tube law employed in [144] accounts also for the viscoelastic properties of vessel wall. However, such viscoelastic tube law has never been parametrized for veins as small as the ones extracted from the MICRO imaging data and included in our venous networks. For this reason, all the simulations presented in this study are performed adopting the elastic tube law (4.10) and a parametrization of the viscoelastic tube law for our MRI-reconstructed cerebral networks will be addressed in the future.

The constant blood density is set to $\rho = 1.060$ g/cm^3, the reference venous pressure in (4.11) is $P_0 = 6666.0$ dyne/cm^2 (≈ 5 mmHg), while we prescribe a constant in space and time external pressure p_{ext},

chosen as the minimum pressure value reached by the time time-varying pressure curve $P_{dist}(t)$ reduced by 5%, that is $p_{ext} = 95\%\min(P_{dist})$.

4.5 Blood flow simulations and results

In this section, we present and discuss the results obtained by performing preliminary blood flow simulations on the MRI-reconstructed cerebral venous networks, calibrated and parametrized as described in Section 4.4. As already pointed out, the main purpose of these simulations is the validation of the proposed processing pipeline itself, to assess whether the obtained cerebral networks are consistent from a physiological and fluid-dynamics point of view and to test their ability to predict physiologically reasonable results in terms of pressure ranges in the corresponding vascular territories.

We carry out two sets of simulations: steady state and transient simulations. In the first case, a constant pressure is prescribed at the outlet nodes of each network, given by the average value of the time-varying pressure curve in the ICV $P_{dist}(t) = P_{ICV}(t)$, while at each inlet node we impose a constant flow rate (no RCR terminal model attached), given by the inflow $Q_{in,j}$ obtained by distributing the total inflow Q_{tot} among all the inlet nodes using Murray's law, for $j = 1, \dots, N_{outlet}$. On the other hand, transient simulations are performed by prescribing the time-varying pressure curve in the ICV $P_{dist}(t)$ at the outlet nodes, wheres inlet nodes are attached to RCR terminal models parametrized as illustrated in Section 4.4, where the time-varying capillary pressure $P_{CP}(t)$ is imposed as inlet pressure to the terminal element (see Figure 4.18).
As initial conditions, we set zero flow and pressure given by the average value of $P_{dist}(t)$ in all vessels, for both steady state and transient simulations. All simulations are performed adopting the second-order path conservative scheme presented in Section 3.4.1.1 and the LTS strategy described in Section 3.4.1.2. The complete set of computational parameters used in the simulations for the MRI-reconstructed venous cerebral networks is reported in Table 4.4. As these are preliminary tests, here fully 1D simulations are performed only.

TABLE 4.4: Computational parameters adopted in the 1D numerical simulations for the MRI-reconstructed venous cerebral networks.

Parameter	Value
Max mesh size, $\Delta x_{\max}$	1 mm
CFL number, CFL	0.9
Cardiac cycle, T_0	0.8 s
Final time, t_{End}	10.0 s

4.5.1 Steady state simulations

Steady state simulations are performed for all the four cerebral vascular networks. Figure 4.20, from panel (A) to (D), shows the venous pressure throughout each cerebral network obtained at steady state. What is immediately observed from these results is that for the venous networks of left and right longitudinal ependymal veins (top row in Figure 4.20) venous pressures are within the expected physiological range, whereas for the cerebral networks corresponding to the left and right septal veins (panels (C)-(D) in Figure 4.20) we obtain very high pressure gradients across the networks, with peaks in the venous pressure of 95-100 mmHg in some districts of these networks, which are completely non-physiological. For instance, in the LSV venous network (see Figure 4.20d), the venous pressure is already considerably increased with respect to the expected physiological range along the two septal veins.

To investigate this scenario thoroughly, for each venous network, from the flow rate obtained at steady state in each vessel we estimate the corresponding wall shear stress (WSS) value. The wall shear stress

distribution as a function of vessel diameter and the histogram of the radius distribution in each cerebral network are displayed in Figures 4.21 and 4.22 for the RLEV and LLEV venous networks, respectively, and in Figures 4.24a and 4.23, for the LSV and RSV cerebral networks, respectively. Firstly, from these plots we observe that in all networks there is very low variability in the values of the radius. In fact, most vessels of each network have a radius around 0.11 mm that is exactly half of the resolution in the x and y directions of the MICRO data we departed form, already prompting that the methodology adopted for the radius estimation in each segment may be not very robust. On the other hand, the wall shear stress results are the confirmation of what previously observed for the steady state pressure results shown in Figure 4.20. Indeed, from Figures 4.21 and 4.22, we can see that, for both RLEV and LLEV venous networks, the estimated values of the wall shear stress are overall reasonable when compared to reference values found in the literature for small veins and venules (see for instance the experimental study presented by Lipowsky *et al.* [86]). In the RLEV network, WSS values in all vessels are below 30 dyne/cm^2; for the LLEV venous network we have larger values in some small internal vessels of the network, up to 80-85 dyne/cm^2, but the range covered by these WSS values is still reasonable. On the other hand, as expected, Figures 4.23 and 4.24a show very high wall shear stress values in both RSV and LSV venous networks, reaching peaks of approximately 600 and 400 dyne/cm^2, respectively. These very large values in the WSS are found in many internal vessels and in the outlet vessels of both networks (blue diamonds in Fig. 4.23 and Fig. 4.24a). Looking back at the pressure results shown in Figure 4.20, we can observe that these two networks present very strong and steep narrowing and discontinuous variations in the radius, with jumps and constrictions that are not consistent and physiological. The radius does not vary and decrease uniformly from the larger to the smaller vessels of each network. This is quite evident in the septal veins of both networks, where in some tracts these vessels are very narrow, while becomes larger in others. On the other hand, for the RLEV and LLEV venous networks, this scenario is not reported. In fact, as we can appreciate from Figure 4.20, in these networks we have that the larger longitudinal ependymal veins overall do not present narrowing or strong reduction in the diameter, which decreases uniformly from the outlet node along the vessel; all smaller veins draining into the larger ones are generally of very similar size.

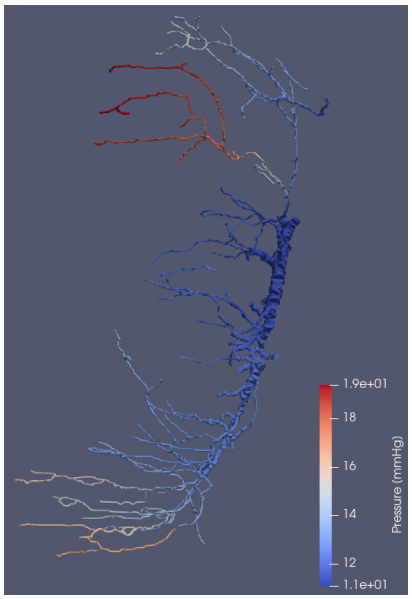
As a consequence, these results lead us to the conclusion that the very high, non-physiological pressure gradients and the large WSS values obtained for the RSV and LSV venous networks are primarily caused by a wrong estimation and distribution of the vessel radii in such networks. This conclusion is also supported by the results obtained by manually modifying the radii of the two septal veins in LSV network. Here, as we can see from Figure 4.20e), a constant radius is adopted for all segments composing the two septal veins, taken as the maximum value of the original radius distribution in these vessels. From this figure we can see that, even though it is still not within the expected physiological range, the venous pressure at steady state is significantly reduced throughout the entire network, with peaks in the venous pressure around 43 mmHg, suggesting that the issues observed in the original network are related to the estimation of the vessel radii. In this modified network, the WSS values are also considerably reduced, especially in the outlet vessels, as shown in Figure 4.24b.

Therefore, this analysis suggests that, in the processing pipeline proposed for the extraction of vascular networks from the high-resolution MICRO imaging data, a more robust algorithm is required to obtain reasonably good estimates of the true radii of a network, especially when dealing with very small vessels.

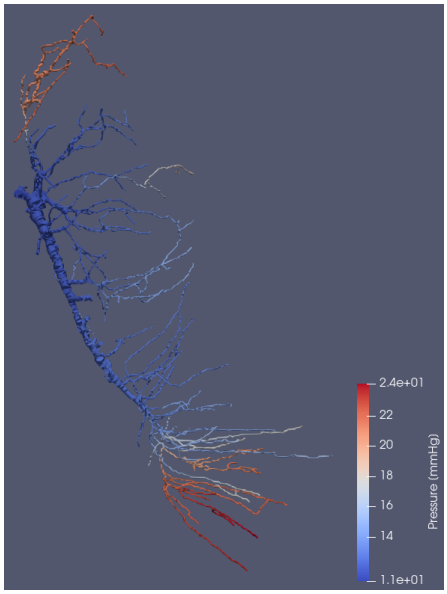
4.5.2 Transient simulations

Transient simulations are then performed only for the venous networks for which physiological results were obtained from the steady state simulations, namely the RLEV and LLEV cerebral networks. Figure 4.25 shows the mean venous pressure throughout each cerebral network over a complete cardiac cycle. We

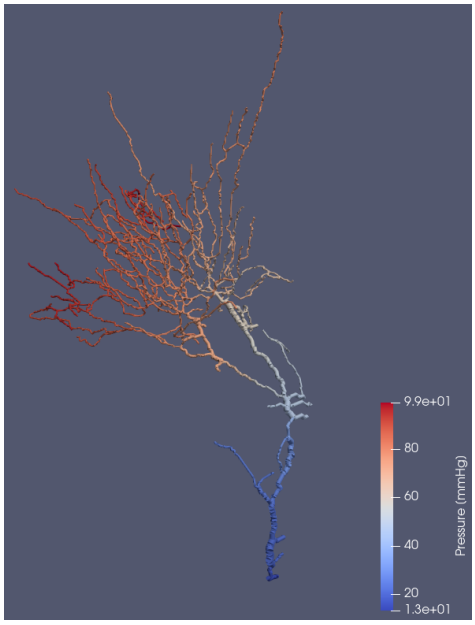
FIGURE 4.20: Venous pressure throughout each cerebral network obtained at steady state. Panel (E) shows the results obtained for the LSV venous network by manually modifying the radii of the larger vessels to remove narrowing and constrictions in these vessels.



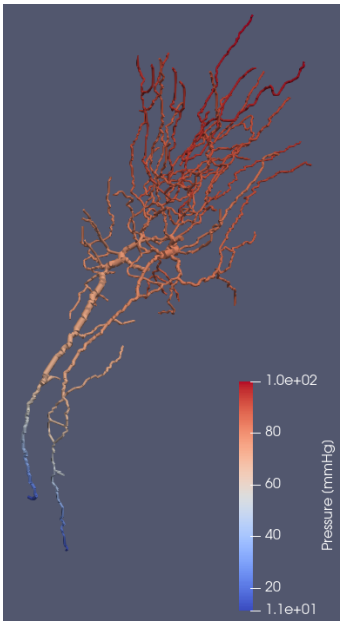
(A) RLEV venous network



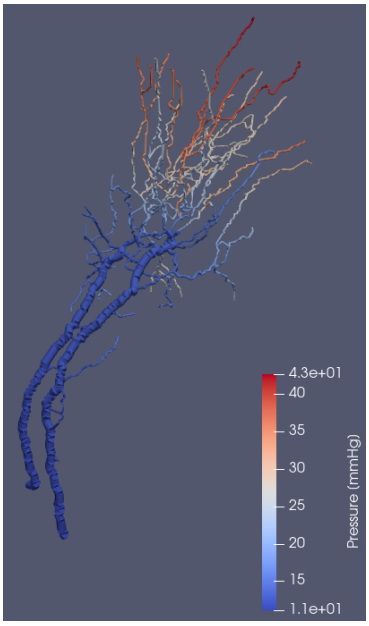
(B) LLEV venous network



(C) RSV venous network



(D) LSV venous network with original radii



(E) LSV venous network with modified radii

can observe that the mean pressure distribution over each venous network is within the expected physiological range, with pressures varying approximately between 11 and 16 mmHg in the RLEV network, and between 11 and 17 mmHg in the LLEV network. From Figure 4.25 we can see that lower values of pressure are found along the longitudinal ependymal veins and in the smaller veins closest to the outlet node(s) of each network; on the other hand, the largest, but still reasonable, values of pressure are reported in the "upper " and "lower" regions of each network, according to the 3D perspective shown Figure 4.25. This suggests that vessels closest to the outlet nodes are more affected by the distal venous pressure, corresponding to the pressure in the ICV, which is prescribed to these nodes, whereas vessels that are more

FIGURE 4.21: Wall shear stress and radius distributions in the RLEV venous network. In each vessel, the wall shear stress is estimated from the flow rate obtained at steady state.

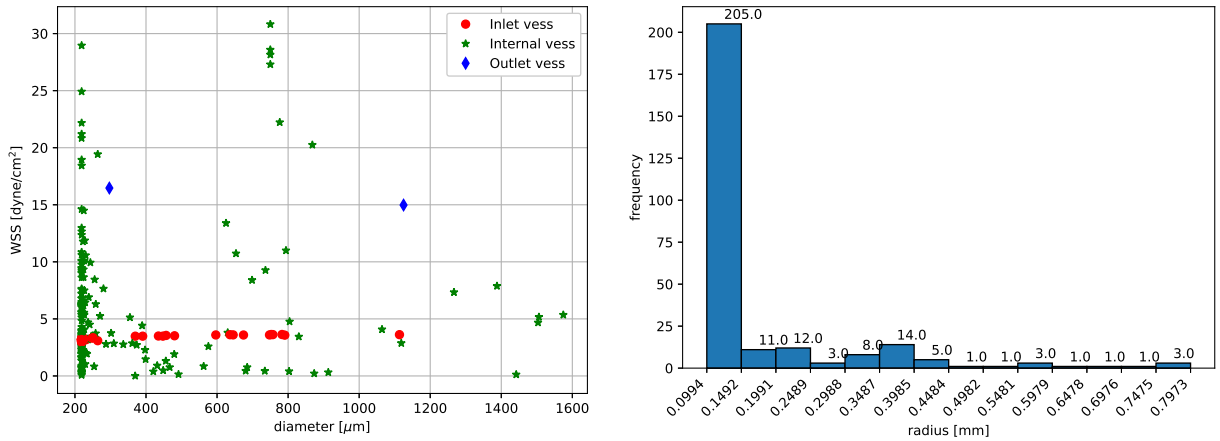


FIGURE 4.22: Wall shear stress and radius distributions in the LLEV venous network. In each vessel, the wall shear stress is estimated from the flow rate obtained at steady state.

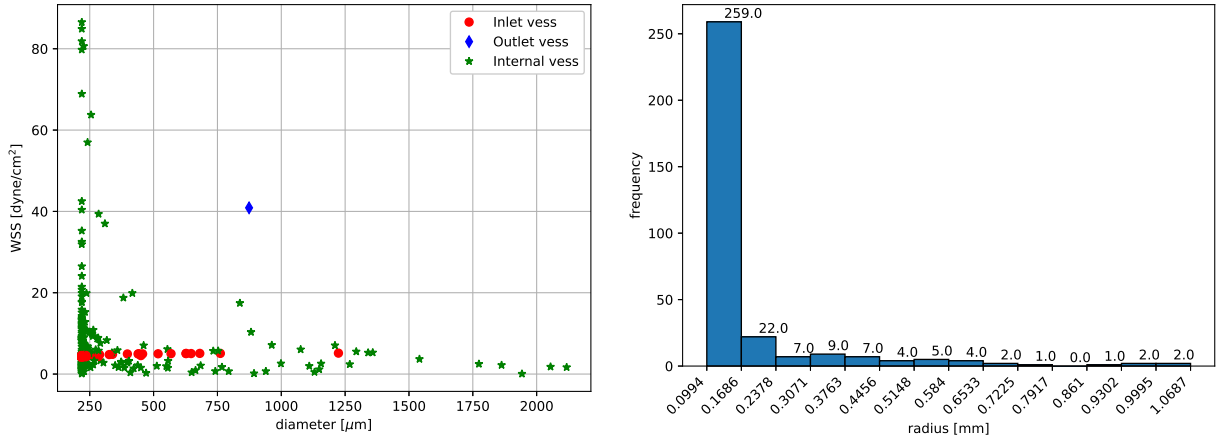
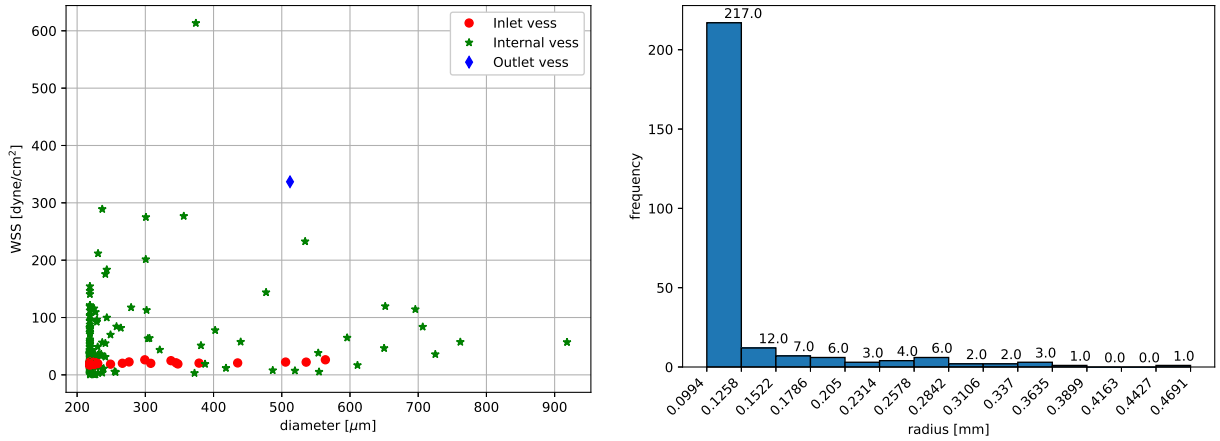
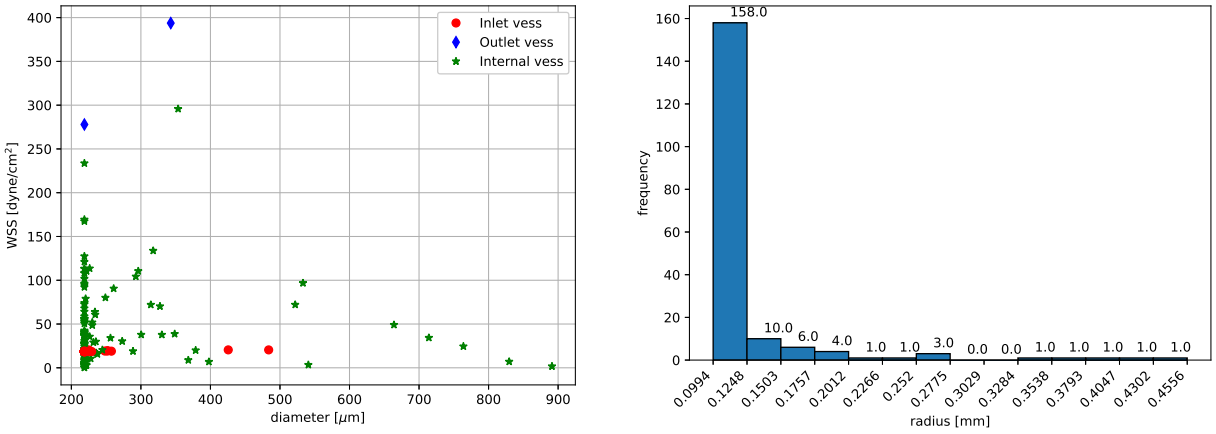


FIGURE 4.23: Wall shear stress and radius distributions in the RSV venous network. In each vessel, the wall shear stress is estimated from the flow rate obtained at steady state.

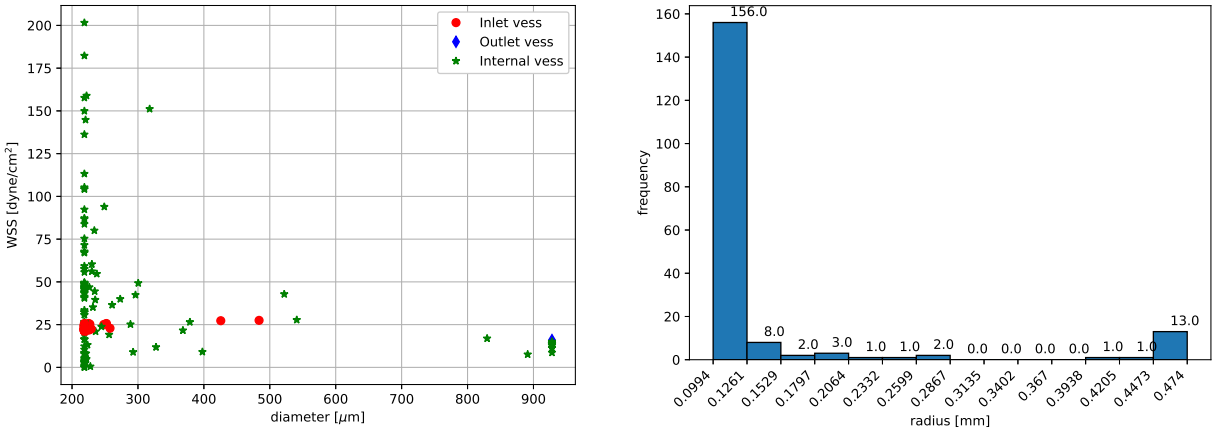


distant undergo a stronger influence coming from the capillary pressure, which is imposed to the *RCR* terminal models attached to the inlet nodes of the network. This pattern is common to both venous networks.

FIGURE 4.24: Wall shear stress and radius distributions in the LSV venous network. In each vessel, the wall shear stress is estimated from the flow rate obtained at steady state. The first row shows the results for the venous network with the original radii, whereas the bottom row displays the results obtained after manually modifying the radii of the larger vessels to remove narrowing and constrictions.



(A) LSV venous network with original radii



(B) LSV venous network with modified radii

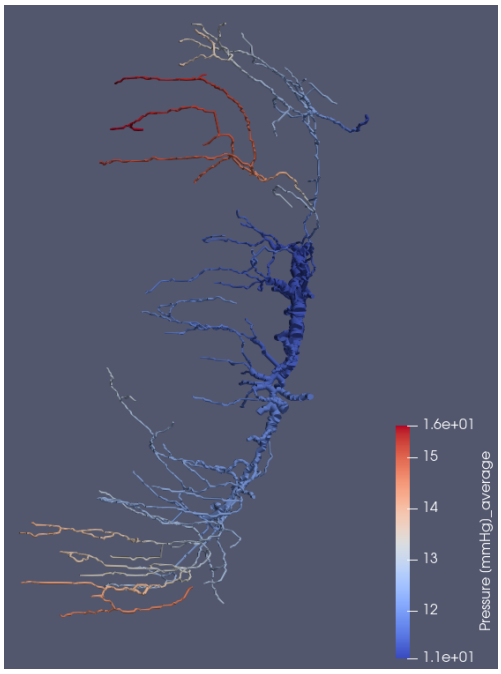
Figures 4.26 and 4.27 display the venous pressure distribution throughout the RLEV and LLEV networks, respectively, at selected time points over a cardiac cycle, to show the variation in both space (over the network) and time (over the cardiac cycle) of the venous cerebral pressure predicted by each vascular network. Once again, we can see that we obtain physiological pressure values over the entire cardiac cycle.

To analyze more in detail the predicted temporal dynamics of pressure and flow in these cerebral networks, Figures 4.28 and 4.29 show pressure and flow waveforms in selected vessels of the RLEV and LLEV networks, respectively, over a complete cardiac cycle and with the solution sampled in time at the midpoint of the vessel. For each venous network, we display the outlet vessels, selected inlet vessels and internal vessels. From these figures, we can observe that pressure and flow waveforms cover reasonable ranges of values in both venous networks. These waves have overall a very similar shape in all the vessels considered; in particular, even if we have very small flow rates, the flow waveforms still present an oscillating behaviour and we can see that, in the first part of the cardiac cycle, are characterized by a pronounced downward peak, which is similar to the one observed in the flow curve of the ICV, shown in Figure 4.19. In some vessels, the shape of the flow rate curve resembles that of the capillary pressure curve prescribed as inlet pressure to the *RCR* terminal models attached to the inlet nodes (see for instance the inlet vessel 54 of the RLEV network in Fig. 4.28, or the inlet vessel 305 of the LLEV network if Fig. 4.29). We also note that, in some vessels, the solution presents small oscillations, especially in the flow results (see for instance

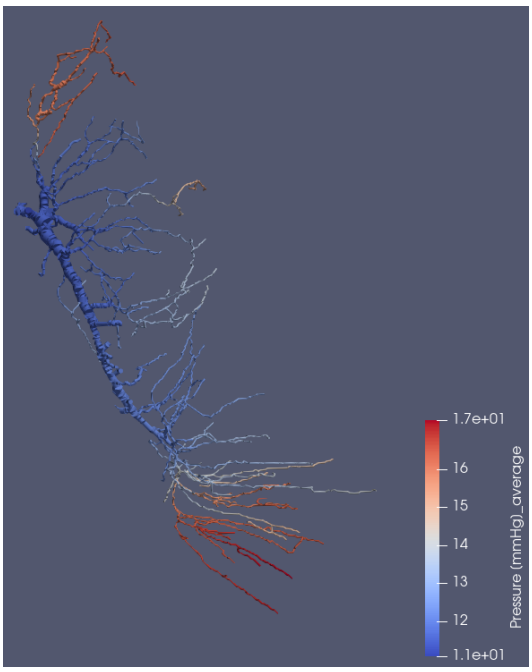
vessels 245, 256 and 226 of the RLEV in Fig. 4.28). A possible explanation could be that these oscillations are small wave reflections caused by the elastic vessel walls. However, the nature of such oscillations has still to be investigated, to understand whether it is related to numerical or modeling issues.

We conclude that the results obtained from the transient simulations performed on the RLEV and LLEV cerebral networks are overall reasonable and satisfactory, even if further investigation is required.

FIGURE 4.25: Mean venous pressure throughout (A) RLEV and (B) LLEV cerebral networks over a complete cardiac cycle ($T_0 = 0.8$ s).



(A) RLEV venous network



(B) LLEV venous network

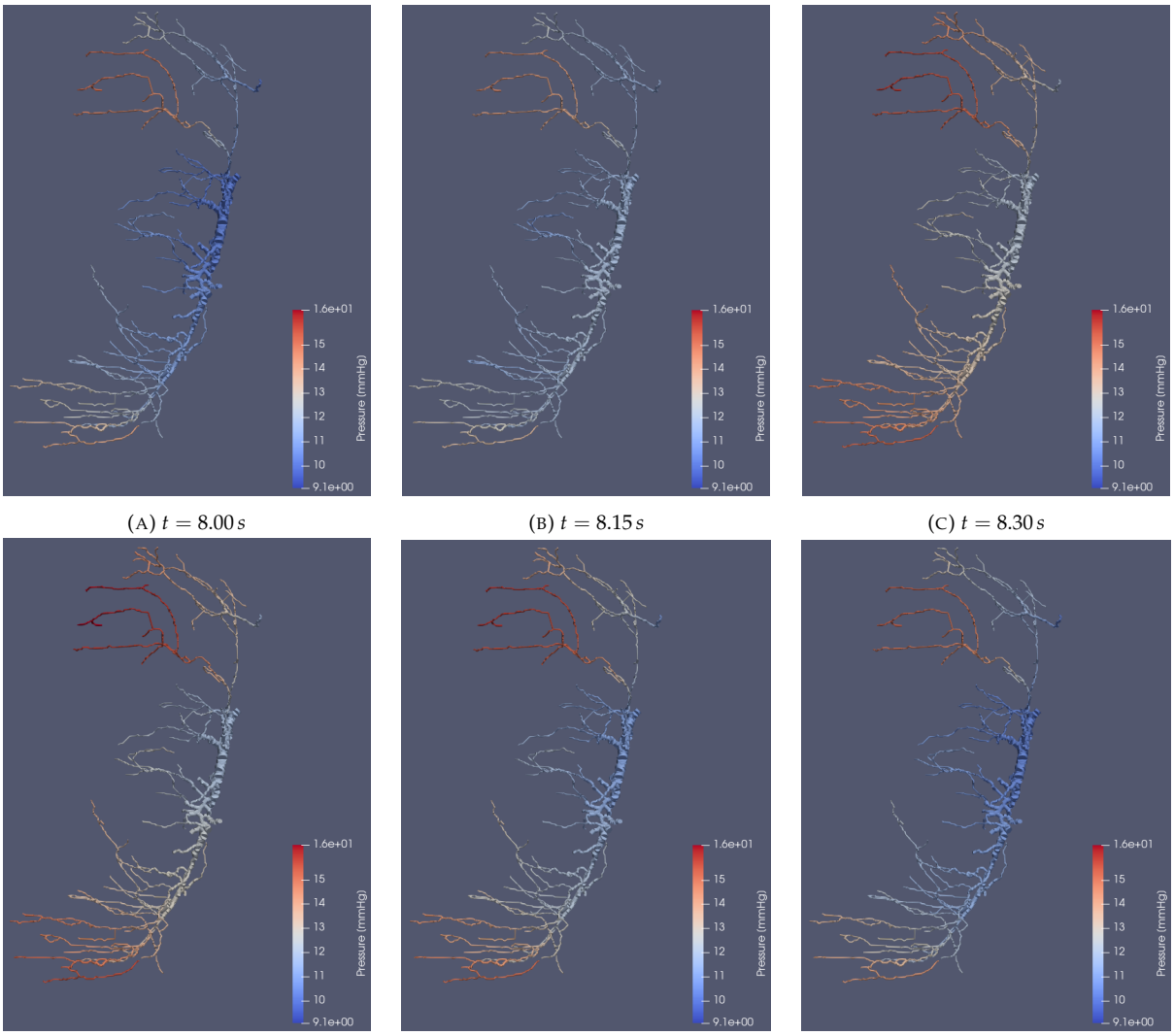
4.5.3 Concluding remarks

The main purpose of the blood flow simulations performed in Sections 4.5.1 and 4.5.2 on the MRI-reconstructed venous networks has been the validation of the processing pipeline proposed to extract and calibrate real cerebral networks from the MICRO imaging data. By exploring the flow and pressure fields generated by the different venous networks, our goal has been to assess whether these networks are suitable to perform blood flow simulations and are able to predict physiologically reasonable results in terms of pressure ranges in the corresponding vascular territories.

We note that this is the first time that the high-resolution MRI data acquired using the novel MICRO imaging method in human brain developed by Prof. E. Mark Haacke and his research group are employed to extract detailed vascular networks of vessels suited to perform simulations of blood flow. In fact, this novel microvascular imaging data were never used before to address such task. As a consequence, the methodology here developed to process these data and, in particular, to reconstruct networks of vessels from the 3D arterio-venous segmentations of cerebral districts of interest and to calibrate and parametrize these networks to simulate blood flow is completely new.

The results obtained lead us to the conclusion that it is feasible to extract subject-specific cerebral networks from the MICRO imaging data and that this work represents a first step towards the definition of an effective processing pipeline for the extraction and parametrization of real cerebral networks and blood flow simulations from subject-specific data, to study and explore cerebral blood flow dynamics (here with

FIGURE 4.26: Venous pressure distribution throughout the RLEV cerebral network at selected time points over a cardiac cycle, showing the temporal variation of the pressure across the network.



(A) $t = 8.00\,s$ (B) $t = 8.15\,s$ (C) $t = 8.30\,s$

(D) $t = 8.45\,s$ (E) $t = 8.60\,s$ (F) $t = 8.75\,s$

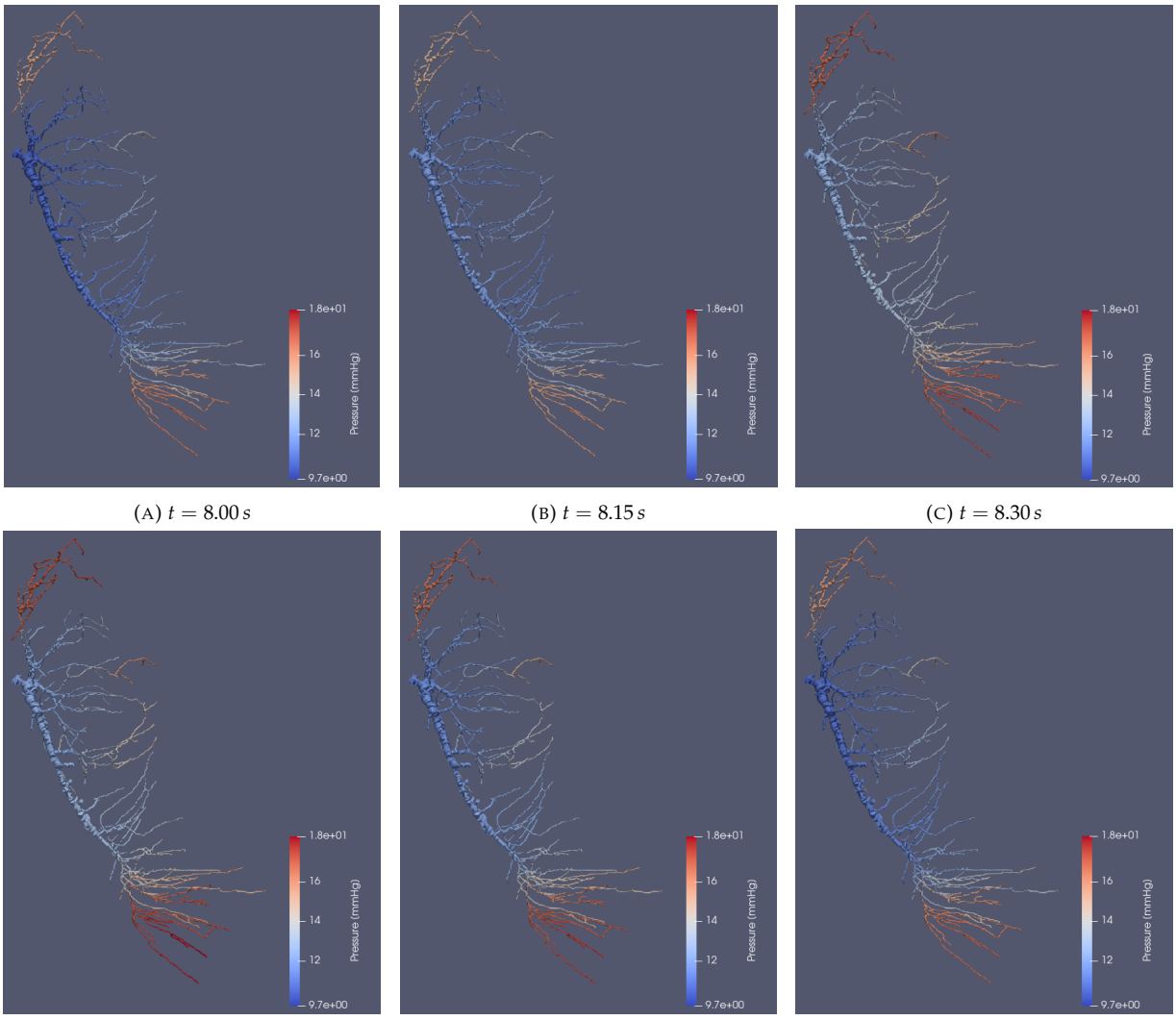
focus on venous blood drainage). In fact, the results obtained from both steady state and transient simulations performed on the RLEV and LLEV cerebral networks are overall good and reasonable, suggesting that these networks are able to correctly predict the dynamics of cerebral blood flow and pressure in the corresponding vascular districts.

On the other hand, the results obtained for the RSV and LSV venous networks have been very useful to identify a major limitation of the proposed processing pipeline related to the estimation/calculation of the vessel radii. Indeed, the very high, non-physiological pressure gradients and the large WSS values obtained in these venous networks are primarily caused by a wrong estimation and distribution of the vessel radii in such networks. Hence, a more robust algorithm is required to obtain reasonably good estimates of the true radii of a network, especially when dealing with very small vessels, to generate vascular networks that are reasonable from a physiological and fluid-dynamics point of view.

Clearly, further investigation is necessary to validate the proposed methodology and, possibly, to identify other limitations and aspects that need to be improved, related to specific steps of the processing pipeline or even to the arterial and venous segmentations we depart form to extract the networks of vessels.

Even though in this work we have focused on the venous side, especially on the small-veins cerebral

FIGURE 4.27: Venous pressure distribution throughout the LLEV cerebral network at selected time points over a cardiac cycle, showing the temporal variation of the pressure across the network.



(A) $t = 8.00\,s$ (B) $t = 8.15\,s$ (C) $t = 8.30\,s$

(D) $t = 8.45\,s$ (E) $t = 8.60\,s$ (F) $t = 8.75\,s$

networks, the next mandatory step will be to perform blood flow simulations also on the vascular networks of main cerebral arteries and main cerebral veins extracted in Section 4.3, after suitable calibration and parametrization, to validate and test also these networks. Finally, we plan to apply the proposed methodology also to the small-arteries masks generated in Section 4.2.6, to reconstruct the arterial network counterpart of the venous networks obtained for the different vascular districts, with the ultimate goal to perform arterio-venous blood flow simulations from subject-specific data.

FIGURE 4.28: Flow and pressure waveforms in selected vessels of the RLEV venous network. The location of these vessels is indicated by the stars in magenta, with corresponding vessel IDs, on the network in the central panel. Results are sampled at the midpoint of the vessel.

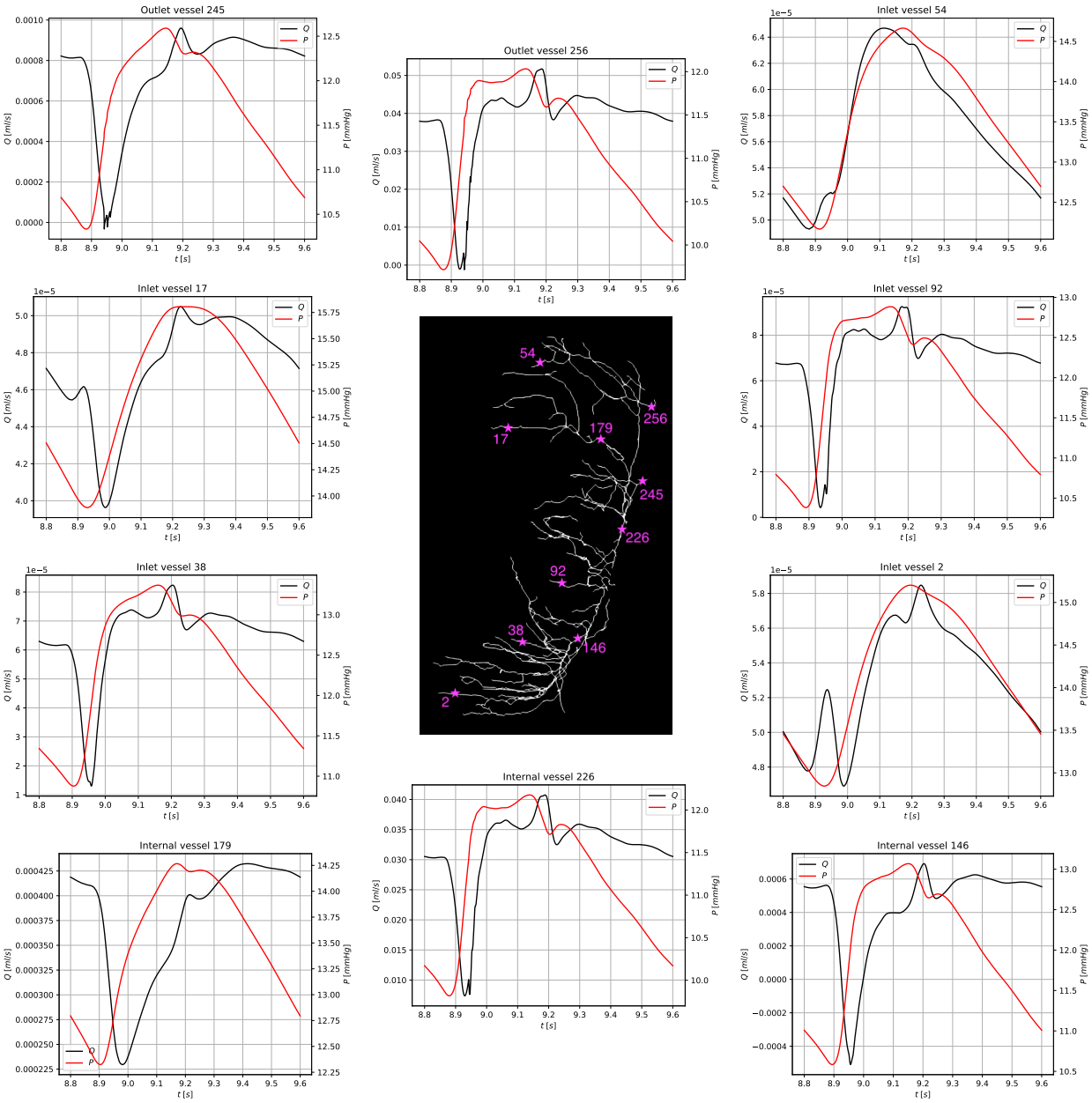
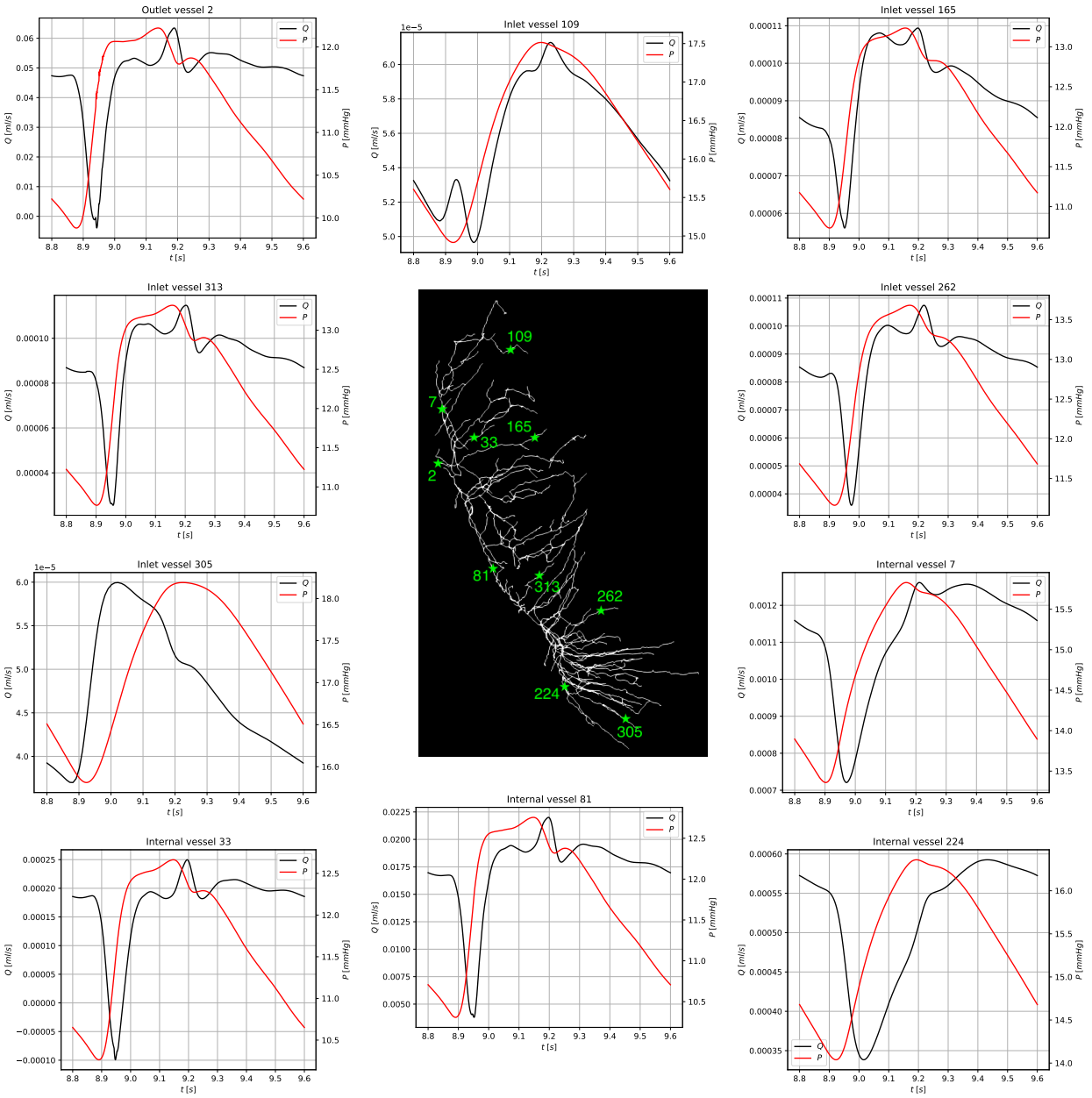


FIGURE 4.29: Flow and pressure waveforms in selected vessels of the LLEV venous network. The location of these vessels is indicated by the stars in green, with corresponding vessel IDs, on the network in the central panel. Results are sampled at the midpoint of the vessel.



Chapter 5

Conclusions

In this chapter we will discuss the achievements accomplished through the results presented in this thesis. Furthermore, motivated by the encountered limitations of the present works, we will suggest several extensions and improvements, as well as possible physiologically relevant applications of the proposed methodologies and topics to be developed in the future.

5.1 Achievements

5.1.1 Nonlinear lumped-parameter models for blood flow

The mathematical model presented in this thesis is based on both a one-dimensional and a lumped-parameter (0D) description of blood flow in compliant vessels, together with the coupling equations that, based on conservation principles, allow to couple 1D and 0D vessels into a network. Departing from a well-established formulation of the 1D blood flow model, here we have extended the traditional approach of deriving 0D models for blood flow in a vascular segment [52, 91, 51], in order to construct 0D models that preserve important nonlinear properties of the original 1D equations. These properties include the nonlinearity in the tube law relating the pressure to the cross-sectional area and pressure-dependent (nonlinear) model parameters, inductance L and resistance R. The nonlinear pressure-area relation, directly derived from the 1D tube law, can be either elastic or viscoelastic, to account for the viscoelastic nature of the vessel wall mechanics. On the other hand, considering the parameters L and R defined in terms of a time-dependent average cross-sectional area, in order to account for vessel cross-section changes under changes of pressure, is also fundamental to derive more realistic and physically consistent 0D blood flow models; this feature is expected to be relevant especially when modeling large deviations from a baseline state, such as hypertension, an haemorrhage or a collapsed state. Along with the nonlinearities included in the newly derived 0D blood flow models, another relevant aspect to be mentioned is that, following the work of Safaei *et al.* [119], these models can be employed to construct networks of vessels where each 1D vessel can be replaced by a 0D element by a per-segment 1D-to-0D mapping, so that the topology of the original 1D network is preserved.

Numerical experiments have shown that this family of nonlinear lumped-parameter models of blood flow is able to predict reasonable good approximations of pressure and flow waveforms in networks of vessels, when compared to the reference 1D solution, at a lower computational cost. For this reason, as the one-dimensional modeling of blood flow in complex and large vascular models and networks can result in computationally expensive simulations, rather than using these nonlinear 0D models as stand-alone tools, they can be coupled and combined with 1D models to construct hybrid networks of 1D-0D vessels, in a way to improve the computational efficiency of simulations, while still preserving a good level of accuracy in the predicted results.

5.1.2 A hybrid network solver for efficient blood flow simulations in complex networks

As already pointed out, the one-dimensional modeling of blood flow in complex vascular networks and models can result in computationally expensive simulations, where the complexity does not only depend on the anatomical detail by which a network is described, but also on the level at which physiological mechanisms and mechanical characteristics of the cardiovascular system are modeled, such as control mechanisms and viscoelasticity of vessel walls. As a consequence, accurate, robust and efficient numerical methods and solvers are needed.

Then, one of the main achievements of the present thesis has been the development of a novel modeling and computational framework which allows to perform efficient and accurate blood flow simulations in complex vascular networks. Departing from both the 1D and nonlinear 0D blood flow models with either elastic or viscoelastic tube laws, we have proposed an efficient hybrid network solver to construct networks of 1D and 0D vessels coupled together and to perform simulations on such networks providing a very good balance between computational efficiency and accuracy in the predicted results. Integrated into an already existing network solver coded in C++, the proposed hybrid methodology is based on (i) suitable coupling equations to couple 1D and/or 0D vessels at junctions, which ensure conservation principles; (ii) efficient numerical methods to solve 1D and 0D vessels, and (iii) high-order numerical coupling strategies for the accurate treatment of hybrid junctions. In particular, we have designed an efficient strategy for solving very large and stiff ODE systems governing the blood flow dynamics in regions of 0D vessels, exploiting existing implicit ODE solvers, but also accounting for the specific features of the problem to be solved. To couple 0D regions, which are evolved using an implicit method, to 1D vessels, that are advanced in time using fully explicit high-order numerical schemes, we have then derived a suitable high-order numerical coupling strategy to solve hybrid junctions of 1D and 0D vessels. The local time-stepping (LTS) algorithm proposed by Müller *et al.* [102] has also been integrated in the hybrid network solver. To instantiate concrete hybrid networks, we have explored different criteria: *a-priori* model selection criteria, such as intravascular volume and vessel compliance, or a region-based criterion. In the first case, we have performed efficiency and error analyses to identify those criteria providing the best trade-off between the computational cost of the simulations and a good level of accuracy in the results. On the other hand, the region-based approach could be adopted in many applications where one or a few vascular regions of interest, where higher accuracy is required, are modeled as 1D regions, while the remaining regions of the vascular model can be turned into 0D regions, with a considerable gain in terms of the computational efficiency of the resulting hybrid simulations.

The proposed hybrid network solver has been applied to solve very complex vascular networks, namely the ADAN model [17, 16] and the ADAN model coupled to CCO-generated cerebral arteriolar networks. The obtained results have shown that this methodology becomes crucial and absolutely necessary to gain computational efficiency when solving networks and models where the heterogeneity of spatial and/or temporal scales is relevant, still ensuring a good level of accuracy in the predicted results. A strong improvement in terms of computational efficiency is already obtained in the ADAN model when adopting a GTS strategy, but not when the LTS algorithm [102] is employed. On the other hand, when dealing with more complex vascular networks where the heterogeneity of spatial and temporal scales is even more relevant, namely the ADAN model coupled to the CCO-generated peripheral beds, adopting the hybrid network solver with LTS strategy determines a tremendous computational improvement, with speed-ups of several orders of magnitude. We have also shown that this hybrid network solver is also able to preserve a good level of accuracy in the predicted results, reproducing good approximations of pressure and flow waveforms in both 1D and 0D vessels of a hybrid network, when compared to the reference 1D results. Hence, the proposed hybrid network solver represents a first step towards a high-performance modeling

and computational framework for the solution of highly complex networks of 1D-0D vessels.

5.1.3 Reconstruction of MRI-derived human cerebral networks for blood flow simulations

Modeling and simulating blood flow in detailed, real arterio-venous cerebral networks may contribute to investigate, quantify and better characterize cerebral blood flow, potentially providing some insights into its complex dynamics and mechanisms. In particular, as pointed out in Section 1.1, the potential venous haemodynamic connection to some neurodegenerative diseases has brought attention to the venous circulation. Motivated by this, we have developed a methodology that, departing from *in-vivo* high-resolution MRI data in human brain, allows to extract subject-specific arterial and venous networks of cerebral districts of interest, which are suitable to perform blood flow simulations. In particular, for the aforementioned motivations, here we have focused on the venous side. We note that the high-resolution MRI data employed in this thesis, acquired using the MICRO imaging method in human brain developed by Prof. E. Mark Haacke and his research group, were never used before to extract networks of vessels that are suitable and good enough, *i.e.* have the necessary properties, to be used for blood flow simulations. So, this has been the first time that a methodology to create and calibrate vascular networks for blood flow simulations from the MICRO imaging data has been developed. The proposed processing pipeline is based on several steps: (i) extraction of detailed arterio-venous segmentation of specific cerebral districts; (ii) reconstruction of networks of vessels from such segmentations, with enough information about geometry and connectivity between vessels to perform blood flow simulations; (iii) calibration and parametrization of these networks; (iv) validation of the MRI-derived cerebral networks by performing preliminary simulations.

The processing pipeline proposed to extract and calibrate real cerebral networks from the MICRO imaging data has been validated by performing preliminary blood flow simulations on the MRI-reconstructed venous networks. By exploring the flow and pressure fields generated by the different venous networks, our goal has been to assess whether these networks are reasonable from a fluid-dynamics point of view and suitable to perform blood flow simulations, predicting physiologically reasonable results in terms of pressure ranges in the corresponding vascular territories. On the one hand, several aspects that need to be improved in this methodology have been identified, with a major limitation given by the algorithm implemented for vessel radius estimation in some of the networks generated. On the other hand, the results obtained have led us to the conclusion that it is feasible to extract subject-specific cerebral networks from the MICRO imaging data which are suitable to perform blood flow simulations and that the MRI-reconstructed cerebral networks are able to predict pressure and flow results that are reasonable in terms of physiological pressure ranges. Hence, this work represents a first step towards the definition of an effective processing pipeline for the extraction and parametrization of real cerebral networks and blood flow simulations from subject-specific data, to study and explore cerebral blood flow dynamics (here with focus on venous blood drainage).

5.2 Future works

Mathematical modeling and fluid dynamics simulations represent a valuable complementary tool to experimental approaches, to describe, study and understand the complex interaction of intracranial fluids of the CNS, including arterial and venous blood, CSF and interstitial fluid. In this thesis, we have focused on one of the main components of this interacting cerebral fluids dynamics, blood flow. However, we plan to apply the framework proposed in this thesis to a more complete mathematical model of the human circulation [99, 100, 144], which allows to account for the interaction of blood, CSF and brain tissue, and where the reconstructed cerebral vascular networks can be integrated to provide a detailed description

of cerebral blood flow dynamics and its interaction with other intracranial fluids. In particular, in [80] a one-dimensional co-axial model has been proposed, extending the original model of Toro *et al.* [143], which describes the coupled blood and CSF flow dynamics in cerebral vessels and surrounding CSF-filled PVS. Based on more detailed approaches modeling CSF flow in a single perivascular space [77, 78], we aim at applying such 1D co-axial model to networks of cerebral vessels and surrounding PVS. Hence, cerebral arterial and venous networks reconstructed with the methodology proposed in this thesis will be the departing point for describing the CSF flow dynamics through PVS surrounding cerebral vessels and its interaction with blood flow, adopting the modeling strategy presented in [80]. Indeed, this framework would allow us to investigate the coupled blood-CSF flow dynamics in the brain and to explore current hypotheses about the nature, mechanisms and driving forces of CSF flow and solute transport through PVS and their role in brain waste clearance. Finally, these 1D models could also be coupled with the 3D elastic tissue of the brain, by following the multiscale coupling approach proposed by Heltai *et al.* [68] for the simulation of vascularized tissues.

In this ambitious and challenging scenario, first of all we plan to improve and extend both the hybrid network solver proposed in Chapter 3 and the methodology developed in Chapter 4 for the reconstruction of MRI-derived human cerebral networks, according to the limitations encountered in the present works. Regarding the hybrid network solver, the development of a more efficient hybrid coupling strategy is already in progress, which will allow to evolve 0D regions with their own time step, not constrained by that of the neighboring 1D vessels. In fact, by using a larger time step for 0D regions, this strategy would significantly reduce the number of updates to be performed for each 0D regions using the implicit ODE solver, making the overall hybrid network methodology much more efficient. We plan also to parallelize the proposed hybrid network solver, for further computational improvement.

The processing pipeline developed to extract and calibrate real cerebral networks from the MICRO imaging data in human brain has also several limitations and aspects that need to be improved. Firstly, as already pointed out, a more robust algorithm is required to obtain reasonably good estimates of the true radii of a network, especially when dealing with very small vessels, to generate vascular networks that are reasonable from a physiological and fluid-dynamics point of view. This aspect will be further investigated to understand whether, in the cerebral networks in which we obtained inconsistent estimates of the vessels diameter, the problem is related to the procedure adopted to calculate the radius of the segments of the network, or to specific characteristics of the original segmentations, that should then be improved. Moreover, even though in this work we have focused on the venous side, especially on the small-veins cerebral networks, the next mandatory step will be to perform blood flow simulations also on the vascular networks of main cerebral arteries and main cerebral veins, after suitable calibration and parametrization, to validate and test also these networks. The proposed methodology will be also applied to the small-arteries masks generated, to create the arterial network counterpart of the venous networks obtained for the different vascular districts, with the ultimate goal to perform arterio-venous blood flow simulations from subject-specific data.

Appendix A

Stability analysis

A.1 First-order ordinary differential equations with periodic forcing function

It is a well-known result that, given a linear homogeneous system of ODEs with constant coefficients, that is

$$\frac{d\boldsymbol{x}(t)}{dt} = \boldsymbol{A}\boldsymbol{x}(t), \tag{A.1}$$

the stability of the exact solution of such ODE system is determined by the real part of the eigenvalues of the coefficient matrix $\boldsymbol{A}$. Precisely, a necessary and sufficient condition for the ODE system (A.1) to be *asymptotically stable* is that all eigenvalues of $\boldsymbol{A}$ have strictly negative real part. If this is the case, then there exist positive constants α, β such that

$$\|e^{\boldsymbol{A}t}\| \leq \beta e^{-\alpha t}, \quad t \geq 0. \tag{A.2}$$

Proof of this result can be found in classical books on ordinary differential equations, see for instance [122, 63].

Here, we want to prove that, when a periodic forcing function $\boldsymbol{b}(t)$ is added to system (A.1) to obtain the inhomogeneous ODE system (2.57), if the homogeneous part is asymptotically stable, then any solution of the complete non-homogeneous system will converge to a periodic solution as t increases. Namely, the periodic solution of the inhomogeneous linear problem (2.57) is an attracting stable solution for the system. The exact solution of system (2.57) obtained with the method of variation of parameters reads

$$\boldsymbol{x}(t) = e^{\boldsymbol{A}t}\boldsymbol{x}_0 + e^{\boldsymbol{A}t}\int_0^t e^{-\boldsymbol{A}s}\boldsymbol{b}(s)\,ds = e^{\boldsymbol{A}t}\boldsymbol{x}_0 + \int_0^t e^{\boldsymbol{A}(t-s)}\boldsymbol{b}(s)\,ds, \tag{A.3}$$

where $\boldsymbol{x}(0) = \boldsymbol{x}_0$ and $e^{\boldsymbol{A}t}$ is the matrix exponential. Under the assumption of periodic forcing function $\boldsymbol{b}(t)$, *i.e.* $\boldsymbol{b}(T_0) = \boldsymbol{b}(0)$ for some period $T_0 > 0$, we are able to obtain a particular solution of (2.57), that is its periodic solution satisfying $\boldsymbol{x}(T_0) = \boldsymbol{x}(0)$, by choosing appropriately the initial condition $\boldsymbol{x}_0$. By enforcing this last condition, after straightforward calculations, we find that the initial condition $\boldsymbol{x}_0^P$ which provides a periodic solution of system (2.57) is given by

$$\boldsymbol{x}_0^P = \left(\boldsymbol{I} - e^{\boldsymbol{A}T_0}\right)^{-1} e^{\boldsymbol{A}T_0}\int_0^{T_0} e^{-\boldsymbol{A}s}\boldsymbol{b}(s)\,ds. \tag{A.4}$$

At this point, we want to show that, if we start from any initial position different from the one which produces the periodic solution, the values of the corresponding solution will converge to the values of the periodic solution as t increases. Let $\boldsymbol{x}^P$ be the periodic solution corresponding to the initial condition $\boldsymbol{x}_0^P$ and let $\boldsymbol{x}^{NP}$ be any other solution of system (2.57) associated to some initial condition $\boldsymbol{x}_0^{NP}$. Then, by computing the norm of the difference between the two solutions and applying (A.2), the following inequality holds

$$\|\boldsymbol{x}^P(t) - \boldsymbol{x}^{NP}(t)\| = \|e^{\boldsymbol{A}t}\left(\boldsymbol{x}_0^P - \boldsymbol{x}_0^{NP}\right)\| \leq \beta e^{-\alpha t}\|\boldsymbol{x}_0^P - \boldsymbol{x}_0^{NP}\|, \tag{A.5}$$

from which it clearly follows that $\beta e^{-\alpha t} \to 0$ as $t \to +\infty$, that is the sought result. In conclusion, if the forcing function $\boldsymbol{b}(t)$ is periodic and if the homogeneous part of system (2.57) is asymptotically stable, then the exact solution of the original inhomogeneous problem will converge to the periodic solution of system (2.57) as t increases, for any admissible choice of the initial condition $\boldsymbol{x}(0) = \boldsymbol{x}_0 = [V(0), Q(0)]^T$. As a consequence, the stability of the exact solution of the complete ODE system (2.57) is determined by the real part of the eigenvalues of the coefficient matrix $\boldsymbol{A}$.

A.2 First-order system of ordinary differential equations with null eigenvalue

Here, as discussed is Section 2.4, we derive the additional assumption on the periodic forcing function $\boldsymbol{b}(t)$, which is needed to preserve the stability of the solution of an inhomogeneous ODE system of the form (2.57) whose coefficient matrix $\boldsymbol{A}$ has a null eigenvalue (and all other eigenvalues with strictly negative real part). This assumption will ensure that the stability of the homogeneous system (which is stable, but not asymptotically stable) is inherited also by the corresponding inhomogeneous system, namely that any solution of (2.57) for any admissible choice of the initial condition will converge to the periodic one as $t \to +\infty$.
This condition on the periodic forcing function is first derived in the scalar case for a single equation; then, the obtained result is extended to the case of a system of ODEs, specifically to system (2.68) governing the linear (Q_{in}, Q_{out})-type 0D vessel.

A.2.1 Scalar case

Let us start from the scalar case of a single ODE and consider the following mass conservation equation

$$\frac{dV}{dt} = Q_{in} - Q_{out}. \tag{A.6}$$

For a scalar ODE, the coefficient matrix $\boldsymbol{A}$ in (2.57) is reduced to a single constant coefficient a, which in the case of the above equation is equal to zero and plays the role of the null eigenvalue of matrix $\boldsymbol{A}$. As a consequence, the right-hand side of equation (A.6) only depends on the scalar, periodic forcing function $b(t) = Q_{in}(t) - Q_{out}(t)$, where $Q_{in}(t)$ and $Q_{out}(t)$ represent the inflow entering the vessel and the outflow leaving the vessel, respectively, and are both periodic signals with the same period $T_0 > 0$. The exact solution of equation (A.6) is

$$V(t) = V(0) + \int_0^t b(s)\, ds, \tag{A.7}$$

with initial condition $V(0)$. At this point, we are interested in studying the asymptotic properties of such a solution, namely the behaviour of $V(t)$ as t approaches $+\infty$.
Let $t = nT_0 + \tau$, with $n \in \mathbb{N}$ sufficiently large and $0 \leq \tau < T_0$. Then, we have

$$\begin{aligned} V(t) = V(nT_0 + \tau) &= V(0) + \int_0^{nT_0+\tau} b(s)\, ds \\ &= V(0) + \int_0^{nT_0} b(s)\, ds + \int_{nT_0}^{nT_0+\tau} b(s)\, ds \\ &= V(0) + n\int_0^{T_0} b(s)\, ds + \int_0^{\tau} b(s)\, ds, \end{aligned} \tag{A.8}$$

where, in the last equality, we have used the periodicity of the forcing term $b(t)$. In the above expression of the exact solution $V(t)$, the initial volume $V(0)$ is a fixed finite quantity, the second integral, $\int_0^{\tau} b(s)\, ds$,

is also finite, since it is the integral of a continuous periodic function over a fraction of its period $[0, T_0]$. Therefore, studying the asymptotic behaviour of the solution $V(t)$, that is

$$\lim_{t\to+\infty} V(t) \tag{A.9}$$

is completely equivalent to study

$$\lim_{n\to+\infty} n\int_0^{T_0} b(s)\,ds. \tag{A.10}$$

We distinguish the following three cases:

$$\lim_{n\to+\infty} n\int_0^{T_0} b(s)\,ds = \begin{cases} +\infty & \text{if } \bar{b} > 0, \\ -\infty & \text{if } \bar{b} < 0, \\ 0 & \text{if } \bar{b} = 0, \end{cases} \tag{A.11}$$

where we have set

$$\bar{b} := \int_0^{T_0} b(s)\,ds. \tag{A.12}$$

In other words, if the integral average of the periodic forcing function $b(t)$ over its period $[0, T_0]$ is different from zero, either positive or negative, then the solution of equation (A.6) will diverge either to $+\infty$ or to $-\infty$, depending on the sign of $\bar{b}$, as $t \to +\infty$. On the other hand, if the integral average of $b(t)$ over its period is zero, then any solution $V(t)$ of (A.6) will be bounded, namely

$$\lim_{t\to+\infty} \big|V(t)\big| < +\infty \quad \Longleftrightarrow \quad \bar{b} = 0 \quad \Longleftrightarrow \quad \frac{1}{T_0}\int_0^{T_0} b(s)\,ds = 0, \tag{A.13}$$

and will converge to the periodic one, that is

$$V(nT_0 + \tau) \xrightarrow{n\to+\infty} V(0) + \int_0^{\tau} b(s)\,ds. \tag{A.14}$$

We point out that this result is also physically consistent. Indeed, for equation (A.6) the condition stated in (A.13) simply becomes

$$\frac{1}{T_0}\int_0^{T_0} \left[Q_{in}(s) - Q_{out}(s)\right] ds = 0 \quad \Longleftrightarrow \quad \int_0^{T_0} Q_{in}(s)\,ds = \int_0^{T_0} Q_{out}(s)\,ds, \tag{A.15}$$

which means that, in order for the volume $V(t)$ not to constantly increase/decrease and asymptotically explode, the inflow entering the vessel and the outflow leaving the vessel must be balanced over each period.

A.2.2 ODE system case

Let us now extend the previous result to the case of a system of ODEs, specifically to system (2.68). For any admissible choice of the initial conditions $\boldsymbol{x}_0 = [V(0), Q(0), V_d(0)]^T$, the general solution of (2.68) is given by the formula in (A.3), where the constant coefficient matrix $\boldsymbol{A}$ and the periodic forcing function $\boldsymbol{b}(t)$ are

$$\boldsymbol{A} = \begin{bmatrix} 0 & -1 & 0 \\ \dfrac{2}{C_0 L_0} & -\dfrac{R_0}{L_0} & -\dfrac{2}{C_0 L_0} \\ 0 & 1 & 0 \end{bmatrix}, \quad \boldsymbol{b}(t) = \begin{bmatrix} Q_{in}(t) \\ 0 \\ -Q_{out}(t) \end{bmatrix}. \tag{A.16}$$

In general, if an $n \times n$ matrix $\boldsymbol{A}$ is diagonalizable, with linearly independent eigenvectors $\boldsymbol{v}_1, \boldsymbol{v}_2, \ldots, \boldsymbol{v}_n$ and corresponding eigenvalues $\lambda_1, \lambda_2, \ldots, \lambda_n$, then, denoted by $\boldsymbol{S}$ the matrix whose columns are the eigenvectors of $\boldsymbol{A}$, we have

$$\boldsymbol{S}^{-1}\boldsymbol{A}\boldsymbol{S} = \begin{bmatrix} \lambda_1 & 0 & \cdots & 0 \\ 0 & \lambda_2 & \cdots & 0 \\ \vdots & \vdots & \ddots & \vdots \\ 0 & 0 & \cdots & \lambda_n \end{bmatrix} = \boldsymbol{D}. \tag{A.17}$$

The exponential of the diagonal matrix $\boldsymbol{D}$ is easily written as

$$e^{\boldsymbol{D}} = \begin{bmatrix} e^{\lambda_1} & 0 & \cdots & 0 \\ 0 & e^{\lambda_2} & \cdots & 0 \\ \vdots & \vdots & \ddots & \vdots \\ 0 & 0 & \cdots & e^{\lambda_n} \end{bmatrix} \tag{A.18}$$

and thus, it is straightforward to check that, under the assumption that $\boldsymbol{A}$ is diagonalizable, the corresponding matrix exponential $e^{\boldsymbol{A}t}$ can be computed as follows

$$e^{\boldsymbol{A}t} = \boldsymbol{S} \begin{bmatrix} e^{\lambda_1 t} & 0 & \cdots & 0 \\ 0 & e^{\lambda_2 t} & \cdots & 0 \\ \vdots & \vdots & \ddots & \vdots \\ 0 & 0 & \cdots & e^{\lambda_n t} \end{bmatrix} \boldsymbol{S}^{-1} = \boldsymbol{S}e^{\boldsymbol{D}t}\boldsymbol{S}^{-1}. \tag{A.19}$$

Then, by introducing the above result in (A.3), the exact solution of an inhomogeneous ODE system of the form (2.57) with diagonalizable coefficient matrix $\boldsymbol{A}$ can be reformulated as

$$\boldsymbol{x}(t) = \left(\boldsymbol{S}e^{\boldsymbol{D}t}\boldsymbol{S}^{-1}\right)\boldsymbol{x}_0 + \int_0^t \left(\boldsymbol{S}e^{\boldsymbol{D}(t-s)}\boldsymbol{S}^{-1}\right)\boldsymbol{b}(s)\,ds, \tag{A.20}$$

As observed at the beginning of this paragraph, if the coefficient matrix $\boldsymbol{A}$ has a zero eigenvalue and all other eigenvalues with strictly negative real part, then the homogeneous part of system (2.57) is stable, but not asymptotically stable, with an attractive line of equilibrium points. Therefore, to study the asymptotic properties of the exact solution of the inhomogeneous system (2.57) obtained by introducing a periodic forcing function $\boldsymbol{b}(t)$, we have to focus on the integral term in (A.20), to study its behaviour as t tends to $+\infty$. We set

$$\widetilde{\boldsymbol{S}}(t) := \boldsymbol{S}e^{\boldsymbol{D}t}\boldsymbol{S}^{-1}. \tag{A.21}$$

By restricting to the order $n = 3$ of the coefficient matrix of system (2.68), after straightforward calculations, we get that the ith component of the integrand vector function in (A.20), obtained by multiplying the ith row of matrix $\widetilde{\boldsymbol{S}}$ by the vector forcing function $\boldsymbol{b}(t)$ and using the fact that $\lambda_1 = 0$, is given by

$$\begin{aligned} (\widetilde{\boldsymbol{S}}(t-s))_i\boldsymbol{b}(s) &= \sum_{j=1}^{3} (\widetilde{\boldsymbol{S}}(t-s))_{ij}\boldsymbol{b}_j(s) \\ &= \frac{1}{|\boldsymbol{S}|}\left[(v_{22}v_{33} - v_{23}v_{32})\,v_{1i} + (v_{23}v_{31} - v_{21}v_{33})\,v_{2i}e^{\lambda_2(t-s)} + (v_{21}v_{32} - v_{22}v_{31})\,v_{3i}e^{\lambda_3(t-s)}\right]\boldsymbol{b}_1(s) \\ &+ \frac{1}{|\boldsymbol{S}|}\left[(v_{13}v_{32} - v_{12}v_{33})\,v_{1i} + (v_{11}v_{33} - v_{13}v_{31})\,v_{2i}e^{\lambda_2(t-s)} + (v_{12}v_{31} - v_{11}v_{32})\,v_{3i}e^{\lambda_3(t-s)}\right]\boldsymbol{b}_2(s) \\ &+ \frac{1}{|\boldsymbol{S}|}\left[(v_{12}v_{23} - v_{13}v_{22})\,v_{1i} + (v_{13}v_{21} - v_{11}v_{23})\,v_{2i}e^{\lambda_2(t-s)} + (v_{11}v_{22} - v_{12}v_{21})\,v_{3i}e^{\lambda_3(t-s)}\right]\boldsymbol{b}_3(s) \end{aligned} \tag{A.22}$$

with $|\boldsymbol{S}| = \det(\boldsymbol{S})$, for $i = 1, \ldots, 3$. As both eigenvalues $\lambda_{2,3}$ have strictly negative real part, the presence of the exponential factors $e^{\lambda_2 t}$ and $e^{\lambda_3 t}$ ensures the convergence of the corresponding terms as $t \to +\infty$,

independently of any assumption on the periodic forcing function $\boldsymbol{b}(t)$. On the other hand, since $e^{\lambda_1 t} = e^0 = 1$ for any $t \geq 0$, when integrating the corresponding terms without decaying exponential factor, namely

$$\int_0^t \frac{\boldsymbol{v}_{1i}}{|\boldsymbol{S}|} \left[(\boldsymbol{v}_{22}\boldsymbol{v}_{33} - \boldsymbol{v}_{23}\boldsymbol{v}_{32})\, \boldsymbol{b}_1(s) + (\boldsymbol{v}_{13}\boldsymbol{v}_{32} - \boldsymbol{v}_{12}\boldsymbol{v}_{33})\, \boldsymbol{b}_2(s) + (\boldsymbol{v}_{12}\boldsymbol{v}_{23} - \boldsymbol{v}_{13}\boldsymbol{v}_{22})\, \boldsymbol{b}_3(s) \right] ds \tag{A.23}$$

for $i = 1, \ldots, 3$, we need to introduce additional assumptions on the periodic forcing function $\boldsymbol{b}(t)$ in order for the above integral terms, and hence the solution of system (2.68), not to explode as $t \to +\infty$.
As done in the scalar case, let $t = nT_0 + \tau$, with $n \in \mathbb{N}$ sufficiently large and $0 \leq \tau < T_0$. Then, using explicit expressions of the components of $\boldsymbol{b}(t)$ given in (A.16), we have that the integral in (A.23) can be rewritten as follows

$$\frac{\boldsymbol{v}_{1i}}{|\boldsymbol{S}|} \int_0^{nT_0+\tau} \left[\alpha_1 Q_{in}(s) - \alpha_2 Q_{out}(s) \right] ds, \quad \text{for } i = 1, \ldots, 3, \tag{A.24}$$

where we have set

$$\alpha_1 := (\boldsymbol{v}_{22}\boldsymbol{v}_{33} - \boldsymbol{v}_{23}\boldsymbol{v}_{32}), \quad \alpha_2 := (\boldsymbol{v}_{12}\boldsymbol{v}_{23} - \boldsymbol{v}_{13}\boldsymbol{v}_{22}). \tag{A.25}$$

If we discard the multiplicative factor $\frac{\boldsymbol{v}_{1i}}{|\boldsymbol{S}|}$, where $\boldsymbol{v}_{1i}$ is the ith element of the eigenvector $\boldsymbol{v}_1$ associated to the null eigenvalue λ_1, for all the three components of the solution of system (2.68) we obtain the same integral, which, by exploiting the periodicity of $Q_{in}(t)$ and $Q_{out}(t)$, becomes

$$\begin{aligned} \int_0^{nT_0+\tau} \left[\alpha_1 Q_{in}(s) - \alpha_2 Q_{out}(s) \right] ds = n \int_0^{T_0} \left[\alpha_1 Q_{in}(s) - \alpha_2 Q_{out}(s) \right] ds \\ + \int_0^{\tau} \left[\alpha_1 Q_{in}(s) - \alpha_2 Q_{out}(s) \right] ds. \end{aligned} \tag{A.26}$$

The second integral in the above expression is finite, since it is the integral of the linear combination of two continuous, periodic functions, with the same period $[0, T_0]$, over a fraction of their period. Then, by means of the same procedure used in the previous scalar case, also here we can observe that, in order for each component of the solution of system (2.68) not to diverge either to $+\infty$ or to $-\infty$ as $t \to +\infty$, namely

$$\lim_{t \to +\infty} |\boldsymbol{x}_i(t)| < +\infty \quad \text{for } i = 1, \ldots, 3, \tag{A.27}$$

and to converge to the periodic solution, a necessary and sufficient condition is

$$\int_0^{T_0} \left[\alpha_1 Q_{in}(s) - \alpha_2 Q_{out}(s) \right] ds = 0 \iff \alpha_1 \int_0^{T_0} Q_{in}(s)\, ds = \alpha_2 \int_0^{T_0} Q_{out}(s)\, ds. \tag{A.28}$$

We recall that this result is strictly valid only in the case where the coefficient matrix $\boldsymbol{A}$ is diagonalizable and, from linear algebra, it is well-known that an $n \times n$ matrix is diagonalizable if it has n independent eigenvectors, which is true, for example, when the matrix has n distinct eigenvalues.
It is easy to check that the matrix $\boldsymbol{A}$ of system (2.68) given in (A.16) is diagonalizable in both cases $\Delta > 0$ and $\Delta < 0$, described in (2.69). If $\Delta > 0$, matrix $\boldsymbol{A}$ has three real and distinct eigenvalues

$$\lambda_1 = 0, \quad \lambda_{2,3} = -\frac{R_0}{2L_0} \pm \frac{\sqrt{\Delta}}{2} \tag{A.29}$$

and corresponding set of linearly independent eigenvectors

$$\boldsymbol{v}_1 = \begin{bmatrix} 1 \\ 0 \\ 1 \end{bmatrix}, \quad \boldsymbol{v}_2 = \begin{bmatrix} 1 \\ \left(\frac{R_0}{2L_0} + \frac{\sqrt{\Delta}}{2} \right) \\ -1 \end{bmatrix}, \quad \boldsymbol{v}_3 = \begin{bmatrix} 1 \\ \left(\frac{R_0}{2L_0} - \frac{\sqrt{\Delta}}{2} \right) \\ -1 \end{bmatrix}; \tag{A.30}$$

while, if $\Delta < 0$, matrix $\boldsymbol{A}$ has three distinct eigenvalues, one equal to zero and the other two complex and conjugate, given by

$$\lambda_1 = 0, \quad \lambda_{2,3} = -\frac{R_0}{2L_0} \pm i\frac{\sqrt{-\Delta}}{2} \tag{A.31}$$

and corresponding set of linearly independent eigenvectors

$$\boldsymbol{v}_1 = \begin{bmatrix} 1 \\ 0 \\ 1 \end{bmatrix}, \quad \boldsymbol{v}_2 = \begin{bmatrix} 1 \\ \left(\frac{R_0}{2L_0} + i\frac{\sqrt{-\Delta}}{2}\right) \\ -1 \end{bmatrix}, \quad \boldsymbol{v}_3 = \begin{bmatrix} 1 \\ \left(\frac{R_0}{2L_0} - i\frac{\sqrt{-\Delta}}{2}\right) \\ -1 \end{bmatrix}. \tag{A.32}$$

Equipped with explicit expressions of the eigenvectors of the coefficient matrix $\boldsymbol{A}$, we can then compute factors α_1 and α_2 given in (A.25) and defining the linear combination between the inflow function $Q_{in}(t)$ and the outflow function $Q_{out}(t)$ in the integral (A.28). We obtain

$$\alpha_1 = \alpha_2 = \begin{cases} -\sqrt{\Delta}, & \text{if } \Delta > 0, \\ -i\sqrt{-\Delta}, & \text{if } \Delta < 0, \end{cases} \tag{A.33}$$

so that condition (A.28) on the periodic forcing function $\boldsymbol{b}(t)$ simply becomes

$$\int_0^{T_0} [Q_{in}(s) - Q_{out}(s)]\, ds = 0 \quad \Longleftrightarrow \quad \int_0^{T_0} Q_{in}(s)\, ds = \int_0^{T_0} Q_{out}(s)\, ds, \tag{A.34}$$

which is exactly the same physically consistent condition found in the scalar case to get asymptotically the periodic solution.

Appendix B

RK4 numerical method and coupling algorithm

As described in Section 3.3.1.1, the first-order, nonlinear ODE systems governing the different configurations of a 0D vessel are solved using the well-established four-step explicit fourth-order Runge-Kutta (RK4) method. For the sake of completeness, we report here the full numerical scheme

$$\begin{cases} \boldsymbol{Y}^{m+1} = \boldsymbol{Y}^m + \Delta t^m \sum_{s=1}^{4} \omega_s \boldsymbol{K}_s, \quad m \geq 0, \\ \boldsymbol{K}_1 = \boldsymbol{B}\left(t^m, \boldsymbol{Y}^m, \boldsymbol{Y}^D\left(t^m\right)\right), \\ \boldsymbol{K}_2 = \boldsymbol{B}\left(t^m + \dfrac{\Delta t^m}{2}, \boldsymbol{Y}^m + \dfrac{\Delta t^m}{2}\boldsymbol{K}_1, \boldsymbol{Y}^D\left(t^m + \dfrac{\Delta t^m}{2}\right)\right), \\ \boldsymbol{K}_3 = \boldsymbol{B}\left(t^m + \dfrac{\Delta t^m}{2}, \boldsymbol{Y}^m + \dfrac{\Delta t^m}{2}\boldsymbol{K}_2, \boldsymbol{Y}^D\left(t^m + \dfrac{\Delta t^m}{2}\right)\right), \\ \boldsymbol{K}_4 = \boldsymbol{B}\left(t^m + \Delta t^m, \boldsymbol{Y}^m + \Delta t^m \boldsymbol{K}_3, \boldsymbol{Y}^D\left(t^m + \Delta t^m\right)\right), \\ \omega_1 = \omega_4 = \dfrac{1}{6}, \quad \omega_2 = \omega_3 = \dfrac{1}{3}, \end{cases} \tag{B.1}$$

with known initial data $\left(t^0, \boldsymbol{Y}^0\right)$.

Furthermore, we display the outline of the algorithm implemented to solve the 0D coupling problem at a junction of 0D vessels, based on the numerical coupling strategy described in Section 3.3.2.1. Given a junction connecting M 0D vessels, at each time step, to update the solution from time t^m to time $t^{m+1} = t^m + \Delta t^m$ in all 0D vessels converging at the junction, schematically we proceed as follows

$$\begin{aligned}
&\texttt{for } \mathtt{m} \geq 0, \\
\texttt{S1:}\ &\left(\mathtt{t^m}, \mathtt{Y_j^m}\right)_{\mathtt{j}=1,\dots,\mathtt{M}} \rightarrow \texttt{compute coupling cond.} \quad \mathtt{Y^{D,m}} = \mathtt{Y^D}\left(\mathtt{Y_1^m}, \dots, \mathtt{Y_M^m}\right) \\
&\rightarrow \texttt{compute } \mathtt{K_{1,j}} = \mathtt{B_j}\left(\mathtt{t^m}, \mathtt{Y_j^m}, \mathtt{Y^{D,m}}\right), \quad \mathtt{j} = 1, \dots, \mathtt{M} \\
&\rightarrow \texttt{compute } \mathtt{Y_j^*} = \mathtt{Y_j^m} + \frac{\Delta \mathtt{t^m}}{2}\mathtt{K_{1,j}}, \quad \mathtt{j} = 1, \dots, \mathtt{M}; \\
\texttt{S2:}\ &\left(\mathtt{t^m} + \frac{\Delta \mathtt{t^m}}{2}, \mathtt{Y_j^*}\right)_{\mathtt{j}=1,\dots,\mathtt{M}} \rightarrow \texttt{compute coupling cond.} \quad \mathtt{Y^{D,*}} = \mathtt{Y^D}\left(\mathtt{Y_1^*}, \dots, \mathtt{Y_M^*}\right) \\
&\rightarrow \texttt{compute } \mathtt{K_{2,j}} = \mathtt{B_j}\left(\mathtt{t^m} + \frac{\Delta \mathtt{t^m}}{2}, \mathtt{Y_j^*}, \mathtt{Y^{D,*}}\right), \quad \mathtt{j} = 1, \dots, \mathtt{M} \\
&\rightarrow \texttt{compute } \mathtt{Y_j^{**}} = \mathtt{Y_j^m} + \frac{\Delta \mathtt{t^m}}{2}\mathtt{K_{2,j}}, \quad \mathtt{j} = 1, \dots, \mathtt{M}; \\
\texttt{S3:}\ &\left(\mathtt{t^m} + \frac{\Delta \mathtt{t^m}}{2}, \mathtt{Y_j^{**}}\right)_{\mathtt{j}=1,\dots,\mathtt{M}} \rightarrow \texttt{compute coupling cond.} \quad \mathtt{Y^{D,**}} = \mathtt{Y^D}\left(\mathtt{Y_1^{**}}, \dots, \mathtt{Y_M^{**}}\right) \\
&\rightarrow \texttt{compute } \mathtt{K_{3,j}} = \mathtt{B_j}\left(\mathtt{t^m} + \frac{\Delta \mathtt{t^m}}{2}, \mathtt{Y_j^{**}}, \mathtt{Y^{D,**}}\right), \quad \mathtt{j} = 1, \dots, \mathtt{M} \\
&\rightarrow \texttt{compute } \mathtt{Y_j^{***}} = \mathtt{Y_j^m} + \Delta \mathtt{t^m}\mathtt{K_{3,j}}, \quad \mathtt{j} = 1, \dots, \mathtt{M};
\end{aligned}$$

S4: $\left(t^m + \Delta t^m, Y_j^{***}\right)_{j=1,\dots,M} \rightarrow$ compute coupling cond. $Y^{D,***} = Y^D\left(Y_1^{***},\dots,Y_M^{***}\right)$
$\rightarrow$ compute $K_{4,j} = B_j\left(t^m + \Delta t^m, Y_j^{***}, Y^{D,***}\right), \quad j = 1,\dots,M;$

$\Longrightarrow$ compute

$$Y_j^{m+1} = Y_j^m + \Delta t^m \sum_{s=1}^{4} w_s K_{s,j}, \quad j = 1,\dots,M.$$

Appendix C

Quantitative error analysis for ADAN model and CCO arteriolar networks

The following tables report relative errors in the results obtained from both the fully 0D and the hybrid network configurations with respect to the reference 1D solution in selected vessels, for

- the elastic ADAN model (Table C.1);
- the viscoelastic ADAN model (Tables C.2-C.4);
- the viscoelastic ADAN model coupled to the CCO-generated peripheral bed of the lenticulostriate artery (Table C.5).

Relative root mean square (RMS), systolic (SYS) and diastolic (DIAS) errors are computed according to the relative error metrics (2.98) for both pressure and flow rate results sampled in time over a complete cardiac cycle, where the solution in the 1D vessels is sampled at the midpoint of the vascular segment. For the hybrid model configuration, we show errors both in vessels that are 1D and in vessels that are 0D in the hybrid network.

TABLE C.1: **Elastic ADAN model.** Relative errors (in %) for pressure and flow results obtained from the fully 0D and the Test 3-hybrid model configurations with respect to the reference 1D results, computed in selected vessels. In the second column of the table, between brackets, it is specified if the vessel is either 1D or 0D in the corresponding hybrid network configuration.

Vessel	**Error**	$\varepsilon_P^{\mathrm{RMS}}(\%)$	$\varepsilon_Q^{\mathrm{RMS}}(\%)$	$\varepsilon_P^{\mathrm{SYS}}(\%)$	$\varepsilon_Q^{\mathrm{SYS}}(\%)$	$\varepsilon_P^{\mathrm{DIAS}}(\%)$	$\varepsilon_Q^{\mathrm{DIAS}}(\%)$
aortic_arch_I	0D *vs* 1D	7.279e-01	4.730e-01	-1.252e-01	4.685e-02	-9.839e-01	-9.378e-01
	hyb (1D) *vs* 1D	6.934e-01	1.121e-01	-2.940e-01	-1.142e-01	-1.271e+00	1.325e-01
aortic_arch_VII	0D *vs* 1D	6.192e-01	2.240e+00	9.780e-01	3.928e-01	-6.037e-01	9.013e-01
	hyb (1D) *vs* 1D	6.791e-01	1.180e+00	-2.115e-01	4.000e-01	-1.224e+00	4.646e-01
abdominal_aorta_X	0D *vs* 1D	8.237e-01	5.059e+00	7.477e-01	-9.136e-01	-2.142e-01	4.247e+00
	hyb (1D) *vs* 1D	7.708e-01	2.007e+00	-4.301e-01	8.458e-01	-1.165e+00	1.670e+00
thoracic_aorta_VIII	0D *vs* 1D	9.740e-01	2.777e+00	1.243e+00	-2.530e+00	-4.023e-01	5.094e-01
	hyb (1D) *vs* 1D	6.812e-01	1.372e+00	-5.251e-01	-5.804e-01	-1.208e+00	-2.994e-01
sup_mesenteric_XI	0D *vs* 1D	1.584e+00	5.566e+00	-2.460e+00	-1.277e+01	-4.323e-01	7.421e-01
	hyb (0D) *vs* 1D	9.494e-01	2.459e+00	-9.147e-01	-2.575e+00	-1.182e+00	-3.279e+00
L_femoral_XI	0D *vs* 1D	2.503e+00	9.112e+00	4.759e-02	-9.109e+00	2.206e+00	-1.940e+00
	hyb (0D) *vs* 1D	1.373e+00	4.542e+00	1.044e+00	-3.738e+00	1.461e-01	-4.048e+00
L_post_tibial_I	0D *vs* 1D	4.513e+00	1.034e+01	-1.779e+00	-1.067e+01	2.758e+00	5.689e-01
	hyb (0D) *vs* 1D	2.923e+00	6.786e+00	-1.478e-02	-5.620e+00	-3.914e-01	-2.803e+00
L_comm_iliac	0D *vs* 1D	1.341e+00	5.646e+00	7.691e-01	-1.825e+00	1.536e-01	5.392e+00
	hyb (0D) *vs* 1D	1.007e+00	2.057e+00	1.728e+00	1.127e+00	-9.259e-01	1.674e+00

L_radial_IV	0D *vs* 1D	1.159e+00	4.571e+00	-4.002e-01	-7.195e+00	7.472e-02	-1.560e+00
	hyb (0D) *vs* 1D	1.149e+00	3.617e+00	-3.630e-01	-2.048e+00	-1.360e+00	-3.551e+00
L_brachial_I	0D *vs* 1D	7.639e-01	2.895e+00	-4.886e-01	-2.927e+00	-6.159e-02	1.413e+00
	hyb (0D) *vs* 1D	9.003e-01	2.058e+00	-5.095e-01	3.401e-01	-1.023e+00	-9.987e-01
L_axillary_III	0D *vs* 1D	8.848e-01	2.447e+00	4.060e-01	-2.945e+00	-2.869e-01	2.160e+00
	hyb (0D) *vs* 1D	1.005e+00	1.874e+00	7.010e-01	4.517e-01	-1.041e+00	-1.876e+00
L_comm_carotid	0D *vs* 1D	7.174e-01	4.409e+00	-4.526e-02	3.386e+00	-5.362e-01	-2.986e+00
	hyb (1D) *vs* 1D	7.106e-01	1.225e+00	-3.891e-01	5.575e-01	-1.235e+00	-7.342e-01
L_int_carotid_I	0D *vs* 1D	1.166e+00	3.999e+00	-2.239e-01	-1.716e+00	-3.239e-01	2.388e+00
	hyb (1D) *vs* 1D	7.489e-01	1.179e+00	-1.924e-01	1.434e+00	-1.233e+00	-9.991e-01
R_int_carotid_VI	0D *vs* 1D	1.772e+00	3.044e+00	2.242e+00	4.243e-01	6.137e-01	9.223e-01
	hyb (1D) *vs* 1D	9.091e-01	1.456e+00	1.378e-01	1.489e+00	-1.147e+00	-1.433e+00
basilar_V	0D *vs* 1D	1.108e+00	1.995e+00	-1.340e-01	-3.535e-01	-3.772e-01	5.082e-01
	hyb (1D) *vs* 1D	8.474e-01	1.742e+00	-1.051e-01	1.510e+00	-1.244e+00	-2.063e+00
L_MCA_post_parietal	0D *vs* 1D	1.551e+00	1.941e+00	-2.416e-01	1.715e+00	-5.745e-01	2.645e-02
	hyb (1D) *vs* 1D	8.864e-01	7.703e-01	-2.310e-01	-4.213e-02	-1.463e+00	-5.919e-01
L_lenticulostriate_II	0D *vs* 1D	1.433e+00	3.093e+00	-5.141e-01	3.567e+00	-3.566e-01	1.375e+00
	hyb (1D) *vs* 1D	8.170e-01	8.407e-01	-1.217e-01	3.126e-01	-1.210e+00	-5.383e-01
L_prefrontal	0D *vs* 1D	2.666e+00	2.834e+00	-1.808e+00	3.733e-01	-8.537e-01	8.182e-03
	hyb (1D) *vs* 1D	8.540e-01	9.166e-01	-2.133e-01	4.279e-01	-1.373e+00	-4.328e-01
R_MCA_middle_temp_branch	0D *vs* 1D	1.353e+00	2.023e+00	-3.298e-01	-1.492e-01	-5.101e-01	7.043e-02
	hyb (1D) *vs* 1D	9.050e-01	1.059e+00	-5.038e-02	-6.897e-01	-1.345e+00	-5.308e-01
comm_hepatic	0D *vs* 1D	8.589e-01	3.168e+00	-7.530e-01	-6.725e+00	-6.730e-02	9.796e-01
	hyb (0D) *vs* 1D	5.885e-01	1.488e+00	-2.196e-01	5.877e-01	-8.945e-01	-1.489e+00

TABLE C.2: **Viscoelastic ADAN model.** Relative errors (in %) for pressure and flow results obtained from the fully 0D and the Test 1-hybrid model configurations with respect to the reference 1D results, computed in selected vessels. In the second column of the table, between brackets, it is specified if the vessel is either 1D or 0D in the corresponding hybrid network configuration.

Vessel	**Error**	$\varepsilon_P^{\mathrm{RMS}}(\%)$	$\varepsilon_Q^{\mathrm{RMS}}(\%)$	$\varepsilon_P^{\mathrm{SYS}}(\%)$	$\varepsilon_Q^{\mathrm{SYS}}(\%)$	$\varepsilon_P^{\mathrm{DIAS}}(\%)$	$\varepsilon_Q^{\mathrm{DIAS}}(\%)$
aortic_arch_I	0D *vs* 1D	6.653e-01	1.950e-01	1.775e-02	6.610e-02	-1.099e+00	-3.419e-01
	hyb (1D) *vs* 1D	8.397e-01	3.692e-02	-7.066e-01	7.046e-02	-1.419e+00	6.836e-02
aortic_arch_VII	0D *vs* 1D	6.269e-01	1.106e+00	7.024e-01	-4.260e-01	-1.013e+00	1.002e+00
	hyb (1D) *vs* 1D	8.411e-01	4.692e-01	-6.108e-01	-4.485e-01	-1.415e+00	-2.832e-03
abdominal_aorta_I	0D *vs* 1D	1.094e+00	3.048e+00	1.790e+00	-4.215e+00	-7.189e-01	1.147e+00
	hyb (1D) *vs* 1D	8.562e-01	7.492e-01	-7.191e-01	-1.347e+00	-1.314e+00	-8.929e-02
abdominal_aorta_IXX	0D *vs* 1D	9.790e-01	4.862e+00	8.264e-01	-4.322e+00	-5.309e-01	2.499e+00
	hyb (1D) *vs* 1D	8.715e-01	1.253e+00	-9.206e-01	-3.122e-01	-1.045e+00	8.578e-01
thoracic_aorta_I	0D *vs* 1D	6.990e-01	1.308e+00	1.249e+00	-9.992e-01	-8.905e-01	7.933e-01
	hyb (1D) *vs* 1D	8.430e-01	5.242e-01	-5.499e-01	-4.698e-01	-1.397e+00	-5.341e-02
thoracic_aorta_VIII	0D *vs* 1D	8.367e-01	1.931e+00	1.485e+00	-2.815e+00	-7.978e-01	4.310e-01
	hyb (1D) *vs* 1D	8.473e-01	6.211e-01	-5.416e-01	-7.338e-01	-1.356e+00	-3.456e-01
sup_mesenteric_I	0D *vs* 1D	7.626e-01	3.350e+00	-7.722e-01	-7.239e+00	-6.664e-01	-6.727e-01
	hyb (0D) *vs* 1D	7.630e-01	6.686e-01	-3.052e-01	5.022e-01	-1.163e+00	-7.566e-01
L_femoral_XI	0D *vs* 1D	2.271e+00	8.512e+00	-7.126e-01	-1.074e+01	2.139e-01	-1.387e+00
	hyb (0D) *vs* 1D	1.219e+00	4.114e+00	6.206e-02	-5.311e+00	-7.046e-01	-2.427e+00
L_popliteal_V	0D *vs* 1D	3.435e+00	9.574e+00	-2.441e+00	-1.402e+01	3.471e-01	-2.569e+00

	hyb (0D) *vs* 1D	2.114e+00	5.604e+00	-1.146e+00	-8.354e+00	-8.467e-01	-3.247e+00
L_int_iliac_III	0D *vs* 1D	1.778e+00	5.455e+00	-1.359e+00	-1.116e+01	-3.398e-01	-1.431e+00
	hyb (0D) *vs* 1D	9.259e-01	1.796e+00	-6.694e-01	-3.964e+00	-9.553e-01	-4.039e-01
L_radial_VI	0D *vs* 1D	1.441e+00	4.120e+00	-6.608e-01	-5.916e+00	-1.040e+00	-5.550e-01
	hyb (0D) *vs* 1D	1.460e+00	3.252e+00	-5.325e-01	-3.484e+00	-1.659e+00	-9.545e-01
L_brachial_I	0D *vs* 1D	6.574e-01	2.492e+00	7.189e-01	-1.977e+00	-8.793e-01	-2.734e-01
	hyb (0D) *vs* 1D	8.337e-01	1.677e+00	5.151e-01	-4.338e-01	-1.418e+00	-7.362e-01
L_comm_carotid	0D *vs* 1D	6.532e-01	2.749e+00	-9.731e-02	1.205e+00	-8.386e-01	-1.958e-01
	hyb (0D) *vs* 1D	8.359e-01	3.107e+00	-1.090e-01	4.987e+00	-1.312e+00	-7.137e-01
L_vertebral_V	0D *vs* 1D	6.794e-01	1.350e+00	-1.944e-01	-8.227e-02	-9.021e-01	-6.046e-01
	hyb (0D) *vs* 1D	8.015e-01	1.595e+00	-1.262e-01	3.283e+00	-1.326e+00	-6.342e-01
R_int_carotid_I	0D *vs* 1D	6.832e-01	1.561e+00	9.584e-02	2.868e-01	-8.757e-01	-4.731e-01
	hyb (0D) *vs* 1D	8.763e-01	1.702e+00	1.294e-01	2.331e+00	-1.330e+00	-5.428e-01
L_MCA_post_parietal	0D *vs* 1D	1.156e+00	1.308e+00	8.178e-02	5.927e-01	-8.243e-01	-5.161e-01
	hyb (0D) *vs* 1D	1.258e+00	1.315e+00	1.984e-01	1.468e+00	-1.377e+00	-7.958e-01
L_post_cerebral_precomm_III	0D *vs* 1D	7.136e-01	1.360e+00	3.938e-01	3.124e+00	-5.663e-01	-7.255e-01
	hyb (0D) *vs* 1D	7.635e-01	1.766e+00	5.665e-01	4.626e+00	-1.046e+00	-1.028e+00
R_MCA_middle_temp_branch	0D *vs* 1D	1.044e+00	1.187e+00	-1.328e-02	1.750e-01	-8.090e-01	-4.843e-01
	hyb (0D) *vs* 1D	1.153e+00	1.194e+00	1.303e-01	1.041e+00	-1.307e+00	-7.785e-01
renal_III	0D *vs* 1D	9.168e-01	1.800e+00	-6.086e-01	-3.489e+00	-4.720e-01	2.646e-01
	hyb (0D) *vs* 1D	5.672e-01	8.080e-01	-2.195e-01	1.924e+00	-9.823e-01	1.123e-02
L_gastric_IV	0D *vs* 1D	1.228e+00	4.286e+00	-8.653e-01	-7.851e+00	-7.858e-01	-2.217e+00
	hyb (0D) *vs* 1D	8.794e-01	1.698e+00	-5.455e-01	2.629e+00	-1.313e+00	-1.835e+00

TABLE C.3: **Viscoelastic ADAN model.** Relative errors (in %) for pressure and flow results obtained from the fully 0D and the Test 2-hybrid model configurations with respect to the reference 1D results, computed in selected vessels. In the second column of the table, between brackets, it is specified if the vessel is either 1D or 0D in the corresponding hybrid network configuration.

Vessel	**Error**	$\varepsilon_P^{\mathrm{RMS}}(\%)$	$\varepsilon_Q^{\mathrm{RMS}}(\%)$	$\varepsilon_P^{\mathrm{SYS}}(\%)$	$\varepsilon_Q^{\mathrm{SYS}}(\%)$	$\varepsilon_P^{\mathrm{DIAS}}(\%)$	$\varepsilon_Q^{\mathrm{DIAS}}(\%)$
aortic_arch_VII	0D *vs* 1D	6.269e-01	1.106e+00	7.024e-01	-4.260e-01	-1.013e+00	1.002e+00
	hyb (1D) *vs* 1D	8.235e-01	4.413e-01	-5.852e-01	-3.597e-01	-1.386e+00	-1.087e-01
abdominal_aorta_IXX	0D *vs* 1D	9.790e-01	4.862e+00	8.264e-01	-4.322e+00	-5.309e-01	2.499e+00
	hyb (1D) *vs* 1D	8.505e-01	1.290e+00	-8.959e-01	-2.203e-01	-1.026e+00	8.318e-01
thoracic_aorta_I	0D *vs* 1D	6.990e-01	1.308e+00	1.249e+00	-9.992e-01	-8.905e-01	7.933e-01
	hyb (1D) *vs* 1D	8.252e-01	5.009e-01	-5.277e-01	-3.811e-01	-1.375e+00	-1.555e-01
sup_mesenteric_XXII	0D *vs* 1D	1.686e+00	3.823e+00	-1.902e+00	-1.055e+01	-8.093e-01	-5.242e-02
	hyb (0D) *vs* 1D	9.954e-01	2.496e+00	-6.492e-01	-7.459e+00	-1.314e+00	-2.907e-01
L_femoral_XV	0D *vs* 1D	2.821e+00	9.150e+00	-1.712e+00	-1.269e+01	3.751e-01	-2.299e+00
	hyb (0D) *vs* 1D	1.576e+00	4.954e+00	-6.432e-01	-6.958e+00	-6.876e-01	-3.076e+00
L_ant_tibial_VI	0D *vs* 1D	4.042e+00	8.741e+00	-2.964e+00	-1.056e+01	3.218e-03	-3.049e-01
	hyb (0D) *vs* 1D	2.950e+00	5.622e+00	-1.498e+00	-5.725e+00	-9.684e-01	-1.548e+00
L_ext_iliac_III	0D *vs* 1D	1.381e+00	6.323e+00	2.069e+00	-6.655e+00	-2.081e-01	1.523e+00
	hyb (0D) *vs* 1D	1.346e+00	2.408e+00	2.671e+00	-2.358e+00	-8.837e-01	-1.106e-01
L_radial_IV	0D *vs* 1D	1.227e+00	3.898e+00	-5.842e-01	-5.131e+00	-9.435e-01	-1.043e+00
	hyb (0D) *vs* 1D	8.290e-01	1.042e+00	-4.771e-01	-5.895e-01	-1.411e+00	-8.368e-01
L_brachial_I	0D *vs* 1D	6.574e-01	2.492e+00	7.189e-01	-1.977e+00	-8.793e-01	-2.734e-01
	hyb (1D) *vs* 1D	8.277e-01	5.988e-01	-5.988e-01	-8.946e-01	-1.367e+00	-4.792e-01

L_brachial_V	0D *vs* 1D	6.992e-01	2.854e+00	1.689e-01	-2.671e+00	-8.790e-01	-6.329e-01
	hyb (1D) *vs* 1D	8.305e-01	6.273e-01	-6.438e-01	-8.450e-01	-1.380e+00	-4.425e-01
L_axillary_III	0D *vs* 1D	6.857e-01	2.051e+00	1.243e+00	-1.971e+00	-8.813e-01	1.371e-01
	hyb (1D) *vs* 1D	8.251e-01	5.645e-01	-5.747e-01	-7.150e-01	-1.370e+00	-3.974e-01
L_ulnar_VII	0D *vs* 1D	1.213e+00	3.499e+00	-6.290e-01	-4.948e+00	-9.484e-01	-1.188e+00
	hyb (0D) *vs* 1D	8.309e-01	6.993e-01	-5.383e-01	-2.991e-01	-1.418e+00	-9.233e-01
L_int_carotid_VI	0D *vs* 1D	1.193e+00	2.046e+00	2.473e+00	-7.390e-01	3.979e-02	-5.600e-01
	hyb (0D) *vs* 1D	1.178e+00	2.103e+00	2.713e+00	3.918e-01	-3.842e-01	-6.664e-01
R_int_carotid_I	0D *vs* 1D	6.832e-01	1.561e+00	9.584e-02	2.868e-01	-8.757e-01	-4.731e-01
	hyb (0D) *vs* 1D	7.841e-01	1.505e+00	1.220e-01	2.717e+00	-1.272e+00	-5.324e-01
basilar_V	0D *vs* 1D	9.180e-01	8.047e-01	-7.924e-02	9.339e-01	-8.961e-01	-7.178e-01
	hyb (0D) *vs* 1D	9.540e-01	1.366e+00	9.578e-02	3.614e+00	-1.287e+00	-9.978e-01
L_dist_medial_striate	0D *vs* 1D	1.481e+00	1.282e+00	-3.796e-01	-3.046e-01	-1.558e+00	-5.196e-01
	hyb (0D) *vs* 1D	1.610e+00	1.267e+00	-1.707e-01	6.978e-01	-1.998e+00	-7.551e-01
L_prefrontal	0D *vs* 1D	1.712e+00	1.233e+00	-1.649e+00	5.804e-01	-9.665e-01	-7.009e-01
	hyb (0D) *vs* 1D	1.808e+00	1.240e+00	-1.638e+00	1.415e+00	-1.448e+00	-9.475e-01
L_ant_parietal	0D *vs* 1D	1.386e+00	1.328e+00	-6.114e-01	6.087e-01	-9.427e-01	-6.294e-01
	hyb (0D) *vs* 1D	1.471e+00	1.313e+00	-5.293e-01	1.489e+00	-1.453e+00	-8.987e-01
comm_hepatic	0D *vs* 1D	8.067e-01	2.520e+00	-3.844e-01	-4.779e+00	-5.080e-01	-2.954e-01
	hyb (0D) *vs* 1D	5.623e-01	6.493e-01	8.554e-03	-2.605e-01	-1.002e+00	-4.324e-01
renal_III	0D *vs* 1D	9.168e-01	1.800e+00	-6.086e-01	-3.489e+00	-4.720e-01	2.646e-01
	hyb (0D) *vs* 1D	5.460e-01	8.173e-01	-1.889e-01	2.010e+00	-9.684e-01	1.613e-02

TABLE C.4: **Viscoelastic ADAN model.** Relative errors (in %) for pressure and flow results obtained from the fully 0D and the Test 3-hybrid model configurations with respect to the reference 1D results, computed in selected vessels. In the second column of the table, between brackets, it is specified if the vessel is either 1D or 0D in the corresponding hybrid network configuration.

Vessel	**Error**	$\varepsilon_P^{\mathrm{RMS}}(\%)$	$\varepsilon_Q^{\mathrm{RMS}}(\%)$	$\varepsilon_P^{\mathrm{SYS}}(\%)$	$\varepsilon_Q^{\mathrm{SYS}}(\%)$	$\varepsilon_P^{\mathrm{DIAS}}(\%)$	$\varepsilon_Q^{\mathrm{DIAS}}(\%)$
aortic_arch_I	0D *vs* 1D	6.653e-01	1.950e-01	1.775e-02	6.610e-02	-1.099e+00	-3.419e-01
	hyb (1D) *vs* 1D	8.105e-01	2.061e-02	-5.808e-01	-9.952e-03	-1.373e+00	2.576e-02
aortic_arch_VII	0D *vs* 1D	6.269e-01	1.106e+00	7.024e-01	-4.260e-01	-1.013e+00	1.002e+00
	hyb (1D) *vs* 1D	8.158e-01	4.112e-01	-5.354e-01	1.497e-02	-1.369e+00	1.842e-01
abdominal_aorta_X	0D *vs* 1D	7.978e-01	4.262e+00	4.807e-01	-4.556e+00	-6.984e-01	2.242e+00
	hyb (1D) *vs* 1D	8.284e-01	1.174e+00	-6.891e-01	-1.058e+00	-1.217e+00	7.959e-01
thoracic_aorta_VIII	0D *vs* 1D	8.367e-01	1.931e+00	1.485e+00	-2.815e+00	-7.978e-01	4.310e-01
	hyb (1D) *vs* 1D	8.223e-01	5.514e-01	-5.062e-01	-2.238e-01	-1.320e+00	-3.092e-01
sup_mesenteric_XI	0D *vs* 1D	1.248e+00	4.002e+00	-1.441e+00	-1.036e+01	-7.597e-01	-2.633e-01
	hyb (0D) *vs* 1D	7.581e-01	1.145e+00	-2.365e-01	-1.680e+00	-1.231e+00	-7.151e-01
L_femoral_XI	0D *vs* 1D	2.271e+00	8.512e+00	-7.126e-01	-1.074e+01	2.139e-01	-1.387e+00
	hyb (0D) *vs* 1D	1.215e+00	4.116e+00	1.452e-01	-4.876e+00	-7.081e-01	-2.494e+00
L_post_tibial_I	0D *vs* 1D	3.784e+00	9.262e+00	-2.521e+00	-1.270e+01	3.698e-01	-2.444e+00
	hyb (0D) *vs* 1D	2.469e+00	5.813e+00	-9.320e-01	-6.972e+00	-9.098e-01	-3.190e+00
L_comm_iliac	0D *vs* 1D	1.135e+00	5.179e+00	5.969e-01	-4.408e+00	-4.493e-01	2.902e+00
	hyb (0D) *vs* 1D	8.945e-01	1.552e+00	1.296e+00	-3.478e-02	-9.915e-01	8.824e-01
L_radial_IV	0D *vs* 1D	1.227e+00	3.898e+00	-5.842e-01	-5.131e+00	-9.435e-01	-1.043e+00
	hyb (0D) *vs* 1D	1.231e+00	3.044e+00	-4.957e-01	-2.422e+00	-1.495e+00	-1.178e+00
L_brachial_I	0D *vs* 1D	6.574e-01	2.492e+00	7.189e-01	-1.977e+00	-8.793e-01	-2.734e-01

	hyb (0D) *vs* 1D	8.072e-01	1.653e+00	5.528e-01	-2.488e-01	-1.343e+00	-5.581e-01
L_axillary_III	0D *vs* 1D	6.857e-01	2.051e+00	1.243e+00	-1.971e+00	-8.813e-01	1.371e-01
	hyb (0D) *vs* 1D	8.489e-01	1.264e+00	1.209e+00	-2.364e-01	-1.316e+00	-4.501e-01
L_comm_carotid	0D *vs* 1D	6.532e-01	2.749e+00	-9.731e-02	1.205e+00	-8.386e-01	-1.958e-01
	hyb (1D) *vs* 1D	8.186e-01	4.526e-01	-5.376e-01	2.216e-01	-1.383e+00	-4.163e-01
L_int_carotid_I	0D *vs* 1D	8.125e-01	2.012e+00	4.603e-01	-6.594e-01	-8.499e-01	-5.253e-01
	hyb (1D) *vs* 1D	8.259e-01	5.440e-01	-5.254e-01	2.847e-01	-1.387e+00	-7.283e-01
R_int_carotid_VI	0D *vs* 1D	1.145e+00	1.422e+00	2.247e+00	-1.504e-01	4.790e-02	-4.983e-01
	hyb (1D) *vs* 1D	8.444e-01	6.747e-01	-5.248e-01	-1.035e+00	-1.393e+00	-8.027e-01
basilar_V	0D *vs* 1D	9.180e-01	8.047e-01	-7.924e-02	9.339e-01	-8.961e-01	-7.178e-01
	hyb (1D) *vs* 1D	8.655e-01	7.456e-01	-5.682e-01	-1.550e+00	-1.416e+00	-7.947e-01
L_MCA_post_parietal	0D *vs* 1D	1.156e+00	1.308e+00	8.178e-02	5.927e-01	-8.243e-01	-5.161e-01
	hyb (1D) *vs* 1D	9.438e-01	7.157e-01	-6.286e-01	-5.791e-01	-1.514e+00	-9.427e-01
L_lenticulostriate_II	0D *vs* 1D	1.057e+00	1.252e+00	2.605e-01	-1.154e-01	-9.285e-01	-5.256e-01
	hyb (1D) *vs* 1D	8.532e-01	6.311e-01	-5.166e-01	-4.688e-01	-1.438e+00	-8.770e-01
L_prefrontal	0D *vs* 1D	1.712e+00	1.233e+00	-1.649e+00	5.804e-01	-9.665e-01	-7.009e-01
	hyb (1D) *vs* 1D	9.134e-01	7.112e-01	-6.092e-01	-5.784e-01	-1.466e+00	-9.425e-01
R_MCA_middle_temp_branch	0D *vs* 1D	1.044e+00	1.187e+00	-1.328e-02	1.750e-01	-8.090e-01	-4.843e-01
	hyb (1D) *vs* 1D	9.169e-01	6.930e-01	-6.175e-01	-6.044e-01	-1.480e+00	-9.093e-01
comm_hepatic	0D *vs* 1D	8.067e-01	2.520e+00	-3.844e-01	-4.779e+00	-5.080e-01	-2.954e-01
	hyb (0D) *vs* 1D	5.640e-01	7.241e-01	9.183e-02	-8.737e-03	-9.863e-01	-4.192e-01

TABLE C.5: **Viscoelastic ADAN model coupled to the CCO arteriolar network of the lenticulostriate artery.** Relative errors (in %) for pressure and flow results obtained from the fully 0D and the hybrid model configurations with respect to the reference 1D results, computed in selected vessels. In the second column of the table, between brackets, it is specified if the vessel is either 1D or 0D in the corresponding hybrid network configuration.

Vessel	**Error**	$\varepsilon_P^{\mathrm{RMS}}(\%)$	$\varepsilon_Q^{\mathrm{RMS}}(\%)$	$\varepsilon_P^{\mathrm{SYS}}(\%)$	$\varepsilon_Q^{\mathrm{SYS}}(\%)$	$\varepsilon_P^{\mathrm{DIAS}}(\%)$	$\varepsilon_Q^{\mathrm{DIAS}}(\%)$
aortic_root	0D *vs* 1D	7.162e-01	4.171e-01	-3.488e-01	1.047e-01	-8.431e-01	-9.544e-01
	hyb (1D) *vs* 1D	3.126e-06	2.481e-07	1.224e-06	1.679e-08	4.917e-06	4.650e-08
L_brachial	0D *vs* 1D	7.797e-01	3.152e+00	1.972e-01	-1.689e+00	-6.593e-01	-2.687e-01
	hyb (1D) *vs* 1D	3.271e-06	2.314e-06	1.551e-06	-3.501e-07	5.149e-06	5.059e-07
L_radial	0D *vs* 1D	1.467e+00	4.492e+00	-5.031e-01	-4.036e+00	-8.956e-01	1.665e+00
	hyb (1D) *vs* 1D	3.303e-06	1.958e-06	1.212e-06	-6.498e-06	5.223e-06	4.190e-07
L_MCA_post_parietal	0D *vs* 1D	1.297e+00	2.010e+00	1.901e-01	2.125e+00	-3.427e-01	-8.883e-02
	hyb (1D) *vs* 1D	1.696e-05	2.263e-05	1.367e-07	-4.735e-08	1.145e-05	6.961e-07
R_dist_medial_striate	0D *vs* 1D	1.644e+00	2.457e+00	1.778e-01	2.283e-01	-9.380e-01	-2.634e-02
	hyb (1D) *vs* 1D	7.896e-06	1.546e-05	3.301e-06	-1.892e-05	2.029e-06	3.812e-06
L_PCA_precomm	0D *vs* 1D	7.866e-01	1.633e+00	6.831e-01	-2.154e+00	-1.620e-02	-2.218e-01
	hyb (1D) *vs* 1D	5.251e-06	4.024e-05	8.257e-06	5.362e-05	5.880e-06	-4.210e-06
L_lenticulostriate	0D *vs* 1D	1.351e+00	1.653e+00	4.242e-01	7.334e-01	-2.986e-01	-2.473e-01
	hyb (1D) *vs* 1D	9.209e-02	2.410e-02	-1.657e-01	3.985e-02	7.649e-02	-6.420e-03
L_prefrontal	0D *vs* 1D	1.734e+00	1.945e+00	-1.705e+00	1.625e+00	-5.161e-01	-2.521e-01
	hyb (1D) *vs* 1D	1.727e-05	2.591e-05	-9.837e-07	1.586e-06	1.016e-05	4.627e-06
R_MCA_temp_branch	0D *vs* 1D	1.308e+00	2.246e+00	3.730e-01	8.868e-01	-2.960e-01	-5.447e-02
	hyb (1D) *vs* 1D	1.7469e-05	2.712e-05	8.965e-06	-6.221e-05	3.092e-06	3.960e-06
L_int_carotid	0D *vs* 1D	1.238e+00	4.211e+00	1.212e+00	-4.182e-02	-1.549e-01	4.884e+00
	hyb (1D) *vs* 1D	3.454e-06	2.283e-05	1.888e-06	3.488e-05	5.283e-06	-4.125e-05

R_int_carotid	0D *vs* 1D	1.044e+00	3.934e+00	-1.071e-01	2.467e+00	-2.718e-01	2.209e+00
	hyb (1D) *vs* 1D	5.325e-06	8.905e-05	6.876e-07	-3.102e-05	5.972e-06	-1.777e-04
basilar	0D *vs* 1D	1.044e+00	3.934e+00	-1.071e-01	2.467e+00	-2.718e-01	2.209e+00
	hyb (1D) *vs* 1D	4.131e-06	1.860e-05	3.802e-06	2.814e-05	5.581e-06	-7.724e-07
L_MCA_ant_parietal	0D *vs* 1D	1.452e+00	1.989e+00	-5.192e-01	1.992e+00	-4.814e-01	-1.959e-01
	hyb (1D) *vs* 1D	1.687e-05	2.315e-05	1.035e-06	6.781e-08	4.645e-06	-1.481e-06
CCO_vess_4042	0D *vs* 1D	1.332e+00	1.626e+00	4.462e-01	6.972e-01	-2.479e-01	-2.543e-01
	hyb (0D) *vs* 1D	2.067e-01	2.722e-02	3.142e-01	5.824e-02	1.595e-01	2.823e-03
CCO_vess_4565	0D *vs* 1D	1.415e+00	1.202e+00	8.396e-04	6.040e-02	-5.705e-01	-2.262e-01
	hyb (0D) *vs* 1D	1.104e-01	5.118e-02	-2.859e-03	2.986e-02	-1.425e-01	4.889e-02
CCO_vess_6074	0D *vs* 1D	1.346e+00	1.286e+00	2.652e-02	1.841e-01	-4.572e-01	-2.624e-01
	hyb (0D) *vs* 1D	4.904e-02	2.567e-02	9.804e-02	5.176e-02	-6.515e-03	1.071e-02
CCO_vess_7536	0D *vs* 1D	1.378e+00	1.323e+00	4.719e-02	2.042e-01	-6.097e-01	-2.819e-01
	hyb (0D) *vs* 1D	1.171e-01	1.946e-02	9.243e-02	4.172e-02	-1.652e-01	-8.452e-03
CCO_vess_4234	0D *vs* 1D	1.406e+00	1.144e+00	-1.617e-01	-1.028e-01	-5.514e-01	-2.849e-01
	hyb (0D) *vs* 1D	6.634e-02	1.871e-02	-1.676e-02	2.691e-02	-8.669e-02	6.706e-03
CCO_vess_5320	0D *vs* 1D	1.388e+00	1.142e+00	-1.627e-01	4.783e-02	-5.535e-01	-2.799e-01
	hyb (0D) *vs* 1D	6.923e-02	6.800e-02	3.196e-03	1.474e-01	-7.875e-02	1.259e-02
CCO_vess_6315	0D *vs* 1D	1.405e+00	1.138e+00	-1.865e-01	-1.455e-01	-5.796e-01	-3.045e-01
	hyb (0D) *vs* 1D	7.683e-02	1.518e-02	-2.902e-02	9.909e-03	-1.067e-01	-5.178e-03
CCO_vess_7942	0D *vs* 1D	1.399e+00	1.171e+00	-1.947e-01	-3.921e-02	-5.620e-01	-2.851e-01
	hyb (0D) *vs* 1D	6.450e-02	1.289e-02	-2.203e-02	2.375e-02	-8.807e-02	-7.740e-04

Bibliography

[1] N.J. Abbott et al. "The Role of Brain Barriers in Fluid Movement in the CNS: Is There a 'Glymphatic' System?" In: *Acta Neuropathol.* 135.3 (2018), pp. 387–407. DOI: 10.1007/s00401-018-1812-4.

[2] J. Alastruey et al. "Lumped Parameter Outflow Models for 1-D Blood Flow Simulations: Effect on Pulse Waves and Parameter Estimation". In: *Commun. Comput. Phys.* 4.2 (Aug. 2008), pp. 317–336.

[3] J. Alastruey et al. "On the Impact of Modelling Assumptions in Multi-Scale, Subject-Specific Models of Aortic Haemodynamics". In: *J R Soc Interface.* 13.119 (2016), p. 20160073. DOI: http://dx.doi.org/10.1098/rsif.2016.0073.

[4] J. Alastruey et al. "Physical Determining Factors of the Arterial Pulse Waveform: Theoretical Analysis and Calculation Using the 1-D Formulation". In: *J Eng Math.* 77 (2012), pp. 19–37. DOI: 10.1007/s10665-012-9555-z.

[5] J. Alastruey et al. "Pulse Wave Propagation in a Model Human Arterial Network: Assessment of 1-D Visco-Elastic Simulations against in Vitro Measurements". In: *Journal of Biomechanics* 44.12 (2011), pp. 2250–2258. ISSN: 00219290. DOI: 10.1016/j.jbiomech.2011.05.041.

[6] J. Alastruey et al. "Reduced Modelling of Blood Flow in the Cerebral Circulation Coupling 1-D, 0-D and Cerebral Auto-Regulation Models". In: *Int. J. Numer. Meth. Fluids* 56 (2008), pp. 1061–1067. DOI: 10.1002/FLD.1606.

[7] L. Antiga et al. "An Image-Based Modeling Framework for Patient-Specific Computational Hemodynamics". In: *Med Biol Eng Comput.* 46 (2008), pp. 1097–1112. DOI: 10.1007/s11517-008-0420-1.

[8] R.L. Armentano et al. "Assessment of Elastin and Collagen Contribution to Aortic Elasticity in Conscious Dogs". In: *Am J Physiol Heart Circ Physiol.* 260.6 Pt 2 (1991), H1870–7. DOI: 10.1152/ajpheart.1991.260.6.H1870.

[9] M. Asgari, D. de Zélicourt, and V. Kurtcuoglu. "Glymphatic Solute Transport Does Not Require Bulk Flow". In: *Sci Rep* 6 (2016), p. 38635. DOI: 10.1038/srep38635.

[10] A.P. Aviolo. "Multi-Branched Model of the Human Arterial System". In: *Med. Biol. Eng. Comput.* 18 (1980), pp. 709–718. DOI: 10.1007/BF02441895.

[11] D.S. Berger and J.K. Li. "Temporal Relationship between Left Ventricular and Arterial System Elastances". In: *IEEE Trans Biomed Eng.* 39.4 (Apr. 1992), pp. 404–410. DOI: 10.1109/10.126613.

[12] D. Bessems et al. "Experimental Validation of a Time-Domain-Based Wave Propagation Model of Blood Flow in Viscoelastic Vessels". In: *J Biomech.* 41.2 (2008), pp. 284–291. DOI: 10.1016/j.jbiomech.2007.09.014.

[13] J. Blacher and M.E. Safar. "Large-Artery Stiffness, Hypertension and Cardiovascular Risk in Older Patients". In: *Nat Clin Pract Cardiovasc Med* 2 (Oct. 2005), pp. 450–5. DOI: 10.1038/ncpcardio0307.

[14] P.J. Blanco, R.A.B. de Queiroz, and R.A. Feijóo. "A Computational Approach to Generate Concurrent Arterial Networks in Vascular Territories". In: *Int J Numer Method Biomed Eng.* 29.5 (2013), pp. 601–14. DOI: 10.1002/cnm.2547.

[15] P.J. Blanco, L.O. Müller, and J.D. Spence. "Blood Pressure Gradients in Cerebral Arteries: A Clue to Pathogenesis of Cerebral Small Vessel Disease". In: *Stroke Vasc Neurol.* 2.3 (2017), pp. 108–117. DOI: 10.1136/svn-2017-000087.

[16] P.J. Blanco et al. "An Anatomically Detailed Arterial Network Model for One-Dimensional Computational Hemodynamics". In: *IEEE Trans Biomed Eng.* 62.2 (2015), pp. 736–53. DOI: 10.1109/TBME.2014.2364522.

[17] P.J. Blanco et al. "Blood Flow Distribution in an Anatomically Detailed Arterial Network Model: Criteria and Algorithms". In: *Biomech Model Mechanobiol.* 13.6 (Mar. 2014), pp. 1303–1330. DOI: 10.1007/s10237-014-0574-8.

[18] P.J. Blanco et al. "Comparison of 1D and 3D Models for the Estimation of Fractional Flow Reserve". In: *Sci Rep* 8.1 (2018), p. 17275. DOI: 10.1038/s41598-018-35344-0.

[19] P.J. Blanco et al. "On the Anatomical Definition of Arterial Networks in Blood Flow Simulations: Comparison of Detailed and Simplified Models". In: *Biomech Model Mechanobiol.* 19.5 (2020), pp. 1663–1678. DOI: 10.1007/s10237-020-01298-4.

[20] P.J. Blanco et al. "On the Integration of the Baroreflex Control Mechanism in a Heterogeneous Model of the Cardiovascular System". In: *Int J Numer Method Biomed Eng.* 28.4 (Apr. 2012), pp. 412–433. ISSN: 20407939. DOI: 10.1002/cnm.1474.

[21] P.J. Blanco et al. "On the Potentialities of 3D-1D Coupled Models in Hemodynamics Simulations". In: *J Biomech* 42.7 (2009), pp. 919–930. DOI: 10.1016/j.jbiomech.2009.01.034.

[22] E. Boileau et al. "A Benchmark Study of Numerical Schemes for One-Dimensional Arterial Blood Flow Modelling". In: *Int J Numer Method Biomed Eng.* 31.10 (2015), e02732. DOI: 10.1002/cnm.2732.

[23] R. Borsche and J. Kall. "High Order Numerical Methods for Networks of Hyperbolic Conservation Laws Coupled with ODEs and Lumped Parameter Models". In: *Journal of Computational Physics* 327 (2016), pp. 678–699. DOI: http://dx.doi.org/10.1016/j.jcp.2016.10.003.

[24] S. Buch et al. "Revealing Vascular Abnormalities and Measuring Small Vessel Density in Multiple Sclerosis Lesions Using USPIO". In: *Neuroimage Clin.* 29 (2021), p. 102525. DOI: 10.1016/j.nicl.2020.102525.

[25] S. Buch et al. "Subvoxel Vascular Imaging of the Midbrain Using USPIO-Enhanced MRI". In: *Neuroimage* 220 (2020), p. 117106. DOI: 10.1016/j.neuroimage.2020.117106.

[26] S. Buch et al. "Vascular Mapping of the Human Hippocampus Using Ferumoxytol-Enhanced MRI". In: *Neuroimage* 250 (2022), p. 118957. DOI: 10.1016/j.neuroimage.2022.118957.

[27] A.C. Burton. "Relation of Structure to Function of the Tissues of the Wall of Blood Vessels". In: *Physiol Rev.* 34.4 (1954), pp. 619–42. DOI: 10.1152/physrev.1954.34.4.619.

[28] A. Cappello, G. Gnudi, and C. Lamberti. "Identification of the Three-Element Windkessel Model Incorporating a Pressure-Dependent Compliance". In: *Ann Biomed Eng.* 23 (2006), pp. 164–177. DOI: 10.1007/BF02368323.

[29] R.O. Carare et al. "Solutes, but Not Cells, Drain from the Brain Parenchyma along Basement Membranes of Capillaries and Arteries: Significance for Cerebral Amyloid Angiopathy and Neuroimmunology". In: *Neuropathol Appl Neurobiol.* 34.2 (2008), pp. 131–144. DOI: doi:10.1111/j.1365-2990.2007.00926.x.

[30] C.E. Castro and E.F. Toro. "Solvers for the High–Order Riemann Problem for Hyperbolic Balance Laws". In: *J. Comput. Phys.* 227.4 (2008), pp. 2481–2513. DOI: 10.1016/j.jcp.2007.11.013.

[31] C. Cattaneo. "A Form of Heat-Conduction Equations Which Eliminates the Paradox of Instantaneous Propagation". In: *Comptes Rendus Math de l'Acad Des Sci.* 247 (1958), pp. 431–433.

[32] M. Celant, E.F. Toro, and L.O. Müller. "Total Effective Vascular Compliance of a Global Mathematical Model for the Cardiovascular System". In: *Symmetry* 13.10 (2021), p. 1858. DOI: 10.3390/sym13101858.

[33] K. Cruickshank et al. "Aortic Pulse-Wave Velocity and Its Relationship to Mortality in Diabetes and Glucose Intolerance". In: *Circulation* 106.16 (2002), pp. 2085–2090. DOI: 10.1161/01.CIR.0000033824.02722.F7.

[34] W. Dauber. *Pocket Atlas of Human Anatomy: Founded by Heinz Feneis*. 5th edn. Thieme Medical Publishers, 2007.

[35] T.A. Davis. "Algorithm 832: UMFPACK, an Unsymmetric-Pattern Multifrontal Method". In: *ACM Trans. Math. Softw.* 30.2 (2004), pp. 196–199. DOI: 10.1145/992200.992206.

[36] T.A. Davis. *Direct Methods for Sparse Linear Systems*. SIAM, 2006.

[37] T.A. Davis and I.S. Duff. "A Combined Unifrontal/Multifrontal Method for Unsymmetric Sparse Matrices". In: *ACM Trans. Math. Softw.* 25.1 (1999), pp. 1–20. DOI: 10.1145/305658.287640.

[38] T.A. Davis and I.S. Duff. "An Unsymmetric-Pattern Multifrontal Method for Sparse LU Factorization". In: *SIAM J. Matrix Anal. Applic.* 18.1 (1997), 140{158. DOI: 10.1137/S0895479894246905.

[39] M. Descoteaux, D.L. Collins, and K. Siddiqi. "A Geometric Flow for Segmenting Vasculature in Proton-Density Weighted MRI". In: *Med Image Anal.* 12.4 (2008), pp. 497–513. DOI: 10.1016/j.media.2008.02.003.

[40] A. d'Esposito et al. "Computational Fluid Dynamics with Imaging of Cleared Tissue and of in Vivo Perfusion Predicts Drug Uptake and Treatment Responses in Tumours". In: *Nat Biomed Eng.* 2 (2018), pp. 773–787. DOI: 10.1038/s41551-018-0306-y.

[41] M. Dumbser, C. Enaux, and E.F. Toro. "Finite Volume Schemes of Very High Order of Accuracy for Stiff Hyperbolic Balance Laws". In: *Journal of Computational Physics* 227.8 (2008), pp. 3971–4001. DOI: 10.1016/j.jcp.2007.12.005.

[42] M. Dumbser and M. Käser. "Arbitrary High Order Non-Oscillatory Finite Volume Schemes on Unstructured Meshes for Linear Hyperbolic Systems". In: *Journal of Computational Physics* 221.2 (2007), pp. 693–723. DOI: 10.1016/j.jcp.2006.06.043.

[43] M. Dumbser and E.F. Toro. "A Simple Extension of the Osher Riemann Solver to Non-Conservative Hyperbolic Systems". In: *Journal of Scientific Computing* 48.1-3 (2011), pp. 70–88. DOI: 10.1007/s10915-010-9400-3.

[44] M. Dumbser and E.F. Toro. "On Universal Osher-type Schemes for General Nonlinear Hyperbolic Conservation Laws". In: *Commun. Comput. Phys.* 10.3 (2011), pp. 635–671. DOI: 10.4208/cicp.170610.021210a.

[45] M. Dumbser et al. "ADER Schemes on Unstructured Meshes for Non-Conservative Hyperbolic Systems: Applications to Geophysical Flows". In: *Computers and Fluids* 38.9 (2009), pp. 1731–1748. DOI: 10.1016/j.compfluid.2009.03.008.

[46] M. Dumbser et al. "FORCE Schemes on Unstructured Meshes II: Non-conservative Hyperbolic Systems". In: *Comput Methods Appl Mech Eng.* 199 (2010), pp. 625–647. DOI: 10.1016/j.cma.2009.10.016.

[47] S. Epstein et al. "Reducing the Number of Parameters in 1D Arterial Blood Flow Modeling: Less Is More for Patient-Specific Simulations". In: *Am J Physiol Heart Circ Physiol* 309.1 (2015), H222–H234. DOI: 10.1152/ajpheart.00857.2014.

[48] L.G. Fernandes et al. "Integrated Cardiorespiratory System Model with Short Timescale Control Mechanisms". In: *Int J Numer Meth Biomed Engng.* 37.11 (2020), e3332. DOI: 10.1002/cnm.3332.

[49] R. Fogliardi, M. Di Donfrancesco, and R. Burattini. "Comparison of Linear and Nonlinear Formulations of the Three-Element Windkessel Model". In: *Am J Physiol Heart Circ Physiol.* 271.6 (1996), H2661–H2668. DOI: 10.1152/ajpheart.1996.271.6.H2661.

[50] L. Formaggia, D. Lamponi, and A. Quarteroni. "One-Dimensional Models for Blood Flow in Arteries". In: *Journal of Engineering Mathematics* 47.3/4 (2003), pp. 251–276. DOI: 10.1023/B:ENGI.0000007980.01347.29.

[51] L. Formaggia, A. Quarteroni, and A. Veneziani, eds. *Cardiovascular Mathematics: Modeling and Simulation of the Circulatory System*. Vol. 1. MS&A: Modeling, Simulation & Applications. Milano: Springer, 2009.

[52] L. Formaggia and A. Veneziani. *Reduced and Multiscale Models for the Human Cardiovascular System*. Tech. rep. Politecnico di Milano, 2003.

[53] L. Formaggia et al. "Numerical Modeling of 1D Arterial Networks Coupled with a Lumped Parameters Description of the Heart". In: *Comput Methods Biomech Biomed Engin.* 9.5 (2006), pp. 273–88. DOI: 10.1080/10255840600857767.

[54] F.E. Fossan et al. "Machine Learning Augmented Reduced-Order Models for FFR-prediction". In: *Comput. Methods Appl. Mech. Engrg.* 384 (2021), p. 113892. DOI: 10.1016/j.cma.2021.113892.

[55] F.E. Fossan et al. "Optimization of Topological Complexity for One-Dimensional Arterial Blood Flow Models". In: *J. R. Soc. Interface* 15.149 (2018), p. 20180546. DOI: 10.1098/rsif.2018.0546.

[56] F.E. Fossan et al. "Uncertainty Quantification and Sensitivity Analysis for Computational FFR Estimation in Stable Coronary Artery Disease". In: *Cardiovasc Eng Technol.* 9.4 (2018), pp. 597–622. DOI: 10.1007/s13239-018-00388-w.

[57] A.F. Frangi et al. "Multiscale Vessel Enhancement Filtering". In: *Wells, W.M., Colchester, A., Delp, S. (Eds) Medical Image Computing and Computer-Assisted Intervention – MICCAI'98*. Springer Berlin Heidelberg, 1998, pp. 130–137. DOI: 10.1007/BFb0056195.

[58] F. Friebel et al. "TiQuant: Software for Tissue Analysis, Quantification and Surface Reconstruction". In: *Bioinformatics* 31.19 (2015), pp. 3234–3236. DOI: 10.1093/bioinformatics/btv346.

[59] S. Fujimoto et al. "Clinical Application of Wave Intensity for the Treatment of Essential Hypertension". In: *Heart and Vessels* 19.1 (Jan. 2004), pp. 19–22. DOI: 10.1007/s00380-003-0725-9.

[60] Y.C. Fung. *Biomechanics: Mechanical Properties of Living Tissues*. Second edn. Springer, 1993.

[61] A. Ghigo. "Reduced-Order Models for Blood Flow in Networks of Large Arteries". PhD thesis. Paris: Université Pierre et Marie Curie, Sept. 2017.

[62] L. Grinberg et al. "Modeling Blood Flow Circulation in Intracranial Arterial Networks: A Comparative 3D/1D Simulation Study". In: *Ann Biomed Eng.* 39.1 (2011), pp. 297–309. DOI: 10.1007/s10439-010-0132-1.

[63] J.K. Hale. *Ordinary Differential Equations*. John Wiley & Sons, Inc., 1969.

[64] S. Hammad et al. "Protocols for Staining of Bile Canalicular and Sinusoidal Networks of Human, Mouse and Pig Livers, Three-dimensional Reconstruction and Quantification of Tissue Microarchitecture by Image Processing and Analysis". In: *Arch Toxicol.* 88.5 (2014), pp. 1161–83. DOI: 10.1007/s00204-014-1243-5.

[65] A. Harten, P.D. Lax, and B. van Leer. "On Upstream Differencing and Godunov–Type Schemes for Hyperbolic Conservation Laws". In: *SIAM Review* 25.1 (1983), pp. 35–61.

[66] A. Harten and S. Osher. "Uniformly High–Order Accurate Nonoscillatory Schemes. I". In: *SIAM Journal on Numerical Analysis* 24.2 (1987), pp. 279–309.

[67] A. Harten et al. "Uniformly High Order Accuracy Essentially Non–Oscillatory Schemes, III". In: *Journal of Computational Physics* 71.2 (1987), pp. 231–303. DOI: 10.1016/0021-9991(87)90031-3.

[68] L. Heltai, A. Caiazzo, and L.O. Müller. "Multiscale Coupling of One-Dimensional Vascular Models and Elastic Tissues". In: *Ann Biomed Eng.* 49.12 (2021), pp. 3243–3254. DOI: 10.1007/s10439-021-02804-0.

[69] S.B. Hladky and M.A. Barrand. "Elimination of Substances from the Brain Parenchyma: Efflux via Perivascular Pathways and via the Blood–Brain Barrier". In: *Fluids Barriers CNS* 15.1 (2018). DOI: 10.1186/s12987-018-0113-6.

[70] S.B. Hladky and M.A. Barrand. "The Glymphatic Hypothesis: The Theory and the Evidence". In: *Fluids Barriers CNS.* 19.1 (Feb. 2022), p. 9. DOI: 10.1186/s12987-021-00282-z.

[71] P.J. Hunter. "Numerical Simulation of Arterial Blood Flow". PhD thesis. Auckland: The University of Auckland (School of Engineering), 1972.

[72] J.J. Iliff et al. "A Paravascular Pathway Facilitates CSF Flow Through the Brain Parenchyma and the Clearance of Interstitial Solutes, Including Amyloid Beta". In: *Sci Transl Med.* 4.147 (2012), 147ra111. DOI: 10.1126/scitranslmed.3003748.

[73] J.J. Iliff et al. "Cerebral Arterial Pulsation Drives Paravascular CSF–Interstitial Fluid Exchange in the Murine Brain". In: *J Neurosci.* 33.46 (2013), pp. 18190–9. DOI: 10.1523/JNEUROSCI.1592-13.2013.

[74] *ITK-SNAP*. www.itksnap.org.

[75] A. Jaeschke, H. Eckert, and L.J. Bray. "Qiber3D–an Open-Source Software Package for the Quantitative Analysis of Networks from 3D Image Stacks". In: *Gigascience* 11.1 (2021), pp. 1–9. DOI: 10.1093/gigascience/giab091.

[76] W. Jin and J. Alastruey. "Arterial Pulse Wave Propagation across Stenoses and Aneurysms: Assessment of One-Dimensional Simulations against Three-Dimensional Simulations and in Vitro Measurements". In: *J R Soc Interface.* 18.177 (2021), p. 20200881. DOI: 10.1098/rsif.2020.0881.

[77] R.T. Kedarasetti, P.J. Drew, and F. Costanzo. "Arterial Pulsations Drive Oscillatory Flow of CSF but Not Directional Pumping". In: *Sci Rep* 10.1 (June 2020), p. 10102. DOI: 10.1038/s41598-020-66887-w.

[78] R.T. Kedarasetti et al. "Functional Hyperemia Drives Fluid Exchange in the Paravascular Space". In: *Fluids Barriers CNS.* 17.1 (Aug. 2020), p. 52. DOI: 10.1186/s12987-020-00214-3.

[79] *Kimimaro*. https://github.com/seung-lab/kimimaro.

[80] B.M. Laudenzi. "Computational Modeling of Blood and CSF Flow Dynamics in Cerebral Vascular-Perivascular Networks". PhD thesis. Trento: University of Trento, 2022.

[81] T.-C. Lee, R.L. Kashyap, and C.-N. Chu. "Building Skeleton Models via 3-D Medial Surface/Axis Thinning Algorithms". In: *CVGIP: Graphical Models and Image Processing* 56.6 (1994), pp. 462–478. DOI: 10.1006/cgip.1994.1042.

[82] J.K. Li, T. Cui, and G.M. Drzewiecki. "A Nonlinear Model of the Arterial System Incorporating a Pressure-Dependent Compliance". In: *IEEE Trans Biomed Eng.* 37.7 (1990), pp. 673–678. DOI: 10.1109/10.55678.

[83] F. Liang et al. "A Computational Model Study of the Influence of the Anatomy of the Circle of Willis on Cerebral Hyperperfusion Following Carotid Artery Surgery". In: *Biomed Eng Online.* 10.1 (2011), p. 84. DOI: 10.1186/1475-925X-10-84.

[84] F. Liang et al. "Multi-Scale Modeling of the Human Cardiovascular System with Applications to Aortic Valvular and Arterial Stenoses". In: *Med Biol Eng Comput.* 47.7 (2009), pp. 743–55. DOI: 10.1007/s11517-009-0449-9.

[85] F.Y. Liang et al. "Biomechanical Characterization of Ventricular–Arterial Coupling during Aging: A Multi-Scale Model Study". In: *J Biomech.* 42.6 (Apr. 2009), pp. 692–704. ISSN: 00219290. DOI: 10.1016/j.jbiomech.2009.01.010.

[86] H.H. Lipowsky, S. Kovalcheck, and Zweifach. "The Distribution of Blood Rheological Parameters in the Microvasculature of Cat Mesentery". In: *Circ Res.* 43.5 (1978), pp. 738–49. DOI: 10.1161/01.res.43.5.738.

[87] S. Liu et al. "Susceptibility Weighted Imaging and Quantitative Susceptibility Mapping of the Cerebral Vasculature Using Ferumoxytol". In: *J Magn Reson Imaging* 47.3 (2018), pp. 621–633. DOI: 10.1002/jmri.25809.

[88] G.D. Maso Talou et al. "Adaptive Constrained Constructive Optimisation for Complex Vascularisation Processes". In: *Sci Rep* 11.1 (2021), p. 6180. DOI: 10.1038/s41598-021-85434-9.

[89] K.S. Matthys et al. "Pulse Wave Propagation in a Model Human Arterial Network: Assessment of 1-D Numerical Simulations against in Vitro Measurements". In: *Journal of Biomechanics* 40.15 (2007), pp. 3476–3486. ISSN: 00219290. DOI: 10.1016/j.jbiomech.2007.05.027.

[90] H. Mestre et al. "Flow of Cerebrospinal Fluid Is Driven by Arterial Pulsations and Is Reduced in Hypertension". In: *Nat Commun.* 9.1 (2018), p. 4878. DOI: 10.1038/s41467-018-07318-3.

[91] V. Milišić and A. Quarteroni. "Analysis of Lumped Parameter Models for Blood Flow Simulations and Their Relation with 1D Models". In: *ESAIM: M2AN* 38.4 (2004), pp. 613–632. DOI: 10.1051/m2an:2004036.

[92] M. Mirramezani and S.C. Shadden. "A Distributed Lumped Parameter Model of Blood Flow". In: *Ann Biomed Eng.* 48.12 (2020), pp. 2870–2886. DOI: 10.1007/s10439-020-02545-6.

[93] G.I. Montecinos, L.O. Müller, and E.F. Toro. "Hyperbolic Reformulation of a 1D Viscoelastic Blood Flow Model and ADER Finite Volume Schemes". In: *Journal of Computational Physics* 266 (2014), pp. 101–123. DOI: 10.1016/j.jcp.2014.02.013.

[94] G.I. Montecinos and E.F. Toro. "Reformulations for General Advection-Diffusion-Reaction Equations and Locally Implicit {{ADER}} Schemes." In: *Journal of Computational Physics* 275 (2014), pp. 415–442. DOI: 10.1016/j.jcp.2014.06.018.

[95] S.M. Moore et al. "One-Dimensional and Three-Dimensional Models of Cerebrovascular Flow". In: *J Biomech Eng.* 127.3 (2005), pp. 440–449. DOI: 10.1115/1.1894350.

[96] L.O. Müller and P.J. Blanco. "A High Order Approximation of Hyperbolic Conservation Laws in Networks: Application to One-Dimensional Blood Flow". In: *Journal of Computational Physics* 300 (2015), pp. 423–437. DOI: 10.1016/j.jcp.2015.07.056.

[97] L.O. Müller, G. Leugering, and P.J. Blanco. "Consistent Treatment of Viscoelastic Effects at Junctions in One-Dimensional Blood Flow Models". In: *Journal of Computational Physics* 314 (2016), pp. 167–193. DOI: 10.1016/j.jcp.2016.03.012.

[98] L.O. Müller, C. Parés, and E.F. Toro. "Well-Balanced High-Order Numerical Schemes for One-Dimensional Blood Flow in Vessels with Varying Mechanical Properties". In: *Journal of Computational Physics* 242 (2013), pp. 53–85. DOI: 10.1016/j.jcp.2013.01.050.

[99] L.O. Müller and E.F. Toro. "A Global Multiscale Mathematical Model for the Human Circulation with Emphasis on the Venous System". In: *Int J Numer Method Biomed Eng.* 30.7 (2014), pp. 681–725. DOI: 10.1002/cnm.2622.

[100] L.O. Müller and E.F. Toro. "Enhanced Global Mathematical Model for Studying Cerebral Venous Blood Flow". In: *J Biomech.* 47.13 (Oct. 2014), pp. 3361–3372. DOI: 10.1016/j.jbiomech.2014.08.005.

[101] L.O. Müller and E.F. Toro. "Well-Balanced High-Order Solver for Blood Flow in Networks of Vessels with Variable Properties". In: *Int J Numer Method Biomed Eng.* 29.12 (2013), pp. 1388–1411. DOI: 10.1002/cnm.2580.

[102] L.O. Müller et al. "A High-Order Local Time Stepping Finite Volume Solver for One-Dimensional Blood Flow Simulations: Application to the ADAN Model". In: *Int J Numer Method Biomed Eng.* 32.10 (2015). DOI: 10.1002/cnm.2761.

[103] L.O. Müller et al. "Impact of Baseline Coronary Flow and Its Distribution on Fractional Flow Reserve Prediction". In: *Int J Numer Method Biomed Eng.* 37.11 (2019), e3246. DOI: 10.1002/cnm.3246.

[104] J.P. Murgo et al. "Aortic Input Impedance in Normal Man: Relationship to Pressure Wave Forms". In: *Circulation* 62.1 (1980), pp. 105–116. DOI: 10.1161/01.CIR.62.1.105.

[105] C.D. Murray. "The Physiological Principle of Minimum Work Applied to the Angle of Branching of Arteries". In: *J. Gen. Physiol.* 9.6 (1926), pp. 835–841. DOI: 10.1085/jgp.9.6.835.

[106] C.D. Murray. "The Physiological Principle of Minimum Work I. The Vascular System and the Cost of Blood Volume". In: *Proc. Natl Acad. Sci. USA* 12.3 (1926), pp. 207–214. DOI: 10.1073/pnas.12.3.207.

[107] J.P. Mynard and P. Nithiarasu. "A 1D Arterial Blood Flow Model Incorporating Ventricular Pressure, Aortic Valve and Regional Coronary Flow Using the Locally Conservative Galerkin (LCG) Method". In: *Commun. Numer. Meth. Engng.* 24.5 (2008), pp. 367–417. DOI: 10.1002/cnm.1117.

[108] J.P. Mynard and J.J. Smolich. "One-Dimensional Haemodynamic Modeling and Wave Dynamics in the Entire Adult Circulation". In: *Ann Biomed Eng.* 43.6 (2015), pp. 1443–1460. DOI: 10.1007/s10439-015-1313-8.

[109] M. Nedergaard. "Garbage Truck of the Brain". In: *Science* 340.6140 (2013), pp. 1529–1530. DOI: 10.1126/science.1240514.

[110] F.H. Netter. *Atlas of Human Anatomy*. 5th edn. Elsevier, 2011.

[111] M.S. Olufsen et al. "Numerical Simulation and Experimental Validation of Blood Flow in Arteries with Structured-Tree Outflow Conditions". In: *Ann Biomed Eng.* 28 (2000), pp. 1281–1299. DOI: 10.1114/1.1326031.

[112] C. Parés. "Numerical Methods for Nonconservative Hyperbolic Systems: A Theoretical Framework". In: *SIAM J. Numer. Anal.* 44.1 (2006), pp. 300–321. DOI: 10.1137/050628052.

[113] A.R. Pries, T.W. Secomb, and P. Gaehtgens. "Biophysical Aspects of Blood Flow in the Microvasculature". In: *Cardiovascular Research* 32.4 (1996), pp. 654–667. DOI: 10.1016/S0008-6363(96)00065-X.

[114] A. Quarteroni, A. Veneziani, and C. Vergara. "Geometric Multiscale Modeling of the Cardiovascular System, between Theory and Practice". In: *Comput. Methods Appl. Mech. Engrg.* 302 (2016), pp. 193–252. DOI: 10.1016/j.cma.2016.01.007.

[115] M.K. Rasmussen, H. Mestre, and M. Nedergaard. "Fluid Transport in the Brain". In: *Physiol Rev.* 102.2 (Apr. 2022), pp. 1025–1151. DOI: 10.1152/physrev.00031.2020.

[116] P. Reymond et al. "Physiological Simulation of Blood Flow in the Aorta: Comparison of Hemodynamic Indices as Predicted by 3-D FSI, 3-D Rigid Wall and 1-D Models". In: *Med Eng Phys.* 35.6 (2013), pp. 784–791. DOI: http://dx.doi.org/10.1016/j.medengphy.2012.08.009.

[117] P. Reymond et al. "Validation of a One-Dimensional Model of the Systemic Arterial Tree". In: *Am J Physiol Heart Circ Physiol.* 297.1 (2009), H208–H222. DOI: 10.1152/ajpheart.00037.2009.

[118] P. Reymond et al. "Validation of a Patient-Specific One-Dimensional Model of the Systemic Arterial Tree". In: *Am J Physiol Heart Circ Physiol.* 301.3 (2011), H1173–82. DOI: 10.1152/ajpheart.00821.2010.

[119] S. Safaei et al. "Bond Graph Model of Cerebral Circulation: Toward Clinically Feasible Systemic Blood Flow Simulations". In: *Front. Physiol.* 9 (2018), p. 148. DOI: 10.3389/fphys.2018.00148.

[120] K. Sagawa, R.K. Lie, and J. Schaefer. "Translation of Otto Frank's Paper "Die Grundform Des Arteriellen Pulses" Zeitschrift Für Biologie 37: 483–526 (1899)". In: *J Mol Cell Cardiol* 22.3 (1990), pp. 253–254. DOI: 10.1016/0022-2828(90)91459-K.

[121] M. Saito et al. "One-Dimensional Model for Propagation of a Pressure Wave in a Model of the Human Arterial Network: Comparison of Theoretical and Experimental Results". In: *J Biomech Eng.* 133.12 (Dec. 2011), p. 121005. DOI: 10.1115/1.4005472.

[122] D.A. Sánchez. *Ordinary Differential Equations and Stability Theory*. Dover Publications, Inc., 1968.

[123] M. Sato et al. "TEASAR: Tree-structure Extraction Algorithm for Accurate and Robust Skeletons". In: *Proceedings the Eighth Pacific Conference on Computer Graphics and Applications*. IEEE, 2000, pp. 281–449. DOI: 10.1109/PCCGA.2000.883951.

[124] W. Schreiner. "Computer Generation of Complex Arterial Tree Models". In: *J Biomed Eng.* 15.2 (1993), pp. 148–50. DOI: 10.1016/0141-5425(93)90046-2.

[125] W. Schreiner and P.F. Buxbaum. "Computer-Optimization of Vascular Trees". In: *IEEE Trans Biomed Eng.* 40.5 (1993), pp. 482–91. DOI: 10.1109/10.243413.PMID:8225337.

[126] Y. Shen et al. "Detecting Sub-Voxel Microvasculature with USPIO-enhanced Susceptibility-Weighted MRI at 7T". In: *Magn Reson Imaging* 67 (2020), pp. 90–100. DOI: 10.1016/j.mri.2019.12.010.

[127] S.J. Sherwin et al. "Computational Modelling of 1D Blood Flow with Variable Mechanical Properties and Its Application to the Simulation of Wave Propagation in the Human Arterial System". In: *Int. J. Numer. Meth. Fluids* 43.6-7 (2003), pp. 673–700. DOI: 10.1002/fld.543.

[128] S.J. Sherwin et al. "One-Dimensional Modelling of a Vascular Network in Space-Time Variables". In: *Journal of Engineering Mathematics* 47.3 (Jan. 2003), pp. 217–250. DOI: 10.1023/B:ENGI.0000007979.32871.e2.

[129] Y. Shi, P. Lawford, and R. Hose. "Review of Zero-D and 1-D Models of Blood Flow in the Cardiovascular System". In: *Biomed Eng Online* 10 (Apr. 2011), p. 33. DOI: 10.1186/1475-925X-10-33.

[130] A. Spilimbergo, E.F. Toro, and L.O. Müller. "One-Dimensional Blood Flow with Discontinuous Properties and Transport: Mathematical Analysis and Numerical Schemes". In: *Commun. Comput. Phys.* 29.3 (2021), pp. 649–697. DOI: 10.4208/cicp.OA-2020-0132.

[131] N. Stergiopulos, D.F. Young, and T.R. Rogge. "Computer Simulation of Arterial Flow with Applications to Arterial and Aortic Stenoses". In: *J Biomech* 25.12 (1992), pp. 1477–88. DOI: 10.1016/0021-9290(92)90060-e.

[132] *SuiteSparse*. http://www.suitesparse.com.

[133] P.W. Sweeney et al. "Modelling the Transport of Fluid through Heterogeneous, Whole Tumours in Silico". In: *PLoS Comput Biol.* 15.6 (2019), e1006751. DOI: 10.1371/journal.pcbi.1006751.

[134] G. Tetteh et al. "DeepVesselNet: Vessel Segmentation, Centerline Prediction, and Bifurcation Detection in 3-D Angiographic Volumes". In: *Front. Neurosci.* 14 (2020), p. 592352. DOI: 10.3389/fnins.2020.592352.

[135] *The Vascular Modeling Toolkit Website*. www.vmtk.org.

[136] M.I. Todorov et al. "Machine Learning Analysis of Whole Mouse Brain Vasculature". In: *Nat Methods.* 17.4 (2020), pp. 442–449. DOI: 0.1038/s41592-020-0792-1.

[137] E.F. Toro. "Brain Venous Haemodynamics, Neurological Diseases and Mathematical Modelling. A Review". In: *Applied Mathematics and Computation* 272 (2016), pp. 542–579. DOI: 10.1016/j.amc.2015.06.066.

[138] E.F. Toro. *Riemann Solvers and Numerical Methods for Fluid Dynamics: A Practical Introduction*. 3rd edn. Springer-Verlag Berlin Heidelberg, 2009.

[139] E.F. Toro, R.C. Millington, and L.A.M. Nejad. "Towards Very High–Order Godunov Schemes". In: *Godunov Methods: Theory and Applications. Edited Review, E. F. Toro (Editor)*, ed. by E.F. Toro. Kluwer Academic/Plenum Publishers, 2001, pp. 905–937.

[140] E.F. Toro and G.I. Montecinos. "Advection-Diffusion-Reaction Equations: Hyperbolization and High-Order ADER Discretizations". In: *SIAM J. Sci. Comput.* 36.5 (2014), A2423–A2457. DOI: 10.1137/130937469.

[141] E.F. Toro and A. Siviglia. "Flow in Collapsible Tubes with Discontinuous Mechanical Properties: Mathematical Model and Exact Solutions". In: *Commun. Comput. Phys.* 13.2 (Feb. 2013), pp. 361–385. DOI: 10.4208/cicp.210611.240212a.

[142] E.F. Toro and V.A. Titarev. "Solution of the Generalized Riemann Problem for Advection–Reaction Equations". In: *Proceedings of the Royal Society A: Mathematical, Physical and Engineering Sciences* 458 (2002), pp. 271–281. DOI: 10.1098/rspa.2001.0926.

[143] E.F. Toro et al. "A Computational Model for the Dynamics of Cerebrospinal Fluid in the Spinal Subarachnoid Space". In: *J Biomech Eng.* 141.1 (Jan. 2019), p. 011004. DOI: 10.1115/1.4041551.

[144] E.F. Toro et al. "Cerebrospinal Fluid Dynamics Coupled to the Global Circulation in Holistic Setting: Mathematical Models, Numerical Methods and Applications". In: *Int. J. Numer. Meth. Biomed. Engng.* 38.1 (2022), e3532. DOI: 10.1002/cnm.3532.

[145] S. Urquiza et al. "Prediction Of Human Arterial Pulse Wave Shape Changes In Aging And Hypertension". In: *Power, H. Hart, R.T. Hosoda, S. et al. (Eds) Computer Simulations in Biomedicine*. Milan, Italy, 1995, pp. 131–138.

[146] M. Ursino. "A Mathematical Model of the Carotid Baroregulation in Pulsating Conditions". In: *IEEE Trans Biomed Eng.* 46.4 (Apr. 1999), pp. 382–392. DOI: 10.1109/10.752935.

[147] M. Ursino, A. Fiorenzi, and E. Belardinelli. "The Role of Pressure Pulsatility in the Carotid Baroreflex Control: A Computer Simulation Study". In: *Comput Biol Med.* 26.4 (1996), pp. 297–314. DOI: 10.1016/0010-4825(96)00012-1.

[148] M. Ursino and C.A. Lodi. "A Simple Mathematical Model of the Interaction between Intracranial Pressure and Cerebral Hemodynamics". In: *J. Appl. Physiol.* 82.4 (1997), pp. 1256–1269. DOI: 10.1152/jappl.1997.82.4.1256.

[149] B. van Leer. "On the Relation between the Upwind–Differencing Schemes of Godunov, Engquist-Osher and Roe". In: *SIAM J. Sci. Stat. Comput.* 5.1 (1985), pp. 1–20.

[150] A. Vasilevskiy and K. Siddiqi. "Flux Maximizing Geometric Flows". In: *IEEE Transactions on Pattern Analysis and Machine Intelligence* 24.12 (2002), pp. 1565–1578. DOI: 10.1109/TPAMI.2002.1114849.

[151] Y.V. Vassilevski, V.Y. Salamatova, and S.S. Simakov. "On the Elasticity of Blood Vessels in One-Dimensional Problems of Hemodynamics". In: *Comput. Math. and Math. Phys.* 55.9 (215), pp. 1567–1578. DOI: 10.1134/S0965542515090134.

[152] S.M. Watanabe, P.J. Blanco, and R.A. Feijóo. "Mathematical Model of Blood Flow in an Anatomically Detailed Arterial Network of the Arm". In: *ESAIM: M2AN* 47.4 (2013), pp. 961–985. DOI: 10.1051/m2an/2012053.

[153] N. Xiao, J. Alastruey, and C.A. Figueroa. "A Systematic Comparison between 1-D and 3-D Hemodynamics in Compliant Arterial Models". In: *Int J Numer Method Biomed Eng* 30.2 (Feb. 2014), pp. 204–231. DOI: 10.1002/cnm.2598.

[154] P.A. Yushkevich et al. "User-Guided 3D Active Contour Segmentation of Anatomical Structures: Significantly Improved Efficiency and Reliability". In: *Neuroimage* 31.3 (2006), pp. 1116–28. DOI: 10.1016/j.neuroimage.2006.01.015.

[155] P. Zamboni et al. "Chronic Cerebrospinal Venous Insufficiency in Patients with Multiple Sclerosis". In: *J Neurol Neurosurg Psychiatry.* 80.4 (2009), pp. 392–399. DOI: 10.1136/jnnp.2008.157164.